FROM ISOMORPHS IN MOLECULAR LIQUIDS AND CONFINEMENT TO MOLECULAR DYNAMICS AT CONSTANT POTENTIAL ENERGY

by

Trond S. Ingebrigtsen

Danish National Research Foundation Centre "Glass and Time",
IMFUFA, Department of Science, Systems and Models,
Roskilde University, Denmark

Supervisor: Prof. Jeppe C. Dyre

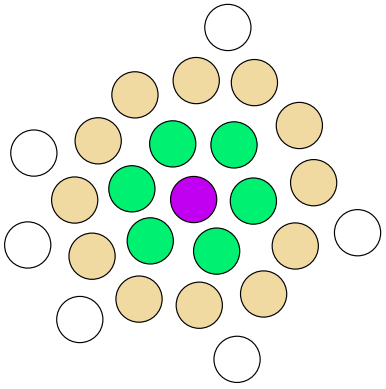

A DISSERTATION

Submitted
to Roskilde University
in partial fulfillment of the requirements
for the degree of

DOCTOR OF PHILOSOPHY

Physics

28th February, 2013

0.1 Abstract

Strongly correlating liquids are defined by having strong correlations in the NVT ensemble between the equilibrium fluctuations of the potential energy U and the virial W. These liquids were discovered by researchers of the "Glass and Time" group, Roskilde University, via molecular dynamics computer simulations and detailed in a series of papers (Bailey *et al.* [2008a,b], Gnan *et al.* [2009], Schrøder *et al.* [2009a, 2011]). Strongly correlating liquids have also been verified in experiments (Gundermann *et al.* [2011]). This thesis expands on the basic understanding of strongly correlating liquids in three directions and uses motivation derived from these liquids to perform research in a fourth direction.

1. We show that strongly correlating liquids have a rather simple thermodynamics in the sense that temperature separates into a product of a function of excess entropy per particle and a function of density. This fact leads to the proposal of a more general scaling procedure, the "isomorph scaling", which is in contrast to the traditional "density scaling" procedure that breaks down when considering larger density changes than usually applied in experiments. In addition, we show that the expressions of Rosenfeld and Tarazona (Rosenfeld and Tarazona [1998]) for the potential energy and heat capacity along an isochore holds to a better approximation for strongly than non-strongly correlating liquids.

2. Strongly correlating liquids are characterized by having isomorphs to a good approximation. Isomorphs are curves in a liquid's phase diagram along which structure and dynamics are invariant in reduced units as well as some thermodynamic quantities. Originally, isomorphs were investigated for bulk atomic systems (Gnan *et al.* [2009]). We extend the concept of isomorphs to systems composed of rigid molecules and show that these systems can have isomorphs to a good approximation, too. We also extend the isomorph concept to confined liquids. Confined liquids exhibit stratification, i.e. the particles of the liquid order themselves in well-defined layers, and position-dependent relaxation processes. Despite of these facts, confined liquids have isomorphs to a good approximation. This observation establishes a connection to a novel excess entropy scaling procedure for predicting confined-liquid behavior via knowledge of their bulk relationships (Mittal *et al.* [2006]).

3. We propose that strongly correlating liquids are to be identified with simple liquids. This new definition of "what is a simple liquid?" is in contrast to the more traditional definition as being systems with radially symmetric pair potentials. The motivation for this new definition is derived from a discovery relating to strongly correlating liquids, namely that structure and dynamics are determined to a good approximation *only* by the interactions within the first coordination shell (FCS), i.e. the nearest-neighbor interactions. In fact, we show that the FCS property holds to a good approximation also in confinement. Bulk and confined liquids are thus more closely related than what is traditionally believed to be the case.

4. We present a new molecular dynamics, NVU dynamics that, instead of conserving the energy E as in standard Newtonian NVE dynamics, conserves the total potential energy U. From simulations and theoretical arguments, we show that NVE and NVU dynamics become equivalent in the thermodynamic limit for both atomic and molecular systems. NVE and NVU dynamics may thus be used interchangeably in simulations for most purposes.

0.2 Resumé

Stærkt korrelerede væsker er definerede ud fra eksistensen af stærke korrelationer i NVT ensemblet mellem ligevægtsfluktuationerne af den potentielle energi U og virialet W. Disse væsker blev opdaget af forskere ved "Glas og Tid", Roskilde Universitet ved anvendelse af molekylær dynamik computer simuleringer og er efterfølgende blevet beskrevet i en serie af artikler (Bailey *et al.* [2008a,b], Gnan *et al.* [2009], Schrøder *et al.* [2009a, 2011]). Eksperimenter har ligeledes påvist eksistensen af stærkt korrelerede væsker (Gundermann *et al.* [2011]). Denne afhandling udvider vor fundamentale forståelse af stærkt korrelerede væsker i tre forskellige retninger og anvender inspiration fra tidligere forskningsresultater vedrørende disse væsker til videreførelse af forskningen i en fjerde retning.

1. Vi viser, at termodynamikken for stærkt korrelerede væsker er af simpel natur, idet temperaturen faktoriserer i et produkt af en funktion af "excess"-entropien per partikel og en funktion af tætheden. Dette faktum fører til en formulering af en mere generel skaleringsmetode, "isomorf-skaleringen", som står i modsætning til den traditionelle skaleringsmetode "tæthedsskalering", der bryder ned ved større tæthedsændringer end typisk anvendt i eksperimenter. Vi viser yderligere, at udtryk formulerede af Rosenfeld og Tarazona (Rosenfeld and Tarazona [1998]) for den potentielle energi og varmekapaciteten langs en "isochore" udgør en bedre approksimation for stærkt korrelerede væsker end for ikke-stærkt korrelerede væsker.

2. Stærkt korrelerede væsker er karakteriserede ved at have isomorfer til en god approksimation. Isomorfer er kurver i en væskes fasediagram, hvor struktur og dynamik er invariant i reducerede enheder, samt yderligere nogle termodynamiske størrelser. Oprindeligt er isomorfer kun blevet undersøgt for "bulk" atomare systemer (Gnan *et al.* [2009]). Vi udvider her isomorf-konceptet til systemer bestående af stive molekyler og viser, at disse systemer til en god approksimation også har isomorfer. Vi udvider ligeledes isomorf-konceptet til "rummeligt begrænsede" væsker. Rummeligt begrænsede væsker udviser stratifikation, dvs. en lagdeling af partiklerne, samt positionsafhængige relaksationsprocesser. Til trods for at rummeligt begrænsede væsker udviser disse fænomener, kan de også have isomorfer til en god approksimation. Denne observation etablerer herved en forbindelse til en ny excess-entropi skaleringsmetode, hvis formål er at forudsige egenskaberne af rummeligt begrænsede væsker ud fra deres bulk sammenhænge (Mittal *et al.* [2006]).

3. Vi foreslår, at stærkt korrelerede væsker identificeres med simple væsker. Denne nye definition af "hvad er en simpel væske?" står i modsætning til den mere traditionelle definition, som værende systemer med radialt-symmetriske par potentialer. Inspiration til formuleringen af denne nye definition er hentet fra en ny opdagelse for stærkt korrelerede væsker, nemlig at struktur og dynamik til en god approksimation *kun* bestemmes af interaktioner inden for første koordinationsskal (FCS) dvs. kun af de nærmeste nabointeraktioner. Tilsvarende viser vi, at denne FCS egenskab også holder for rummeligt begrænsede væsker. Bulk og rummeligt begrænsede væsker er således mere nært beslægtede end hvad der er den almindelige opfattelse.

4. Vi præsenterer en ny molekylær dynamik metode, NVU dynamik, der bevarer den totale potentielle energi U i stedet for at bevare energien E, som er tilfældet for Newtonsk NVE dynamik. Ud fra simuleringer samt teoretiske overvejelser viser vi, at NVE og NVU dynamik er ækvivalente i den termodynamiske grænse for både atomare og molekylære systemer. NVE og NVU dynamik kan således anvendes i flæng i simuleringer til de fleste formål.

0.3 Preface

This is the philosophiae doctor (Ph.D.) thesis of Trond Sylvan Ingebrigtsen. The Ph.D. was initiated March 1st, 2010, and the thesis was submitted February 28th, 2013, thus lasting the three years of the Danish Ph.D. programme. The thesis has been supervised by Prof. Jeppe C. Dyre, "Glass and Time", Roskilde University. The thesis has 8 companion papers as follows (see Appendix E).

Papers

I. *Communication: Thermodynamics of condensed matter with strong pressure-energy correlations.*
T. S. Ingebrigtsen, L. Bøhling, T. B. Schrøder, and J. C. Dyre, J. Chem. Phys., **136**, 061102, 2012.

II. *Scaling of viscous dynamics in simple liquids: theory, simulation and experiment.*
L. Bøhling, T. S. Ingebrigtsen, A. Grzybowski, M. Paluch, J. C. Dyre, and T. B. Schrøder, New J. Phys., **14**, 113035, 2012.

III. *What Is a Simple Liquid?*
T. S. Ingebrigtsen, T. B. Schrøder, and J. C. Dyre, Phys. Rev. X, **2**, 011011, 2012.

IV. *Do the repulsive and attractive pair forces play separate roles for the physics of liquids?*
L. Bøhling, A. A. Veldhorst, T. S. Ingebrigtsen, N. P. Bailey, J. S. Hansen, S. Toxvaerd, T. B. Schrøder, and J. C. Dyre, J. Phys.: Condens. Matter, **25**, 032101, 2013.

V. *Isomorphs in Model Molecular Liquids.*
T. S. Ingebrigtsen, T. B. Schrøder, and J. C. Dyre, J. Phys. Chem. B, **116**, 1018, 2012.

VI. *NVU dynamics. I. Geodesic motion on the constant-potential-energy hypersurface.*
T. S. Ingebrigtsen, S. Toxvaerd, O. J. Heilmann, T. B. Schrøder, and J. C. Dyre, J. Chem. Phys., **135**, 104101, 2011. **Editors' Choice 2011**.

VII. *NVU dynamics. II. Comparing to four other dynamics.*
T. S. Ingebrigtsen, S. Toxvaerd, T. B. Schrøder, and J. C. Dyre, J. Chem. Phys., **135**, 104102, 2011.

VIII. *NVU dynamics. III. Simulating molecules at constant potential energy.*
T. S. Ingebrigtsen, and J. C. Dyre, J. Chem. Phys., **137**, 244101, 2012.

The thesis contains ten chapters and assumes no prior knowledge of the papers listed above. References are, however, made throughout the text to these articles, and the thesis does not cover all aspects. Thus, for a detailed understanding, the thesis should be accompanied by the associated papers. In addition, basic knowledge about computer simulations, mathematics and statistical mechanics is assumed. The thesis is organized as follows.

1. *Chapter 1* establishes a background for the thesis by considering the topics of molecular dynamics, simulations via graphics cards (GPUs), as well as supercooled liquids and the glass transition.

2. *Chapter 2* introduces the so-called "strongly correlating liquids" (Pedersen *et al.* [2008]), their isomorphs (Gnan *et al.* [2009]) and the consequences of isomorphs in a liquid's phase diagram.

3. *Chapter 3* develops the thermodynamics of strongly correlating liquids (Paper I) with the remarkable simple result that temperature separates into a product of a function of excess entropy per particle and a function of density. In addition, the so-called "isomorph scaling" is introduced (Papers I and II) which stands in contrast to the more traditional "density scaling" (Tölle [2001]) often used to describe viscous liquids.

4. *Chapter 4* investigates whether the expressions proposed by Rosenfeld and Tarazona (Rosenfeld and Tarazona [1998]) for the potential energy and isochoric heat capacity along an isochore are a better approximation for strongly correlating liquids than for non-strongly correlating liquids.

5. *Chapter 5* details a new "chemical" characterization of strongly correlating liquids via the role of the first coordination shell interactions for these liquids. A new definition of: *What is a simple liquid*? is also proposed (Papers III and IV).

6. *Chapter 6* extends the concept of isomorphs for atomic systems (Gnan *et al.* [2009]) to molecular systems composed of rigid molecules (Paper V).

7. *Chapter 7* extends the concept of isomorphs to confined systems.

8. *Chapter 8* investigates the new definition of simplicity in the context of a confined system. It is shown that confined liquids, although exhibiting stratification and position-dependent relaxation processes, in essence are as simple as bulk liquids.

9. *Chapter 9* presents a new molecular dynamics that conserves the total potential energy, i.e., *NVU* dynamics (Papers VI, VII and VIII). Via simulations and theoretical arguments it is concluded that *NVU* dynamics becomes equivalent to standard energy-conserving Newtonian *NVE* dynamics in the thermodynamic limit. Framework for simulating both atomic and molecular systems at constant potential energy is considered.

10. *Chapter 10* concludes and presents new, exciting topics for future research.

Many different numerical model systems are encountered in the present work and for the convenience of the reader, all the specific model details are given in Appendix A. The reader is referred to this appendix whenever a new model system is mentioned in the text.

0.4 Acknowledgements

First and foremost, I acknowledge my supervisor Prof. Jeppe C. Dyre for three years of great science and extensive fun and for teaching a chemist (me) the secret ways of physics. In alphabetical order, I also acknowledge the entire "Glass and Time" group, current as well as former members:

Nicholas P. Bailey, Lasse Bøhling, Tage Christensen, Nicoletta Gnan, Ditte Gundermann, Jesper S. Hansen, Tina Hecksher, Bo Jakobsen, Heine Larsen, Ebbe H. Larsen, Claudio Maggi, Albena Nielsen, Kristine Niss, Preben Olsen, Niels B. Olsen, Jon J. Papini, Ib H. Pedersen, Ulf R. Pedersen, Torben Rasmussen, Lisa A. Roed, Thomas B. Schrøder, Søren Toxvaerd, and Arno A. Veldhorst.

All of these persons have inspired this thesis in one way or the other. In particular, Lasse was my "partner in crime" for the three years of the Ph.D. study. Arno and Jesper, with whom I both shared office, great fun and good discussions. Furthermore, Jesper taught me the art of teaching classical mechanics. With Nick, Søren, and Thomas I had valuable discussions about anything from prewetting to isomorphs. Heine always repaired the graphics cards (with a smile!) and provided me with a *personal* backup server for the 5.4 Terabytes (2^{40} bytes) of data that my local account currently stores.

I acknowledge Prof. Thomas M. Truskett for taking good care of me during my 3 months stay at the University of Texas at Austin, Austin, Texas. Discussing isomorphs with Tom and his group, especially Avni Jain, was a true pleasure. A special thanks goes to Prof. Jeffrey R. Errington from The State University of New York, Buffalo, New York for extensive calculations of the excess entropy and for great patience when receiving "yet another mail" about calculating the excess entropy for additional state points or just for science in general. My stay in Austin was also made extremely pleasant due to Dr. Blinda E. McClelland and Prof. Howard M. Liljestrand; by whom I rented a cottage.

Furthermore a special thanks to:

Benjamin Dalton, Asli Deniz, Elsje S. Fraser, Lasse A. Grinderslev, Johanne Gudmand-Høyer, Kasper B. S. Jensen, Claire A. Lemarchand, Luciana L. A. Lomonaco, Sergio de Luca, Kenneth H. M. Nielsen, Thomas N. Nielsen, Trine H. Rose, Leila Separdar, and Sif I. M. Skjoldager,

for enriching my life further during the three years. A thanks to the guys at Savsmuld for providing a deeper insight into this covert association at IMFUFA. Also thanks to the people at IMFUFA for just being themselves.

At last, I thank my family for proofreading the entire Ph.D. thesis and the published thesis articles.

Thesis Disclaimer: No graphics cards were intentionally harmed or overheated during the

making of this thesis.

TABLE OF CONTENTS

Chapter 1

BACKGROUND

Throughout the last 60 years the interaction between humans and computers has been steadily increasing (Shneiderman and Plaisant [2005]). This is in particular true for the use of computers in science. The first molecular dynamics (MD) computer simulations were performed by Alder and Wainwright in 1957 who studied a system composed of hard-sphere particles (Allen and Tildesley [1987]). Since then, computers have been used to solve fundamental problems that even real experiments could not resolve, for instance, whether a purely entropic system can have a first-order phase transition (Frenkel and Smit [2002]).

Computer simulations are not a replacement for real experiments, as emphasized recently in a letter by Buchenau [2012] in The Journal of Physical Chemistry Letters with the title "*Simulation and Experiment – A Difficult Interaction*". Computer simulations may, however, form the basis of testing the applicability and validity of new theories which could be difficult to verify through experiments. Simulations can also serve as a catalyst for the creation of new theories which in the end may be tested experimentally. A recent example of the latter case derives from a series of articles of the "Glass and Time" group, Roskilde University (Bailey *et al.* [2008a,b], Gnan *et al.* [2009], Schrøder *et al.* [2009a, 2011]). Here, a new class of liquids was identified via MD computer simulations. An iterative process between simulations and "theory making" improved the basic understanding of these liquids and ultimately enabled the first experimental verification of this class of liquids in a paper by Gundermann *et al.* [2011] from 2011 in Nature Physics.

The present thesis is a continuation of the understanding of these liquids. These new liquids are introduced more rigorously in Chapter 2. The thesis work is based on MD computer simulations, and to establish a foundation for the results presented here the framework of MD is introduced in Section 1.1. The main focus of the "Glass and Time" group is the study of vitrification and of the preceeding supercooled liquid phase. Terminology associated with supercooled liquids and the glass transition is introduced in Section 1.3. Performing computer simulations of highly viscous supercooled liquids is not an easy task, since changing temperature by a few percentage may change relaxation times orders of magnitude. There is thus a "need for speed" in the study of viscous liquids, and Section 1.2 briefly reviews state-of-the-art graphics card (GPU) computing.

1.1 Molecular Dynamics. Solving Newton's 2nd law

Standing on the prominent shoulders of Galileo and Brahe/Kepler, Sir Isaac Newton formulated in 1687 his famous laws of motion (Newton [1687]). The second law of Newton states

$$\mathbf{F} = m\mathbf{a}, \tag{1.1}$$

where $\mathbf{F}$ is the force, $\mathbf{a}$ the acceleration, and m the inertial mass of a given particle. For a particle undergoing a free fall, i.e. the particle is only affected by gravity, Newton's 2nd law reads

$$mg = m\frac{d^2y}{dt^2}. \tag{1.2}$$

Here g is the acceleration due to gravity, and a coordinate system is applied with the y-axis in the direction of the force on the particle. This second-order, inhomogenous, ordinary differential equation can easily be solved, and its solution is usually the first thing students of classical mechanics meet (Knudsen and Hjorth [2002]). The solution to Eq. (1.2) is

$$y = \frac{1}{2}gt^2 + v_{0y}t + y_0, \tag{1.3}$$

where v_{0y} and y_0 are integration constants. Equation (1.3) uniquely detemines the motion of the particle in the past, present, and future. Suppose now, we consider an electrically charged particle in a constant and spatially homogenous magnetic field. The force is here given by the famous Lorentz Force, $\mathbf{F} = q(\mathbf{v} \times \mathbf{B})$, where $\mathbf{v}$ and q are, respectively, the velocity and charge of the particle, and $\mathbf{B}$ is the magnetic-field vector. Newton's 2nd law now produces a set of coupled differential equations, as follows (taking the z-axis to be aligned with the field)

$$qB_z v_y = m\frac{dv_x}{dt}, \tag{1.4}$$

$$-qB_z v_x = m\frac{dv_y}{dt}, \tag{1.5}$$

$$0 = m\frac{dv_z}{dt}. \tag{1.6}$$

These equations may be solved, although not as easily as the free fall, and the general solution is the "helix" curve (Knudsen and Hjorth [2002]).

Increasing the complexity; suppose we have a system of N particles each affected by a force derived from a potential function U via $\mathbf{F} = -\nabla U(\mathbf{r}_1, ..., \mathbf{r}_N)$, where $\mathbf{r}_k$ is the position vector of particle k and ∇ the gradient operator. This potential function could be a sum of pair potentials $U = \sum_{i<j} v(r_{ij})$, in which r_{ij} is the distance between particles i and j. An example of a typical pair potential v is given in Fig. 1.1 and is the famous Lennard-Jones (LJ) pair potential (Allen and Tildesley [1987]).

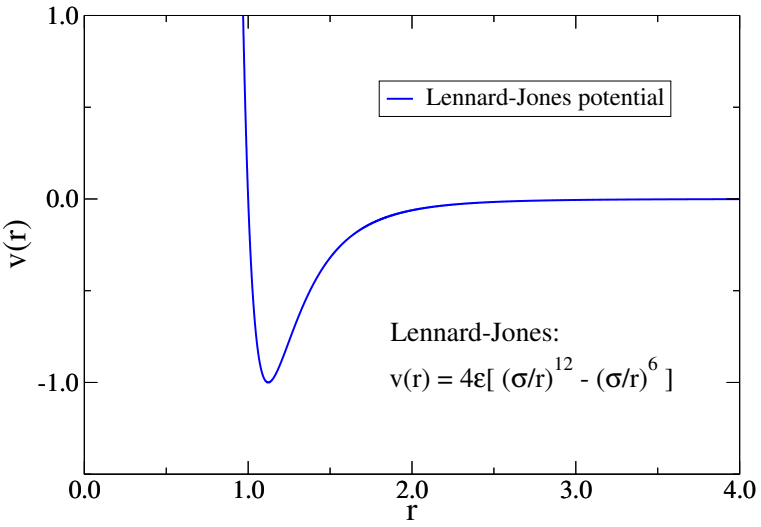

Figure 1.1: *The Lennard-Jones (LJ) pair potential* $v(r) = 4\epsilon[(\sigma/r)^{12} - (\sigma/r)^6]$*, where* σ *and* ϵ *define, respectively, the length and energy scales of the potential. The LJ potential diverges at* $r = 0$ *and goes to zero at infinity. This potential was used in some of the first MD simulations, more specific by Rahman in 1964 (Allen and Tildesley [1987]).*

In this case, solving Newton's 2nd law is not as easy as the former two examples, as the force on a given particle is now dependent on the position of all the other N particles. In fact, solving this analytically is not possible and is known as the N-body problem[1] in mechanics (Goldstein *et al.* [2002]).

Molecular dynamics, in all its simplicity, solves the N-body problem. However, since it cannot be solved analytically, MD resorts to a numerical integration of the equations of motion, using a so-called numerical integrator. As an example of a numerical integrator, we may write Eq. (1.1), applying to the acceleration $\mathbf{a}$ what is known as a central-difference discretization (Allen and Tildesley [1987]), as

$$\mathbf{F}(t) \approx m\frac{\frac{\mathbf{r}(t+\Delta t)-\mathbf{r}(t)}{\Delta t} - \frac{\mathbf{r}(t)-\mathbf{r}(t-\Delta t)}{\Delta t}}{\Delta t}, \tag{1.7}$$

where Δt is a "small" time step increment. Rearranging this equation leads to a numerical integrator known as the "Verlet algorithm" (Verlet [1967])

$$\mathbf{r}(t+\Delta t) = 2\mathbf{r}(t) - \mathbf{r}(t-\Delta t) + \frac{(\Delta t)^2}{m}\mathbf{F}(t). \tag{1.8}$$

Supposing the initial positions $\mathbf{r}$ at times $t - \Delta t$ and t are given, then the recursion formula of Eq. (1.8) can be used to track the motion of all N particles (choosing some appropriate time step Δt).

The careful reader will at this point object that the solution generated by Eq. (1.8) may have nothing to do with the analytical solution. This is indeed an active research area and

[1] One typically refers to the N-body problem when the force is gravitational, but we disregard this minor detail.

may justify a thesis (or two) on its own. The interested reader is referred to the extensive literature about this particular issue (see, for instance, Toxvaerd *et al.* [2012] and references therein).

The motion of the N particles is in MD limited to a box of volume V. To avoid surface effects, box edges are often eliminated via so-called periodic boundary conditions (Frenkel and Smit [2002]), where replicates of the simulation box are translated in a space-filling manner around the "main" box itself (see Fig. 1.2). Since the motion in all replicate boxes is identical, the number of particles N is still conserved (along with the volume).

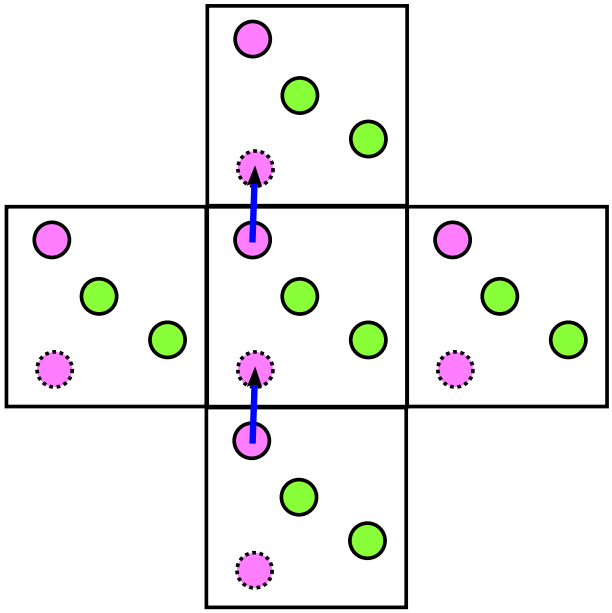

Figure 1.2: *An illustration of periodic boundary conditions. Replicates of the simulation box are translated in a space-filling manner around the main box itself (middle box). The purple atom moves as indicated by the blue arrow, and enters on the other side of the box due to periodic boundary conditions. The motion in all replicate boxes is identical and is thus not stored explicitly.*

If the force field is conservative (Knudsen and Hjorth [2002]), then Newton's 2nd law conserves the total energy $E = K + U$, in which K is the kinetic energy, and MD simulations are often referred to as NVE simulations. The MD technique has since its introduction evolved rapidly, and simulations at constant temperature NVT (Hoover [1985], Nosé [1984]), constant pressure NPT (Frenkel and Smit [2002], Nosé [1984]), or even constant chemical potential μVT (Lynch and Pettitt [1997]) can now be carried out. In Chapter 9, a new MD technique is derived conserving the total potential energy, NVU.

Molecular dynamics is thus a very versatile technique, but why apply MD in the first place? The main advantage of MD is that the microscopic motion of the individual particles is known exactly (within the classical mechanical picture) and enables the calculation of virtually any observable on a routine basis; observables that may be difficult or even impossible to realise in real experiments. Molecular dynamics has thus been applied to a wide range of fields ranging from non-equilibrium flow of water in nano-confinement (Hansen *et al.*

[2011]) to the study of the mechanism behind the human immunodeficiency virus (Wartha *et al.* [2005]). Supercooled liquids and the glass transition are in this respect no exception where, for instance, growing length scales and cooperative dynamics (Cavagna [2009], Dyre [2006]) cannot be measured in real experiments as easily as they can through computer simulations. Every technique has, however, its limitations, and the main limitation of MD is that the time step Δt is governed by the femtosecond vibrations; thus to study the relaxation of an experimental glass forming liquid on the order of 10^{17} time steps are needed. There is thus not only a need, but a dire "need for speed" in this field of research, and here graphics cards (GPUs) enter the scene.

1.2 State-of-the-art molecular dynamics

The MD simulations presented in this thesis have used the Roskilde University Molecular Dynamics (RUMD) program, which is an open-source MD program (avaliable at `http://rumd.org`) that utilizes graphics cards (GPUs). RUMD is developed in the "Glass and Time" group and written using the graphics card vendor NVIDIA's CUDA programming model (NVIDIA [2012]). CUDA[2] is a general purpose parallel computing architecture that also provides an extension of the C programming language (Deitel and Deitel [2001]) to enable easy interaction with the GPU.

In this section, we first give a non-exhaustive introduction to GPU computing using CUDA, and then we give an introduction to the basic ideas behind the RUMD program. The introduction becomes technical and is best understood with knowledge of standard computer hardware (see also NVIDIA [2012]). NVIDIA has released different generations of their GPUs that utilize CUDA where each generation provides different features and changes certain hardware specifications. In the following, we assume the so-called "Tesla" architecture[3] from NVIDIA. The RUMD program currently only uses features related to this architecture to ensure compatibility of the code with older and newer graphics cards (and maintaining just one "version" of the code).

1.2.1 GPU computing using CUDA

Figure 1.3 shows a drawing of the GPU hardware in the Tesla architecture.

[2] CUDA stands for Compute Unified Device Architecture, and we use the term loosely to describe all the features provided by NVIDIA for GPU computing.

[3] The latest architecture anno 2012 is the "Keplar" architecture which is two generations after Tesla.

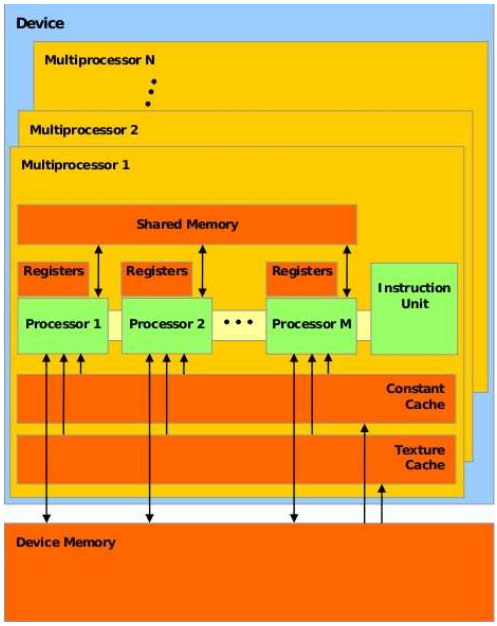

Figure 1.3: *A drawing of the GPU hardware in the "Tesla" architecture (taken from NVIDIA [2012]). The GPU consists of N (≈ 30) multi-processors each with M ($= 8$) cores. The M cores are synchronized to execute the same instruction but are able to operate on different data.*

The GPU consists of N (≈ 30) multi-processors each with M ($= 8$) cores. Each of these cores is comparable to a standard CPU and can execute a single instruction. The M cores are, however, synchronized to execute the same instruction but can operate on different data (in computer science called a Single Instruction Multiple Data or Single Instruction Multiple Thread architecture). For example, if the code to be executed on the GPU contains an IF-statement that some cores evaluate to be *true* while others evaluate it to be *false*; then each of these IF-clauses must be executed serialized (with an associated penalty on performance). The M cores share a fast local memory called "shared memory" where reading from the shared memory is as fast as reading from the registers (within certain restrictions, see NVIDIA [2012]). The size of the shared memory is 16KB. In comparison, all the multi-processors have access to a slower global "device memory" on the GPU of the order of 1GB of storage. The device memory (in the Tesla architecture) is, however, not cached as in the usual CPU, and the typical workflow of a CUDA-program starts by reading data from device memory into shared memory for efficient calculations.

The piece of code, written in CUDA, to be executed on the GPU is called a "kernel". It is specified in the execution of this kernel, how many threads[4] should be spawned from the code. The threads are then divided (by the programmer) into a number of blocks. Each block is then executed on a given multi-processor, where one core handles the execution of a single thread. As a technical detail, the GPU partitions the threads of a given block into so-called "warps" of size n ($= 32$), and it is among these n threads the execution of a single instruction must remain synchronized. A GPU is ideally suited to execute MD programs,

[4] A thread, in general, is the smallest unit of work that can be performed.

since the (pair) force calculation of a typical MD program takes up 90% of the total run time of the program (Allen and Tildesley [1987]) but involves mostly arithmetic operations applied to the different data for the atoms. The GPU has dedicated most of its hardware to these kinds of operations and do not have any logic to handle, for instance, branch prediction, e.g. deciding when an IF-statement or recursive loops are taken.

In the above many details related to GPU computing using CUDA are left out, and the reader is referred to, for instance, NVIDIA [2012] for much more detail. Equipped with this small introduction to GPU computing, the next section introduces the basic ideas behind the RUMD program for running efficient MD on the GPU, i.e., we focus on evaluating the pair forces efficiently on the GPU.

1.2.2 Roskilde University Molecular Dynamics. RUMD

The basic framework of the RUMD program is constructed from the so-called "N-body" program (Nyland *et al.* [2008]) that calculates gravitational interactions on the GPU among N interacting "atoms". In the N-body program, the calculation of the forces is an $\mathrm{O}(N^2)$ algorithm since all pair interactions must be evaluated explicitly with this kind of long-ranged force. The latter corresponds to filling the entries of a (anti-symmetric) $N \times N$ force matrix, where each entry corresponds to the force (i.e. x, y, z-components) among a pair of atoms.

A sketch of the force calculation in the N-body program is shown in Fig. 1.4. The $N \times N$ force matrix is divided into "tiles" (for the first tiles, see colors in Fig. 1.4), and the forces are evaluated by filling the entries of each tile, from the left to the right. The force calculation proceeds in the following way. A thread is created for each atom (row), and the N threads are divided into N/p blocks, i.e., p threads per block. In a given block, the p threads read p atomic positions from device into shared memory[5]. The forces of a given tile (of size p^2) are then calculated by the p threads using the data in shared memory. Afterwards, another batch of p atomic positions is read into shared memory (see arrows), and the forces of the next tile are calculated. This procedure continues until all the tiles have had their interactions evaluated. In this scheme, there is thus a trade-off between a large value for p which reduces the number of reads from device memory, and small value for p which creates more blocks to be executed on the GPU. It should also be noted that the above approach does not utilize Newton's third law, which is common to MD programs, and is because arithmetic operations are fast on the GPU.

[5] In this way, only $(N/p)^2 \cdot p = N^2/p$ reads from device memory (instead of N^2) are performed.

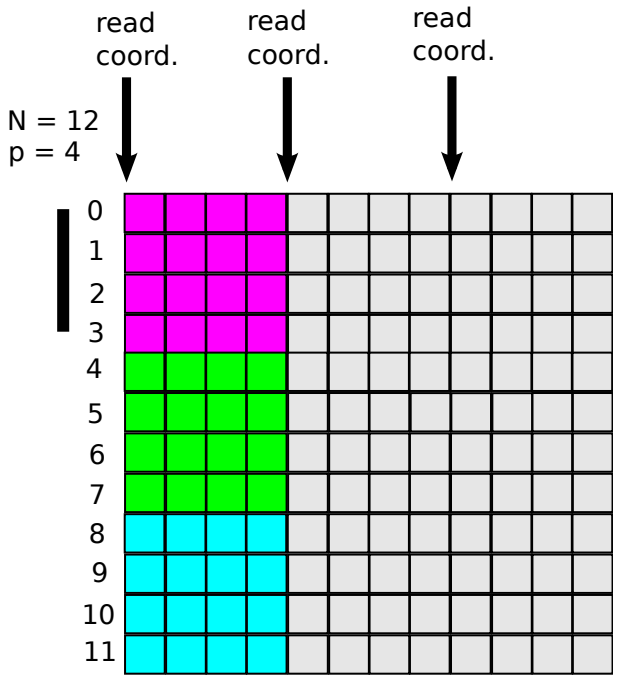

Figure 1.4: *Evaluation of the $N \times N$ force matrix in the N-body program. The forces are calculated by filling the entries of a given tile from the left to the right. The force calculation proceeds as follows. A thread is created for each particle (row), and the N threads are divided into N/p blocks (in this example 3 blocks). In a given block, the p threads read p atomic positions from device into shared memory, and the shared memory is then used to calculate the forces of a given tile (the different colors show the evaluation of the first tiles). Afterwards, another batch of coordinates is read into shared memory (see arrows) and the forces of the next tile are calculated. This procedure continues until all the tiles (here 9 tiles) have had their interactions evaluated.*

As mentioned previously, the device memory is not cached, and the GPU hides the memory latency[6] by executing different warps (recall that the execution was synchronous only among a warp) while fetching data from the device memory (NVIDIA [2012]). A simple optimization of the brute-force scheme is thus to use q "threads per atom". The additional $q - 1$ threads calculate the forces of the remaining tiles concurrently with the "original" thread (Nyland *et al.* [2008]). This is shown in Fig. 1.5 using $q = 2$ threads per atom (row). The speed-up gained using more threads per atom is small at larger sample sizes, as the multi-processors have a large pool of threads to schedule from.

[6] A request from data in global memory involves not only the time taken to transfer data into local memory, but also time spent waiting for the request to be performed. This is called memory latency and may be of the order of many hundreds of instructions.

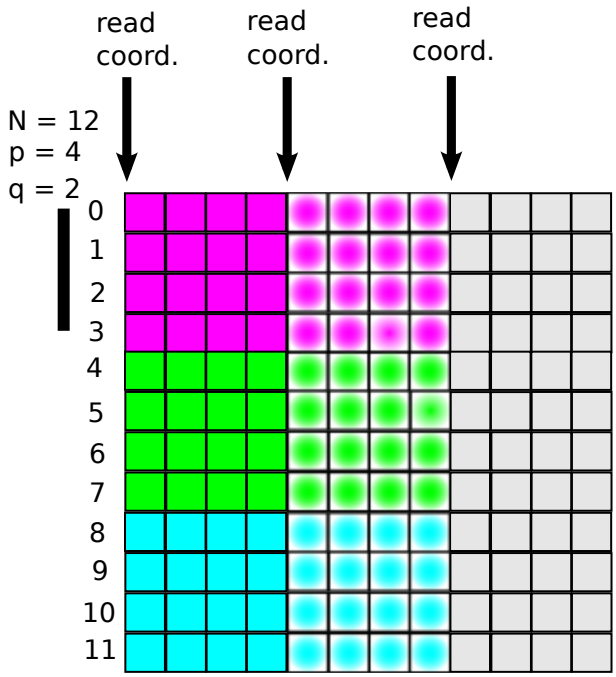

Figure 1.5: *Evaluation of the $N \times N$ force matrix in the N-body program. Here, the basic scheme is optimized by using q "threads per atom" enabling the possibility of better memory latency hiding. In the example of the figure, $q = 2$, and the first two tiles are being evaluated concurrently by the threads. For larger system sizes this scheme does not provide a significant speed-up as the GPU has a large pool of threads to schedule from (Nyland* et al. *[2008]).*

By using the N-body program with LJ instead of gravitational interactions, a good speedup is obtained for small system sizes (roughly a factor of 3) over a highly optimized serial MD program. However, to develop an efficient MD program, RUMD has optimized in different ways on this basic $\mathrm{O}(N^2)$ brute-force scheme for calculating the forces. In MD, a pair potential cutoff at a distance r_c is often introduced after which the forces are neglected. Doing so, the complexity of the force calculation may be reduced to $\mathrm{O}(N)$, by using a so-called "Verlet neighbor-list" that specifies the interactions among the atoms within the cutoff distance r_c (Allen and Tildesley [1987]). In RUMD, the neighbor-list is implemented using a bit-pattern for each (CUDA) block and atom (for instance; the pattern 0110, where 1 specifies interaction among a pair of atoms). This bit-pattern is represented by integer values (of 32-bits) and may be efficiently decoded using the intrinsic CUDA `__ffs` function (NVIDIA [2012]) that returns the position of the least significant non-zero bit of the pattern.

For larger system sizes, additional optimizations must be introduced as the forces are evaluated from the neighbor-list as the particles happen to appear in memory at the program start (i.e. starting from the particle with index 0 and stopping at the particle with index $N - 1$). This may result in a large number of blocks with a few or no interactions. In this scheme of evaluating the forces, all the relevant interactions should ideally be grouped together in a single block. RUMD solves this problem by using a spatial sorting of the atoms based on their coordinates in space.

1.3 Supercooled liquids and the glass transition

We consider here briefly a few key issues associated with supercooled liquids and the glass transition. Reviews may be found in, for instance, Cavagna [2009], Debenedetti and Stillinger [2001], Dyre [2006]. When a liquid is cooled below its freezing temperature (see T_m in Fig. 1.6) and avoids crystallization, it is termed "supercooled". The liquid is here thermodynamically unstable with regards to the crystal, however, the supercooled liquid state may be rather long-lived[7]. It is thus possible to equilibrate the liquid below its melting temperature, and with respect to all measurements one cannot detect that it is indeed the crystal that is the thermodynamically stable state (unless the system actually crystallizes). Some liquids supercool more easily than others, but is not a topic that we will discuss here. However, with a suitable cooling rate most liquids can be cooled below their freezing temperatures and become supercooled.

The supercooling of the liquid is associated with an increase in characteristic relaxation times, in particular, those associated with the relaxation of the structure of the liquid; there is thus also an increase in the viscosity μ upon cooling. Monitoring, for instance, the entropy vs temperature (see Fig. 1.6); the entropy decreases as the temperature is lowered, however, at some point, there is a sudden change in the slope from the liquid value to a slope similar to the crystal; the system here forms a glass. The temperature at which it forms a glass is denoted T_g. Since the structural relaxation time τ increases upon cooling, this value will at some point become comparable to the cooling rate, and at the point where the system is not given enough time to equilibrate; the system forms a glass. The glass is thus a highly viscous out-of-equilibrium liquid. The glass transition temperature T_g is then not well-defined as it depends on the cooling rate (red, orange, and yellow curves correspond to different cooling rates). It is often only weakly dependent as we will see below.

[7] Crystallization involves both nucleation, i.e., the formation of a critical nucleus, as well as growth, i.e., the diffusion of particles into the critical nucleus.

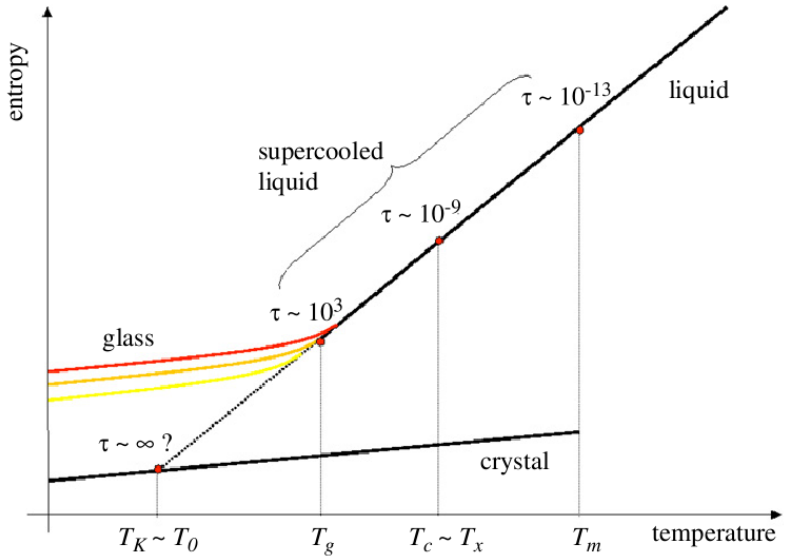

Figure 1.6: *An illustration of the supercooled liquid and its path to becoming a glass (taken from Cavagna [2009]). The entropy is monitored as the liquid is cooled below its freezing temperature T_m; the entropy decreases as the temperature is lowered. However, at some point there is a change in slope from the liquid value to a slope similar to the crystal; at this point the liquid forms a glass. The observed change in the slope is, however, not associated with any discontinuity as seen in the transition from liquid to crystal. The remaining temperatures are associated with different theories and aspects relating to the glass transition, see Cavagna [2009].*

The so-called "Angell plot" is shown in Fig. 1.7, where the logarithm of the viscosity is plotted against T_g/T, for a number of different liquids. Some liquids show an Arrhenius-type behavior (i.e., a straight line), while others show a dramatic increase in the viscosity when the temperature is lowered (non/super-Arrhenius behavior). The latter is typically referred to as, respectively, "strong"[8] and "fragile" behavior. We see that a prime example of a fragile liquid is *o*-terphenyl (OTP); three benzene molecules bonded together in the ortho-position. Since there is such a dramatic increase in viscosity (or relaxation time), the temperature at which the liquid forms a glass is only weakly dependent on the cooling rate. The explanation of the non-Arrhenius-type behavior is one the most important challenges relevant for understanding the glass transition, and many different theories have been proposed (see, for instance, Cavagna [2009], Dyre [2006], Shintani and Tanaka [2006] and references therein).

[8] This term is not to be mistaken with the use of "strongly correlating liquids".

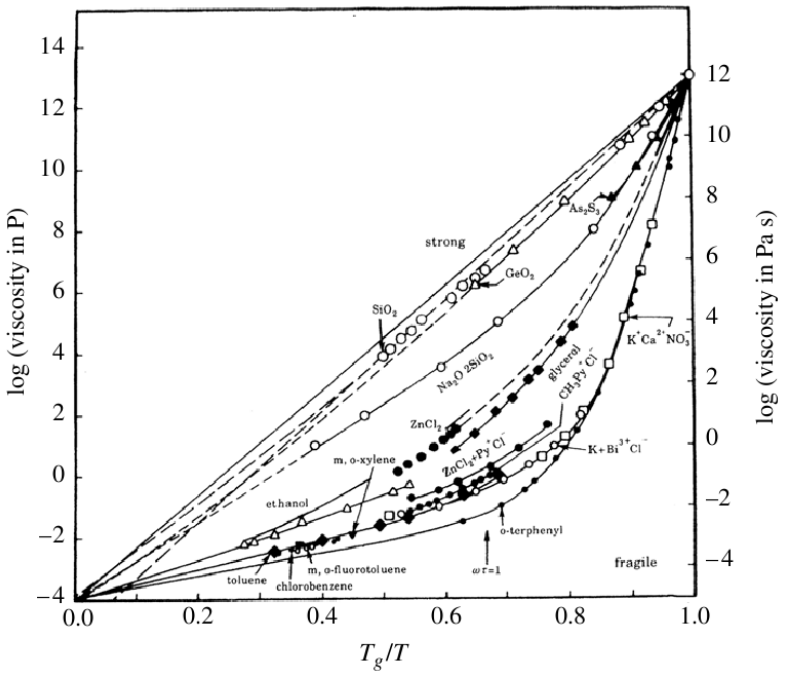

Figure 1.7: *The so-called "Angell plot" (taken from Cavagna [2009]) where the logarithm of the viscosity μ is plotted against T_g/T, where T_g is the glass transition temperature. Some liquids show an Arrhenius-type behavior (i.e., a straight line), while others show a dramatic increase in the viscosity, when the temperature is lowered. This behavior is referred to as, respectively, "strong" and "fragile" behavior.*

In the next section, we introduce and consider properties of the so-called "strongly correlating liquids". These liquids, as we shall see, appear simpler than other types of liquids. The latter statement includes the supercooled liquid phase and the glass. Thus, the understanding of these liquids may also appear fruitful for the understanding of supercooled liquids and the glass transition, in general (Angell and Klein [2011], Gundermann *et al.* [2011]).

Chapter 2

INTRODUCTION TO STRONGLY CORRELATING LIQUIDS

In a recent series of articles (Bailey *et al.* [2008a,b], Gnan *et al.* [2009], Schrøder *et al.* [2009a, 2011]) a new class of liquids was identified, namely the class of "strongly correlating liquids". An example of a strongly correlating liquid is the famous single-component LJ liquid with more than 95% correlation (see next section) in large parts of its phase diagram. Although the term "liquid" is used frequently, crystals or glasses are not excluded from being strongly correlating (Bailey *et al.* [2008a]). In fact, crystals and glasses are typically as strongly correlating as the preceeding liquid phase from which they are derived. In the gas phase or near the critical point, however, a system ceases to be strongly correlating.

Strongly correlating liquids are characterized by having "isomorphs"[1] to a good approximation (Gnan *et al.* [2009]). Isomorphs are curves in a liquid's phase diagram along which certain thermodynamic properties, structure and dynamics are invariant in so-called "reduced units". The concept of isomorphs, itself, refers only to configurational Boltzmann factors and not to a specific system or phase behavior. The only system for which isomorphs are exact is the inverse power-law r^{-n} (IPL) system[2]. For any other model system or real experimental liquids, isomorphs are an approximate concept. The success of the isomorph concept is captured in the fact, that for many systems; *it is a good approximation*. Only computer simulations of the actual system may, so far, give insight into how good an approximation it is. We now introduce more rigorously strongly correlating liquids and their isomorphs (Gnan *et al.* [2009]).

2.1 What is a strongly correlating liquid?

A strongly correlating liquid is defined by having strong correlations in the NVT ensemble between the equilibrium fluctuations of the potential energy U and the virial W (Bailey *et al.* [2008a]). Recall, that the instantaneous energy E and pressure p can both be written as a sum of a (fluctuating) kinetic part and a (fluctuating) configurational part, as follows

[1] The term "isomorph" is inspired from the mathematical concept of isomorphism meaning essentially same mathematical "structure". The physical reason for this name will become apparent later.

[2] More precisely, all potential functions that are Euler homogenous $U(\lambda\mathbf{R}) = \lambda^k U(\mathbf{R})$ (in which $\mathbf{R} \equiv (\mathbf{r}_1, ..., \mathbf{r}_N)$) have exact isomorphs. Thus, systems with 3-body, 4-body, etc. interactions can also have exact isomorphs assuming these interactions scale in the same way. In this chapter, we refer to the Euler homogenous systems simply as inverse power-law systems, but the latter fact should always be kept in mind.

$$E = K + U, \tag{2.1}$$

$$pV = Nk_BT + W, \tag{2.2}$$

where K is the kinetic energy, V the system volume and N the number of atoms. The virial W (Allen and Tildesley [1987]) is then the contribution to the pressure coming from the interactions between the particles of the system, and it is defined by[3]

$$W \equiv \frac{1}{3}\sum_i \mathbf{r}_i \cdot \mathbf{F}_i, \tag{2.3}$$

where $\mathbf{r}_i$ and $\mathbf{F}_i$ are, respectively, the position and force of particle i. For the LJ system (see Fig. 1.1) with $U = U_{LJ} = \sum_{i<j} v(r_{ij})$, the virial is $W = W_{LJ} = -\sum_{i<j} r_{ij}v'(r_{ij})/3$. The correlation between U and W is quantified via the correlation coefficient[4] R ($-1 \leq R \leq 1$) given by

$$R = \frac{\langle \Delta W \Delta U \rangle}{\sqrt{\langle (\Delta W)^2 \rangle}\sqrt{\langle (\Delta U)^2 \rangle}}, \tag{2.4}$$

where $\Delta U = U - \langle U \rangle$, $\Delta W = W - \langle W \rangle$, and $\langle ... \rangle$ denotes NVT ensemble average. The class of strongly correlating liquids is defined by $R \geq 0.90$ (Pedersen *et al.* [2008]), and only IPL systems r^{-n} are perfectly correlating, i.e., $R = 1$ (since $\Delta W = (n/3)\Delta U$ for all microconfigurations).

An illustration of strong virial/potential energy correlation for the asymmetric dumbbell model (see Appendix A for model details) is given in Fig. 2.1. Figure 2.1(a) shows the normalized time evolution of U and W from a molecular dynamics simulation, while Fig. 2.1(b) shows a scatter plot of the instantaneous values of U and W. It is clear that the latter two quantities are highly correlated, and in this case the correlation coefficient is $R = 0.96$.

[3] This chapter is mainly concerned with systems of atoms whereas later chapters consider systems composed of molecules.

[4] The correlation coefficient R is a common measure of linear correlation between two quantities in statistics.

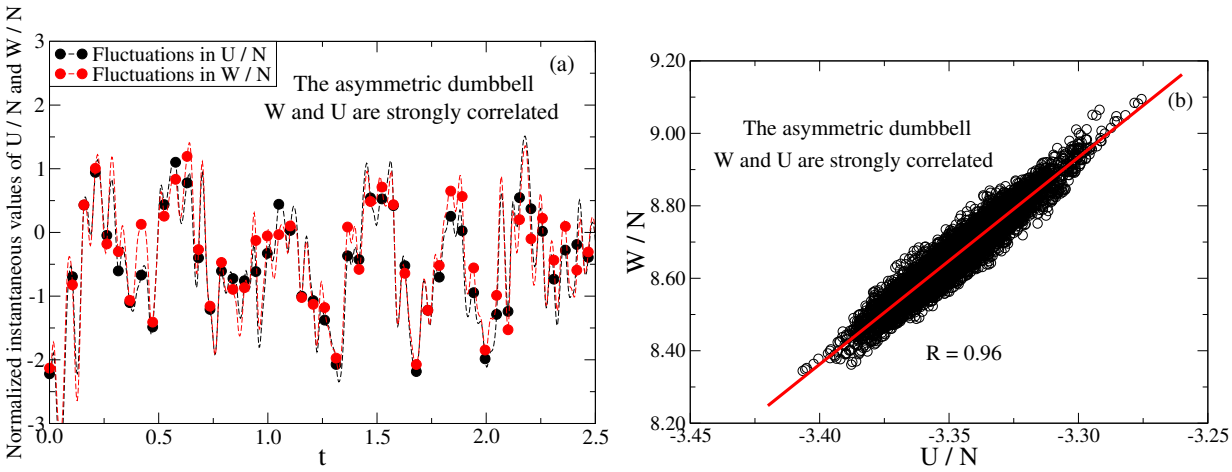

Figure 2.1: *Two different ways of visualizing (taken from Paper V) the strong virial/potential energy correlation for the asymmetric dumbbell model at* $\rho = 0.932$ *and* $T = 0.465$ *(see Appendix A for model details and the units used). (a) The time evolution of* U *(black) and* W *(red) per particle normalized to zero mean and unity standard deviation. (b) A scatter plot of the instantaneous values of* U *and* W *per particle. The correlation coefficient* R *is* 0.96.

Many different model systems have been identified to belong to the class of strongly correlating liquids (Bailey *et al.* [2008a,b], Coslovich and Roland [2008, 2009], Pedersen [2009], Pedersen *et al.* [2008, 2010a], Schrøder *et al.* [2009b], Veldhorst *et al.* [2012]), and include

- The standard single-component LJ liquid (SCLJ),
- The Kob-Andersen binary LJ mixture (KABLJ),
- The Wahnström binary LJ mixture (WABLJ),
- The asymmetric dumbbell model,
- The Lewis-Wahnström *o-terphenyl* model (OTP),
- And several others.

In addition, strong WU correlation has experimentally been verified for

- Tetramethyl-tetraphenyl-trisiloxane which is a molecular van der Waals liquid (Gundermann *et al.* [2011]),
- Supercritical argon (Pedersen *et al.* [2008]).

The class of strongly correlating liquids is believed to include most or all van der Waals and metallic liquids, whereas covalently, hydrogen-bonding or strongly ionic or dipolar liquids are not strongly correlating (Bailey *et al.* [2008a]). The latter reflects the fact that competing

interactions tend to destroy the strong correlation. A recent study indicates, however, that all liquids may become strongly correlating at sufficiently high pressures if crystallization is avoided (Papini *et al.* [2011]). This would, however, often imply pressures in the GPa range which is nevertheless still geological relevant pressures (Goel *et al.* [2011]).

2.1.1 The cause of strong WU correlation in the SCLJ liquid

We consider here the cause of strong WU correlation in the SCLJ liquid. This explanation holds[5] for many of the strongly correlating liquids (Bailey *et al.* [2008b], Pedersen *et al.* [2011]). As mentioned previously, only r^{-n} systems are perfectly correlating with $R = 1$.

It was, however, shown in Bailey *et al.* [2008b] that the first and second moments of the fluctuations in U and W (i.e. the quantities appearing in Eq. (2.4)) have contributions due to pair distances, corresponding to the entire first peak of the radial distribution function (Hansen and McDonald [2006]); with larger distances making negligible contributions. Over this range, the LJ potential usually has attractions (see Fig. 2.2(a)), and thus it is not at all obvious how the strong WU correlation in the SCLJ system connects to IPL systems.

Figure 2.2(a) shows the LJ pair potential and the difference between this potential and an appropriately chosen $v_{IPL} \propto r^{-18}$ approximating the repulsive part of the LJ potential[6]. It is observed from the figure that the difference between these two potentials to a good approximation is linear over the first peak (red curve). As shown in Fig. 2.2(b), the LJ potential may thus be approximated by $v_{LJ} \approx v_{IPL} + B + Cr$ over most of the first peak (also called an extended IPL pair potential).

[5] An exception is strong correlations in the Weeks-Chandler-Andersen (WCA) system (Weeks *et al.* [1971]) where the potential is truncated at the minimum. In the WCA system, the correlation is a single particle-pair effect (Gnan [2010]).

[6] Note that the exponent needed is larger than 12, as would be expected from the repulsive term of the LJ potential (Pedersen *et al.* [2010b]).

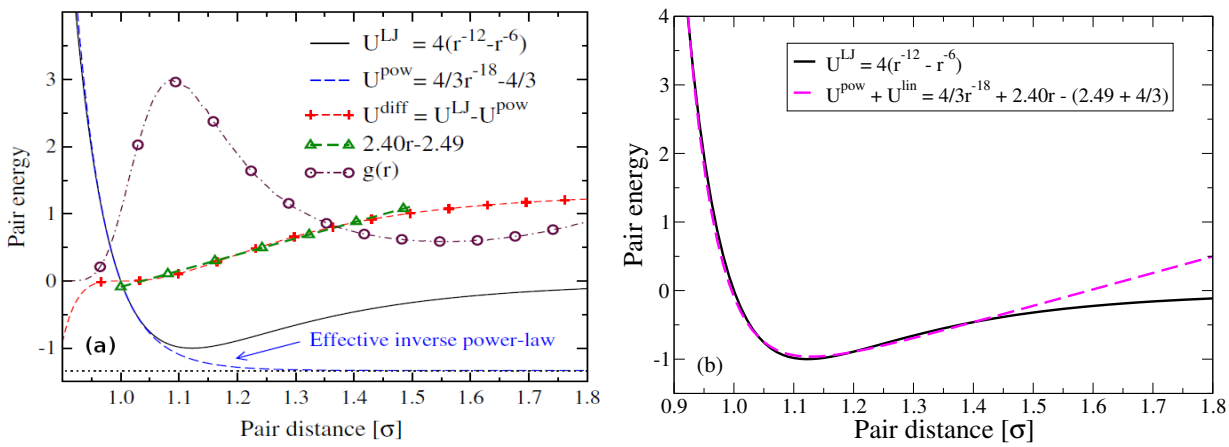

Figure 2.2: *(a) Approximation of the LJ potential by an effective IPL potential proportional to* r^{-18} *(taken from Pedersen* et al. *[2011]). The open circles mark the radial distribution function at a typical low-pressure state point. The blue dotted curve marks the IPL potential which approximates the LJ potential quite well* below *the minimum. The difference between the LJ potential and the IPL potential is approximately linear in* r *over the first peak (red curve). (b) Approximation of the LJ potential by an extended IPL potential* $v_{IPL} + B + Cr$ *(magenta curve) with* $v_{IPL} \propto r^{-18}$*. This approximation holds for most of the first peak.*

In addition, it was argued in Bailey *et al.* [2008b] that the linear term $B+Cr$ at constant volume approximately sums to a constant over the nearest neighbors and does not contribute much to the fluctuations. In this way, the SCLJ liquid becomes strongly correlating, but only after summation over the nearest neighbors; it is thus a collective phenomenon. The strong correlation will also disappear, should the volume fluctuate as in the constant pressure ensembles.

2.2 Isomorphs. Invariance curves in the phase diagram

This section introduces the concept of isomorphs for strongly correlating liquids (Gnan *et al.* [2009]). Consider two state points in a liquid's thermodynamical phase diagram with density and temperature (ρ_1, T_1) and (ρ_2, T_2). These two state points are defined to be isomorphic if the following holds: Whenever a microconfiguration of state point (1) and one of state point (2) have the same reduced coordinates (for all particles $i = 1, ..., N$ and $\rho = N/V$ in which V is the system volume)

$$\rho_1^{1/3}\mathbf{r}_i^{(1)} = \rho_2^{1/3}\mathbf{r}_i^{(2)}, \tag{2.5}$$

these two configurations have proportional Boltzmann factors, i.e.,

$$e^{-U(\mathbf{r}_1^{(1)},...,\mathbf{r}_N^{(1)})/k_BT_1} = C_{12}e^{-U(\mathbf{r}_1^{(2)},...,\mathbf{r}_N^{(2)})/k_BT_2}. \tag{2.6}$$

Here C_{12} is a constant that depends only on the state points (1) and (2) and not on the microconfigurations. An isomorph is then defined as a continuous curve of state points that are all pairwise isomorphic.

From statistical thermodynamics (Hill [1986]) it is well-known that Boltzmann factors determine the canonical ensemble averages, and from this fact it follows that different quantities will be invariant along an isomorph, since the constant C_{12} vanishes when normalizing the canonical probabilities. For instance, Sec. 2.2.1 proves the invariance of structure in reduced units along an isomorph. The invariance is, however, not limited to static quantities, but also the dynamics in reduced units is invariant along an isomorph (details follow in Sec. 2.2.2). The reduced units are defined as follows: Measuring length, energy and mass in terms of macroscopic properties, i.e., $\rho^{-1/3}$, k_BT and $\langle m \rangle$, the units of other properties follow (Allen and Tildesley [1987]). Quantities can then be made dimensionless ("reduced") via expressions like (in which t is time)

- $\tilde{\mathbf{r}} = \rho^{1/3}\mathbf{r}$,
- $\tilde{U} = U/k_BT$,
- $\tilde{m} = m/\langle m \rangle$,
- $\tilde{t} = t\,\rho^{1/3}\sqrt{k_BT/\langle m \rangle}$,
- and so forth.

Whenever the phrase "reduced units" is mentioned in this thesis, the above scalings are implied. Only IPL systems have exact isomorphs, with $C_{12} = 1$, and are characterized by having $\rho^\gamma/T = const$ where $\gamma = n/3$. For IPL systems, isomorphs thus capture the well-known scaling properties for thermodynamics (Hoover *et al.* [1970], Klein [1919], Stishov [1975]) and dynamics (Hiwatari *et al.* [1974], Hoover and Ross [1971], Zhakhovskii [1994]).

For any other strongly correlating model system, however, $C_{12} \neq 1$ and has the consequence that only some of the scaling properties of pure IPL systems generalize to the class of strongly correlating liquids. The quantities that typically do not generalize to become isomorph invariants relate to a volume derivative of the excess Helmholtz free energy $F_{\rm ex}$ (Gnan *et al.* [2009]). For instance, the (reduced) excess pressure coefficient $\beta_V^{\rm ex} \equiv -\partial^2 F_{\rm ex}/\partial T \partial V$ is not an isomorph invariant. A list of some important isomorph invariants for this thesis is given below (Gnan *et al.* [2009]).

1. The structure in reduced units,
2. The dynamics in reduced units,
3. The excess entropy $S_{\rm ex} = S - S_{\rm id}$[7],
4. The excess isochoric heat capacity $C_V^{\rm ex} = (\partial U/\partial T)_V$,
5. Any reduced relaxation time $\tilde{\tau}_\alpha$.

[7] $S_{\rm id}$ is the ideal-gas entropy at the same density and temperature as the liquid.

We will now prove the invariance of some of the isomorph invariants mentioned above (Gnan *et al.* [2009]). Before doing so, we note that there are additional consequences of isomorphs beyond isomorph invariants. One consequence is; since by Eq. (2.6), two isomorphic state points have identical canonical probabilities, an instantaneous change of temperature and of density from an equilibrated state point to an isomorphic state point does not lead to any relaxation. This fact is independent of the relaxation time of the state points and is called an "isomorphic jump" (Gnan *et al.* [2009]).

2.2.1 Invariance of the structure in reduced units along an isomorph

We show here that the structure in reduced units is invariant along an isomorph. The NVT configurational probability is given by (where $\mathbf{R} \equiv (\mathbf{r}_1, ..., \mathbf{r}_N)$, $d\mathbf{R} \equiv d\mathbf{r}_1 ... d\mathbf{r}_N$, and $\tilde{\mathbf{R}} \equiv \rho^{1/3}\mathbf{R}$)

$$\hat{P}(\mathbf{R}) = \frac{e^{-U(\mathbf{R})/k_BT}}{\int e^{-U(\mathbf{R})/k_BT} d\mathbf{R}}. \tag{2.7}$$

The probability distribution of the reduced structure is thus (the mapping is bijective)

$$\tilde{P}(\tilde{\mathbf{R}}) = \hat{P}(\rho^{-1/3}\tilde{\mathbf{R}})|\mathbf{J}| = \rho^{-N}\hat{P}(\rho^{-1/3}\tilde{\mathbf{R}}), \tag{2.8}$$

where $|\mathbf{J}| = \rho^{-N}$ is the determinant of the Jacobian of the transformation. The probability to observe a given reduced structure $\tilde{P}(\tilde{\mathbf{R}})d\tilde{\mathbf{R}}$ at state point (1) is related to state point (2) via ($d\tilde{\mathbf{R}} = \rho^N d\mathbf{R}$)

$$\tilde{P}(\tilde{\mathbf{R}}^{(1)})d\tilde{\mathbf{R}}^{(1)} = \frac{e^{-U(\mathbf{R}^{(1)})/k_BT_1}}{\int e^{-U(\mathbf{R}^{(1)})/k_BT_1} d\mathbf{R}^{(1)}} d\mathbf{R}^{(1)}, \tag{2.9}$$

$$= \frac{C_{12}\, e^{-U(\mathbf{R}^{(2)})/k_BT_2}}{C_{12}\int e^{-U(\mathbf{R}^{(2)})/k_BT_2}\left(\frac{\rho_2}{\rho_1}\right)^N d\mathbf{R}^{(2)}} \left(\frac{\rho_2}{\rho_1}\right)^N d\mathbf{R}^{(2)}, \tag{2.10}$$

$$= \frac{e^{-U(\mathbf{R}^{(2)})/k_BT_2}}{\int e^{-U(\mathbf{R}^{(2)})/k_BT_2} d\mathbf{R}^{(2)}} d\mathbf{R}^{(2)}, \tag{2.11}$$

$$= \tilde{P}(\tilde{\mathbf{R}}^{(2)})d\tilde{\mathbf{R}}^{(2)}, \tag{2.12}$$

where the second equation applies Eq. (2.6). Since $\tilde{\mathbf{R}}$ was chosen arbitrarily, the structure in reduced units is invariant along an isomorph.

2.2.2 Invariance of the dynamics in reduced units along an isomorph

We now consider the invariance of the dynamics in reduced units along an isomorph. The dynamics is assumed to be Newtonian dynamics, i.e. governed by Newton's 2nd law;

$$\mathbf{F}_i = m_i \mathbf{a}_i. \tag{2.13}$$

Applying the reduced units introduced previously, Newton's 2nd law reads (with $\tilde{\mathbf{F}}_i = \rho^{-1/3}\mathbf{F}_i/k_BT$, $\tilde{m}_i = m_i/\langle m\rangle$, and $\tilde{\mathbf{a}}_i = \langle m\rangle\rho^{-1/3}\mathbf{a}_i/k_BT$)

$$k_BT\rho^{1/3}\tilde{\mathbf{F}}_i = \frac{\langle m\rangle \tilde{m}_i\, k_BT\rho^{1/3}}{\langle m\rangle}\tilde{\mathbf{a}}_i. \tag{2.14}$$

Eliminating the common factors, we have

$$\tilde{\mathbf{F}}_i = \tilde{m}_i\tilde{\mathbf{a}}_i. \tag{2.15}$$

Taking now the logarithm of the isomorph definition Eq. (2.6), we have the following relation (recall $\tilde{\mathbf{R}} \equiv \rho^{1/3}\mathbf{R}$)

$$-U(\rho_1^{-1/3}\tilde{\mathbf{R}})/k_BT_1 = -U(\rho_2^{-1/3}\tilde{\mathbf{R}})/k_BT_2 + \ln C_{12}. \tag{2.16}$$

Applying the gradient $\nabla_{\tilde{\mathbf{r}}_i}$, the constant disappears, and we conclude

$$\tilde{\mathbf{F}}_i^{(1)} = \tilde{\mathbf{F}}_i^{(2)}. \tag{2.17}$$

This equation states that the reduced force is the same for scaled microconfigurations of isomorphic state points. The invariance of Newtonian dynamics in reduced units then follows immediately from Eq. (2.15). The microscopic dynamics is not limited to deterministic dynamics, but also stochastic dynamics can be invariant (see Gnan *et al.* [2009]).

2.2.3 Invariance of the heat capacity along an isomorph

The invariance of the excess isochoric heat capacity (in which $\Delta U = U - \langle U\rangle$)

$$C_V^{\text{ex}} = \frac{\langle(\Delta U)^2\rangle}{k_BT^2}, \tag{2.18}$$

along an isomorph can be seen rather easily (recall also $C_V^{\text{ex}} = -T(\partial^2 F_{\text{ex}}/\partial T^2)_V$). Defining $X \equiv U/k_BT$, we may write Eq. (2.18) as (where $\Delta X = X - \langle X\rangle$)

$$C_V^{\text{ex}} = k_B\langle(\Delta X)^2\rangle. \tag{2.19}$$

From the logarithm of Eq. (2.6), we have

$$U(\mathbf{R}^{(1)})/k_BT_1 = U(\mathbf{R}^{(2)})/k_BT_2 - \ln C_{12}. \tag{2.20}$$

From this equation, we conclude that

$$(\Delta X^{(1)})^2 = (\Delta X^{(2)})^2. \tag{2.21}$$

Thus, since scaled microconfigurations have identical values for $(\Delta X)^2$ and identical Boltzmann probabilities, the invariance of C_V^{ex} along an isomorph now follows. The ideal-gas

contribution to the heat capacity only gives a constant contribution, and thus the invariance of the full heat capacity also follows (Gnan *et al.* [2009]). In the next section, we consider how to verify the existence of isomorphs in a given system via the so-called "direct isomorph check".

2.2.4 Direct isomorph check

Taking again the logarithm of Eq. (2.6), and rearranging, we get (recall $\mathbf{R} \equiv (\mathbf{r}_1, ..., \mathbf{r}_N)$)

$$U(\mathbf{R}^{(2)}) = \frac{T_2}{T_1} U(\mathbf{R}^{(1)}) + k_B T_2 \ln C_{12}. \tag{2.22}$$

Equation (2.22) is called the "direct isomorph check" (Gnan *et al.* [2009]) as it provides a convenient way of testing for isomorphs. The procedure is as follows: A simulation is performed at one state point (1), and the obtained configurations are scaled to a different density ρ_2 where the potential energy is evaluated. The respective potential energies of the two state points are then plotted against each other. According to Eq. (2.22), this procedure should give a near straight line (see discussion below) if the system has isomorphs. The temperature T_2 of the isomorphic state point with density ρ_2 can be calculated from the slope of a linear regression fit by multiplying with T_1. Afterwards, a simulation can be performed at the state point (ρ_2, T_2) to verify the invariance of the aforementioned properties.

A direct isomorph check for the KABLJ mixture is shown in Fig. 2.3 for a 15% density increase where the correlation coefficient of the direct isomorph check is $R_{DI} = 0.98$. We note from Fig. 2.3 that the intersection is non-zero, and thus $C_{12} \neq 1$ for the KABLJ mixture.

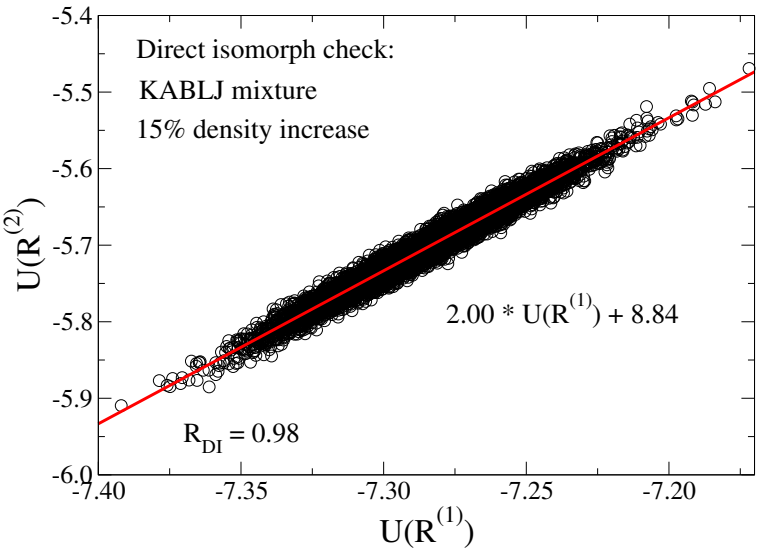

Figure 2.3: *Direct isomorph check for the KABLJ mixture. During a simulation at state point* $(\rho_1, T_1) = (1.204, 0.600)$ *the positions* $(\boldsymbol{R} \equiv (\boldsymbol{r}_1, ..., \boldsymbol{r}_N))$ *are scaled to density* $\rho_2 = 1.385$*. The potential energy is then evaluated from the scaled configurations and plotted against the potential energy of the unscaled configurations. According to Eq. (2.22), this procedure should give a (near) straight line if the system has isomorphs.*

For any system, if the change in density is sufficiently small R_{DI} will trivially be high. Is this fact equivalent to all systems having isomorphs? It is only for strongly correlating liquids a high R_{DI} is observed when the density increase is large. The latter fact may be justified from a relation derived in Appendix C of Gnan *et al.* [2009] between the correlation coefficient R (Eq. (2.4)) and that of the direct isomorph check R_{DI}. The relation is given by

$$\frac{1}{R_{DI}^2} - 1 = (d\ln T)^2 \Big(\frac{1}{R^2} - 1 \Big). \tag{2.23}$$

From this equation, it follows that $R_{DI} \to 1$ when either $d\ln\rho \to 0$ (and thus $d\ln T \to 0$) and/or when $R \to 1$. It is also shown in Appendix A of Gnan *et al.* [2009], in a different way, that a liquid has isomorphs to a good approximation *if and only if* it is strongly correlating.

2.2.5 What do isomorphs look like?

At the current point in time, isomorphs may seem like a rather abstract concept, and we delay the discussion of how to actually generate an isomorph in a liquid's phase diagram to later chapters (Gnan *et al.* [2009], Schrøder *et al.* [2011]). Isomorphs may, however, be visualized rather easily for a strongly correlating liquid by "just" knowing the phase diagram. Figure 2.4 shows the SCLJ phase diagram in terms of temperature T and density ρ (Andersen *et al.* [1976], Hansen and Verlet [1969]).

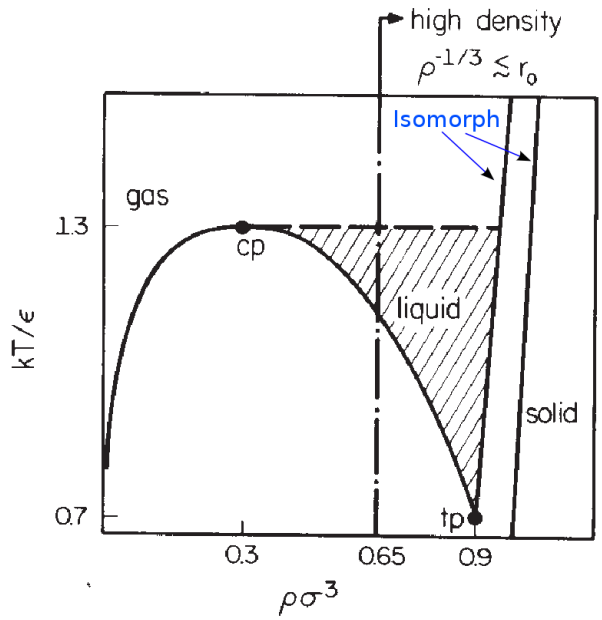

Figure 2.4: *The SCLJ phase diagram (taken from Andersen* et al. *[1976] and modified slightly) in terms of temperature T and density ρ. The melting line is itself an isomorph (Gnan* et al. *[2009], Schrøder* et al. *[2011]).*

It is argued in Gnan *et al.* [2009] and Schrøder *et al.* [2011] that the *melting line* is itself an isomorph, and explains a number of simple observations along the melting line (Andrade [1931], Gnan *et al.* [2009], Khrapak and Morfill [2011], Schrøder *et al.* [2011]). Since two different isomorphs cannot intersect[8], the isomorphs of the liquid-part of the phase diagram run "parallel" to the liquid-side of the coexistence line (see the blue arrow), where the vertical dashed line gives a good estimate of where in the phase diagram the properties of isomorphs start to vanish, e.g. close to the critical point and in the gas phase. Isomorphs extend far into the super-critical fluid region and also run (Albrechtsen and Olsen [2013]) in the crystalline-part of the phase diagram (even inside the solid-liquid coexistence region). From simulations, it has been observed that liquid isomorphs can be metastable inside the liquid-gas coexistence region, and a conjecture is that they are simply limited by the spinodal (Brazhkin and Trachenko [2012]). Thus, isomorphs are not just some abstract curves, but they are actually of high relevance for both liquid and solid-state physics and can be visualized rather easily by just following the melting line of a strongly correlating liquid.

[8] Two different isomorphs cannot intersect as this would violate the basic property of isomorphs (Gnan *et al.* [2009], Schrøder *et al.* [2011]).

Chapter 3

THERMODYNAMICS OF STRONGLY CORRELATING LIQUIDS (PAPERS I AND II)

The previous chapter argued that the excess isochoric heat capacity $C_V^{\rm ex}$ and the excess entropy $S_{\rm ex}$ are invariant along an isomorph. This observation is now used to show a rather unusual property of strongly correlating liquids, namely that temperature separates into a product of a function of excess entropy per particle and a function of density. In the following, the number of particles N is kept fixed. Since $C_V^{\rm ex}$ and $S_{\rm ex}$ are both invariant along an isomorph, we may write

$$C_V^{\rm ex} = f(S_{\rm ex}), \tag{3.1}$$

where f is some function. From the thermodynamic identity $C_V^{\rm ex} = T(\partial S_{\rm ex}/\partial T)_V = (\partial S_{\rm ex}/\partial \ln T)_V$, keeping the volume V fixed, it then follows from Eq. (3.1) that

$$d\ln T = \frac{dS_{\rm ex}}{f(S_{\rm ex})}. \tag{3.2}$$

Integrating this equation (at constant volume) we get

$$\ln T = \phi(S_{\rm ex}) + \chi(V). \tag{3.3}$$

Taking then the exponential function, we arrive at the result ($s_{\rm ex} \equiv S_{\rm ex}/N$)

$$T = g(S_{\rm ex})h(V) = g(s_{\rm ex})h(\rho). \tag{3.4}$$

For a strongly correlating liquid, temperature thus separates into a product of a function of excess entropy per particle and a function of density. An analytical expression for the function $h(\rho)$ is derived in the next section for a particular system with isomorphs.

3.1 An analytical expression for $h(\rho)$

Consider a system for which the total *average* potential energy U is written as a sum of IPLs r^{-n}, i.e.,

$$U = \sum_n v_n \sum_{i<j} \langle r_{ij}^{-n} \rangle. \tag{3.5}$$

Here $\langle ... \rangle$ denotes ensemble average, r_{ij} is the distance between particles i and j and v_n is a factor[1] depending on the exponent n. In the case of the LJ system (recall Fig. 1.1), U

[1] For simplicity in the notation we consider only single-component systems, but the results are entirely general.

would contain only the terms $v_6 = -4\epsilon\sigma^6$ and $v_{12} = 4\epsilon\sigma^{12}$. Applying the reduced units of Eq. (2.5) ($\tilde{r} = \rho^{1/3}r$), we may write

$$U = \sum_n v_n \sum_{i<j} \langle \tilde{r}_{ij}^{-n} \rangle \rho^{n/3} = \sum_n H_n(S_{\rm ex}) \rho^{n/3}. \tag{3.6}$$

The last equation utilizes that $\langle \tilde{r}_{ij}^{-n} \rangle$ is an isomorph invariant since the structure in reduced units is also invariant along an isomorph; thus

$$\langle \tilde{r}_{ij}^{-n} \rangle = F_n(S_{\rm ex}) \propto H_n(S_{\rm ex}). \tag{3.7}$$

Taking now the derivative with respect to temperature at constant volume of Eq. (3.6), it follows that (where $C_V^{\rm ex} = (\partial U/\partial T)_V = T(\partial S_{\rm ex}/\partial T)_V$)

$$T\big(\frac{\partial S_{\rm ex}}{\partial T}\big)_V = \sum_n H_n'(S_{\rm ex}) \big(\frac{\partial S_{\rm ex}}{\partial T}\big)_V \rho^{n/3}. \tag{3.8}$$

In the equation above $H_n'(S_{\rm ex}) \equiv dH_n/dS_{\rm ex}$. Dividing then by $(\partial S_{\rm ex}/\partial T)_V$ gives

$$T = \sum_n H_n'(S_{\rm ex}) \rho^{n/3}. \tag{3.9}$$

Since temperature by Eq. (3.4) separates into a product of a function of excess entropy and a function of density, Eq. (3.9) can only be consistent with this result if $H_n'(S_{\rm ex})$ (for all n) is proportional to some function $\Phi(S_{\rm ex})$. This function $\Phi(S_{\rm ex})$ is within a multiplicative constant given by $g(S_{\rm ex})$. We thus identify (within a multiplicative constant)

$$h(\rho) = \sum_n C_n \rho^{n/3}. \tag{3.10}$$

In the case of a LJ-type system (i.e., a system with only v_6 and v_{12} appearing in U), we have

$$h(\rho) = C_6\rho^2 + C_{12}\rho^4. \tag{3.11}$$

Since $h(\rho)$ is only defined within a multiplicative constant, we can multiply $h(\rho)$ with $1/(C_6 + C_{12})$ giving

$$h(\rho) = (1-\alpha)\rho^2 + \alpha\rho^4, \tag{3.12}$$

where $\alpha \equiv C_{12}/(C_6 + C_{12})$. There is thus only one free parameter α in $h(\rho)$ for a LJ-type system, and this parameter can be determined from simulations at a single state point (see Papers I or II for more details). It is also shown in Paper II that the constants C_n are actually related to the heat capacities of the individual IPL terms appearing in U. For a LJ-type system with $U = U_6 + U_{12}$ we have $C_6 = C_{V,6}^{\rm ex}/C_V^{\rm ex}$ and $C_{12} = C_{V,12}^{\rm ex}/C_V^{\rm ex}$, where $C_{V,n}^{\rm ex} \equiv \langle (\Delta U_n)^2 \rangle / k_B T^2$. These "heat capacities" may, however, be either positive or negative with the restriction that their sum $C_V^{\rm ex}$ remains positive.

Since isomorphs are approximate, the derived theory must also be tested via simulations. For a LJ-type system it was argued above that $H_{12}'(S_{\rm ex}) \propto H_6'(S_{\rm ex})$. Integrating this

equation gives $H_{12} = \alpha H_6 + \beta$, where β does not depend on volume since H_{12} is a function of excess entropy only. In Fig. 3.1, H_{12} is plotted against H_6 for the KABLJ mixture (i.e. a LJ-type system) over a range of state points where density is varied by a factor of eight and temperature by a factor of 40 000. The non-perfect, although quite good, collapse of the data points reflects the approximative nature of the theory.

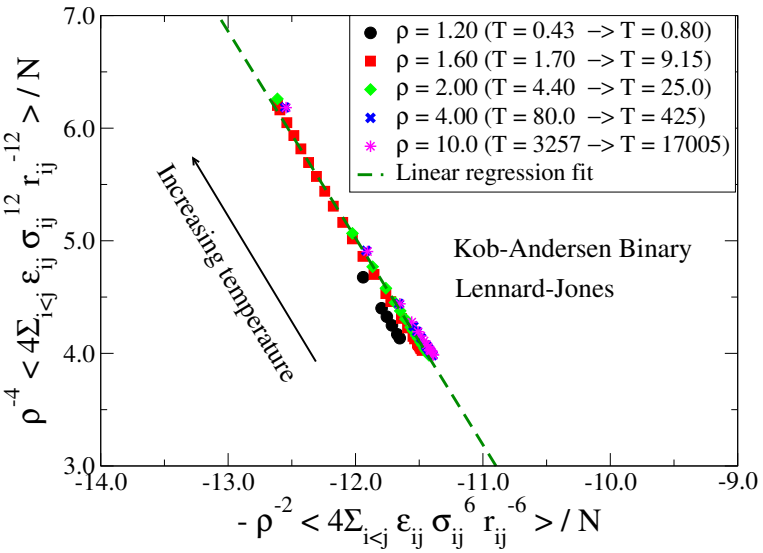

Figure 3.1: *H_{12} as a function of H_6 for the KABLJ mixture (taken from Paper I). The isomorph theory predicts that $H_{12} = \alpha H_6 + \beta$. A good collapse is seen, although density is varied by a factor of eight and temperature by a factor of 40 000.*

3.2 Beyond density scaling. Defining the isomorph scaling

As mentioned previously, the excess entropy is invariant along an isomorph, and from the separation identity of Eq. (3.4) we conclude that $h(\rho)/T$ is also an isomorph invariant. Since any reduced relaxation time $\tilde{\tau}_\alpha$ is also invariant, we may write

$$\tilde{\tau}_\alpha = G\Big(\frac{h(\rho)}{T}\Big). \tag{3.13}$$

This equation defines the so-called "isomorph scaling" (Papers I and II). For an IPL system, we see from Eq. (3.10) that $h(\rho) = \rho^\gamma$ where $\gamma = n/3$, and in this particular case Eq. (3.13) becomes

$$\tilde{\tau}_\alpha = G\Big(\frac{\rho^\gamma}{T}\Big). \tag{3.14}$$

Equation (3.14) defines what is known as "density scaling" (Tölle [2001]), and the origin behind the term ρ^γ/T for highly viscous liquids, in general, has been the topic of much debate in the literature (see, for instance, Alba-Simionesco *et al.* [2004], Casalini and Roland [2004], Dreyfus *et al.* [2003, 2004], Fragiadakis and Roland [2011]). In the concept of density scaling, the exponent γ is a constant such that

$$\gamma = \Big(\frac{\partial \ln T}{\partial \ln \rho}\Big)_{\tilde{\tau}_\alpha}. \tag{3.15}$$

We now consider whether density scaling holds for all strongly correlating liquids, taking Eq. (3.15) as a *general* definition of the density scaling exponent. By the separation identity $T = g(S_{\rm ex})h(\rho)$, we may write (by taking the logarithm)

$$d\ln T = d\ln g(S_{\rm ex}) + d\ln h(\rho). \tag{3.16}$$

Along an isomorph both $S_{\rm ex}$ and $\tilde{\tau}_\alpha$ are constant, and the first term on the right-hand side is then zero. We then have $d\ln T = d\ln h(\rho)$, and using these facts, Eq. (3.15) becomes

$$\gamma = \Big(\frac{\partial \ln T}{\partial \ln \rho}\Big)_{S_{\rm ex}} = \Big(\frac{d\ln h(\rho)}{d\ln \rho}\Big)_{S_{\rm ex}} = \frac{d\ln h(\rho)}{d\ln \rho} = \gamma(\rho). \tag{3.17}$$

In the general case, we expect γ to change along an isomorph since h is a function of density and depends on the particular system. If γ changes significantly along an isomorph, we thus expect a break down of density scaling as the latter assumes a constant γ. The isomorph scaling (Eq. (3.13)) is nevertheless expected to hold as this is based only on the assumption of isomorphs (and not on constant γ).

This conclusion is confirmed via simulations of the KABLJ mixture; Fig. 3.2(a) shows that density scaling breaks down when larger density variations are considered than typically chosen in experiments (usually 10%). The isomorph scaling of Fig. 3.2(b) shows no sign of a breakdown. Isomorph scaling is thus not merely a "higher-order" approximation to density scaling (in terms of the function $h(\rho)$) but rather a fundamental fact of the isomorph theory, as shown above. In fact, as mentioned previously, $h(\rho)$ contains only one free parameter for the KABLJ mixture that may be determined from simulations at a single state point.

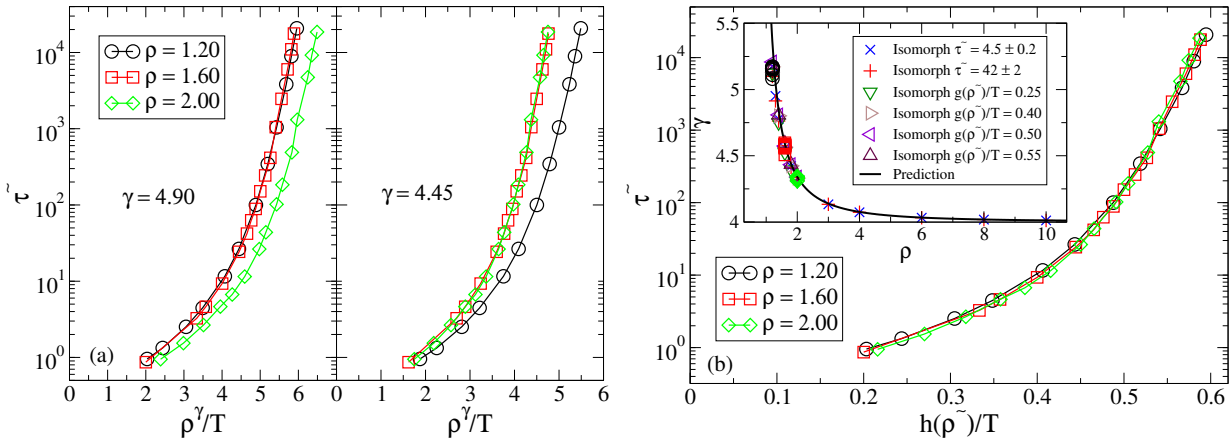

Figure 3.2: *Reduced average structural relaxation times $\tilde{\tau}_\alpha$ along three different isochores for the KABLJ mixture (taken from Paper II). (a) Density scaling $\tilde{\tau}_\alpha = G(\rho^\gamma/T)$ is applied. Two individual isochores can be scaled to superpose whereas the remaining isochore fails to scale. (b) Isomorph scaling $\tilde{\tau}_\alpha = G(h(\rho)/T)$ is applied. All three isochores scale to superpose. Recall that for LJ-type systems $h(\rho)$ has only one free parameter (see Sec. 3.1). The inset shows $\gamma = \langle \Delta U \Delta W \rangle / \langle (\Delta U)^2 \rangle$ (see Gnan* et al. *[2009]) calculated from the fluctuations of U and W at a single state point along different isochores and isomorphs, as well as $\gamma(\rho)$ calculated via Eq. (3.17) from $h(\rho)$. The agreement between simulations and theory is excellent.*

3.3 Grüneisen-type configurational equation of state

The Grüneisen equation of state is given by (Burakovsky and Preston [2004], Ross and Young [1993])

$$p = \gamma_g(\rho) E_{vib} + p_0(\rho), \tag{3.18}$$

where p is the pressure, E_{vib} the vibrational energy, γ_g the Grüneisen parameter (per unit volume), and p_0 a function of density. This equation is frequently used as an equation of state for high pressure solids (Burakovsky and Preston [2004], Ross and Young [1993]). It is now shown that a similar type equation of state applies for the configurational degrees of freedom of a strongly correlating liquid. The fundamental equation of thermodynamics is given by ($p_{\rm ex} \equiv W/V$ and $dV/V = d\ln V = -d\ln\rho$ for fixed N)

$$dU = TdS_{\rm ex} - p_{\rm ex}dV = TdS_{\rm ex} + Wd\ln\rho, \tag{3.19}$$

and produces the relations

$$T = \left(\frac{\partial U}{\partial S_{\rm ex}}\right)_\rho, \tag{3.20}$$

$$W = \left(\frac{\partial U}{\partial \ln\rho}\right)_{S_{\rm ex}}. \tag{3.21}$$

Since $T = g(S_{\rm ex})h(\rho)$, we conclude via integration of Eq. (3.20) that

$$U = G(S_{\rm ex})h(\rho) + \phi(\rho). \tag{3.22}$$

Taking the logarithmic derivative of this equation with respect to density (at constant $S_{\rm ex}$), and using Eq. (3.21), we get

$$W = G(S_{\rm ex})\frac{dh(\rho)}{d\ln\rho} + \frac{d\phi(\rho)}{d\ln\rho}. \tag{3.23}$$

Applying, from Eq. (3.22), then the relation

$$G(S_{\rm ex}) = \frac{U - \phi(\rho)}{h(\rho)}, \tag{3.24}$$

gives the following expression

$$W = \frac{d\ln h(\rho)}{d\ln\rho}U + \Phi(\rho) = \gamma(\rho)U + \Phi(\rho). \tag{3.25}$$

Equation (3.25) is the configurational version of Eq. (3.18). The virial W plotted versus the potential energy U along an isochore is then a straight line with slope γ (Bailey *et al.* [2008a], Schrøder *et al.* [2011]). Appendix B proves the converse statement that the Grüneisen-type configurational equation of state implies a separation of temperature.

Chapter 4

INVESTIGATION OF ROSENFELD-TARAZONA FOR VARIOUS LIQUIDS

Rosenfeld and Tarazona (Rosenfeld and Tarazona [1998]) derived via liquid-state density functional theory (a review of DFT may be found in Evans [1979]), a temperature expansion of the average potential energy which to leading order reads

$$U(\rho, T) = \alpha(\rho)T^{3/5} + \beta(\rho), \tag{4.1}$$

where $\alpha(\rho)$ and $\beta(\rho)$ are functions of density. From Eq. (4.1), an expression for the excess isochoric heat capacity may also be obtained (recall $C_V^{\text{ex}} = (\partial U/\partial T)_V$)

$$C_V^{\text{ex}} = 3/5\alpha(\rho)T^{-2/5}. \tag{4.2}$$

Rosenfeld and Tarazona concluded that these (truncated) expressions should hold to a high degree of accuracy for IPL fluids and confirmed this via simulations. Later on, different authors (Agarwal *et al.* [2010], Chopra *et al.* [2010b], Gebremichael *et al.* [2005], May and Mausbach [2012], Mossa *et al.* [2002]) investigated the applicability of Eq. (4.1), and its related equations, to describe as diverse liquids as Lewis-Wahnström OTP, SPC/E water, Dzugutov liquid, Gaussian core model (GCM), and more. In general, the authors concluded that Eq. (4.1) is a good approximation to the potential energy (and heat capacity) of these systems. However, some authors did notice deviations for liquids such as the Dzugutov and GCM. The latter two liquids do not belong to the class of strongly correlating liquids. It is thus natural to investigate, since IPL fluids are perfectly correlating, whether Eqs. (4.1) and (4.2) better describe strongly than non-strongly correlating liquids. Recall that $C_V^{\text{ex}} = \langle(\Delta U)^2\rangle/k_B T^2$ and can be calculated independently from the potential energy. It is also possible to calculate, for instance, the excess entropy, but it is a much more computational intensive task.

We start the investigation by showing in Fig. 4.1 the potential energy U and excess isochoric heat capacity C_V^{ex} along a single isochore for each of 18 different model systems, including both strongly and non-strongly correlating liquids. For reference, all the investigated model systems are listed in Table 4.1 along with selected data presented in this chapter.

System	ρ	S_U	$S_{C_V^{\mathrm{ex}}}$	R
Strongly correlating liquids (14)				
Dumbbell	0.93	$9.99997 \cdot 10^{-1}$	$9.99346 \cdot 10^{-1}$	0.96
Confined dumbbell	0.93	$9.99996 \cdot 10^{-1}$	$9.97617 \cdot 10^{-1}$	0.91
Girifalco	0.40	$9.98785 \cdot 10^{-1}$	$-6.63833 \cdot 10^{-1}$	0.91
KABLJ	1.20	$9.99983 \cdot 10^{-1}$	$9.84013 \cdot 10^{-1}$	0.93
IPL 6	0.85	$9.99986 \cdot 10^{-1}$	$9.97261 \cdot 10^{-1}$	1.00
IPL 12	0.85	$9.99997 \cdot 10^{-1}$	$9.99501 \cdot 10^{-1}$	1.00
IPL 18	0.85	$9.99967 \cdot 10^{-1}$	$9.88366 \cdot 10^{-1}$	1.00
LJC 10	1.00	$9.99993 \cdot 10^{-1}$	$9.98303 \cdot 10^{-1}$	0.86
LJC 4	1.00	$9.99990 \cdot 10^{-1}$	$9.91327 \cdot 10^{-1}$	0.90
OTP	0.33	$9.99982 \cdot 10^{-1}$	$9.95318 \cdot 10^{-1}$	0.91
Repulsive LJ	1.00	$9.99979 \cdot 10^{-1}$	$9.95072 \cdot 10^{-1}$	1.00
SCB	1.00	$9.99979 \cdot 10^{-1}$	$9.91343 \cdot 10^{-1}$	0.99
SCLJ	0.85	$9.99927 \cdot 10^{-1}$	$9.73529 \cdot 10^{-1}$	0.96
WABLJ	1.30	$9.99851 \cdot 10^{-1}$	$9.10703 \cdot 10^{-1}$	0.98
Non-strongly correlating liquids (4)				
Core soft water	0.40	$9.73950 \cdot 10^{-1}$	$4.72855 \cdot 10^{-1}$	0.097
Dzugutov	0.80	$9.96993 \cdot 10^{-1}$	$7.86436 \cdot 10^{-1}$	0.71
Molten salt	0.37	$9.99839 \cdot 10^{-1}$	$9.51729 \cdot 10^{-1}$	0.15
SPC/E water	1.00	$9.86504 \cdot 10^{-1}$	$5.58319 \cdot 10^{-1}$	0.067

Table 4.1: *Model systems (see Appendix A) investigated with respect to the expressions of Rosenfeld and Tarazona in Eqs. (4.1) and (4.2). S_U and $S_{C_V^{\mathrm{ex}}}$ are, respectively, the coefficient of determination (Eq. (4.3)) for the potential energy and heat capacity along the isochore of density ρ. The correlation coefficient R is given for the lowest temperature state points along the isochores.*

In general, we observe from the figure that for all liquids C_V^{ex} decreases with increasing temperature.

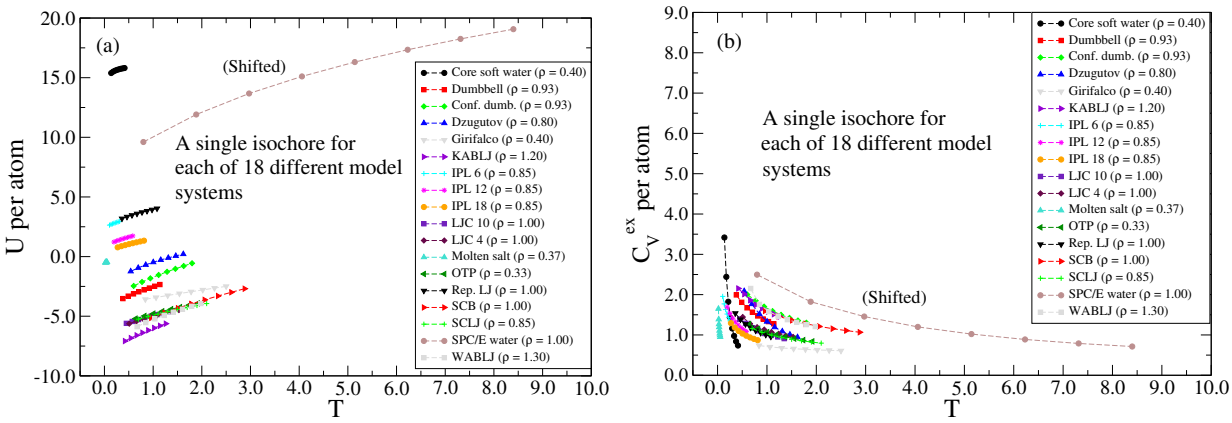

Figure 4.1: *A single isochore for each of 18 different model systems including both strongly and non-strongly correlating liquids. (a) The potential energy U per atom as a function of temperature. The values for SPC/E water have been shifted for clarity with -3 in the x-direction and 33 in the y-direction. (b) The excess isochoric heat capacity $C_V^{ex} = \langle(\Delta U)^2\rangle/k_B T^2$ per atom as a function of temperature. The values for SPC/E water have been shifted for clarity with -3 in the x-direction. For all liquids C_V^{ex} decreases with increasing temperature.*

Turning now to the expressions of Rosenfeld and Tarazona, we show in, respectively, Figs. 4.2(a) and (b) the coefficient of determination S_X (Steel and Torrie [1960]) for the potential energy U and excess isochoric heat capacity $C_V^{\rm ex}$ as a function[1] of $1 - R$. The coefficient of determination S_X is defined via the expression

$$S_X = 1 - \frac{\sum_{i=1}^{N} \left(X_i - f_{X_i}\right)^2}{\sum_{i=1}^{N} (X_i - \langle X \rangle)^2}, \tag{4.3}$$

where X is a generic quantity, and the average $\langle X \rangle$ is taken over a set of data points with elements $\mathbf{X} = \{X_1, ..., X_N\}$. f_X is a function that provides the "model" values for each X_i (with $i = 1, ..., N$), and is in our case given by fits to the data points in $\mathbf{X}$ (as a function of temperature T) using, respectively, $f_U = A_0\, T^{3/5} + A_1$, and $f_{C_V^{\rm ex}} = 3/5 A_2\, T^{-2/5}$, where A_0, A_1, and A_2 are constants (since density is fixed by using a single isochore).

[1] The value of R is given for the lowest temperature state points along the isochores.

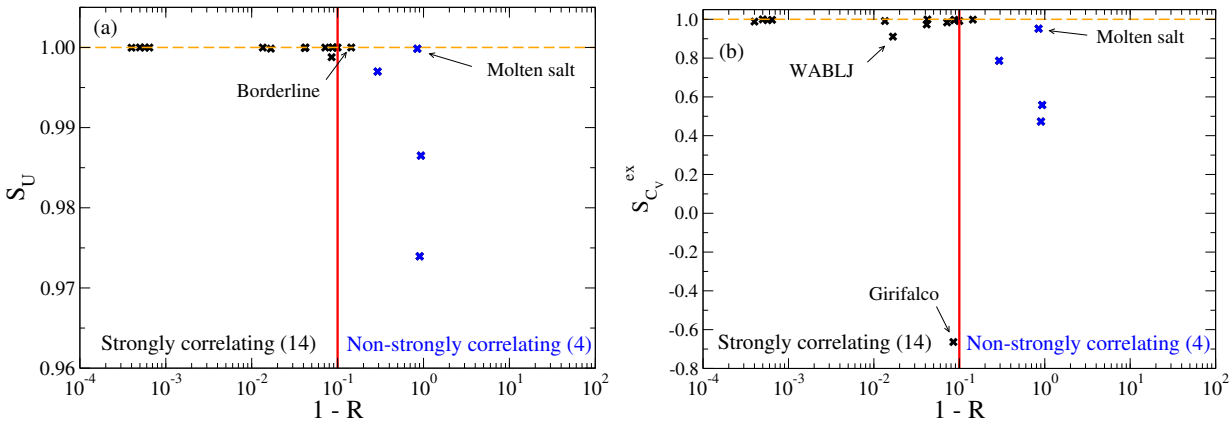

Figure 4.2: *The coefficient of determination S_X (Eq. (4.3)) as a function of $1-R$ calculated from data along a single isochore for each of 18 different model systems, including both strongly and non-strongly correlating liquids. (a) S_U is calculated via the potential energy. (b) $S_{C_V^{\rm ex}}$ is calculated via the excess isochoric heat capacity.*

S_X is a measure of the proportion of variability in a data set that is accounted for by the statistical model (Steel and Torrie [1960]). A value of $S_X = 1$ implies perfect account of the variability and is independent on the (energy) scale used. The elements of $\mathbf{X} = \mathbf{U}$ and $\mathbf{X} = \mathbf{C}_V^{\rm ex}$ (shown in Fig. 4.1) have been generated as follows.

1. First, the system is isochoric cooled until either of the following happens: 1) The system crystallizes. 2) The pressure becomes negative. 3) The relaxation time is on the order of 10^5 time units. After the cooling, the temperature T_{min} is noted and the system simulated to equilibrium; in the case of crystallization or negative pressure, the temperature is increased slightly in order to have a stable phase.

2. Next, the temperature is increased from T_{min} by a factor of three (i.e., up to $T_{max} = 3T_{min}$), probing state points along the isochore with a spacing of $\Delta T = (T_{max} - T_{min})/7$. A total of 8 equilibrium state points are hereby generated.

3. Finally, the 8 generated state points are then used to calculate the elements of $\mathbf{X} = \mathbf{U}$ and $\mathbf{X} = \mathbf{C}_V^{\rm ex}$.

We see from Fig. 4.2(a) that for both strongly and non-strongly correlating liquids S_U gives a value close to 1. Nevertheless, for all non-strongly correlating liquids (except the molten salt model) a lower value is obtained than for the strongly correlating liquids. In the case of $S_{C_V^{\rm ex}}$ in Fig. 4.2(b), the data shows a bit more scatter due to the uncertainty in estimating the heat capacity from the fluctuations. A similar behavior is nevertheless observed (note the change of scale), as for S_U, except that the Girifalco system now gives a value for $S_{C_V^{\rm ex}}$ significantly different than from any other strongly or non-strongly correlating system. The Girifalco system is rather unusual (see Apppendix A) in the sense that it diverges at a non-zero distance, representing the effective interaction between two C_{60} molecules (Girifalco [1992]). If we disregard, for the moment, the Girifalco system, the results indicate that the expression

of Rosenfeld-Tarazona for $C_V^{\rm ex}$ is a better approximation for strongly correlating liquids, too. The second lowest value for $S_{C_V^{\rm ex}} \approx 0.91$ of the strongly correlating liquids is obtained for the WABLJ mixture that in the supercooled regime creates crystal-like structures in terms of Frank-Casper bonds (Pedersen *et al.* [2010c]).

Turning now to the Girifalco system, we plot in Fig. 4.3, $S_{C_V^{\rm ex}}$ as function of $1-R$, but using the expression $f_{C_V^{\rm ex}} = 3/5 A_2 T^{-2/5} + A_3$, i.e., the system is allowed to have a non-vanishing excess isochoric heat capacity at very high temperatures. This time, the Girifalco system follows to a good approximation the chosen power-law $T^{-2/5}$. Physically, however, this approach is questionable, but it is nevertheless interesting that the same exponent is applicable.

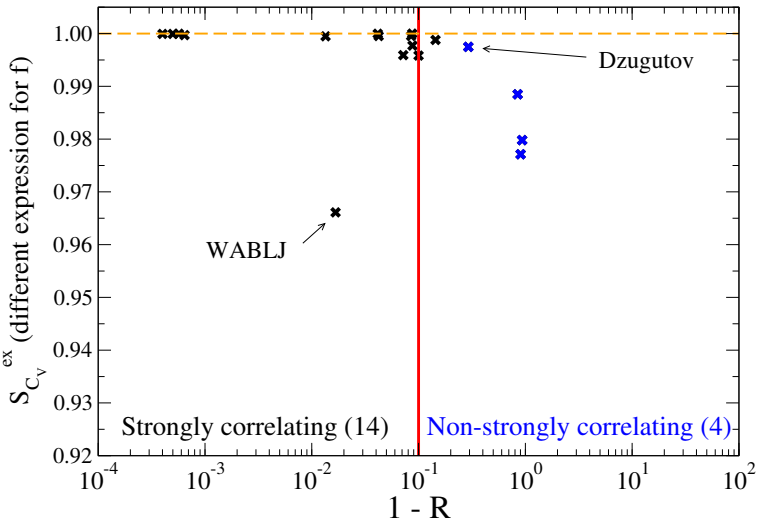

Figure 4.3: *The coefficient of determination for the excess isochoric heat capacity* $S_{C_V^{\rm ex}}$ *as a function of* $1-R$ *calculated from data along a single isochore for each of* 18 *different model systems, including both strongly and non-strongly correlating liquids. A different model expression than in Fig. 4.2 is applied, namely* $f_{C_V^{\rm ex}} = 3/5 A_2 T^{-2/5} + A_3$*, where* A_3 *is a constant.*

We conclude that the expressions of Rosenfeld and Tarazona may be used to a fair approximation for most systems (depending on the quantity of interest), but a better approximation is obtained when the system is strongly correlating in the range of state points in question. It should be noted that for non-strongly correlating liquids, we observe no clear connection between the value of R and the "goodness" of Rosenfeld-Tarazona.

We now consider how the function $\alpha(\rho)$ in the Rosenfeld-Tarazona expression relates to $h(\rho)$ (see Eq. (3.10)) for strongly correlating liquids. Along an isomorph both $C_V^{\rm ex}$ and $h(\rho)/T$ are invariant, thus

$$C_V^{\rm ex} = F\Big(\frac{h(\rho)}{T}\Big). \tag{4.4}$$

Since by Rosenfeld-Tarazona; $C_V^{\rm ex} = 3/5\alpha(\rho)T^{-2/5} = 3/5\big(\alpha(\rho)^{5/2}/T\big)^{2/5}$, it follows that

$$h(\rho) = \alpha(\rho)^{5/2}. \tag{4.5}$$

Equation (4.5) is tested in Fig. 4.4 for the repulsive LJ system (see Appendix A), where density is changed by a factor of eight[2]. The function $h(\rho)$ is determined via the expression

$$h(\rho) = (\gamma_0/2 - 1)\rho^4 + (2 - \gamma_0/2)\rho^2, \tag{4.6}$$

with $\gamma_0 = 3.56$. This expression appears after using the identity $\gamma(\rho) = d\ln h(\rho)/d\ln\rho$ at the reference state point of $\rho = 1$ and $T = 1$ (see Paper I for details). We determine $\alpha(\rho)$ from the constant A_0 by fitting the expression $A_0\,T^{3/5} + A_1$ to the potential energy as a function of temperature (since the potential energy has better statistics) along six different isochores of the repulsive LJ system (with ρ in the range 0.50 - 4.00). Fig. 4.4 shows that $\alpha(\rho)$ to a very good approximation is given by $h(\rho)^{2/5}$.

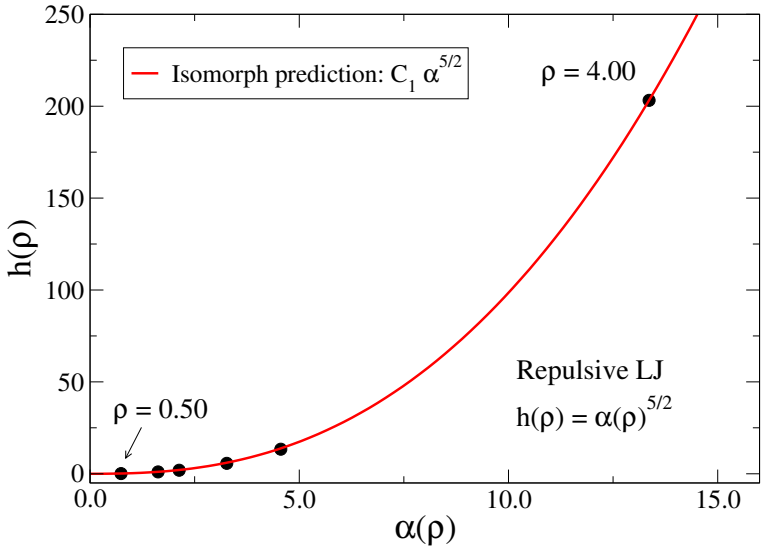

Figure 4.4: *The function $h(\rho)$, given by Eq. (4.6), plotted as a function of $\alpha(\rho)$ in the Rosenfeld-Tarazona expression, for six different densities of the repulsive LJ system (black data points). The red curve gives $C_1\,\alpha^{5/2}$, where C_1 is a constant uniquely determined from the state point $\rho = 4.00$; $h(\rho)$ is only determined within a multiplicative constant.*

[2] A similar test using power-law density scaling can be found in Pedersen *et al.* [2010b].

Chapter 5

THE FIRST COORDINATION SHELL CHARACTERIZATION OF STRONGLY CORRELATING LIQUIDS (PAPERS III AND IV)

In this chapter, we present a new "chemical" characterization of strongly correlating liquids via the role of the first coordination shell (FCS) interactions for these liquids (Paper III). The FCS (Chandler [1987]) is defined as the nearest-neighbor molecules around a given molecule and is illustrated schematically in Fig. 5.1 for a (two-dimensional) LJ liquid. A LJ liquid has approximately 12 nearest neighbors (in two dimensions: 6 nearest neighbors), whereas the FCS of water, due to its local tetrahedral nature, comprises between 4 and 5 molecules (Hujo *et al.* [2011]). The concept of nearest neighbors is derived from solids but is often applied to liquids as it provides a useful way of thinking on liquids.

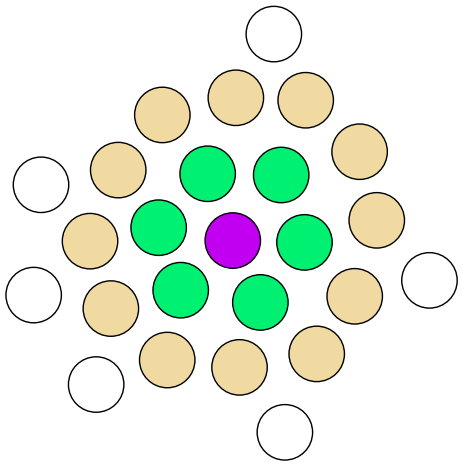

Figure 5.1: *A schematic snap-shot of a configuration of a two-dimensional LJ liquid. The purple atom is surrounded by its nearest neighbors (green atoms), second-nearest neighbors (yellow), etc. For a strongly correlating liquid (see text below) it is the interactions between the purple and green atoms that to a good approximation determine structure and dynamics.*

In two recent articles, Toxvaerd and Dyre (Toxvaerd and Dyre [2011a,b]) studied the use of shifted-force (SF) pair potential cutoffs in molecular dynamics computer simulations of the SCLJ liquid and the KABLJ mixture. If the pair potential is $v(r)$ and the pair force is $f(r) = -v'(r)$, the SF is given by

$$f_{SF}(r) = \begin{cases} f(r) - f(r_c) & \text{if } r \leq r_c\,, \\ 0 & \text{if } r > r_c\,. \end{cases} \tag{5.1}$$

The force remains continuous at the cutoff distance r_c, after which it is set to zero. An SF cutoff corresponds to the use of the following pair potential below r_c

$$v_{SF}(r) = v(r) - v'(r_c)(r - r_c) - v(r_c). \tag{5.2}$$

An SF cutoff thus adds a linear term to the "original" pair potential $v(r)$ which does not affect structure nor dynamics (recall the discussion of Sec. 2.1.1). The linear term does, however, affect some of the thermodynamical quantities, for instance, the energy and pressure are different from the original $v(r)$ system. These properties may, however, also be extracted from the radial distribution function (RDF) using the original potential $v(r)$ (Chandler [1987], Hansen and McDonald [2006]), and thus this is not a crucial problem (Toxvaerd and Dyre [2011a,b]).

It was discovered by Toxvaerd and Dyre that at low cutoff distances, the use of SF cutoffs was crucial to ensuring reliable simulation results due to an otherwise large force discontinuity. In addition, the authors found for the SCLJ liquid and the KABLJ mixture that an SF cutoff at the distance of the first minimum of the RDF gave identical results, for both structure and dynamics, to simulations with a very large pair potential cutoff. The first minimum of the RDF is the standard way of delimiting the FCS (Chandler [1987]), and we denote from now on this particular type of cutoff; an FCS cutoff. The SCLJ liquid and KABLJ mixture are both strongly correlating liquids (see Sec. 2.1). Recent studies by Fennell and Gezelter [2006] found, however, that for SPC/E water, an SF cutoff at distances beyond the FCS is needed to ensure good simulation results. Water is a prime example of a non-strongly correlating liquid. These results thus motivate the following conjecture (Paper III):

The FCS interactions determine to a good approximation structure and dynamics, if and only if, the liquid at the state point in question is strongly correlating.

This conjecture is investigated in more detail in the next few sections by applying an FCS cutoff to a number of different systems[1], both strongly and non-strongly correlating liquids, and probing the resulting structure and dynamics. A total number of 21 systems were studied in Paper III, and we present here only representatives for these systems. Additional systems besides those presented in Paper III are also studied here (recall that model details are given in Appendix A).

5.1 Single-component inverse power-law fluids

We study here four different single-component IPL fluids with exponents $n = 3$, 4, 12, 18. The IPL pair potentials are shown in Fig. 5.2, ranging from harsh repulsive ($n = 18$) to quite soft and long-ranged ($n = 3$).

[1] As a technical detail, in the case of systems with more than one particle-pair interactions, we apply cutoffs in units of the largest particle; see also Paper III.

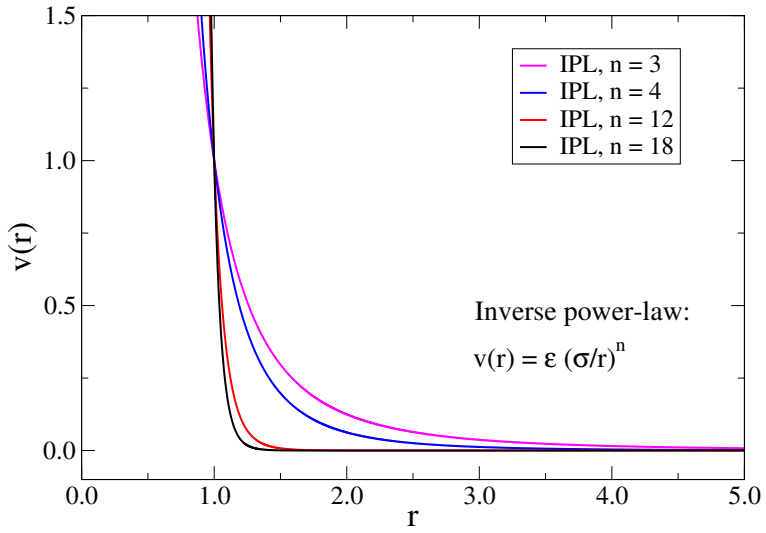

Figure 5.2: *Four different IPL pair potentials with exponents $n = 3$, 4, 12, 18, ranging from harsh repulsive ($n = 18$) to quite soft and long-ranged ($n = 3$).*

Figures 5.3(a)-(d) then quantify the structure of the IPL fluids via the RDF at $\rho = 0.85$ and two different temperatures applying, in simulations, different types of cutoffs. The black and orange curves correspond to simulations with a very large SF cutoff (we denote this reference simulations), whereas the red and green circles correspond to simulations with an FCS cutoff. In all figures, the FCS is marked by the vertical red dashed lines. In addition, the insets quantify the deviations in the RDF from the reference RDF as functions of the SF cutoff.

For all four investigated IPL fluids, excellent agreement is seen between the FCS cutoff and the large SF cutoff. In particular, we see from the insets that the deviations increase dramatically when the cutoff enters the FCS (blue crosses). Considering, however, the $n = 3$ IPL fluid some deviation is noted near the first peak of the RDF. This deviation is suspected to be related to the dimensionality of the system ($d = 3$) with respect to the IPL exponent ($n = 3$). One possible way to verify this conjecture would be to simulate a two-dimensional system using the $n = 3$ exponent; in this case the FCS approach should work perfectly again.

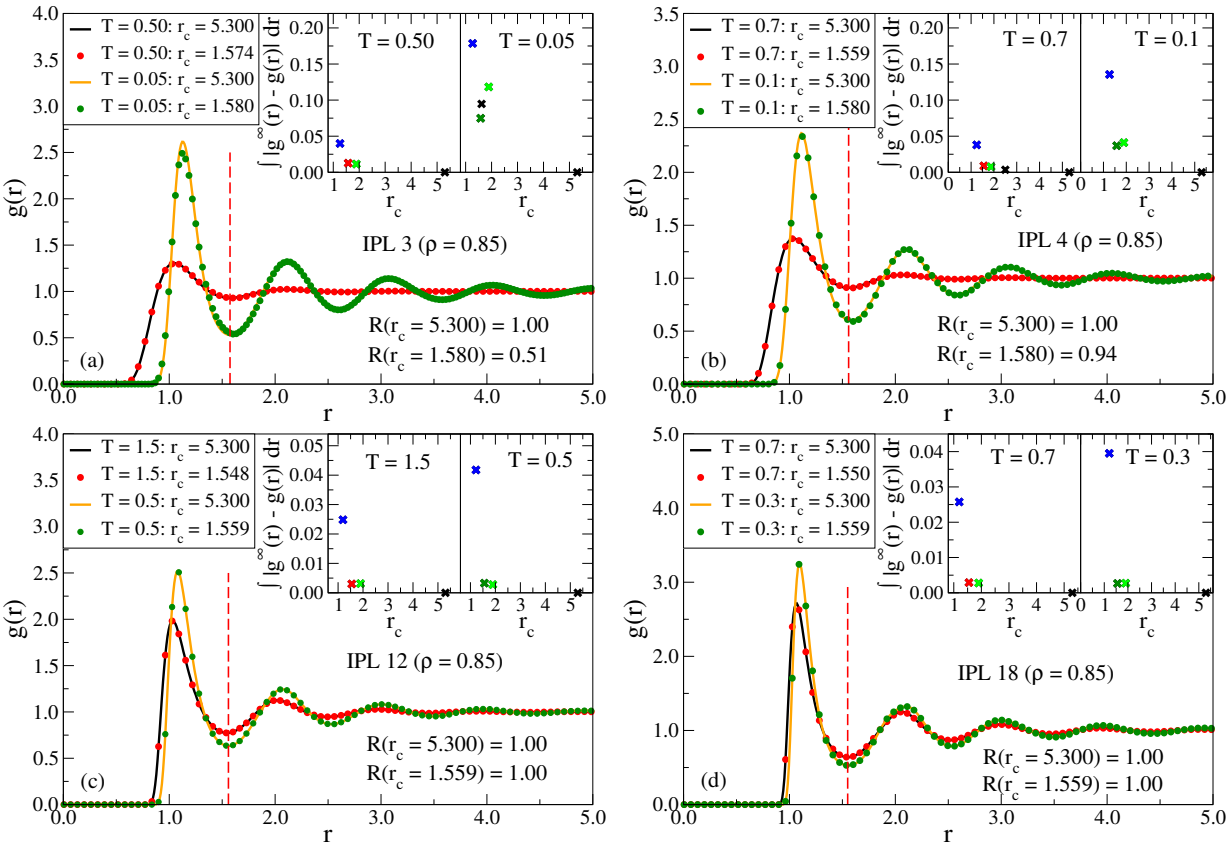

Figure 5.3: *RDFs for single-component IPL fluids with exponents $n = 3, 4, 12, 18$, each simulated at two temperatures and density $\rho = 0.85$ (Figs. 5.3(b) and (d) are taken from Paper III). The black and orange curves show reference simulation results using a large SF cutoff representing the true IPL behavior, whereas the red and green circles give results from simulations with an FCS cutoff (marked by the vertical red dashed lines). The insets quantify the deviations in the RDF from the reference RDF as functions of the SF cutoff; deviations increase dramatically when the cutoff enters the FCS (blue crosses). In all panels, the virial/potential energy correlation coefficient R is given for the lowest temperature state point ($R = 1$ for IPL systems with infinite cutoff). (a) $n = 3$, $T = 0.50$ and $T = 0.05$. (b) $n = 4$, $T = 0.70$ and $T = 0.10$. (c) $n = 12$, $T = 1.5$ and $T = 0.50$. (d) $n = 18$, $T = 0.70$ and $T = 0.30$.*

Next, we consider in Figs. 5.4(a)-(d) the dynamics of the IPL fluids by showing the incoherent intermediate scattering function (ISF) defined by (Hansen and McDonald [2006])

$$F_s(\mathbf{q}, t) = \langle \exp[i\mathbf{q} \cdot (\mathbf{r}(t) - \mathbf{r}(0))] \rangle, \tag{5.3}$$

for the lowest temperature state points of Fig. 5.3. We average over wave vectors $\mathbf{q}$ in, respectively, the x, y, and z-direction and present results for $\mathrm{q} = |\mathbf{q}|$ which corresponds approximately to the first diffraction peak in the static structure factor of the liquid.

The black and red curves show, respectively, a large SF cutoff and an FCS cutoff. The blue curves show an SF cutoff at the distance of the half-height from the first minimum of the RDF towards the first maximum. The green curves show a cutoff to the right of the first

minimum of the RDF, at the same difference in distance between the red and blue curves. To a good approximation, for all IPL fluids, the dynamics attained using the FCS cutoff is identical to that of the large SF cutoff. Interestingly for the $n = 3$ IPL fluid, a larger SF cutoff (green curve) provides a slightly worse approximation to the dynamics than the FCS cutoff.

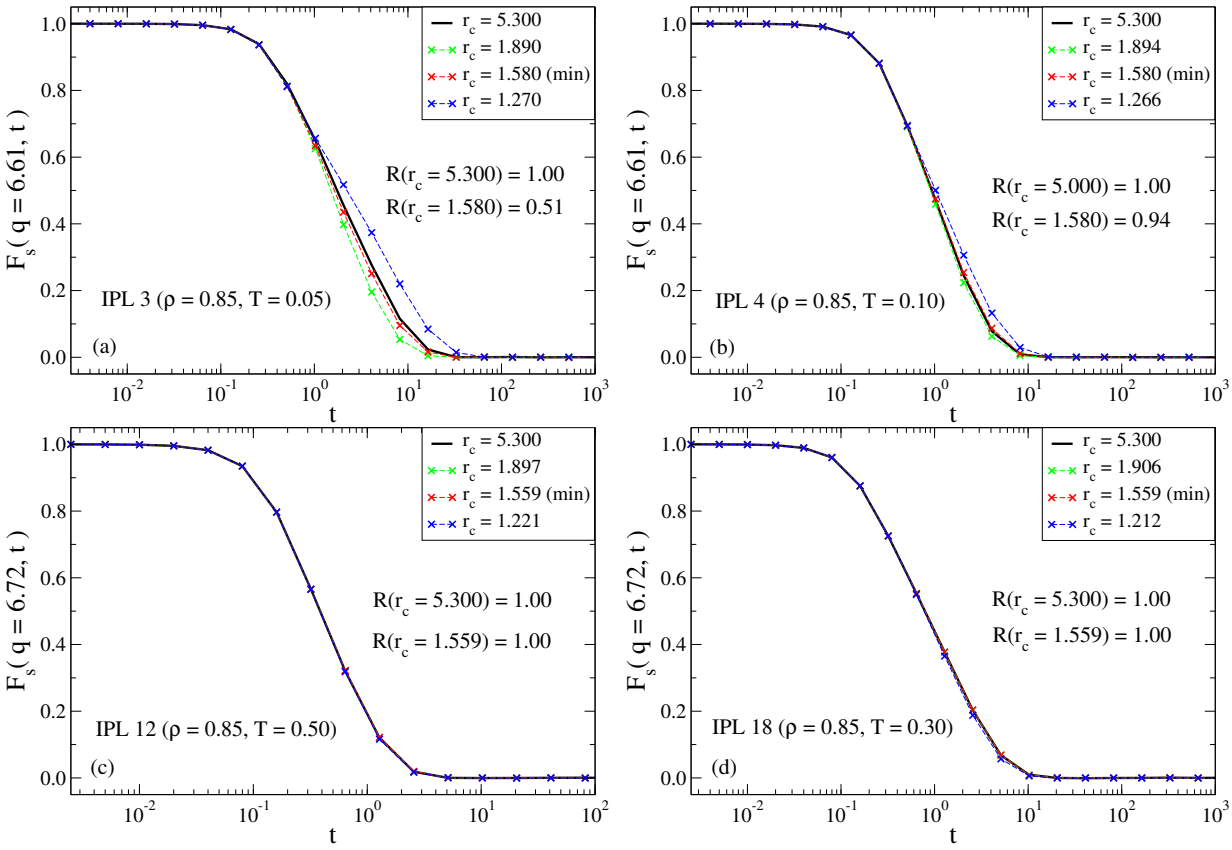

Figure 5.4: *Incoherent ISFs for the IPL fluids at the lowest temperature state points of Fig. 5.3 (Figs. 5.4(b) and (d) are taken from Paper III). The black curves give results for a large cutoff, the red crosses for an FCS cutoff (marked by the vertical red dashed lines in Fig. 5.3). In all panels, the virial/potential energy correlation coefficient R is given at the simulated state point ($R = 1$ for IPL systems with infinite cutoff). (a) $n = 3$, $T = 0.05$. (b) $n = 4$, $T = 0.10$. (c) $n = 12$, $T = 0.50$. (d) $n = 18$, $T = 0.30$.*

IPL fluids with infinite cutoff are perfectly correlating with $R = 1$, and the results presented in this section thus call for further investigations into whether the proposed conjecture also holds when the virial/potential energy correlation decreases.

5.2 Generalized Kob-Andersen binary LJ mixtures

In this section, we consider the application of FCS cutoffs to generalized KABLJ mixtures (see Appendix A) with repulsive exponent $m = 12$ and attractive exponents $n = 4, 6$. These

systems are both strongly correlating liquids. Figure 5.5 shows the AA-particle pair potentials of these systems.

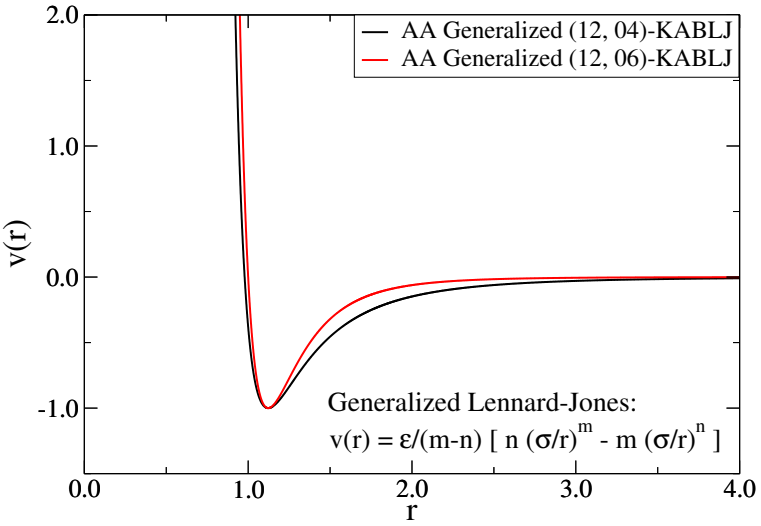

Figure 5.5: *AA-particle generalized KABLJ pair potentials with repulsive exponent $m = 12$ and attractive exponents $n = 4, 6$.*

Here and in the forthcoming sections, we use the definitions and meanings introduced in Sec. 5.1 with respect to the figures. Figure 5.6 shows AA-particle RDFs of the generalized KABLJ mixtures applying an FCS cutoff and a very large cutoff. For both systems, we again observe excellent agreement between these two cutoff schemes.

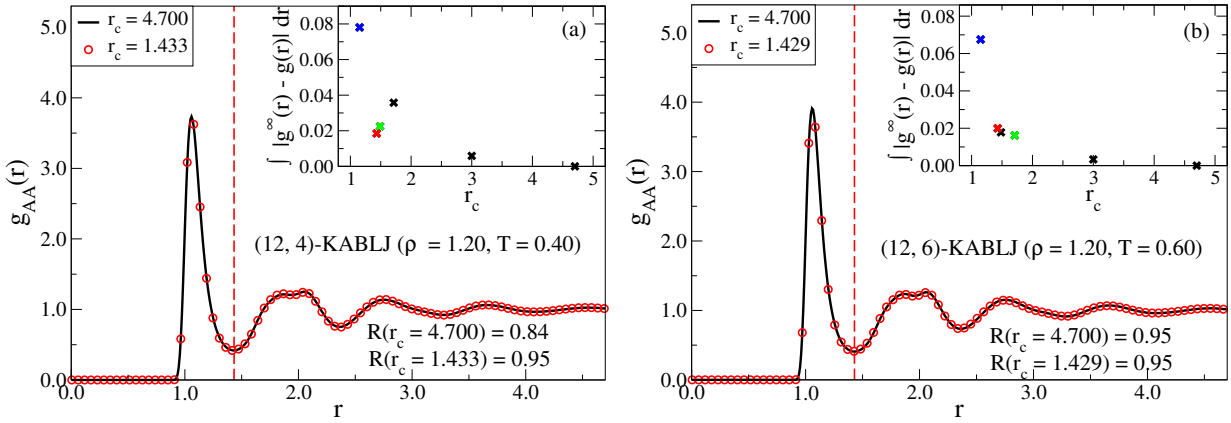

Figure 5.6: *AA-particle RDFs of generalized KABLJ mixtures (Fig. 5.6(a) is taken from Paper III) with repulsive exponent $m = 12$ and attractive exponent n using an FCS cutoff (red) and a very large cutoff (black). (a) $n = 4$, $\rho = 1.20$, and $T = 0.40$. (b) $n = 6$, $\rho = 1.20$, and $T = 0.60$.*

Turning then to the dynamics, the A-particle incoherent ISFs are shown in Fig. 5.7 for the same state points as in Fig. 5.6. The FCS cutoff gives an excellent approximation to

the true dynamics (black curve). We note, however, very minor deviations between the FCS cutoff and the reference simulation, and it is related to the way we delimit the FCS. The interested reader is referred to Appendix B of Paper III for more details on a different way of delimiting the FCS.

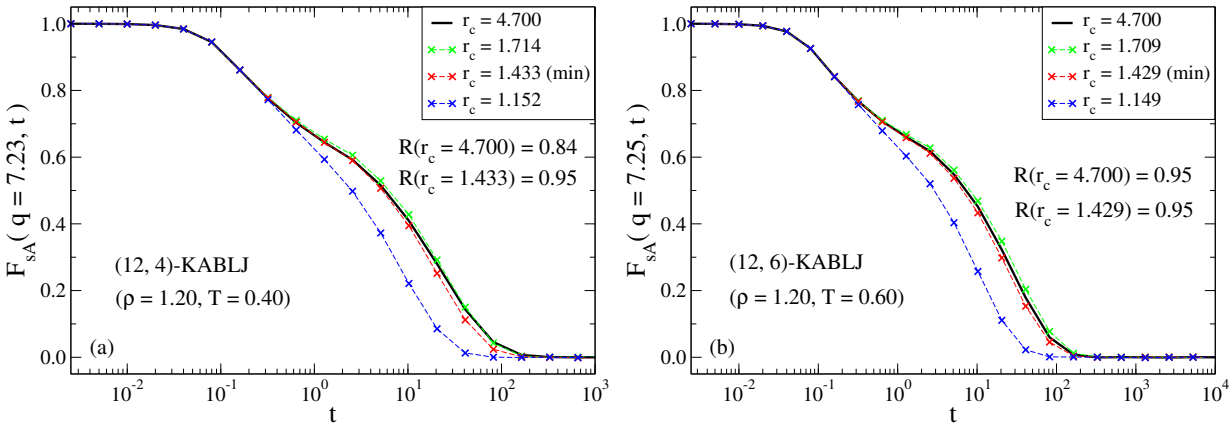

Figure 5.7: *A-particle incoherent ISFs of generalized KABLJ mixtures (Fig. 5.7(a) is taken from Paper III) with repulsive exponent $m = 12$ and attractive exponent n using an FCS cutoff (red) and a very large cutoff (black). The blue curves give results within the FCS. (a) $n = 4$, $\rho = 1.20$, and $T = 0.40$. (b) $n = 6$, $\rho = 1.20$, and $T = 0.60$.*

Paper III additionally shows results for the generalized KABLJ mixture with attractive exponent $n = 10$, and the Wahnström binary LJ mixture which are both strongly correlating liquids. For both of these systems we arrive at results similar to those shown in this section, i.e., the FCS cutoff gives a good approximation to the true structure and dynamics.

5.3 Dzugutov liquid

We have so far only studied systems that are strongly correlating, and we now therefore turn to study systems with $R < 0.90$, i.e., non-strongly correlating liquids. An example of which is the Dzugutov (DZ) liquid (Dzugutov [1992]) with $R \approx 0.71$. Figure 5.8 shows the DZ pair potential which was originally proposed as a candidate for a good model glass former, since it penalizes the distances corresponding to the next-nearest neighbors of the face-centered cubic lattice. The DZ liquid was, however, found upon medium supercooling to create quasi-crystals (Dzugutov [1993]).

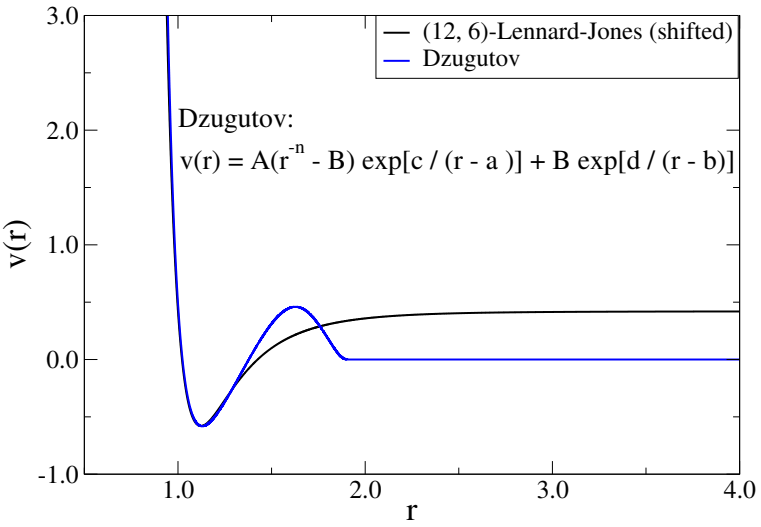

Figure 5.8: *The DZ pair potential (blue curve, taken from Paper III). Also shown is the LJ pair potential (black curve). The DZ potential approximates the LJ potential around the first minimum but has a maximum at larger distances corresponding to the next-nearest neighbors of the face-centered cubic lattice. See Appendix A for definitions of the constants.*

Figure 5.9 shows RDFs and ISFs of the DZ liquid in, respectively, Figs. 5.9(a) and (b), applying an FCS cutoff and a very large SF cutoff. We see that both the structure and the dynamics of the DZ liquid are not approximated well when using an FCS cutoff. This is not surprising given the fact that using an FCS cutoff removes the maximum of the DZ potential. What is important here, however, is that the poor FCS-cutoff results correlate with the fairly weak virial potential-energy correlations ($R \approx 0.71$). This suggests studying other non-strongly correlating liquids in order to investigate whether this is a general trend.

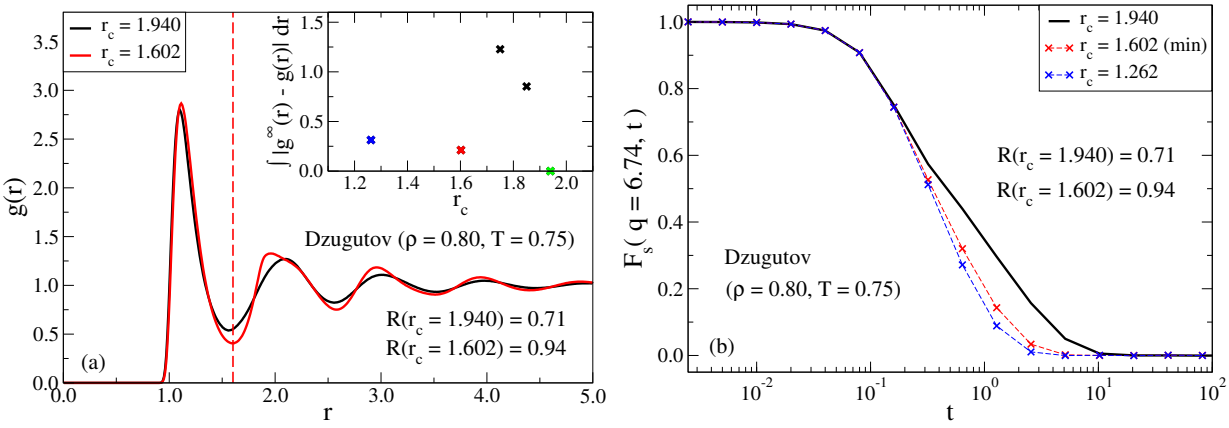

Figure 5.9: *The effect on the structure and dynamics (taken from Paper III) when the cutoff for the DZ liquid at $\rho = 0.80$ and $T = 0.75$ ($R = 0.71$) is varied. The red and black curves give, respectively, results for an FCS cutoff and a large cutoff. (a) RDFs. The inset quantifies the deviation in the RDF from the reference RDF as a function of the cutoff. (b) The incoherent ISF, including results for a cutoff within the FCS (blue crosses).*

5.4 Hansen-McDonald molten salt

We consider here a model of a singly-charged molten salt (i.e., a two-component model with $R = 0.15$) due to Hansen and McDonald (Hansen and McDonald [1975]). Figure 5.10 shows the results for structure and dynamics. The structure is poorly approximated using an FCS cutoff, whereas the dynamics to a good approximation is identical to the large SF cutoff. These results are consistent with recent results of Hansen *et al.* [2012] who studied the Hansen-McDonald molten salt model and concluded that large SF cutoffs are needed in order to get good simulation results.

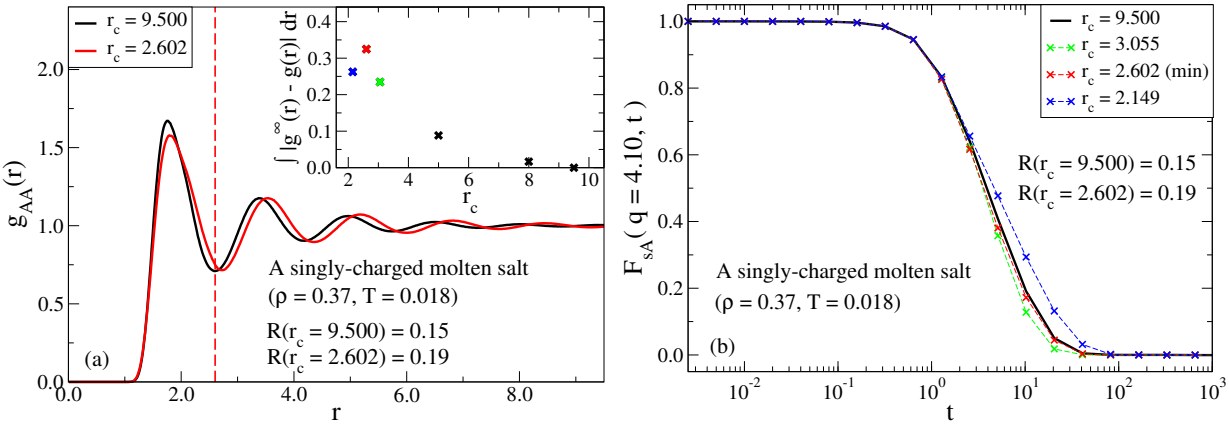

Figure 5.10: *The effect on the structure and dynamics (taken from Paper III) when the cutoff for the Hansen-McDonald molten salt at $\rho = 0.37$ and $T = 0.018$ ($R = 0.15$) is varied. The red and black curves give, respectively, results for an FCS cutoff and a large reference cutoff. (a) AA-RDFs. The inset quantifies the deviation in RDF from the reference RDF as a function of the cutoff. (b) The A-particle incoherent ISF including results for a cutoff within the FCS (blue crosses).*

5.5 Lewis-Wahnström OTP

Turning the study to molecules, we investigate the Lewis-Wahnström OTP model; a rigid molecule with the shape of an isosceles triangle (see Appendix A). The structure and dynamics of this model, when an FCS cutoff and a large SF cutoff are applied, are given in Fig. 5.11. The spikes of the RDFs derive from the rigid-bonds of the model. We observe good results using the FCS cutoff also for molecules, consistent with the fact that this model is strongly correlating ($R = 0.91$). Again, the small deviations in the dynamics are related to delimiting the FCS (see Paper III).

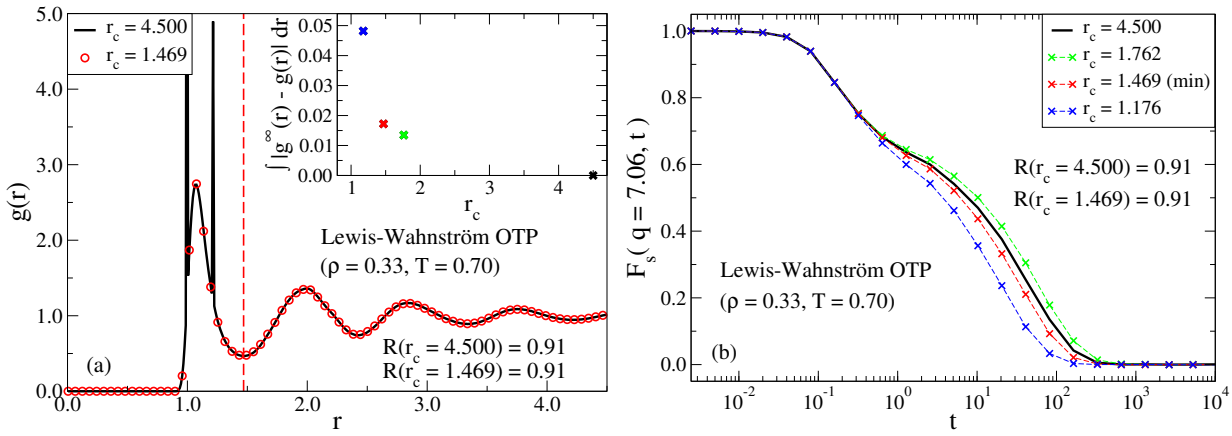

Figure 5.11: *The effect on the structure and dynamics (taken from Paper III) when the cutoff for the Lewis-Wahnström OTP model at $\rho = 0.33$ and $T = 0.70$ ($R = 0.91$) is varied. The red and black curves give, respectively, results for an FCS cutoff and a large reference cutoff. (a) RDFs. The inset quantifies the deviation in RDF from the reference RDF as a function of the cutoff. (b) The incoherent ISF including results for a cutoff within the FCS (blue crosses).*

5.6 Rigid SPC/E water

As the last example we consider the rigid SPC/E water model in Fig. 5.12. This model is not strongly correlating at ambient conditions, a fact that directly reflects water's well-known density maximum (Bailey *et al.* [2008a]). The FCS cutoff fails to approximate the structure, however, as is the case with the Hansen-McDonald molten salt model, the dynamics seems to be very well approximated using the FCS cutoff. Interestingly, using an SF cutoff at $r_c = 0.924$ (blue curve in Fig. 5.12(b)) the dynamics slows down many orders of magnitude and is related to crystallization of the model.

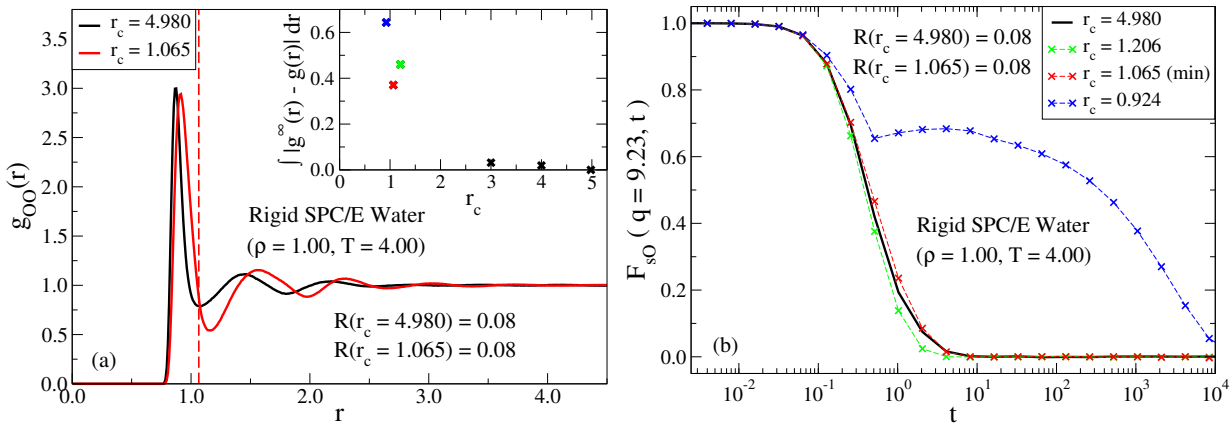

Figure 5.12: *The effect on the structure and dynamics (taken from Paper III) when the cutoff for the rigid SPC/E water model at $\rho = 1.00$ and $T = 4.00$ ($R = 0.08$) is varied. The red and black curves give, respectively, results for an FCS cutoff and a large reference cutoff. (a) Oxygen-oxygen RDFs. The inset quantifies the deviation in RDF from the reference RDF as a function of the cutoff. (b) The oxygen incoherent ISF including results for a cutoff within the FCS (blue crosses).*

This hereby concludes our investigation on FCS cutoffs in strongly and non-strongly correlating liquids, where the next section summarizes the observed results. Recall that more model systems are avaliable in Paper III.

5.7 Summarizing the FCS results

Paper III and the previous sections showed that structure and dynamics are well approximated in simulations using an FCS cutoff for the following atomic and molecular systems:

- IPL fluids ($n = 3, 4, 6, 12, 18$),
- SCLJ liquid at density $\rho = 0.85$,
- Generalized KABLJ mixtures,
- Wahnström binary LJ mixture,
- Single-component Buckingham liquid,
- The Lewis-Wahnström OTP model,
- The asymmetric dumbbell model.

These systems are all strongly correlating (Bailey *et al.* [2008a,b], Gnan *et al.* [2009], Schrøder *et al.* [2009a, 2011]). Thus for strongly correlating liquids it is enough to know the intermolecular interactions within the FCS in order to accurately simulate structure and dynamics.

The simulations showed further that for all of the following atomic and molecular systems structure and/or dynamics are not properly reproduced, when an FCS cutoff is used:

- Dzugutov liquid,
- Lennard-Jones Gaussian liquid,
- Gaussian core model,
- Hansen-McDonald molten salt model,
- Rigid SPC/E water model.

None of these liquids are strongly correlating. For all these systems larger cutoffs are needed in order to faithfully reproduce the system's physics (Fennell and Gezelter [2006], Hansen *et al.* [2012]).

In conclusion, a shifted-forces FCS cutoff leads to accurate results *if and only if* the liquid is strongly correlating at the state point in question. This suggests that strongly correlating liquids are *characterized* by the fact that intermolecular interactions beyond the FCS can be ignored which was the conjecture proposed at the start of this chapter. These results then question some of the major assumptions in liquid-state physics (Weeks *et al.* [1971], Widom [1967]), and we touch upon this issue in the next section (see also Paper III).

5.8 Is the Weeks-Chandler-Andersen approach to liquids correct?

In a seminal paper by B. Widom in Science from 1967 (Widom [1967]), the following picture of simple uniform liquids is proposed,

"*..., in a fluid as dense as a liquid at its triple point, the attractive forces exerted on any molecule by its neighbors largely cancel, while the negative potentials largely add, ...*".

This and other works (for instance, Reiss [1965]) later inspired the Weeks-Chandler-Andersen (WCA) approach to liquids (Weeks *et al.* [1971]), where the liquid is related to a reference system with pair interactions that are truncated at the potential minimum. The WCA method was shown to give a good approximation to the structure of simple liquids, and later on the method was conjectured to work for the dynamics too (see Andersen *et al.* [1976], and references therein).

We have in the previous sections seen that for strongly correlating liquids, it is the FCS interactions that determine the structure and dynamics of the liquid, and not simply the repulsive forces. Is the picture proposed by Widom and others then correct? As an example, the minimum of the LJ potential is located at the fixed distance $r_c = 2^{1/6}\sigma \approx 1.12\sigma$, and near the LJ triple point, the FCS is located at $r_c \approx 1.50\sigma$. The WCA method does then not take into account all the relevant interactions for the determination of the structure and dynamics of the liquid. Berthier and Tarjus also showed that using the WCA method in the supercooled liquid regime gave rise to a significantly different dynamics for the KABLJ

mixture (Berthier and Tarjus [2009, 2011]). The location of the FCS does, however, depend on state point and implies that at extremely high densities the WCA method takes into account all the relevant interactions, since the FCS, here, is "pushed" to the left of the potential minimum. This was exactly a point made by Toxvaerd and Dyre (Toxvaerd and Dyre [2011b]). It should, however, be noted that in doing so, some of the WCA repulsion may then also be removed.

5.9 What is a simple liquid?

In the light of the results presented in the previous sections, the class of strongly correlating liquids may now be characterized in three, but equivalent, ways as follows

1. The FCS interactions determine structure and dynamics (chemical).
2. The existence of isomorphs in the phase diagram (physical).
3. Invariance curves of the reduced constant-potential-energy hypersurface $\tilde{\Omega}$ in the phase diagram (mathematical).

The chemical characterization was detailed in the previous sections (see also Paper III), the physical characterization in Chapter 2, and the mathematical characterization of strongly correlating liquids is shown in Appendix A of Gnan *et al.* [2009]. We will return to the mathematical characterization in Chapter 9 and simply state it for now. From each of these characterizations, the simpler properties of strongly correlating liquids may be derived; perhaps most easily from the physical characterization.

Since the class of strongly correlating liquids is characterized in three distinct ways this fact implies that the class is *fundamental*. In addition, since the properties derived from these concepts are simpler than what is known for other types of liquids it suggests that the class of strongly correlating liquids should be identified with the "class of simple liquids". We thus propose that

Strongly correlating liquid = Simple liquid

Traditionally, a simple liquid is defined as systems with, *nearly spherical, nonpolar molecules (particles) interacting via radially symmetric pair potentials* (Hansen and McDonald [2006]). The new definition of a simple liquid thus has a certain overlap with this traditional viewpoint, but also important difference. For instance, in the new definition;

1. Simplicity is quantified by the continuous variable R and varies throughout the phase diagram; it is not an on/off property.
2. All systems may become simple at very high pressures if crystallization is avoided (this is a conjecture based on results in Papini *et al.* [2011]).
3. $R = 1$ (IPL liquid) is the prime example or "gold standard" of a simple liquid.

4. Not all atomic systems with radially symmetric pair potentials are simple at low pressures (i.e., Dzugutov liquid, GCM, and Hansen-McDonald molten salt).

5. Elongated non-spherical molecules may also be simple (for instance, small polymers Veldhorst [2013]).

In defining strongly correlating liquids as simple liquids one obtains a quantitative criterion via R for when a liquid is simple at a given state point, however, the answer is not *yes* or *no* anymore based on the given system. A priori, there is no particular reason as to why this definition should be clear-cut, and it is argued in Paper III that the latter is actually not to be expected due to the diversity of liquids in general.

Chapter 6

ISOMORPHS IN MODEL MOLECULAR LIQUIDS (PAPER V)

Chapter II introduced the concept of isomorphs for atomic systems (Gnan *et al.* [2009]) and considered their implications. For example, it was shown in Chapter III that isomorphs imply a separation of temperature into a product of a function of excess entropy per particle and a function of density. In this connection, one may wonder whether it is possible to extend the isomorphic framework beyond atomic systems to help improve the understanding of more "complex" systems. This could perhaps be liquids composed of molecules, liquids undergoing a homogenous shear flow (Evans and Morriss [1984], Ladd [1984], Separdar *et al.* [2012]), or even liquids that are spatially confined. Let us take liquids that are spatially confined as an example. Confined liquids exhibit stratification, i.e., the particles of the liquid order themselves in well-defined layers, creating a non-uniform density profile in the liquid (Schoen *et al.* [1987], Toxvaerd [1981]). In addition to stratification there may be strong interactions with the confining walls that can have a significant impact on the structure and dynamics of the liquid. Extending isomorphs beyond atomic systems could thus appear problematic due to new and rich phenomenology encountered in "complex" systems.

Truskett, Errington, and co-workers studied in a number of articles (Chopra *et al.* [2010a], Goel *et al.* [2008, 2009], Mittal *et al.* [2006, 2007]) the effect of confinement on Rosenfeld's excess entropy scaling (Rosenfeld [1977, 1999]), i.e. that a reduced transport coefficient $\tilde{X}$ can be written as some function of excess entropy $\tilde{X} = f(S_{\rm ex})$. They concluded that Rosenfeld's excess entropy scaling is also valid for confined systems and that the functional form f to a good approximation is unaffected by the degree of confinement. Additionally, Schrøder *et al.* [2009b] studied scaling of structure and dynamics for systems composed of rigid molecules: the asymmetric dumbbell model and the Lewis-Wahnström OTP model. More specifically, they considered state points in the phase diagram with identical ρ^γ/T, as motivated by pure IPL systems, and tested for collapse of, for instance, the reduced unit radial distribution function. A good collapse of the considered quantities was hereby achieved.

The previous observations are all consistent with the properties of isomorphs for (bulk) atomic systems. In the case of Schrøder *et al.* [2009b], the reduced-unit radial distribution function is identical for isomorphic state points, and in the case of Truskett, Errington, and co-workers, since $\tilde{X}$ and $S_{\rm ex}$ are both invariant along an isomorph, a reduced transport coefficient can be written as some function of excess entropy. These results thus motivate further investigations into extending the isomorphic framework to these types of "complex" systems, and such an investigation is performed in this chapter for systems of rigid molecules, whereas the next chapter considers confined systems.

6.1 Extending the isomorph concept

We consider here the extension of isomorphs to systems composed of rigid (non-flexible) molecules. In the definition of isomorphs for atomic systems (see Sec. 2.2), the mapping among microconfigurations of isomorphic state points is defined via an isotropic scaling of the atomic coordinates. This mapping thus violates the rigid structure of the molecules, and the first task is to formulate a definition of isomorphs that preserves the rigidity of the molecules. A simple modification of isomorphs is to redefine the mapping among microconfigurations in terms of the molecular center-of-masses. In this way, the mapping does not violate the rigid structure of the molecules.

We thus define two state points (ρ_1, T_1) and (ρ_2, T_2) in the phase diagram of a liquid composed of rigid molecules to be isomorphic if the following holds: Whenever two configurations of state points (1) and (2) for all molecules i have identical reduced center-of-mass coordinates

$$\rho_1^{1/3}\mathbf{r}_{CM,i}^{(1)} = \rho_2^{1/3}\mathbf{r}_{CM,i}^{(2)}, \tag{6.1}$$

and identical Eulerian angles (Gray and Gubbins [1984])

$$\phi_i^{(1)} = \phi_i^{(2)},\ \theta_i^{(1)} = \theta_i^{(2)},\ \chi_i^{(1)} = \chi_i^{(2)}, \tag{6.2}$$

these two configurations have proportional Boltzmann factors, i.e., [where $\mathbf{R} \equiv (\mathbf{r}_{CM,1}, \phi_1, \theta_1, \chi_1, ..., \mathbf{r}_{CM,N}, \phi_N, \theta_N, \chi_N)$]

$$e^{-U(\mathbf{R}^{(1)})/k_BT_1} = C_{12}e^{-U(\mathbf{R}^{(2)})/k_BT_2}. \tag{6.3}$$

As for atomic isomorphs, C_{12} is a constant that depends only on the state points (1) and (2). In contrast to atomic systems, since the bonds do not follow the overall scaling of the system, the above definition of isomorphs does not imply the existence of exact isomorphs for rigid molecules with intermolecular IPL interactions.

Having defined isomorphs for systems composed of rigid molecules, we may use the direct isomorph check in analogy to atomic systems (see Section 2.2.4) in order to examine the presence of isomorphs in specific model systems. Figure 6.1 performs a direct isomorph check for the asymmetric dumbbell model, the model that was also investigated by Schrøder *et al.* [2009b].

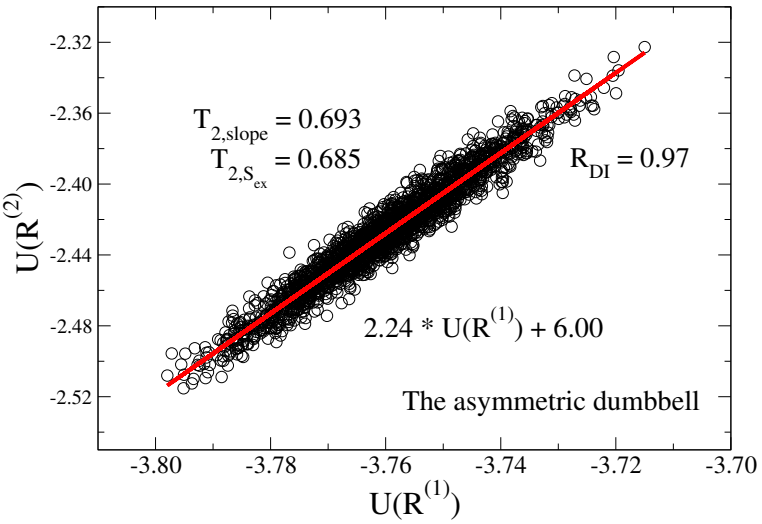

Figure 6.1: *Direct isomorph check for the asymmetric dumbbell model (taken from Paper V). During a simulation at state point (ρ_1, T_1) = (0.868, 0.309) the center-of-mass of each dumbbell is scaled to density $\rho_2 = 0.999$, keeping the Eulerian angles fixed. The potential energy is evaluated from the scaled configurations and plotted against the potential energy of the unscaled configurations. The temperature $T_{2,slope}$ of the isomorphic state point at density ρ_2 is calculated by multiplying the linear regression slope with T_1. $T_{2,S_{ex}}$ is the temperature of the isomorphic state point calculated by keeping the excess entropy constant (see Sec. 6.3).*

For a 15% density increase, the correlation coefficient of the direct isomorph check is $R_{DI} = 0.97$ and indicates (recall the discussion of Sec. 2.2.4) that the asymmetric dumbbell model has isomorphs in the above meaning of the term. These isomorphs are considered in more detail in Sec. 6.4. Additionally, we note from Fig. 6.1 that the intersection of the linear regression fit is non-zero, and thus $C_{12} \neq 1$.

6.2 Isomorph invariants in liquids composed of rigid molecules

The isomorphs defined in the last section for systems composed of rigid molecules differ slightly from the atomic case. A natural question is then: *Do all isomorph invariants for atomic systems generalize to molecular systems*? Most of the isomorph invariants for atomic systems generalize directly to molecular systems, however, some invariants must be modified to be consistent with the rigid molecular structure. For instance, it is easy to show (see Appendix B of Paper V) that the dynamics in reduced units of the individual particles, constituting a rigid molecule, is not invariant along an isomorph. In this case, it is necessary to consider the center-of-mass motion and the motion relative to the center-of-mass separately.

The canonical configurational probability for a system of N rigid molecules (Gray and Gubbins [1984]) is given by (where $d\mathbf{R} \equiv d\mathbf{r}_{CM,1} d\tau_1 \ldots d\mathbf{r}_{CM,N} d\tau_N$ with $\tau \equiv (\phi, \theta, \chi)$ and $d\tau = sin\ \theta\ d\theta\, d\phi\, d\chi$)

$$\hat{P}(\mathbf{R}) = \frac{e^{-U(\mathbf{R})/k_BT}}{\int e^{-U(\mathbf{R})/k_BT} d\mathbf{R}}. \tag{6.4}$$

In combination with Eq. (6.3), it follows that all mapped configurations of state points (1) and (2) have identical Boltzmann probabilities, i.e.,

$$\hat{P}(\mathbf{R}^{(1)}) d\mathbf{R}^{(1)} = \hat{P}(\mathbf{R}^{(2)}) d\mathbf{R}^{(2)}. \tag{6.5}$$

The proof of isomorph invariants, such as the center-of-mass structure, is thus similar to the derivation shown in Chapter II for atomic systems (see Sec. II of Paper V). For the dynamics, the center-of-mass motion is simply governed by Newton's 2nd law[1]

$$\mathbf{F}_{CM,i} = M_i \mathbf{a}_{CM,i}, \tag{6.6}$$

and we can use the same arguments here, too. For example, the following quantities appear as isomorph invariants for liquids composed of rigid molecules.

1. The center-of-mass structure in reduced units,
2. The center-of-mass dynamics in reduced units,
3. The excess entropy S_{ex},
4. The excess isochoric heat capacity C_V^{ex},
5. Any molecular relaxation time $\tilde{\tau}_\alpha$,
6. And more.

As for atomic systems by Eq. (6.5), isomorphic jumps (see Sec. 2.2) are also a property of isomorphs for systems composed of rigid molecules, where isomorphic jumps for the asymmetric dumbbell and Lewis-Wahnström OTP models can be found in Paper V.

6.3 Generating isomorphs for rigid molecules

As of this chapter, we have not considered how isomorphs in the phase diagram can be generated from a chosen state point. For atomic systems, an isomorph is generated by keeping the excess entropy constant (Gnan *et al.* [2009]). In the NVT ensemble, the excess entropy can conveniently be kept constant via the following exact relation

$$\gamma \equiv \frac{\langle \Delta W \Delta U \rangle}{\langle (\Delta U)^2 \rangle} = \Big(\frac{\partial \ln T}{\partial \ln \rho} \Big)_{S_{\text{ex}}}. \tag{6.7}$$

[1] The constraint force maintaining rigidity is an internal force and does not contribute to the center-of-mass motion. See Paper V for details on simulating molecules.

The procedure for generating an isomorph is as follows: 1) The left-hand side is calculated from the fluctuations at a given state point. 2) A new state point is identified by a discretization of Eq. (6.7) by changing the density by 1%. The temperature of the isomorphic state point is calculated from $\Delta \ln T = \gamma \Delta \ln \rho$. 3) The procedure is repeated, and in this way an isomorph is generated in the phase diagram.

The above procedure for generating isomorphs of atomic systems can be generalized to systems of rigid molecules since the excess entropy is also constant for isomorphs of molecular systems. It should, however, be noted that in going from atomic to molecular systems, there are different contributions to the potential energy U and virial W. For a system of rigid molecules interacting via the LJ potential (see Fig. 1.1), the potential energy and virial are

$$U = U_{LJ}, \tag{6.8}$$

$$W = W_{LJ} + W_{CON}. \tag{6.9}$$

The new term W_{CON} is the contribution to the virial deriving from the rigid bonds (see also Appendix A of Paper V). In generating an isomorph, the virial W must thus include this additional contribution.

6.4 The isomorphs of the asymmetric dumbbell model

We now consider the isomorphs of the asymmetric dumbbell model applying the procedure described in the former section for generating an isomorph. The corresponding results for isomorphs of the Lewis-Wahnström OTP model and a symmetric IPL dumbbell model can be found in Paper V. A drawing of the asymmetric dumbbell model (see Appendix A) is shown in Fig. 6.2 and is a simplistic computer model of Toluene. The asymmetric dumbbell model is a convenient model system to simulate, as it is not prone to crystallization, and can be cooled into a highly viscous state.

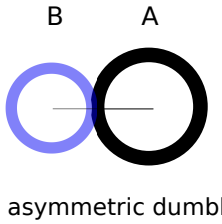

Figure 6.2: *A drawing of the asymmetric dumbbell model; a simplistic computer model of Toluene. The model details are found in Appendix A.*

Figure 6.3(a) shows molecular center-of-mass radial distribution functions in reduced units along an isomorph with 19% density increase. For comparison, an isotherm with 12% density increase is shown in Fig. 6.3(b). The structure is to a good approximation invariant along the isomorph whereas the isotherm shows slightly larger deviations in the scaling, especially near the second peak.

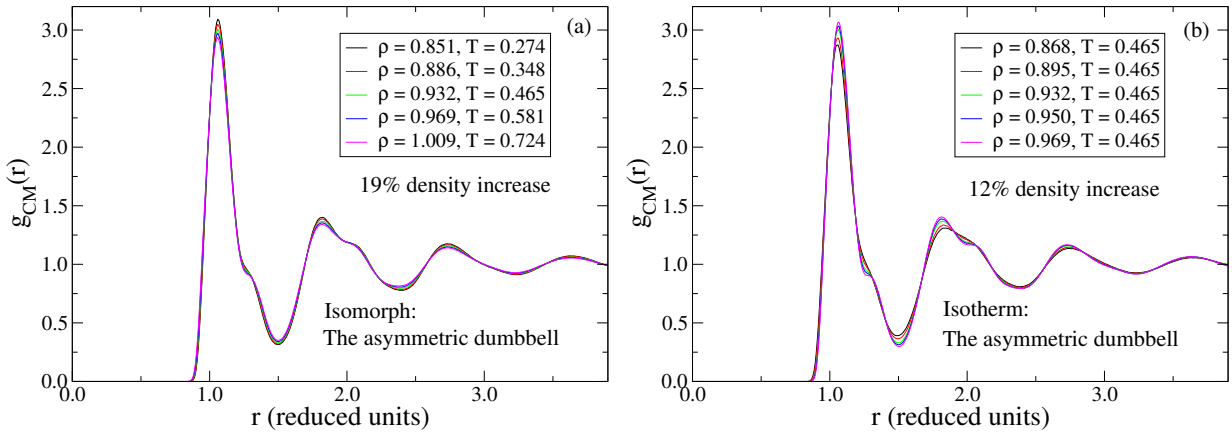

Figure 6.3: *Molecular center-of-mass radial distribution functions in reduced units ($\tilde{r} = \rho^{1/3} r$) for the asymmetric dumbbell model (taken from Paper V). (a) Along an isomorph with 19% density increase. (b) Along an isotherm with 12% density increase.*

Next, the invariance of the dynamics is quantified in Fig. 6.4 by probing the molecular center-of-mass incoherent intermediate scattering function at a wave vector q corresponding approximately to the first peak of the static structure factor. This function is shown along the same isomorph and isotherm as Fig. 6.3. An excellent collapse is seen for the dynamics along the isomorph while the isotherm shows approximately three orders of magnitude variation in the dynamics.

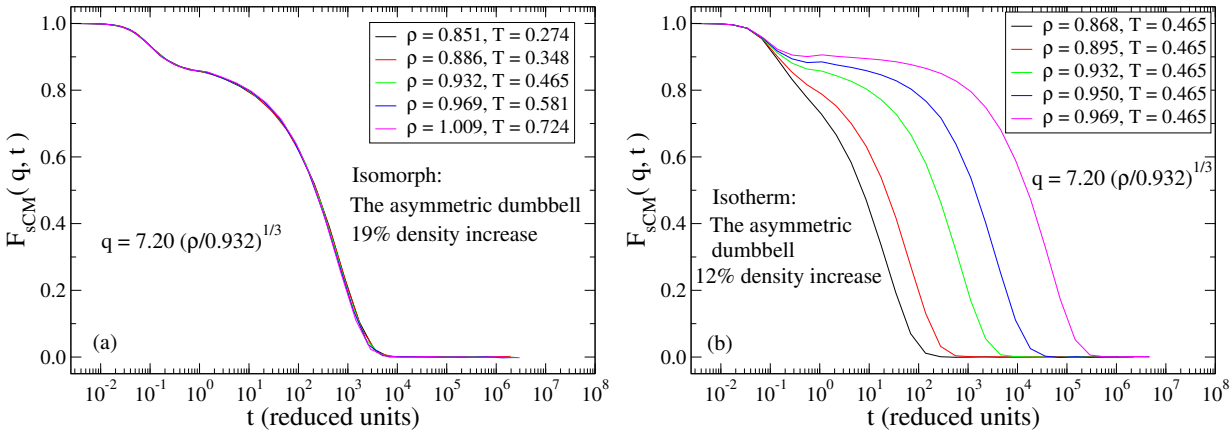

Figure 6.4: *Molecular center-of-mass incoherent intermediate scattering functions in reduced units ($\tilde{r} = \rho^{1/3} r$) for the asymmetric dumbbell model keeping the reduced wave vector q constant (taken from Paper V). (a) Along the isomorph of Fig. 6.3 with 19% density increase. (b) Along the isotherm of Fig. 6.3 with 12% density increase.*

The excess isochoric heat capacity $C_V^{\rm ex}$ (i.e., $C_V^{\rm ex} = C_V - C_V^{\rm id}$) was in Sec. 6.2 predicted to be invariant along an isomorph (recall, however, that $C_V^{\rm id}$ only adds a state point independent constant contribution). Figure 6.5 shows $C_V^{\rm ex}$ as a function of density along the previous isomorph and isotherm. The excess isochoric heat capacity changes less than 2% along the

isomorph while the isotherm shows a 25% increase. The heat capacity is thus to a good approximation invariant along an isomorph, but not along an isotherm.

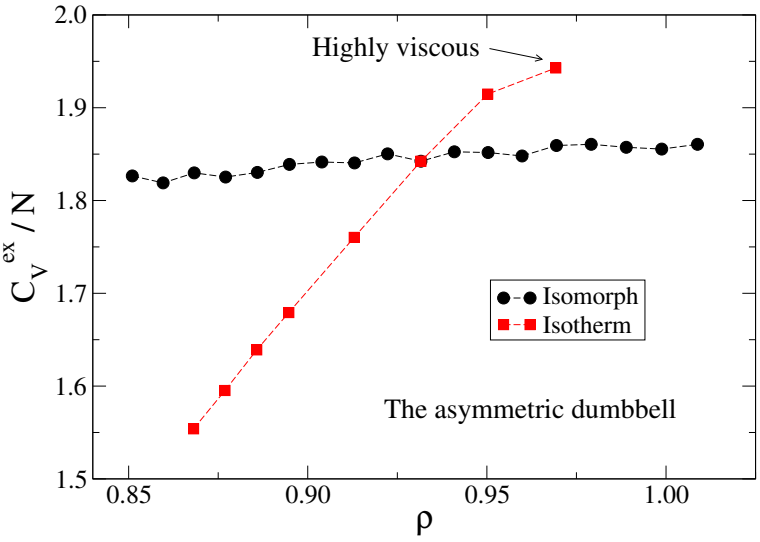

Figure 6.5: *The excess isochoric heat capacity per particle C_V^{ex}/N for the asymmetric dumbbell model (taken from Paper V) as a function of density along the isomorph (black) and isotherm (red, $T = 0.465$) of Figs. 6.3-6.4. The density increase is 19% and 12%, respectively. The excess isochoric heat capacity increases less than 2% along the isomorph while the isotherm shows a 25% increase. For the isotherm the dynamics becomes very slow for densities higher than $\rho = 0.950$ and the system becomes difficult to equilibrate properly.*

We conclude from the results presented here and in Paper V that systems composed of rigid molecules can also have isomorphs. This is the first example in extending isomorphs beyond the atomic system.

6.5 The approximative nature of isomorphs

In the study of supercooled liquids and the glass transition, it is an unresolved issue of what controls the average structural relaxation time $\tilde{\tau}_\alpha$. As in all parts of physics a theory is searched for which explains the phenomena and at the same time captures the very diverse spectrum of liquids. Any proposed universal theory must certainly hold for strongly correlating liquids.

The (reduced) average structural relaxation time is an isomorph invariant and can thus only be controlled by another isomorph invariant, for instance, the excess entropy. This observation is called the "isomorphic filter" (Gnan *et al.* [2009]) as it can be used to filter out some existing (universal) theories of the glass transition. The usual version of the theory of Adam and Gibbs (Adam and Gibbs [1965]) states that $\tilde{\tau}_\alpha \propto \exp[A/TS_c]$ (in which A is a constant and S_c is the configurational entropy) and does not pass the isomorphic filter since TS_c is not an isomorph invariant. The Adam-Gibbs relation does, however, pass the isomorphic filter if A is assumed to be the function of density $\mathrm{A}(\rho) = h(\rho)$.

Isomorphs are, however, approximate, and not all isomorph invariants for a strongly correlating liquid may be equally good in capturing a relaxation time. Figure 6.6 shows a reduced molecular relaxation time $\tilde{\tau}_\alpha$, extracted from the molecular center-of-mass intermediate scattering function when $F_{sCM}(\tilde{\tau}_\alpha) = 0.2$, for the asymmetric dumbbell model as a function of (a) excess entropy and (b) excess isochoric heat capacity. Both quantities are predicted to be invariant along an isomorph (see Sec. 6.2). It is clear from Fig. 6.6, that the heat capacity for this particular system does not describe $\tilde{\tau}_\alpha$ as well as the excess entropy and reflects the approximative nature of isomorphs. The correlation between $\tilde{\tau}_\alpha$ and C_V^{ex} is nevertheless high as expected from the isomorph theory.

The excess entropy at a given state point has been calculated from the thermodynamic relation $S_{\mathrm{ex}} = (U - F_{\mathrm{ex}})/k_B T$ using an approach similar to that outlined in Chopra *et al.* [2010a]. We first employ grand canonical transition matrix Monte Carlo simulation (Fitzgerald *et al.* [1999]) to obtain the density dependence of the absolute Helmholtz free energy of the fluid at relatively high temperature. We then use expanded ensemble Monte Carlo simulation (Lyubartsev *et al.* [1992]) to follow the variation in the Helmholtz free energy with temperature and density. For example, when moving along an isochore, we create a series of subensembles with variable T and fixed ρ. The potential energy U is obtained from an ensemble average within the relevant subensemble. A system of volume $V = 1000$ is used to complete grand canonical simulations. All expanded ensemble simulations employ $n = 1000$ molecules.

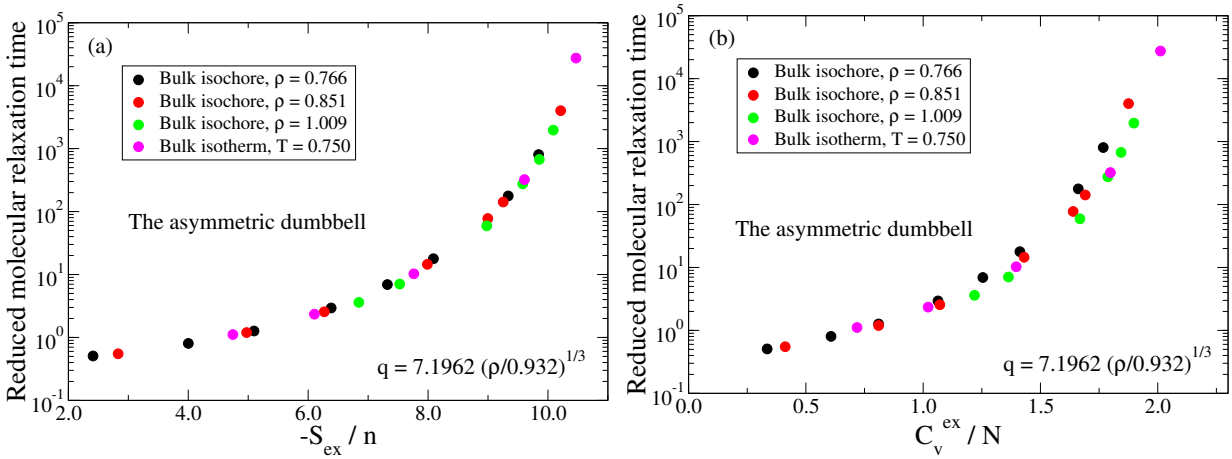

Figure 6.6: *Reduced molecular relaxation times $\tilde{\tau}_\alpha$ extracted from the molecular center-of-mass intermediate scattering function for the asymmetric dumbbell model along three different isochores and an isotherm. (a) As a function of excess entropy per molecule. (b) As a function of excess isochoric heat capacity per atom.*

In the next section, we consider briefly a more technical topic relating to isomorphs, namely the shape of isomorphs in the (U, W)-phase diagram (Schrøder *et al.* [2011]). This is a new phase diagram that provides a useful framework for studying isomorphs as shown in Schrøder *et al.* [2011].

6.6 The shape of isomorphs in the (U,W)-phase diagram

Schrøder *et al.* [2011] studied isomorphs of atomic single-component and multi-component LJ liquids with generalized exponents m and n. It was found that for given exponents (m, n) all isomorphs have the same shape in the (U,W)-phase diagram; i.e., a so-called master isomorph exists from which all isomorphs can be generated via a simple scaling of the WU-coordinates. For instance, the shape of isomorphs in the (U,W)-phase diagram of the SCLJ liquid and of the KABLJ mixture is the same. The proof of this fact uses that the structure (in reduced units) of the atomic positions to a good approximation is invariant along an isomorph. The shape of isomorphs for a LJ system (i.e. a system with $m = 12$ and $n = 6$) was shown to be given by the expressions below ($\tilde{\rho} \equiv \rho/\rho^*$ and the superscript $*$ denotes reference state point)

$$U = U_{LJ} = U_m^* \tilde{\rho}^4 + U_n^* \tilde{\rho}^2, \tag{6.10}$$

$$W = W_{LJ} = 4U_m^* \tilde{\rho}^4 + 2U_n^* \tilde{\rho}^2. \tag{6.11}$$

Here (U_m^*, U_n^*) are reference coefficients calculated from a chosen state point along the isomorph (see Schrøder *et al.* [2011] for details). For rigid molecular systems, however, the virial W has several contributions as follows (see Sec. 6.3)

$$U = U_{LJ}, \tag{6.12}$$

$$W = W_{LJ} + W_{CON}. \tag{6.13}$$

In addition, it is the molecular center-of-mass structure that is invariant along an isomorph. It is thus natural to wonder whether the above facts affect the presence of master isomorphs in rigid molecular systems with (generalized) intermolecular LJ interactions.

Figure 6.7 investigates this aspect in more detail, where Fig. 6.7(a) shows three different isomorphs in the (U,W)-phase diagram for the asymmetric dumbbell model[2] in two different versions: One for the total virial W and one replacing W with W_{LJ} along the isomorph. Figure 6.7(b) shows the same isomorphs as in (a), but after scaling each isomorph to superpose with a factor identified by trial and error. We see for both versions of the virial that all isomorphs collapse onto a single curve, i.e., a master isomorph still exists.

[2] Recall from Appendix A that the asymmetric dumbbell model has intermolecular LJ interactions, i.e. $m = 12$ and $n = 6$.

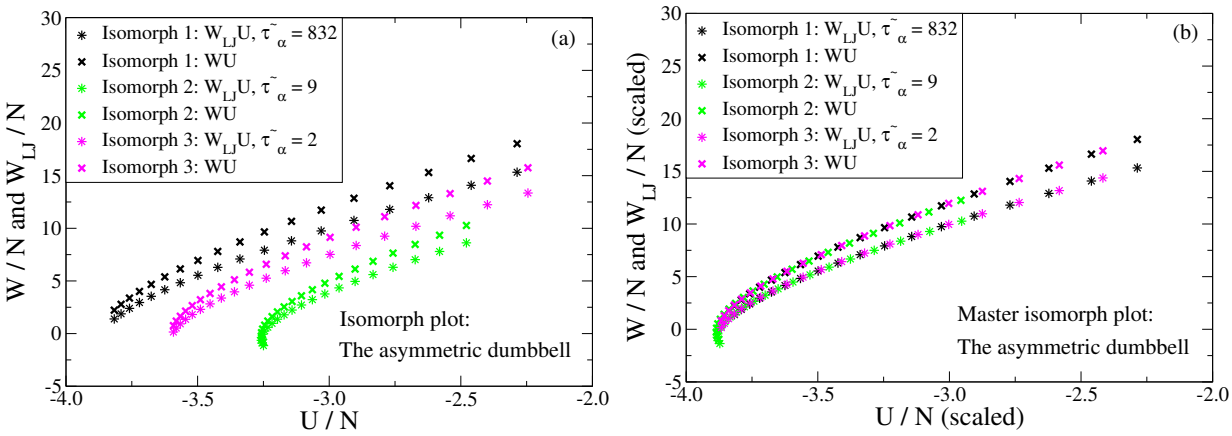

Figure 6.7: *(a) Three different isomorphs for the asymmetric dumbbell model in two different versions with 19%, 21% and 22% density increase, respectively (black, magenta and green). The crosses give the total virial W, the asterisks give $W_{LJ} = W - W_{CON}$. $\tilde{\tau}_\alpha$ is the reduced relaxation time extracted from the incoherent intermediate scattering function. (b) The same isomorphs as in (a) where WU and $W_{LJ}U$ are each scaled to superpose with a factor identified by trial and error. The black points have unity scaling factor. The figures have been taken from Paper V.*

A priori, however, the shape of isomorphs for molecular systems is expected to depend also on the topology of the molecule; taking the limit of vanishing bond length d for the asymmetric dumbbell model, one expects to recover the shape of isomorphs for atomic systems given by Eqs. (6.10) and (6.11). Figures 6.8(a) and (b) show four different isomorphs scaled to superpose in, respectively, the (U,W_{LJ}) and (U,W)-phase diagrams, corresponding to four dumbbells of length $d = 0.0400$, 0.184, 0.584, 0.784. The parameters are that of the asymmetric dumbbell model, and it is only the bond length that is changed in this study. The shape of isomorphs, in both versions of the virial, is seen to depend strongly on the length of the dumbbell.

The expressions of Eqs. (6.10) and (6.11), for atomic systems, given by the orange curve capture the shape of isomorphs for the dumbbell of length $d = 0.0400$. Considering, however, larger lengths ($d > 0.184$), deviations from the atomic shape start to occur. This is consistent with the fact that it is the molecular center-of-mass structure that is invariant along an isomorph (see Paper V). In addition, Paper V showed the existence of a "general" master isomorph in the (U,W_{LJ})-phase diagram between the asymmetric dumbbell model and the Lewis-Wahnström OTP model. Here, we see that this result depends on the specific molecular topology chosen to perform the comparison. In general, a theory for the shape of isomorphs in the (U,W_{LJ}) or (U,W)-phase diagrams for rigid molecules is also missing (see Paper V for additional details).

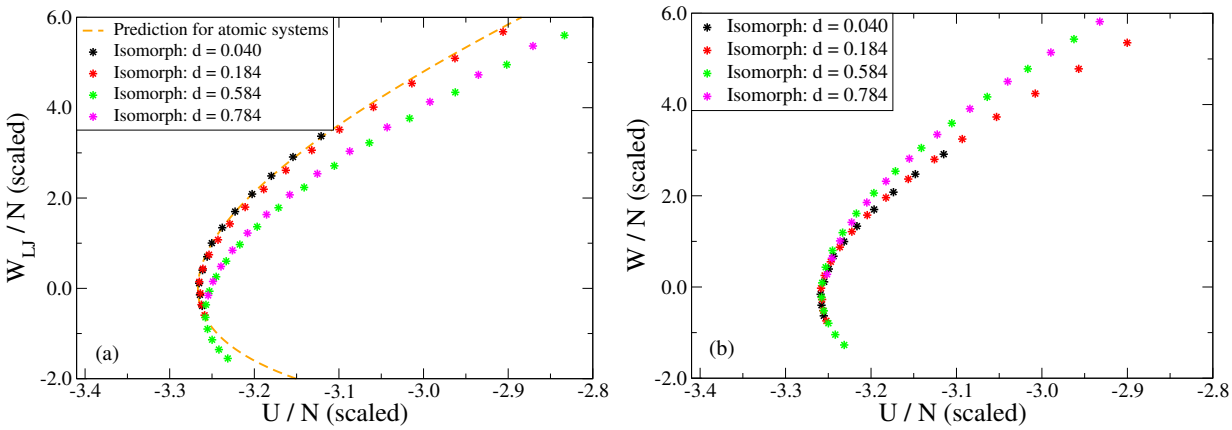

Figure 6.8: *Four different isomorphs scaled to superpose (the green curve has unity scaling factor) corresponding to four dumbbell models of lengths* $d = 0.0400, 0.184, 0.584, 0.784$. *The dumbbell of length* $d = 0.584$ *is the asymmetric dumbbell model, and it is only the bond length that is changed in the current study. (a) Isomorphs in the* (U, W_{LJ})*-phase diagram. The orange curve is calculated from Eqs. (6.10) and (6.11) and gives the shape of isomorphs for atomic systems. (b) Isomorphs in the* (U, W)*-phase diagram.*

Chapter 7

ISOMORPHS IN MODEL CONFINED LIQUIDS

Having established isomorphs for systems composed of rigid molecules in the previous chapter, we now leave bulk equilibrium liquids to study the existence of isomorphs in liquids that are spatially confined. Reviews of nanoscale-confined liquid's behavior may be found in, for instance, Alcoutlabi and McKenna [2005], Baschnagel and Varnik [2005], Richert [2011]. There exist many different forms of confining geometries relevant for the study of liquids in confinement, but we limit the investigation to a study of the so-called "slit-pore" geometry. The slit-pore is shown in Fig. 7.1 and consists of two identical and parallel walls confining the liquid in the direction normal to the walls (z-direction). The slit-pore remains infinite in the directions parallel to the walls (x and y-directions) and is thus a quasi two-dimensional system (Diestler and Schoen [1995]).

The phase diagram of the bulk (equilibrium) liquid may be described in terms of two variables, for example, density and temperature or pressure and temperature. The phase diagram of a liquid confined to a slit-pore is extended by an additional variable, namely with the width of the slit-pore H (Diestler and Schoen [1995]). The phase diagram is thus three-dimensional and may be described in terms of the variables (H, A, T), where A is the interfacial area of the slit-pore (Diestler and Schoen [1995]). The variables H and A appear as the analogs of volume for bulk systems. For very large H, the three-dimensional phase-diagram must, of course, "collapse" into the two-dimensional phase-diagram of the bulk system.

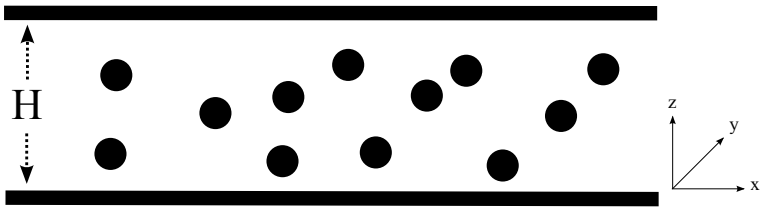

Figure 7.1: *A schematic picture of a slit-pore. Two identical and parallel walls confine the liquid in the direction normal to the walls (z-direction). H is the width of the slit-pore, i.e. the distance between the two confining walls. The system remains infinite in the directions parallel to the walls (x and y-directions), where A is the interfacial area of the slit-pore (Diestler and Schoen [1995]).*

As we have seen in the previous sections, the hallmark of isomorphs is the proportionality of Boltzmann factors of scaled microconfigurations. A priori, there is no particular reason to think that confinement should call for a change of the proportionality of Boltzmann factors. However, since the phase diagram of a confined liquid is three-dimensional, it is possible to define surfaces as well as curves where properties are constant. Isomorphs are curves in the phase-diagram of the bulk equilibrium liquid, but is the latter also the case for confined

systems? And if isomorphs remain curves, how should H and A be varied? These questions are studied in more detail in the next section.

7.1 Isomorphs in a three-dimensional phase diagram

As mentioned above, the proportionality of Boltzmann factors of scaled microconfigurations is expected to remain the hallmark of isomorphs in confinement. Similar to the bulk system, we may then use the "direct isomorph check" (see Sec. 2.2.4) to search for isomorphic state points in the phase diagram, and by doing so to clarify the nature of isomorphs in confinement.

Figure 7.2 shows four different direct isomorph checks for the asymmetric dumbbell model in a slit-pore where H and A are varied in different ways[1]. We consider the following direct isomorph checks:

1. A is varied by scaling the x and y-coordinates of the molecular center-of-masses with $\rho_r^{1/3}$ (where $\rho_r = 0.932/1.071$), keeping H constant.
2. H is varied by scaling the z-coordinates of the walls and the molecular center-of-masses with $\rho_r^{1/3}$, keeping A constant.
3. H and A are varied by scaling all lengths with $\rho_r^{1/3}$.
4. H and A are varied by scaling the x and y-coordinates with $\rho_r^{1/3}$, and the z-coordinates with $(1 + \rho_r^{1/3})/2$.

The highest correlation coefficient of the direct isomorph checks ($R_{DI} = 0.95$) is achieved when all lengths are scaled with the same factor whereas for constant H or A the correlation coefficient is significantly lower ($R_{DI} < 0.90$). The latter suggests that isomorphs are curves in the confined phase diagram rather than surfaces where properties are constant (recall that the phase diagram is three-dimensional). It should also be noted that the scaling of the z-coordinates by half the factor (scheme 4) gives a lower correlation coefficient ($R_{DI} = 0.93$) than scaling all lengths equally.

Thus it appears that isomorphs in the confined phase diagram are similar to bulk isomorphs. In defining isomorphs of the bulk system, however, the coordinates are scaled isotropically with $\rho^{1/3}$. The phase diagram of the confined liquid is three-dimensional, and the variables H and A should not appear in a definition of isomorphs in confinement, only via their product HA, but should reflect their independence.

[1] We delay the discussion of defining H in simulations to Sec. 7.3.

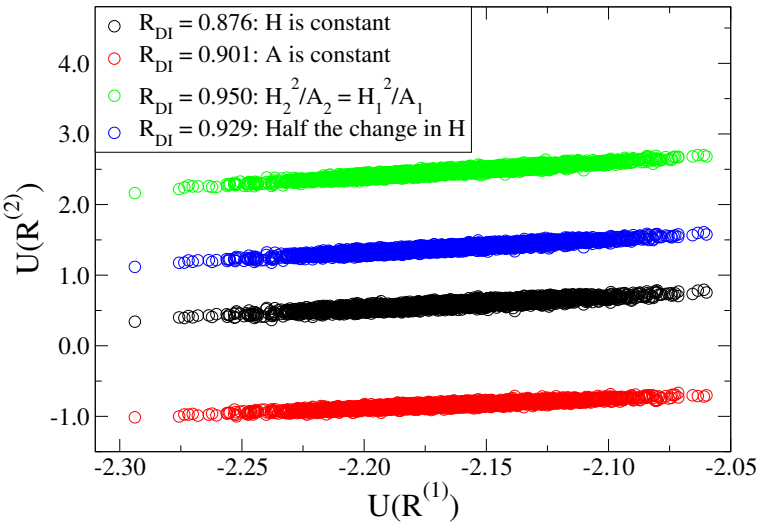

Figure 7.2: *Four different "direct isomorph checks" for the asymmetric dumbbell model in a slit-pore initiated from the state point $\rho = 0.932$, $T = 0.750$, $H = 8.13$. Black circles: A is varied by scaling the x and y-coordinates of the molecular center-of-masses with $\rho_r^{1/3}$ (where $\rho_r = 0.932/1.071$), keeping H constant. Red circles: H is varied by scaling the z-coordinates of the walls and the molecular center-of-masses with $\rho_r^{1/3}$, keeping A constant. Green circles: H and A are varied by scaling all lengths with $\rho_r^{1/3}$. Blue circles: H and A are varied by scaling the x and y-coordinates with $\rho_r^{1/3}$ and the z-coordinates with $(1+\rho_r^{1/3})/2$.*

The above results and discussion motivate the following definition of isomorphs in confinement: We define two state points (H_1, A_1, T_1) and (H_2, A_2, T_2) in the phase diagram of a liquid confined to a slit-pore, where the state variables are related via

$$\frac{H_1^2}{A_1} = \frac{H_2^2}{A_2}, \tag{7.1}$$

to be isomorphic if the following holds: Whenever two configurations of state points (1) and (2) for all molecules i have identical reduced center-of-mass coordinates ($\rho_H \equiv n/H$, $\rho_A \equiv n/A$, and n is the number of molecules)

$$\rho_{A_1}^{1/2}\, x_{CM,i}^{(1)} = \rho_{A_2}^{1/2}\, x_{CM,i}^{(2)}, \tag{7.2}$$

$$\rho_{A_1}^{1/2}\, y_{CM,i}^{(1)} = \rho_{A_2}^{1/2}\, y_{CM,i}^{(2)}, \tag{7.3}$$

$$\rho_{H_1}\, z_{CM,i}^{(1)} = \rho_{H_2}\, z_{CM,i}^{(2)}, \tag{7.4}$$

and identical Eulerian angles (Gray and Gubbins [1984])

$$\phi_i^{(1)} = \phi_i^{(2)},\ \theta_i^{(1)} = \theta_i^{(2)},\ \chi_i^{(1)} = \chi_i^{(2)}, \tag{7.5}$$

these two configurations have proportional Boltzmann factors, i.e., [where $\mathbf{R} \equiv (\mathbf{r}_{CM,1}, \phi_1, \theta_1, \chi_1, ..., \mathbf{r}_{CM,N}, \phi_N, \theta_N, \chi_N)$]

$$e^{-U(\mathbf{R}^{(1)})/k_BT_1} = C_{12}e^{-U(\mathbf{R}^{(2)})/k_BT_2}. \tag{7.6}$$

As before, C_{12} is a constant and depends only on the state points (1) and (2). The scalings introduced in Eqs. (7.2) - (7.4) take into account the independence[2] of the state variables H and A.

7.2 Isomorph invariants of liquids in a slit-pore

The canonical configurational probability for a liquid in a slit-pore is given by (Diestler and Schoen [1995])

$$\hat{P}(\mathbf{R}) = \frac{e^{-U(\mathbf{R})/k_BT}}{\int e^{-U(\mathbf{R})/k_BT} d\mathbf{R}}. \tag{7.7}$$

In the case of a LJ liquid $U = U_{LJ} + U_{WALL}$, and the only difference between bulk and confined systems is therefore the appearance of the term U_{WALL} in the Boltzmann factor and a restriction of the coordinates in the z-direction. Since the isomorph definition is merely based on the proportionality of Boltzmann factors of scaled microconfigurations, isomorph invariants of the slit-pore follow completely analogous to the bulk system (see Chapter 2 for derivation). We then have the following isomorph invariants in a confined system.

1. The center-of-mass structure in reduced units,
2. The center-of-mass dynamics in reduced units,
3. The excess entropy[3] S_{ex},
4. The excess isochoric heat capacity $C_V^{\text{ex}} \equiv (\partial U/\partial T)_{H,A}$,
5. And more.

As for bulk systems, isomorphic jumps are also expected to be properties of confined isomorphs. The next section considers the generation of isomorphs in simulations of confined systems.

7.3 Generating isomorphs in a slit-pore

In the bulk system, an isomorph was generated by keeping the excess entropy constant (Sec. 6.3). In appendix C, we derive the following equation for keeping the excess entropy constant in a slit-pore

[2] When we consider isomorphs in confinement via simulations, we use for simplicity the factor $\rho^{1/3}$ (with $\rho = n/(HA)$) to perform the scaling to reduced units.

[3] The reference state for the excess entropy is defined as an ideal gas of volume $V \equiv HA$.

$$\gamma \equiv \frac{\langle \Delta W \Delta U \rangle}{\langle (\Delta U)^2 \rangle} = -2/3 \Big(\frac{\partial \ln T}{\partial \ln A} \Big)_{S_{\rm ex},H} - 1/3 \Big(\frac{\partial \ln T}{\partial \ln H} \Big)_{S_{\rm ex},A}, \tag{7.8}$$

$$= -\Big(\frac{\partial \ln T}{\partial \ln HA} \Big)_{S_{\rm ex}}^{d \ln H = d \ln A/2}. \tag{7.9}$$

The (fluctuating) virial W is defined equivalent to the bulk system as

$$W \equiv -\frac{HA}{3} \Big[S_{\rm xx} + S_{\rm yy} + S_{\rm zz} \Big], \tag{7.10}$$

where $S_{\rm xx}$, $S_{\rm yy}$, and $S_{\rm zz}$ are, respectively, the xx, yy, and zz-components of the configurational part of the stress tensor[4], i.e. the kinetic degrees of freedom have been subtracted. Since the slit-pore is isotropic in the radial direction, the average stress tensor components parallel to the walls $\langle S_{\rm xx} \rangle = \langle S_{\rm yy} \rangle \equiv S_{||}$ are identical whereas the average off-diagonal components are zero (Diestler and Schoen [1995]).

As for the bulk system, the potential energy U and virial W have several contributions. For a rigid molecular LJ system confined to a slit-pore, they are given by

$$U = U_{LJ} + U_{WALL}, \tag{7.11}$$

$$W = W_{LJ} + W_{CON} + W_{WALL}. \tag{7.12}$$

The new terms with respect to the bulk system are U_{WALL} and W_{WALL}, i.e., the contributions to the potential energy and virial deriving from the confining walls of the slit-pore. In our study, U_{WALL} is defined via ($z_{lower} < 0 < z_{upper}$)

$$U_{WALL} = \sum_i \Big(v_{9,3}(z_{upper} - z_i) + u_{9,3}(z_i - z_{lower}) \Big), \tag{7.13}$$

where

$$v_{9,3}(z) = \frac{4\pi \epsilon_{iw} \rho_w \sigma_{iw}^3}{3} \Big[\frac{1}{15} \Big(\frac{\sigma_{iw}}{z} \Big)^9 - \frac{1}{2} \Big(\frac{\sigma_{iw}}{z} \Big)^3 \Big]. \tag{7.14}$$

Here, z is the distance between the divergence of the potential and the particle in question. σ_{iw} and ϵ_{iw} are parameters similar to the LJ potential, and ρ_w defines the density of the confining solid. The confining walls are thus modelled via a smooth potential (Eq. (7.14)) that appears after considering the total interaction of a LJ particle with a semi-infinite solid continuum of LJ particles (Steele [1973], Toxvaerd [1981]). This potential is also known as the "Steele" potential.

Hence $S_{\rm xx}$, $S_{\rm yy}$ and $S_{\rm zz}$ may be calculated (disregarding the rigid bonds) using the following expressions (Diestler and Schoen [2000], Varnik *et al.* [2000])

[4] The negative of the pressure tensor is the stress tensor.

$$S_{\alpha\alpha} = \frac{1}{2HA}\sum_{i=1}^{N}\sum_{j=1\neq i}^{N}\frac{v'(r_{ij})\alpha_{ij}^2}{r_{ij}},\ \alpha = x, y, \tag{7.15}$$

$$S_{\mathrm{ZZ}} = \frac{1}{2HA}\sum_{i=1}^{N}\sum_{j=1\neq i}^{N}\frac{v'(r_{ij})z_{ij}^2}{r_{ij}} \tag{7.16}$$

$$-\frac{1}{V}\sum_{i=1}^{N}\Big[f_{9,3}(z_{upper}-z_i)\cdot\big(H/2-z_i\big)+f_{9,3}(z_i-z_{lower})\cdot(z_i+H/2)\big)\Big]. \tag{7.17}$$

Equation (7.17) is a new term representing the contribution to the (configurational) pressure coming from the interactions with the walls. The walls are taken to be particles of infinite mass, and hence have no contribution to the kinetic energy (Diestler and Schoen [2000], Varnik *et al.* [2000]).

To generate an isomorph via Eq. (7.9) one needs to define H. Here and henceforth, we define H as the distance between the two points where the wall potentials diverge, i.e.; $H = z_{upper} - z_{lower}$. This definition is, however, not unique (more on this issue to come). Thus, to investigate the consistency of Eq. (7.9) with this definition of H, we take a different approach to generate an isomorph than in the bulk system. Instead, we generate an isomorph via the direct isomorph check (recall Sec. 2.2.4)

$$U(\mathbf{R}^{(2)}) = \frac{T_2}{T_1}U(\mathbf{R}^{(1)}) + k_B T_2 \ln C_{12}, \tag{7.18}$$

changing H and A according to Eq. (7.1) by a few percentage. The linear regression slope of the direct isomorph check provides the ratio T_2/T_1, and T_2 can thus be calculated by multiplying with T_1. This procedure is repeated for each state point along the isomorph until a curve in the phase diagram is generated.

In the next two sections we consider the isomorphs of the KABLJ mixture and the asymmetric dumbbell model (see Appendix A) confined to a slit-pore via the Steele potential. We apply periodic boundary conditions in the (x,y)-directions. The simulations are performed in the NVT ensemble using the Nosé-Hoover algorithm, and the solid density ρ_w is kept constant for all simulations (the asymmetric dumbbell has $\rho_w = 0.932$ and KABLJ mixture $\rho_w = 1.204$). A shifted-potential cutoff at the distance r_c (Allen and Tildesley [1987]) is used for the LJ interactions with $r_c = 5.00\sigma_{\alpha\beta}$ and $r_c = 2.50\sigma_{\alpha\beta}$ for, respectively, the KABLJ mixture and the asymmetric dumbbell model. The Steele potential interacts with the entire slit-pore region, i.e., no cutoff is applied. We use $\sigma_{Aw} = 1$, $\epsilon_{Aw} = 1$, $\sigma_{Bw} = (1+\sigma_{BB})/2$, $\epsilon_{Bw} = \sqrt{1\cdot\epsilon_{BB}}$.

7.4 Isomorphs of the Kob-Andersen binary LJ mixture in a slit-pore

A liquid that is spatially confined exhibits stratification (Schoen *et al.* [1987], Toxvaerd [1981]), i.e., the particles of the liquid order themselves in well-defined layers. The density of

the liquid $\rho(\mathbf{r}_i)$ is then a varying function of space and is not constant as in the bulk liquid. The Steele potential depends only on the distance z, and hence the density is a function of z_i only $\rho(\mathbf{r}_i) = \rho(z_i)$. In addition, the pair-correlation function $g(\mathbf{r}_i, \mathbf{r}_j)$ depends on the cylindrical coordinates $(r_{ij},\ z_{ij})$ of particle j with respect to particle i, that is $g(\mathbf{r}_i, \mathbf{r}_j) = g(z_i, r_{ij}, z_{ij})$ (Schoen *et al.* [1987, 1988]).

In Fig. 7.3 we show the A-particle density profile (in reduced units) of the KABLJ mixture in a slit-pore along an isotherm and isomorph with, respectively, 5% and 27% density increase. The density profile is to a fair approximation invariant in reduced units along both the isotherm and isomorph (noting the difference in density increase). However, the isomorph shows a better invariance of the second peak.

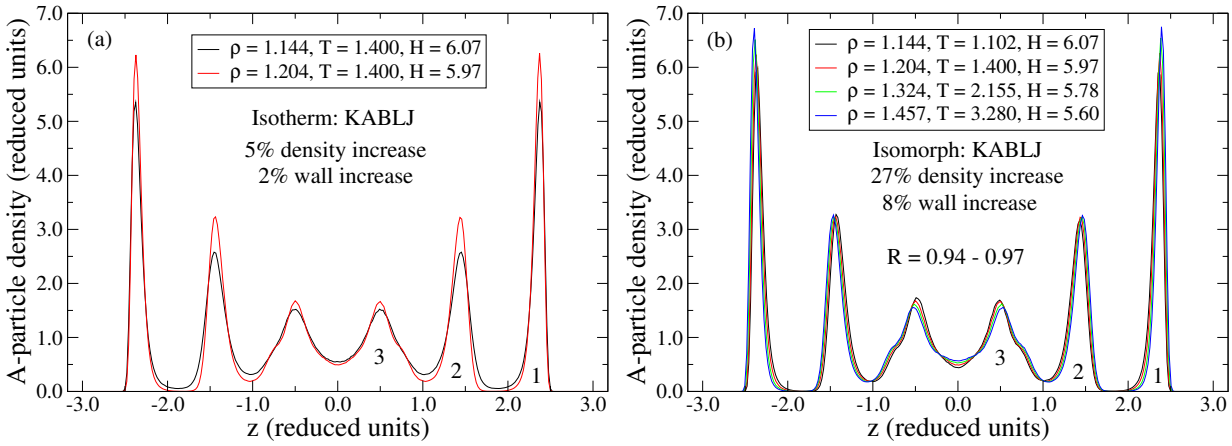

Figure 7.3: *A-particle density profiles (in reduced units $\tilde{z} = \rho^{1/3} z$) of the KABLJ mixture in a slit-pore. The numbers identify the layers. (a) Along an isotherm with 5% density increase. (b) Along an isomorph with 27% density increase.*

Continuing the investigation of the structure of the liquid, we study the pair-correlation function. Since $g(z_i, r_{ij}, z_{ij})$ is a function of three variables, we consider only the so-called "in-plane" pair-correlation function, i.e., $g(z_i, r_{ij}, z_{ij} = 0)$. To increase the statistics; all the particles of a given layer are considered to have the same coordinates of z_i and $z_{ij} = 0$ (Schoen *et al.* [1987, 1988]). Here and henceforth, we define a layer of the liquid (referring to the density profile) as the particles enclosed within two imaginary planes located at $z = z_1$ and $z = z_2$ (the chosen values for z_1 and z_2 correspond approximately to adjacent minima). The delimitation of selected layers are given in Table 7.1 (see also Fig. 7.3) where reduced units are used to specify the planes (the density profile is state point dependent). In addition, we average over the layer in question and its reflection in the mirror plane at $z = 0$ (since the walls of the slit-pore are identical).

Layer	$\tilde{z}_1$	$\tilde{z}_2$
1	1.827	2.549
3	0	1.031

Table 7.1: *Delimitation of selected layers (referring to the A-particle density profile in Fig. 7.3) by imaginary planes located at $\tilde{z} = \tilde{z}_1$ and $\tilde{z} = \tilde{z}_2$ for the KABLJ mixture in a slit-pore ($\tilde{z} = \rho^{1/3} z$).*

We consider in Fig. 7.4 the *AA*-radial distribution functions (RDF) for layers 1 and 3 along the previous isotherm and isomorph. We note that the RDF of layer 1 is solid-like whereas the RDF of layer 3 resembles that of a bulk liquid (Schoen *et al.* [1987]). Nevertheless, the structure of both layers is to a good approximation invariant along the isomorph, with some deviation noted for the second peak of layer 3. On the isotherm, the RDF is also invariant for layer 3, however, in layer 1 the solid-like structure "thaws" and becomes bulk-liquid-like; the structure on the isotherm is thus not invariant.

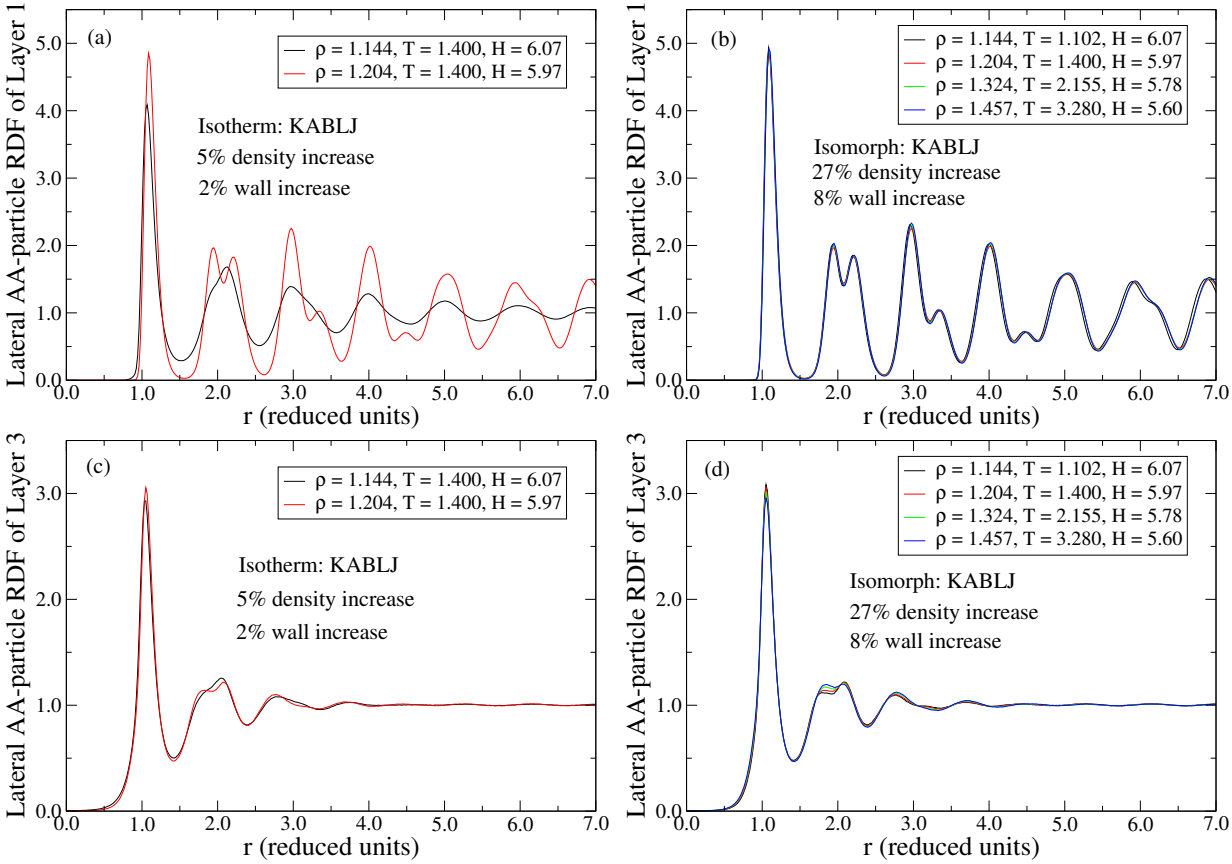

Figure 7.4: *AA-particle RDFs (in reduced units) for different layers (see Fig. 7.3 and Table 7.1) of the KABLJ mixture in a slit-pore along the isotherm and isomorph of Fig. 7.3. (a) Isotherm, layer 1. (b) Isomorph, layer 1. (c) Isotherm, layer 3. (d) Isomorph, layer 3.*

The corresponding dynamics of the two layers is shown in Fig. 7.5 by probing the *A*-

particle incoherent intermediate scattering function (ISF) for constant reduced wave vector parallel to the walls. The dynamics is to a good approximation invariant along the isomorph whereas the dynamics on the isotherm, for both layers, is not. For layer 1 on the isomorph (Fig. 7.5(b)), the red curve corresponding to $\rho = 1.204$ deviates more significantly than the general trend of the other scaled curves; we currently have no explanation for this behavior.

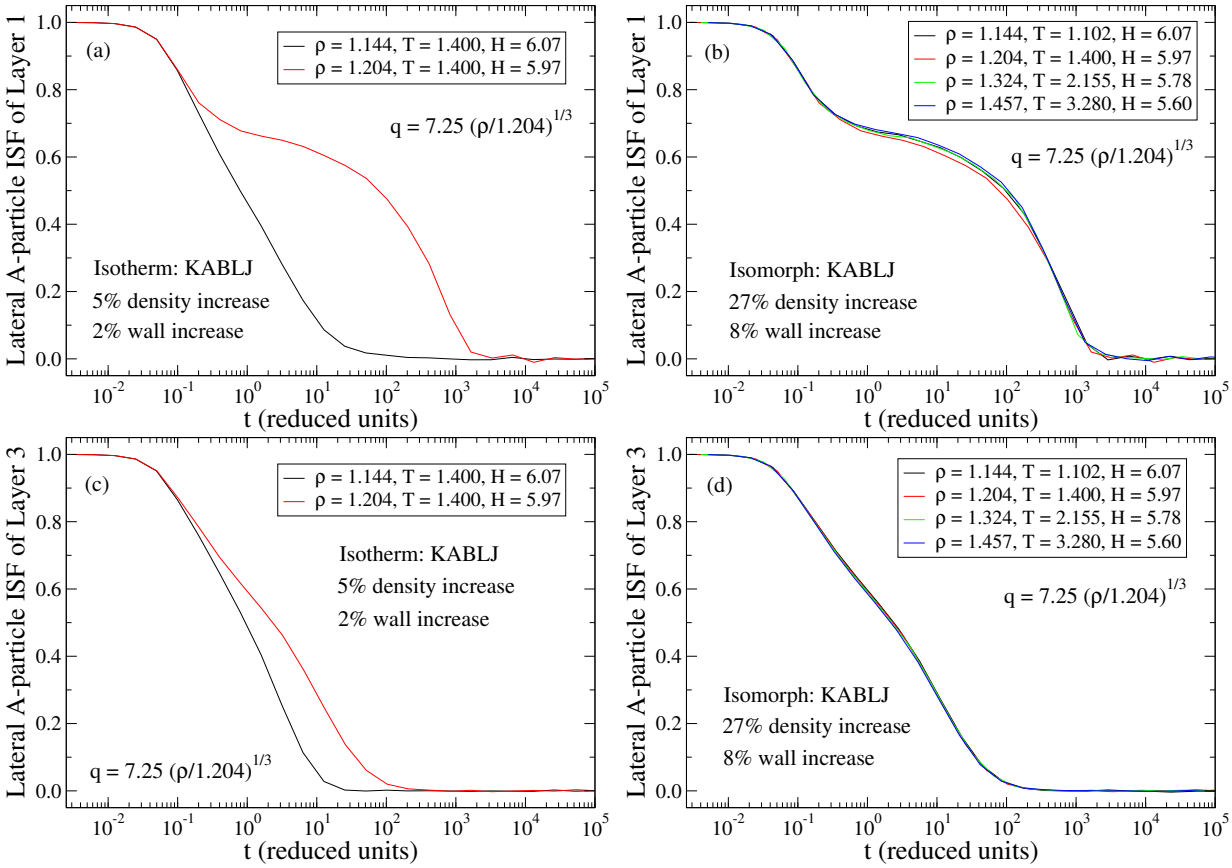

Figure 7.5: *A-particle incoherent ISFs (in reduced units) for constant reduced wave vector parallel to the walls for different layers of the KABLJ mixture in a slit-pore. The isotherm and isomorph of Figs. 7.3-7.4 are shown. (a) Isotherm, layer 1. (b) Isomorph, layer 1. (c) Isotherm, layer 3. (d) Isomorph, layer 3.*

7.5 Isomorphs of the asymmetric dumbbell model in a slit-pore

The isomorphs of the asymmetric dumbbell model in a slit-pore are now considered. Figure 7.6 shows the molecular center-of-mass (CM) density profile (in reduced units) along an isotherm and isomorph with, respectively, 8% and 20% density increase. As with the KABLJ mixture, the density profile is to a good approximation invariant both on the isotherm and the isomorph.

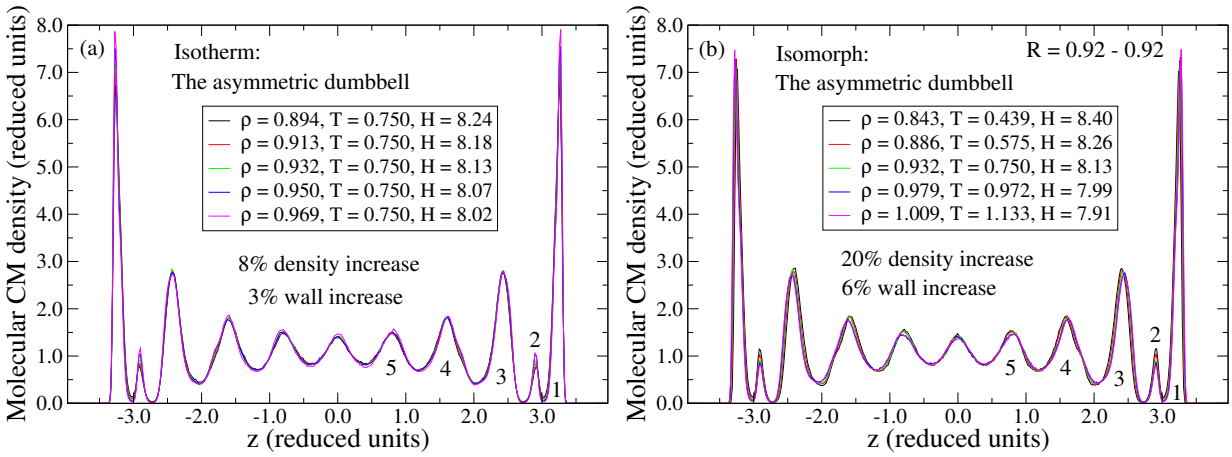

Figure 7.6: *Molecular CM density profiles in (reduced units) for the asymmetric dumbbell model in a slit-pore. The numbers identify the layers. (a) Along an isotherm with 8% density increase. (b) Along an isomorph with 20% density increase.*

Next, we consider in Fig. 7.7 the molecular CM RDFs for layers 1 and 5 (see Fig. 7.6 and Table 7.2) along the previous isotherm and isomorph. The RDFs seem equally invariant for the isotherm and isomorph. The density increase on the isomorph is, however, a factor of two larger than the density increase on the isotherm.

Layer	$\tilde{z}_1$	$\tilde{z}_2$
1	3.021	3.400
5	0.408	1.203

Table 7.2: *Delimitation of selected layers (referring to the CM density profile in Fig. 7.6) by imaginary planes located at $\tilde{z} = \tilde{z}_1$ and $\tilde{z} = \tilde{z}_2$ for the asymmetric dumbbell model in a slit-pore ($\tilde{z} = \rho^{1/3} z$).*

We note from Figs. 7.7(a) and (b) that layer 1, i.e., the contact layer of the liquid, shows no sign of solidification as was the case for the KABLJ mixture, and the RDF resembles that of a bulk liquid.

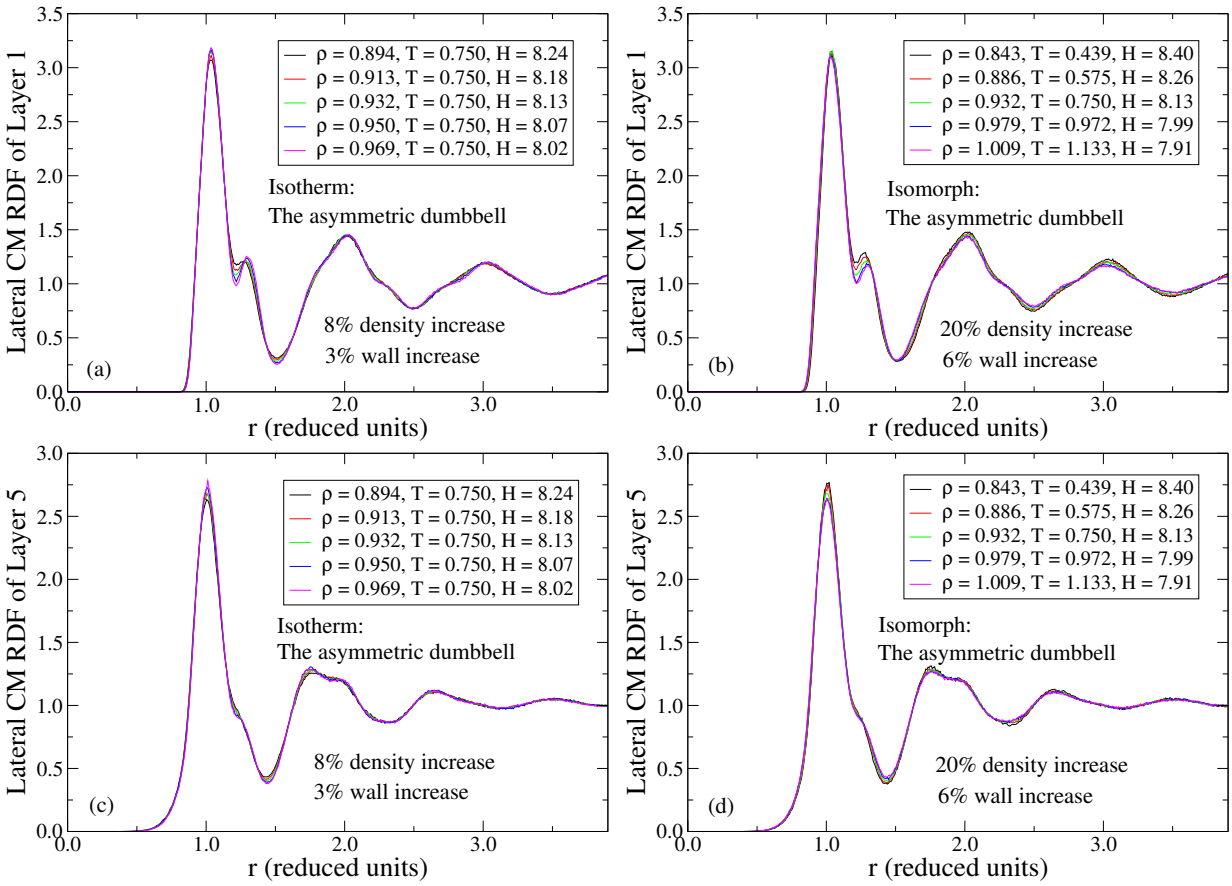

Figure 7.7: *Molecular CM RDFs (in reduced units) for different layers (see Table 7.2) of the asymmetric dumbbell model in a slit-pore along the isotherm and isomorph of Fig. 7.6. (a) Isotherm, layer 1. (b) Isomorph, layer 1. (c) Isotherm, layer 5. (d) Isomorph, layer 5.*

Focusing the study on the dynamics of the liquid, Fig. 7.8 shows the molecular CM incoherent ISF for constant reduced wave vector parallel to the walls. This function is averaged over the entire slit-pore. The dynamics is to a good approximation invariant along the isomorph while the isotherm shows approximately three orders of magnitude change in the dynamics.

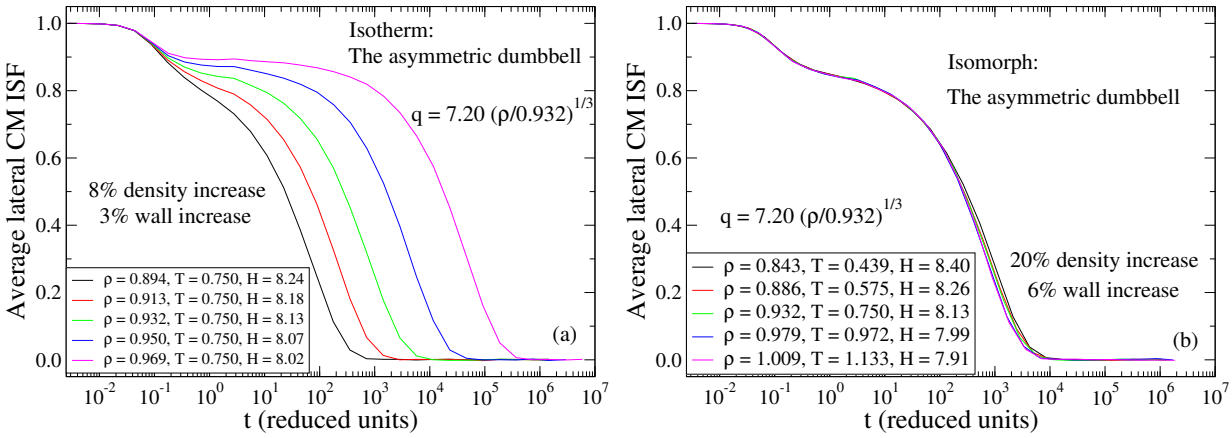

Figure 7.8: *Molecular CM incoherent ISFs (in reduced units) for constant reduced wave vector parallel to the walls. (a) Along the isotherm of Figs. 7.6-7.7. (b) Along the isomorph of Figs. 7.6-7.7.*

Figure 7.9 shows the corresponding dynamics in layers 1 and 5. Both layers show excellent scaling on the isomorph while the isotherm shows a significant change in the dynamics. It should be noted that the dynamics of the contact layer (layer 1) is only slightly slower than the dynamics in the middle of the slit-pore (layer 5).

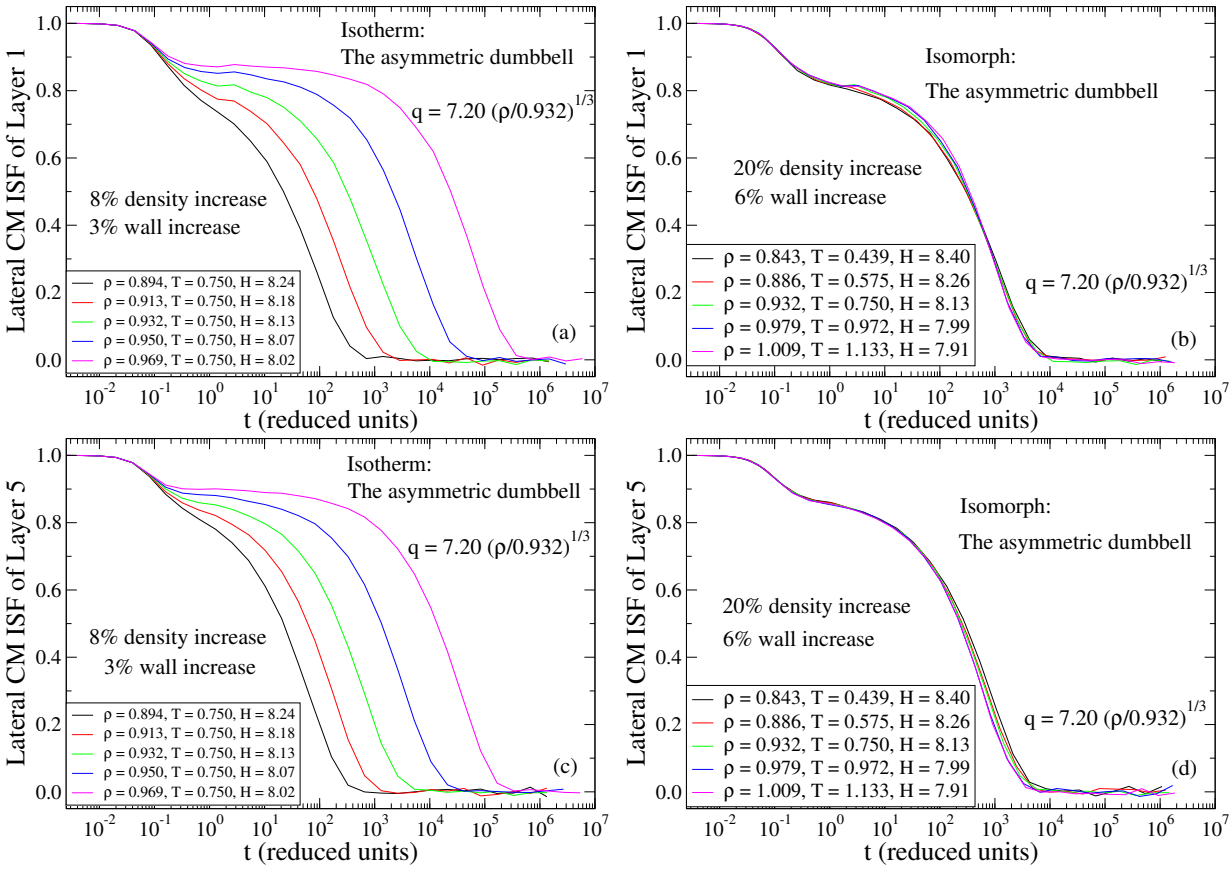

Figure 7.9: *Molecular CM incoherent ISF (in reduced units) for constant reduced wave vector parallel to the walls for different layers of the asymmetric dumbbell model in a slit-pore. The isotherm and isomorph of Figs. 7.6-7.8 are shown. (a) Isotherm, layer 1. (b) Isomorph, layer 1. (c) Isotherm, layer 5. (d) Isomorph, layer 5.*

Finally in Fig. 7.10, we study the mean-square displacement in the z-direction of the molecular CM along the previous isomorph. The figure shows an excellent collapse also for the dynamics normal to the confining walls. The long-time limit of the particle mean-square displacement is given by $H^2/6$ (Schoen *et al.* [1988]). Concluding on the investigation of the isomorph, structure was observed to be almost equally invariant along the isotherm and isomorph. However, for the dynamics the observation was different. A striking difference in the dynamics between the isotherm and the isomorph was observed, with the isomorph showing excellent invariance.

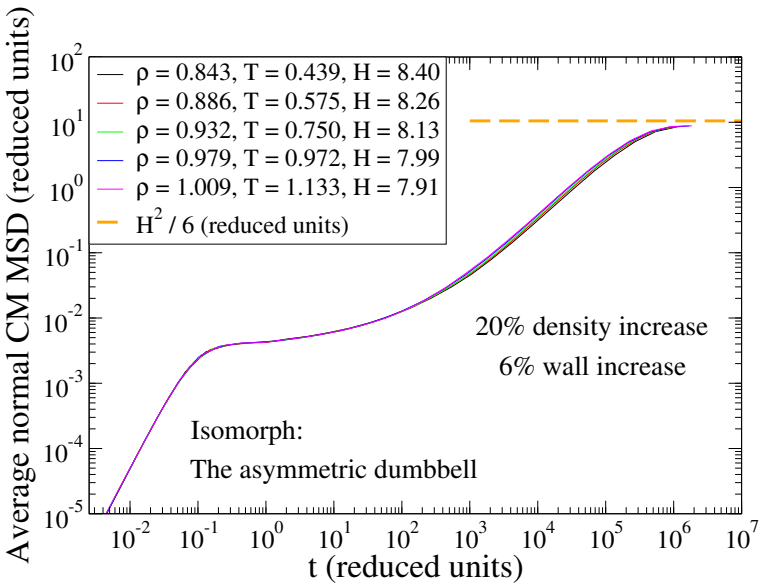

Figure 7.10: *Molecular CM mean-square displacements (in reduced units) of the asymmetric dumbbell normal to the confining walls. The isomorph of Figs. 7.6-7.9 is shown. The long-time limit of the particle mean-square displacement is given by* $H^2/6$ *(Schoen* et al. *[1988]).*

7.5.1 Increasing the degree of confinement

It is also interesting to study the effect on isomorphs by increasing the degree of confinement (i.e., making H smaller). Here we study this aspect using again the asymmetric dumbbell model in a slit-pore. Figure 7.11 shows the density profile of the molecular CM along an isotherm and an isomorph with 33% density increase and $H \approx 4$. We now observe larger deviations for the density profile along the isomorph, and is consistent with the lower correlation coefficient for the investigated state points (R is in the range $0.87 - 0.90$). The structure along the isotherm displays a qualitative change at the density of $\rho = 0.737$ and is thus less invariant compared to the isomorph (note, however, the slight asymmetry in the density profile at $\rho = 0.979$ which indicates that this state point is not fully equilibrated).

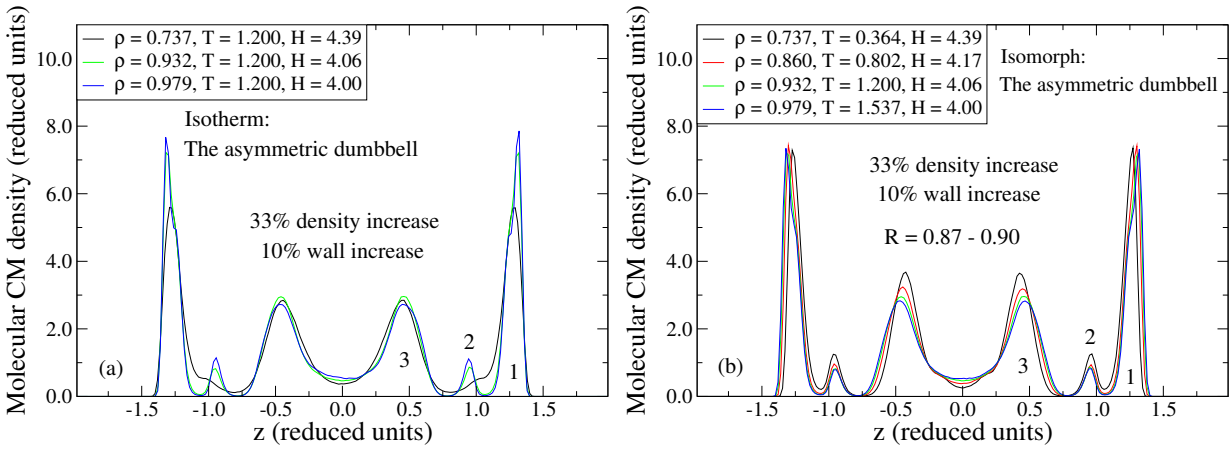

Figure 7.11: *Molecular CM density profiles in (reduced units) for the asymmetric dumbbell model in a slit-pore ($H \approx 4$). The numbers identify the layers. (a) Along an isotherm with 33% density increase. (b) Along an isomorph with 33% density increase.*

Figure 7.12 shows the incoherent ISF averaged over the entire slit-pore for the same isotherm and isomorph. The dynamics is to a good approximation invariant along the isomorph whereas the dynamics along the isotherm shows a striking five orders of magnitude change. For the density $\rho = 0.737$, along the isomorph, we observe (black curve) a worse scaling at longer times than what would be estimated from the behavior of the other curves. We currently have no explanation for this observation.

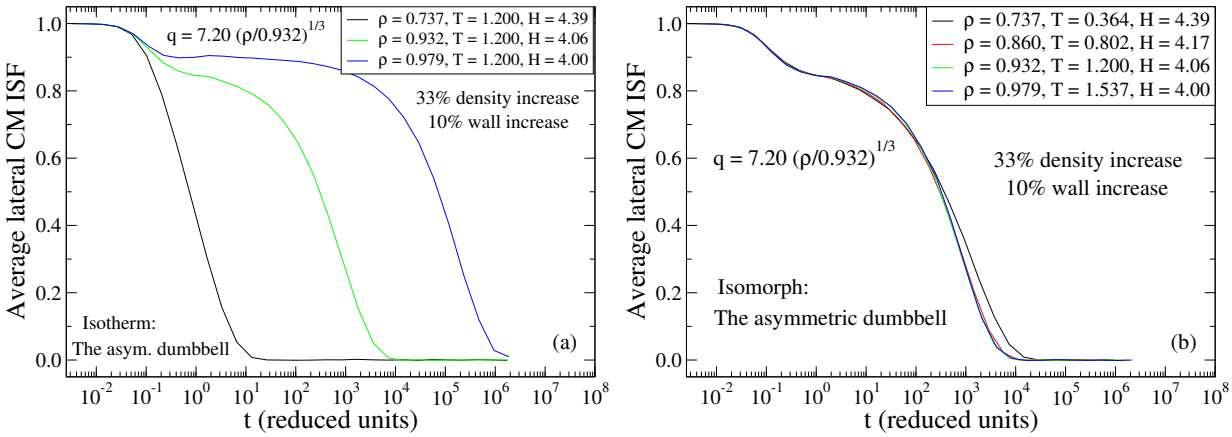

Figure 7.12: *Molecular CM incoherent ISFs (in reduced units) for constant reduced wave vector parallel to the walls ($H \approx 4$). (a) Along the isotherm of Fig. 7.11. (b) Along the isomorph of Fig. 7.11.*

Investigating now the layer properties, Fig. 7.13 shows the molecular CM RDFs of the two main layers of the slit-pore (bulk and contact layer, see Fig. 7.11) along the previous isotherm and isomorph. Along the isomorph, clear deviations in the structure are noted for both layers where the structure of the contact layer (layer 1) shows a better invariance than the structure of the layer in the center of the pore (layer 3). We suspect that this is

a consequence of the significantly higher density of the contact layer. The aforementioned qualitative change in the structure along the isotherm is most prominent for the contact layer whereas the structure of layer 3 shows a similar "invariance" to the isomorph.

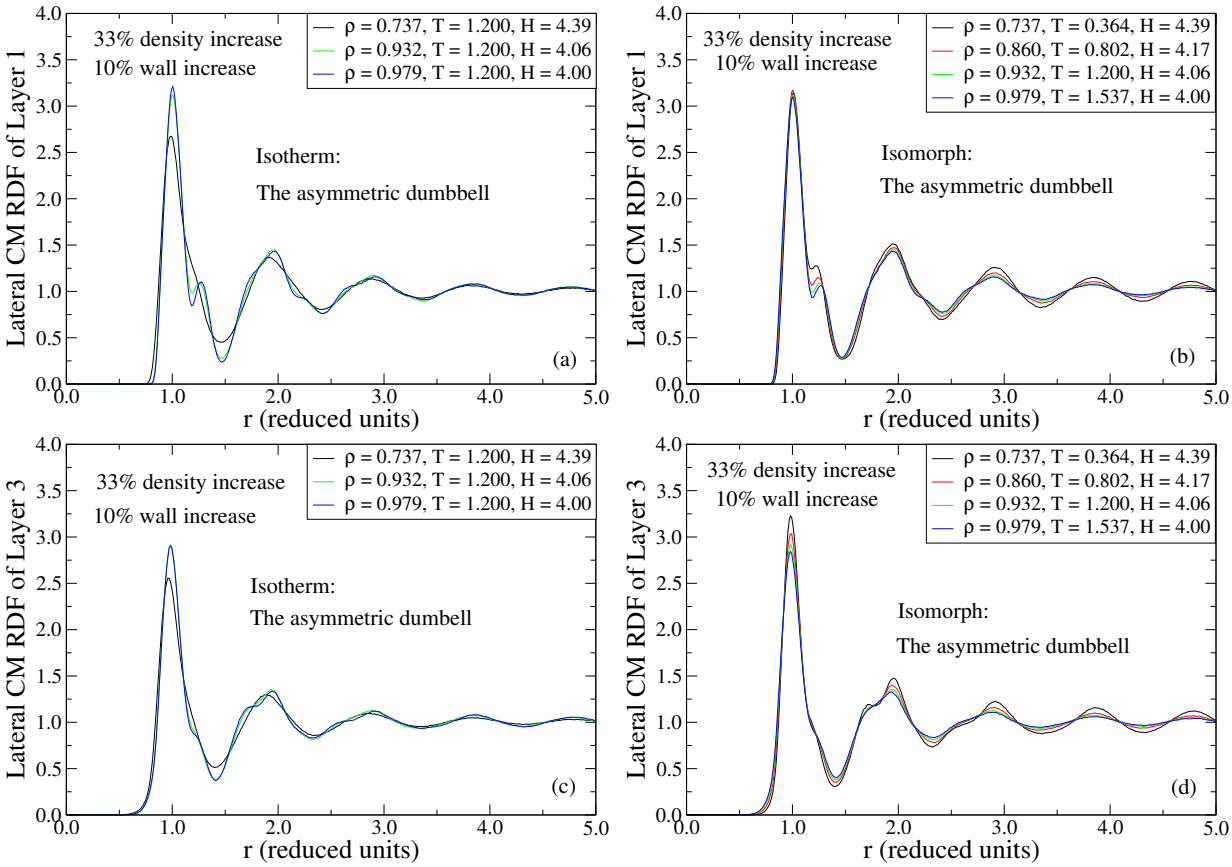

Figure 7.13: *Molecular CM RDFs (in reduced units) for different layers (see Fig. 7.11) of the asymmetric dumbbell model in a slit-pore along the isotherm and isomorph of Figs. 7.11-7.12. (a) Isotherm, layer 1. (b) Isomorph, layer 1. (c) Isotherm, layer 3. (d) Isomorph, layer 3.*

Additionally, we show in Fig. 7.14 the molecular CM incoherent ISFs of the two previous layers, and again we observe deviations in the scalings along the isomorph. On the other hand, the isotherm shows a significant change in the dynamics similar to the behavior observed for the average dynamics.

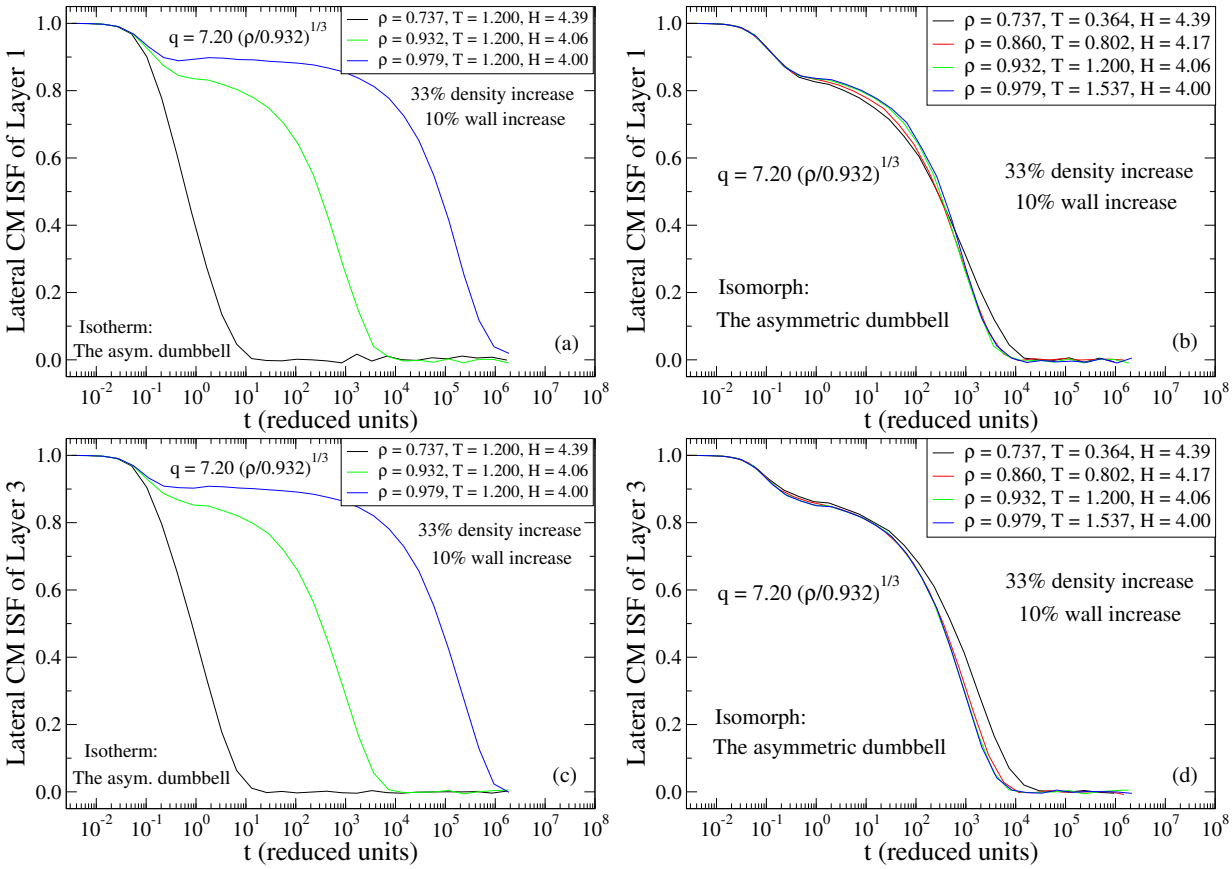

Figure 7.14: *Molecular CM incoherent ISF (in reduced units) for constant reduced wave vector parallel to the walls for different layers of the asymmetric dumbbell model in a slit-pore. The isotherm and isomorph of Figs. 7.11-7.13 are shown. (a) Isotherm, layer 1. (b) Isomorph, layer 1. (c) Isotherm, layer 3. (d) Isomorph, layer 3.*

7.6 Is the definition of the width of the slit-pore H meaningful?

The excess entropy in confinement can be kept constant via the relation (recall the discussion in Sec. 7.3)

$$\gamma \equiv \frac{\langle \Delta W \Delta U \rangle}{\langle (\Delta U)^2 \rangle} = -\Big(\frac{\partial \ln T}{\partial \ln HA}\Big)_{S_{\rm ex}}^{d\ln H = d\ln A/2}. \tag{7.19}$$

In the previous sections we defined H as the distance between the two points where the wall potentials diverge. We now examine this definition of H for consistency with Eq. (7.19) using the state points of the two previously generated isomorphs for the asymmetric dumbbell model. Recall from Sec. 7.3 that we used the direct isomorph check to generate the isomorphs; only for perfect isomorphs does this imply that $S_{\rm ex}$ is rigorously constant.

Figure 7.15 shows γ calculated from the fluctuations via the left-hand side of Eq. (7.19) $\langle \Delta W \Delta U \rangle / \langle (\Delta U)^2 \rangle$ (black and red circles) and calculated from the state points of the isomorphs via the right-hand side $-(\partial \ln T/\partial \ln HA)_{S_{\rm ex}}^{d\ln H = d\ln A/2}$ (magenta and cyan aster-

isks). An excellent agreement between the two expressions is obtained and implies that the definition of H is not only meaningful, but also that $S_{\rm ex}$ to excellent approximation is invariant along the isomorph. Figure 7.16 shows $S_{\rm ex}$ along an isotherm and "Isomorph 1" of Fig. 7.15, confirming the latter conclusion (the excess entropy has been calculated via the methods mentioned in Sec. 6.5). In this connection it is important to note that we have only tested one particular definition of H in connection with isomorph, and thus the results does not exclude other meaningful definitions of the width of the slit-pore. However, the chosen definition is certainly the most simple.

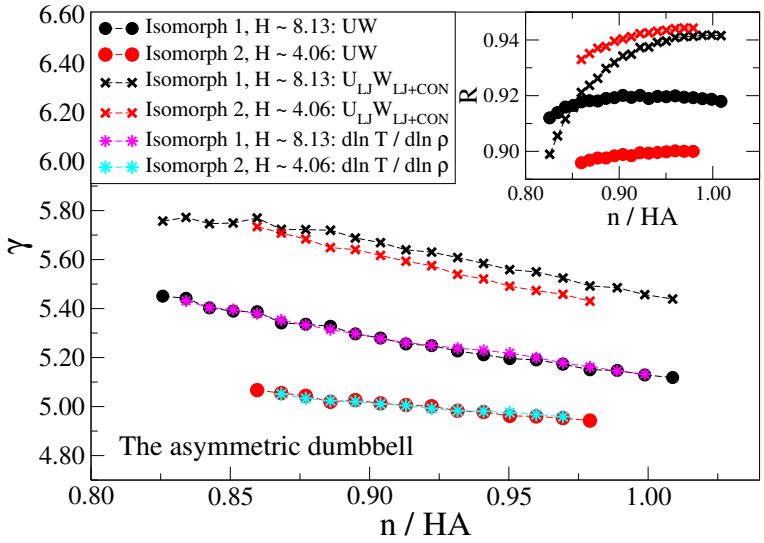

Figure 7.15: *$\gamma = \langle \Delta W \Delta U \rangle / \langle (\Delta U)^2 \rangle$ as a function of $n/(HA) \equiv \rho$ calculated via UW and $U_{LJ}W_{LJ+CON}$ (i.e., excluding the wall contributions to UW) along the two previous isomorphs of the asymmetric dumbbell model in a slit-pore (black and red data points). Also shown is $d\ln T/d\ln\rho = -d\ln T/d\ln HA$ of Eq. (7.19) along the same isomorphs (magenta and cyan asterisks). The inset shows corresponding quantities for the correlation coefficient $R = \langle \Delta W \Delta U \rangle / \sqrt{\langle (\Delta W)^2 \rangle} \sqrt{\langle (\Delta U)^2 \rangle}$.*

We note additionally from Fig. 7.15 that γ calculated using $U_{LJ}W_{LJ+CON}$ is different from γ calculated using UW by approximately 10%. Thus, the contribution from the wall potentials to the fluctuations in U and W cannot in general be neglected.

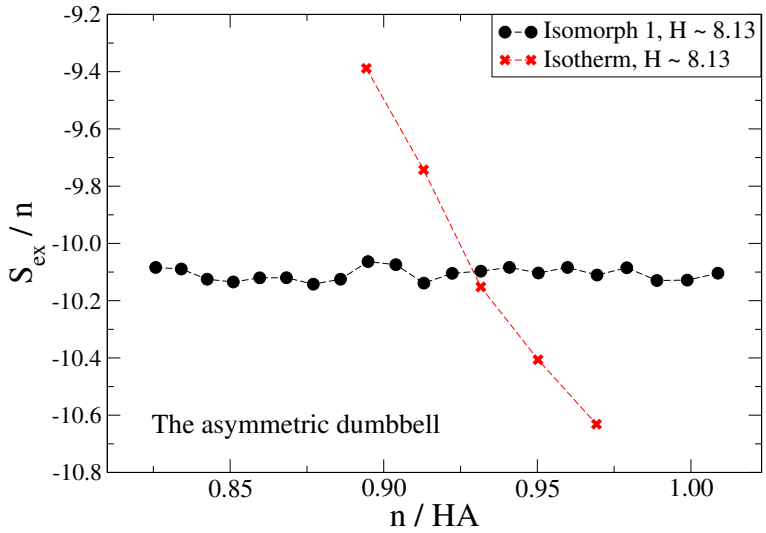

Figure 7.16: *The excess entropy S_{ex} per molecule along an isotherm (red crosses) and "Isomorph 1" of Fig. 7.15 (black circles) for the asymmetric dumbbell model in a slit-pore. The middle point on the isotherm is slightly lower than the isomorph due to the uncertainty in the simulations. The reference state for the excess entropy of the confined system is an uncorrelated ideal gas with volume $V = HA$ (see the next section). S_{ex} is to an excellent approximation invariant along the isomorph, but not on the isotherm.*

7.7 Excess entropy scaling in bulk and confinement

Truskett, Errington, and co-workers (see the introduction to Chapter 6) established a relationship between bulk and confined systems via excess entropy (Chopra *et al.* [2010a], Goel *et al.* [2008], Mittal *et al.* [2006, 2007]). They found that Rosenfeld's excess entropy scaling is also valid for confined systems and that the functional form f to a good approximation is unaffected by the degree of confinement. Since isomorphs have now been established for confined systems, it is natural to ask whether the invariance (upon confinement) of the function f can be understood in terms of isomorphs.

We start by verifying the bulk/confined excess entropy scaling relationship for the asymmetric dumbbell model. In confined systems, different reference states for defining the excess entropy have been proposed. For instance, one may define a reference state of an ideal gas having the same one-body spatial and oriential distribution as the liquid. Chopra *et al.* [2010a] investigated different versions of the excess entropy with the purpose of collapsing the confined state points onto the bulk excess entropy curve. They found that a reference state of an uncorrelated ideal gas with volume $V \equiv H^{\text{eff}}A$ was the most succesful where H^{eff} is the distance[5] H between the two walls corrected for the "non-accessible" volume of the particles near the walls. The non-accessible volume appears as a consequence of the wall-

[5] Recall that H is defined as the distance between the two points where the wall potentials diverge, i.e.; $H = z_{upper} - z_{lower}$.

fluid interactions and makes the density of the system higher than what would be estimated from $V = HA$.

In this study, we follow the procedure outlined in Chopra *et al.* [2010a] to calculate H^{eff} with the only exception that the absolute minimum of the effective wall-liquid interaction potential is used as a shift. The procedure is as follows.

1. We start by constructing the potential of mean force of the wall $u_{\text{eff}}(z)/k_BT = -\ln(\rho(z))$ from the total particle density profile $\rho(z)$.

2. The potential $u_{\text{eff},0}(z)/k_BT$ is then constructed by shifting the $u_{\text{eff}}(z)/k_BT$ curve by an amount that corresponds to the absolute minimum in $u_{\text{eff}}(z)/k_BT$.

3. Finally, we locate the first point at which $u_{\text{eff},0}(z)/k_BT = 1$. The distance of this point σ_{HS} marks the location of an effective "hard" wall. We then calculate $H^{\text{eff}} = H - 2\sigma_{HS}$ since the slit-pore is symmetric.

The outlined procedure is performed for every confined state point to calculate H^{eff} (Chopra *et al.* [2010a]) but it must be stressed that this is not a state point dependent "fitting" procedure onto the bulk curve. Alternatively, one could also use the particle density profile itself to estimate H^{eff}.

Figure 7.17 shows a reduced molecular relaxation time $\tilde{\tau}_\alpha$, extracted from the molecular center-of-mass incoherent intermediate scattering function when $F_{sCM}(\tilde{\tau}_\alpha) = 0.2$, as a function of excess entropy for the asymmetric dumbbell model in the bulk (black data points) and in a slit-pore (red data points). Figure 7.17(a) applies a reference state for the excess entropy of an uncorrelated ideal gas with volume $V = HA$, and Fig. 7.17(b) applies a version with $V = H^{\text{eff}}A$. The version of excess entropy defined via H^{eff} collapses, to a good approximation, all the data points into a single curve while the version of excess entropy defined via H shows some scatter in the data points. The latter confirms the observations of Chopra *et al.* [2010a].

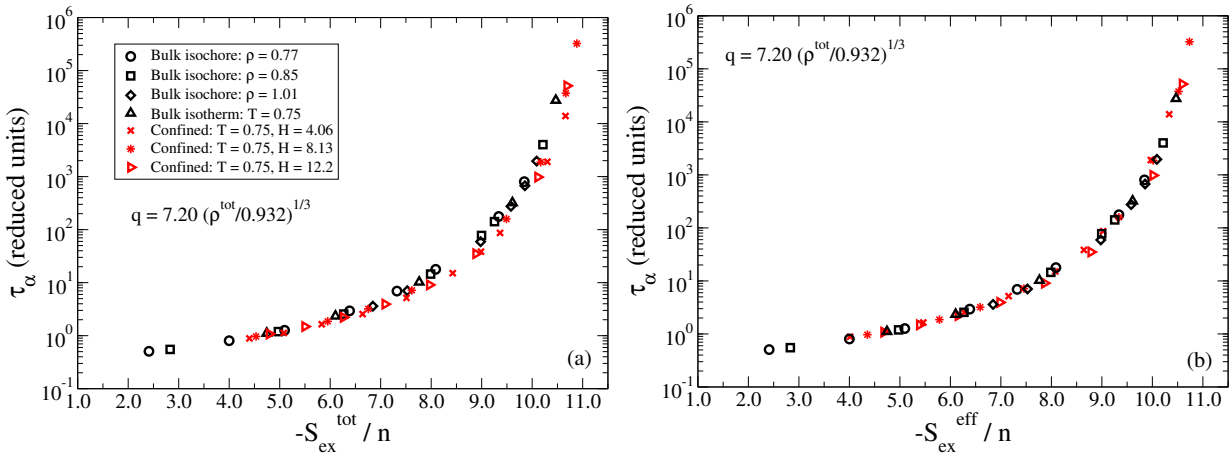

Figure 7.17: *A reduced molecular relaxation time $\tilde{\tau}_\alpha$ extracted from the molecular center-of-mass incoherent intermediate scattering function as a function of excess entropy (per molecule) for the asymmetric dumbbell model in the bulk (black data points) and in a slit-pore (red data points). The reference state for the excess entropy in the slit-pore is an uncorrelated ideal gas with volume V. (a) $V = HA$. (b) $V = H^{eff}A$ where H^{eff} is the distance H corrected for the "non-accessible" volume of the particles near the walls (see the text).*

It was argued in the previous sections that isomorphs are curves and not surfaces in the confined three-dimensional phase diagram. If isomorphs were surfaces, only one number[6] is needed to specify the isomorph, for instance, the excess entropy. The latter implies that

$$\tilde{\tau}_\alpha = f\big(S_{\rm ex}\big), \tag{7.20}$$

thus explaining the invariance of the function f upon confinement. Isomorphs are, however, curves in the phase diagram of the confined liquid, and two numbers are needed to specify an isomorph. Considering the surfaces in the phase diagram where $S_{\rm ex}$ and C_V^{ex} are constant and assuming that these surfaces do not coincide, the intersection of these surfaces identifies the isomorph. Thus, one concludes

$$\tilde{\tau}_\alpha = f\big(S_{\rm ex}, C_V^{\rm ex}\big), \tag{7.21}$$

and cannot *a priori* expect a single-parameter collapse as in the bulk case. In this sense, Fig. 7.17(a) is consistent with isomorphs in confinement while Fig. 7.17(b) cannot be explained directly in terms of isomorphs.

The excellent collapse of the bulk/confined excess entropy scaling, however, also raises the question: Is the collapse of dynamical quantities onto the bulk curve (Mittal [2009], Mittal *et al.* [2006]) a unique property of excess entropy? Figure 7.18(a) shows the reduced molecular relaxation times of Fig. 7.17 as a function of excess isochoric heat capacity (an isomorph invariant). Here, it is important to note that the excess isochoric heat capacity, itself, is not dependent on the definition of the width of the slit-pore. Within the scattering

[6] One number specifies a level surface in the confined phase diagram.

of the bulk data, the confined state points collapse onto the bulk curve. In comparison, Figs. 7.18(b) and (c) show the same state points plotted as a function of total density $\rho^{\text{tot}} = n/(HA)$ and effective density $\rho^{\text{eff}} = n/(H^{\text{eff}}A)$; here, no collapse is seen.

Thus, one concludes that the collapse of the confined data points onto the bulk curve is not a unique property of excess entropy as the excess heat capacity may also be used (although, the excess entropy gave a better collapse than the excess heat capacity). The isomorph theory, itself, does not imply any causality among the properties that are invariant along an isomorph, and a conjecture is thus that all isomorph invariants can be used to perform the bulk/confined scaling; this, however, remains to be verified.

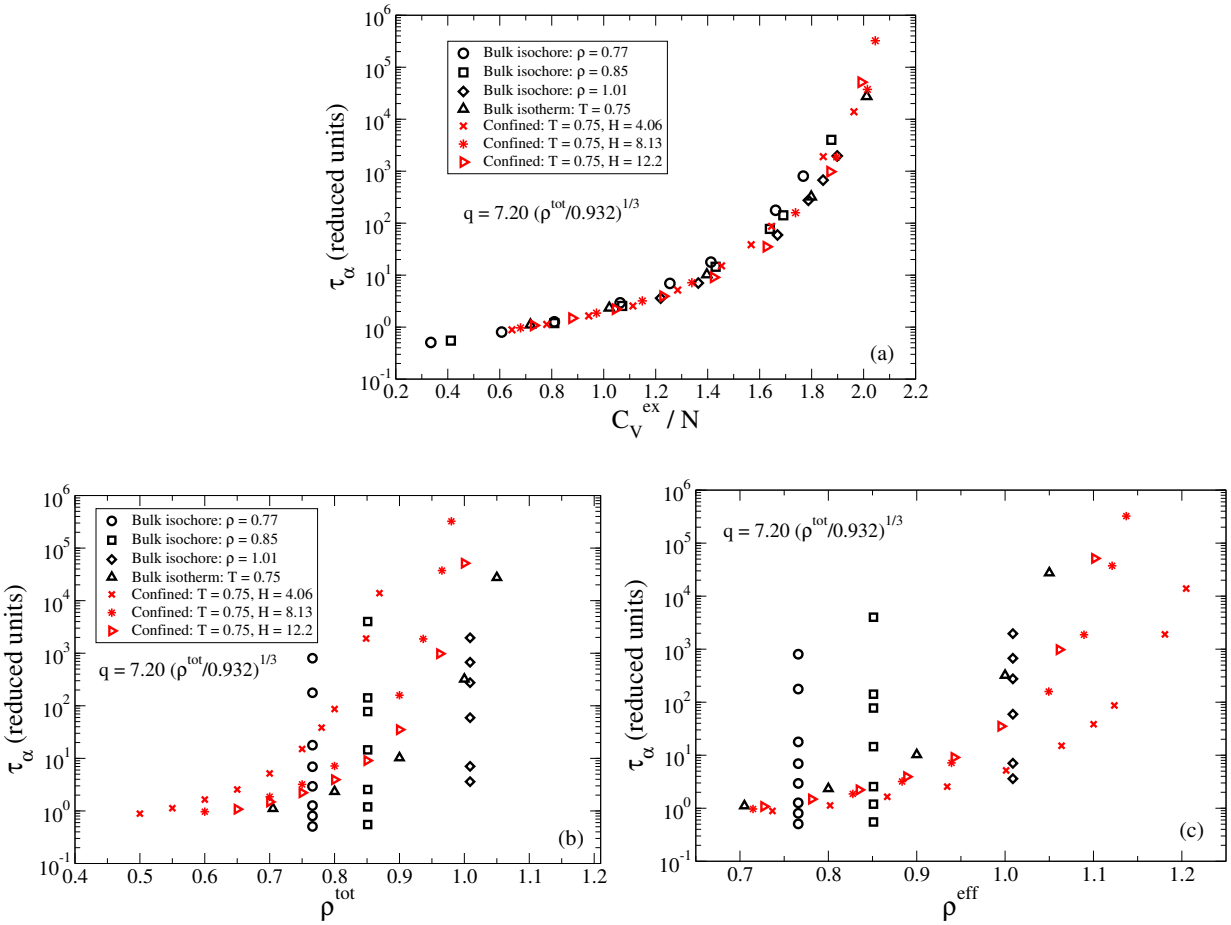

Figure 7.18: *Reduced molecular relaxation times $\tilde{\tau}_\alpha$ of Fig. 7.17 for the asymmetric dumbbell model in the bulk (black data points) and in confinement (red data points). (a) As a function of excess isochoric heat capacity. (b) As a function of total density $\rho^{tot} = n/(HA)$. (c) As a function of effective density $\rho^{eff} = n/(H^{eff}A)$, see text.*

Finally, we show in Fig. 7.19 that density scaling (Tölle [2001]) also works in confinement. The relaxation time $\tilde{\tau}_\alpha$ has been defined analogous to the aforementioned definition.

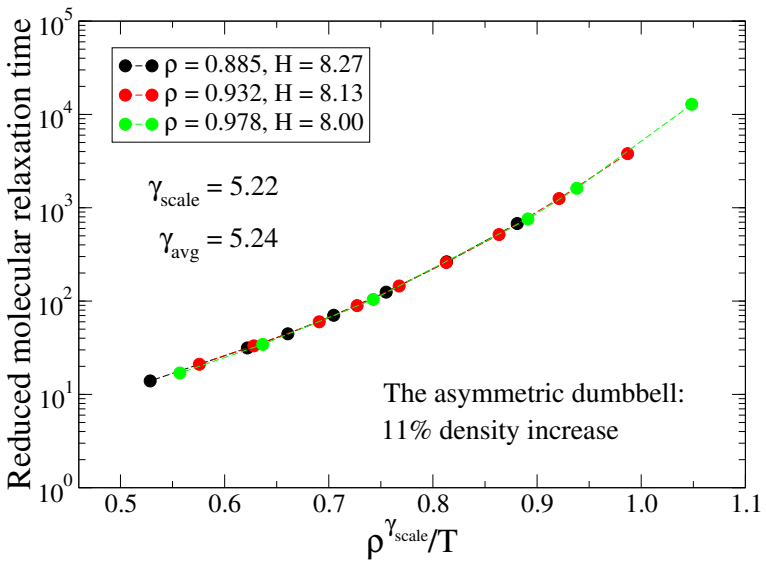

Figure 7.19: *Density scaling* $\tilde{\tau}_\alpha = G\big(\rho^\gamma/T\big)$ *for the asymmetric dumbbell model in a slit-pore* ($\rho \equiv n/(HA)$). *The exponent* γ_{scale} *is estimated using trial and error, and the exponent* γ_{avg} *is the average of* $\gamma = \langle \Delta W \Delta U \rangle / \langle (\Delta U)^2 \rangle$ *over all the state points of the figure.*

Chapter 8

ARE LIQUIDS IN NANOSCALE CONFINEMENT SIMPLE?

We consider here some very recent and *unfinished* research relating to the role of the FCS for liquids in confinement. We learned in Chapter 5 that simple liquids are characterized by the fact, in addition to having isomorphs, that the FCS interactions determine to a good approximation their structure and dynamics. We have in the previous chapter detailed the existence of isomorphs for liquids in confinement, but is the FCS property still meaningful for confined liquids? And in this case, how should the wall-liquid interactions be treated in this picture? These questions are studied below.

In Fig. 8.1, we show the density profile and the "layer RDF" for each layer (layers 1-3) of the SCLJ liquid confined to the slit-pore at $\rho = 0.85$, $T = 1.80$, and $H = 6.13$. The confining potential is throughout this chapter still the Steele potential, see Sec. 7.3. From Fig. 8.1(b), we see that the structure depends significantly on the distance to the wall; the distance at which the RDFs attain their first local minimum is seen to be largest for the contact layer (layer 1). Thus, a simple FCS scheme for the liquid-liquid interactions is to choose an FCS cutoff from this particular layer (see the red dashed line in Fig. 8.1(b)) and to apply it to all the layers of the liquid (i.e. the usual cutoff procedure in molecular dynamics simulations).

Next, we consider the wall-liquid interactions. The density profile given in Fig. 8.1(a) can be thought of as the RDF of a particle with infinite radius (the wall itself), and the stratification in confined liquids thus appears similar to the ordering in nearest-neighbor shells of the bulk liquid (Diestler *et al.* [1991]). A conjecture is then that the wall-liquid interactions, for a strongly correlating liquid, extend no further than to the first local minimum of the density profile (see the red dashed lines in Fig. 8.1(a)), i.e., the analog of the FCS cutoff for the liquid-liquid interactions.

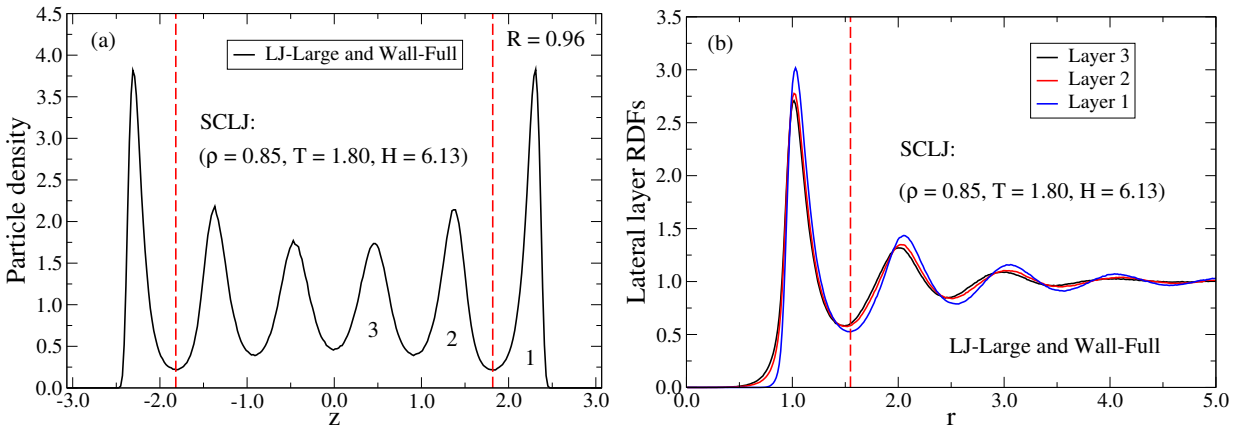

Figure 8.1: *(a) Density profile for the SCLJ liquid in a slit-pore at $\rho = 0.85$, $T = 1.80$, and $H = 6.13$ with pair potential cutoff $r_c = 5.000$. The red dashed line marks the FCS of the wall "particle" at the distance $r = 1.250$ from the wall. (b) Lateral RDFs of layers 1-3 (layer 1 being the contact layer, and layer 3 the bulk layer) of the density profile in (a). The red dashed line marks the FCS of layer 1 at $r = 1.549$.*

Having now chosen a scheme for the FCS cutoffs in a confined system, we are faced with an additional challenge before the proposed picture can be tested. As noted in Chapter 5 an SF truncation scheme is needed to ensure reliable results for bulk systems at low cutoff distances (Toxvaerd and Dyre [2011a]). It is, however, known that using an SF cutoff near interfaces can lead to spurious behavior (Allen and Tildesley [1987]) and may be understood as follows. An SF truncation scheme is equivalent to adding a linear term to the pair potential, however, for this linear term to sum to a constant (and not effect the structure and dynamics), the neighbors of a given atom must have a fairly uniform distribution around the main atom itself. The atoms near the walls are, however, missing (in loose terms) "half a coordination shell". Thus, for the linear term not to modify the structure and dynamics, the wall must compensate for the missing atoms.

We have empirically found from simulations that using an SF truncation scheme on the wall-liquid interactions will compensate some amount, but not enough. Instead, we choose here an ad-hoc based correction on the wall-liquid interactions that seems to work well in practice. The procedure is as follows: We first apply an SF truncation on the liquid-liquid and wall-liquid interactions, separately. Afterwards, an additional term is added to the force from the wall given by the absolute difference in the SF corrections, i.e., the term $\Delta F = |f_{LJ}(r_c) - f_{WALL}(r_c)|$ is added to the force from the wall, where $f(r_c)$ is the force at the cutoff distance r_c. It must be stressed that we have not yet found a rigorous theoretical argument for adding this particular term to the force from the wall, and it is based merely on the observation that it works well for a range of simulated state points and model systems.

8.1 The single-component LJ liquid in a slit-pore. $\rho = 0.85$

Applying the above FCS scheme to the state point of Fig. 8.1 ($R = 0.96$), we arrive at the results presented in Fig. 8.2. Figure 8.2(a) shows the density profile whereas Fig. 8.2(b) shows the RDF of layer 1 (i.e., the contact layer). The black curves give a simulation with a very large pair potential cutoff in combination with no cutoff for the wall-liquid interactions. The red curves give an FCS cutoff for both the liquid and wall interactions, while the turquoise curves give, for comparison, a WCA-type cutoff[1] (Weeks *et al.* [1971]) for the liquid and wall interactions. By comparing to the WCA method, we do not imply that this picture is supposed to be applicable to confined systems, but it provides merely for now a good reference system. The FCS cutoff gives excellent results whereas the WCA-type cutoff shows slight deviations in the density profile (Fig. 8.2(a)).

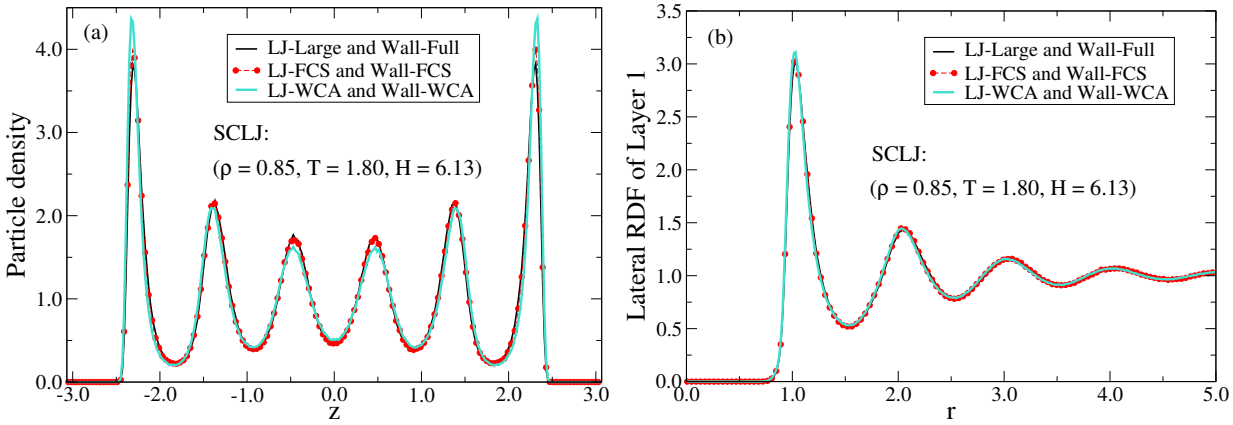

Figure 8.2: *FCS and WCA-type cutoff simulations for the SCLJ liquid confined to a slit-pore. The black curves give a large pair potential cutoff in combination with no cutoff for the wall interactions. The red curves give a cutoff at the FCS for the liquid and wall interactions whereas the turquoise curves give a WCA-type cutoff for the liquid and wall interactions. (a) Density profiles. (b) Lateral RDFs of layer 1 (see Fig. 8.1).*

The RDFs of layer 2 and 3 are shown in Fig. 8.3. Again, the FCS cutoff gives a good approximation to the structure in these two layers whereas the WCA-type cutoff shows a slightly larger deviation than seen for layer 1.

[1] Recall that the WCA method truncates at the potential minimum.

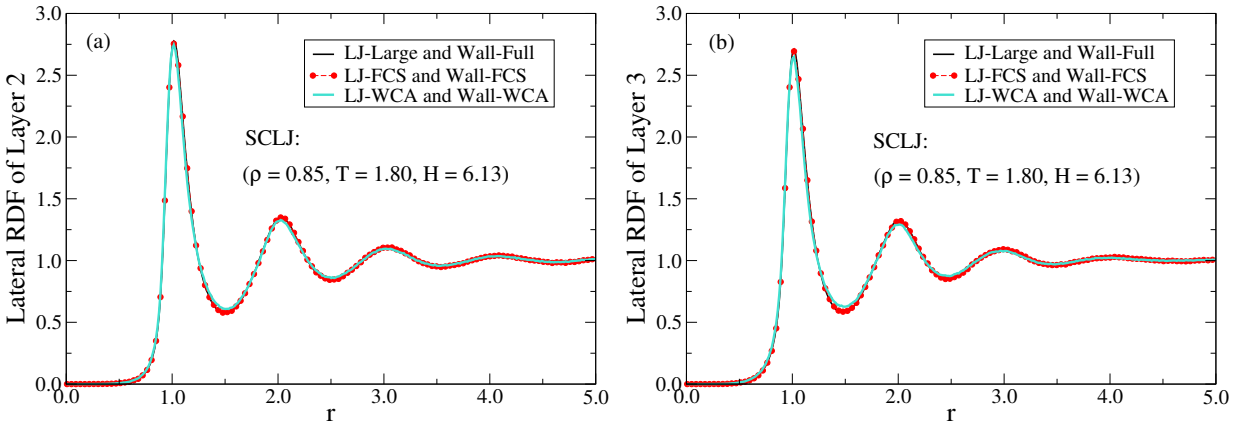

Figure 8.3: *FCS and WCA-type cutoff simulations for the SCLJ liquid confined to a slit-pore. The black curves give a large pair potential cutoff in combination with no cutoff for the wall interactions. The red curves give a cutoff at the FCS for the liquid and wall interactions whereas the turquoise curves give a WCA-type cutoff for the liquid and wall interactions. (a) Lateral RDFs of layer 2. (b) Lateral RDFs of layer 3.*

Next, we consider the incoherent ISF for a wave vector parallel to the walls (chosen to be the same for all layers) in Fig. 8.4. For all layers, the FCS cutoff approximates well the dynamics while the WCA-type cutoff shows slight deviations in layers 2 and 3.

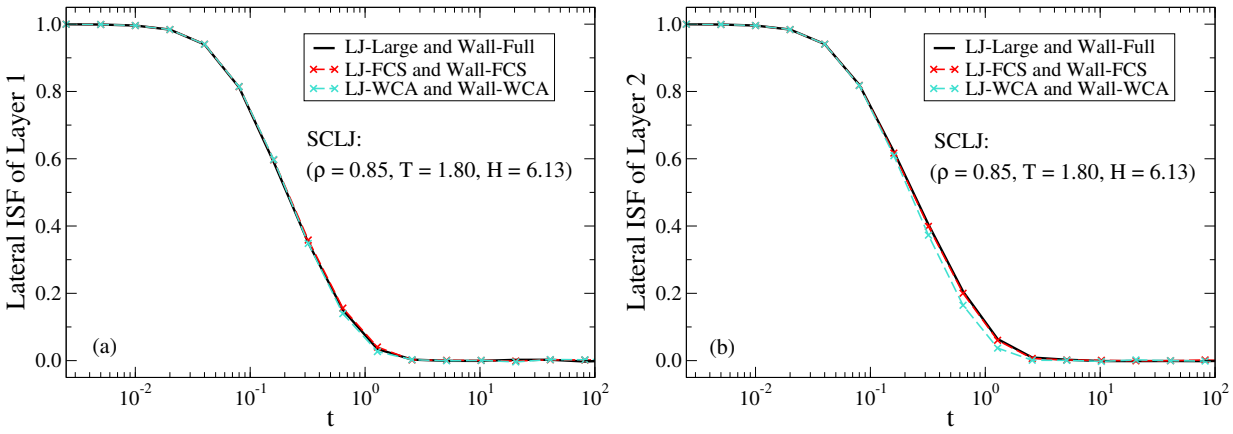

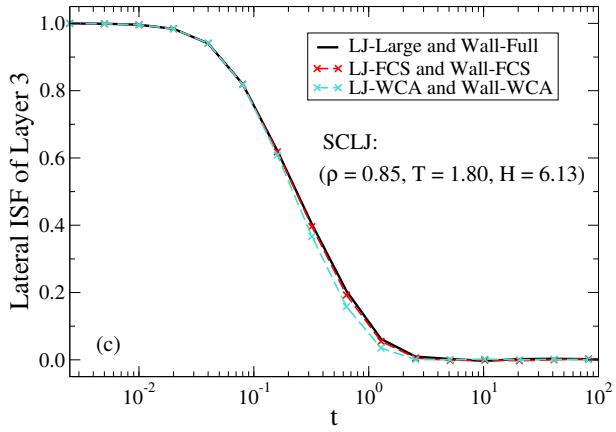

Figure 8.4: *FCS and WCA-type cutoff simulations for the SCLJ liquid confined to a slit-pore. The black curves give a large pair potential cutoff in combination with no cutoff for the wall interactions. The red curves give a cutoff at the FCS for the liquid and wall interactions whereas the turquoise curves give a WCA-type cutoff for the liquid and wall interactions. (a) Lateral ISFs of layer 1. (b) Lateral ISFs of layer 2. (c) Lateral ISFs of layer 3.*

In the following two sections, we lower the density of the slit-pore for the SCLJ system, keeping H constant, and compare the effect on using an FCS cutoff. In doing so, the correlation coefficient R is seen to decrease, and the FCS results are expected to become more approximative. Throughout the chapter, we use the same definitions and meanings introduced in this section (unless specified otherwise).

8.2 The single-component LJ liquid in a slit-pore. $\rho = 0.75$

We show in Fig. 8.5 the density profile and layer RDFs for the SCLJ liquid at $\rho = 0.75$, $T = 0.80$, and $H = 6.13$ ($R = 0.87$).

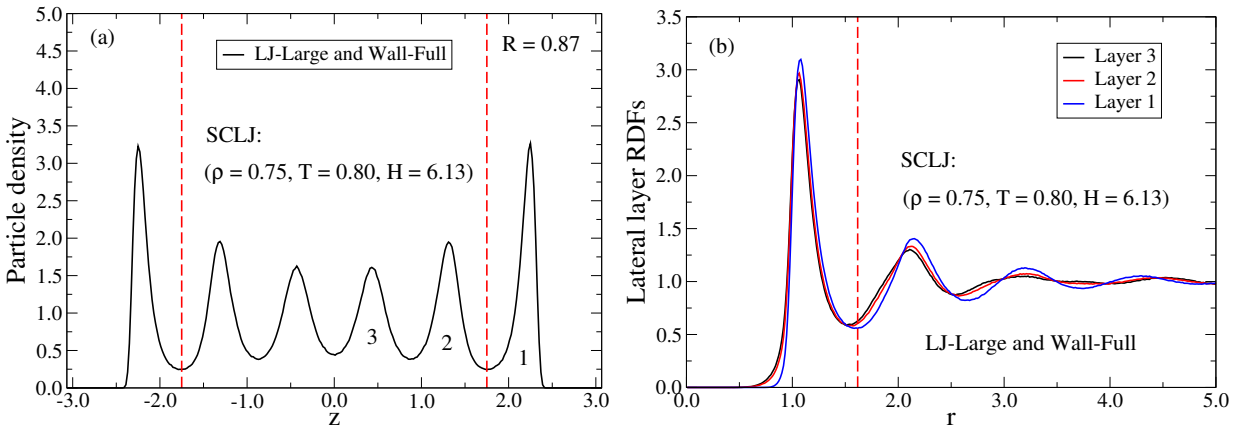

Figure 8.5: *(a) Density profile for the SCLJ liquid in a slit-pore at $\rho = 0.75$, $T = 0.80$, and $H = 6.13$ with pair potential cutoff $r_c = 5.000$. The red dashed line marks the FCS of the wall "particle" at the distance $r = 1.317$ from the wall. (b) Lateral RDFs of layers 1-3 (layer 1 being the contact layer, and layer 3 the bulk layer) of the density profile in (a). The red dashed line marks the FCS of layer 1 at $r = 1.617$.*

Figure 8.6 then shows results for the density profile and contact-layer RDF (layer 1) using the FCS cutoff. The FCS cutoff gives a good approximation to the structure where the WCA-type cutoff shows only minor deviations and is similar to the behavior observed for $\rho = 0.85$.

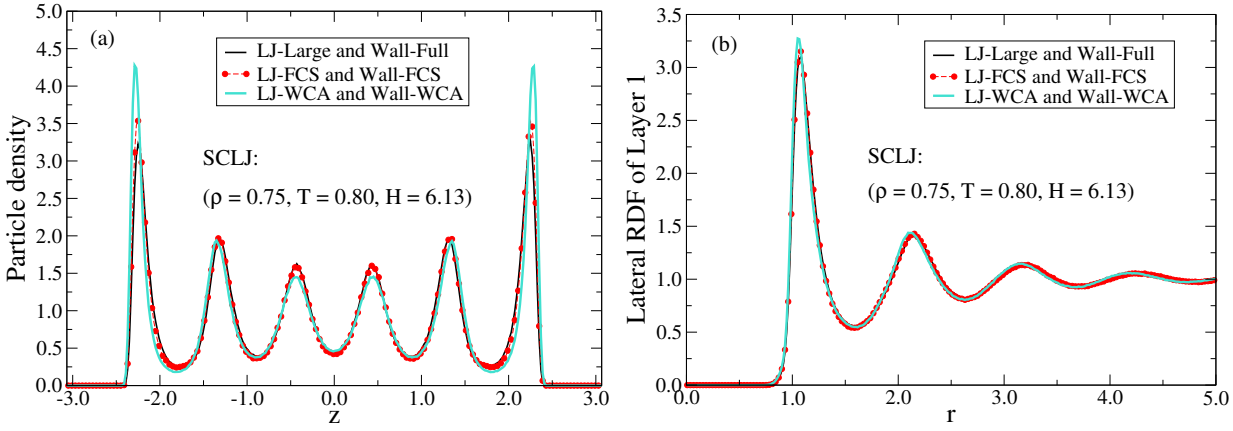

Figure 8.6: *FCS and WCA-type cutoff simulations for the SCLJ liquid confined to a slit-pore. The black curves give a large pair potential cutoff in combination with no cutoff for the wall interactions. The red curves give a cutoff at the FCS for the liquid and wall interactions whereas the turquoise curves give a WCA-type cutoff for the liquid and wall interactions. (a) Density profiles. (b) Lateral RDFs of layer 1.*

Considering the layer RDFs of layer 2 and 3 in Fig. 8.7, we now observe larger deviations for the WCA-type cutoff whereas the FCS cutoff still gives an excellent approximation to the structure of the liquid.

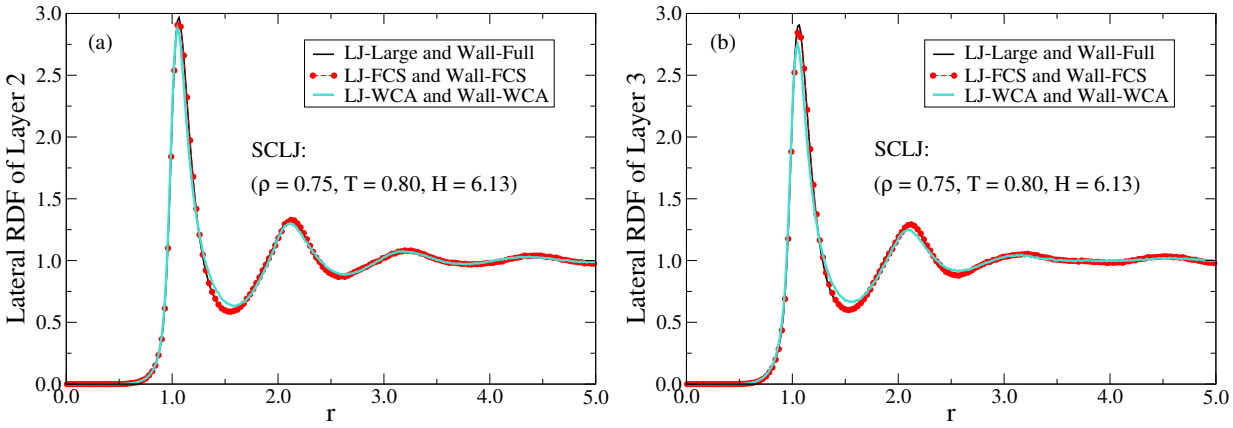

Figure 8.7: *FCS and WCA-type cutoff simulations for the SCLJ liquid confined to a slit-pore. The black curves give a large pair potential cutoff in combination with no cutoff for the wall interactions. The red curves give a cutoff at the FCS for the liquid and wall interactions whereas the turquoise curves give a WCA-type cutoff for the liquid and wall interactions. (a) Lateral RDFs of layer 2. (b) Lateral RDFs of layer 3.*

Probing then the dynamics of all layers in Fig. 8.8 via the incoherent ISF, we observe also larger deviations for the WCA-type cutoff than at the density $\rho = 0.85$. The FCS cutoff only shows slight deviations for layer 3 and is consistent with the border-line correlation coefficient of $R = 0.87$ at this state point.

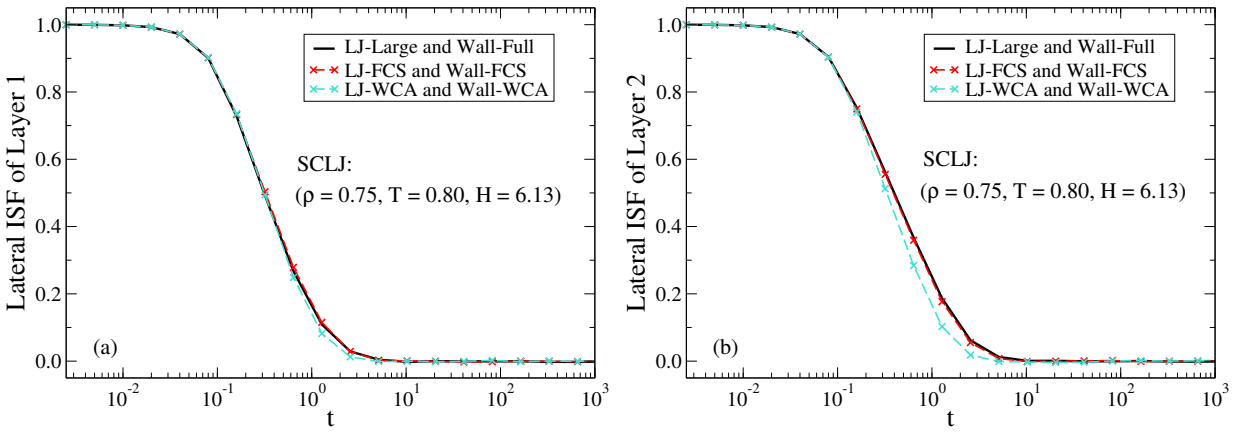

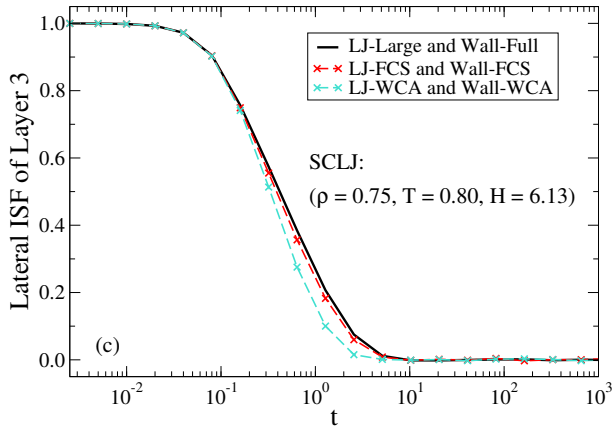

Figure 8.8: *FCS and WCA-type cutoff simulations for the SCLJ liquid confined to a slit-pore. The black curves give a large pair potential cutoff in combination with no cutoff for the wall interactions. The red curves give a cutoff at the FCS for the liquid and wall interactions whereas the turquoise curves give a WCA-type cutoff for the liquid and wall interactions. (a) Lateral ISFs of layer 1. (b) Lateral ISFs of layer 2. (c) Lateral ISFs of layer 3.*

8.3 The single-component LJ liquid in a slit-pore. $\rho = 0.65$

Decreasing now the density even more to $\rho = 0.65$, we arrive at a state point that is not strongly correlating with $R = 0.74$. Again, for reference, Fig. 8.9 shows the density profile and layer RDFs for this state point.

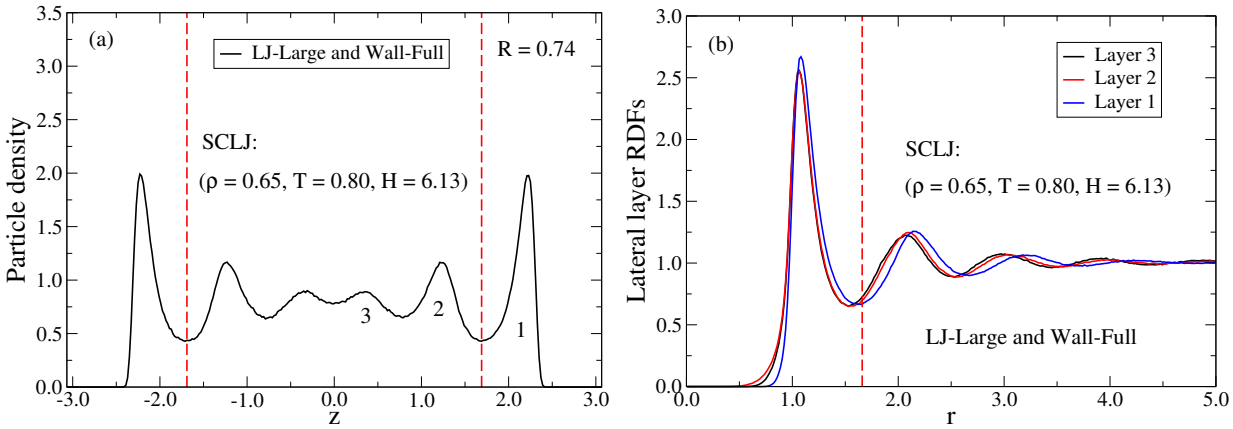

Figure 8.9: *(a) Density profile for the SCLJ liquid in a slit-pore at $\rho = 0.65$, $T = 0.80$, and $H = 6.13$ with pair potential cutoff $r_c = 7.500$. The red dashed line marks the FCS of the wall "particle" at the distance $r = 1.377$ from the wall. (b) Lateral RDFs of layers 1-3 (layer 1 being the contact layer, and layer 3 the bulk layer) of the density profile in (a). The red dashed line marks the FCS of layer 1 at $r = 1.660$.*

As before, we show in Fig. 8.10 results for the density profile and contact-layer RDF using the FCS cutoff. The density profile now displays more deviations using the FCS cutoff

whereas the WCA-type cutoff shows significant deviations, in particular near the walls. On the other hand, for the layer RDF only very minor deviations are seen for either cutoff scheme.

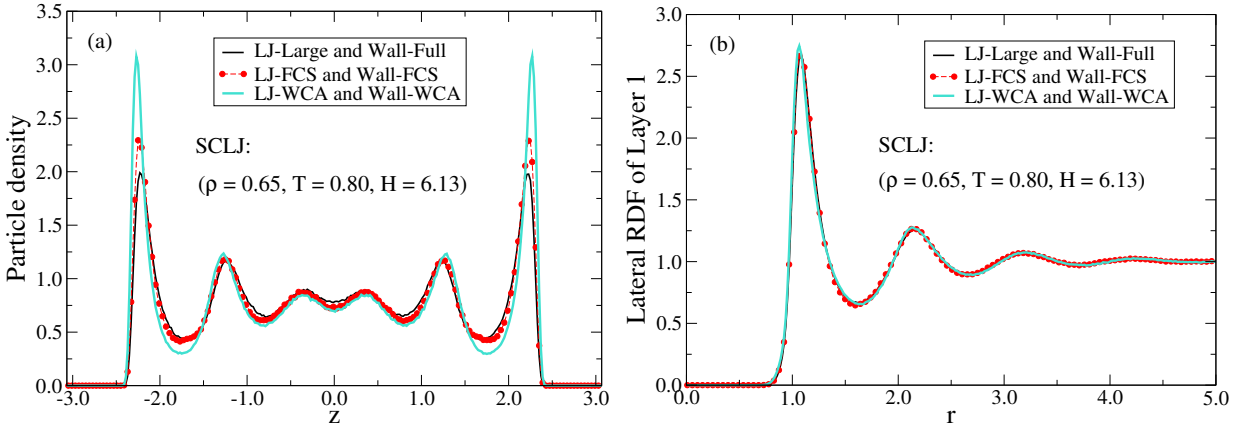

Figure 8.10: *FCS and WCA-type cutoff simulations for the SCLJ liquid confined to a slit-pore. The black curves give a large pair potential cutoff in combination with no cutoff for the wall interactions. The red curves give a cutoff at the FCS for the liquid and wall interactions whereas the turquoise curves give a WCA-type cutoff for the liquid and wall interactions. (a) Density profiles. (b) Lateral RDFs of layer 1.*

In contrast to the results for the contact-layer, the WCA-type cutoff shows clear deviations for layers 2 and 3 in Fig. 8.11. The FCS cutoff gives a good approximation to the structure in both layers.

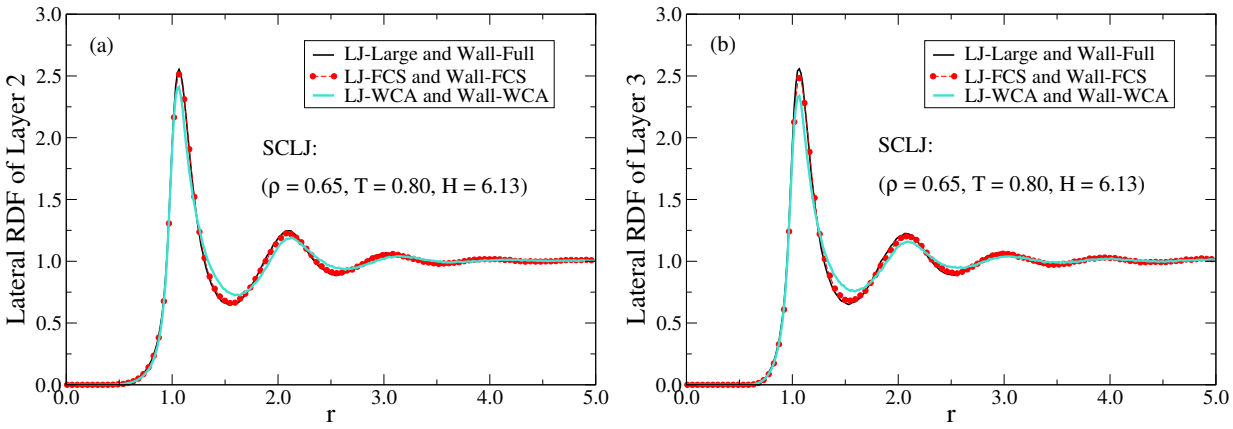

Figure 8.11: *FCS and WCA-type cutoff simulations for the SCLJ liquid confined to a slit-pore. The black curves give a large pair potential cutoff in combination with no cutoff for the wall interactions. The red curves give a cutoff at the FCS for the liquid and wall interactions whereas the turquoise curves give a WCA-type cutoff for the liquid and wall interactions. (a) Lateral RDFs of layer 2. (b) Lateral RDFs of layer 3.*

The dynamics of the three layers are shown in Fig. 8.12. We observe minor deviations using the WCA-type cutoff. Thus, although this state point is not strongly correlating

($R = 0.74$), and the results for the FCS cutoff are seen to become more approximate, it still gives a good approximation to both the structure and the dynamics of the liquid.

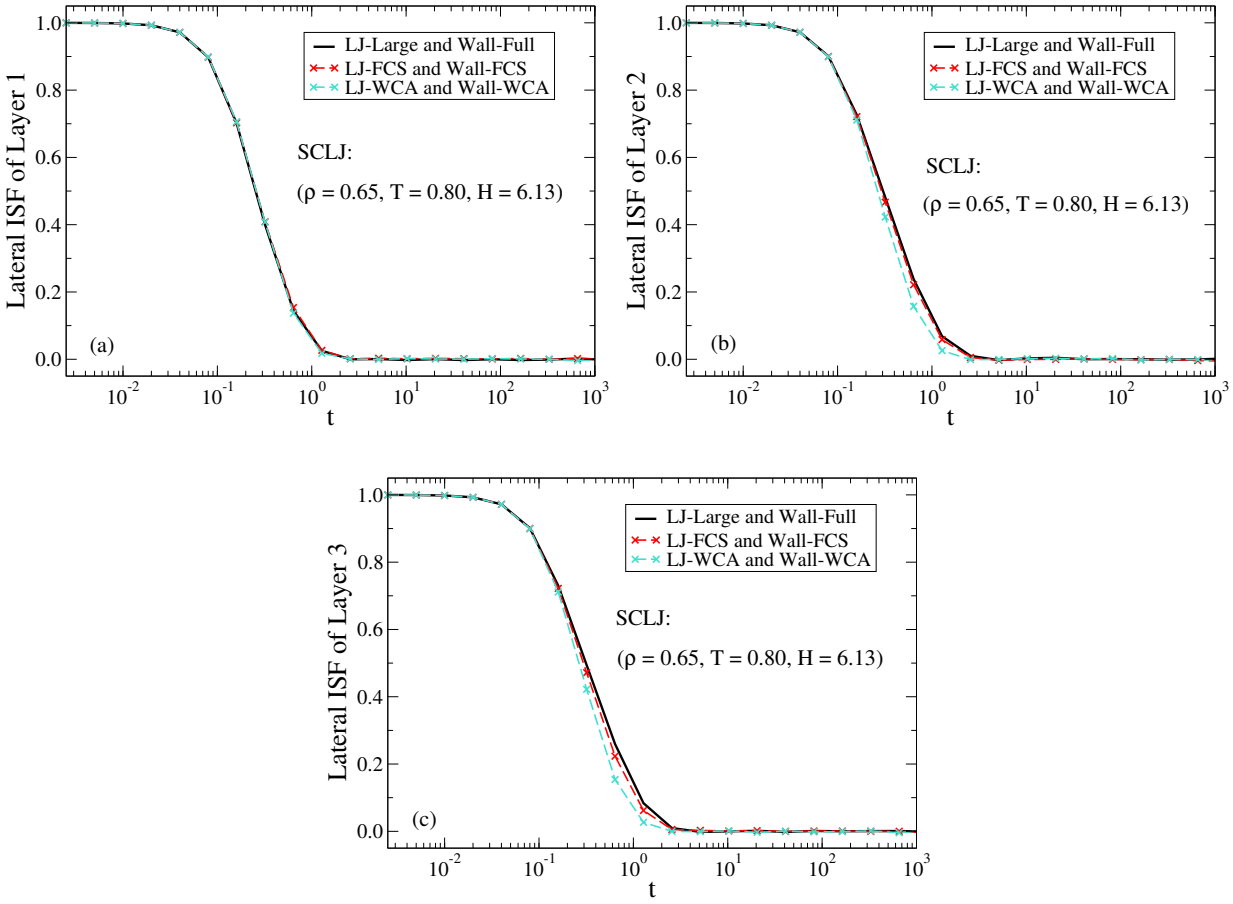

Figure 8.12: *FCS and WCA-type cutoff simulations for the SCLJ liquid confined to a slit-pore. The black curves give a large pair potential cutoff in combination with no cutoff for the wall interactions. The red curves give a cutoff at the FCS for the liquid and wall interactions whereas the turquoise curves give a WCA-type cutoff for the liquid and wall interactions. (a) Lateral ISFs of layer 1. (b) Lateral ISFs of layer 2. (c) Lateral ISFs of layer 3.*

8.4 The single-component LJ liquid in a slit-pore. $\rho = 4.00$

As a final example for the SCLJ system, it is illustrative to consider a state point for which the location of the FCS is pushed to the left of the potential minimum for both the liquid-liquid and wall-liquid interactions. Having the discussion presented in Sec. 5.8 in mind, one expects that a WCA-type cutoff works satisfactorily, and we thus show no results using the WCA approach. In Fig. 8.13 we show the density profile and the layer RDF for each layer of the SCLJ liquid at $\rho = 4.00$, $T = 1179$, and $H = 3.66$ with $R = 0.99$. We see that the FCS (delimited by the red dashed lines) is indeed "pushed" to smaller distances than,

respectively, $2^{1/6}\sigma$ and $(2/5)^{1/6}\sigma_w$ for the pair and wall interactions. These values define the distances of the minima for the simulated potentials ($\sigma = \sigma_w = 1$).

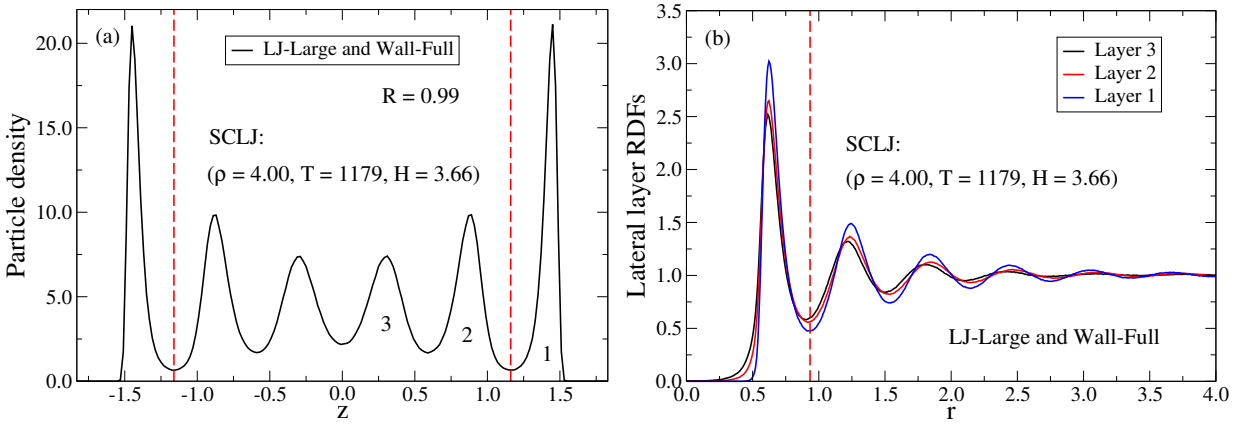

Figure 8.13: *(a) Density profile for the SCLJ liquid in a slit-pore at $\rho = 4.00$, $T = 1179$, and $H = 3.66$ with pair potential cutoff $r_c = 5.000$. The red dashed line marks the FCS of the wall "particle" at the distance $r = 0.669$ from the wall. (b) Lateral RDFs of layers 1-3 (layer 1 being the contact layer, and layer 3 the bulk layer) of the density profile in (a). The red dashed line marks the FCS of layer 1 at $r = 0.934$.*

Figure 8.14 shows the density profile and layer RDF of layer 1 using different cutoffs. The black and red curves give, respectively, reference and FCS simulations. The blue curves give an SF-type cutoff for the liquid and wall interactions at the distance of the first maximum for, respectively, the RDF of layer 1 and the density profile. We see that the FCS cutoff gives an excellent approximation to the structure although the pair and wall potential cutoffs are quite small, respectively, $r_c = 0.934$ and $r_w = 0.669$. In comparison, applying a cutoff inside the FCS (blue curves) shows significant deviations.

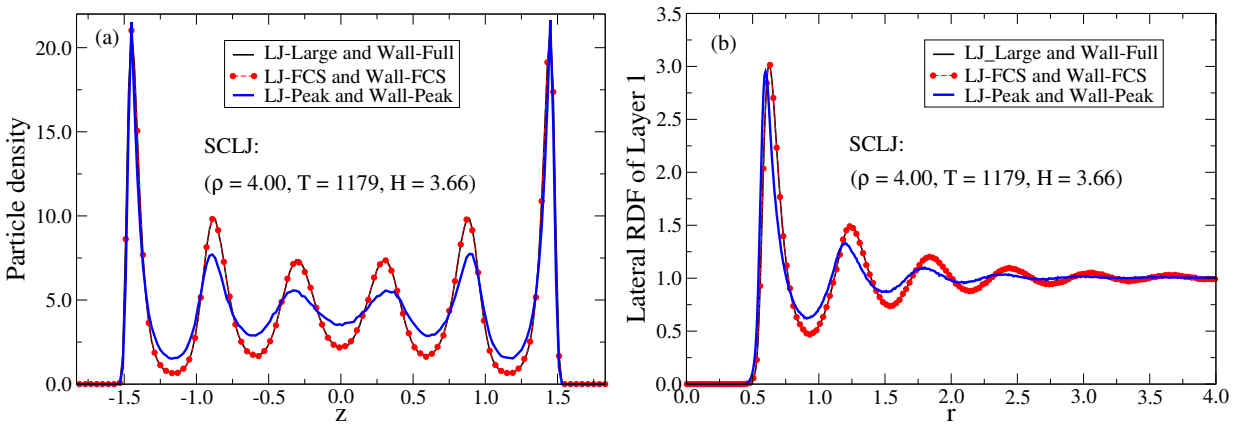

Figure 8.14: *FCS and first-maximum-type cutoff simulations for the SCLJ liquid confined to a slit-pore. The black curves give a large pair potential cutoff in combination with no cutoff for the wall interactions. The red curves give a cutoff at the FCS for the liquid and wall interactions whereas the blue curves give an SF-type cutoff for the liquid and wall interactions at the distance of the first maximum for, respectively, the RDF of layer 1 and the density profile. (a) Density profiles. (b) Lateral RDFs of layer 1 (see Fig. 8.13).*

The same conclusion is reached considering the RDFs of layers 2 and 3 in Fig. 8.15.

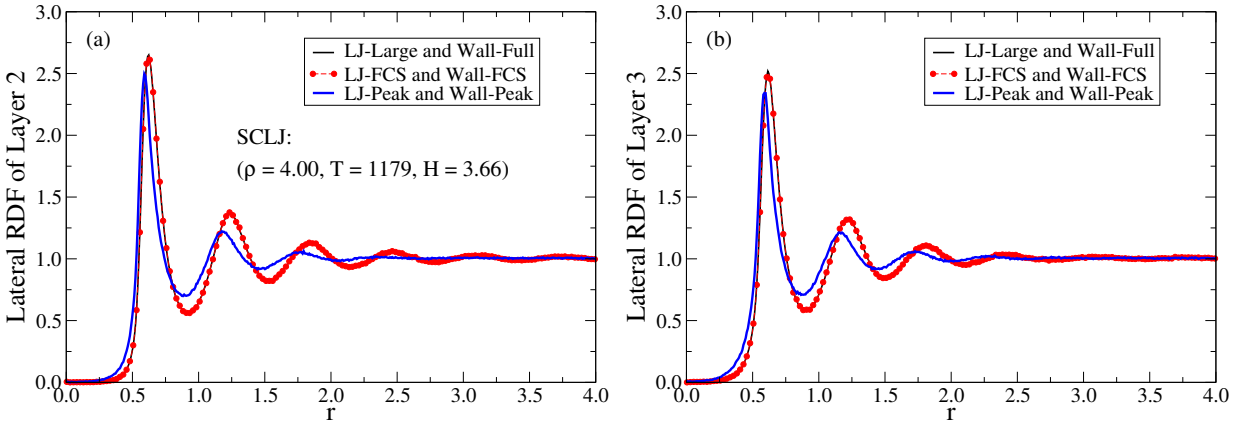

Figure 8.15: *FCS and first-maximum-type cutoff simulations for the SCLJ liquid confined to a slit-pore. The black curves give a large pair potential cutoff in combination with no cutoff for the wall interactions. The red curves give a cutoff at the FCS for the liquid and wall interactions whereas the blue curves give an SF-type cutoff for the liquid and wall interactions at the distance of the first maximum for, respectively, the RDF of layer 1 and the density profile. (a) Lateral RDFs of layer 2. (b) Lateral RDFs of layer 3.*

Turning now to the dynamics via the self-part of the ISF in Fig. 8.16. The same behavior as for the structure is observed where the FCS cutoff gives an excellent approximation to the dynamics whereas applying a cutoff inside the FCS shows deviations.

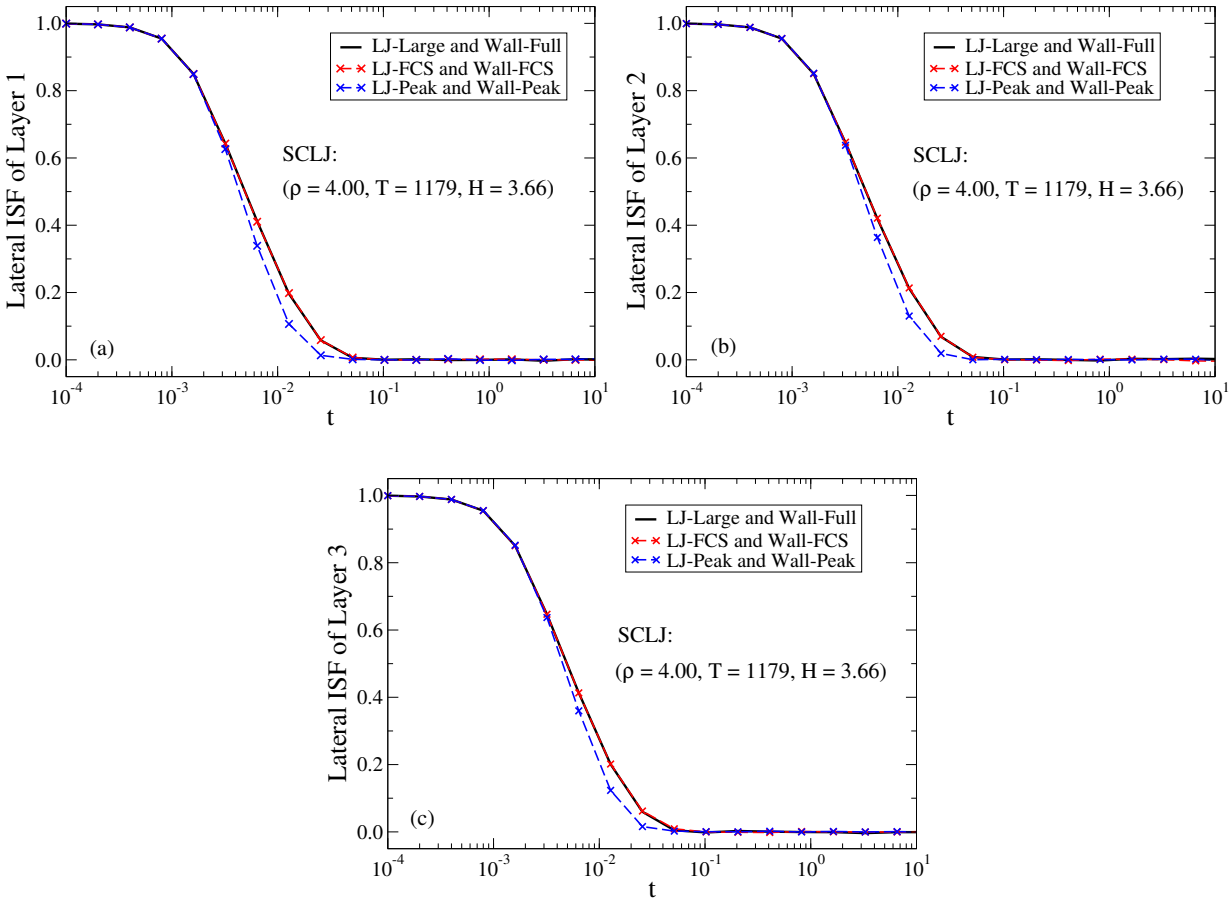

Figure 8.16: *FCS and first-maximum-type cutoff simulations for the SCLJ liquid confined to a slit-pore. The black curves give a large pair potential cutoff in combination with no cutoff for the wall interactions. The red curves give a cutoff at the FCS for the liquid and wall interactions whereas the blue curves give an SF-type cutoff for the liquid and wall interactions at the distance of the first maximum for, respectively, the RDF of layer 1 and the density profile. (a) Lateral ISFs of layer 1. (b) Lateral ISFs of layer 2. (c) Lateral ISFs of layer 3.*

8.5 The Kob-Andersen binary LJ mixture in a slit-pore

We now consider the application of an FCS cutoff to the KABLJ mixture that was also investigated for isomorphs in Sec. 7.4. Figure 8.17(a) shows the A and B-particle density profiles for the KABLJ mixture confined to a slit-pore at $\rho = 1.20$, $T = 1.40$, and $H = 5.97$ ($R = 0.95$) while Fig. 8.17(b) shows the AA-particle RDF for each layer. As mentioned in Sec. 7.4, the contact layer (layer 1) shows clear sign of solidification.

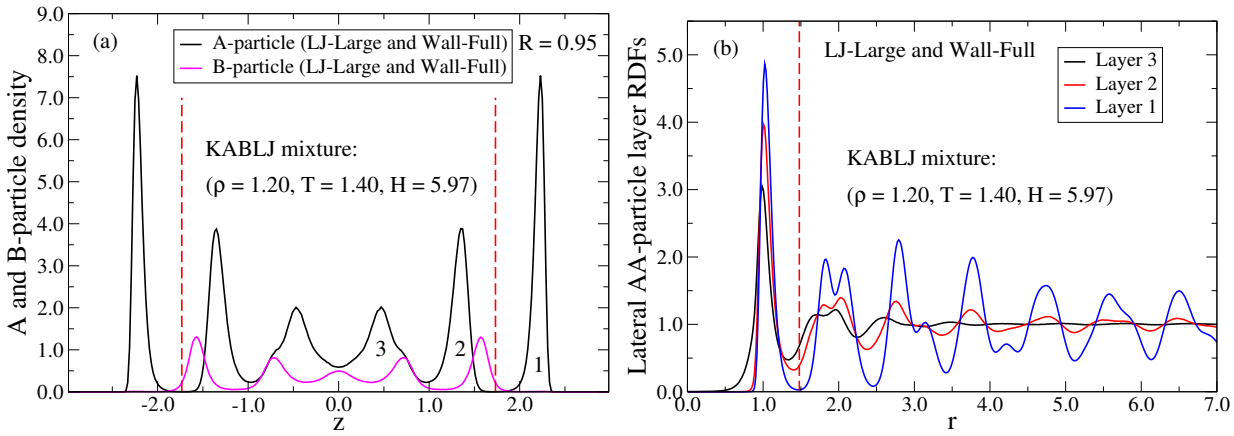

Figure 8.17: *(a) A and B-particle density profiles for the KABLJ mixture confined to a slit-pore at $\rho = 1.20$, $T = 1.40$, and $H = 5.97$ with pair potential cutoff $r_c = 8.000$. The red dashed line marks the FCS of the wall "particle" at the distance $r = 1.252$ from the wall. (b) Lateral AA-particle RDFs of layers 1-3 (layer 1 being the contact layer, and layer 3 the bulk layer) of the A-particle density profile in (a). The red dashed line marks the FCS of layer 1 at $r = 1.479$.*

Probing now the density profile for both particles using an FCS cutoff in Fig. 8.18, we see excellent agreement with the reference simulations (black curves), whereas using a WCA-type cutoff shows some deviation. In particular for the WCA-type cutoff, we note for the B-particle density profile of Fig. 8.18(b) that a small amount of excess B-particles have been absorbed into the A-particle rich contact layer (turquoise curve and around $z \approx 2.2$).

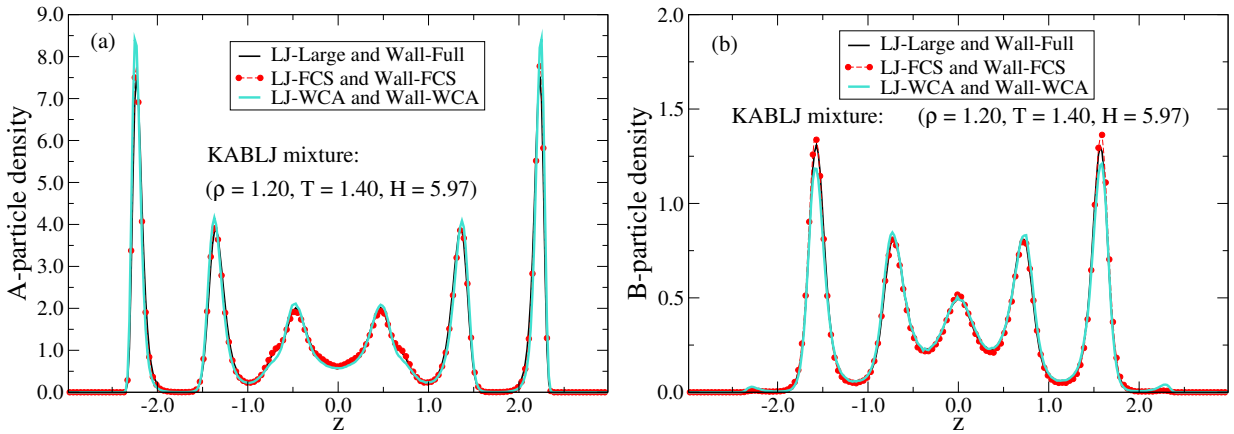

Figure 8.18: *Density profiles of the KABLJ mixture confined to slit-pore. The black curves give a large pair potential cutoff in combination with no cutoff for the wall interactions. The red curves give a cutoff at the FCS for the liquid and wall interactions, and the turquoise curves give a WCA-type cutoff for the liquid and wall interactions. (a) A-particle density profiles. (b) B-particle density profiles.*

Considering in Fig. 8.19 the AA-particle RDF for each layer, the FCS simulations show nearly perfect agreement with the reference simulations. In comparison, the WCA-type

cutoff shows clear deviations for all layers, in particular, for the contact layer.

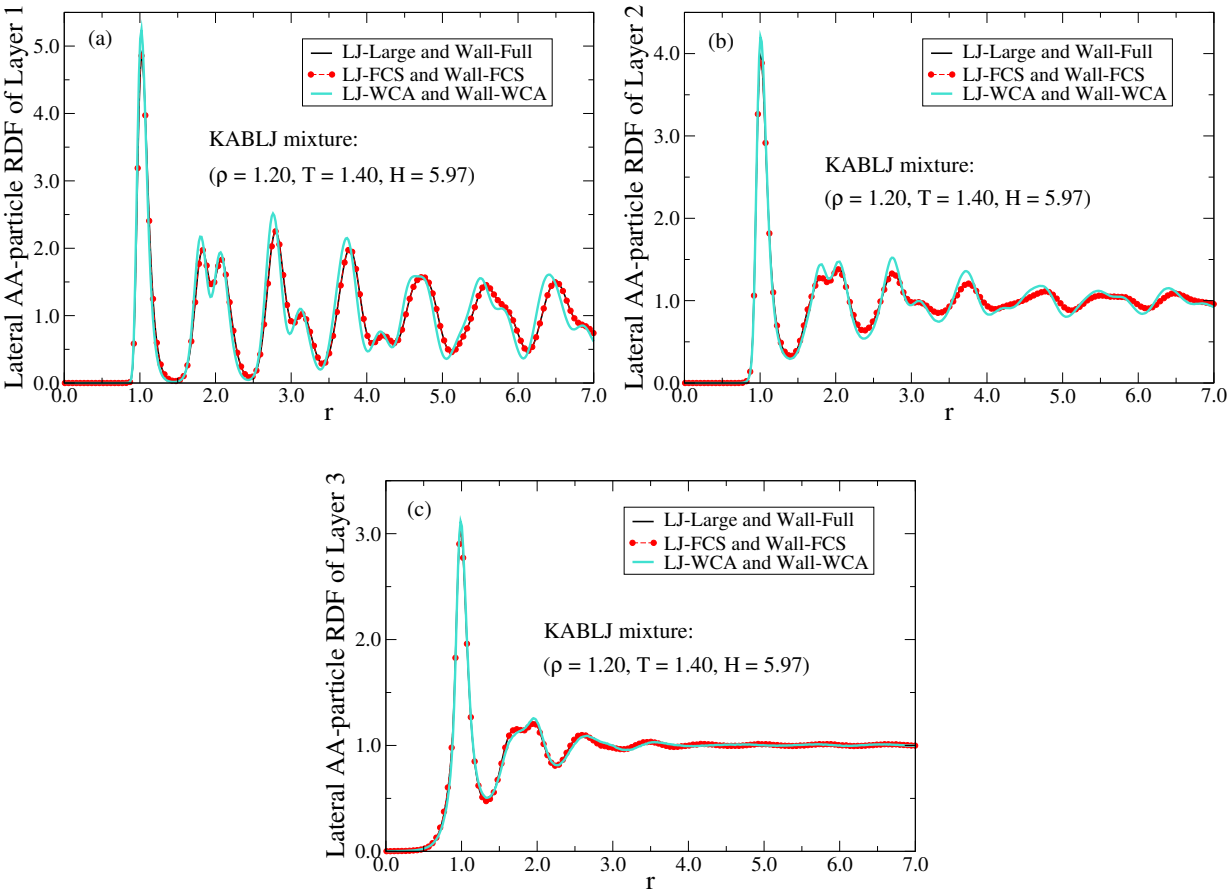

Figure 8.19: *FCS and WCA-type cutoff simulations for the KABLJ mixture confined to a slit-pore. The black curves give a large pair potential cutoff in combination with no cutoff for the wall interactions. The red curves give a cutoff at the FCS for the liquid and wall interactions whereas the turquoise curves give a WCA-type cutoff for the liquid and wall interactions. (a) Lateral AA-particle RDFs of layer 1. (b) Lateral AA-particle RDFs of layer 2. (c) Lateral AA-particle RDFs of layer 3.*

Finally, we consider the corresponding dynamics of each layer in Fig. 8.20. Again, the agreement with the FCS simulations is excellent while the WCA-type cutoff mimics the behavior seen in the RDFs, i.e., showing pronounced deviations for the contact layer. Appendix D shows simulations of two additional model systems: the WABLJ mixture and the asymmetric dumbbell model. These systems give rise to the same conclusions.

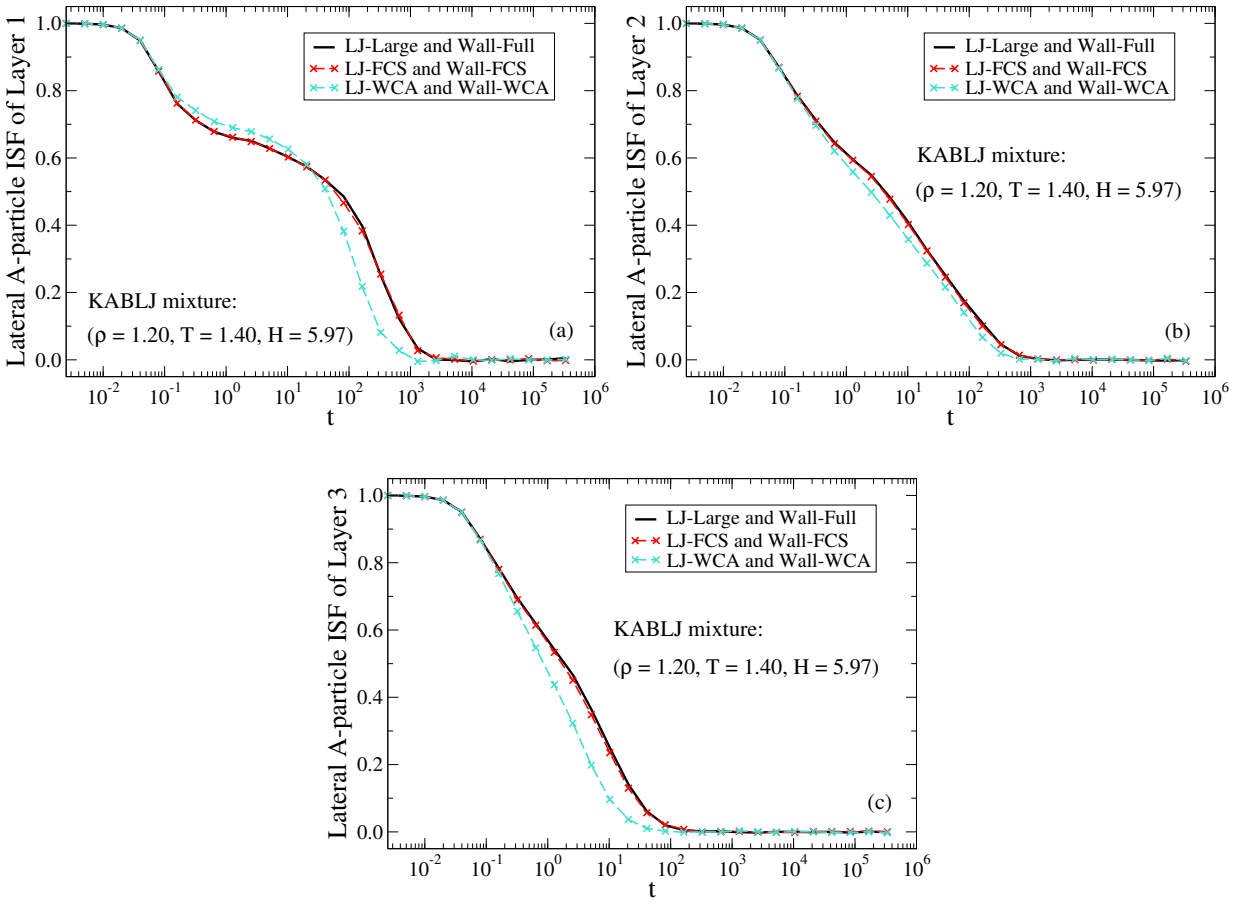

Figure 8.20: *FCS and WCA-type cutoff simulations for the KABLJ mixture confined to a slit-pore. The black curves give a large pair potential cutoff in combination with no cutoff for the wall interactions. The red curves give a cutoff at the FCS for the liquid and wall interactions whereas the turquoise curves give a WCA-type cutoff for the liquid and wall interactions. (a) Lateral A-particle ISFs of layer 1. (b) Lateral A-particle ISFs of layer 2. (c) Lateral A-particle ISFs of layer 3.*

8.6 Concluding on the FCS results for confined liquids

In conclusion, the above results (and Appendix D) suggest that also for a confined system, it is merely the interactions within the FCS that determine the structure and dynamics. The latter also holds to a good approximation near the interface, and, as such, the interfacial layer is no more special than any other layer of the liquid. In addition, the wall influences only particles at distances beyond the first layer, indirectly, via their interactions with the particles of the contact layer. A similar effect is seen for completely hard walls with specular or "Maxwellian" microscopic roughness where the memory of colliding with the walls is lost in the contact layer (Diestler *et al.* [1991]). At first sight, a confined system appears complex due to stratification and a significant change in the dynamics compared to the bulk system, however, as shown here; the physics can still be quite simple. It must, however, be noted

that these results are expected to hold only for liquids that are strongly correlating in the confinement.

Alternatively, one may argue (Weeks [2012]) that some of the state points studied for the SCLJ system are high density and high temperature states with an external wall potential with attractions such that the original WCA force cancellation arguments (Widom [1967]) work pretty well for the fluid between the walls. Applying then a cutoff at large distances as in the FCS approach would then appear trivial. We observed, however, large deviations using the WCA-type approach on the liquid-liquid and wall-liquid interactions at high density for the KABLJ mixture, the WABLJ mixture (see Appendix D), the asymmetric dumbbell, and for the SCLJ liquid at somewhat lower densities ($\rho = 0.75, 0.65$). In all cases the FCS cutoff gave an excellent approximation to the structure and dynamics. The most striking evidence, however, for the proposed FCS picture in confined systems is supplied by the SCLJ system at $\rho = 4.00$ where cutoffs well below the WCA minima could safely be applied to the liquid-liquid and wall-liquid interactions.

The investigation in this chapter is limited to one particular confining potential, the Steele potential, and the generality of the FCS results for a variety of external fields remains to be shown.

8.7 Other methods for approximating non-uniform liquids

The FCS approach outlined above seems to be a promising new way to approximate confined liquids. There exist, however, other more general approaches to describing non-uniform liquids:

- Mode-coupling theory (Götze [2009]), which relates the dynamic density correlations of a viscous fluid to its static structure, has been extended to treat simple model fluids (e.g. hard-sphere) under confinement (Biroli *et al.* [2006], Krakoviack [2005, 2011], Lang *et al.* [2010, 2012]).

- Local Molecular Field (LMF) theory by Weeks and co-workers (Rodgers and Weeks [2008], Weeks *et al.* [1995, 1997, 1998]). LMF theory,

  "*...generally accounts for the averaged effects of long-ranged components of the intermolecular interactions by using an effective or restructured external field. The derivation starts from the exact Yvon–Born Green hierarchy and shows that the approximation can be very accurate when the interactions averaged over are slowly varying at characteristic nearest-neighbor distances.*" (Rodgers and Weeks [2008]).

  A specific example of the method (Weeks *et al.* [1995]) would be to use the WCA approximation for the liquid in confinement and then account for the long-ranged part of the potential using the effective external field determined in a self-consistent manner. The LMF theory has been applied to a wide range of systems ranging from weak dispersion interactions to systems with strong electrostatic interactions with good results. The theory has, however, only been developed to approximate static quantities and does not yet incorperate dynamics (Rodgers and Weeks [2008]).

- Mathematical force-error estimate approaches for inhomogeneous systems (Wang *et al.* [2012]).

In general, for systems with strong electrostatic interactions, the FCS approach is not expected to work as competing interactions tend to destroy the strong correlation.

Chapter 9

NVU DYNAMICS (PAPERS VI, VII AND VIII)

Molecular dynamics (MD) has since its introduction evolved rapidly and is now a very versatile technique being applied to simulations at constant temperature NVT (Hoover [1985], Nosé [1984]), constant pressure NPT (Frenkel and Smit [2002]), or even constant chemical potential μVT (Lynch and Pettitt [1997]). In this chapter, we consider a new MD method that conserves the total potential energy NVU (Papers VI, VII, and VIII).

NVU dynamics is defined by motion that traces out a geodesic curve (see below) on the constant-potential-energy hypersurface Ω given by

$$\Omega = \{\mathbf{R} \in R^{3N} \mid U(\mathbf{R}) = U_0\}. \tag{9.1}$$

Here $\mathbf{R} \equiv \{\mathbf{r}^{(1)}, ..., \mathbf{r}^{(N)}\}$ in which $\mathbf{r}^{(k)}$ is the position vector of the k'te particle, U is the potential-energy function of a N-particle classical system, and U_0 is a constant. Equation (9.1) specifies a $(3N-1)$-dimensional hypersurface (a level surface) embedded in the Euclidean $3N$-dimensional configuration space and is a so-called Riemannian differential manifold (Gallot *et al.* [2004], Schlichtkrull [2009, 2010]).

A geodesic on Ω is then a curve that satisfies the condition of stationary length for fixed endpoints $\mathbf{R}_A$ and $\mathbf{R}_B$ (Gallot *et al.* [2004], Kopeikin *et al.* [2011]), i.e.,

$$\delta \int_{\mathbf{R}_A}^{\mathbf{R}_B} dl \; \Bigg|_{\Omega} = 0, \tag{9.2}$$

where dl is the line element of the metric, and here and henceforth δ denotes the variation of variational calculus (Hansen [1973]). The condition of Eq. (9.2) expresses that small perturbations of the curve on Ω, keeping the endpoints fixed, to lowest order do not change the curve length (Hansen [1973]). The shortest path between any two points is thus a geodesic. Geodesics and their fascinating properties have been studied extensively in pure mathematics, physics as well as computer science see, for instance, Baek *et al.* [2007], Caselles *et al.* [1997], Cheng *et al.* [2002], Kimmel and Sethian [1998], Kopeikin *et al.* [2011], Schlichtkrull [2010] and references therein. Physically, traversing a geodesic at constant velocity corresponds simply to a generalization of Newton's first law, i.e. the law of inertia, to a curved space (the surface itself). NVU dynamics may thus simply be imagined as going "straight ahead" on the hypersurface Ω.

An illustration of geodesics on a sphere in three dimensions (called great circles) is shown via the black curves in Fig. 9.1. We observe that between the two poles there exist an infinite number of geodesics, and geodesics may thus in general intersect each other.

Figure 9.1: *An illustration of geodesics on a sphere (black curves, taken from Schiller-Institute [2013]). The geodesics may be derived by intersecting the sphere with a plane containing the central point of the sphere. There exist an infinite number of geodesics between the two poles; the shortest path between any two points is a geodesic.*

The motivation to study *NVU* dynamics derives from the theory of strongly correlating liquids. If a liquid to a good approximation has isomorphs in the phase diagram, then along these curves the reduced coordinate constant-potential-energy hypersurface $\tilde{\Omega}$ defined by (recall $\tilde{\mathbf{R}} = \rho^{1/3}\mathbf{R}$)

$$\tilde{\Omega} = \{\tilde{\mathbf{R}} \in R^{3N} \mid U(\rho^{-1/3}\tilde{\mathbf{R}}) = \langle U \rangle\}, \tag{9.3}$$

is also (approximately) invariant (Dyre [2013], Gnan *et al.* [2009]). In this equation $\langle U \rangle$ denotes the average potential energy of the respective state points along the isomorph. Thus, it is natural to speculate that the isomorph invariants are simply encoded in the geometry of $\tilde{\Omega}$. However, to understand the dynamical invariants of the isomorph, one needs a dynamics that refers exclusively to $\tilde{\Omega}$, and the simplest deterministic dynamics is geodesic dynamics. In fact, all liquids have constant-potential-energy hypersurfaces Ω (Eq. (9.1)), and *NVU* dynamics is consequently defined for any liquid, not just the strongly correlating liquids.

Molecular dynamics at constant potential energy has previously been considered by a number of authors.

- Cotterill, Madsen and co-workers (Cotterill and Madsen [1986, 2006], Li *et al.* [1992]) used dynamics at constant potential energy to understand the differences between crystalline and non-crystalline states of matter in terms of the geometry of Ω. The authors used an algorithm similar to the one presented in this chapter. However, no connection to geodesics was made, and the applied algorithm violates the usual stability criteria for algorithms in MD (see Paper VI).

- Scala *et al.* [2002] studied diffusive dynamics on Ω focusing on the entropic nature of barriers in the potential energy landscape (i.e., the graph of $U(\mathbf{R})$) by regarding these as "bottlenecks". A picture shared by Cotterill, Madsen and co-workers who imagined Ω as consisting of pockets connected by "tubes".

- Stratt and co-workers (Nguyen and Stratt [2010], Nguyen *et al.* [2012], Wang and Stratt [2007a,b]) considered geodesic pathways in the "potential-energy-landscape

ensemble". This novel ensemble is defined by including all configurations with potential energy less than or equal to some potential energy U_0. A geodesic in the potential-energy-landscape ensemble consists of a curve that is partly geodesic on the constant-potential-energy surface Ω, partly a straight line in the space defined by $U < U_0$. In this approach, the picture shifts, "*perspective from finding stationary points on the potential energy landscape to finding and characterizing the accessible pathways through the landscape. Within this perspective pathways would be slow, not because they have to climb over high barriers, but because they have to take a long and tortuous route to avoid such barriers...*" (Wang and Stratt [2007a]). Thus, the more "convoluted and labyrinthine" the geodesic pathways are, the slower is the dynamics.

In the next section, we derive a numerical algorithm for performing NVU geodesic motion on Ω in the case of atomic systems (Papers VI and VII) whereas in Sec. 9.2 we extend this algorithm in order to simulate molecular systems with rigid bonds (Paper VIII). Simulations of rigid bonds, in general, are rather involved, as it requires solving systems of nonlinear equations (see, for instance, Ingebrigtsen *et al.* [2010], Ryckaert *et al.* [1977], Toxvaerd *et al.* [2009]).

9.1 Discrete geodesic motion on Ω for atomic systems

The geodesics of Ω were in Eq. (9.2) defined via the variation over the arc length (Hansen [1973]). However, geodesics on Ω may also be defined[1] via second-order, nonlinear differential equations given as (Schlichtkrull [2010])

$$\frac{d^2u_i(t)}{dt^2} + \sum_{j,k} \Gamma^i_{jk}(\gamma(t)) \frac{du_j(t)}{dt} \frac{du_k(t)}{dt} = 0, \tag{9.4}$$

where $u_i(t)$ are coordinates of the curve $\gamma(t)$ parameterized by t, and Γ^i_{jk} are the Christoffel symbols (Schlichtkrull [2009, 2010]), having somewhat complicated expressions and for clarity of presentation left out (see Schlichtkrull [2010]). These equations are also called the "geodesic equations", and finding geodesics is usually a matter of solving these differential equations.

In analogy, classical mechanics may also be formulated via Hamilton's principle (Goldstein *et al.* [2002]), instead of Newton's second law ($\mathbf{F}_i - m_i\ddot{\mathbf{r}}_i = 0$), given by

$$\delta \int_{t_1}^{t_2} L \, dt = 0. \tag{9.5}$$

Here $L = K - U$ is the Lagrangian function, K is the kinetic energy, and in Eq. (9.5) one considers a path in configuration space between times t_1 and t_2 and requires the "action" to be stationary (Goldstein *et al.* [2002]).

[1] In fact, the geodesic equations follow by carrying out the variational principle (Kopeikin *et al.* [2011]).

Lately, a new class of numerical integrators was proposed, the so-called "variational time integrators" (Kane *et al.* [1999], Lew [2003], Marsden and West [2001], Stern and Desbrun [2006], West [2004]). In this approach, the numerical integrator is derived *directly* from a variational principle, i.e., by first discretizing the variational principle and then carrying out the variation. The motivation behind variational time integrators is that by deriving the discrete algorithm from a variational principle, the intrinsic geometrical properties of the flow are maintained. It has been shown that the variational approach generates algorithms with equivalent or superior stability to the usual numerical approaches for differential equations (Kane *et al.* [1999], Lew [2003], Marsden and West [2001], Stern and Desbrun [2006], West [2004]). As an example, applying the variational integration technique to Hamilton's principle (Eq. (9.5)) results in the Verlet algorithm (see West [2004] for a derivation).

In this spirit, we take Eq. (9.2) as the starting point for developing the numerical *NVU* algorithm rather than using the geodesic equations. Before proceeding, however, we must define the measure of length appearing in Eq. (9.2). Motivated by the results to come, we define dl via the expression

$$dl^2 \equiv \sum_k \tilde{m}_k \big(d\mathbf{r}^{(k)}\big)^2, \tag{9.6}$$

where $\tilde{m}_k = m_k/\langle m\rangle$ is the "reduced" mass of particle k. Equation (9.6) is not the standard Euclidean measure of length (except when all masses are equal), it is rather derived from a metric proposed by Heinrich Hertz (Hertz [1894], Lützen [2005]). The point of choosing this particular metric, as we shall see, is that it ensures equivalence between *NVU* and standard energy-conserving Newtonian *NVE* dynamics in the thermodynamic limit for systems of varying masses. Thus, although we consider only the configuration space in *NVU* dynamics, the (relative) masses still enter via the definition of length.

With this choice for dl, a discretization of Eq. (9.2) can now be performed in different ways (Stern and Desbrun [2006]), and one possibility is

$$\delta S \equiv \delta\Big(\sum_i \sqrt{\sum_k \tilde{m}_k \big(\mathbf{r}_i^{(k)} - \mathbf{r}_{i-1}^{(k)}\big)^2} - \sum_i \lambda_i U(\mathbf{R}_i)\Big) = 0. \tag{9.7}$$

In this expression, the path is divided into a number of discrete points indexed by i (starting from $\mathbf{R}_A$ and ending at $\mathbf{R}_B$), and one Lagrangian multiplier λ_i is introduced for every point i to keep the potential energy constant (Hansen [1973]). The expression of Eq. (9.7) is dependent on all the k particles and discrete points i. For the variation to vanish, this corresponds simply to (see Stern and Desbrun [2006])

$$\partial S/\partial \mathbf{r}_i^{(k)} = 0, \tag{9.8}$$

for all $k = 1, ..., N$ and discrete points[2] i. In addition, we also make an Ansatz[3] of constant step length l_0 (Paper VI), i.e.,

[2] We neglect here the endpoints A and B as they are fixed.

[3] This corresponds simply to a constant time step length Δt in Newtonian dynamics.

$$\sum_k \tilde{m}_k \left(\mathbf{r}_i^{(k)} - \mathbf{r}_{i-1}^{(k)}\right)^2 \equiv l_0^2. \tag{9.9}$$

Taking then the partial derivative $\partial S/\partial \mathbf{r}_i^{(k)} = 0$ and applying Eq. (9.9) gives

$$\tilde{m}_k\big(\mathbf{r}_i^{(k)} - \mathbf{r}_{i-1}^{(k)}\big) + \tilde{m}_k\big(\mathbf{r}_i^{(k)} - \mathbf{r}_{i+1}^{(k)}\big) + l_0\lambda_i \mathbf{f}_i^{(k)} \;=\; 0, \tag{9.10}$$

where $\mathbf{f}_i^{(k)} = -\nabla_{\mathbf{r}_i^{(k)}} U$. Equivalently, the NVU algorithm can be written

$$\mathbf{r}_{i+1}^{(k)} = 2\mathbf{r}_i^{(k)} - \mathbf{r}_{i-1}^{(k)} + l_0\lambda_i \langle m\rangle\, \mathbf{f}_i^{(k)}/m_k. \tag{9.11}$$

Equation (9.11) constitutes the NVU algorithm for atomic systems with varying mass. However, to complete the NVU algorithm an expression for the Lagrangian multipliers λ_i must be determined.

9.1.1 Determining the discrete *NVU* Lagrangian multipliers

We determine the Lagrangian multipliers λ_i as follows. Defining first

$$\mathbf{a}_i^{(k)} \equiv \mathbf{r}_i^{(k)} - \mathbf{r}_{i-1}^{(k)}, \tag{9.12}$$

$$\mathbf{b}_i^{(k)} \equiv \mathbf{r}_i^{(k)} - \mathbf{r}_{i+1}^{(k)}. \tag{9.13}$$

The Ansatz of Eq. (9.9) then expresses that

$$\sum_k \tilde{m}_k((\mathbf{a}_i^{(k)})^2 - (\mathbf{b}_i^{(k)})^2) = \sum_k \tilde{m}_k(\mathbf{a}_i^{(k)} + \mathbf{b}_i^{(k)}) \cdot (\mathbf{a}_i^{(k)} - \mathbf{b}_i^{(k)}) = 0, \tag{9.14}$$

and via Eq. (9.10) we have

$$\sum_k \tilde{m}_k\big(-l_0\lambda_i \mathbf{f}_i^{(k)}/\tilde{m}_k\big) \cdot \big(\mathbf{r}_{i+1}^{(k)} - \mathbf{r}_{i-1}^{(k)}\big) = 0. \tag{9.15}$$

Equivalently,

$$\sum_k \mathbf{f}_i^{(k)} \cdot \mathbf{r}_{i+1}^{(k)} = \sum_k \mathbf{f}_i^{(k)} \cdot \mathbf{r}_{i-1}^{(k)}. \tag{9.16}$$

Combining Eq. (9.16) with the discrete NVU algorithm of Eq. (9.10) gives the following result

$$l_0\lambda_i = \frac{-2\sum_k \mathbf{f}_i^{(k)} \cdot (\mathbf{r}_i^{(k)} - \mathbf{r}_{i-1}^{(k)})}{\sum_k (\mathbf{f}_i^{(k)})^2/\tilde{m}_k}. \tag{9.17}$$

The atomic NVU algorithm with varying masses is then given by

$$\mathbf{r}_{i+1}^{(k)} = 2\mathbf{r}_i^{(k)} - \mathbf{r}_{i-1}^{(k)} - \frac{2\sum_k \mathbf{f}_i^{(k)} \cdot (\mathbf{r}_i^{(k)} - \mathbf{r}_{i-1}^{(k)})}{\sum_k (\mathbf{f}_i^{(k)})^2/\tilde{m}_k} \mathbf{f}_i^{(k)}/\tilde{m}_k. \tag{9.18}$$

We denote this the "basic" *NVU* algorithm. Similar to the Verlet algorithm of *NVE* dynamics (recall Eq. (1.8)), if we are given the positions at step $i-1$ and i, the algorithm of Eq. (9.18) can be used to generate a geodesic on Ω.

In addition, note that a switch of the index $i-1$ with $i+1$ results in the same discrete algorithm; the *NVU* algorithm is thus reversible in the configuration space. In the Appendix of Paper VI, it is also shown that the *NVU* algorithm is symplectic (Goldstein *et al.* [2002]) in the same sense as the standard Verlet algorithm. The *NVU* algorithm has thus all the properties normally associated with stability of molecular dynamics algorithms (Frenkel and Smit [2002]). Paper VI additionally shows that the Ansatz of constant step length is obeyed in the discrete algorithm of Eq. (9.18).

The basic *NVU* algorithm (Eq. (9.18)) may also be reformulated in the following form (defining $\boldsymbol{\delta}_{i+1/2}^{(k)} \equiv \mathbf{r}_{i+1}^{(k)} - \mathbf{r}_i^{(k)}$)

$$\boldsymbol{\delta}_{i+1/2}^{(k)} = \boldsymbol{\delta}_{i-1/2}^{(k)} - \frac{2\sum_k \mathbf{f}_i^{(k)} \cdot \boldsymbol{\delta}_{i-1/2}^{(k)}}{\sum_k (\mathbf{f}_i^{(k)})^2/\tilde{m}_k} \mathbf{f}_i^{(k)}/\tilde{m}_k, \tag{9.19}$$

$$\mathbf{r}_{i+1}^{(k)} = \mathbf{r}_i^{(k)} + \boldsymbol{\delta}_{i+1/2}^{(k)}. \tag{9.20}$$

This is the Leap-frog version (Allen and Tildesley [1987]) of the basic *NVU* algorithm.

9.1.2 Properties of the basic *NVU* algorithm

We consider here properties[4] of the basic *NVU* algorithm given in Eq. (9.18). Figure 9.2(a) shows an *NVU* simulation for the SCLJ liquid at $\rho = 0.85$ and $T = 0.70$ started from two consecutive (equilibrium) *NVE* configurations that were randomly chosen, and provide the positions at step i and $i-1$.

[4] The simulations are actually performed using Eqs. (9.19) and (9.20) but the discussion is easier to understand in the Verlet form of Eq. (9.18).

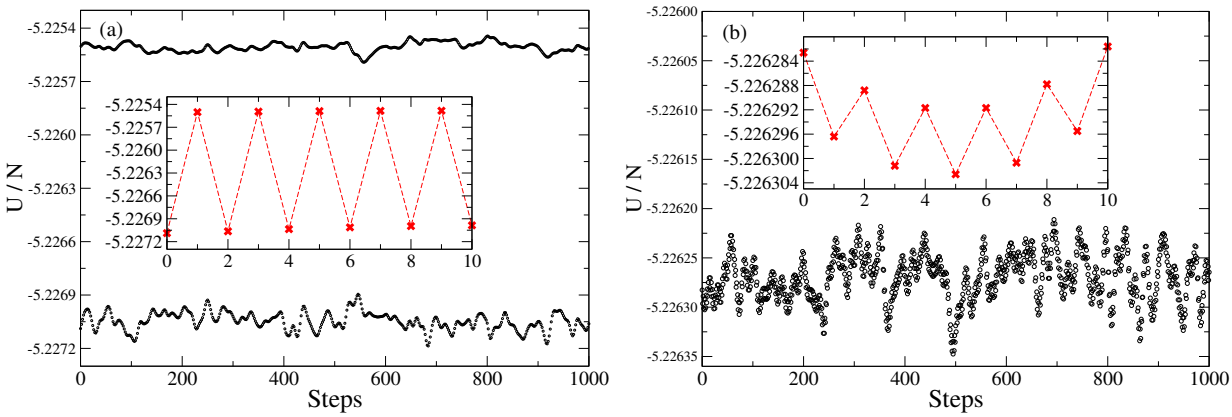

Figure 9.2: *The potential energy as a function of integration step number in NVU dynamics (using the basic NVU algorithm) for the SCLJ liquid at $\rho = 0.85$ and $T = 0.70$ (taken from Paper VI). The insets show the first 10 integration steps. (a) The NVU simulation is started from two randomly chosen consecutive NVE configurations. (b) The NVU simulation is started from two consecutive configurations of an NVE simulation with a very small potential energy difference.*

The *NVU* algorithm seems to show motion on two distinct "hypersurfaces" where the inset of Fig. 9.2(a) shows that the algorithm actually jumps every second step between these two surfaces. The *NVU* algorithm was constructed to perform motion on a *single* hypersurface Ω, thus: How can we understand this behavior?

Introducing the notation $U_{i-1} \equiv U(\mathbf{R}_{i-1})$, $U_i \equiv U(\mathbf{R}_i)$, etc., and Taylor expanding U_{i+1} and U_{i-1} around U_i we have (in which $\mathbf{F}_i \equiv -\nabla_{\mathbf{R}_i} U$)

$$U_{i+1} = U_i - \mathbf{F}_i \cdot (\mathbf{R}_{i+1} - \mathbf{R}_i) + O(l_0^2), \tag{9.21}$$

$$U_{i-1} = U_i - \mathbf{F}_i \cdot (\mathbf{R}_{i-1} - \mathbf{R}_i) + O(l_0^2). \tag{9.22}$$

Subtracting these two equations, we get

$$U_{i+1} = U_{i-1} - \mathbf{F}_i \cdot (\mathbf{R}_{i+1} - \mathbf{R}_{i-1}) + O(l_0^2), \tag{9.23}$$

Equation (9.16) expresses that $\mathbf{F}_i \cdot (\mathbf{R}_{i+1} - \mathbf{R}_{i-1}) = 0$, and Eq. (9.23) then becomes[5]

$$U_{i+1} = U_{i-1} + O(l_0^2). \tag{9.24}$$

Equation (9.24) states that the potential energy of *NVU* algorithm is conserved, but only every second step. Thus, starting the *NVU* algorithm from two randomly chosen consecutive configurations of an *NVE* simulation, in which the potential energy fluctuates, will result in motion between two distinct hypersurfaces.

[5] In the case of identical particle masses the order is $O(l_0^3)$; see Paper VI.

In this understanding, if the two consecutive *NVE* configurations are carefully chosen to have a small potential energy difference, the *NVU* algorithm should still show motion between two hypersurfaces, but on a much smaller potential energy scale. Figure 9.2(b) shows that this is indeed the case. In addition, Fig. 9.3 supports this conclusion where the distribution of the term $l_0\lambda_i$ (Eq. (9.17)) is shown for Figs. 9.2(a) and (b). A bimodal distribution is observed for the two randomly chosen configurations (green) whereas only one peak is observed when carefully choosing the *NVE* starting configurations to have a small potential energy difference (blue).

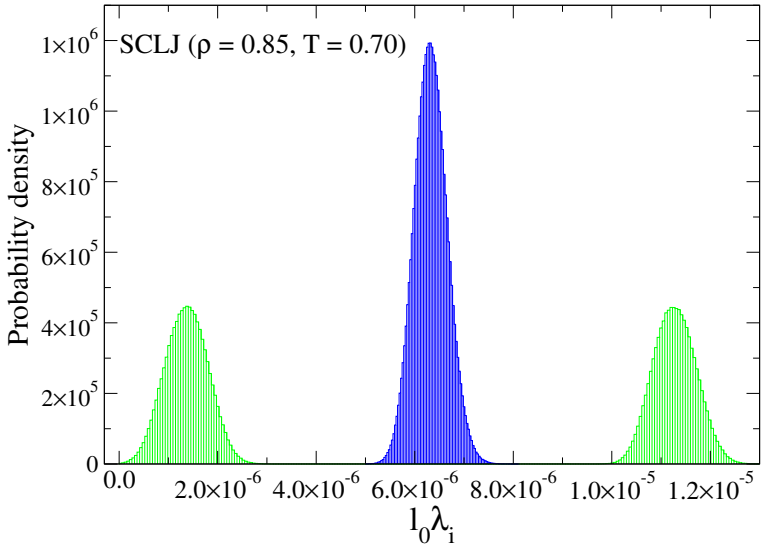

Figure 9.3: *The distribution of $l_0\lambda_i$ (Eq. (9.17)) for Figs. 9.2(a) and (b). The distribution of Fig. 9.2(a) shows a bimodal distribution (green) whereas the distribution of Fig. 9.2(b) shows a single peak (blue). The figure is taken from Paper VI.*

9.1.3 Developing a stabilized *NVU* algorithm

In Fig. 9.4 we show the potential energy and step length, for the SCLJ liquid at $\rho = 0.85$ and $T = 0.70$, as functions of integration step number for a long simulation using the basic *NVU* algorithm (red curves). For the long simulation, both quantities are seen to drift due to accumulating round-off errors. The observed drift of the *NVU* algorithm is no more serious than what is seen for the energy using the (*NVE*) Verlet algorithm[6]. However, to perform very long simulations, e.g. as is needed for viscous liquids, a completely stable *NVU* algorithm needs to be developed for a fully practical use in any situation.

[6] The simulations are performed in single-precision floating point arithmetic.

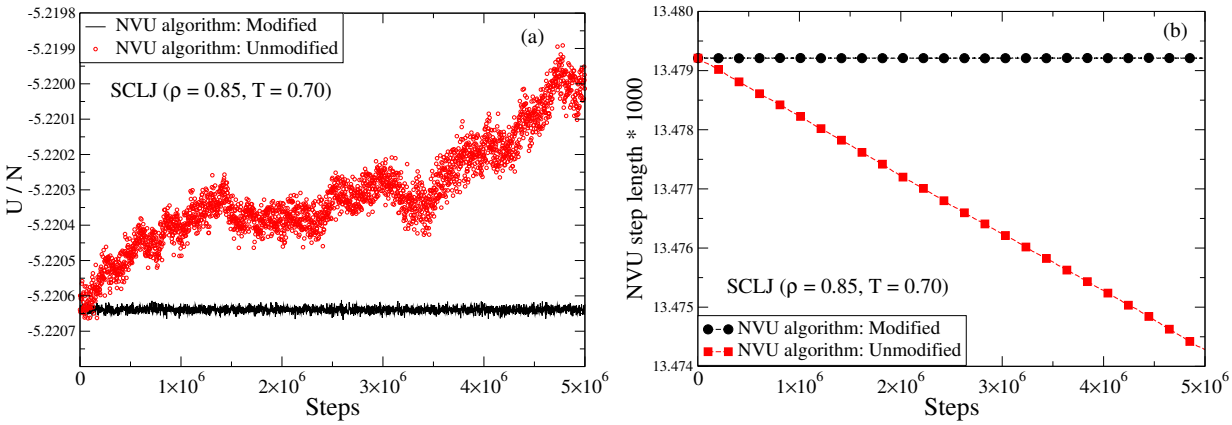

Figure 9.4: *Simulations using the basic (red) and stabilized (black) NVU algorithm for the SCLJ liquid at $\rho = 0.85$ and $T = 0.70$ (taken from Paper VI). (a) The potential energy as a function of integration step number. The stabilized algorithm uses U_0 = -5.220638. (b) The step length $(\sum_k \tilde{m}_k(\boldsymbol{\delta}^{(k)}_{i+1/2})^2)^{1/2}$ as a function of integration step number. The stabilized algorithm uses $l_0 = 0.01347921$.*

We stabilize the *NVU* algorithm in two steps. First, the potential energy drift is eliminated by modifying the basic algorithm as given below

$$\boldsymbol{\delta}^{(k)}_{i+1/2} = \boldsymbol{\delta}^{(k)}_{i-1/2} - \frac{2\sum_k \mathbf{f}^{(k)}_i \cdot \boldsymbol{\delta}^{(k)}_{i-1/2} + U_0 - U_{i-1}}{\sum_k (\mathbf{f}^{(k)}_i)^2/\tilde{m}_k} \mathbf{f}^{(k)}_i/\tilde{m}_k. \tag{9.25}$$

From this equation, we have

$$\sum_k \mathbf{f}^{(k)}_i \cdot (\mathbf{r}^{(k)}_{i+1} - \mathbf{r}^{(k)}_{i-1}) = \sum_k \mathbf{f}^{(k)}_i \cdot (\boldsymbol{\delta}^{(k)}_{i+1/2} + \boldsymbol{\delta}^{(k)}_{i-1/2}) = U_{i-1} - U_0. \tag{9.26}$$

It then follows by Eq. (9.23) that

$$U_{i+1} = U_0 + O(l_0^2). \tag{9.27}$$

In this way, the potential energy is set equal to U_0 (the constant defining Ω) at every integration step, and no numerical drift can occur. Next, the step length is stabilized by introducing a normalizing factor in the algorithm, as follows

$$\boldsymbol{\delta}^{(k)}_{i+1/2} = l_0 \frac{\boldsymbol{\chi}^{(k)}_{i+1/2}}{\sqrt{\sum_k \tilde{m}_k (\boldsymbol{\chi}^{(k)}_{i+1/2})^2}}, \tag{9.28}$$

$$\mathbf{r}^{(k)}_{i+1} = \mathbf{r}^{(k)}_i + \boldsymbol{\delta}^{(k)}_{i+1/2}, \tag{9.29}$$

where

$$\boldsymbol{\chi}_{i+1/2}^{(k)} \equiv \boldsymbol{\delta}_{i-1/2}^{(k)} - \frac{2\sum_k \mathbf{f}_i^{(k)} \cdot \boldsymbol{\delta}_{i-1/2}^{(k)} + U_0 - U_{i-1}}{\sum_k (\mathbf{f}_i^{(k)})^2/\tilde{m}_k} \mathbf{f}_i^{(k)}/\tilde{m}_k. \tag{9.30}$$

As shown in Fig. 9.5, the normalizing factor is close to unity and is thus a small perturbation of the basic algorithm. It ensures trivially $\sum_k \tilde{m}_k (\boldsymbol{\delta}_{i+1/2}^{(k)})^2 = l_0^2$, i.e., that the step length is conserved. Formally, we should now also show the effect of the step length stabilization on the properties derived above; these details are, however, found in Paper VI with the conclusion that the properties shown above still apply. It should, however, be noted that in the stabilized version, it is not possible to prove that the *NVU* algorithm is reversible in the configuration space. Motivated by the simulation results to come, we suspect that this is still the case.

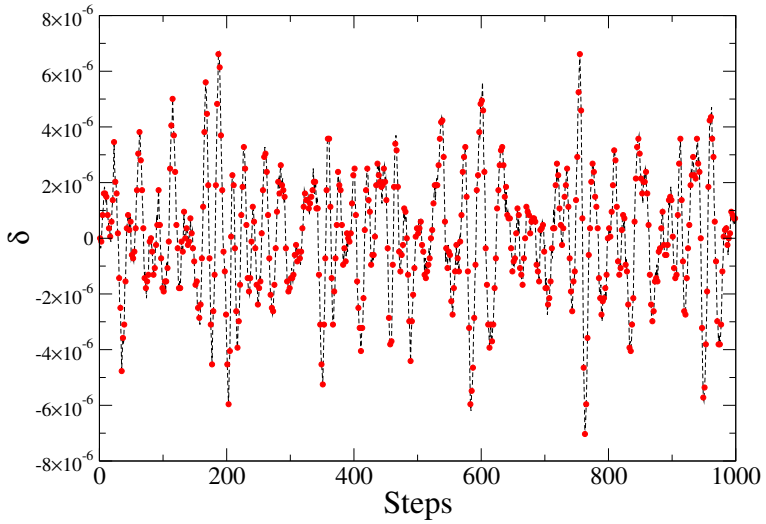

Figure 9.5: *$\delta_i \equiv 1 - l_0/(\sum_k \tilde{m}_k (\boldsymbol{\chi}_{i+1/2}^{(k)})^2)^{1/2}$ as a function of integration step number for the SCLJ liquid at $\rho = 0.85$ and $T = 0.70$ (taken from Paper VI). The dotted lines serve as a guide to the eye. The step length perturbation of the basic NVU algorithm is seen to be small.*

In fact, Fig. 9.4 shows that the *NVU* algorithm is now absolutely stable (black curves) conserving both potential energy and step length for any number of integration steps. The stabilized *NVU* algorithm was in Paper VI tested by probing the structure of the SCLJ liquid at various state points. Instead, we focus here on the sampling properties for the KABLJ mixture (Paper VII). The dynamics for this system is very sensitive to small "errors" in the supercooled liquid phase (Berthier and Tarjus [2009, 2011]) and thus serves as a good reference system for testing the *NVU* algorithm.

9.1.4 Sampling properties for the Kob-Andersen binary LJ mixture

The sampling properties of the stabilized *NVU* algorithm, described in the previous section, for the KABLJ mixture are investigated in this section by comparing the results of *NVU* dynamics to other well-known dynamics, in particular, to Newtonian *NVE* dynamics. For a comparison of *NVE* dynamics to other types of dynamics see, for instance, Berthier [2007], Berthier and Kob [2007], Flenner and Szamel [2005], Gleim *et al.* [1998], Szamel and Flenner [2004].

In *NVU* dynamics there is, as such, no measure of time since the geodesic can be traversed with any velocity on the manifold. Thus, to be able to compare to *NVE* dynamics a measure of time is needed. In fact, by comparing the *NVU* algorithm (Eq. (9.11)) to the (*NVE*) Verlet algorithm

$$\mathbf{r}_{i+1}^{(k)} = 2\mathbf{r}_i^{(k)} - \mathbf{r}_{i-1}^{(k)} + (\Delta t)^2 \mathbf{f}_i^{(k)}/m_k, \tag{9.31}$$

one can define a step-dependent "time step" of *NVU* algorithm via the definition

$$(\Delta t_{i,NVU})^2 \equiv l_0 \lambda_i \langle m \rangle. \tag{9.32}$$

This identification enables a comparison of dynamical quantities with *NVE* dynamics, and the average of Eq. (9.32) is used for simplicity in the following. We compare as follows. First, an *NVE* simulation at a given state point is performed to provide an equilibrated starting configuration for *NVU* dynamics. Afterwards, the value of U_0 is chosen as the average potential energy of the *NVE* simulation, and l_0 is chosen to give an *NVU* "time step" comparable to the *NVE* simulation.

Figure 9.6 shows radial distribution functions for the KABLJ mixture at two different state points corresponding to $\rho = 1.20$ and $T = 2.00$ and 0.405. The black curves give *NVE* simulations whereas the colored circles give the corresponding *NVU* simulations. For all pair-correlation functions, a quantitative agreement between *NVE* and *NVU* dynamics is obtained; even at the highly viscous state point of $T = 0.405$.

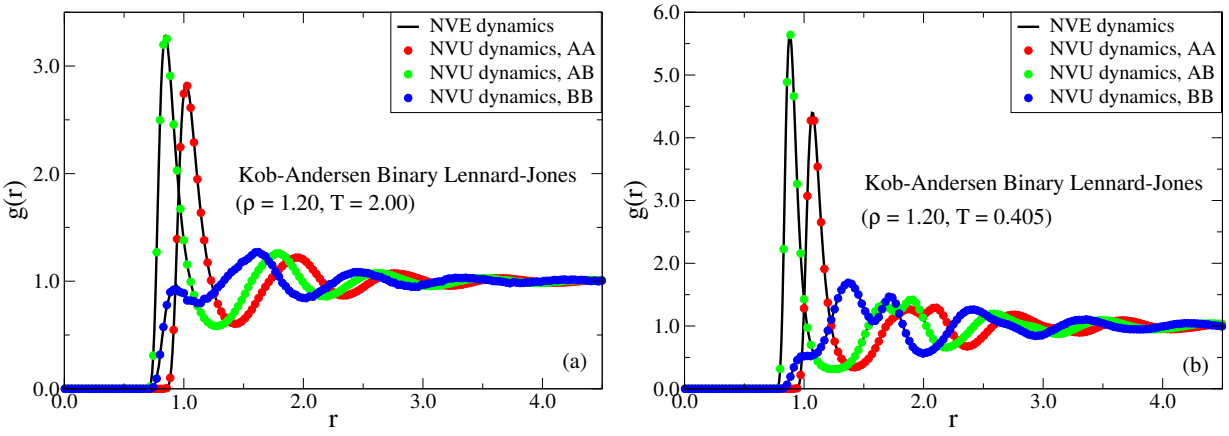

Figure 9.6: *Comparison of radial distributions functions in NVE (black curves) and NVU dynamics (colored circles) for the KABLJ mixture at $\rho = 1.20$ (taken from Paper VII). (a) $T = 2.00$. (b) $T = 0.405$.*

Turning now to the dynamics in Fig. 9.7, we show the A-particle mean-square displacement and incoherent intermediate scattering functions over a range of state points with $\rho = 1.20$ and $T = 2.00$, 0.80, 0.60, 0.50, 0.44, 0.42, 0.405. Although the dynamics changes roughly five orders of magnitude over this temperature range, the agreement between NVE and NVU dynamics remains quantitative and quite striking for both dynamical quantities.

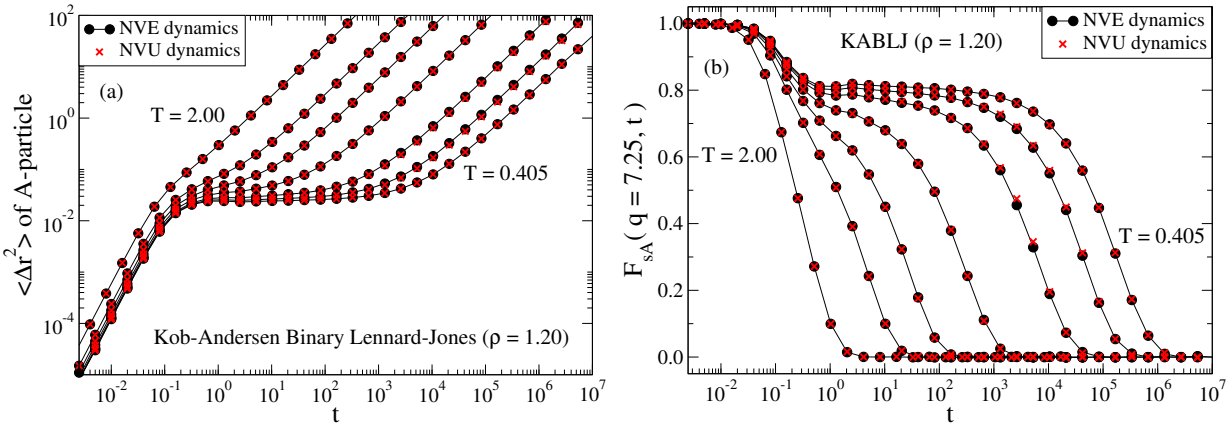

Figure 9.7: *Comparison of dynamical quantities in NVE (black curves) and NVU dynamics (red crosses) for the KABLJ mixture at $\rho = 1.20$ and $T = 2.00$, 0.80, 0.60, 0.50, 0.44, 0.42, 0.405 (taken from Paper VII). (a) The A-particle mean-square displacement. (b). The A-particle incoherent intermediate scattering function.*

It has previously been reported (Berthier [2007], Berthier and Kob [2007]) that different microscopic dynamics should have different dynamical fluctuations. For instance, Berthier and Kob [2007] showed that the dynamical fluctuations for the KABLJ mixture quantified via $\chi_{4,A} = N_A[\langle F_{sA}^2(\mathbf{q},t)\rangle - \langle F_{sA}(\mathbf{q},t)\rangle^2]$ between NVE and NVT dynamics are not the same. We now investigate whether this is also true for NVU dynamics. In Fig. 9.8(a) we show χ_4 for the KABLJ mixture at three different temperatures in NVE and NVU dynamics. Here, deviations are noted between the two dynamics, and considering a twice as large system in Fig. 9.8(b) does not seem to improve the behavior.

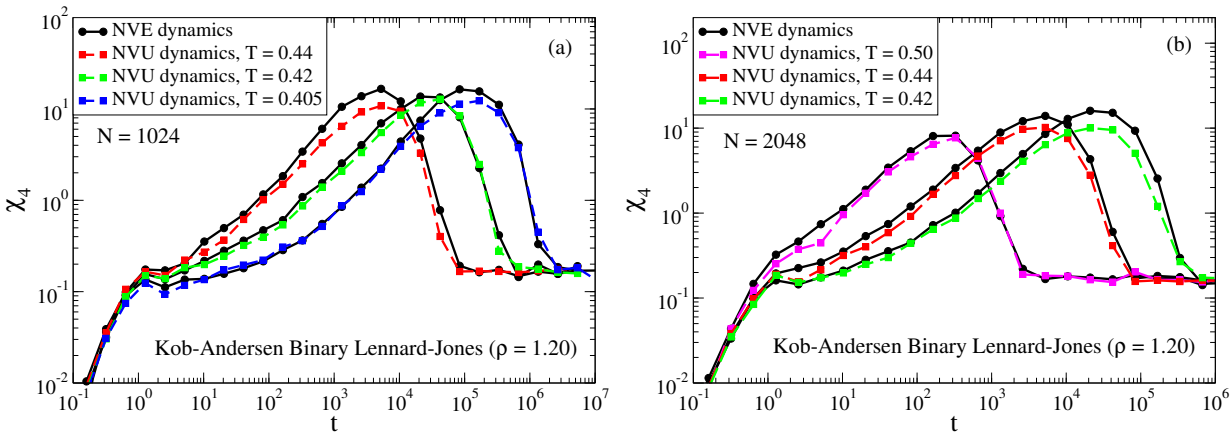

Figure 9.8: *Comparison of dynamical fluctuations via* $\chi_{4,A} = N_A[\langle F_{sA}^2(\mathbf{q},t)\rangle - \langle F_{sA}(\mathbf{q},t)\rangle^2]$ *between NVE (black curves) and NVU dynamics (colored curves) for the KABLJ mixture at* $\rho = 1.20$. *(a)* $N = 1024$ *particles and* $T = 0.44, 0.42, 0.405$. *(b)* $N = 2048$ *particles and* $T = 0.50, 0.44, 0.42$.

Finally, we consider in Fig. 9.9 the A-particle incoherent intermediate scattering function for the KABLJ mixture at $\rho = 1.20$ comparing now five different dynamics. We consider *NVE* dynamics, *NVT* dynamics, *NVU* dynamics, Metropolis *NVT* Monte-Carlo, and a random-walk on Ω (see Paper VII for a description of the algorithms used). It has previously been reported that the long-time behavior of viscous liquids is independent of the microscopic dynamics (Gleim *et al.* [1998], Szamel and Flenner [2004]). This may be understood as the dynamics becomes more and more influenced by barriers in the landscape, and so the microscopic details of the dynamics become less important. Figure 9.9 shows quantitative agreement between the deterministic dynamics at all temperatures whereas the long-time behavior of the stochastic and deterministic dynamics becomes identical only in the low-temperature limit (here, less than $T = 0.80$).

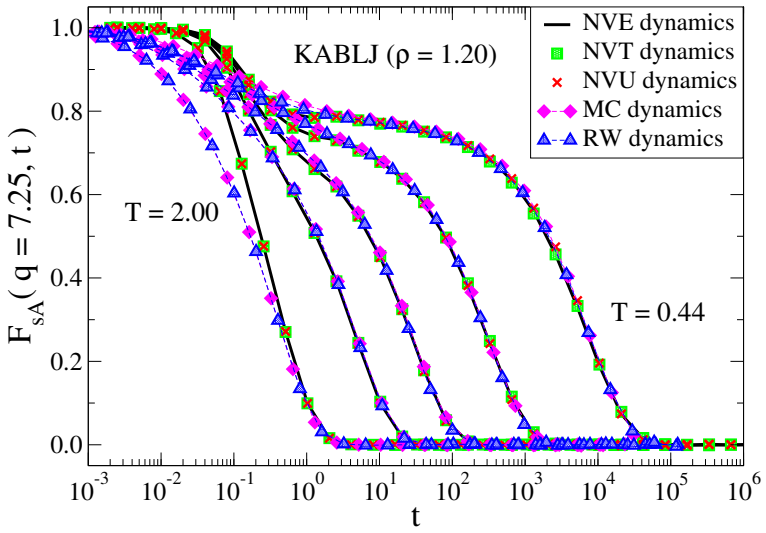

Figure 9.9: *The incoherent intermediate scattering function for the KABLJ mixture at* $\rho = 1.20$ *and* $T = 2.00, 0.80, 0.60, 0.50, 0.44$ *comparing five different dynamics (taken from Paper VII). The dynamics are as follows: NVE dynamics (black curves), NVT dynamics (green squares), NVU dynamics (red crosses), Metropolis NVT Monte-Carlo (purple diamonds), and a random-walk on* Ω *(blue triangles). For a description of the algorithms used, see Paper VII.*

9.1.5 Equivalence between *NVE* and *NVU* dynamics in the thermodynamic limit

The previous section detailed a quantitative agreement between *NVE* and *NVU* dynamics and naturally raises the question whether the two dynamics are related in some well-defined sense? Figure 9.10 shows the distribution of the *NVU* "time step" $(\Delta t_{i,NVU})^2 \equiv l_0 \lambda_i \langle m \rangle$ (Eq. (9.32)) for different system sizes of the SCLJ liquid: $N = 256, 1024, 8192$ particles.

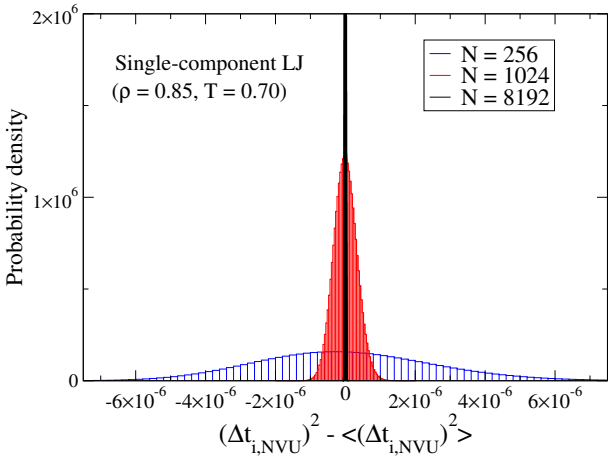

Figure 9.10: *Distribution of* $(\Delta_{i,NVU})^2 \equiv l_0\lambda_i\langle m\rangle$ *(see Eq. (9.32)) for different system sizes of the SCLJ liquid:* $N = 256, 1024, 8192$ *particles (taken from Paper VII). The relative variation of the NVU "time step" becomes smaller as the number of particles increases.*

A narrowing of this distribution is observed as the number of particles increases, in fact, the relative variation becomes smaller, as N increases. As the number of particles increases, it becomes a better and better approximation to treat this term as constant. Comparing the NVU algorithm

$$\mathbf{r}_{i+1}^{(k)} = 2\mathbf{r}_i^{(k)} + \mathbf{r}_{i-1}^{(k)} + l_0\lambda_i\langle m\rangle\,\mathbf{f}_i^{(k)}/m_k, \tag{9.33}$$

to the Verlet algorithm in Eq. (9.31), one expects from the latter observation that NVE and NVU dynamics become equivalent in the thermodynamic limit. The latter statement should be understood in the sense that, for instance, the relative deviations between NVE and NVU time auto-correlation functions go to zero as $N \to \infty$. The simulations of the former section used $N \approx 1000$ particles, however, simulations as few as $N = 65$ particles were simulated with quantitative agreement.

It should be noted, however, that Fig. 9.8 showed that the dynamical fluctuations were not identical between NVE and NVU dynamics. Consider also for the moment the famous example of Newton's falling apple. NVU dynamics predicts that this apple remains fixed in (level) space to keep the potential energy constant whereas Newton's second law predicts that the apple should fall to the ground converting potential into kinetic energy. Thus, for very few degrees of freedom one does not expect quantitative agreement between NVE and NVU dynamics.

It is also natural to ask, for large enough system sizes: Does the agreement depend on the functional choice of U? In general, one could construct functional forms of U where the observed equivalence would break down. However, potential functions representing real-world systems have a complex energy surface, including anharmonicity, and for these systems one would expect to find a quantitative agreement between NVE and NVU dynamics.

9.2 Discrete geodesic motion on Ω for molecular systems

The *NVU* algorithm detailed above was in Paper VIII extended to simulate molecules at constant potential energy. Molecular systems are in general simulated by using flexible and/or rigid bonds in the modelling. Introducing flexible bonds in the simulations merely adds additional contributions to the total potential energy, and the *NVU* algorithm can therefore readily simulate flexible bonds. The rigid bonds, however, introduce a number G of constraints among the particle coordinates of the system ($\alpha = 1, ..., G$)

$$\sigma_\alpha(\mathbf{R}) \equiv (\mathbf{r}^{(k_\alpha)} - \mathbf{r}^{(l_\alpha)})^2 \equiv (\mathbf{r}^\alpha)^2 = C_\alpha^2. \tag{9.34}$$

Equation (9.34) expresses that the distance between particles k_α and l_α is a constant, C_α. The geodesic motion on Ω with rigid bonds is thus restricted to a submanifold ω of Ω where the rigid-bond constraints are satisfied, i.e., the motion is restricted to

$$\omega = \{\mathbf{R} \in \Omega \mid \sigma_\alpha(\mathbf{R}) = C_\alpha^2 \ , \ \alpha = 1, ..., G\}. \tag{9.35}$$

If the bond constraints are independent, ω is a $(3N - G - 1)$-dimensional compact Riemannian differential manifold (Schlichtkrull [2009]). The variational principle defining *NVU* dynamics with rigid bonds is then given by (compare Eq. (9.2))

$$\delta \int_{\mathbf{R}_A}^{\mathbf{R}_B} dl = 0 \ \Big|_\omega \ . \tag{9.36}$$

Applying now the variational integration technique to Eq. (9.36) gives

$$\delta \left(\sum_i \sqrt{\sum_k \tilde{m}_k \left(\mathbf{r}_i^{(k)} - \mathbf{r}_{i-1}^{(k)} \right)^2} - \sum_i \lambda_i U(\mathbf{R}_i) + \sum_{i,\alpha} \Lambda_{\alpha i} \sigma_\alpha(\mathbf{R}_i) \right) \ = \ 0 \, . \tag{9.37}$$

The path is divided into a number of discrete points, and one Lagrangian multiplier $\Lambda_{\alpha i}$ is introduced for each constraint α at every point i. Following standard notation for constraint molecular dynamics (Goldstein *et al.* [2002], Ryckaert *et al.* [1977]), the Lagrangian multipliers of the bond constraints are chosen with a positive sign. Applying the Ansatz of constant step length l_0, i.e.,

$$\sum_k \tilde{m}_k \left(\mathbf{r}_i^{(k)} - \mathbf{r}_{i-1}^{(k)} \right)^2 \equiv l_0^2, \tag{9.38}$$

and carrying out the variation of Eq. (9.37) using Eq. (9.38) leads to

$$\mathbf{r}_{i+1}^{(k)} = 2\mathbf{r}_i^{(k)} - \mathbf{r}_{i-1}^{(k)} + \frac{l_0}{\tilde{m}_k} \lambda_i \mathbf{f}_i^{(k)} + \frac{l_0}{\tilde{m}_k} \nabla_{\mathbf{r}_i^{(k)}} \sum_\alpha \Lambda_{\alpha i} \sigma_\alpha. \tag{9.39}$$

This equation constitutes the *NVU* algorithm with rigid bonds. It has a close resemblance to the Lagrangian equations of motion with holonomic constraints (Goldstein *et al.* [2002]), i.e., rigid-bond *NVE* dynamics (Ryckaert *et al.* [1977]). Equation (9.39) contains $G + 1$

Lagrangian multipliers for each integration step which must be determined to complete the rigid-bond *NVU* algorithm. This procedure is very technical as it involves solving systems of non-linear equations, and the reader is instead referred to Paper VIII for details on calculating the Lagrangian multipliers (see also Ingebrigtsen *et al.* [2010], Toxvaerd *et al.* [2009] for rigid-bonds in general). Nevertheless, the basic idea behind rigid bonds in *NVU* dynamics is detailed in the above text.

In the next section, we show the sampling properties of the rigid-bond *NVU* algorithm for two rigid molecules: the asymmetric dumbbell model and SPC/E water (model details are available in Appendix A). Paper VIII additionally shows simulations of the Lewis-Wahnström OTP model.

9.2.1 Sampling properties for the asymmetric dumbbell model

Figure 9.11(a) and (b) show, respectively, the molecular center-of-mass (CM) radial distribution functions (RDF) and molecular CM incoherent intermediate scattering functions (ISF) for the asymmetric dumbbell model. The black curves give *NVT* dynamics simulations whereas the red crosses give *NVU* dynamics. We do not compare, as before, to *NVE* dynamics as it is well-known that *NVE* and *NVT* dynamics give equivalent results (Evans and Holian [1985]).

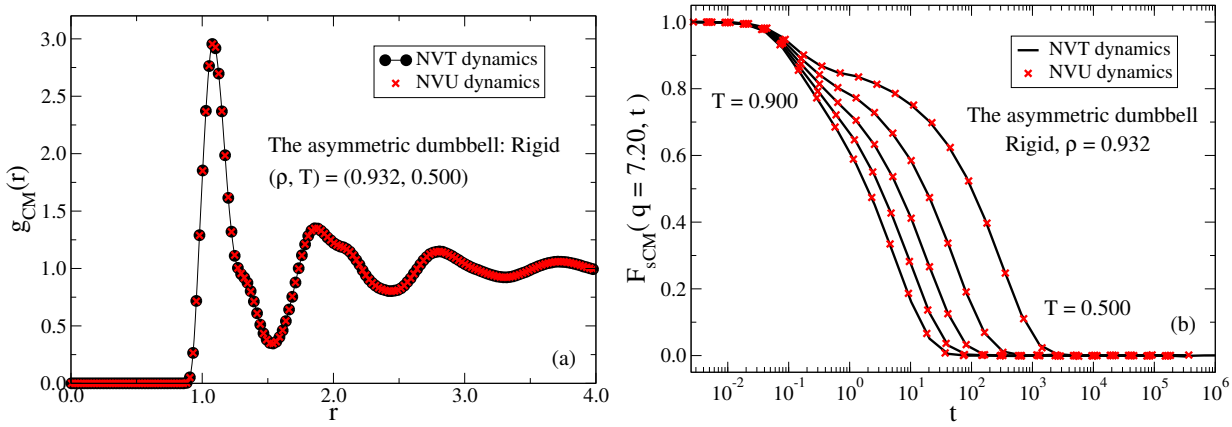

Figure 9.11: *Comparison of structure and dynamics in NVU and NVT simulations of the rigid asymmetric dumbbell model (taken from Paper VIII). The black circles and curves give NVT, the red crosses NVU simulation results. (a) The molecular CM RDFs at $\rho = 0.932$ and $T = 0.500$. (b) The molecular CM incoherent ISFs at $\rho = 0.932$ and $T = 0.500$, 0.600, 0.700, 0.800, 0.900.*

For both structure and dynamics, an excellent agreement between *NVT* and *NVU* dynamics is obtained. Paper VIII shows simulations for a flexible dumbbell model where the same conclusion is reached.

9.2.2 Sampling properties for rigid SPC/E water

Applying the same meanings and notations as for the asymmetric dumbbell, the molecular CM RDFs and ISFs are shown in Fig. 9.12 for rigid SPC/E water. The same conclusion is reached as for the asymmetric dumbbell model. It should be noted that the rigid SPC/E water is a prime example of a non-strongly correlating liquid.

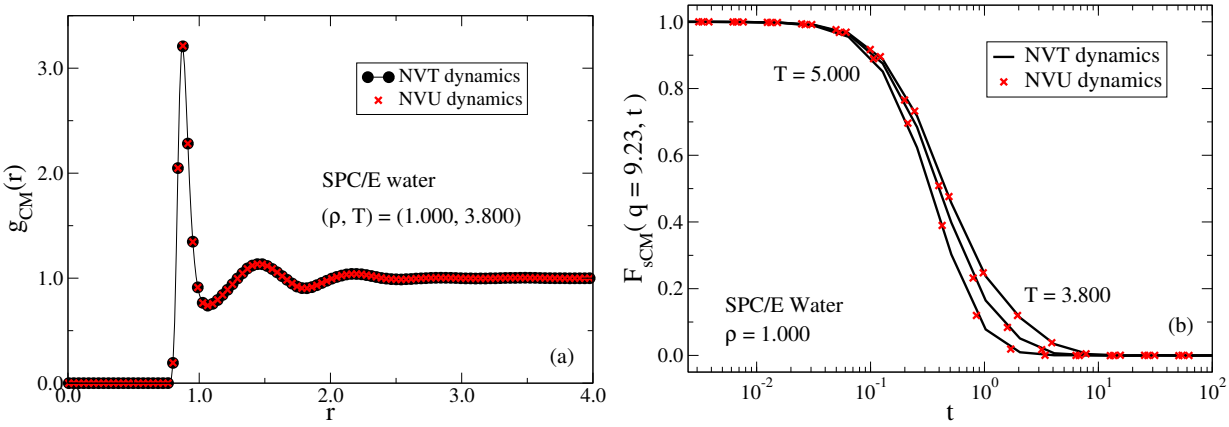

Figure 9.12: *Comparison of structure and dynamics in NVU and NVT simulations of rigid SPC/E water (taken from Paper VIII). The black circles and curves give NVT, the red crosses NVU simulation results. (a) The molecular CM RDFs at $\rho = 1.000$ and $T = 3.800$. (b) The molecular CM ISFs at $\rho = 1.000$ and $T = 3.800$, 4.200, 5.000.*

We thus conclude from the results presented here (and in Paper VIII) that also for molecular systems do *NVE* and *NVU* dynamics become equivalent in the thermodynamic limit, since *NVE* and *NVT* dynamics are known to give equivalent results (Evans and Holian [1985]).

Chapter 10

CONCLUDING REMARKS

This thesis has focused on developing a further understanding of the properties of strongly correlating liquids or in the terminology of this thesis, "simple liquids" (Paper III). In this chapter, we shall refer to this class *only* as simple liquids.

10.1 Brief summary of results

The thermodynamics of simple liquids (Paper I) was shown to be simple as temperature separates into a product of a function of excess entropy per particle and a function of density, i.e.,

$$T = g(s_{\mathrm{ex}})h(\rho). \tag{10.1}$$

This fact leads to a more general scaling, the "isomorph scaling" (Papers I and II), in contrast to the traditional "density scaling" which breaks down when considering larger density changes than usually applied in experiments. Originally, the theory of simple liquids was investigated for bulk atomic systems (Gnan *et al.* [2009], Schrøder *et al.* [2011]). We have, however, seen that this theory is not limited to systems of atoms but also extends to systems composed of rigid molecules (Paper V). In fact, it has recently been shown that even flexible polymer models can have isomorphs to a good approximation (Veldhorst [2013]). A new characterization of simple liquids was also discovered as for these liquids the structure and dynamics are determined to a good approximation only by the interactions within the first coordination shell (Paper III).

Biological relevant liquids often occur in confined spaces with a resultant change in structure and dynamics from the bulk liquid. As a first step, we investigated isomorphs and the first coordination shell property of simple liquids in a "neutral" external field (see Chapters 7 and 8). It was shown that these systems, too, have isomorphs to a good approximation; an observation that connects to a novel excess entropy scaling behavior of bulk and confined systems (Mittal *et al.* [2006]). By itself, isomorphs in confined systems provide a way to understand the dynamical changes that occur when liquids are confined spatially[1]. Motivated also by the theory, a new molecular dynamics, *NVU* dynamics, was proposed and shown to be equivalent to standard Newtonian *NVE* dynamics for both atomic and molecular systems (Papers VI, VII, and VIII).

As emphasized in Chapter 1 simulations are not a replacement for real experiments (Buchenau [2012]), and thus the experimental counterparts of these simulations are missing. A milestone for the future would be to test, for instance, density or excess entropy scaling in a nanoscale confined system.

[1] The additional state variable H does, however, not change much along the isomorph itself.

10.2 Additional considerations

We identified in this thesis the class of strongly correlating liquids with the class of "simple liquids". However, at the end of the day; is this choice just another way of introducing a perhaps more broad appealing name for the same class of liquids? It was argued that this class is fundamental as it may be characterized in four equivalent ways, and the properties derived from these concepts have been considered to be simple liquid behavior for many years (Rosenfeld [1977]). The properties of simple liquids also generalize beyond the bulk equilibrium system to both confined equilibrium liquids, crystals (Albrechtsen and Olsen [2013]), as well as liquids undergoing homogenous shear flow (Separdar *et al.* [2012]). In fact, preliminary work has shown that even the first coordination shell property of simple liquids generalizes to confined systems. It is also likely that a connection can be established to continuum descriptions (Navier-Stokes equations) of nanoscale confined liquids (Travis *et al.* [1997]). The answer to the former question must thus be considered to be *no*. It will be interesting to see how far and to what situations the theory of simple liquids may be extended.

Inspired also from the theory of simple liquids, this thesis detailed a new molecular dynamics that conserves the total potential energy, i.e., NVU dynamics. However, will NVU dynamics become a standard simulation tool in the future as, for instance, NVT dynamics is today? The first thing to note is that NVU dynamics is not faster than NVE or NVT dynamics. There is thus no performance gain in using NVU dynamics as a replacement for NVE or NVT dynamics. NVU dynamics does, however, provide a new way of thinking on the dynamics of a classical mechanical system. A new way of thinking that has already proven useful (Dyre [2013]) to understand quasi-universal observations among single-component atomic systems (see, for instance, Andrade [1931], Dzugutov [1996], Rosenfeld [1977], Young and Andersen [2003, 2005]). The introduction of NVT dynamics (Nosé [1984]) had its obvious advantage in the control of temperature instead of the energy. Whether NVU dynamics also has such a practical advantage remains, however, to be seen. In the next section, we consider a few of the possible paths for new research that the current thesis work motivates.

10.3 Future research topics

The work presented in this thesis opens up for new paths of research related to the theory of simple liquids. Listed below are a few such topics.

1. **Liquid-vapor interfaces**.
   Isomorphs of nanoscale confined systems were investigated in Chapter 7. In generel, however, one may ask: What kind of interfaces are strong enough to break the potential energy/virial correlation entirely? In the above understanding, gasses are not simple, and one may speculate that systems with liquid-vapor interfaces are not simple either. The (reduced) surface tension has been observed to exhibit near universal behavior (Grosfils and Lutsko [2009], Guggenheim [1945]) for liquid films surrounded by their vapor when plotted against $(\rho_l - \rho_v)/\rho_c$ (Galliero [2010]), where ρ_c is the

critical density. "*Concerning hydrogen-bonding fluids, reduced surface tensions of both methanol and water clearly deviate from the universal Parachor behavior*" (Galliero [2010]). Water and methanol are not simple liquids, and this fact motivates that the near universal observation might be related to a property of simple liquids.

2. **Simple liquids in a variety of external fields**.
   A related topic to the above is the study of simple liquids in different external fields used to model solids. The surfaces encountered in nature are atomistically discrete, have defects, charges, different chemical compositions, and so forth. All of these features will affect the strong correlation (and thus also isomorphs), but to what extent? Is the oil present in pores of chalk layers (Stipp *et al.* [1998]), simple? If the latter is the case, excess entropy or heat capacity scaling of the *bulk* system can be used to predict the dynamics in the confinement. A natural extension is also to study the effect of the external field on the first coordination shell property as was initiated in Chapter 8.

3. **Excess entropy or heat capacity scaling in non-equilibrium systems?**
   Recently, it was shown that non-equilibrium systems can also have isomorphs (Separdar *et al.* [2012]). More specific, it was shown that liquids undergoing a Couette shear flow via the SLLOD equations of motion (Evans and Morriss [1984], Ladd [1984]) have isomorphs to a good approximation. The isomorphs extend into the non-trivial region of the phase diagram where so-called "shear thinning" is observed. Defining entropy and temperature in a non-equilibrium system is still highly speculative (Evans and Morriss [2008]), however, it is natural to ask: Does excess entropy and/or heat capacity scaling (observed for the confined equilibrium liquid) extend to non-equilibrium liquids?

   This method would then be an alternative to other approaches for predicting non-equilibrium behavior (Suzuki and Hayakawa [2013]). In addition, should such a connection exist, one would have a mapping not only between an equilibrium and a non-equilibrium liquid, but also between a non-equilibrium and a nanoscale-confined liquid. This would result in a highly non-trivial and quite puzzling quasi-universality relation.

4. **What separates a liquid from a gas?**
   Near the triple point, some liquids are simple in the above meaning of the term and have certain features associated with the liquid phase, for instance, the role of the FCS interactions. These features are not present in the gas phase. Thus, for these kinds of liquids it may be possible to use the correlation coefficient R as a quantitative criterion for where in the critical region the liquid properties start to diminish when going from liquid to gas beyond the critical point. This topic of research is motivated by recent work of Brazhkin and Trachenko [2012] who ask the exact title question. Liquids such as water can, however, not be included in this type of investigation as they are not strongly correlating.

5. **Does polydispersity affect intrinsic liquid properties?**
   The KABLJ mixture is more than 95% correlating in large parts of its phase diagram. On the other hand, the WABLJ mixture is 99% strongly correlating; both are binary mixtures. Inspired by this observation, a more general question might be: How does

polydispersity affect intrinsic liquid properties? Polydispersity is often used in colloidal systems to avoid crystallization, but in this process: Is the essence of the physics lost?

6. **A study of liquid crystals**.
   A liquid crystal is an interesting phase with both liquid and crystal-like properties. The modelling of this phase is often taken as the Gay-Berne potential (Gay and Berne [1981]). The Gay-Berne potential is an anisotropic form of the LJ pair potential. It would thus be interesting and highly relevant for practical purposes (modern televisions use liquid crystals in their displays) to investigate how simple this phase truly is.

7. **Medium-Range Crystalline Order and simple liquids**.
   Recently, an explanation was presented by H. Tanaka and co-workers (Kawasaki *et al.* [2007], Leocmach and Tanaka [2012], Shintani and Tanaka [2006], Watanabe and Tanaka [2008]) of the viscous slow down seen in supercooled, glass-forming liquids in terms of the growth of "medium-range crystalline order" (MRCO). MRCO are regions of the supercooled liquid with high crystalline symmetry but appear as part of the supercooled liquid's natural thermal fluctuations. Growth of MRCO, upon cooling, has been observed both in simulations (Kawasaki *et al.* [2007], Shintani and Tanaka [2006]) as well as experiments (Leocmach and Tanaka [2012], Watanabe and Tanaka [2008]), and it is believed to be closely related to the increase in dynamical heterogeneity seen in glass-forming liquids upon cooling. It is also believed that MRCO is related to the increase in average structural relaxation time τ_α. In the MRCO picture $\tau_\alpha = f(\varepsilon)$, where ε is the characteristic size of the MRCO regions. In addition, a connection between ε and S_2 was also observed (Kawasaki *et al.* [2007]). S_2 is the two-particle contribution to the excess entropy and is an isomorph invariant (Gnan *et al.* [2009]).

   Simple liquids and their isomorphs imply the relationship $\tau_\alpha = f(S_2)$ whereas MRCO suggests $S_2 = f(\varepsilon)$. The latter then leads to $\tau_\alpha = f(\varepsilon)$ as proposed by the MRCO theory. It is thus natural to ask if the two concepts are related in some well-defined sense?

The above mentioned projects are only a few of the possible paths one may follow; other obvious paths are a more in-depth study of isomorphs in mixtures of molecules, for instance, a mixture of water and oil (and possibly a surfactant): At what mole fraction does the correlation break?

Trond S. Ingebrigtsen, "Glass and Time", Roskilde University.

BIBLIOGRAPHY

Abraham, J. Y., Buldyrev, S. V., and Giovambattista, N. *Liquid and Glass Polymorphism in a Monatomic System with Isotropic, Smooth Pair Interactions.* J. Phys. Chem. B, **115**, 14229, 2011.

Adam, G. and Gibbs, J. H. *On the Temperature Dependence of Cooperative Relaxation Properties in Glass-Forming Liquids.* J. Chem. Phys., **43**, 139, 1965.

Agarwal, M., Singh, M., Sharma, R., Alam, M. P., and Chakravarty, C. *Relationship between Structure, Entropy, and Diffusivity in Water and Water-Like Liquids.* J. Phys. Chem. B, **114**, 6995, 2010.

Alba-Simionesco, C., Cailliaux, A., Alegría, A., and Tarjus, G. *Scaling out the density dependence of the α relaxation in glass-forming polymers.* Europhys. Lett., **68**, 58, 2004.

Albrechtsen, D. and Olsen, A. E. Unpublished data, 2013.

Alcoutlabi, M. and McKenna, G. B. *Effects of confinement on material behaviour at the nanometre size scale.* J. Phys.: Condens. Matter, **17**, 461, 2005.

Allen, M. P. and Tildesley, D. J. *Computer Simulation of Liquids.* Oxford University Press: New York, 1987.

Andersen, H. C., Chandler, D., and Weeks, J. D. Roles of Repulsive and Attractive Forces in Liquids: The Equilibrium Theory of Classical Fluids. In Prigogine, I. and Rice, S. A., editors, *Advances in Chemical Physics*, volume 34, page 105. John Wiley and Sons, Inc., 1976.

Andrade, E. N. C. *Viscosity of Liquids.* Nature, **128**, 835, 1931.

Angell, C. A. and Klein, I. S. *Prigogine and Defay say relax.* Nat. Phys., **7**, 750, 2011.

Baek, J., Deopurkar, A., and Redfield, K. *Finding Geodesics on Surfaces.* Standford University, 2007.

Bailey, N. P., Pedersen, U. R., Gnan, N., Schrøder, T. B., and Dyre, J. C. *Pressure-energy correlations in liquids. I. Results from computer simulations.* J. Chem. Phys., **129**, 184507, 2008a.

Bailey, N. P., Pedersen, U. R., Gnan, N., Schrøder, T. B., and Dyre, J. C. *Pressure-energy correlations in liquids. II. Analysis and consequences.* J. Chem. Phys., **129**, 184508, 2008b.

Baschnagel, J. and Varnik, F. *Computer simulations of supercooled polymer melts in the bulk and in confined geometry.* J. Phys.: Condens. Matter, **17**, 851, 2005.

Berendsen, H. J. C., Grigera, J. R., and Straatsma, T. P. *The Missing Term In Effective Pair Potentials.* J. Phys. Chem., **91**, 6269, 1987.

Berthier, L. *Revisiting the slow dynamics of a silica melt using Monte Carlo simulations.* Phys. Rev. E, **76**, 011507, 2007.

Berthier, L. and Kob, W. *The Monte Carlo dynamics of a binary Lennard-Jones glass-forming mixture.* J. Phys.: Condens. Matter, **19**, 205130, 2007.

Berthier, L. and Tarjus, G. *Nonperturbative Effect of Attractive Forces in Viscous Liquids.* Phys. Rev. Lett., **103**, 170601, 2009.

Berthier, L. and Tarjus, G. *The role of attractive forces in viscous liquids.* J. Chem. Phys., **134**, 214503, 2011.

Biroli, G., Bouchaud, J.-P., Miyazaki, K., and Reichman, D. R. *Inhomogeneous Mode-Coupling Theory and Growing Dynamic Length in Supercooled Liquids.* Phys. Rev. Lett., **97**, 195701, 2006.

Brazhkin, V. V. and Trachenko, K. *What separates a liquid from a gas?* Phys. Today, **65**, 68, 2012.

Buchenau, U. *Simulation and Experiment – A Difficult Interaction.* J. Phys. Chem. Lett., **3**, 760, 2012.

Buckingham, R. A. *The classical equation of state of gaseous helium, neon and argon.* Proc. R. Soc. London A, **168**, 264, 1938.

Burakovsky, L. and Preston, D. L. *Analytic model of the Grüneisen parameter all densities.* J. Phys. Chem. Solids, **65**, 1581, 2004.

Casalini, R. and Roland, C. M. *Thermodynamical scaling of the glass transition dynamics.* Phys. Rev. E, **69**, 062501, 2004.

Caselles, V., Kimmel, R., and Sapiro, G. *Geodesic Active Contours.* Int. J. Comput. Vision, **22**, 61, 1997.

Cavagna, A. *Supercooled liquids for pedestrians.* Phys. Rep., **476**, 51, 2009.

Chandler, D. *Introduction to Modern Statistical Mechanics.* Oxford University Press: New York, 1987.

Cheng, L.-T., Burchard, P., Merriman, B., and Osher, S. *Motion of Curves Constrained on Surfaces Using a Level-Set Approach.* J. Comput. Phys., **175**, 604, 2002.

Chopra, R., Truskett, T. M., and Errington, J. R. *Excess-entropy scaling of dynamics for a confined fluid of dumbbell-shaped particles.* Phys. Rev. E, **82**, 041201, 2010a.

Chopra, R., Truskett, T. M., and Errington, J. R. *On the Use of Excess Entropy Scaling to Describe the Dynamic Properties of Water.* J. Phys. Chem. B, **114**, 10558, 2010b.

Coslovich, D. and Roland, C. M. *Thermodynamic Scaling of Diffusion in Supercooled Lennard-Jones Liquids.* J. Phys. Chem. B, **112**, 1329, 2008.

Coslovich, D. and Roland, C. M. *Pressure-energy correlations and thermodynamic scaling in viscous Lennard-Jones liquids.* J. Chem. Phys., **130**, 014508, 2009.

Cotterill, R. M. J. and Madsen, J. U. *Localized fluidity modes and the topology of the constant-potential-energy hypersurfaces of Lennard-Jones matter.* Phys. Rev. B, **33**, 262, 1986.

Cotterill, R. M. J. and Madsen, J. U. *The glass state: characterizing energy landscape features.* J. Phys.: Condens. Matter, **18**, 6507, 2006.

de Oliveira, A. B., Netz, P. A., Colla, T., and Barbosa, M. C. *Thermodynamic and dynamic anomalies for a three-dimensional isotropic core-softened potential.* J. Chem. Phys., **124**, 084505, 2006.

Debenedetti, P. G. and Stillinger, F. H. *Supercooled liquids and the glass transition.* Nature, **410**, 259, 2001.

Deitel, H. M. and Deitel, P. J. *C++ How To Program.* Prentice-Hall, Inc., third edition, 2001.

Diestler, D. J. and Schoen, M. *Statistical thermodynamics of confined thin films.* Acta Chim. Hung., **132**, 45, 1995.

Diestler, D. J. and Schoen, M. *Correlation of stress and structure in a simple fluid confined to a pore with furrowed walls.* Phys. Rev. E, **62**, 6615, 2000.

Diestler, D. J., Schoen, M., Hertzner, A. W., and Cushman, J. H. *Fluids in micropores. III. Self-diffusion in a slit-pore with rough hard walls.* J. Chem. Phys., **95**, 5432, 1991.

Dreyfus, C., Aouadi, A., Gapinski, J., Matos-Lopes, M., Steffen, W., Patkowski, A., and Pick, R. M. *Temperature and pressure study of Brillouin transverse modes in the organic glass-forming liquid orthoterphenyl.* Phys. Rev. E, **68**, 011204, 2003.

Dreyfus, C., Grand, A. Le, Gapinski, J., Steffen, W., and Patkowski, A. *Scaling the α-relaxation time of supercooled fragile organic liquids.* Eur. Phys. J. B, **42**, 309, 2004.

Dyre, J. C. *Colloquium: The glass transition and elastic models of glass-forming liquids.* Rev. Mod. Phys., **78**, 953, 2006.

Dyre, J. C. *NVU perspective on simple liquids' quasiuniversality.* Phys. Rev. E, **87**, 022106, 2013.

Dzugutov, M. *Glass formation in a simple monatomic liquid with icosahedral inherent local order.* Phys. Rev. A, **46**, 2984, 1992.

Dzugutov, M. *Formation of a dodecagonal quasicrystalline phase in a simple monatomic liquid.* Phys. Rev. Lett, **70**, 2924, 1993.

Dzugutov, M. *A universal scaling law for atomic diffusion in condensed matter.* Nature, **381**, 137, 1996.

Engel, M. and Trebin, H.-R. *Self-Assembly of Monatomic Complex Crystals and Quasicrystals with a Double-Well Interaction Potential*. Phys. Rev. Lett., **98**, 225505, 2007.

Evans, D. J. and Holian, B. L. *The Nose-Hoover thermostat*. J. Chem. Phys., **83**, 4069, 1985.

Evans, D. J. and Morriss, G. *Statistical Mechanics of Nonequilibrium Liquids*. Cambridge University Press, second edition, 2008.

Evans, D. J. and Morriss, G. P. *Nonlinear-response theory for steady planar Couette flow*. Phys. Rev. A, **30**, 1528, 1984.

Evans, R. *The nature of the liquid-vapour interface and other topics in the statistical mechanics of non-uniform, classical fluids*. Adv. Phys., **28**, 143, 1979.

Fennell, C. J. and Gezelter, J. D. *Is the Ewald summation still necessary? Pairwise alternatives to the accepted standard for long-range electrostatics*. J. Chem. Phys., **124**, 234104, 2006.

Fitzgerald, M., Picard, R. R., and Silver, R. N. *Canonical transition probabilities for adaptive Metropolis simulation*. Europhys. Lett., **46**, 282, 1999.

Flenner, E. and Szamel, G. *Relaxation in a glassy binary mixture: Mode-coupling-like power laws, dynamic heterogeneity, and a new non-Gaussian parameter*. Phys. Rev. E, **72**, 011205, 2005.

Fomin, Yu. D., Gribova, N. V., Ryzhov, V. N., Stishov, S. M., and Frenkel, D. *Quasibinary amorphous phase in a three-dimensional system of particles with repulsive-shoulder interactions*. J. Chem. Phys., **129**, 064512, 2008.

Fragiadakis, D. and Roland, C. M. *On the density scaling of liquid dynamics*. J. Chem. Phys., **134**, 044504, 2011.

Frenkel, D. and Smit, B. *Understanding Molecular Simulation*. Academic Press: San Diego, second edition, 2002.

Galliero, G. *Surface tension of short flexible Lennard-Jones chains: Corresponding states behavior*. J. Chem. Phys., **133**, 074705, 2010.

Gallot, S., Hulin, D., and Lafontaine, J. *Riemannian Geometry*. Springer-Verlag: Berlin, third edition, 2004.

Gay, J. G. and Berne, B. J. *Modification of the overlap potential to mimic a linear site–site potential*. J. Chem. Phys., **74**, 3316, 1981.

Gebremichael, Y., Vogel, M., Bergroth, M. N. J., Starr, F. W., and Glotzer, S. C. *Spatially Heterogeneous Dynamics and the Adam-Gibbs Relation in the Dzugutov Liquid*. J. Phys. Chem. B, **109**, 15068, 2005.

Girifalco, L. A. *Molecular Properties of C_{60} In the Gas and Solid Phases.* J. Phys. Chem., **96**, 858, 1992.

Gleim, T., Kob, W., and Binder, K. *How Does the Relaxation of a Supercooled Liquid Depend on Its Microscopic Dynamics?* Phys. Rev. Lett., **81**, 4404, 1998.

Gnan, N. *Viscous liquid dynamics in and out of equilibrium: from isomorphic curves in the phase diagram to effective temperatures in ageing.* PhD thesis, Roskilde University, 2010.

Gnan, N., Schrøder, T. B., Pedersen, U. R., Bailey, N. P., and Dyre, J. C. *Pressure-energy correlations in liquids. IV. "Isomorphs" in liquid phase diagrams.* J. Chem. Phys., **131**, 234504, 2009.

Goel, G., Krekelberg, W. P., Errington, J. R., and Truskett, T. M. *Tuning Density Profiles and Mobility of Inhomogeneous Fluids.* Phys. Rev. Lett., **100**, 106001, 2008.

Goel, G., Krekelberg, W. P., Pond, M. J., Mittal, J., Shen, V. K., Errington, J. R., and Truskett, T. M. *Available states and available space: static properties that predict self-diffusivity of confined fluids.* J. Stat. Mech. Theor. Exp., **4**, 04006, 2009.

Goel, G., Lacks, D. J., and Orman, J. A. Van. *Transport coefficients in silicate melts from structural data via a structure-thermodynamics-dynamics relationship.* Phys. Rev. E, **84**, 051506, 2011.

Goldstein, H., Poole, C., and Safko, J. *Classical Mechanics.* Addison-Wesley: San Francisco, third edition, 2002.

Götze, W. *Complex Dynamics of Glass-Forming Liquids: A Mode-coupling theory.* Oxford University Press: New York, first edition, 2009.

Gray, C. G. and Gubbins, K. E. *Theory of Molecular Fluids.* Oxford University Press: Oxford, 1984.

Grosfils, P. and Lutsko, J. F. *Dependence of the liquid-vapor surface tension on the range of interaction: A test of the law of corresponding states.* J. Chem. Phys., **130**, 054703, 2009.

Guggenheim, E. A. *The Principle of Corresponding States.* J. Chem. Phys., **13**, 253, 1945.

Gundermann, D., Pedersen, U. R., Hecksher, T., Bailey, N. P., Jakobsen, B., Christensen, T., Olsen, N. B., Schrøder, T. B., Fragiadakis, D., Casalini, R., Roland, C. M., Dyre, J. C., and Niss, K. *Predicting the density-scaling exponent of a glass-forming liquid from Prigogine–Defay ratio measurements.* Nat. Phys., **7**, 816, 2011.

Hansen, E. *Variationsregning.* Polyteknisk Forlag, second edition, 1973.

Hansen, J. P. and McDonald, I. R. *Statistical mechanics of dense ionized matter. IV. Density and charge fluctuations in a simple molten salt.* Phys. Rev. A, **11**, 2111, 1975.

Hansen, J.-P. and McDonald, I. R. *Theory of Simple Liquids.* Academic Press: Amsterdam, third edition, 2006.

Hansen, J.-P. and Verlet, L. *Phase Transitions of the Lennard-Jones System.* Phys. Rev., **184**, 151, 1969.

Hansen, J. S., Dyre, J. C., Daivis, P. J., Todd, B. D., and Bruus, H. *Nanoflow hydrodynamics.* Phys. Rev. E, **84**, 036311, 2011.

Hansen, J. S., Schrøder, T. B., and Dyre, J. C. *Simplistic Coulomb Forces in Molecular Dynamics: Comparing the Wolf and Shifted-Force Approximations.* J. Phys. Chem. B, **116**, 5738, 2012.

Hertz, H. *Die Prinzipien der Mechanik, in Neuem Zusammenhange Dargestellt.* Johann Ambrosius Barth: Leipzig, 1894.

Hill, T. L. *An Introduction to Statistical Thermodynamics.* Dover Publications, Inc.: New York, 1986.

Hiwatari, Y., Matsuda, H., Ogawa, T., Ogita, N., and Ueda, A. *Molecular Dynamics Studies on the Soft-Core Model.* Prog. Theor. Phys., **52**, 1105, 1974.

Hoang, V. V. and Odagaki, T. *Glasses of simple liquids with double-well interaction potential.* Physica B, **403**, 3910, 2008.

Hoover, W. G. *Canonical dynamics: Equilibrium phase-space distributions.* Phys. Rev. A, **31**, 1695, 1985.

Hoover, W. G. and Ross, M. *Statistical Theories of Melting.* Contemp. Phys., **12**, 339, 1971.

Hoover, W. G., Ross, M., Johnson, K. W., Henderson, D., Barker, J. A., and Brown, B. C. *Soft-Sphere Equation of State.* J. Chem. Phys., **52**, 4931, 1970.

Hujo, W., Jabes, B. S., Rana, V. K., Chakravarty, C., and Molinero, V. *The Rise and Fall of Anomalies in Tetrahedral Liquids.* J. Stat. Phys., **145**, 293, 2011.

Ingebrigtsen, T., Heilmann, O. J., Toxvaerd, S., and Dyre, J. C. *Time reversible molecular dynamics algorithms with holonomic bond constraints in the NPH and NPT ensembles using molecular scaling.* J. Chem. Phys, **132**, 154106, 2010.

Kane, C., Marsden, J. E., and Ortiz, M. *Symplectic-energy-momentum preserving variational integrators.* J. Math. Phys., **40**, 3353, 1999.

Kawasaki, T., Araki, T., and Tanaka, H. *Correlation between Dynamic Heterogeneity and Medium-Range Order in Two-Dimensional Glass-Forming Liquids.* Phys. Rev. Lett., **99**, 215701, 2007.

Khrapak, S. A. and Morfill, G. E. *Accurate freezing and melting equations for the Lennard-Jones system.* J. Chem. Phys., **134**, 094108, 2011.

Kimmel, R. and Sethian, J. A. *Computing geodesic paths on manifolds.* Proc. Natl. Acad. Sci., **95**, 8431, 1998.

Klein, O. *Om det osmotiska trycket hos en elektrolyt.* Medd. Vetenskapsakad. Nobelinst., **5**, 1, 1919.

Knudsen, J. M. and Hjorth, P. G. *Elements of Newtonian Mechanics.* Springer-Verlag: Berlin, third edition, 2002.

Kob, W. and Andersen, H. C. *Testing mode-coupling theory for a supercooled binary Lennard-Jones mixture: The van Hove correlation function.* Phys. Rev. E, **51**, 4626, 1995a.

Kob, W. and Andersen, H. C. *Testing mode-coupling theory for a supercooled binary Lennard-Jones mixture. II. Intermediate scattering function and dynamic susceptibility.* Phys. Rev. E, **52**, 4134, 1995b.

Kopeikin, S., Efroimsky, M., and Kaplan, G. *Relativistic Celestial Mechanics of the Solar System.* Wiley-VCH, 2011.

Krakoviack, V. *Liquid-Glass Transition of a Fluid Confined in a Disordered Porous Matrix: A Mode-Coupling Theory.* Phys. Rev. Lett., **94**, 065703, 2005.

Krakoviack, V. *Mode-coupling theory predictions for the dynamical transitions of partly pinned fluid systems.* Phys. Rev. E, **84**, 050501, 2011.

Kremer, K. and Grest, G. S. *Dynamics of entangled linear polymer melts: A molecular-dynamics simulation.* J. Chem. Phys., **92**, 5057, 1990.

Ladd, A. J. C. *Equations of motion for non-equilibrium molecular dynamics simulations of viscous flow in molecular fluids.* Mol. Phys., **53**, 459, 1984.

Lang, S., Botan, V., Oettel, M., Hajnal, D., Franosch, T., and Schilling, R. *Glass Transition in Confined Geometry.* Phys. Rev. Lett., **105**, 125701, 2010.

Lang, S., Schilling, R., Krakoviack, V., and Franosch, T. *Mode-coupling theory of the glass transition for confined fluids.* Phys. Rev. E, **86**, 021502, 2012.

Leocmach, M. and Tanaka, H. *Roles of icosahedral and crystal-like order in the hard spheres glass transition.* Nat. Commun., **3**, 974, 2012.

Lew, A. *Variational time integrators in computational solid mechanics.* PhD thesis, California Institute of Technology, 2003.

Lewis, L. J. and Wahnström, G. *Rotational dynamics in ortho-terphenyl: a microscopic view.* J. Non-Cryst. Solids, **172-174**, 69, 1994a.

Lewis, L. J. and Wahnström, G. *Molecular-dynamics study of supercooled ortho-terphenyl.* Phys. Rev. E, **50**, 3865, 1994b.

Li, J., Platt, E., Waszkowycz, B., Cotterill, R., and Robson, B. *Exploration of the phase space of molecular systems: Assessment of established and new methods.* Biophys. Chem., **43**, 221, 1992.

Lützen, J. *Mechanistic Images in Geometric Form: Heinrich Hertz's "Principles of Mechanics"*. Oxford University Press: Oxford, 2005.

Lynch, G. C. and Pettitt, B. M. *Grand canonical ensemble molecular dynamics simulations: Reformulation of extended system dynamics approaches*. J. Chem. Phys., **107**, 8594, 1997.

Lyubartsev, A. P., Martsinovski, A. A., Shevkunov, S. V., and Vorontsov-Velyaminov, P. N. *New approach to Monte Carlo calculation of the free energy: Method of expanded ensembles*. J. Chem. Phys., **96**, 1776, 1992.

Marsden, J. E. and West, M. *Discrete mechanics and variational integrators*. Acta Numer., **1**, 357, 2001.

May, H.-O. and Mausbach, P. *Thermodynamic excess properties and their scaling behavior for the Gaussian core model fluid*. Fluid Phase Equilib., **313**, 156, 2012.

Mittal, J. *Using Compressibility Factor as a Predictor of Confined Hard-Sphere Fluid Dynamics*. J. Phys. Chem. B, **113**, 13800, 2009.

Mittal, J., Errington, J. R., and Truskett, T. M. *Thermodynamics Predicts How Confinement Modifies the Dynamics of the Equilibrium Hard-Sphere Fluid*. Phys. Rev. Lett., **96**, 177804, 2006.

Mittal, J., Errington, J. R., and Truskett, T. M. *Relationships between Self-Diffusivity, Packing Fraction, and Excess Entropy in Simple Bulk and Confined Fluids*. J. Phys. Chem. B, **111**, 10054, 2007.

Mossa, S., Nave, E. La, Stanley, H. E., Donati, C., Sciortino, F., and Tartaglia, P. *Dynamics and configurational entropy in the Lewis-Wahnström model for supercooled orthoterphenyl*. Phys. Rev. E, **65**, 041205, 2002.

Newton, Sir I. *Philosophiae Naturalis Principia Mathematica*. I. Newton, 1687.

Nguyen, C. N. and Stratt, R. M. *Preferential solvation dynamics in liquids: How geodesic pathways through the potential energy landscape reveal mechanistic details about solute relaxation in liquids*. J. Chem. Phys., **133**, 124503, 2010.

Nguyen, C. N., Isaacson, J. I., Shimmyo, K. B., Chen, A., and Stratt, R. M. *How dominant is the most efficient pathway through the potential energy landscape of a slowly diffusing disordered system?* J. Chem. Phys., **136**, 184504, 2012.

Nosé, S. *A unified formulation of the constant temperature molecular dynamics methods*. J. Chem. Phys., **81**, 511, 1984.

NVIDIA. *CUDA C Programming Guide Version 4.2*, 2012.

Nyland, L., Harris, M., and Prins, J. Fast N-Body Simulation with CUDA. In Nguyen, H., editor, *GPU Gems 3*. Addison-Wesley: Kendallville, second edition, 2008.

Papini, J. J., Schrøder, T. B., and Dyre, J. C. *Do all liquids become strongly correlating at high pressure?* arXiv, **1**, 1103.4954v2, 2011.

Pedersen, U. R. *Long-time simulations of viscous liquids: from strong correlations to crystallization.* PhD thesis, Roskilde University, 2009.

Pedersen, U. R., Bailey, N. P., Schrøder, T. B., and Dyre, J. C. *Strong Pressure-Energy Correlations in van der Waals Liquids.* Phys. Rev. Lett., **100**, 015701, 2008.

Pedersen, U. R., Peters, G. H., Schrøder, T. B., and Dyre, J. C. *Correlated Volume-Energy Fluctuations of Phospholipid Membranes: A Simulation Study.* J. Phys. Chem. B, **114**, 2124, 2010a.

Pedersen, U. R., Schrøder, T. B., and Dyre, J. C. *Repulsive Reference Potential Reproducing the Dynamics of a Liquid with Attractions.* Phys. Rev. Lett., **105**, 157801, 2010b.

Pedersen, U. R., Schrøder, T. B., Dyre, J. C., and Harrowell, P. *Geometry of Slow Structural Fluctuations in a Supercooled Binary Alloy.* Phys. Rev. Lett., **104**, 105701, 2010c.

Pedersen, U. R., Gnan, N., Bailey, N. P., Schrøder, T. B., and Dyre, J. C. *Strongly correlating liquids and their isomorphs.* J. Non-Cryst. Solids, **357**, 320, 2011.

Reiss, H. Scaled Particle Methods in the Statistical Thermodynamics of Fluids. In Prigogine, I., editor, *Advances in Chemical Physics*, volume 9, page 1. John Wiley and Sons, Inc., 1965.

Richert, R. *Dynamics of Nanoconfined Supercooled Liquids.* Annu. Rev. Phys. Chem., **62**, 65, 2011.

Rodgers, J. M. and Weeks, J. D. *Local molecular field theory for the treatment of electrostatics.* J. Phys.: Condens. Matter, **20**, 494206, 2008.

Rosenfeld, Y. *Relation between the transport coefficients and the internal entropy of simple systems.* Phys. Rev. A, **15**, 2545, 1977.

Rosenfeld, Y. *A quasi-universal scaling law for atomic transport in simple fluids.* J. Phys.: Condens. Matter, **11**, 5415, 1999.

Rosenfeld, Y. and Tarazona, P. *Density functional theory and the asymptotic high density expansion of the free energy of classical solids and fluids.* Mol. Phys., **95**, 141, 1998.

Ross, M. and Young, D. A. *Theory of the Equation of State at High Pressure.* Annu. Rev. Phys. Chem., **44**, 61, 1993.

Ryckaert, J.-P., Ciccotti, G., and Berendsen, H. J. C. *Numerical integration of the Cartesian Equations of Motion of a System with Constraints: Molecular Dynamics of n-Alkanes.* J. Comput. Phys., **23**, 327, 1977.

Scala, A., Angelani, L., Leonardo, R. Di, Ruocco, G., and Sciortino, F. *A stroll in the energy landscape.* Philos. Mag. B., **82**, 151, 2002.

Schiller-Institute, 2013. URL http://www.schillerinstitute.org/fid_02-06/031_long_life_catenary.html.

Schlichtkrull, H. *Differentiable Manifolds. Lecture Notes for Geometry 2.* University of Copenhagen, 2009.

Schlichtkrull, H. *Curves and Surfaces. Lecture Notes for Geometry 1.* University of Copenhagen, 2010.

Schoen, M., Diestler, D. J., and Cushman, J. H. *Fluids in micropores. I. Structure of a simple classical fluid in a slit-pore.* J. Chem. Phys., **87**, 5464, 1987.

Schoen, M., Cushman, J. H., Diestler, D. J., and Rhykerd, C. L. *Fluids in micropores. II. Self-diffusion in a simple classical fluid in a slit pore.* J. Chem. Phys., **88**, 1394, 1988.

Schrøder, T. B., Bailey, N. P., Pedersen, U. R., Gnan, N., and Dyre, J. C. *Pressure-energy correlations in liquids. III. Statistical mechanics and thermodynamics of liquids with hidden scale invariance.* J. Chem. Phys., **131**, 234503, 2009a.

Schrøder, T. B., Pedersen, U. R., Bailey, N. P., Toxvaerd, S., and Dyre, J. C. *Hidden scale invariance in molecular van der Waals liquids: A simulation study.* Phys. Rev. E, **80**, 041502, 2009b.

Schrøder, T. B., Gnan, N., Pedersen, U. R., Bailey, N. P., and Dyre, J. C. *Pressure-energy correlations in liquids. V. Isomorphs in generalized Lennard-Jones systems.* J. Chem. Phys., **134**, 164505, 2011.

Separdar, L., Bailey, N. P., Schrøder, T. B., Davatolhagh, S., and Dyre, J. C. *Isomorph invariance of Couette shear flows simulated by the SLLOD equations of motion.* arXiv, **1**, 1212.4480v1, 2012.

Shintani, H. and Tanaka, H. *Frustration on the way to crystallization in glass.* Nature, **2**, 200, 2006.

Shneiderman, B. and Plaisant, C. *Designing the User Interface.* Addison-Wesley, fourth edition, 2005.

Steel, R. G. D. and Torrie, J. H. *Principles and Procedures of Statistics.* McGraw-Hill: New York, 1960.

Steele, W. A. *The physical interaction of gases with crystalline solids: I. Gas-solid energies and properties of isolated adsorbed atoms.* Surf. Sci., **36**, 317, 1973.

Stern, A. and Desbrun, M. *Discrete Geometric Mechanics for Variational Time Integrators.* Proceeding: SIGGRAPH, **1**, 75, 2006.

Stillinger, F. H. *Phase transitions in the Gaussian core system.* J. Chem. Phys., **65**, 3968, 1976.

Stipp, S. L. S., Konnerup-Madsen, J., Franzreb, K., Kulik, A., and Mathieu, H. J. *Spontaneous movement of ions through calcite at standard temperature and pressure.* Nature, **396**, 356, 1998.

Stishov, S. M. *The thermodynamics of melting of simple substances.* Sov. Phys. Usp., **17**, 625, 1975.

Suzuki, K. and Hayakawa, H. *Nonequilibrium mode-coupling theory for uniformly sheared underdamped systems.* Phys. Rev. E, **87**, 012304, 2013.

Szamel, G. and Flenner, E. *Independence of the relaxation of a supercooled fluid from its microscopic dynamics: Need for yet another extension of the mode-coupling theory.* Europhys. Lett., **67**, 779, 2004.

Tölle, A. *Neutron scattering studies of the model glass former ortho-terphenyl.* Rep. Prog. Phys., **64**, 1473, 2001.

Toxvaerd, S. *The structure and thermodynamics of a solid-fluid interface.* J. Chem. Phys., **74**, 1998, 1981.

Toxvaerd, S. and Dyre, J. C. *Communication: Shifted forces in molecular dynamics.* J. Chem. Phys., **134**, 081102, 2011a.

Toxvaerd, S. and Dyre, J. C. *Role of the first coordination shell in determining the equilibrium structure and dynamics of simple liquids.* J. Chem. Phys., **135**, 134501, 2011b.

Toxvaerd, S., Heilmann, O. J., Ingebrigtsen, T., Schrøder, T. B., and Dyre, J. C. *Time-reversible molecular dynamics algorithms with bond constraints.* J. Chem. Phys., **131**, 064102, 2009.

Toxvaerd, S., Heilmann, O. J., and Dyre, J. C. *Energy conservation in molecular dynamics simulations of classical systems.* J. Chem. Phys., **136**, 224106, 2012.

Travis, K. P., Todd, B. D., and Evans, D. J. *Departure from Navier-Stokes hydrodynamics in confined liquids.* Phys. Rev. E, **55**, 4288, 1997.

Varnik, F., Baschnagel, J., and Binder, K. *Molecular dynamics results on the pressure tensor of polymer films.* J. Chem. Phys., **113**, 4444, 2000.

Veldhorst, A. A. Unpublished data, 2013.

Veldhorst, A. A., Bøhling, L., Dyre, J. C., and Schrøder, T. B. *Isomorphs in the phase diagram of a model liquid without inverse power law repulsion.* Eur. Phys. J. B, **85**, 21, 2012.

Verlet, L. *Computer "Experiments" on Classical Fluids. I. Thermodynamical Properties of Lennard-Jones Molecules.* Phys. Rev., **159**, 98, 1967.

Wahnström, G. *Molecular-dynamics study of a supercooled two-component Lennard-Jones system.* Phys. Rev. A, **44**, 3752, 1991.

Wang, C. and Stratt, R. M. *Global perspectives on the energy landscapes of liquids, supercooled liquids, and glassy systems: The potential energy landscape ensemble.* J. Chem. Phys., **127**, 224503, 2007a.

Wang, C. and Stratt, R. M. *Global perspectives on the energy landscapes of liquids, supercooled liquids, and glassy systems: Geodesic pathways through the potential energy landscape.* J. Chem. Phys., **127**, 224504, 2007b.

Wang, H., Schütte, C., and Zhang, P. *Error estimate of short-range force calculation in inhomogeneous molecular systems.* Phys. Rev. E, **86**, 026704, 2012.

Wartha, F., Horn, A. H. C., Meiselbach, H., and Sticht, H. *Molecular Dynamics Simulations of HIV-1 Protease Suggest Different Mechanisms Contributing to Drug Resistance.* J. Chem. Theory Comput., **1**, 315, 2005.

Watanabe, K. and Tanaka, H. *Direct Observation of Medium-Range Crystalline Order in Granular Liquids Near the Glass Transition.* Phys. Rev. Lett., **100**, 158002, 2008.

Weeks, J. D. Private communication, 2012.

Weeks, J. D., Chandler, D., and Andersen, H. C. *Role of Repulsive Forces in Determining the Equilibrium Structure of Simple Liquids.* J. Chem. Phys., **54**, 5237, 1971.

Weeks, J. D., Selinger, R. L. B., and Broughton, J. Q. *Self-Consistent Treatment of Repulsive and Attractive Forces in Nonuniform Liquids.* Phys. Rev. Lett., **75**, 2694, 1995.

Weeks, J. D., Vollmayr, K., and Katsov, K. *Intermolecular forces and the structure of uniform and nonuniform fluids.* Physica A, **244**, 461, 1997.

Weeks, J. D., Katsov, K., and Vollmayr, K. *Roles of Repulsive and Attractive Forces in Determining the Structure of Nonuniform Liquids: Generalized Mean Field Theory.* Phys. Rev. Lett., **81**, 4400, 1998.

West, M. *Variational integrators.* PhD thesis, California Institute of Technology, 2004.

Widom, B. *Intermolecular Forces and the Nature of the Liquid State.* Science, **157**, 3787, 1967.

Young, T. and Andersen, H. C. *A scaling principle for the dynamics of density fluctuations in atomic liquids.* J. Chem. Phys., **118**, 3447, 2003.

Young, T. and Andersen, H. C. *Tests of an Approximate Scaling Principle for Dynamics of Classical Fluids.* J. Phys. Chem. B, **109**, 2985, 2005.

Zhakhovskii, V. V. *Melting curve of systems with a homogeneous potential function.* J. Exp. Theor. Phys., **78**, 871, 1994.

APPENDIX

Appendix A

NUMERICAL MODEL SYSTEMS

The model systems appearing in the thesis (and their abbreviations) are presented below where quantities are given in dimensionless units defined by setting $\epsilon = \sigma = 1$. Masses that are not specified are unity.

1. *Single-component inverse power-law (IPL) fluids*:
   N particles interacting via $v(r) = \epsilon(\sigma/r)^n$.

2. *Single-component Lennard-Jones (SCLJ) liquid*:
   N particles interacting via $v(r) = 4\epsilon[(\sigma/r)^{12} - (\sigma/r)^6]$.

3. *Single-component repulsive LJ liquid* (Paper I):
   N particles interacting via $v(r) = 4\epsilon[(\sigma/r)^{12} + (\sigma/r)^6]$. The parameters are $\sigma = 1$, $\epsilon = 1/8$.

4. *Buckingham liquid* (Buckingham [1938], Veldhorst *et al.* [2012]):
   N particles interacting via $v(r) = \epsilon\big[6/(\alpha-6)\exp[\alpha(1-r/r_m)]$ - $\alpha/(\alpha-6)(r_m/r)^6\big]$. The parameters are $\epsilon = 1$, $\alpha = 14.5$, $r_m = 2^{1/6}$.

5. *Generalized Kob-Andersen binary LJ (KABLJ) mixture* (Kob and Andersen [1995a,b]):
   A binary mixture of 80% A particles and 20% B particles interacting via $v(r) = \epsilon_{\alpha\beta}/(12-n)\left[n(\sigma_{\alpha\beta}/r)^{12} - 12(\sigma_{\alpha\beta}/r)^n\right]$. The parameters are $\epsilon_{AB} = 1.5$, $\epsilon_{BB} = 0.5$, $\sigma_{AA} = 2^{1/6}$, $\sigma_{AB} = 0.8 \cdot 2^{1/6}$, $\sigma_{BB} = 0.88 \cdot 2^{1/6}$.

6. *Wahnström binary LJ (WABLJ) mixture* (Wahnström [1991]):
   An equimolar binary mixture of A and B particles interacting via the LJ potential. The parameters are $\epsilon_{AA} = \epsilon_{AB} = \epsilon_{BB} = 1$, $\sigma_{AA} = 1, \sigma_{BB} = 1/1.2, \sigma_{AB} = (\sigma_{AA}+\sigma_{BB})/2$, $m_A = 2$, $m_B = 1$.

7. *Dzugutov (DZ) liquid* (Dzugutov [1992]):
   N particles interacting via $v(r) = v_1 + v_2$, where $v_1 = A(r^{-n} - B)\exp(c/(r-a))$ and $v_2 = B\exp(d/(r-b))$ and $r \geq a \Rightarrow v_1 = 0$, $r \geq b \Rightarrow v_2 = 0$ $(a < b)$. The parameters are $a = 1.87$, $b = 1.94$, $c = 1.1$, $d = 0.27$, $A = 5.82$, $B = 1.28$, $n = 16$.

8. *Lennard-Jones Gaussian (LJG) liquid* (Engel and Trebin [2007], Hoang and Odagaki [2008]):
   N particles interacting via $v(r) = \epsilon\left((\sigma/r)^{12} - 2(\sigma/r)^6 - \epsilon_0\exp[-(r-r_0)^2/2\sigma_0^2]\right)$. The parameters are $\sigma_0^2 = 0.02$, $\epsilon_0 = 1.50$, $r_0 = 1.47$.

9. *Gaussian core model (GCM)* (Stillinger [1976]):
   N particles interacting via $v(r) = \epsilon\exp\left[-(r/\sigma)^2\right]$.

10. *Girifalco* (Girifalco [1992]):
N particles interacting via $v(r) = -\alpha\big[1/s(s-1)^3+1/s(s+1)^3-2/s^4\big]+\beta\big[1/s(s-1)^9+1/s(s+1)^9-2/s^{10}\big]$ with $s = r/\sigma$. The parameters are $\alpha = 0.17$, $\beta = 3.08397 \cdot 10^{-4}$.

11. *Core soft water* (de Oliveira *et al.* [2006]):
N particles interacting via the LJG potential. The parameters are $\sigma = 2^{1/6}$, $\epsilon = 1$, $\sigma_0^2 = 1/2$, $\epsilon_0 = -5$, $r_0 = 0.7$.

12. *Fermi Jagla* (Abraham *et al.* [2011]):
N particles interacting via $v(r) = \epsilon\big[(\sigma/r)^n + A_0/(1+\exp[A_1/A_0(r/\sigma - A_2)]) - B_0/(1+\exp[B_1/B_0(r/\sigma - B_2)])\big]$. The parameters are $n = 20$, $A_0 = 4.56$, $A_1 = 28.88$, $A_2 = 1.36$, $B_0 = 1$, $B_1 = 3.57$, $B_2 = 2.36$.

13. *Smooth Repulsive Shoulder* (Fomin *et al.* [2008]):
N particles interacting via $v(r) = (\sigma/r)^n + \epsilon[1 - \tanh(k_0(r - \sigma_s))]/2$. The parameters are $n = 14$, $k_0 = 10$, $\sigma_s = 1.35$.

14. *Hansen-McDonald molten salt* (Hansen and McDonald [1975]):
An equimolar binary mixture of singly-charged cations (+) and anions (−). The potential between two particles of charge q_α and q_β is given by $v(r) = (1/9)r^{-9} + q_\alpha q_\beta/r$, where $q_+ = 1$, $q_- = -1$.

15. *Lennard-Jones Chain (LJC)* (Kremer and Grest [1990]):
We simulated linear chains of $N = 4$ and $N = 10$ LJ particles that were rigidly bonded with bond distance $r = 1$. Only the nearest-neighbor LJ interactions are removed.

16. *The asymmetric dumbbell* (Schrøder *et al.* [2009b]):
A large (A) and a small (B) LJ particle rigidly bonded with bond distance $r_{AB} = 0.29/0.4963$. The parameters are $\sigma_{BB} = 0.3910/0.4963$, $\epsilon_{BB} = 0.66944/5.726$, $m_B = 15.035/77.106$. The A-B interaction in different molecules is determined by the Lorentz-Berthelot mixing rule (Allen and Tildesley [1987]).

17. *Lewis-Wahnström OTP* (Lewis and Wahnström [1994a,b]):
Three identical LJ particles rigidly bonded in an isosceles triangle with unity sides and top-angle of 75°.

18. *Rigid SPC/E water* (Berendsen *et al.* [1987]):
A rigid isosceles triangle with sides $r_{OH} = 1/3.166$ and base line $2r_{OH}\sin(109.47/2)$. The O-O intermolecular interactions are given by the LJ pair potential ($\epsilon_{OO} = 1$, $\sigma_{OO} = 1$, $m_O = 15.9994/1.00794$) with no intermolecular LJ interactions for H-H and H-O. The three particles are charged with $q_O = -0.8476e/(8.2316\pi\,\varepsilon_0\,\text{Å}\,kJ/mol)^{1/2}$ and $q_H = |q_O|/2$.

Appendix B

A GRÜNEISEN-TYPE CONFIGURATIONAL EQUATION OF STATE IMPLIES A SEPARATION OF TEMPERATURE

In this appendix we prove that a Grüneisen-type configurational equation of state implies a separation of temperature into a product of a function of excess entropy and a function of density. The Grüneisen-type equation of state is given by

$$W = \gamma(\rho)U + \Phi(\rho). \tag{B.1}$$

The fundamental equation of thermodynamics ($p_{\rm ex} \equiv W/V$)

$$dU = TdS_{\rm ex} - p_{\rm ex}dV = TdS_{\rm ex} + Wd\ln\rho, \tag{B.2}$$

produces the relations

$$T = \Big(\frac{\partial U}{\partial S_{\rm ex}}\Big)_{\rho}, \tag{B.3}$$

$$W = \Big(\frac{\partial U}{\partial \ln\rho}\Big)_{S_{\rm ex}}. \tag{B.4}$$

Taking the derivative of Eq. (B.1) with respect to excess entropy (at constant density), and applying Eq. (B.3), gives

$$\Big(\frac{\partial W}{\partial S_{\rm ex}}\Big)_{\rho} = \gamma(\rho)\Big(\frac{\partial U}{\partial S_{\rm ex}}\Big)_{\rho} = \gamma(\rho)T. \tag{B.5}$$

The left-hand side of Eq. (B.5) can also be written as

$$\Big(\frac{\partial W}{\partial S_{\rm ex}}\Big)_{\rho} = \frac{\partial}{\partial S_{\rm ex}}\Big|_{\rho}\frac{\partial}{\partial\ln\rho}\Big|_{S_{\rm ex}}U = \frac{\partial}{\partial\ln\rho}\Big|_{S_{\rm ex}}T, \tag{B.6}$$

by using Eqs. (B.3) and (B.4). We then conclude via Eq. (B.5) that

$$\Big(\frac{\partial\ln T}{\partial\ln\rho}\Big)_{S_{\rm ex}} = \gamma(\rho). \tag{B.7}$$

The separation identity of temperature now follows via integration.

Appendix C

KEEPING EXCESS ENTROPY CONSTANT IN A SLIT-PORE

This appendix considers how to keep the excess entropy constant in a slit-pore (see Fig. 7.1, page 71 for a description of the slit-pore). The fundamental equations of thermodynamics for a slit-pore are (Diestler and Schoen [1995])

$$dU = TdS_{\rm ex} + S_{||}HdA + S_{\rm zz}AdH, \tag{C.1}$$

$$dF_{\rm ex} = -S_{\rm ex}dT + S_{||}HdA + S_{\rm zz}AdH, \tag{C.2}$$

where $F_{\rm ex}$ is the excess Helmholtz free energy, $S_{||}$ and $S_{\rm zz}$ are, respectively, the configurational stress tensor components parallel and normal to the slit-pore. From Eq. (C.2), we have the following Maxwell relations

$$-\Big(\frac{\partial S_{\rm ex}}{\partial A}\Big)_{T,H} = H\Big(\frac{\partial S_{||}}{\partial T}\Big)_{H,A}, \tag{C.3}$$

$$-\Big(\frac{\partial S_{\rm ex}}{\partial H}\Big)_{T,A} = A\Big(\frac{\partial S_{\rm zz}}{\partial T}\Big)_{H,A}, \tag{C.4}$$

$$\Big(\frac{\partial S_{||}H}{\partial H}\Big)_{T,A} = \Big(\frac{\partial S_{\rm zz}A}{\partial A}\Big)_{T,H}. \tag{C.5}$$

We define the average virial W of the slit-pore in analogy to bulk systems as

$$W \equiv -\frac{HA}{3}\Big[2S_{||} + S_{\rm zz}\Big]. \tag{C.6}$$

Combining the above Maxwell relations with standard fluctuation formulas in the NVT ensemble (see Appendix B of Bailey *et al.* [2008a]) gives the following expression

$$\gamma \equiv \frac{\langle \Delta W \Delta U\rangle}{\langle (\Delta U)^2\rangle} = \frac{\big(\frac{\partial W}{\partial T}\big)_{H,A}}{\big(\frac{\partial U}{\partial T}\big)_{H,A}}, \tag{C.7}$$

$$= \frac{-2HA/3\Big(\frac{\partial S_{||}}{\partial T}\Big)_{H,A} - HA/3\big(\frac{\partial S_{\rm zz}}{\partial T}\big)_{H,A}}{T\big(\frac{\partial S_{\rm ex}}{\partial T}\big)_{H,A}}, \tag{C.8}$$

$$= \frac{2A/3\big(\frac{\partial S_{\rm ex}}{\partial A}\big)_{T,H} + H/3\big(\frac{\partial S_{\rm ex}}{\partial H}\big)_{T,A}}{T\big(\frac{\partial S_{\rm ex}}{\partial T}\big)_{H,A}}, \tag{C.9}$$

where we have used from Eq. (C.1) that $(\partial U/\partial T)_{H,A} = T(\partial S_{\rm ex}/\partial T)_{H,A}$. Note that $\langle \Delta W \Delta U\rangle/\langle (\Delta U)^2\rangle$ refer to the instantaneous virial/potential energy whereas $(\partial W/\partial T)_{H,A}$,

etc. refers to ensemble averages; for ease of notation this is left out. If we keep the excess entropy constant, we may write

$$dS_{\mathrm{ex}} = \Big(\frac{\partial S_{\mathrm{ex}}}{\partial A}\Big)_{T,H} dA + \Big(\frac{\partial S_{\mathrm{ex}}}{\partial H}\Big)_{T,A} dH + \Big(\frac{\partial S_{\mathrm{ex}}}{\partial T}\Big)_{H,A} dT = 0. \tag{C.10}$$

From this equation, it then follows that

$$\Big(\frac{\partial S_{\mathrm{ex}}}{\partial A}\Big)_{T,H} = -\Big(\frac{\partial S_{\mathrm{ex}}}{\partial T}\Big)_{H,A}\Big(\frac{\partial T}{\partial A}\Big)_{S_{\mathrm{ex}},H}, \tag{C.11}$$

$$\Big(\frac{\partial S_{\mathrm{ex}}}{\partial H}\Big)_{T,A} = -\Big(\frac{\partial S_{\mathrm{ex}}}{\partial T}\Big)_{H,A}\Big(\frac{\partial T}{\partial H}\Big)_{S_{\mathrm{ex}},A}. \tag{C.12}$$

Applying Eqs. (C.11) and (C.12) to Eq. (C.9) gives

$$\gamma = \frac{\langle \Delta W \Delta U\rangle}{\langle (\Delta U)^2\rangle} = -2/3\Big(\frac{\partial \ln T}{\partial \ln A}\Big)_{S_{\mathrm{ex}},H} - 1/3\Big(\frac{\partial \ln T}{\partial \ln H}\Big)_{S_{\mathrm{ex}},A}, \tag{C.13}$$

$$= -\Big(\frac{\partial \ln T}{\partial \ln HA}\Big)^{d\ln H = d\ln A/2}_{S_{\mathrm{ex}}}, \tag{C.14}$$

where the condition on the superscript is motivated by Eq. (7.1). Equation (C.14) provides via discretization a procedure for keeping the excess entropy constant in a slit-pore (see Sec. 6.3 for bulk systems).

Appendix D

SIMULATIONS OF FIRST COORDINATION SHELL CUTOFFS IN CONFINED LIQUIDS

This appendix presents results from simulations of FCS cutoffs for liquids confined to a slit-pore and expands on the results shown in Chapter 8. A description of each simulation is given in the figure captions.

D.1 The Wahnström binary LJ mixture in a slit-pore

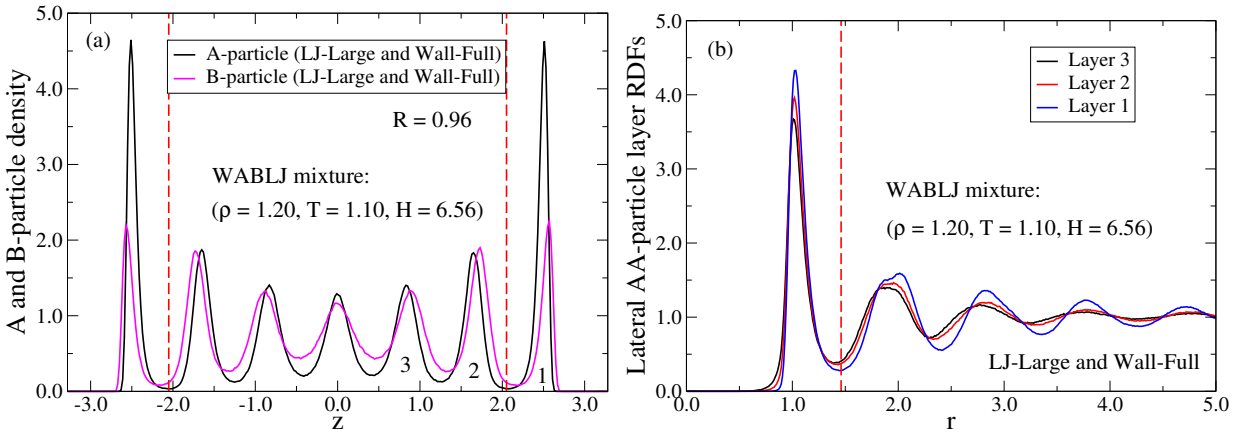

Figure D.1: *(a) A and B-particle density profiles for the WABLJ mixture in a slit-pore at $\rho = 1.20$, $T = 1.10$, and $H = 6.56$ with pair potential cutoff $r_c = 4.500$. The red dashed line marks the FCS of the wall "particle" at the distance $r = 1.229$ from the wall. (b) Lateral AA-particle RDFs of layers 1-3 (layer 1 being the contact layer, and layer 3 the bulk layer) of the A-particle density profile in (a). The red dashed line marks the FCS of layer 1 at $r = 1.460$.*

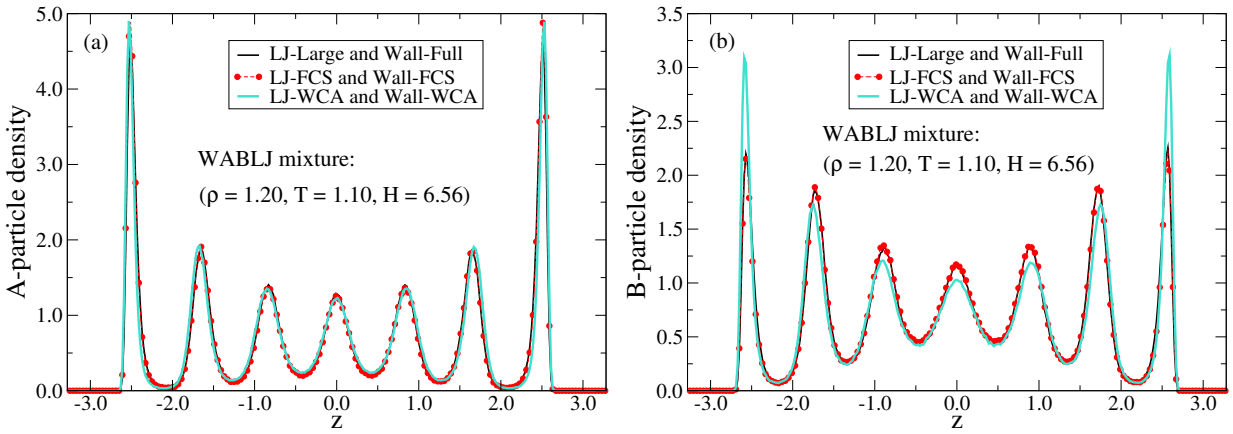

Figure D.2: *Density profiles of the WABLJ mixture confined to a slit-pore. The black curves give a large pair potential cutoff in combination with no cutoff for the wall interactions. The red curves give a cutoff at the FCS for the liquid and wall interactions, and the turquoise curves a WCA-type cutoff for the liquid and wall interactions. (a) A-particle density profile. (b) B-particle density profile.*

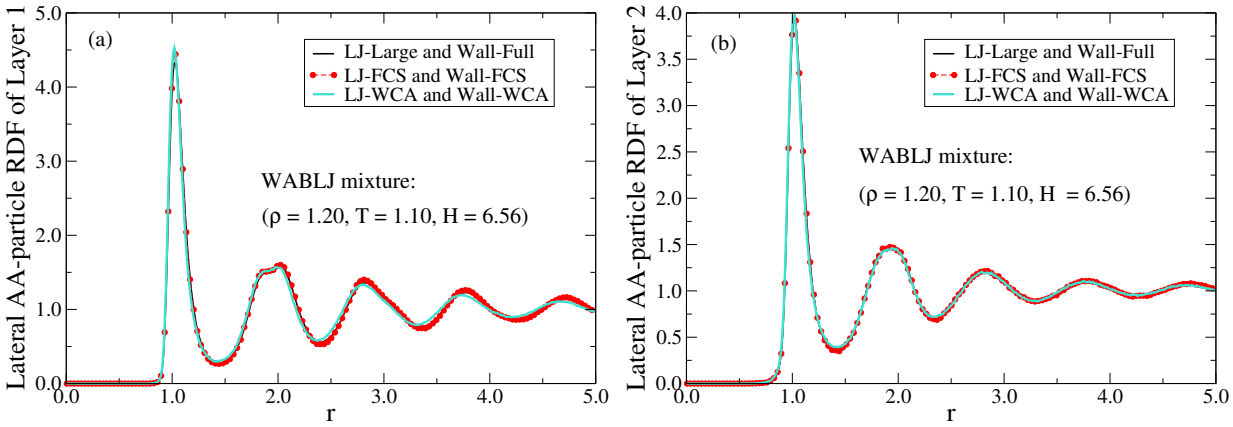

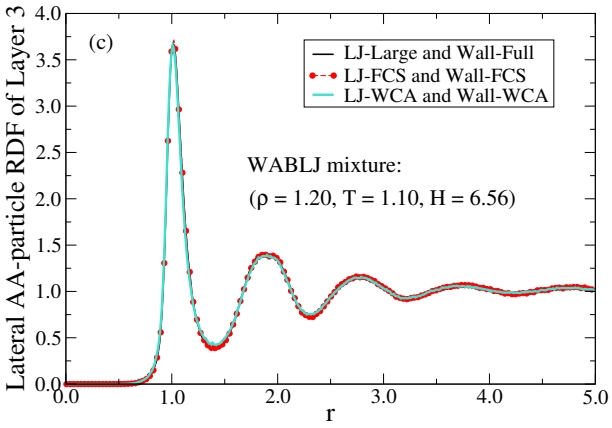

Figure D.3: *FCS and WCA-type cutoff simulations for the WABLJ mixture confined to a slit-pore. The black curves give a large pair potential cutoff in combination with no cutoff for the wall interactions. The red curves give a cutoff at the FCS for the liquid and wall interactions whereas the turquoise curves give a WCA-type cutoff for the liquid and wall interactions. (a) Lateral AA-particle RDFs of layer 1. (b) Lateral AA-particle RDFs of layer 2. (c) Lateral AA-particle RDFs of layer 3.*

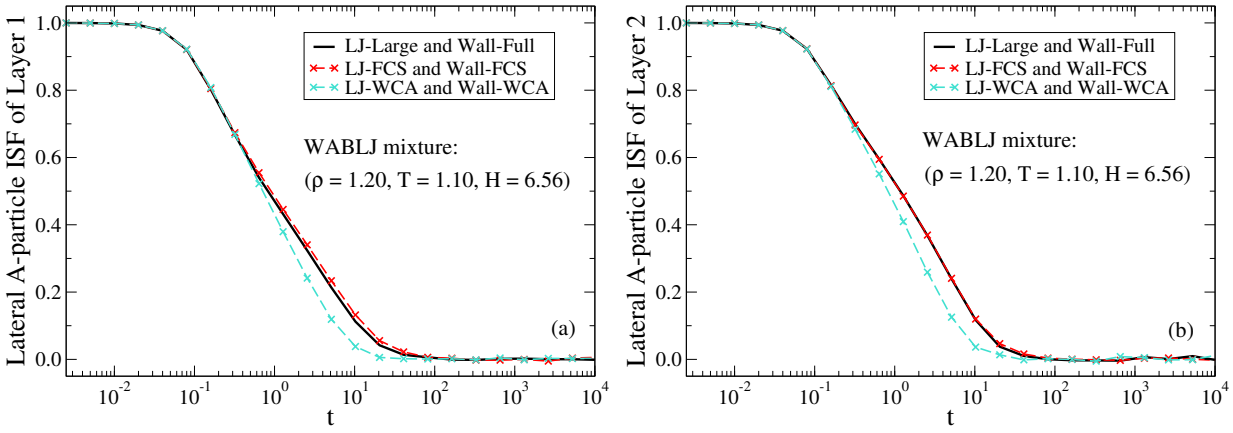

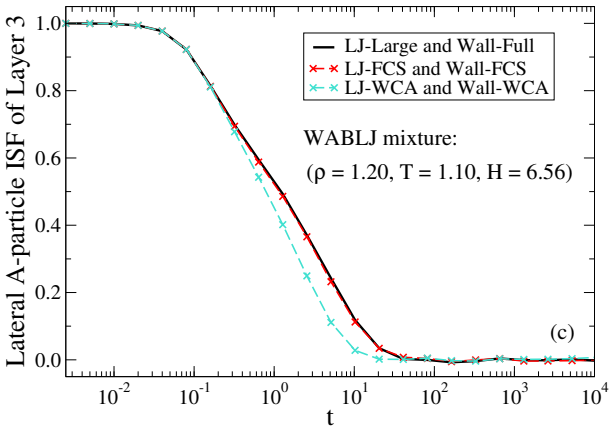

Figure D.4: *FCS and WCA-type cutoff simulations for the WABLJ mixture confined to a slit-pore. The black curves give a large pair potential cutoff in combination with no cutoff for the wall interactions. The red curves give a cutoff at the FCS for the liquid and wall interactions whereas the turquoise curves give a WCA-type cutoff for the liquid and wall interactions. (a) Lateral A-particle ISFs of layer 1. (b) Lateral A-particle ISFs of layer 2. (c) Lateral A-particle ISFs of layer 3.*

D.2 The asymmetric dumbbell model in a slit-pore

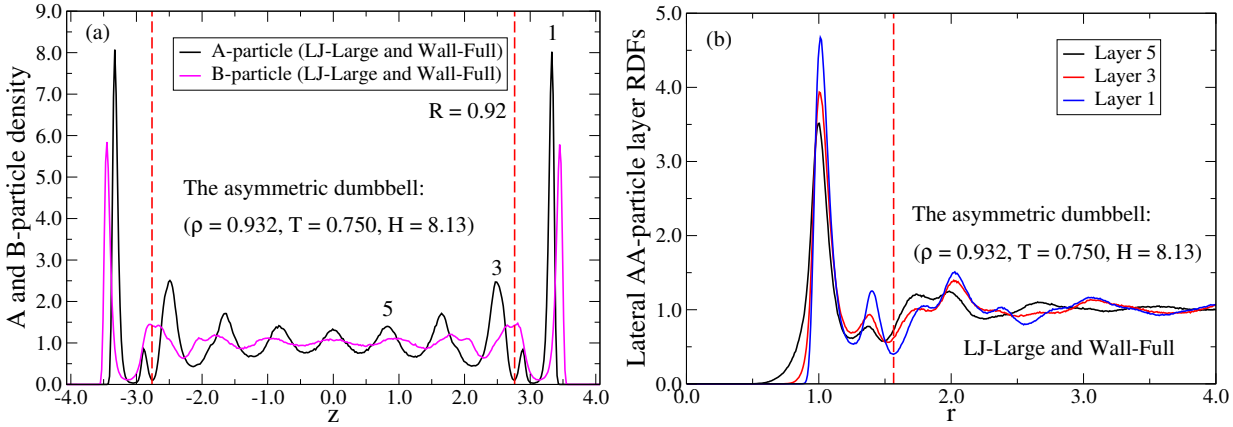

Figure D.5: *(a) A and B-particle density profiles for the asymmetric dumbbell model in a slit-pore at $\rho = 0.932$, $T = 0.750$, and $H = 8.13$ with pair potential cutoff $r_c = 4.000$. The red dashed line marks the FCS of the wall "particle" at the distance $r = 1.300$ from the wall. (b) Lateral AA-particle RDFs of layers 1, 3, 5 (layer 1 being the contact layer, and layer 5 the bulk layer) of the A-particle density profile in (a). The red dashed line marks the FCS of layer 1 at $r = 1.565$.*

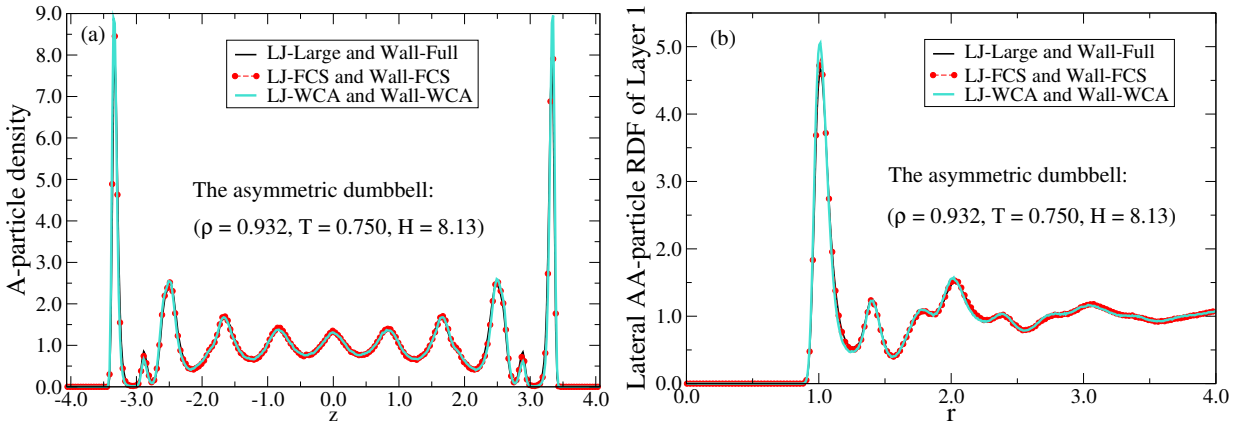

Figure D.6: *FCS and WCA-type cutoff simulations for the asymmetric dumbbell model confined to a slit-pore. The black curves give a large pair potential cutoff in combination with no cutoff for the wall interactions. The red curves give a cutoff at the FCS for the liquid and wall interactions whereas the turquoise curves give a WCA-type cutoff for the liquid and wall interactions. (a) A-particle density profiles. (b) Lateral AA-particle RDFs of layer 1.*

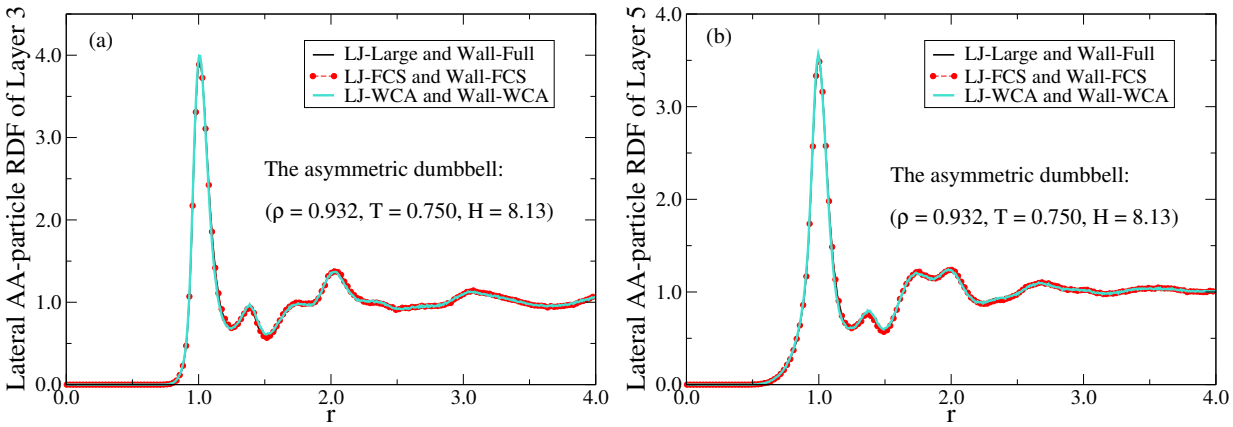

Figure D.7: *FCS and WCA-type cutoff simulations for the asymmetric dumbbell model confined to a slit-pore. The black curves give a large pair potential cutoff in combination with no cutoff for the wall interactions. The red curves give a cutoff at the FCS for the liquid and wall interactions whereas the turquoise curves give a WCA-type cutoff for the liquid and wall interactions. (a) Lateral AA-particle RDFs of layer 3. (b) Lateral AA-particle RDFs of layer 5.*

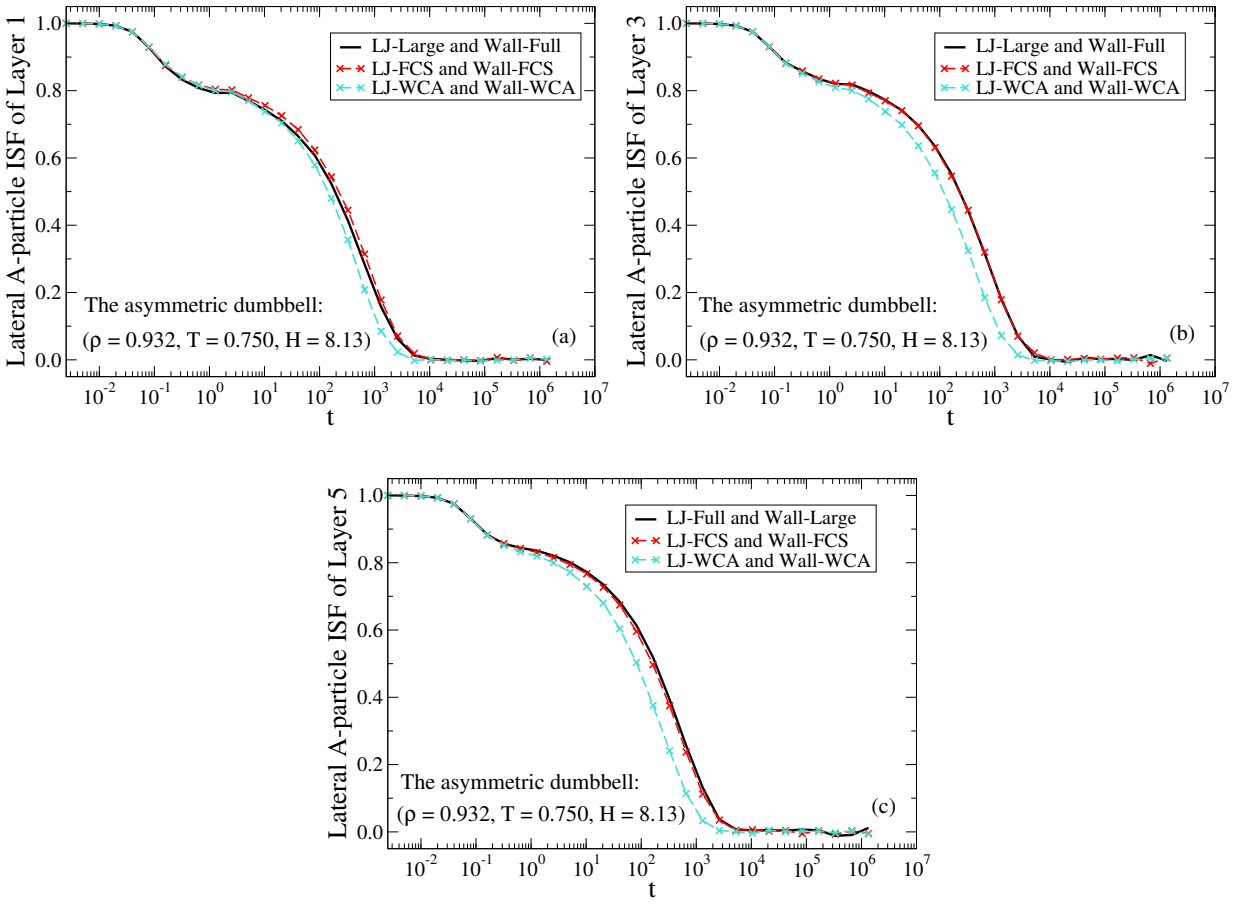

Figure D.8: *FCS and WCA-type cutoff simulations for the asymmetric dumbbell model confined to a slit-pore. The black curves give a large pair potential cutoff in combination with no cutoff for the wall interactions. The red curves give a cutoff at the FCS for the liquid and wall interactions whereas the turquoise curves give a WCA-type cutoff for the liquid and wall interactions. (a) Lateral A-particle ISFs of layer 1. (b) Lateral A-particle ISFs of layer 3. (c) Lateral A-particle ISFs of layer 5.*

Appendix E

REPRINT OF THESIS ARTICLES

Communication: Thermodynamics of condensed matter with strong pressure-energy correlations

Trond S. Ingebrigtsen, Lasse Bøhling, Thomas B. Schrøder, and Jeppe C. Dyre[a)]
DNRF Centre "Glass and Time", IMFUFA, Department of Sciences, Roskilde University, P.O. Box 260, DK-4000 Roskilde, Denmark

(Received 20 December 2011; accepted 31 January 2012; published online 14 February 2012)

We show that for any liquid or solid with strong correlation between its *NVT* virial and potential-energy equilibrium fluctuations, the temperature is a product of a function of excess entropy per particle and a function of density, $T = f(s)h(\rho)$. This implies that (1) the system's isomorphs (curves in the phase diagram of invariant structure and dynamics) are described by $h(\rho)/T = \text{Const.}$, (2) the density-scaling exponent is a function of density only, and (3) a Grüneisen-type equation of state applies for the configurational degrees of freedom. For strongly correlating atomic systems one has $h(\rho) = \sum_n C_n \rho^{n/3}$ in which the only non-zero terms are those appearing in the pair potential expanded as $v(r) = \sum_n v_n r^{-n}$. Molecular dynamics simulations of Lennard-Jones type systems confirm the theory. © *2012 American Institute of Physics*. [http://dx.doi.org/10.1063/1.3685804]

The class of strongly correlating liquids was introduced in Refs. 1 and 2. These liquids are defined by having a correlation coefficient above 0.9 of the constant-volume equilibrium fluctuations of virial W and potential energy U. The WU correlation coefficient varies with state point, but we found from computer simulations that a system has either poor WU correlations in the entire phase diagram or is strongly correlating at most of its condensed-phase state points.[1–5] Van der Waals and metallic liquids are generally strongly correlating, whereas hydrogen-bonded, ionic, and covalently bonded liquids are generally not. The solid phase is usually at least as strongly correlating as the liquid phase. Theoretical arguments, numerical evidence, and experiments show that strongly correlating liquids are simpler than liquids in general.[1–7]

The simplicity of strongly correlating liquids compared to liquids in general[8] derives from the fact that the former have "isomorphs" in their phase diagram, which are curves of isomorphic state points. Two state points with particle density and temperature (ρ_1, T_1) and (ρ_2, T_2) are termed *isomorphic*[3] if all pairs of physically relevant microconfigurations of the state points that trivially scale into one another (i.e., $\rho_1^{1/3}\mathbf{r}_i^{(1)} = \rho_2^{1/3}\mathbf{r}_i^{(2)}$ for all particles i) have proportional configurational Boltzmann factors:

$$e^{-U(\mathbf{r}_1^{(1)},\ldots,\mathbf{r}_N^{(1)})/k_BT_1} = C_{12}\, e^{-U(\mathbf{r}_1^{(2)},\ldots,\mathbf{r}_N^{(2)})/k_BT_2}. \qquad (1)$$

Only inverse-power-law liquids[9] have exact isomorphs (here $C_{12} = 1$), but as shown in Appendix A of Ref. 3 a system is strongly correlating if and only if it has isomorphs to a good approximation.

The invariance of the canonical probabilities of scaled microconfigurations along an isomorph has several implications, for instance:[1–3] (1) the excess entropy and the isochoric specific heat are isomorph invariants, (2) the reduced-unit dynamics is isomorph invariant for both Newtonian and stochastic dynamics, (3) all reduced-unit static correlation functions are isomorph invariant, and (4) a jump between isomorphic state points takes the system instantaneously to equilibrium. Using reduced units means measuring length in terms of the unit $\rho^{-1/3}$ and time in units of $\rho^{-1/3}\sqrt{m/k_BT}$ where m is the average particle mass. Since isomorphs are generally approximate, isomorph properties are likewise rarely rigorously obeyed.

All thermodynamic quantities considered below are excess quantities, i.e., in excess of those of an ideal gas at the same density and temperature. Thus, S is the *excess* entropy ($S < 0$), C_V is the *excess* isochoric specific heat, p is the *excess* pressure (i.e., $p = W/V$), etc.

Briefly, the reason that S and C_V are isomorph invariants is the following.[3] The entropy is determined by the canonical probabilities, which are identical for scaled microconfigurations of two isomorphic state points. From Einstein's formula $C_V = \langle(\Delta U)^2\rangle/k_BT^2$ the isomorph invariance of C_V follows easily by taking the logarithm of Eq. (1) and making use of the isomorph invariance of scaled microconfiguration probabilities.

Since S and C_V are invariant along the same curves in the phase diagram, C_V is a function of S: $C_V = \phi(S)$. Thus, $T(\partial S/\partial T)_V = \phi(S)$ or at constant volume: $\mathrm{d}S/\phi(S) = \mathrm{d}T/T$. Integrating this leads to an expression of the form $\psi(S) = \ln(T) + k(V)$, which implies $T = \exp[\psi(S)]\exp[-k(V)]$. The generic version of this involves only intensive quantities ($s \equiv S/N$):

$$T = f(s)h(\rho). \qquad (2)$$

For inverse-power-law interactions ($\propto r^{-n}$) the entropy is well known to be a function of ρ^γ/T where $\gamma = n/3$: $S = K(\rho^\gamma/T)$. Applying the inverse of the function K shows that these perfectly correlating systems obey Eq. (2) with $h(\rho) = \rho^\gamma$.

The thermodynamic separation identity Eq. (2) is the main result of this communication. We proceed to discuss some consequences and numerical tests.

a)Electronic mail: dyre@ruc.dk.

Density scaling: Since entropy is an isomorph invariant, it follows from Eq. (2) that the variable characterizing an isomorph may be chosen as $h(\rho)/T$. In particular, the reduced relaxation time $\tilde{\tau}$, which is also an isomorph invariant, may be written for some function G:

$$\tilde{\tau} = G\left(\frac{h(\rho)}{T}\right). \tag{3}$$

This is the form of "density scaling" proposed by Alba-Simionesco *et al.* in 2004 from different arguments;[10] at the same time Dreyfus *et al.*, as well as Casalini and Roland, favored the more specific form $\tilde{\tau} = G(\rho^{\gamma}/T)$.[10] Isochrones for many supercooled liquids and polymers follow to a good approximation the latter "power-law density scaling" relation.[11] For large density changes, however, it was recently shown that the density-scaling exponent varies significantly in both simulations and experiments;[12] these cases conform to the more general equation (3).

An expression for the density-scaling exponent: The general, state-point dependent density-scaling exponent γ is defined[2,3] by

$$\gamma \equiv \left(\frac{\partial \ln T}{\partial \ln \rho}\right)_S = \left(\frac{\partial \ln T}{\partial \ln \rho}\right)_{\tilde{\tau}}. \tag{4}$$

The physical interpretation of Eq. (4) is the following. If density is increased by 1%, temperature should be increased by γ% for the system to have the same entropy and reduced relaxation time. Equation (2) implies $\mathrm{d}\ln T = \mathrm{d}\ln f(s) + \mathrm{d}\ln h(\rho)$; thus along an isomorph one has $\mathrm{d}\ln T = \mathrm{d}\ln h$. Via Eq. (4) this implies

$$\gamma = \frac{\mathrm{d}\ln h}{\mathrm{d}\ln \rho}. \tag{5}$$

In particular, γ depends only on density: $\gamma = \gamma(\rho)$.[3]

Configurational Grüneisen equation of state: The Grüneisen equation of state expresses that pressure equals a density-dependent number times energy plus a term that is a function of density only.[13] This equation of state is used routinely for describing condensed matter at high pressures and temperatures. We proceed to show that strongly correlating systems obey the configurational version of the Grüneisen equation of state, which as suggested by Casalini *et al.*[14] has the density-scaling exponent as the proportionality constant:[3,4]

$$W = \gamma(\rho)U + \Phi(\rho). \tag{6}$$

To prove this, note first that $(\partial U/\partial S)_\rho = T = f(S)h(\rho)$ by integration implies $U = F(S)h(\rho) + k(\rho)$ where $F'(S) = f(S)$ (S is the extensive entropy). Since $W = (\partial U/\partial \ln \rho)_S$ (which follows from the standard identity $T\mathrm{d}S = \mathrm{d}U + p\mathrm{d}V$), we get $W = F(S)\mathrm{d}h/\mathrm{d}\ln\rho + \mathrm{d}k/\mathrm{d}\ln\rho$. Substituting into the latter expression $F(S)$ isolated from $U = F(S)h(\rho) + k(\rho)$ leads to Eq. (6), in which $\gamma(\rho)$ is given by Eq. (5). It is straightforward to show that, conversely, Eq. (6) implies the thermodynamic separation identity Eq. (2).

The isomorphs of atomic systems: We consider now predictions for systems of "atomic" particles interacting via pair potentials of the form[15] (where r is the distance between two particles)

$$v(r) = \sum_n v_n r^{-n}. \tag{7}$$

For simplicity only the case of identical particles is considered, but the arguments generalize trivially to multicomponent systems. Consider the thermal average $\langle r^{-n}\rangle$. Switching to reduced units defined by $\tilde{r} \equiv \rho^{1/3} r$, we have $\langle r^{-n}\rangle = \langle \tilde{r}^{-n}\rangle \rho^{n/3}$. Since structure is isomorph invariant in reduced units, $\langle \tilde{r}^{-n}\rangle$ is an isomorph invariant. Consequently, it is a function of any other isomorph invariant, for instance the entropy: $\langle \tilde{r}^{-n}\rangle = G_n(S)$. Noting that the average potential energy is a sum of Eq. (7) over all particle pairs, we conclude that (where $H_n(S) \propto v_n G_n(S)$)

$$U = \sum_n H_n(S)\rho^{n/3}. \tag{8}$$

Taking the derivative of this equation with respect to temperature at constant volume leads to

$$\left(\frac{\partial U}{\partial T}\right)_V = \sum_n H_n'(S)\left(\frac{\partial S}{\partial T}\right)_V \rho^{n/3}. \tag{9}$$

The left-hand side is $T(\partial S/\partial T)_V$, so Eq. (9) implies

$$T = \sum_n H_n'(S)\rho^{n/3}. \tag{10}$$

This is consistent with the thermodynamic separation identity Eq. (2) only if all the functions $H_n'(S)$ are proportional to some function, i.e., if one can write $H_n'(S) = C_n\phi(S)$. We identify $\phi(S)$ as the function $f(s)$ of Eq. (2), which means that

$$h(\rho) = \sum_n C_n \rho^{n/3}. \tag{11}$$

Thus, for strongly correlating atomic liquids, the thermodynamic function $h(\rho)$ has an analytical structure, which is inherited from $v(r)$ in the sense that the only non-zero terms of $h(\rho)$ are those corresponding to non-zero terms of $v(r)$. Note that not all systems with potentials of Eq. (7) are strongly correlating and that the derivation applies only if this is the case.

As an illustration we present results from *NVT* simulations of the Kob-Andersen binary Lennard-Jones (KABLJ) liquid,[16] which is strongly correlating at its condensed-phase state points.[1–3] The application of the above to LJ systems predicts that $H_{12}'(S) \propto H_6'(S)$, where $H_{12}(S)$ is the reduced coordinate average of the r^{-12} term of U. Integrating this leads to $H_{12}(S) = \alpha H_6(S) + \beta$, implying that if the repulsive term in U is plotted against the attractive term in reduced units, all points are predicted to fall onto a common line. Figure 1 presents data where density was changed by a factor of eight and temperature by a factor of 40 000. The data collapse is good but not exact, which reminds us that the relations derived are approximate.

The theory implies a simple mathematical description of the isomorphs in the (ρ, T) phase diagram. From the fact that the potential energy contains only r^{-12} and r^{-6} terms, it follows that $h(\rho) = A\rho^4 - B\rho^2$. Consequently, LJ isomorphs are given by

$$\frac{A\rho^4 - B\rho^2}{T} = \text{Const.} \tag{12}$$

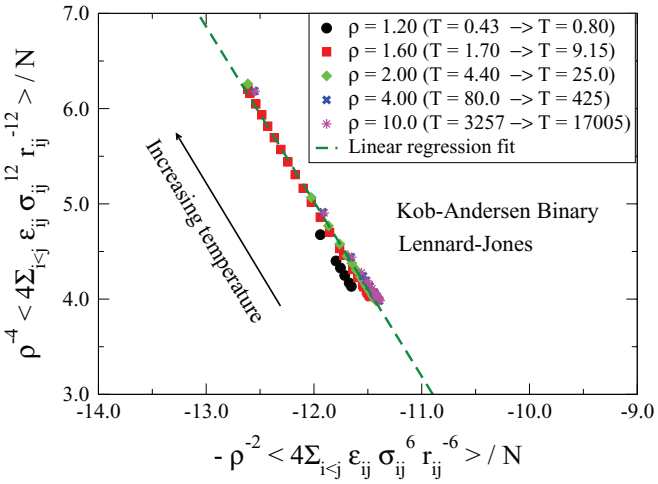

FIG. 1. The thermal average of r^{-12} versus that of $-r^{-6}$ in reduced units for a large range of state points of the Kob-Andersen binary Lennard-Jones liquid simulated with 1000 particles ($\varepsilon_{AA} = \sigma_{AA} = 1$). These quantities correspond to $H_{12}(S)$ and $H_6(S)$ in Eq. (8). The theory predicts that $H'_{12}(S) \propto H'_6(S)$, implying that all data points should fall onto a common line according to $H_{12}(S) = \alpha H_6(S) + \beta$.

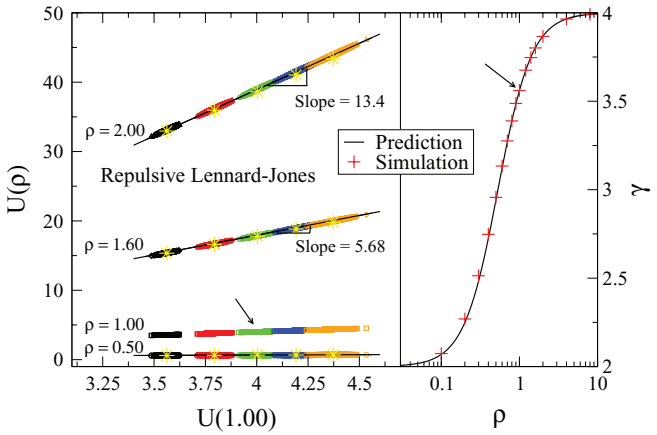

FIG. 2. "Multiple direct isomorph check" applied to simulations of $N = 1000$ particles of the repulsive LJ fluid defined by the pair potential $(r^{-12} + r^{-6})/2$. The left panel shows a scatter plot of the potential energies of pairs of microconfigurations, where the potential energy of a given microconfiguration at density 1.0 is denoted $U(1.00)$ and that of the same microconfiguration scaled to density ρ is denoted $U(\rho)$ ($\rho = 0.5$, 1.6, 2.0). This was done for $T = 0.6$, 0.8, 1.0, 1.2, 1.4. The yellow asterisks mark the average of each scatter plot. The black lines are the predictions (see the text) with slopes determined via Eq. (13) from the fluctuations calculated at the state point $(\rho, T) = (1, 1)$ marked by an arrow. The right panel shows the density-scaling exponent along an isomorph predicted from Eqs. (5) and (13) (full curve) and the exponent calculated at each state point from the fluctuation formula $\gamma = \langle \Delta W \Delta U \rangle / \langle (\Delta U)^2 \rangle$ (Ref. 3) (red crosses). The arrow marks the state point $(\rho, T) = (1, 1)$.

The invariance of the Boltzmann statistical weights of scaled microconfigurations implies that an isomorph cannot cross the liquid-solid coexistence curve. In particular, the coexistence curve is itself predicted to be an isomorph,[3] which was recently confirmed by simulations of generalized LJ liquids.[4,17] Consequently, the coexistence line is given by Eq. (12). This validates a recent conjecture of Khrapak and Morfill.[18]

Predictions for the repulsive Lennard-Jones fluid: As a final illustration we consider the "repulsive" single-component LJ fluid defined by the pair potential $v(r) = (r^{-12} + r^{-6})/2$, a system with *WU* correlation coefficient above 99.9% in its entire phase diagram. At low densities ($\rho \ll 1$) the repulsive LJ fluid behaves as an r^{-6} fluid, whereas it for $\rho \gg 1$ is effectively an r^{-12} fluid. Thus, the density-scaling exponent $\gamma(\rho)$ varies from 2 to 4 as density increases, a much larger variation than that of previously studied strongly correlating systems.

Since $h(\rho)$ is only defined within an overall multiplicative constant, one can write for the repulsive LJ fluid $h(\rho) = \alpha\rho^4 + (1-\alpha)\rho^2$. This leads via Eq. (5) to $\gamma_0 = 2 + 2\alpha$, where γ_0 is the density-scaling exponent at reference density unity, implying that

$$h(\rho) = (\gamma_0/2 - 1)\rho^4 + (2 - \gamma_0/2)\rho^2 . \quad (13)$$

Our simulations identified from the expression $\gamma_0 = \langle \Delta W \Delta U \rangle / \langle (\Delta U)^2 \rangle$ (Ref. 3) the exponent $\gamma_0 = 3.56$ at the state point $(\rho, T) = (1, 1)$. Equation (13) with $\gamma_0 = 3.56$ was tested in two different ways. First, we compared at each state point along an isomorph the exponent $\gamma(\rho)$ predicted from Eqs. (5) and (13) with that calculated from the fluctuations via $\gamma = \langle \Delta W \Delta U \rangle / \langle (\Delta U)^2 \rangle$ (right panel of Fig. 2). The left panel presents a second test of Eq. (13) by showing results from simulating five temperatures at $\rho = 1$, plotting for each temperature instantaneous values of the potential energy versus the potential energy of the same microconfigurations scaled to three other densities ($\rho = 0.5$, 1.6, 2.0). The theory behind the observed straight lines is the following. Consider two isomorphic state points (ρ_0, T_0) and (ρ, T) and suppose each temperature is changed a little, keeping both densities constant. If the two new state points are also isomorphic, the entropy change is the same for both: $dU_0/T_0 = dU/T$. This implies $dU/dU_0 = T/T_0$, i.e., $(\partial U/\partial U_0)_{\rho_0,\rho} = T/T_0$. Since $h(\rho)/T$ is constant along an isomorph, this implies $(\partial U/\partial U_0)_{\rho_0,\rho} = h(\rho)/h(\rho_0)$. Integrating this at constant ρ_0 and ρ leads to $U = [h(\rho)/h(\rho_0)]U_0 + \phi(\rho_0, \rho)$. In our case of reference density unity $\rho_0 = 1$ and $h(\rho_0) = 1$. Thus, plotting U versus U_0 is predicted to result in straight lines with slope $h(\rho)$ (yellow asterisks in the left panel of Fig. 2). The scaled state points are isomorphic to the original $\rho = 1$ state points, with temperatures given by $T = T_0 h(\rho)$. Via the "direct isomorph check"[3] this implies that the scaled microconfigurations form elongated ovals also with slope $h(\rho)$.

In summary, we have shown that for strongly correlating liquids or solids, temperature separates into a function of entropy times a function of density. For these systems the energy scale is consequently determined by density alone. It is an open question whether, conversely, the thermodynamic separation identity equation (2) implies that the system in question is strongly correlating. We anticipate that this is the case, at least for realistic potentials.

The centre for viscous liquid dynamics "Glass and Time" is sponsored by the Danish National Research Foundation (DNRF).

[1]N. P. Bailey, U. R. Pedersen, N. Gnan, T. B. Schrøder, and J. C. Dyre, J. Chem. Phys. **128**, 184507 (2008); N. P. Bailey, U. R. Pedersen, N. Gnan, T. B. Schrøder, and J. C. Dyre, *ibid.* **129**, 184508 (2008); T. B. Schrøder,

N. P. Bailey, U. R. Pedersen, N. Gnan, and J. C. Dyre, *ibid.* **131**, 234503 (2009).
[2]U. R. Pedersen, N. P. Bailey, T. B. Schrøder, and J. C. Dyre, Phys. Rev. Lett. **100**, 015701 (2008); N. Gnan, C. Maggi, T. B. Schrøder, and J. C. Dyre, *ibid.* **104**, 125902 (2010); U. R. Pedersen, T. B. Schrøder, and J. C. Dyre, *ibid.* **105**, 157801 (2010).
[3]N. Gnan, T. B. Schrøder, U. R. Pedersen, N. P. Bailey, and J. C. Dyre, J. Chem. Phys. **131**, 234504 (2009).
[4]T. B. Schrøder, N. Gnan, U. R. Pedersen, N. P. Bailey, and J. C. Dyre, J. Chem. Phys. **134**, 164505 (2011).
[5]U. R. Pedersen, N. Gnan, N. P. Bailey, T. B. Schrøder, and J. C. Dyre, J. Non-Cryst. Solids **357**, 320 (2011).
[6]D. Gundermann, U. R. Pedersen, T. Hecksher, N. P. Bailey, B. Jakobsen, T. Christensen, N. B. Olsen, T. B. Schrøder, D. Fragiadakis, R. Casalini, C. M. Roland, J. C. Dyre, and K. Niss, Nat. Phys. **7**, 816 (2011).
[7]T. S. Ingebrigtsen, T. B. Schrøder, and J. C. Dyre, e-print arXiv:1111.3557 (2011).
[8]O. Hirschfelder, C. F. Curtiss, and R. B. Bird, *Molecular Theory of Gases and Liquids* (Wiley, New York, 1954); J. P. Boon and S. Yip, *Molecular Hydrodynamics* (McGraw-Hill, New York, 1980); J. S. Rowlinson and B. Widom, *Molecular Theory of Capillarity* (Clarendon, Oxford, 1982); M. P. Allen and D. J. Tildesley, *Computer Simulation of Liquids* (Oxford Science Publications, Oxford, 1987); D. Chandler, *Introduction to Modern Statistical Mechanics* (Oxford University Press, New York, 1987); P. G. Debenedetti, *Metastable Liquids: Concepts and Principles* (Princeton University, Princeton, NJ, 1996); N. H. March and M. P. Tosi, *Introduction to Liquid State Physics* (World Scientific, Singapore, 2002); J.-L. Barrat and J.-P. Hansen, *Basic Concepts for Simple and Complex Liquids* (Cambridge University Press, Cambridge, England, 2003); J.-P. Hansen and J. R. McDonald, *Theory of Simple Liquids*, 3rd ed. (Academic, New York, 2005).
[9]O. Klein, Medd. Vetenskapsakad. Nobelinst. **5**, 1 (1919); T. H. Berlin and E. W. Montroll, J. Chem. Phys. **20**, 75 (1952); W. G. Hoover, M. Ross, K. W. Johnson, D. Henderson, J. A. Barker, and B. C. Brown, *ibid.* **52**, 4931 (1970); W. G. Hoover, S. G. Gray, and K. W. Johnson, *ibid.* **55**, 1128 (1971); Y. Hiwatari, H. Matsuda, T. Ogawa, N. Ogita, and A. Ueda, Prog. Theor. Phys. **52**, 1105 (1974); D. M. Heyes and A. C. Branka, J. Chem. Phys. **122**, 234504 (2005); A. C. Branka and D. M. Heyes, Phys. Rev. E **74**, 031202 (2006).
[10]C. Alba-Simionesco, D. Kivelson, and G. Tarjus, J. Chem. Phys. **116**, 5033 (2002); C. Dreyfuss, A. Aouadi, J. Gapinski, M. Matos-Lopes, W. Steffen, A. Patkowski, and R. M. Pick, Phys. Rev. E **68**, 011204 (2003); C. Alba-Simionesco, A. Cailliaux, A. Alegria, and G. Tarjus, Europhys. Lett. **68**, 58 (2004); R. Casalini and C. M. Roland, Phys. Rev. E **69**, 062501 (2004).
[11]C. M. Roland, S. Hensel-Bielowka, M. Paluch, and R. Casalini, Rep. Prog. Phys. **68**, 1405 (2005); G. Floudas, M. Paluch, A. Grzybowski, and K. L. Ngai, *Molecular Dynamics of Glass-Forming Systems: Effects of Pressure* (Springer, New York, 2010); D. Fragiadakis and C. M. Roland, J. Chem. Phys. **134**, 044504 (2011).
[12]L. Bøhling, T. S. Ingebrigtsen, A. Grzybowski, M. Paluch, J. C. Dyre, and T. B. Schrøder, e-print arXiv:1112.1602 (2011).
[13]M. Born and K. Huang, *Dynamical Theory of Crystal Lattices* (Oxford University Press, Oxford, U.K., 1954); M. Ross and D. A. Young, Annu. Rev. Phys. Chem. **44**, 61 (1993); L. Burakovsky and D. L. Preston, J. Phys. Chem. Solids **65**, 1581 (2004).
[14]R. Casalini, U. Mohanty, and C. M. Roland, J. Chem. Phys. **125**, 014505 (2006).
[15]Y. Rosenfeld, Phys. Rev. A **26**, 3633 (1982).
[16]W. Kob and H. C. Andersen, Phys. Rev. Lett. **73**, 1376 (1994).
[17]A. Ahmed and R. J. Sadus, J. Chem. Phys. **131**, 174504 (2009).
[18]S. A. Khrapak and G. E. Morfill, J. Chem. Phys. **134**, 094108 (2011).

New Journal of Physics
The open access journal for physics

Scaling of viscous dynamics in simple liquids: theory, simulation and experiment

L Bøhling[1], T S Ingebrigtsen[1], A Grzybowski[2], M Paluch[2], J C Dyre[1] and T B Schrøder[1,3]

[1] DNRF Centre 'Glass and Time', IMFUFA, Department of Sciences, Roskilde University, Post Box 260, DK-4000 Roskilde, Denmark
[2] Institute of Physics, University of Silesia, ul. Uniwersytecka 4, 40-007 Katowice, Poland
E-mail: tbs@ruc.dk

New Journal of Physics **14** (2012) 113035 (12pp)
Received 11 April 2012
Published 26 November 2012
Online at http://www.njp.org/
doi:10.1088/1367-2630/14/11/113035

Abstract. Supercooled liquids are characterized by relaxation times that increase dramatically by cooling or compression. From a single assumption follows a scaling law according to which the relaxation time is a function of $h(\rho)$ over temperature, where ρ is the density and the function $h(\rho)$ depends on the liquid in question. This scaling is demonstrated to work well for simulations of the Kob–Andersen binary Lennard-Jones mixture and two molecular models, as well as for the experimental results for two van der Waals liquids, dibutyl phthalate and decahydroisoquinoline. The often used power-law density scaling, $h(\rho) \propto \rho^{\gamma}$, is an approximation to the more general form of scaling discussed here. A thermodynamic derivation was previously given for an explicit expression for $h(\rho)$ for liquids of particles interacting via the generalized Lennard-Jones potential. Here a statistical mechanics derivation is given, and the prediction is shown to agree very well with simulations over large density changes. Our findings effectively reduce the problem of understanding the viscous slowing down from being a quest for a function of two variables to a search for a single-variable function.

[3] Author to whom any correspondence should be addressed.

The relaxation time of a supercooled liquid increases markedly upon cooling, in some cases by a factor of 10 or more when the temperature decreases by just 1% [1–11]. This phenomenon lies behind glass formation, which the takes place when a liquid upon cooling is no longer able to equilibrate on laboratory time scales due to its extremely long relaxation time. It has long been known that increasing the pressure at constant temperature increases the relaxation time in much the same way as does cooling at ambient pressure. Only during the last decade, however, have large amounts of data become available on how the relaxation time varies with temperature and density. Following pioneering works by Tölle [12], it was demonstrated by Dreyfus *et al* [13], Alba-Simionesco *et al* [14] as well as Casalini and Roland [15] that for many liquids and polymers the relaxation time is a function of a single variable. Roland *et al* [16] reviewed the field and demonstrated that for a large number of molecular liquids and polymers the relaxation time to a good approximation is a function of ρ^γ/T, where γ is an empirical material-dependent parameter. For recent works on this 'power-law density scaling', or 'thermodynamic scaling', see, e.g., [17–20]. The consensus is now that van der Waals liquids and most polymers conform to the scaling, whereas hydrogen-bonding liquids disobey it.

A standard model in simulation studies of viscous liquids is the Kob–Andersen binary Lennard-Jones (KABLJ) mixture [21], which can be cooled to a highly viscous state and only crystallizes for extraordinarily long simulations [22]. The system consists of 80% large Lennard-Jones (LJ) particles (A) interacting strongly with 20% smaller LJ particles (B). The KABLJ mixture was shown by Coslovich and Roland [23] to obey power-law density scaling to a good approximation with $\gamma = 5.1$ for the density range $\rho \equiv N/V = 1.15$ to $\rho = 1.35$, whereas Pedersen *et al* [24] used the slightly different value $\gamma = 5.16$ to scale the density range 1.1–1.4. Figure 1 demonstrates, however, that power-law density scaling breaks down when considering a larger density range. Relaxation time data for the isochores $\rho = 1.2$ and 1.6 collapse very well using $\gamma = 4.90$, whereas the isochores $\rho = 1.6$ and 2.0 collapse using $\gamma = 4.45$; in both cases the third isochore deviates significantly. In the following, we show that power-law density scaling is an approximation to a more general form of scaling, which is derived from the theory of isomorphs [25, 26]. We further show that given that the two lowest densities of figure 1 obey power-law density scaling with $\gamma = 4.90$, the isomorph theory predicts that the two highest densities scale with $\gamma = 4.45$, as indeed seen in figure 1.

What causes power-law density scaling and its breakdown for large density variations? A justification of density scaling may be given by reference to inverse power-law (IPL) potentials ($\propto r^{-n}$), where r is the distance between particles. For such unrealistic, purely repulsive systems, density scaling is rigorously obeyed with $\gamma = n/3$ [27]. Assuming that power-law density scaling reflects an underlying effective power-law potential, the scaling exponent γ can be found from the NVT equilibrium fluctuations of the potential energy U and the virial $W = pV - NkT$ (IPL potentials have $W = (n/3)U$) as follows:

$$\gamma = \frac{\langle \Delta W \Delta U \rangle}{\langle (\Delta U)^2 \rangle}. \tag{1}$$

This was confirmed for the KABLJ mixture by Coslovich and Roland [23] and Pedersen *et al* [24]. Pedersen *et al* [24] further supported this 'hidden scale invariance' explanation by demonstrating that for the investigated density range the dynamics and structure of the KABLJ mixture are accurately reproduced by an IPL mixture with exponent chosen in accordance with equation (1).

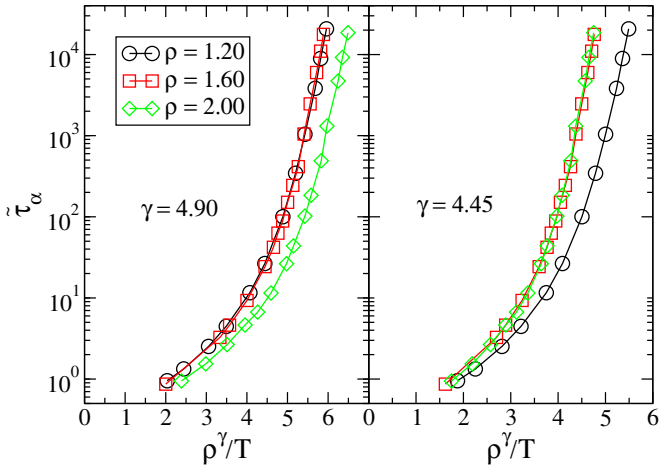

Figure 1. Breakdown of power-law density scaling for the reduced structural relaxation time $\tilde{\tau}_\alpha$ in the KABLJ mixture, $\tilde{\tau}_\alpha \equiv \rho^{1/3}(k_B T/m)^{1/2}\tau_\alpha$, where τ_α is the time at which the self-intermediate scattering function ($F_s(q,t)$, $q = 7.25(\rho/1.2)^{1/3}$) for the A particles has decayed to $1/e$. Molecular dynamics (MD) simulations in the NVT ensemble ($N = 1000$) were performed using RUMD, an MD package optimized for state-of-the-art GPU computing (see http://rumd.org). The time step was kept constant in reduced units, $\tilde{h} = 0.0025$. $\tilde{\tau}_\alpha$ is plotted for three isochores as a function of the density-scaling variable ρ^γ/T, where γ is an empirical scaling parameter. Left panel: $\gamma = 4.90$ collapses the data for the two lowest densities. Right panel: $\gamma = 4.45$ collapses the data for the two highest densities. It is not possible to find a single exponent that collapses all the data; even though the two exponents differ by only 10%, power-law scaling with a single exponent clearly fails.

The hidden scale invariance is not just a feature of the KABLJ mixture but of 'strongly correlating liquids' in general [28–31]. These are defined by having strong correlations between equilibrium NVT fluctuations of the potential energy and the virial (correlation coefficients larger than 0.9). Also molecular models can be strongly correlating; examples include the Lewis–Wahnstrom model of ortho-terphenyl and an asymmetric dumbell model. Both models are strongly correlating and obey power-law density scaling with exponents consistent with equation (1) for density increases of 8 and 16%, respectively [32]. Very recently, Gundermann *et al* [20] investigated the van der Waals liquid tetramethyl-tetraphenyl-trisiloxane, and gave the first experimental confirmation of the relation between the power-law density scaling exponent and equation (1).

For any potential that is *not* an IPL the exponent γ as calculated from equation (1) depends on the state point. Power-law density scaling corresponds to disregarding this state-point dependence. It is thus not surprising that power-law density scaling breaks down when large density changes are involved, but interestingly a more fundamental and robust form of scaling can be derived [33]. In the following, we proceed to derive the new scaling by a different route than used in [33].

Strongly correlating liquids have 'isomorphs' in their phase diagram, which are curves along which the structure and dynamics in reduced units are invariant to a good approximation [25, 26]. The invariance of structure implies invariance of the configurational ('excess') entropy, $S_{\rm ex}$; thus the isomorphs are the configurational adiabats. Gnan *et al* [25] discussed in detail the consequences of a liquid having isomorphs and also showed that a liquid is strongly correlating if and only if it has isomorphs to a good approximation. The precise definition of an isomorph [25] is that this is an equivalence class of state points, where two state points are termed equivalent ('isomorphic') if all pairs of physically relevant micro-configurations of the two state points, which trivially scale into one another, have proportional configurational Boltzmann's factors. From this single assumption several predictions can be derived, including isomorph invariance of structure and dynamics in reduced units and that jumps between isomorphic state points take the system instantaneously to equilibrium [25].

Letting $\mathbf{R}$ denote a micro-configuration (all particle coordinates) of a reference state point (ρ_*, T_*), the condition for state point (ρ, T) to be isomorphic with (ρ_*, T_*), i.e. the proportionality of pairs of Boltzmann's factors can, by taking the logarithm and rearranging, be expressed as

$$U\left(\tilde{\rho}^{-\frac{1}{3}}\mathbf{R}\right) = \frac{T}{T_*}U\left(\mathbf{R}\right) + K, \quad \tilde{\rho} \equiv \rho/\rho_*, \tag{2}$$

where K is a constant that only depends on the two state points. Equation (2) is the basis of the so-called *direct isomorph check* [25]: (a) draw micro-configurations $\mathbf{R}$ from a simulation at (ρ_*, T_*), (b) evaluate the potential energies of these configurations scaled to density ρ, and plot them in a scatter plot against the potential energies at ρ_*. If a state point (ρ, T) exists that to a good approximation is isomorphic with (ρ_*, T_*), this scatter plot will be close to a straight line and the new temperature T is determined as T_* multiplied by the slope.

In the following, we consider systems where the interaction potential between particles i and j is given by a sum of IPLs:

$$\phi_{ij}(r_{ij}) = \sum_n \epsilon_{n,ij}\left(\frac{\sigma}{r_{ij}}\right)^n. \tag{3}$$

This includes the standard 12-6 LJ potential, but also, e.g., potentials with more than two power-law terms. We note that some systems interacting via equation (3) will *not* be strongly correlating and thus not have good isomorphs. In the following, properties are derived for those systems that *do* have good isomorphs.

The total potential energy of a given micro-configuration $\mathbf{R}$ at density ρ_* is a sum over contributions from the power-law terms, $U = \sum_n U_n$. When scaling $\mathbf{R}$ to the density ρ, keeping the structure invariant in reduced units, each power-law term is scaled by $\tilde{\rho}^{\frac{n}{3}} = (\rho/\rho_*)^{n/3}$, and the potential energy at the new density $U' = U(\tilde{\rho}^{-1/3}\mathbf{R})$ is [26]

$$U' = \sum_n \tilde{\rho}^{\frac{n}{3}} U_n. \tag{4}$$

Thus, the linear regression slope of the U', U-scatter plot in the direct isomorph check is given by (where all averages refer to the reference state point (ρ_*, T_*))

$$\frac{\langle \Delta U' \Delta U\rangle}{\langle (\Delta U)^2\rangle} = \sum_n \tilde{\rho}^{\frac{n}{3}} \frac{\langle \Delta U_n \Delta U\rangle}{\langle (\Delta U)^2\rangle}. \tag{5}$$

Using Einstein's fluctuation formula for the excess isochoric heat capacity and the corresponding formula for the 'partial' heat capacities (which can be negative),

$$C_{v,n}^{\mathrm{ex}} \equiv \left(\frac{\partial \langle U_n \rangle}{\partial T}\right)_V = \frac{\langle \Delta U_n \Delta U \rangle}{k_{\mathrm{B}} T_*^2}, \tag{6}$$

we obtain an expression for the new temperature T relative to the reference temperature T_* (compare equation (2)):

$$\frac{T}{T_*} = \frac{\langle \Delta U' \Delta U \rangle}{\langle (\Delta U)^2 \rangle} = \sum_n \tilde{\rho}^{\frac{n}{3}} \frac{C_{v,n}^{\mathrm{ex}}}{C_v^{\mathrm{ex}}} \equiv h(\tilde{\rho}). \tag{7}$$

Since $C_v^{\mathrm{ex}} = \sum_n C_{v,n}^{\mathrm{ex}}$ the number of parameters in the scaling function $h(\tilde{\rho})$ is one less than the number of terms in the potential (equation (3)). In particular, for the standard 12-6 LJ potential, $h(\tilde{\rho})$ contains just a single parameter:

$$h(\tilde{\rho}) = \tilde{\rho}^4 c + \tilde{\rho}^2 (1-c), \quad c \equiv C_{v,12}^{\mathrm{ex}}/C_v^{\mathrm{ex}}. \tag{8}$$

Using that $U_{12} = W/2 - U$ for 12-6 LJ systems [26], $h(\tilde{\rho})$ can be conveniently expressed in terms of γ_* defined as equation (1) evaluated at the reference density ρ_*:

$$h(\tilde{\rho}) = \tilde{\rho}^4 (\gamma_*/2 - 1) - \tilde{\rho}^2 (\gamma_*/2 - 2). \tag{9}$$

Equation (7) provides a convenient method for numerically tracing out an isomorph—previously this could only be done by changing density by a small amount, e.g. 1%, and then adjusting temperature to keep the excess entropy constant, using that γ (equation (1)) can also be expressed as [25]

$$\gamma = \left(\frac{\partial \ln T}{\partial \ln \rho}\right)_{S_{\mathrm{ex}}}. \tag{10}$$

It is a prediction of the isomorph theory that γ depends only on density [25, 26]. This means that the same differential equation, equation (10), determines the temperature on all isomorphs, implying that $h(\tilde{\rho})$ is the same for all isomorphs—what changes between different isomorphs is T_*. Thus $h(\tilde{\rho})/T$ is an isomorph invariant (compare equation (7)), which can be used as a scaling variable for the reduced relaxation time $\tilde{\tau}$ that is also an isomorph invariant [25] $\tilde{\tau} = f(h(\tilde{\rho})/T)$. This form of scaling was first proposed by Alba-Simionesco *et al* [14]. Here a theoretical derivation has been provided, as well as an explicit expression for $h(\tilde{\rho})$ for systems interacting via generalized LJ potentials (equation (3)).

What is the difference between the derivation presented here and the derivation presented in [33]? The derivation in [33] is thermodynamic in nature—from the invariance of excess entropy and heat capacity along the same curves in the phase diagram (the isomorphs) follows directly the general form of the scaling $h(\tilde{\rho})/T = \mathrm{const}$. In contrast, the derivation presented here is statistical-mechanical in nature—from the direct isomorph check (equation (2)) and the invariance of structure on isomorphs follows directly the specific form of the scaling for generalized LJ systems (equation (7)).

From the scaling $\tilde{\tau} = f(h(\tilde{\rho})/T)$ it follows that power-law density scaling *is* obeyed when considering only *pairs* of isochores: choosing one of the densities as the reference density, γ is uniquely determined so that $\tilde{\rho}^\gamma = h(\tilde{\rho})$ where $\tilde{\rho}$ is the other density divided by the reference density. Since the power law is then equal to $h(\tilde{\rho})$ at the two densities involved ($h(\tilde{\rho}=1)=1$, see equation (7)), it follows that the two isochores obey power-law density scaling with the exponent γ. This is indeed what is seen in figure 1. Choosing $\rho_* = 1.6$ as the reference density,

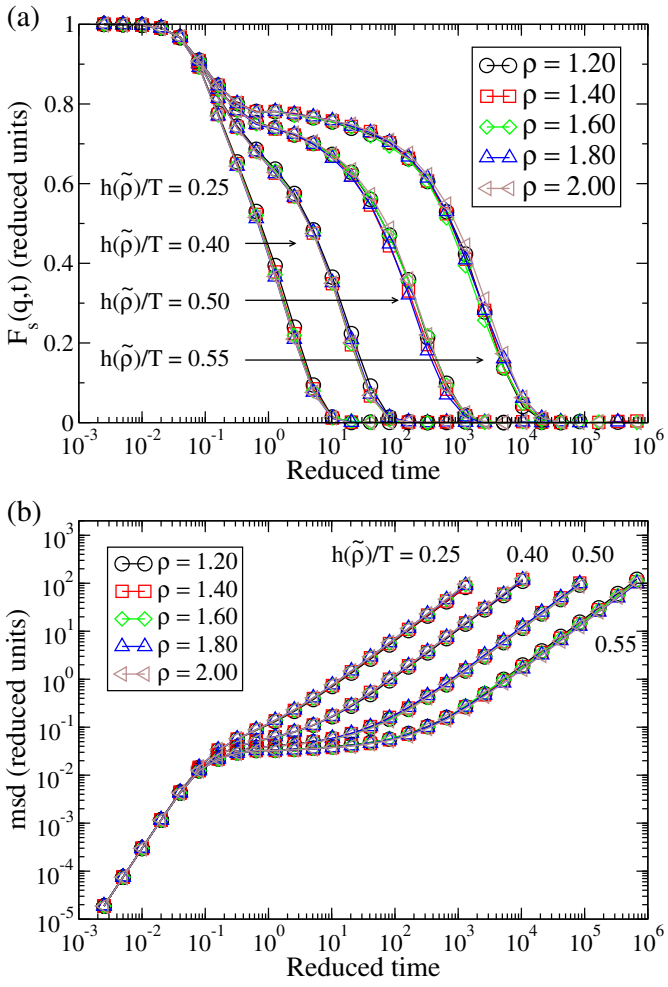

Figure 2. Four different isomorphs in the KABLJ mixture, each generated from the condition $h(\tilde{\rho})/T = \text{const}$. Densities range from 1.2 to 2.0, and $h(\tilde{\rho}) = \tilde{\rho}^4\,(\gamma_*/2-1) - \tilde{\rho}^2\,(\gamma_*/2-2)$ (equation (9)) with $\gamma_* = 4.59$ determined from the scaling in figure 1, see text ($\tilde{\rho} \equiv \rho/\rho_*$, $\rho_* = 1.6$). (a) Self part of intermediate scattering functions in reduced units. (b) Mean-square displacements in reduced units. The data collapse confirms that true isomorphs have been identified.

the scaling in the left panel of figure 1 corresponds to $h(1.2/1.6) = (1.2/1.6)^{4.90}$ which via equation (9) leads to $\gamma_* = 4.59$. Using this value we find that $h(2.0/1.6) = 2.70 = (2.0/1.6)^{4.45}$. Thus from one power-law scaling exponent in figure 1, the other is uniquely predicted. Moreover, the value $\gamma_* = 4.59$ is consistent with what is found by evaluating equation (1) at the reference isochore $\rho_* = 1.6$ in the temperature range $T = 1.7$–5, which leads to values of γ_* decreasing from 4.6 to 4.5. In the following figures reporting the results for the KABLJ mixture, we use $\gamma_* = 4.59$ as estimated from the left panel of figure 1, i.e. no further fitting or adjustment of parameters was applied.

As mentioned, the scaling function $h(\tilde{\rho})$ was derived *assuming* that good isomorphs exist. In figure 2 we test this for the KABLJ mixture using the most sensitive isomorph invariant—the

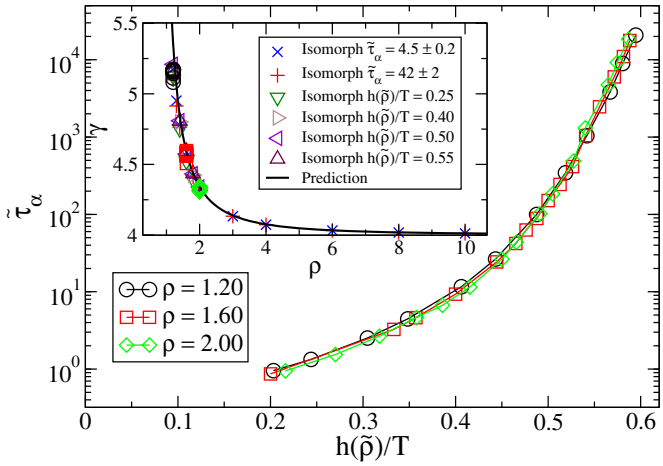

Figure 3. Reduced relaxation times for the KABLJ mixture scaled according to the isomorph theory (same data as in figure 1). The scaling function $h(\tilde{\rho})$ is the same as in figure 2 (equation (9), $\gamma_* = 4.59$). Inset: comparing γ computed from simulations (equation (1)) to the prediction of the isomorph theory, $\gamma = \mathrm{d}\ln h/\mathrm{d}\ln\rho$ (black curve). Isomorphs denoted by a reduced relaxation time are each generated from a single reference point using equations (7) and (9), with '$\pm$' quantifying the resulting variation of the reduced relaxation time on the isomorph. Isochores are plotted with the same symbols as in the main figure.

dynamics of viscous states. State points with the same $h(\tilde{\rho})/T$, predicted to be on the same isomorph, are seen to have very similar dynamics even though the density varies from 1.2 to 2.0.

Figure 3 tests the proposed scaling for the KABLJ mixture using the data of figure 1. Clearly, the new form of scaling works well. Combining equation (10) with the definition of $h(\tilde{\rho})$ (equation (7)) shows that γ is the logarithmic derivative of $h(\tilde{\rho})$, $\gamma = \mathrm{d}\ln h/\mathrm{d}\ln\rho$. The inset of figure 3 demonstrates that this prediction agrees well with simulations even when going to large densities (where the purely repulsive r^{-12} limit is approached).

We now turn briefly to molecular models. In this case it is still a prediction of the isomorph theory that an expression of the form $h(\tilde{\rho})/T$ is the right scaling variable [33], but we do not have an explicit expression for $h(\tilde{\rho})$. Figure 4 demonstrates how power-law density scaling breaks down for the Lewis–Wahnstrom model of ortho-terphenyl and an asymmetric dumbell model when considering larger density changes than previously studied [32]. Like in figure 1, power-law scaling works when considering pairs of isochores, consistent with the right scaling variable being of the form $h(\tilde{\rho})/T$. The insets of figure 4 test the isomorph prediction that γ to a good approximation is a function of density only, the assumption used to derive the new scaling. The prediction agrees well with simulations: γ is found to be much more dependent on density than on temperature. For more results on isomorphs in these model molecular liquids, see [34].

Finally, we present in figure 5 a new analysis of experimental data for the two van der Waals liquids dibutyl phthalate (DBP) and decahydroisoquinoline (DHIQ), using larger density increases than usually studied in scaling experiments (20 and 18%, respectively). For DBP, dielectric relaxation times were taken from [35], and densities were calculated from the Tait

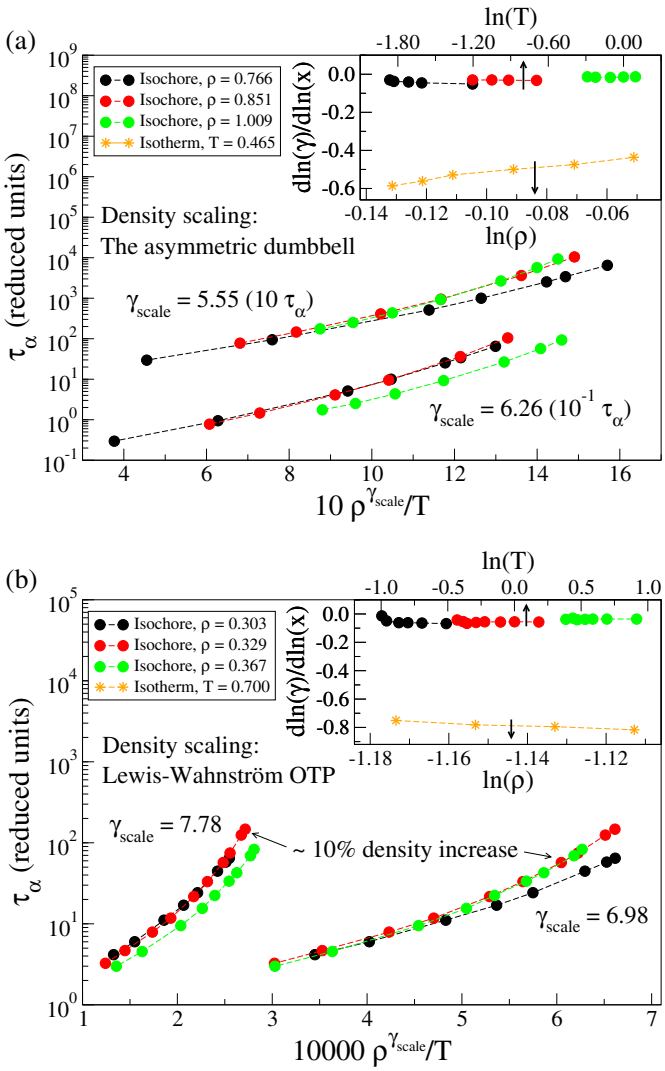

Figure 4. Breakdown of power-law density scaling in two molecular models. In accordance with the scaling derived in the present work, power-law scaling *does* work when considering only pairs of isochores. (a) The asymmetric dumbbell model. (b) The Lewis–Wahnstrom model of ortho-terphenyl (OTP). Insets: $(\partial \ln \gamma / \partial \ln T)_\rho$ plotted against $\ln T$ (circles) and $(\partial \ln \gamma / \partial \ln \rho)_T$ plotted against $\ln \rho$ (stars). Consistent with the isomorph theory, γ is found to be much more dependent on density than on temperature.

equation of state [36] fitted to PVT data from Bridgman [37]. For DHIQ, dielectric relaxation times were taken from [38], and the Tait equation of state with parameters estimated by Casalini *et al* [39] was used to calculate densities. We find that the isochronal dependences $\log_{10} T$ versus $\log_{10} \rho$ determined at given structural relaxation times in reduced units, $\tilde{\tau} = \tau v_m^{-1/3} (k_B T/m)^{1/2}$, where v_m and m are the molecular volume and mass, are nonlinear (figures 5(b) and (e)). This implies breakdown of power-law density scaling. The isochrones can be superposed after

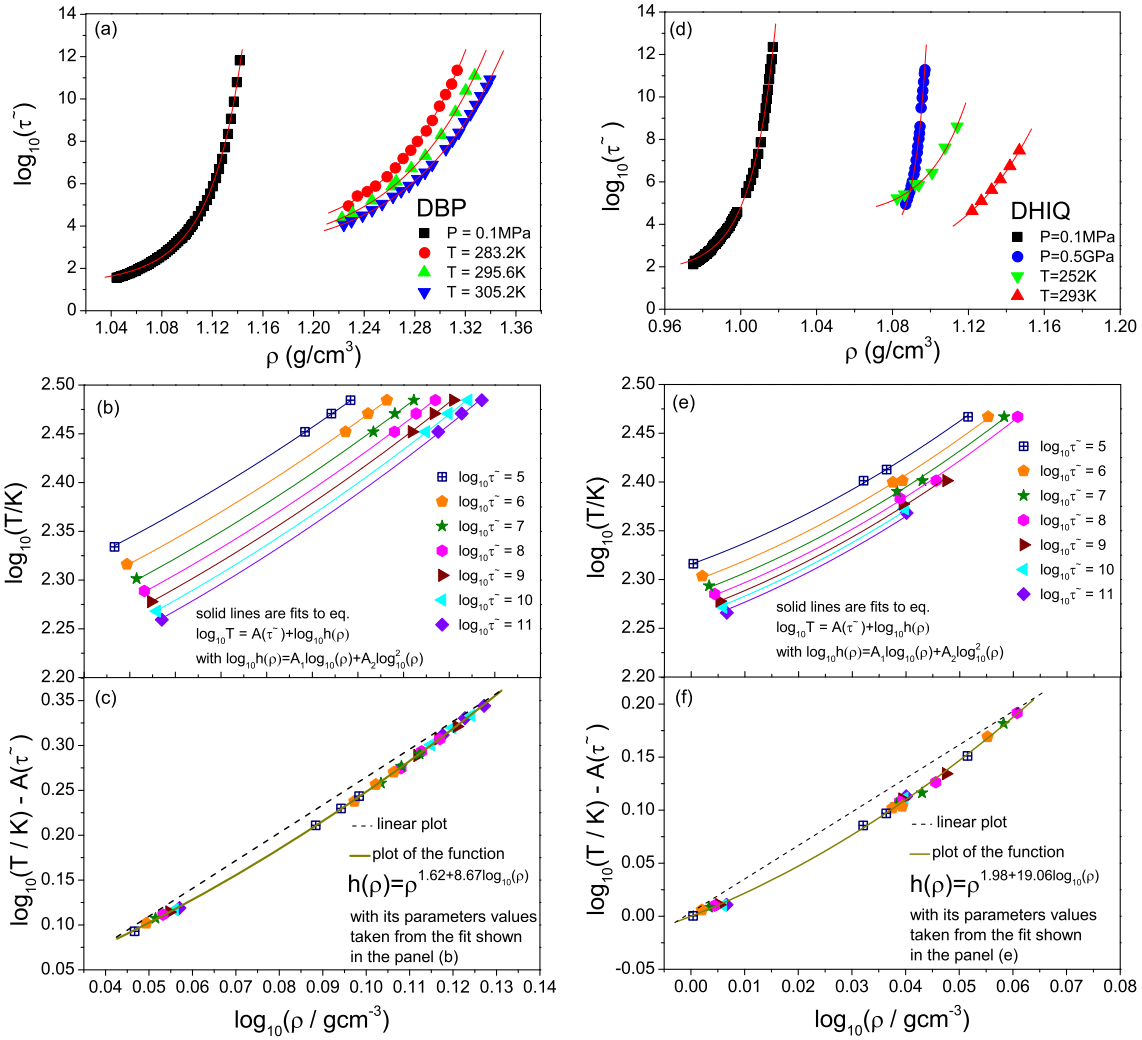

Figure 5. Deviation from power-law scaling in DBP ((a)–(c)) and DHIQ ((d)–(f)). (a) and (d) Density dependence of isobaric and isothermal structural relaxation times $\tilde{\tau}$ in reduced units. Solid lines represent separate fits to the modified Avramov model [40]. (b) and (e) The isochronal dependences $\log_{10} T$ versus $\log_{10} \rho$ determined at a given $\tilde{\tau}$. Fits are done to all isochrones simultaneously. (c) and (f) The isochrones vertically shifted by the fitted values $A(\tilde{\tau})$. Deviations from power-law scaling (straight dashed lines) are evident. The fitted $h(\rho)$'s correspond to γ values increasing from 2.6 to 3.9 (DBP) and from 2.0 to 4.3 (DHIQ).

vertical shifting, however (figures 5(c) and (f)), which implies that a scaling variable exists of the form $h(\rho)/T$. The isochrones can be described by a phenomenological form of the scaling function $\log_{10}(h)(\rho) = A_1 \log_{10} \rho + A_2 \log_{10}^2 \rho$, chosen here simply to take into account the curvature. Our results for DBP are consistent with those reported by Niss *et al* [41]. We conclude that for DBP and DHIQ, power-law density scaling breaks down at large density variations in the way predicted by the isomorph theory. Interestingly, the density dependence

of γ is stronger than for the model systems and in the opposite direction; for the experimental systems γ *increases* with density.

What are the perspectives of our findings? Based on the theory of isomorphs in dense liquids we have now a form of density scaling that is more fundamental and more robust than power-law density scaling and which is consistent with both simulations and experiments. This 'isomorph scaling'—in its mathematical form originally proposed by Alba-Simionesco *et al* [14]—is predicted to apply for all strongly correlating liquids, i.e. van der Waals and metallic liquids, but not, e.g., for hydrogen-bonding liquids. Our results should *not* be used to abandon power-law density scaling—it is a useful approximation to isomorph scaling when the scaling function $h(\rho)$ is unknown and only moderate density changes are considered. Under these conditions the isomorph theory predicts that power-law density scaling works with an exponent determined by equation (1). Isomorph scaling provides a deeper understanding of why—and when—power-law density scaling works.

An interesting perspective is to what extent isomorph scaling can be generalized to Brownian dynamics in colloidal or nanoparticle suspensions. A necessary—but not sufficient—condition is that the diffusion coefficient in appropriate reduced units [25] is a single-valued function of excess entropy, since these are both isomorph invariants. This condition rules out, e.g., the Gaussian core, Hertzian and effective star-polymer models [42]. On the other hand, it does leave open the possibility that, e.g., the Yukawa potential used to model charge-stabilized colloidal suspensions and complex (dusty) plasmas has isomorphs, and thus obeys isomorph scaling [43, 44].

Isomorph scaling has important consequences for the most fundamental open question in the field of viscous liquids and glass transition: what controls the dramatic viscous slowing down? In general, this question has to be considered as a search for a physically justified function of *two* variables, temperature and density (or temperature and pressure). Our results imply that this problem is now effectively reduced to a search for a function of a single variable, at least for the class of strongly correlating liquids. This is particularly striking for LJ-type systems such as the KABLJ mixture, where we have a prediction for the scaling function that agrees very well with simulations for much larger density variations than usually considered. The fact that the LJ scaling function contains just a single parameter—i.e. no more parameters than power-law density scaling—confirms that isomorph scaling is more fundamental and not merely a higher-order approximation compared to power-law density scaling. Isomorph scaling must be taken into account in theories of the viscous slowing down: since the relaxation time in reduced units obeys isomorph scaling, any quantity proposed to control the relaxation time must also obey isomorph scaling [25].

Acknowledgments

The Centre for Viscous Liquid Dynamics 'Glass and Time' is sponsored by the Danish National Research Foundation. AG and MP gratefully acknowledge support from the Polish National Science Centre (the project MAESTRO 2).

References

[1] Kauzmann W 1948 *Chem. Rev.* **43** 219
[2] Harrison G 1976 *The Dynamic Properties of Supercooled Liquids* (New York: Academic)

[3] Brawer S 1985 *Relaxation in Viscous Liquids and Glasses* (Columbus, OH: American Ceramic Society)
[4] Gutzow I and Schmelzer J 1995 *The Vitreous State: Thermodynamics, Structure, Rheology and Crystallization* (Berlin: Springer)
[5] Ediger M D, Angell C A and Nagel S R 1996 *J. Phys. Chem.* **100** 13200
[6] Angell C A, Ngai K L, McKenna G B, McMillan P F and Martin S W 2000 *J. Appl. Phys.* **88** 3113
[7] Alba-Simionesco C 2001 *C. R. Acad. Sci., Paris (IV)* **2** 203
[8] Debenedetti P G and Stillinger F H 2001 *Nature* **410** 259
[9] Binder K and Kob W 2005 *Glassy Materials and Disordered Solids: An Introduction to their Statistical Mechanics* (Singapore: World Scientific)
[10] Sciortino F 2005 *J. Stat. Mech.* (2005) P05015
[11] Dyre J C 2006 *Rev. Mod. Phys.* **78** 953
[12] Tölle A 2001 *Rep. Prog. Phys.* **64** 1473
[13] Dreyfus C, Aouadi A, Gapinski J, Matos-Lopes M, Steffen W, Patkowski A and Pick R M 2003 *Phys. Rev.* E **68** 011204
Dreyfus C, Le Grand A, Gapinski J, Steffen W and Patkowski A 2004 *Eur. Phys. J.* B **42** 309–19
[14] Alba-Simionesco C, Kivelson D and Tarjus G 2002 *J. Chem. Phys.* **116** 5033
Tarjus G, Kivelson D, Mossa S and Alba-Simionesco C 2004 *J. Chem. Phys.* **120** 6135
Alba-Simionesco C, Cailliaux A, Alegria A and Tarjus G 2004 *Europhys. Lett.* **68** 58
Alba-Simionesco C and Tarjus G 2006 *J. Non-Cryst. Solids* **352** 4888
[15] Casalini R and Roland C M 2004 *Phys. Rev.* E **69** 062501
Roland C M and Casalini R 2004 *J. Chem. Phys.* **121** 11503
[16] Roland C M, Hensel-Bielowka S, Paluch M and Casalini R 2005 *Rep. Prog. Phys.* **68** 1405
[17] Roland C M 2010 *Macromolecules* **43** 7875
[18] Floudas G, Paluch M, Grzybowski A and Ngai K 2011 *Molecular Dynamics of Glass-Forming Systems: Effects of Pressure* (Berlin: Springer)
[19] Lopez E R, Pensado A S, Comunas M J P, Padua A A H, Fernandez J and Harris K R 2011 *J. Chem. Phys.* **134** 144507
[20] Gundermann D *et al* 2011 *Nature Phys.* **7** 816
[21] Kob W and Andersen H C 1994 *Phys. Rev. Lett.* **73** 1376
[22] Toxvaerd S, Pedersen U R, Schrøder T B and Dyre J C 2009 *J. Chem. Phys.* **130** 224501
[23] Coslovich D and Roland C M 2009 *J. Chem. Phys.* **115** 151103
[24] Pedersen U R, Schrøder T B and Dyre J C 2010 *Phys. Rev. Lett.* **105** 157801
[25] Gnan N, Schrøder T B, Pedersen U R, Bailey N P and Dyre J C 2009 *J. Chem. Phys.* **131** 234504
[26] Schrøder T B, Gnan N, Pedersen U R, Bailey N P and Dyre J C 2011 *J. Chem. Phys.* **134** 164505
[27] Klein O 1919 *Medd. Vetenskapsakad. Nobelinst.* **5** 1
Berlin T H and Montroll E W 1952 *J. Chem. Phys.* **20** 75
Hoover W G, Ross M, Johnson K W, Henderson D, Barker J A and Brown B C 1970 *J. Chem. Phys.* **52** 4931
Hoover W G, Gray S G and Johnson K W 1971 *J. Chem. Phys.* **55** 1128
Hiwatari Y, Matsuda H, Ogawa T, Ogita N and Ueda A 1974 *Prog. Theor. Phys.* **52** 1105
Heyes D M and Branka A C 2005 *J. Chem. Phys.* **122** 234504
Branka A C and Heyes D M 2006 *Phys. Rev.* E **74** 031202
[28] Pedersen U R, Bailey N P, Schrøder T B and Dyre J C 2008 *Phys. Rev. Lett.* **100** 015701
[29] Bailey N P, Pedersen U R, Gnan N, Schrøder T B and Dyre J C 2008 *J. Chem. Phys.* **129** 184507
[30] Bailey N P, Pedersen U R, Gnan N, Schrøder T B and Dyre J C 2008 *J. Chem. Phys.* **129** 184508
[31] Schrøder T B, Bailey N P, Pedersen U R, Gnan N and Dyre J C 2009 *J. Chem. Phys.* **131** 234503
[32] Schrøder T B, Pedersen U R, Bailey N P, Toxvaerd S and Dyre J C 2009 *Phys. Rev.* E **80** 041502
[33] Ingebrigtsen T S, Bøhling L, Schrøder T B and Dyre J C 2012 *J. Chem. Phys.* **136** 061102
[34] Ingebrigtsen T S, Schrøder T B and Dyre J C 2012 *J. Phys. Chem.* B **116** 1018

[35] Paluch M, Roland C M, Pawlus S, Zioło J and Ngai K L 2003 *Phys. Rev. Lett.* **91** 115701
Sekula M, Pawlus S, Hensel-Bielowka S, Ziolo J, Paluch M and Roland C M 2004 *J. Phys. Chem.* B **108** 4997
[36] Tait P G 1888 *Physics and Chemistry of the Voyage of H. M. S. Challenger* vol 2, part 2 (London: HMSO)
[37] Bridgman P W 1932 *Proc. Am. Acad. Arts Sci.* **67** 1
[38] Paluch M, Pawlus S, Hensel-Bielowka S, Kaminska E, Prevosto D, Capaccioli S, Rolla P A and Ngai K L 2005 *J. Chem. Phys.* **122** 234506
[39] Casalini R, McGrath K J and Roland C M 2006 *J. Non-Cryst. Solids* **352** 4905
[40] Casalini R, Mohanty U and Roland C M 2006 *J. Chem. Phys.* **125** 014505
[41] Niss K, Dalle-Ferrier C, Tarjus G and Alba-Simionesco C 2007 *J. Phys.: Condens. Matter* **19** 076102
[42] Pond M K, Errington J R and Truskett T M 2011 *Soft Matter* **7** 9859
[43] Rosenfeld Y 2001 *J. Phys.: Condens. Matter* **13** L39
[45] Khrapak S A, Vaulina O S and Morfill G E 2012 *Phys. Plasma* **19** 034503

What Is a Simple Liquid?

Trond S. Ingebrigtsen, Thomas B. Schrøder, and Jeppe C. Dyre*

DNRF Centre "Glass and Time," IMFUFA, Department of Sciences, Roskilde University, Postbox 260, DK-4000 Roskilde, Denmark

(Received 16 November 2011; published 15 March 2012)

This paper is an attempt to identify the *real essence* of simplicity of liquids in John Locke's understanding of the term. Simple liquids are traditionally defined as many-body systems of classical particles interacting via radially symmetric pair potentials. We suggest that a simple liquid should be defined instead by the property of having strong correlations between virial and potential-energy equilibrium fluctuations in the *NVT* ensemble. There is considerable overlap between the two definitions, but also some notable differences. For instance, in the new definition simplicity is not a direct property of the intermolecular potential because a liquid is usually only strongly correlating in part of its phase diagram. Moreover, not all simple liquids are atomic (i.e., with radially symmetric pair potentials) and not all atomic liquids are simple. The main part of the paper motivates the new definition of liquid simplicity by presenting evidence that a liquid is strongly correlating if and only if its intermolecular interactions may be ignored beyond the first coordination shell (FCS). This is demonstrated by *NVT* simulations of the structure and dynamics of several atomic and three molecular model liquids with a shifted-forces cutoff placed at the first minimum of the radial distribution function. The liquids studied are inverse power-law systems (r^{-n} pair potentials with $n = 18, 6, 4$), Lennard-Jones (LJ) models (the standard LJ model, two generalized Kob-Andersen binary LJ mixtures, and the Wahnstrom binary LJ mixture), the Buckingham model, the Dzugutov model, the LJ Gaussian model, the Gaussian core model, the Hansen-McDonald molten salt model, the Lewis-Wahnstrom ortho-terphenyl model, the asymmetric dumbbell model, and the single-point charge water model. The final part of the paper summarizes properties of strongly correlating liquids, emphasizing that these are simpler than liquids in general. Simple liquids, as defined here, may be characterized in three quite different ways: (1) *chemically* by the fact that the liquid's properties are fully determined by interactions from the molecules within the FCS, (2) *physically* by the fact that there are isomorphs in the phase diagram, i.e., curves along which several properties like excess entropy, structure, and dynamics, are invariant in reduced units, and (3) *mathematically* by the fact that throughout the phase diagram the reduced-coordinate constant-potential-energy hypersurfaces define a one-parameter family of compact Riemannian manifolds. No proof is given that the chemical characterization follows from the strong correlation property, but we show that this FCS characterization is consistent with the existence of isomorphs in strongly correlating liquids' phase diagram. Finally, we note that the FCS characterization of simple liquids calls into question the physical basis of standard perturbation theory, according to which the repulsive and attractive forces play fundamentally different roles for the physics of liquids.

DOI: 10.1103/PhysRevX.2.011011 Subject Areas: Chemical Physics, Condensed Matter Physics, Statistical Physics

I. INTRODUCTION

Going back to Plato, classification or categorization is the epistemological process that groups objects based on similar properties [1]. Having primarily biological examples in mind, Aristotle defined categories as discrete entities characterized by properties shared by their members [2]. Aristotle, and Locke in 1690 in much more detail, distinguished between the *nominal essence* and the *real essence* of an object [3]. The nominal essence comes from experience and represents the object's appearance, whereas the real essence represents the object's deeper, constituting features. For instance, the real essence of a material thing is its atomic constitution, because this is the causal basis of all the thing's observable properties [4]. A scientific classification is particularly useful if it reflects the *real* essence of the objects in question by identifying their underlying common features, from which the more obvious and easily observable *nominal* properties follow. Having in mind Locke's concept of real essence, we argue below for a new definition of the class of simple liquids.

Physicists love simple systems. This reflects the fundamental paradigm that, in order to capture a given phenomenon, simpler is better. Most classifications in physics are clear-cut, for example, the classification of elementary particles into baryons and leptons, whereas classifications in other sciences usually have a wealth of borderline cases. Because of the diversity of molecules, it is reasonable to expect a definition of "simple liquids" to be of the latter type.

*dyre@ruc.dk

The concept of a simple liquid is old, but it remains central as evidenced by the 2003 book entitled *Basic Concepts for Simple and Complex Liquids* [5] or the review of nonsimple liquids entitled *Theory of Complicated Liquids* from 2007 [6]. Generations of liquid-state theorists were introduced to this exciting topic by studying Hansen and McDonald's textbook *Theory of Simple Liquids* [7]. This book first appeared in 1976, following a period of spectacular progress in the theory of liquids, catalyzed by some of the very first scientific computer simulations.

In Ref. [7] a simple liquid is defined as a classical system of approximately spherical, nonpolar molecules interacting via pair potentials. This and closely related definitions of liquid simplicity have been standard for many years [8–12]. In this definition, simple liquids have much in common with the chemists' ''nonassociated liquids'' [13], but there are some significant differences. Chemists generally regard a liquid as simple even if it consists of elongated molecules, as long as these are without internal degrees of freedom and interact primarily via van der Waals forces. Many physicists would probably disagree. Thus, it is far from trivial to ask: What characterizes a simple liquid? More accurately: Given a classical system of rigid bodies with potential energy as a function of the bodies' centers of masses and their spatial orientations, is it possible to give a quantitative criterion for how simple the system is? If yes, is simplicity encoded uniquely in the potential-energy function or may the degree of simplicity vary throughout the phase diagram?

Recent works identified and described the properties of what we have termed strongly correlating liquids [14–25]. By definition, in these liquids the virial W and the potential energy U correlate strongly in their constant-volume thermal-equilibrium fluctuations. Recall that the average virial $\langle W\rangle$ gives the contribution to the pressure from intermolecular interactions, which is added to the ideal-gas term Nk_BT, deriving from momentum transport via particle motion (below p is the pressure, V the volume, N the number of particles, k_B Boltzmann's constant, and T the temperature):

$$pV = Nk_BT + \langle W\rangle. \tag{1}$$

The term strongly correlating liquid refers to the case when the WU correlation coefficient in the NVT ensemble is larger than 0.9 [17]. If angular brackets denote an NVT ensemble average, the correlation coefficient R is defined by

$$R = \frac{\langle \Delta W \Delta U\rangle}{\sqrt{\langle (\Delta W)^2\rangle \langle (\Delta U)^2\rangle}}. \tag{2}$$

An example of a strongly correlating liquid is the standard Lennard-Jones (LJ) liquid at typical condensed-phase state points. Many other systems, including some molecular models, have been shown to be strongly correlating; we refer the reader to papers that derive and document the several simple properties of strongly correlating liquids [14–25]. These properties are summarized briefly in Sec. IV A after the presentation of the simulation results.

The present work is motivated by developments initiated by recent findings by Berthier and Tarjus [26,27]. These authors showed that for the viscous Kob-Andersen binary Lennard-Jones mixture [28,29] the dynamics is not reproduced properly by cutting the potentials at their minima according to the well-known Weeks-Chandler-Andersen (WCA) recipe [30]. The role of the cutoff was subsequently studied in two papers [31,32], showing that placing a shifted-forces cutoff at the first minimum of the pair correlation function—thus defining the first coordination shell (FCS)—gives good results for Lennard-Jones–type systems. This is the case not only at moderate densities, but also at very high densities. Applying the same cutoff to water does not work properly [33]. Water is an example of a nonstrongly correlating liquid with $R \approx 0$ at ambient conditions, a consequence of water's density maximum [17]. These findings led us to speculate whether it is a general property of strongly correlating liquids that the intermolecular interactions may be ignored beyond the FCS without compromising accuracy to any significant extent. The main part of this paper shows that, indeed, using such an ''FCS cutoff'' gives accurate simulation results if the liquid is strongly correlating.

The paper presents results obtained from computer simulations of several different systems, only some of which are strongly correlating. We investigate the role of the FCS in determining liquid structure and dynamics. Structure is probed by the radial distribution function (RDF), dynamics by the incoherent or, in a few cases, coherent intermediate scattering function (ISF) at the wave vector defined by the maximum of the static structure factor. The numerical evidence is clear. By varying the cutoff of the intermolecular forces, we find that in order to get accurate simulation results it is enough to take into account merely the interactions within the FCS *if and only if* the liquid is strongly correlating. In other words, for strongly correlating liquids, interactions beyond the FCS are unimportant, and this applies only for these liquids. At present there are no compelling arguments for this empirical ''FCS property,'' but we argue briefly in Sec. IV B that it is consistent with known properties of strongly correlating liquids.

The FCS property of strongly correlating liquids shows that these are simpler than liquids in general. A number of other simple properties of strongly correlating liquids have been identified previously [14–25]. Altogether, these facts motivate our new definition of liquid simplicity.

Section II presents the results from molecular dynamics simulations and Sec. III summarizes the results. Section IV gives an overview of the many simple properties of strongly correlating liquids, motivating our suggestion that a liquid is to be defined as simple if it is strongly correlating at the state point in question. Section V gives a few concluding remarks.

II. MOLECULAR DYNAMICS SIMULATIONS OF ATOMIC AND MOLECULAR LIQUIDS

In a computer simulation, the interactions, which usually extend in principle to infinity, are truncated at some cutoff distance r_c beyond which they are ignored. To avoid a discontinuity in the force, which can severely affect the results [31,34], the simulations reported below use potentials modified such that the force goes continuously to zero at r_c. This is done by applying a so-called shifted-forces (SF) cutoff [34–36] where, if the pair potential is $v(r)$ and the pair force is $f(r) = -v'(r)$, the shifted force is given by

$$f_{\mathrm{SF}}(r) = \begin{cases} f(r) - f(r_c) & \text{if } r < r_c \\ 0 & \text{if } r > r_c. \end{cases} \tag{3}$$

This corresponds to using the following pair potential below r_c: $v_{\mathrm{SF}}(r) = v(r) - v'(r_c)(r - r_c) - v(r_c)$. Using a SF cutoff gives more accurate results and better numerical stability than using the standard shifted-potential (SP) cutoff [31]. This is so despite the fact that a SF cutoff does not have the correct pair force for any r, whereas the pair force is correct below r_c for a SP cutoff. Apparently, avoiding discontinuity of the force at r_c is more important than maintaining the correct force. It was recently discussed [18] why adding a linear term to the pair potential affects neither structure nor dynamics to any significant extent. The reason is that, when one nearest-neighbor distance decreases, others increase in such a way that their sum is virtually constant. This argument is exact in one dimension and holds to a good approximation in 3D constant-volume simulations [18] (in constant-pressure simulations the volume fluctuates and the argument no longer applies). Coulomb interactions have also been treated by the SF cutoff procedure. Although the Coulomb interaction is long ranged and conditionally convergent, when r_c is sufficiently large, a SF cutoff gives results close to those of the standard, much more involved, Ewald summation method [37,38].

All simulations were performed in the NVT ensemble with periodic boundary conditions using the Nose-Hoover algorithm [39–41]. We used the Roskilde University Molecular Dynamics package developed for state-of-the-art graphics processing unit (GPU) computing [42]. For the molecular models, bond lengths were held fixed using the time-symmetrical central-difference algorithm [43–45].

The effect on the structure and dynamics of varying the pair-potential cutoff r_c was recently investigated for the single-component Lennard-Jones liquid and the Kob-Andersen binary LJ mixture [31,32]. For both systems, it was found that if a SF cutoff is applied instead of the commonly used SP cutoff, the standard cutoff $r_c = 2.5\sigma$ can be decreased to 1.5σ and still give the correct physics. The value $r_c = 1.5\sigma$ is close to the first minimum of the RDF, implying that all nearest-neighbor interactions are accounted for. Decreasing the cutoff further quickly affects the simulations, an effect that is quite pronounced for the dynamics in the viscous regime [26,27].

In the following we investigate, for several systems, whether it is possible to choose a FCS cutoff and still get the correct physics. We start by studying strongly correlating atomic liquids. Then, data are presented for a few atomic liquids that are not strongly correlating. Finally, data are given for two strongly correlating molecular liquids and a water model. Details of the models studied, the number of particles, etc., are given in Appendix A.

A. Three inverse-power-law fluids

We consider first systems with 100% correlation between virial and potential-energy equilibrium fluctuations in the NVT ensemble. It follows from the definition of the virial $W = -1/3 \sum \mathbf{r}_i \cdot \nabla_i U$ [34] that a necessary and sufficient condition for W to correlate perfectly with U is that the potential energy is an Euler homogeneous function of the particle coordinates $\mathbf{r}_i$. This is clearly the case for systems with inverse power-law (IPL) pair potentials [$v(r) \propto r^{-n}$], but note that potentials with nontrivial angular dependence may also be Euler homogeneous.

We simulated single-component IPL pair-potential systems with exponents $n = 18, 6, 4$ at density $\rho = 0.85$. Each system was studied at two temperatures. The simulated systems range from $n = 18$, which is very harsh and repulsive, to $n = 4$, which is quite soft and long ranged. The role of the cutoff is investigated by choosing three different, fairly small cutoffs: one placed at the first minimum of the RDF (red), one corresponding to the half height of the RDF from its minimum to its maximum (blue), and one placed to the right of the RDF first minimum (green), displaced the same amount as the difference between the first and the second cutoff.

The RDFs $g(r)$ are shown for $n = 18, 6, 4$ in Fig. 1; $n = 12$ gives similar results (not shown). The simulations with a SF cutoff at the first minimum of the RDF—referred to as FCS-cutoff simulations—give a faithful representation of the structure. The insets show, as functions of the cutoff, the deviations in RDF between the results for a FCS cutoff and the "true" large-cutoff results, quantified by integrating the numerical difference in the pair correlation function. Clearly, deviations increase sharply when the cutoff enters the FCS (blue crosses).

We simulated also the $n = 3$ and $n = 1$ IPL fluids. For both systems, a FCS cutoff does not lead to the correct physics. Both models do not have a proper thermodynamic limit, for which the exponent must be larger than the dimension [46]. For the $n = 1$ IPL (Coulomb) fluid, this problem may be solved by introducing a uniform, neutralizing background of opposite charges, resulting in the well-known one-component plasma model [47]. An indication that a FCS cutoff works poorly when the IPL exponent approaches the dimension is seen for the $n = 4$ simulation, for which the WU correlation coefficient for the FCS cutoff starts to deviate significantly from unity. Moreover, but almost

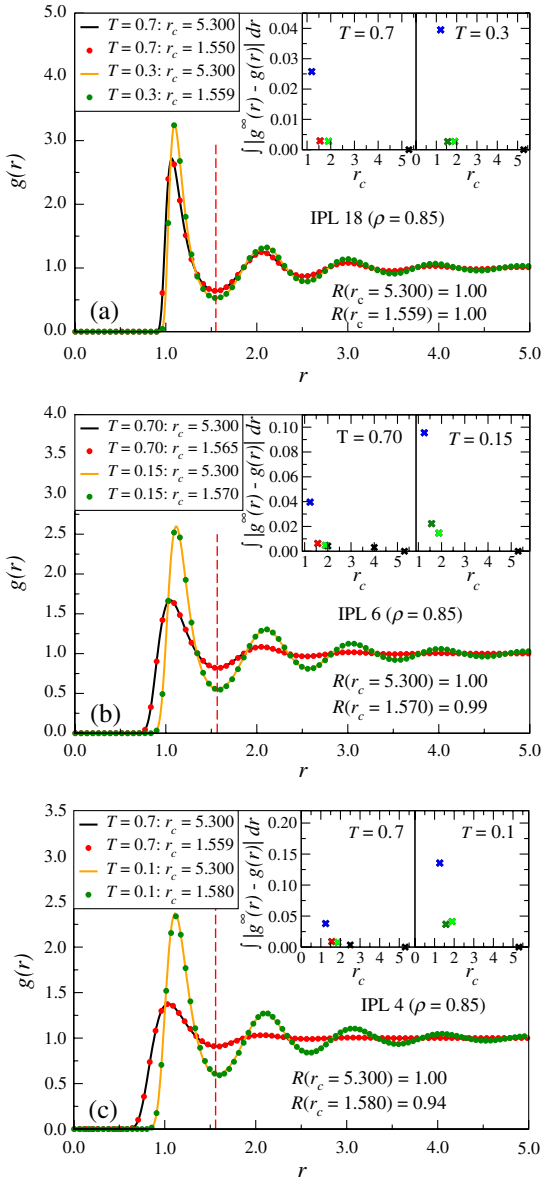

FIG. 1. RDFs for single-component IPL fluids with exponents $n = 18, 6, 4$, each simulated at two temperatures at density $\rho = 0.85$. The black and orange curves show reference simulation results with large cutoffs representing the true IPL behavior, the red and green dots give results from simulations with a FCS cutoff (marked by the vertical red dashed lines). The insets quantify the deviations in the RDF from the reference RDF as functions of the cutoff; deviations increase dramatically when the cutoff enters the FCS (blue crosses). In panels (a), (b), and (c) the virial potential-energy correlation coefficient R is given for the lowest temperature (this quantity is exactly unity for IPL systems with infinite cutoff).

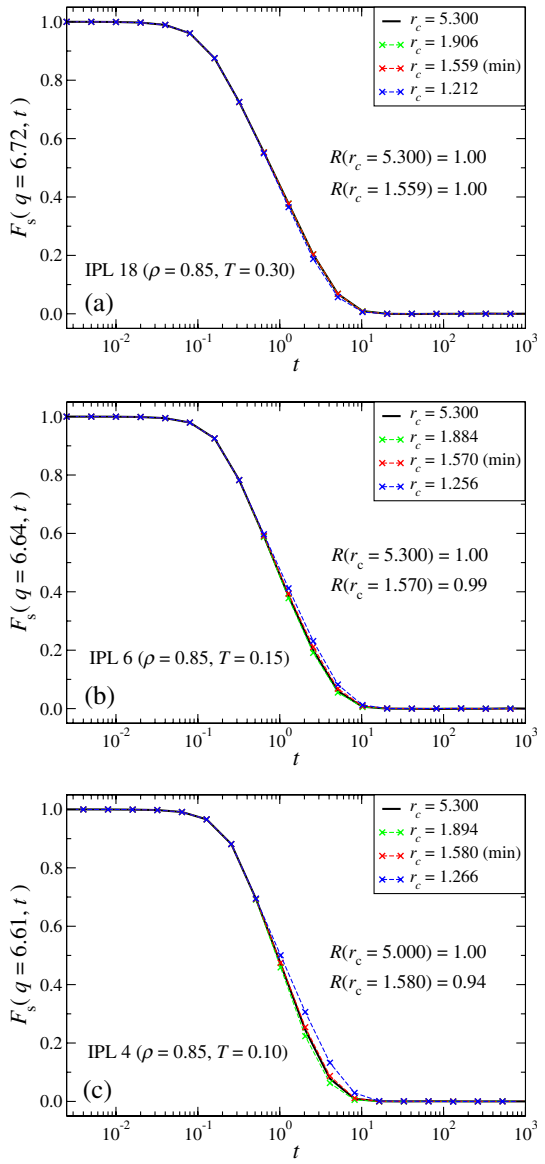

FIG. 2. Incoherent ISFs for the IPL fluids at the lowest-temperature state points of Fig. 1. The black curves give results for a large cutoff, the red crosses for a FCS cutoff (marked by the vertical red dashed lines in Fig. 1). (a) $n = 18$, $T = 0.30$; (b) $n = 6$, $T = 0.15$; (c) $n = 4$, $T = 0.10$.

invisible in the figure, the $n = 4$ pair correlation function's first maximum deviates slightly when comparing FCS and true simulations.

Figure 2 shows the incoherent ISFs evaluated at the wave vector corresponding to the first maximum of the static structure factor for the low-temperature state points of each of the three IPL systems. A good representation of the dynamics is obtained for all systems when the FCS cutoff is used.

B. Lennard-Jones liquids

Next, we consider what is probably the most studied potential in the history of computer simulations, the LJ pair potential,

$$v_{\mathrm{LJ}}(r) = 4\epsilon\left[\left(\frac{\sigma}{r}\right)^{12} - \left(\frac{\sigma}{r}\right)^{6}\right]. \tag{4}$$

Here, σ and ϵ define, respectively, the length and energy scale of the interaction (dimensionless units defined by

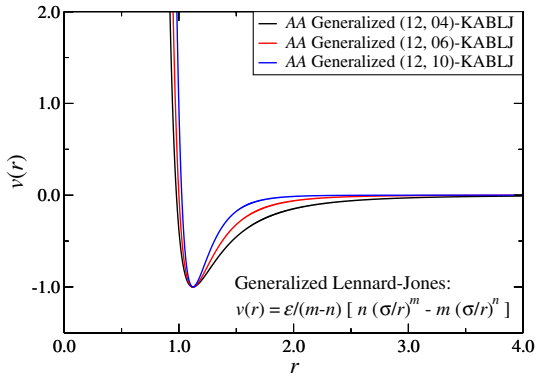

FIG. 3. The *AA*-particle generalized KABLJ pair potentials with fixed repulsive exponent 12 and three different attractive exponents $n = 4, 6, 10$. The model parameters are given in Appendix A.

$\sigma = \epsilon = 1$ are used below). This potential does not have 100% virial potential-energy correlations, but has still quite strong correlations with correlation coefficients $R > 0.9$ in the condensed-fluid part of the phase diagram (and also in the crystalline phase [18]). We studied the single-component LJ (SCLJ) liquid, two generalized 80/20 Kob-Andersen binary LJ (KABLJ) mixtures with repulsive exponent 12 and attractive exponents $n = 4, 10$, and the Wahnstrom 50/50 binary LJ mixture (Fig. 3 and Appendix A give model details). The influence of a SF cutoff on simulation accuracy was investigated recently for the SCLJ liquid and the standard KABLJ mixture ($n = 6$) [31,32], but for completeness we include results for the SCLJ system here as well. See also Table I.

The role of the cutoff is again investigated by choosing three different cutoffs: one placed at the first minimum of the RDF (red color in Figs. 4–8), one corresponding to the half height of the RDF from its minimum to its maximum (blue color in Figs. 4–8), and one displaced to the right of the minimum by the same amount as the difference between the first and the second cutoff (green color in Figs. 4–8).

In Fig. 4, RDFs are shown for the SCLJ liquid at three different state points. The red circles and curve show results from simulations with a FCS cutoff (marked by the vertical red dashed line); the black curves show the corresponding simulations with a large cutoff (reference system). The insets quantify the deviations in the simulated RDF from the reference RDF as a function of the cutoff. The reference RDF of Figs. 4(a) and 4(b) is clearly well represented using a FCS cutoff, while choosing the cutoff inside the FCS results in significant deterioration. At low density [Fig. 4(c)], deviations occur between FCS-cutoff simulations and the reference system. As mentioned, the SCLJ liquid is strongly correlating in large parts of its phase

TABLE I. The results for five state points of the SCLJ liquid. For each state point is given density, temperature, correlation coefficient, maximum deviation from the true RDF using a FCS cutoff, and maximum deviation from the true ISF using a FCS cutoff. The deviations clearly increase as the *WU* correlation decreases.

System	ρ	T	R	$\lvert\Delta\text{RDF}\rvert_{\max}$	$\lvert\Delta\text{ISF}\rvert_{\max}$
SCLJ	0.85	1.00	0.97	1.31×10^{-2}	5.10×10^{-3}
SCLJ	0.85	0.70	0.96	1.68×10^{-2}	8.28×10^{-3}
SCLJ	0.85	0.65	0.96	1.63×10^{-2}	8.96×10^{-3}
SCLJ	0.50	1.50	0.69	11.2×10^{-2}	7.94×10^{-3}
SCLJ	0.55	1.13	0.50	15.2×10^{-2}	12.0×10^{-3}

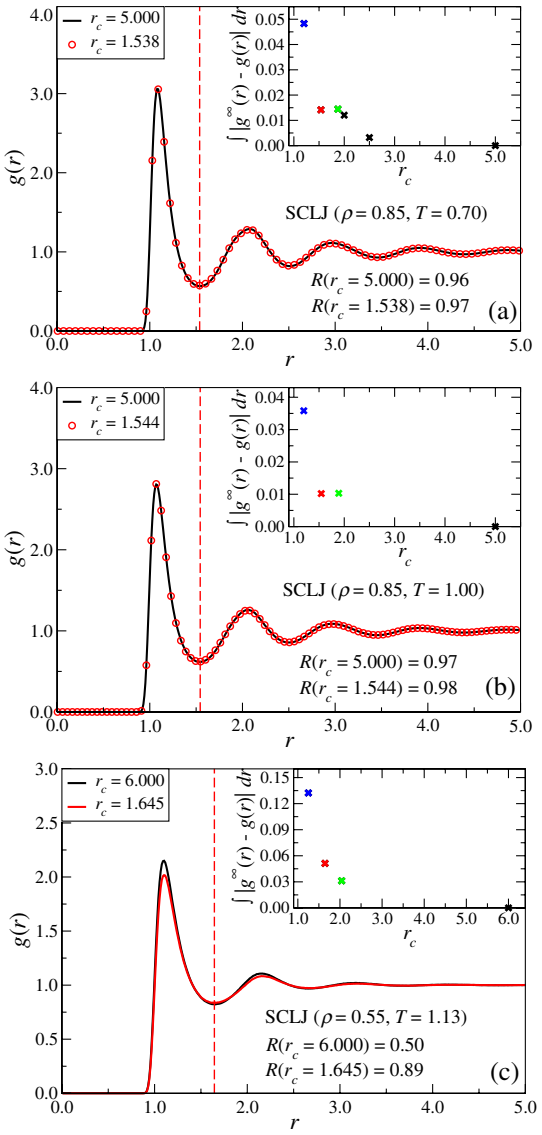

FIG. 4. RDFs for the SCLJ liquid at three different state points: (a) $\rho = 0.85, T = 0.70$ ($R = 0.96$); (b) $\rho = 0.85, T = 1.00$ ($R = 0.97$); (c) $\rho = 0.55, T = 1.13$ ($R = 0.50$). The black curves show reference simulations with large cutoffs; the red dots and curve show results from simulations with a FCS cutoff (marked by the vertical red dashed lines). The insets quantify the deviation in RDF from the reference RDF as functions of the cutoff. At all three state points, deviations increase significantly when the cutoff enters the FCS (blue crosses in the insets). For state points (a) and (b), which are strongly correlating ($R > 0.9$), a FCS cutoff leads to accurate results. This is not the case for state point (c).

diagram, but as density is lowered, the correlations decrease gradually and the liquid is no longer strongly correlating at state point (c), where $R = 0.50$. These simulations suggest that only when a liquid is strongly correlating, is it possible to ignore interactions beyond the FCS.

Next, we investigated the SCLJ dynamics at the same three state points. The dynamics is studied via the incoherent ISF. The ISFs are shown in Fig. 5; at all state points the dynamics is well represented using a FCS cutoff.

We proceed to investigate mixtures of two different particles (A and B) interacting with LJ type potentials.

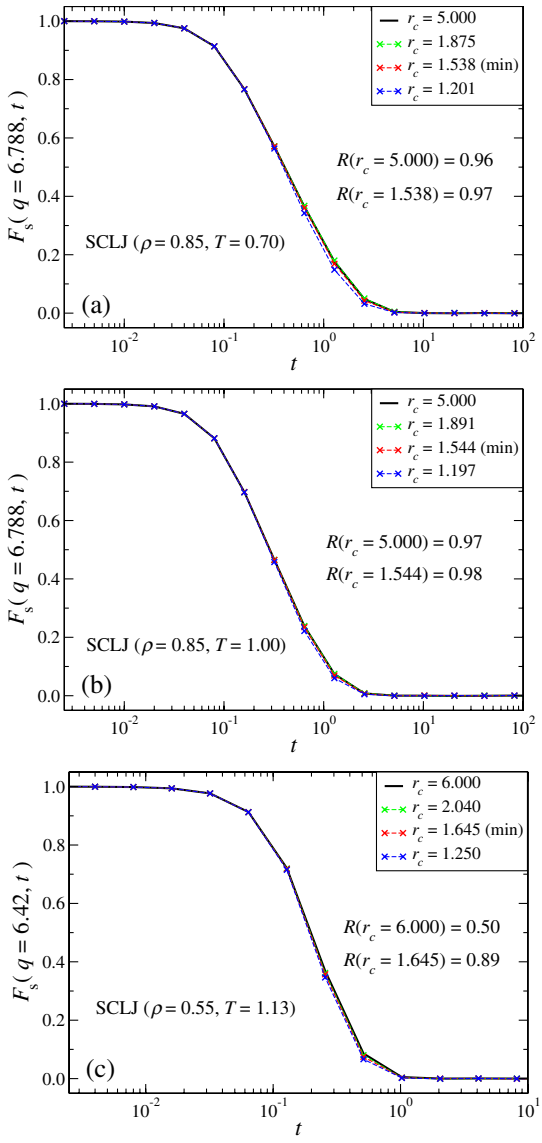

FIG. 5. Incoherent ISFs for the SCLJ liquid at the state points of Fig. 4. The black curves give the reference cutoff results, the red curves give the FCS-cutoff results, the blue curves give results for a cutoff at the half-height towards the first maximum of the RDF, and the green curves give results for a cutoff to the right of the minimum. (a) $\rho = 0.85$, $T = 0.70$ ($R = 0.96$); (b) $\rho = 0.85$, $T = 1.00$ ($R = 0.97$); (c) $\rho = 0.55$, $T = 1.13$ ($R = 0.50$).

The cutoff used for all three interactions (AA, AB, BB) is placed at the same distance, referring to σ_{AA}. In Fig. 6 the reference and FCS-cutoff results are shown for the AA-particle RDFs of generalized KABLJ mixtures with repulsive exponent 12 and attractive exponents $n = 4, 10$. For all investigated state points a FCS cutoff gives accurate results. We found the same using the standard repulsive exponent $n = 6$ (results not shown) [32].

The A-particle ISFs for the state points of Fig. 6 are shown in Fig. 7. For the KABLJ mixture also, placing the cutoff inside the FCS (blue curves) fails to reproduce the dynamics properly, whereas the dynamics is well approximated using a FCS cutoff (red). Slight deviations are noted for the red curves, an issue considered in Appendix B, which discusses alternatives for delimiting the FCS. Similar results are found for the B particles (results not shown).

We also simulated the Wahnstrom 50/50 binary LJ mixture [48], finding again that whenever $R > 0.9$, the structure and dynamics are well reproduced using a FCS cutoff. We do not show these results, but show instead results for the AA coherent ISF at one state point (Fig. 8). Again, the FCS cutoff (red crosses) gives the correct

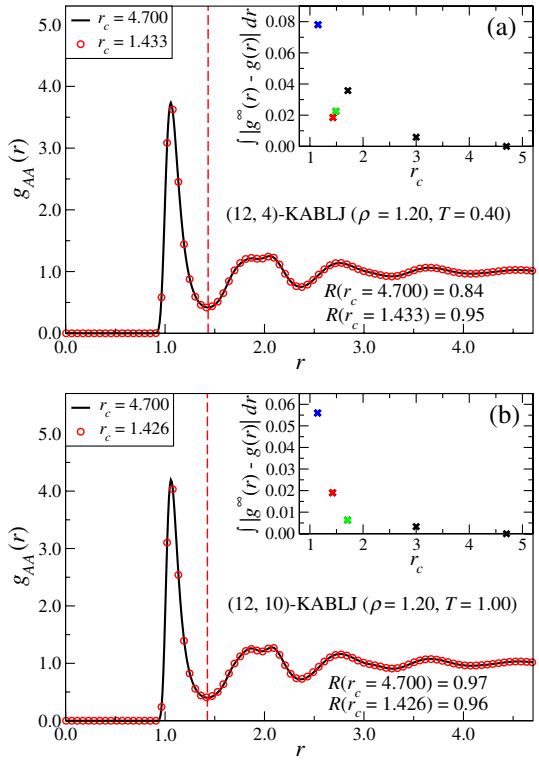

FIG. 6. RDFs for generalized KABLJ mixtures with repulsive exponent 12 and attractive exponents $n = 4, 10$. The black curves give the reference cutoff results; the red circles give the FCS-cutoff results. The insets quantify the deviation in RDF from the reference RDF as functions of the cutoff. (a) $n = 4$, $\rho = 1.20$, $T = 0.40$ ($R = 0.84$); (b) $n = 10$, $\rho = 1.20$, $T = 1.00$ ($R = 0.97$).

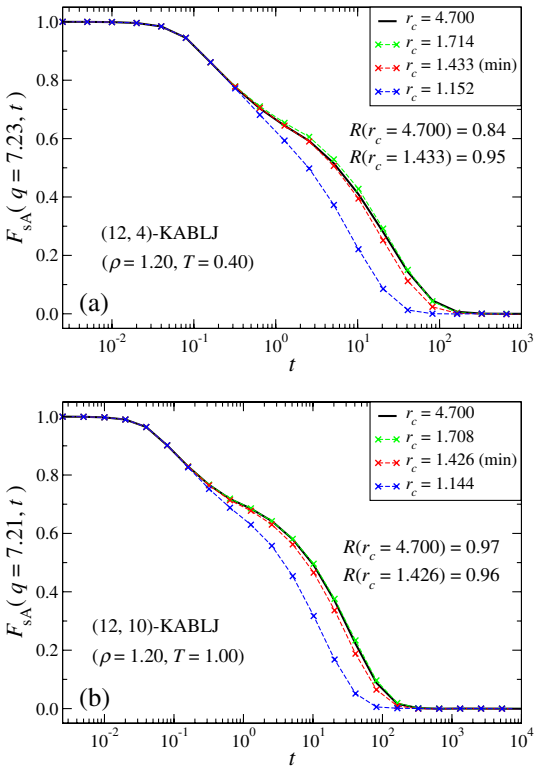

FIG. 7. Incoherent ISFs for generalized KABLJ mixtures with repulsive exponent 12 and attractive exponents $n = 4, 10$. The red and black curves give, respectively, results for FCS cutoffs and large reference cutoffs. (a) $n = 4$, $\rho = 1.20$, $T = 0.40$ ($R = 0.84$); (b) $n = 10$, $\rho = 1.20$, $T = 1.00$ ($R = 0.97$).

dynamics, whereas reducing the cutoff further does not give proper results (blue crosses).

In summary, for all LJ–type systems, whenever there are strong virial potential-energy correlations ($R > 0.9$), a FCS cutoff gives accurate results for both the structure and dynamics.

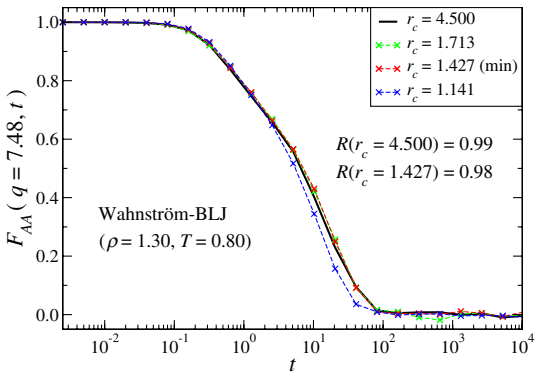

FIG. 8. Coherent ISF of the A particles for the Wahnstrom 50/50 binary LJ liquid at the wave vector defined by the static structure factor maximum. The red and black curves give, respectively, results for a FCS cutoff and large reference cutoff at the state point where $\rho = 1.30$ and $T = 0.80$.

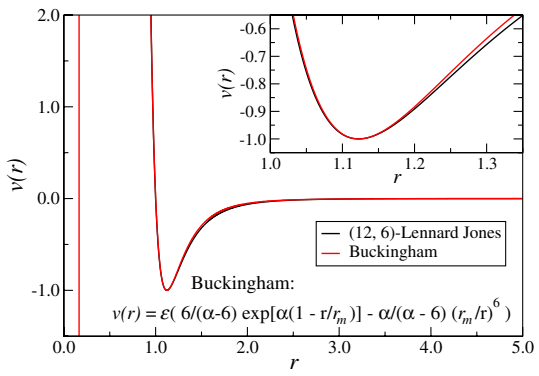

FIG. 9. The Buckingham pair potential (red) and the LJ pair potential (black). The parameters of the Buckingham potential were chosen such that the LJ potential is well approximated in the repulsive region.

C. Buckingham liquid

Next, we consider the single-component Buckingham liquid (SCB). The Buckingham potential [49,50] is similar to the LJ potential, but does not have an IPL repulsive term; instead the potential's short-distance behavior follows a steep exponential (Fig. 9). Consequently, the Buckingham potential does not diverge at $r = 0$. The parameters of the

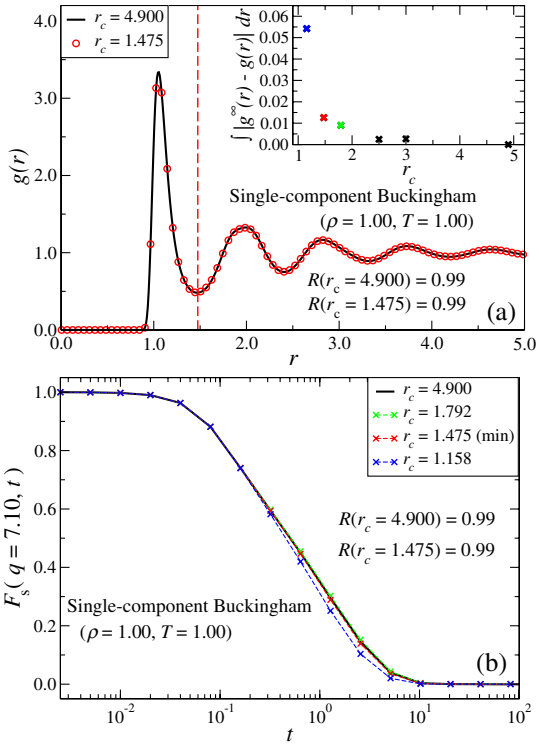

FIG. 10. The effect on the structure and dynamics of varying the cutoff for the SCB liquid. The red and black curves give, respectively, results for a FCS cutoff and a large reference cutoff. (a) RDF at $\rho = 1.00$ and $T = 1.00$ ($R = 0.99$). The inset quantifies the deviation in RDF from the reference RDF as a function of the cutoff. (b) Incoherent ISF at the same state point.

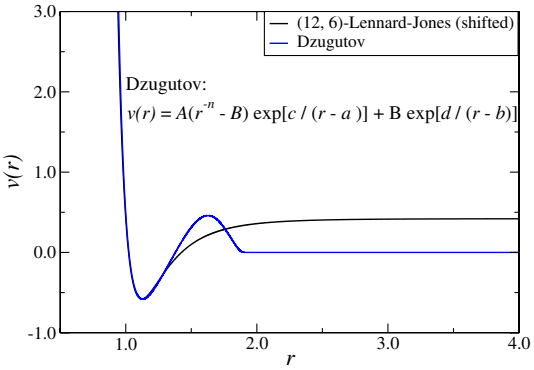

FIG. 11. The DZ pair potential [51] (blue curve). Also shown is the LJ pair potential (black curve). The DZ potential approximates the LJ potential around the first minimum, but has a maximum at larger distances.

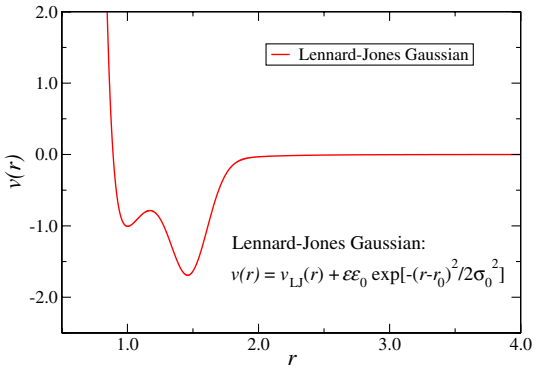

FIG. 13. The LJG pair potential [52] constructed by adding a Gaussian to the LJ potential. Two distinct minima are present.

Buckingham potential (Appendix A) were chosen such that the LJ potential is well approximated in the lower-energy repulsive part of the potential (Fig. 9).

Figures 10(a) and 10(b) show, respectively, the RDF and ISF for the SCB liquid. The SCB liquid is strongly correlating [50] and a FCS cutoff works well.

D. Dzugutov liquid

Figure 11 shows the Dzugutov (DZ) pair potential [51], which was originally suggested as a model potential for which crystallization is impeded by energetically punishing particle separations corresponding to the next-nearest-neighbor distance of crystallographic local order. At short distances the DZ pair potential approximates the LJ potential.

Figures 12(a) and 12(b) show, respectively, the RDF and the coherent ISF of the DZ system. For this system, the use of a FCS cutoff leads to poor results. This is not surprising given the fact that using a FCS cutoff removes the maximum of the DZ potential. What is important here, however, is that the poor FCS-cutoff results correlate with the fairly weak virial potential-energy correlations ($R = 0.71$). This suggests studying other non-strongly correlating liquids in order to investigate whether this is a general trend.

E. Lennard-Jones Gaussian liquid

The Lennard-Jones Gaussian (LJG) liquid [52] is a non-strongly correlating liquid with the two-minimum pair potential shown in Fig. 13. The parameters of the LJG model (Appendix A) are such that the LJG potential minimum does not coincide with that of the SCLJ system [53].

Results from the simulating structure and dynamics of the LJG liquid are shown in Figs. 14(a) and 14(b). The FCS cutoff does not give the correct RDF. Deviations in the dynamics are fairly small, likely due to the fact that the dynamics is fast [compare, e.g., the time scale of the decay to that of the DZ liquid in Fig. 12(b)].

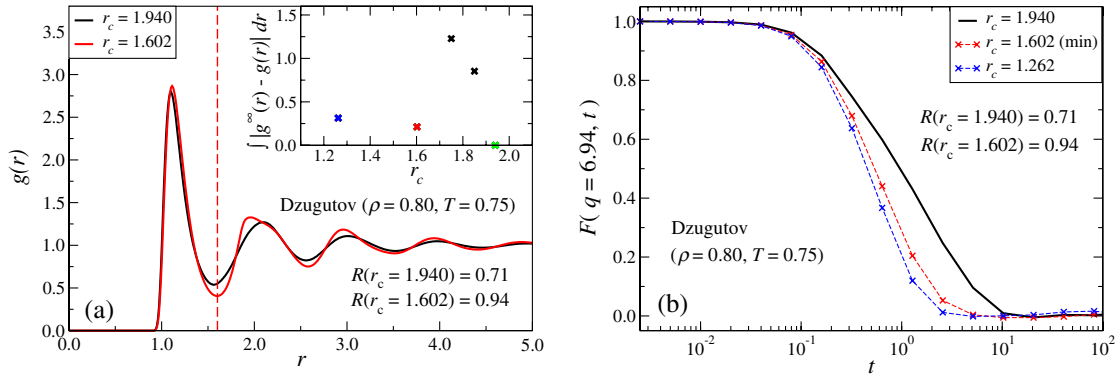

FIG. 12. The effect on the structure and dynamics of varying the cutoff for the DZ liquid at $\rho = 0.80$ and $T = 0.75$ ($R = 0.71$). The red and black curves give, respectively, results for a FCS cutoff and a large reference cutoff. (a) RDF. The inset quantifies the deviation in RDF from the reference RDF as a function of the cutoff. (b) The coherent ISF at the same state point, including here results for a cutoff within the FCS (blue crosses).

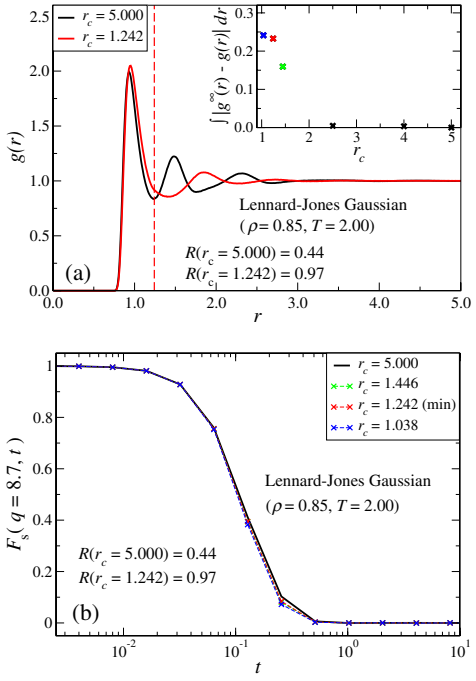

FIG. 14. The effect of the cutoff on the structure and dynamics for the LJG liquid. The red and black curves give, respectively, results for a FCS cutoff and a large reference cutoff. (a) RDF at $\rho = 0.85$ and $T = 2.00$ ($R = 0.44$). The inset quantifies the deviation in RDF from the reference RDF (black curve) as a function of the cutoff. (b) Incoherent ISF at the same state point.

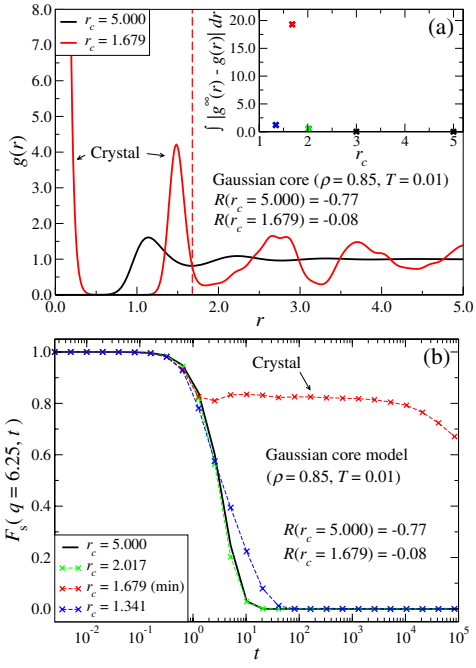

FIG. 15. The effect on the structure and dynamics of varying the cutoff for the GCM liquid. The red and black curves give, respectively, results for a FCS cutoff and a large reference cutoff. (a) RDF at $\rho = 0.85$ and $T = 0.01$ ($R = -0.77$). The inset quantifies the deviation in RDF from the reference RDF as a function of the cutoff. The red curve represents a crystallized state. (b) Incoherent ISF at the same state point.

F. Gaussian core model

The Gaussian core model (GCM) [54,55], which is not strongly correlating, is defined by a Gaussian pair potential and thus has a finite potential energy at zero separation. The high-density regime of the GCM model ($\rho > 1.5$) has recently received attention as a single-component model glass former [56], because it is not prone to crystallization and shows the characteristic features of glass-forming liquids (large viscosity, two-step relaxation, etc.).

Figure 15 shows the RDF and ISF for the GCM liquid. The GCM crystallizes when a FCS cutoff is used. For this reason, obviously, a FCS cutoff is not able to reproduce the structure and dynamics of the reference system. Note, however, that crystallization does not occur when the cutoff is chosen in the neighborhood of the FCS cutoff (see the inset).

G. The Hansen-McDonald molten salt model

The final atomic system we studied is the so-called singly charged molten salt model proposed by Hansen and McDonald [57]. In Fig. 16 we see that the structure

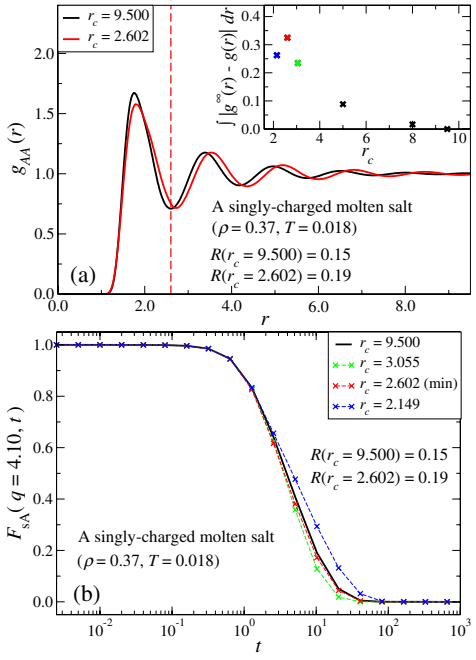

FIG. 16. The effect on the structure and dynamics of varying the cutoff for the Hansen-McDonald single-charged molten salt model. Because of the competing interactions (Coulomb and $n = 9$ repulsive IPL) this model is not strongly correlating. The red and black curves give, respectively, results for a FCS cutoff and a large reference cutoff. (a) AA-particle RDF at $\rho = 0.37$ and $T = 0.018$ ($R = 0.15$). The inset quantifies the deviation in RDF from the reference RDF as a function of the cutoff. (b) A-particle incoherent ISF at the same state point.

is not represented well by a FCS cutoff. Interestingly, the dynamics is well reproduced using this cutoff—even better, in fact, than for a larger cutoff [Fig. 16(b), green curve].

H. Two strongly correlating molecular model liquids

We finish the presentation of the numerical results by giving data for three molecular model liquids. In this subsection, data are given for two strongly correlating molecular liquid models, the Lewis-Wahnstrom ortho-terphenyl (OTP) model [58,59] and the asymmetric dumbbell model [19], which represent a molecule by three and two rigidly bonded LJ spheres, respectively. The next subsection gives data for a rigid water model.

Figures 17(a) and 17(b) show the LJ particle RDF and ISF of the OTP model. Both quantities are well approximated using a FCS cutoff, although slight deviations are noted for the ISF (red curve, see Appendix B for considerations concerning this). The OTP model is a borderline strongly correlating liquid ($R = 0.91$).

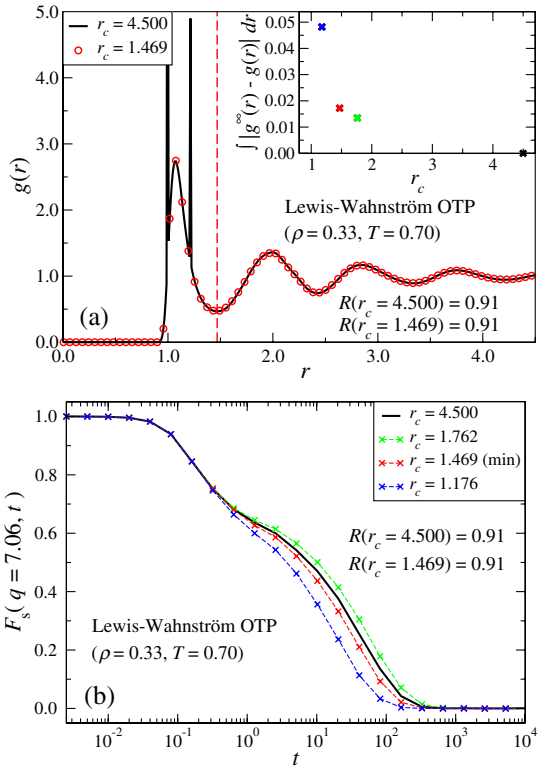

FIG. 17. The effect on the structure and dynamics of varying the cutoff for the Lewis-Wahnstrom OTP model. The red and black curves give, respectively, results for a FCS cutoff and a large reference cutoff. (a) RDF of the LJ particles at $\rho = 0.33$ and $T = 0.70$ ($R = 0.91$). The inset quantifies the deviation in RDF from the reference RDF as a function of the cutoff. The spikes derive from the bonds. (b) Incoherent ISF at the same state point.

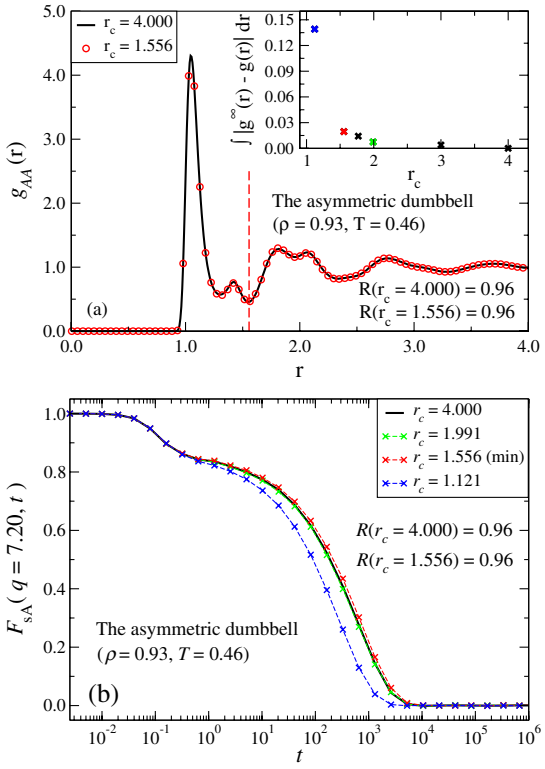

FIG. 18. The effect on the structure and dynamics of varying the cutoff for the asymmetric dumbbell model. The red and black curves give, respectively, results for a FCS cutoff and a large reference cutoff. Note that in this case the FCS cutoff is defined by using the second minimum (the first minimum is not the absolute minimum). (a) RDF at $\rho = 0.93$ and $T = 0.46$ ($R = 0.96$). The inset quantifies the deviation in RDF from the reference RDF (black curve) as a function of the cutoff. (b) A-particle incoherent ISF at the same state point. For the lowest cutoff the system crystallized.

Figures 18(a) and 18(b) show corresponding figures for the large (A) particle of the asymmetric dumbbell model at a viscous state point. The use of a FCS cutoff gives accurate results for both the structure and dynamics. The FCS cutoff was placed at the *second* minimum of the AA RDF, because the AA RDF has here a lower value than at the first minimum. If the cutoff is placed at the first minimum, clear deviations are found (data not shown).

I. Rigid SPC/E water model

We consider finally the rigid single-point charge (SPC/E) water model [60] (Fig. 19). This model is not strongly correlating at ambient conditions, a fact that directly reflects water's well-known density maximum [18]. The structure of the SPC/E water model is not well represented using a FCS cutoff. Interestingly, the FCS-cutoff dynamics shows only slight deviations from that of the reference curve (black).

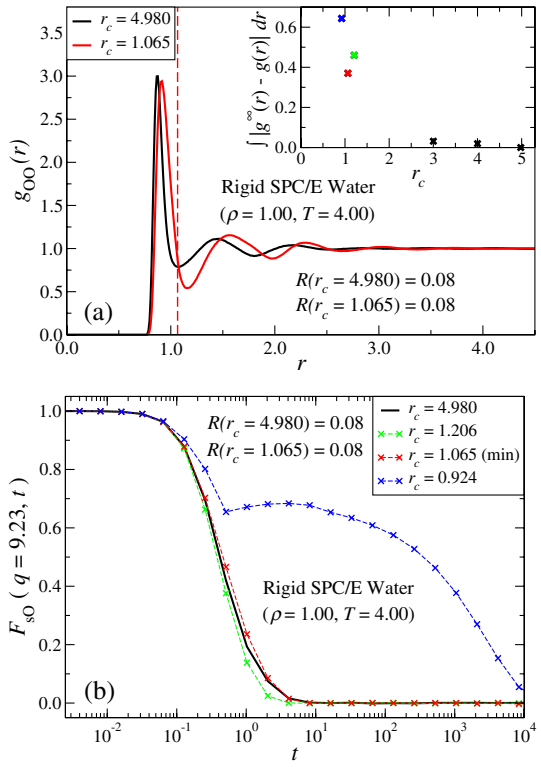

FIG. 19. The effect on the structure and dynamics of varying the cutoff for the rigid SPC/E water model [60]. The red and black curves give, respectively, results for a FCS cutoff and a large reference cutoff. (a) Oxygen-oxygen RDF at $\rho = 1.00$ and $T = 4.00$ ($R = 0.08$). The inset quantifies the deviation in RDF from the reference RDF as a function of the cutoff. (b) Oxygen incoherent ISF at the same state point.

III. SUMMARIZING THE SIMULATION RESULTS

The previous section showed that the structure and dynamics are well approximated in simulations using a FCS cutoff for the following atomic and molecular systems:

(1) Inverse power-law systems ($n = 18, 6, 4$),
(2) single-component Lennard-Jones liquid at density $\rho = 0.85$,
(3) generalized Kob-Andersen binary Lennard-Jones mixtures,
(4) Wahnstrom binary Lennard-Jones mixture,
(5) single-component Buckingham liquid,
(6) Lewis-Wahnstrom OTP model,
(7) asymmetric dumbbell model.

These systems are all strongly correlating [17,18,20,21,24]. Thus, for strongly correlating liquids, it is enough to know the intermolecular interactions within the FCS in order to accurately simulate the structure and dynamics.

The simulations showed further that for all of the following atomic and molecular systems, structure and/or dynamics are not properly reproduced when a FCS cutoff is used:

(1) single-component Lennard-Jones liquid at density $\rho = 0.55$,
(2) Dzugutov liquid,
(3) Lennard-Jones Gaussian liquid,
(4) Gaussian core model,
(5) Hansen-McDonald molten salt model,
(6) rigid SPC/E water model.

For all these systems, larger cutoffs are needed in order to faithfully reproduce the system's physics. None of the latter liquids are strongly correlating.

In conclusion, a shifted-forces FCS cutoff leads to accurate results *if and only if* the liquid is strongly correlating at the state point in question. We know of no exceptions to this empirical rule. This suggests that strongly correlating liquids are characterized by the property that intermolecular interactions beyond the FCS can be safely ignored.

IV. THE REAL ESSENCE OF SIMPLICITY OF LIQUIDS

As discussed in the Introduction, a definition of simple liquids is most useful if it identifies their real essence in Locke's understanding of the term [3], the underlying fundamental characteristic from which these liquids' simple features, their nominal essences, follow. We suggest below that the class of simple liquids is to be identified with the class of strongly correlating liquids (Sec. IV C). This is motivated by first summarizing the many simple properties of strongly correlating liquids (Sec. IV A), then showing that this class of liquids can be characterized from three different perspectives: mathematically, physically, and chemically (Sec. IV B). This gives three very different characterizations, indicating that the class of strongly correlating liquids is fundamental, and further motivating the suggestion that the real essence of liquid simplicity is the existence of strong correlations of virial potential-energy equilibrium NVT fluctuations. By connecting to the chemists' concept of nonassociated liquids, we then discuss which real-world liquids are simple (Sec. IV D), liquids near interfaces (Sec. IV E), and give examples of complex liquid properties (Sec. IV F). Finally, Sec. IV G points out that our results call into question the physical basis of traditional perturbation theory, which assumes quite different roles of the attractive and the repulsive forces; this distinction is not deep and fundamental for simple liquids.

A. Strongly correlating liquids and their properties

The simple properties of strongly correlating liquids follow from the existence of "isomorphs" in their phase diagram (see below). Some simple properties were identified before isomorphs were defined in 2009 [21], however, for instance that

(1) all eight fundamental thermoviscoelastic response functions are given in terms of just one, i.e., the dynamic Prigogine-Defay ratio is close to unity [16],

(2) aging may be described in terms of merely one extra parameter [18,20],
(3) power-law density scaling [61] is obeyed to a good approximation; i.e., for varying density and temperature, the relaxation time is a function of ρ^γ/T [19].

An isomorph is an equivalence class of state points in the phase diagram. Two state points (ρ_1, T_1) and (ρ_2, T_2) are defined to be isomorphic [21] if the following holds: Whenever one microconfiguration of state point (1) and one of state point (2) have the same reduced coordinates [i.e., $\rho_1^{1/3}\mathbf{r}_i^{(1)} = \rho_2^{1/3} r_i^{(2)}$ for all particles i], these two microconfigurations have proportional configurational Boltzmann factors,

$$e^{-U(\mathbf{r}_1^{(1)},\ldots,\mathbf{r}_N^{(1)})/k_BT_1} = C_{12}e^{-U(\mathbf{r}_1^{(2)},\ldots,\mathbf{r}_N^{(2)})/k_BT_2}. \quad (5)$$

For most systems, the isomorph concept is approximate just as *WU* correlations are rarely perfect. Thus, we do not require Eq. (5) to be rigorously obeyed for all microconfigurations, but only to a good approximation for all *physically relevant* microconfigurations. By this we mean microconfigurations that are not *a priori* unimportant for the physics. An isomorph defines a continuous curve of state points in the liquid's phase diagram.

Appendix A of Ref. [21] showed that a liquid is strongly correlating if and only if it has isomorphs to a good approximation. This was confirmed in Refs. [21,24], which showed that Lennard-Jones–type atomic liquids have good isomorphs. Likewise, Ref. [62] recently showed that the strongly correlating Lewis-Wahnstrom OTP and asymmetric dumbbell models have good isomorphs.

Equation (5) has many consequences. These were derived and discussed in detail in the original isomorph paper from 2009 (Ref. [21]), to which the reader is referred. Basically, the structure and dynamics at two isomorphic state points are identical in reduced units. Quantities that are invariant along an isomorph include (but are not limited to)

(1) The excess entropy, i.e., the entropy in excess of the ideal-gas entropy at the same density and temperature—this is the configurational contribution to the entropy (a quantity that is negative because a liquid is always more ordered than an ideal gas at same density and temperature).
(2) All N-body entropy terms. Recall that the excess entropy can be expanded in a series of two-body, three-body, etc., terms; each term is invariant along an isomorph [21].
(3) The isochoric heat capacity.
(4) The structure in reduced units (defined by $\tilde{\mathbf{r}}_i \equiv \rho^{1/3}\mathbf{r}_i$ for all particles i). Not only the radial distribution function, but all higher-order distribution functions are isomorph invariant in reduced units.
(5) The Newtonian NVE and Nosé-Hoover NVT equations of motion in reduced units; likewise Brownian dynamics.
(6) All autocorrelation functions in reduced units.
(7) All average relaxation times in reduced units.
(8) Reduced transport coefficients such as the diffusion coefficient, viscosity, etc.

Isomorphs have the further interesting property that there is no relaxation for an instantaneous change of temperature and density when jumping from an equilibrated state point to a different state point isomorphic with the initial state. The absence of relaxation derives from the fact that the Boltzmann probabilities of scaled microconfigurations are identical. Such "isomorph jumps" have been shown to work very well for the KABLJ liquid [21], for the asymmetric dumbbell and for the Lewis-Wahnstrom OTP molecular models [62]. Moreover, the effective temperature of a glass prepared by a temperature-density jump from an equilibrium state of a strongly correlating liquid depends only on the final density [22]; this provides yet another example of a simple feature of these liquids.

Some further predictions for the class of strongly correlating liquids deriving from the existence of isomorphs are

(1) The solid-liquid coexistence curve is an isomorph [21,24]. This implies invariance along the coexistence curve of the reduced structure factor, the reduced viscosity, the reduced diffusion constant, etc., as well as pressure invariance of the melting entropy and the reduced-unit Lindemann melting criterion [21].
(2) Collapse of the two-order-parameter maps of Debenedetti *et al.* [63–67] to one-dimensional curves [21].
(3) Isochronal superposition [68], i.e., the fact that when pressure and temperature are varied, the average relaxation time determines the entire relaxation spectrum [21].

The above listed properties of strongly correlating liquids all reflect one or the other kind of simplicity of strongly correlating liquids. A final, recently established simple property is a thermodynamic separation identity: For all strongly correlating liquids, if s is the excess entropy per particle, the temperature as a function of s and density ρ factorizes as follows [69]:

$$T = f(s)h(\rho). \quad (6)$$

Equation (6) has a number of consequences [69], for instance, the configurational Gruneisen equation of state and that the isomorphs of LJ liquids—in particular, the LJ solid-liquid coexistence curve—are given by $(A\rho^4 - B\rho^2)/T = \text{const}$ [70,71].

B. Mathematical, physical, and chemical characterization of strongly correlating liquids

At a given state point, if the average potential energy is denoted by $\langle U \rangle$, the constant-potential-energy

hypersurface is defined by $\Omega = \{(\mathbf{r}_1, \ldots, \mathbf{r}_N) \in R^{3N} | U(\mathbf{r}_1, \ldots, \mathbf{r}_N) = \langle U \rangle\}$. This is a compact, Riemannian $(3N-1)$-dimensional differentiable manifold. Each state point has its own such hypersurface. In this way, a family of high-dimensional manifolds is defined throughout the phase diagram. In Appendix A of Ref. [21] it was shown that the reduced-unit constant-potential-energy manifold is invariant along a strongly correlating liquid's isomorphs, and that, conversely, invariance curves exist for these manifolds only for strongly correlating liquids. Thus, for such liquids, these manifolds constitute a one-parameter family of manifolds, not two-parameter families as expected from the fact that the phase diagram is two-dimensional. This provides a mathematical characterization of the class of strongly correlating liquids.

The physical characterization of this class was discussed already: A liquid is strongly correlating if and only if it has isomorphs to a good approximation; this is shown in Appendix A of Ref. [21]. The proof utilizes that a liquid is strongly correlating if and only if its constant-virial hypersurfaces in the $3N$-dimensional configuration space are (almost) identical to its constant-potential-energy hypersurfaces.

The chemical characterization of strongly correlating liquids is the property documented in the present paper: A liquid is strongly correlating at a given state point if and only if the liquid's structure and dynamics are accurately calculated by simulations that ignore interactions beyond the first coordination shell. This is an empirical finding for which we have, at present, no compelling argument. How can one justify this FCS characterization of strongly correlating liquids? Note first that the property of insignificance of interactions beyond the FCS is an isomorph invariant: If a liquid has good isomorphs and if a FCS cutoff works well at one state point, FCS cutoffs must work well for all its isomorphic state points. Thus, the chemical characterization of strongly correlating liquids is consistent with the fact that these liquids have isomorphs. Note further that it has been shown for the Lennard-Jones liquid that almost all of the fluctuations in virial and potential energy come from interparticle separations within the FCS [18]. Finally, we give an nonrigorous argument that a SF cutoff works well for any strongly correlating liquid: Consider an atomic liquid with pair interaction $v(r)$ that is strongly correlating at the state point in question. Since virial and potential-energy fluctuations correlate, one can replace $v(r)$ by $\lambda r v'(r)$ where λ is some constant. Thus the radial force $f(r) = -v'(r)$ can be replaced by $-\lambda[rv'(r)]' = \lambda[f(r) + rf'(r)]$. This implies for some constant μ that $f(r) \sim \mu r f'(r)$ where $\sim$ indicates equivalence in MD simulations. Assuming the SF cutoff system is likewise strongly correlating, we get $f_{\mathrm{SF}}(r) \sim \mu r f'_{\mathrm{SF}}(r)$. Since $f'(r) = f'_{\mathrm{SF}}(r)$, one concludes that $f(r) \sim f_{\mathrm{SF}}(r)$.

Most likely it is the existence of a well-defined FCS that implies the almost cancellation of the linear term of the shifted-force potential. The fact that interactions beyond the FCS may be ignored shows that interactions are effectively short ranged, which means that the structure is dominated by what may be termed packing effects.

C. Defining the class of simple liquids

Section IV A listed several simple properties of strongly correlating liquids. Section IV B showed that this liquid class may be characterized from three quite different perspectives. It appears that the class of strongly correlating liquids is fundamental. Since the properties of strongly correlating liquids are generally simpler than those of liquids in general, we now propose the following definition: Simple liquid=strongly correlating liquid. This is the basic message of the present paper, which implies a quantification of the degree of simplicity via the number R of Eq. (2), the NVT ensemble equilibrium virial potential-energy correlation coefficient.

Compared to the standard definition of simple liquids as those with radially symmetric pair interactions, there are some notable differences:

(1) Simplicity is quantified by a continuous variable, it is not an on/off property.
(2) The degree of simplicity generally varies throughout the phase diagram. Consequently, simplicity is not merely encoded in a liquid's intermolecular interactions. In fact, most strongly correlating liquids lose this property as density is lowered and the gas phase is approached.
(3) Not all "atomic" liquids (i.e., with radially symmetric pair interactions) have simple regions in the low-pressure part of the phase diagram (compare the Dzugutov, Lennard-Jones Gaussian, Gaussian core, and molten salt models);
(4) Not all simple liquids are atomic (compare the Wahnstrom OTP and the asymmetric dumbbell models).

According to the new definition of liquid simplicity, the case where the potential energy is an Euler homogeneous function of the particle positions ($R = 1$) sets the gold standard for simplicity. This is consistent with the many simple properties of these liquids. Usually one has in mind IPL systems with pair interactions that scale with the distance as r^{-n}. However, $R = 1$ systems as mentioned also include some with angular dependencies in the potential energy, as long as these scale with distance the same way as all other interactions. Because of the absence of attractions, IPL fluids have no liquid-gas phase transition. In this sense it may seem strange to claim that IPL fluids are the simplest liquids. However, more realistic strongly correlating liquids like the LJ liquid cease to be so when the liquid-vapor coexistence line is approached, showing that this phase transition cannot be understood in the framework of simple

liquids. This contrasts with the liquid-solid phase transition, where, for instance, the fact that the coexistence line for simple liquids is an isomorph—confirmed for the LJ liquid [24]—explains several previously noted regularities [21].

Is the hard-sphere fluid simple? One may define a configurational virial function for this system, but it is not obvious how to define a potential-energy function that is different from zero. Thus, there is no meaningful correlation coefficient R for hard-sphere fluids. On the other hand, the hard-sphere liquid may be regarded as the $n \to \infty$ limit of an IPL liquid, and it is well known that, for instance, the hard-sphere radial distribution function is close to that of, e.g., an r^{-20} IPL liquid at a suitably chosen temperature. This would indicate that hard-sphere liquids are simple, which is consistent with the prevailing point of view. Another interesting case is that of the WCA version of the LJ liquid, which cuts off all attractions by putting the force equal to zero beyond the potential-energy minimum. This liquid is strongly correlating [72]. Despite this, we found in simulations that the WCALJ liquid has somewhat poorer isomorphs than the LJ liquid.

It is possible that the hard-sphere liquid and the WCALJ liquid should be both excluded from the class of simple liquids on the grounds that their potentials are not analytic. For systems interacting via pair potentials, it could make good sense to add the extra requirement that the pair potential is an analytical function of the inverse pair distance, i.e., that an expansion exists of the form $v(r) = \sum_n v_n r^{-n}$. Such an extra analyticity requirement would not exclude any strongly correlating liquids occurring in nature where all potentials are expected to be analytic.

D. Which liquids in the real world are simple?

Real-world liquids may be classified according to the nature of the chemical bonds between the molecules. There are five types of bonds [73], which are listed below with a few typical examples (polymeric systems may be added as a separate class):

(1) Van der Waals bonds (e.g., argon, toluene, butane, etc.);
(2) Metallic bonds (e.g., gold, aluminum, alloys, etc.);
(3) Hydrogen bonds (e.g., water, glycerol, ethanol, etc.);
(4) Ionic bonds (e.g., molten sodium chloride, molten potassium nitrate, room-temperature ionic liquids, etc.);
(5) Covalent bonds (e.g., silica and borate melts, etc.).

Most liquids involve elements of more than one type of chemical bond. For instance, van der Waals forces are present in all liquids; the first class consists merely of those liquids that only have van der Waals forces. Another borderline example is a dipolar organic liquid like di-butylphthalate, where van der Waals as well as Coulomb forces are present; the hydrogen-bonded liquid glycerol also has strong dipolar interactions, i.e., an element of the ionic bonds, etc.

Based on computer simulations and known properties of liquids, we believe that most or all van der Waals and metallic liquids are strongly correlating [14,16,18], i.e., simple. Liquids that are not simple are the hydrogen, ionically, and covalently bonding liquids. In these cases, the virial potential-energy correlations are weakened by the existence of competing interactions, either with different r dependences (the ionically bonding liquids) or because angular and radial forces have different r scaling (the hydrogen and covalently bonded liquids).

Metals play a special role as simple liquids, because their interatomic forces derive from collective interactions between ion cores and free electrons [8]. The resulting interaction is a nondirectional interaction between symmetric ion cores, i.e., these systems are simple in the traditional sense. Preliminary computer simulations show that metals are strongly correlating [17], so metals are also simple in the sense of the present paper. However, not all isomorph invariants are expected to apply for metals. For instance, the electron gas can influence the collective dynamics without any structural and relaxational counterpart [74,75], so isomorph invariance most likely breaks down for these (fast) collective degrees of freedom.

It should be emphasized that the above considerations refer to ambient or moderate pressure conditions. It was recently suggested that all liquids become strongly correlating at high pressure [76]. Thus, e.g., the molten silicates of the Earth's upper mantle are predicted to be simpler than molten silicates at ambient pressure.

E. Liquids near interfaces

It is interesting to consider liquids under more general circumstances, for instance under confinement or generally near interfaces. Liquids near interfaces show rich and complicated behavior. For instance, a liquid confined to the nanoscale may change its dynamic properties several orders of magnitude compared to the bulk system. Predicting these changes is an important challenge relevant for biological systems, engineered devices, etc. Recently, it was shown that some liquids retain bulk liquid behavior in confinement [77–80]. More specifically, it was shown that Rosenfeld's excess entropy scaling in the bulk persists in confinement and is, to a good approximation, independent of the wall-fluid interaction strength. This was shown for LJ and hard-sphere liquids, suggesting the possibility of extending the concept of a simple liquid beyond bulk systems. More work is needed, however, to clarify the relevance and consequences of the present definition of liquid simplicity near interfaces [81,82].

F. A note on complex liquid behavior

Here we give a brief example showing that liquids, which are not simple in the above defined sense, often

have complex properties [65,83–86]. Water with its correlation coefficient close to zero at ambient conditions is a prime example of a complex liquid. It is well known for water that a certain region of state points in the density-temperature phase diagram exhibits anomalous thermodynamic behavior in the sense that isobaric heating implies densification. Numerical evidence indicates that these state points lie within a larger region with a diffusion anomaly, i.e., an increased diffusivity upon isothermal compression [65], a region that, in turn, lies within a larger region of a structural anomaly characterized by decreasing order upon isothermal compression [65].

Different order parameters exist for characterizing the structural order of liquids, some of which relate purely to an integral over the RDF [83–85]. In this way, it is possible to calculate the contribution to structural anomalies from the different coordination shells [83–85]. It has been shown [84,85] that the structural anomaly of water and waterlike liquids is not a ''first-shell effect. Rather, they reflect how structuring in second and more distant coordination shells responds to changes in thermodynamic or system parameters'' [84,85]. Thus, the anomalous behavior of water derives from interactions beyond the FCS [83,85]. This is consistent with the results presented in this paper—water is not simple—since the structure and dynamics of strongly correlating liquids are given exclusively by the interactions within the FCS.

G. To which extent do the assumptions of standard pertubation theory hold?

The finding that the FCS plays a crucial role for a large class of systems may be taken as a modern demonstration of the classic van der Waals picture of liquids, in the sense that such liquids can be understood in terms of packing effects [87]. On the other hand, our results call into question the basis of traditional perturbation theory, which is conceptually also usually traced back to van der Waals [88]. Perturbation theory is based on the assumption of entirely different roles being played by the repulsive and the attractive forces [7,30,81,87–90]: The repulsive forces largely determine the structure and reduce the entropy compared to that of an ideal gas at same density and temperature; the attractive forces reduce the pressure and energy compared to that of an ideal gas. From the findings of this and a previous paper [32] it is clear, however, that this picture applies only at such low pressures that the FCS coincides with the region around the pair-potential minimum. At high pressure, the entire FCS is within the range of the repulsive forces; here, the attractive forces play little role for simple liquids. In general, what is important for a strongly correlating liquid is to take into account properly all forces from particles within the FCS—and only these. Thus, the well-known WCA reference system, which ignores the attractions, is a good reference only at such high pressure that all forces from particles within the FCS are repulsive [26,27,32].

The dominance of the FCS for simple liquids reflects the fundamental physics that the characteristic length defining the pair-potential minimum (e.g., σ of the LJ potential) is much less important than generally believed: σ determines the density of the low-pressure-condensed phase, but for simple liquids that is all. The physically relevant length for these liquids is the one given by the macroscopic density: $\rho^{-1/3}$. At low pressure, this length is roughly that of the potential-energy minimum, thus explaining why the latter has been generally assumed to be important.

The above considerations apply only for simple liquids; in general, both lengths play important roles for the physics. The irrelevance of any length defined by the microscopic potential emphasizes that the class of strongly correlating liquids is at the one end of the ''complexity scale'' where, at the other end, one finds systems like macromolecules, electrolytes, interfaces, micelles, or enzymes, for which multiple length scales are important [91].

V. CONCLUDING REMARKS

If you ask a chemist what is a simple liquid, he or she may likely answer that nonassociated liquids are simple, whereas associated liquids are generally much more complex. These two concepts are defined as follows in Chandler's textbook [13]. The intermolecular structure of a nonassociated liquid ''can be understood in terms of packing. There are no highly specific interactions in these systems.'' In contrast, water is an example of an associated liquid, and its ''linear hydrogen bonding tends to produce a local tetrahedral ordering that is distinct from what would be predicted by only considering the size and shape of the molecule'' [13].

Packing usually refers to purely entropic, hard-sphere-like behavior. Given that no realistic potentials are infinitely repulsive, it makes good sense to interpret packing more generally as all short-ranged effects of the intermolecular interactions. If one accepts this interpretation, the crucial role of the FCS for strongly correlating liquids is consistent with the understanding that the properties of nonassociated liquids can be interpreted in terms of packing: *Once the forces from particles within the FCS are known, basically everything is known.*

In other words, for a simple liquid there are no important long-range interactions, and ''considering the size and shape of the molecule'' [13] is enough to account for the liquid's physical properties. This applies even for the r^{-4} IPL fluid, which one would *a priori* regard as systems with fairly long-ranged interactions.

The present definition of the class of simple liquids is thus consistent with the chemists' general picture of simple liquids. The new definition goes further, however, by quantifying simplicity via the virial potential-energy correlation coefficient R of Eq. (2). In particular, simplicity is

not an on/off property of the potential, but varies continuously with the state point. Thus, even a complex liquid like water is expected to approach simple behavior under sufficiently high pressure [76] and, conversely, the prototype strongly correlating LJ liquid becomes gradually more complex as density is lowered and the critical region and the gas phase are approached. Is this a problem, given that everyone agrees that the gas phase is simple? We do not think so. In fact, the gas phase is simple for an entirely different reason, namely, that molecules move freely most of the time, only interrupted by occasional fast and violent collisions with other molecules. It would be strange if a system exhibiting one form of simplicity could be transformed continuously in the phase diagram, maintaining its simplicity, into a system of an entirely different form of simplicity; one would expect the intermediate phase to be complex.

Liquid simplicity is characterized by the correlation coefficient R of Eq. (2) being close to unity, i.e., that $1 - R$ is a small number. This situation is typical in physics, where simplifying features always appear when some dimensionless number is small. The obvious question arises whether a statistical-mechanical perturbation theory may be constructed around simple liquids, embracing the more complex ones. Only time will tell whether this is possible, but it presents a challenge because the properties of IPL fluids ($R = 1$) cannot be worked out analytically.

A potentially annoying feature of defining liquid simplicity from the existence of strong correlations of the virial potential-energy fluctuations is that one cannot determine whether or not a given liquid is simple directly from the potential. We believe one should accept this as an acceptable cost for precisely defining the class of simple liquids. With the power of today's computers, this is much less of a problem than previously. For most systems, a brief simulation will determine whether or not the liquid is strongly correlating at the state point in question. Nevertheless, it would be nice to have an analytical criterion for liquid simplicity, i.e., for estimating whether $R > 0.9$.

Except for IPL fluids, no system is simple in the entire fluid phase. This paper focused on the condensed liquid phase, not too far from the solid-liquid-coexistence line, but far from the critical point and the gas phase—it is here that some liquids are simple. The present focus on liquids is not meant to imply a limitation to the liquid phase, however. Simulations show that when a strongly correlating liquid crystallizes, the crystal is at least as strongly correlating [18]. A theory has been developed for (classical) strongly correlating crystals, showing that the property of strong virial potential-energy equilibrium fluctuations in the NVT ensemble is an anharmonic effect that survives as $T \to 0$ [18]. Of course, low-temperature crystals are not classical systems, and for both liquids and crystals an interesting topic for future work is the implication of the proposed simplicity definition for the quantum description.

Section IVA summarized the several nominal essences of simple liquids. What is the real essence of liquid simplicity? Given that three fundamental characterizations of strongly correlating liquids are equivalent—the mathematical, the physical, and the new chemical (FCS) characterizations—this question cannot be answered unequivocally. At the end of the day, it is a matter of taste whether one defines liquid simplicity from the existence of strong virial potential-energy correlations, from the existence of isomorphs, from the existence of invariance curves in the phase diagram of constant-potential-energy hypersurfaces, or from the property that interactions beyond the FCS play little role.

ACKNOWLEDGMENTS

We gratefully acknowledge useful input from Livia Bove, Jesper Schmidt Hansen, Peter Harder, Mogens Niss, and Søren Toxværd. The centre for viscous liquid dynamics "Glass and Time" is sponsored by the Danish National Research Foundation (DNRF).

APPENDIX A: MODEL DETAILS

The model systems investigated are listed below. Quantities are given in rationalized units defined by putting $\epsilon = \sigma = 1$. Masses that are not specified are unity.

Single-component inverse-power-law (IPL) fluids.—$N = 1024$ particles interacting via $v(r) = \epsilon(\sigma/r)^n$. Three different fluids were studied ($n = 18, 6, 4$).

Single-component Lennard-Jones liquid.—$N = 1024$ particles interacting via Eq. (4).

Generalized Kob-Andersen binary mixture [28,29].—A binary mixture of 820 A particles and 204 B particles interacting via $v(r) = \epsilon_{\alpha\beta}/(12-n)[n(\sigma_{\alpha\beta}/r)^{12} - 12(\sigma_{\alpha\beta}/r)^n]$. Binary mixtures with $n = 4, 10$ were studied. The parameters used are $\epsilon_{AA} = 1$, $\epsilon_{AB} = 1.5$, $\epsilon_{BB} = 0.5$, $\sigma_{AA} = 2^{1/6}$, $\sigma_{AB} = 0.8 \cdot 2^{1/6}$, $\sigma_{BB} = 0.88 \cdot 2^{1/6}$.

Wahnstrom binary LJ mixture.—An equimolar binary mixture of A and B particles ($N = 1024$) interacting via the LJ potential. The parameters are $\epsilon_{AA} = \epsilon_{AB} = \epsilon_{BB} = 1$, $\sigma_{AA} = 1$, $\sigma_{BB} = 1/1.2$, $\sigma_{AB} = (\sigma_{AA} + \sigma_{BB})/2$, $m_A = 2$, $m_B = 1$.

Buckingham liquid.—$N = 1000$ particles interacting via $v(r) = \epsilon\{6/(\alpha-6)\exp[\alpha(1 - r/r_m)] - \alpha/(\alpha-6) \times (r_m/r)^6\}$. The parameters used are $\epsilon = 1$, $\alpha = 14.5$, $r_m = 2^{1/6}$.

Dzugutov liquid [51].—$N = 1024$ particles interacting via $v(r) = v_1 + v_2$ where $v_1 = \{A(r^{-n} - B)\exp[c/(r-a)]\}$ and $v_2 = B\exp[d/(r-b)]$ and $r \geq a \Rightarrow v_1 = 0$, $r \geq b \Rightarrow v_2 = 0$ ($a < b$). The parameters used are $a = 1.87$, $b = 1.94$, $c = 1.1$, $d = 0.27$, $A = 5.82$, $B = 1.28$, $n = 16$.

Lennard-Jones Gaussian liquid [52].—$N = 1024$ particles interacting via $v(r) = \epsilon\{(\sigma/r)^{12} - 2(\sigma/r)^6 - \epsilon_0 \exp[-(r - r_0)^2/2\sigma_0^2]\}$. The parameters used are $\sigma_0^2 = 0.02$, $\epsilon_0 = 1.50$, $r_0 = 1.47$.

Gaussian core model [52].—$N = 1024$ particles interacting via $v(r) = \epsilon \exp[-(r/\sigma)^2]$.

The Hansen-McDonald molten salt model [57].—$N = 2744$ particles forming an equimolar binary mixture of singly charged cations and anions. The potential between two particles of charge q_α and q_β is given by $v(r) = (1/9)r^{-9} + q_\alpha q_\beta/r$, where $q_+ = 1$, $q_- = -1$.

Lewis-Wahnstrom OTP [58,59].—The Lewis-Wahnstrom OTP model consists of three identical LJ particles rigidly bonded in an isosceles triangle with unity sides and a top angle of 75° (number of molecules studied: $N = 320$).

The asymmetric dumbbell model [19].—This molecular model consists of a large (A) and a small (B) LJ particle, rigidly bonded with a bond distance of 0.29/0.4963 (number of molecules studied: 500). This model has $\sigma_{BB} = 0.391/0.4963$, $\epsilon_{BB} = 0.669\,44/5.726$, and $m_B = 15.035/77.106$. The AB interaction between different molecules is determined by the Lorentz-Berthelot mixing rule.

Rigid SPC/E water [60].—This water model is an isosceles triangle with sides 1/3.166 and base line 0.52 (number of molecules studied: 1000). The oxygen-oxygen intermolecular interactions are given by the LJ pair potential ($\epsilon_{OO} = 1$, $\sigma_{OO} = 1$, and $m_O = 16$). There are no intermolecular LJ interactions for H-H or H-O. The three particles are charged with $q_O = -22.0$ and $q_H = 11.0$.

APPENDIX B: HOW TO DELIMIT THE FIRST COORDINATION SHELL?

In all simulations, the FCS cutoff was defined by placing the cutoff at the first minimum of the RDF, which is the standard definition of the FCS for liquids [13]. An alternative definition goes back to van der Waals [87]. The FCS is here identified with a sphere of radius determined by requiring that the average density $\rho_{\text{integrated}}$ within the FCS equals the overall average density ρ_{mean}. For the single-component LJ liquid, this leads to virtually the same FCS [31]. Some change occurs for the standard KABLJ mixture, however. This is clear from Fig. 20 in which the integrated local density of A particles calculated from the RDF (including the particle at the center) is shown as a function of the distance to the origin. The van der Waals distance is slightly larger than the first minimum of the RDF.

We applied this alternative definition of a FCS cutoff in Fig. 21, which shows the A-particle ISF for the (12, 6)-KABLJ mixture of Fig. 20 simulated with, respectively, a cutoff at the first minimum of the RDF [Fig. 21(a)] and a van der Waals cutoff [Fig. 21(b)]. Although the difference is merely 0.05, the van der Waals cutoff approx-

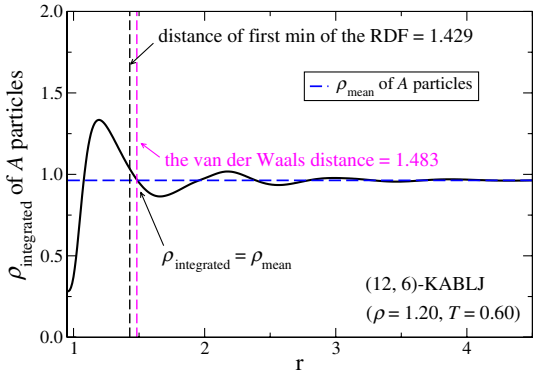

FIG. 20. Integrated local density $\rho_{\text{integrated}}$ of the A particles of the standard KABLJ mixture plotted as a function of distance to the origin (calculated from the A-particle RDF). The dashed black line gives the distance of the minimum of the first peak of the RDF, the dashed magenta line gives the van der Waals distance, i.e., the distance at which the integrated local density equals the overall average density of the system. The horizontal dashed blue line marks the mean density ρ_{mean} of A particles in the simulated system ($\rho_{\text{mean}} = 0.8 * 1.2$).

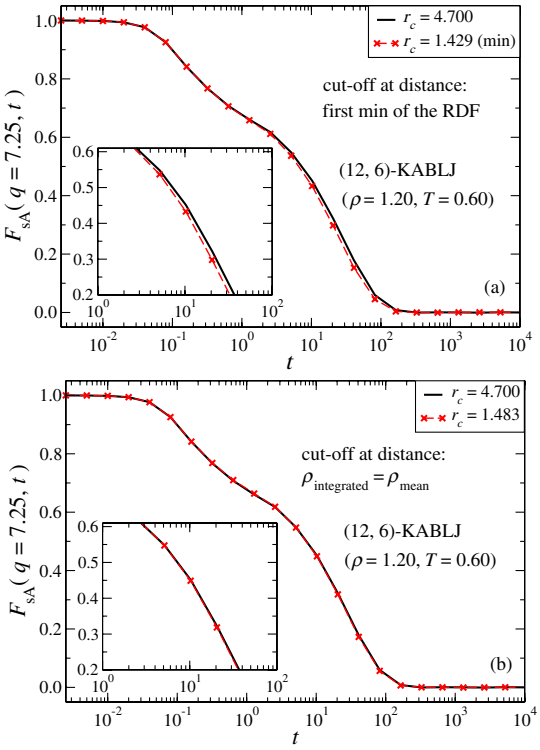

FIG. 21. Effect on the A-particle incoherent ISF for the standard KABLJ mixture of different of ways of delimiting the FCS. (a) FCS identified from the minimum beyond the first peak of the AA-particle RDF. (b) FCS identified by the van der Waals distance, i.e., the distance at which the integrated local density equals the mean density of the system. The van der Waals distance is slightly larger than the RDF minimum. Using this as defining the FCS-cutoff radius gives a better representation of the dynamics.

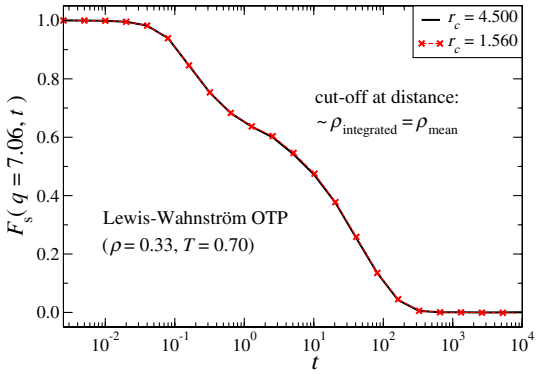

FIG. 22. Results for the incoherent ISF of the Wahnstrom OTP model with a cutoff at $r_c = 1.56$ (red), and a large reference cutoff (black). The deviations of Fig. 17(b), in which $r_c = 1.47$, disappear by choosing this slightly larger cutoff, not far from the van der Waals cutoff (1.53).

imates the reference ISF better than does the RDF minimum cutoff. Thus, it is possible that the van der Waals distance may serve as a better definition of the FCS than the standard FCS definition.

Identifying the exact size of the FCS for molecular systems is less straightforward, especially when different intermolecular interactions are involved. It is noteworthy how well the simple cutoff scheme in Fig. 18 represents the dynamics of the asymmetric dumbbell model. The slight deviations observed for the OTP model [Fig. 17(b)] disappear when the cutoff is increased from $r_c = 1.47$ to $r_c = 1.56$ (Fig. 22). This distance is close, but not identical, to the van der Waals distance calculated from the particle RDF (approximately 1.53). More work is needed to clarify the best way to delimit the FCS and define the FCS cutoff.

[1] Plato, *Statesman (Dialogue), in Plato: Complete Works*, edited by J. M. Cooper and D. S. Hutchinson (Hackett Publishing Co. Inc., Indianapolis, 1997).

[2] Aristotle, Categories (http://www.classicallibrary.org/aristotle/categories/index.htm, 2001).

[3] J. Locke, An Essay Concerning Human Understanding, Book III (http://etext.lib.virginia.edu/modeng/modengL.browse.html, 2002).

[4] http://en.wikipedia.org/wiki/classification.

[5] J. L. Barrat and J. P. Hansen, *Basic Concepts for Simple and Complex Liquids* (Cambridge University Press, Cambridge, 2003).

[6] B. Kirchner, *Theory of Complicated Liquids: Investigation of Liquids, Solvents and Solvent Effects with Modern Theoretical Methods*, Phys. Rep. **440**, 1 (2007).

[7] J. P. Hansen and J. R. McDonald, *Theory of Simple Liquids* (Academic, New York, 2005), 3rd ed.

[8] I. Z. Fisher, *Statistical Theory of Liquids* (University of Chicago, Chicago, 1964).

[9] S. A. Rice and P. Gray, *The Statistical Mechanics of Simple Liquids* (Interscience, New York, 1965).

[10] H. N. V. Temperley, J. S. Rowlinson, and G. S. Rushbrooke, *Physics of Simple Liquids* (Wiley, New York, 1968).

[11] N. K. Ailawadi, *Equilibrium Theories of Classical Fluids*, Phys. Rep. **57**, 241 (1980).

[12] C. G. Gray and K. E. Gubbins, *Theory of Molecular Fluids* (Oxford University, New York 1984).

[13] D. Chandler, *Introduction to Modern Statistical Mechanics* (Oxford University, New York, 1987).

[14] U. R. Pedersen, N. P. Bailey, T. B. Schrøder, and J. C. Dyre, *Strong Pressure-Energy Correlations in van der Waals Liquids*, Phys. Rev. Lett. **100**, 015701 (2008).

[15] U. R. Pedersen, T. Christensen, T. B. Schrøder, and J. C. Dyre, *Feasibility of a Single-Parameter Description of Equilibrium Viscous Liquid Dynamics*, Phys. Rev. E **77**, 011201 (2008).

[16] N. P. Bailey, T. Christensen, B. Jakobsen, K. Niss, N. B. Olsen, U. R. Pedersen, T. B. Schrøder, and J. C. Dyre, *Glass-Forming Liquids: One or More "Order" Parameters?*, J. Phys. Condens. Matter **20**, 244113 (2008).

[17] N. P. Bailey, U. R. Pedersen, N. Gnan, T. B. Schrøder, and J. C. Dyre, *Pressure-Energy Correlations in Liquids. I. Results from Computer Simulations*, J. Chem. Phys. **129**, 184507 (2008).

[18] N. P. Bailey, U. R. Pedersen, N. Gnan, T. B. Schrøder, and J. C. Dyre, *Pressure-Energy Correlations in Liquids. II. Analysis and Consequences*, J. Chem. Phys. **129**, 184508 (2008).

[19] T. B. Schrøder, U. R. Pedersen, N. P. Bailey, S. Toxvaerd, and J. C. Dyre, *Hidden Scale Invariance in Molecular van der Waals Liquids: A Simulation Study*, Phys. Rev. E **80**, 041502 (2009).

[20] T. B. Schrøder, N. P. Bailey, U. R. Pedersen, N. Gnan, and J. C. Dyre, *Pressure-Energy Correlations in Liquids. III. Statistical Mechanics and Thermodynamics of Liquids with Hidden Scale Invariance*, J. Chem. Phys. **131**, 234503 (2009).

[21] N. Gnan, T. B. Schrøder, U. R. Pedersen, N. P. Bailey, and J. C. Dyre, *Pressure-Energy Correlations in Liquids. IV. "Isomorphs" in Liquid Phase Diagrams*, J. Chem. Phys. **131**, 234504 (2009).

[22] N. Gnan, C. Maggi, T. B. Schrøder, and J. C. Dyre, *Predicting the Effective Temperature of a Glass*, Phys. Rev. Lett. **104**, 125902 (2010).

[23] U. R. Pedersen, T. B. Schrøder, and J. C. Dyre, *Repulsive Reference Potential Reproducing the Dynamics of a Liquid with Attractions*, Phys. Rev. Lett. **105**, 157801 (2010).

[24] T. B. Schrøder, N. Gnan, U. R. Pedersen, N. P. Bailey, and J. C. Dyre, *Pressure-Energy Correlations in Liquids. V. Isomorphs in Generalized Lennard-Jones Systems*, J. Chem. Phys. **134**, 164505 (2011).

[25] U. R. Pedersen, N. Gnan, N. P. Bailey, T. B. Schrøder, and J. C. Dyre, *Strongly Correlating Liquids and their Isomorphs*, J. Non-Cryst. Solids **357**, 320 (2011).

[26] L. Berthier and G. Tarjus, *Nonperturbative Effect of Attractive Forces in Viscous Liquids*, Phys. Rev. Lett. **103**, 170601 (2009).

[27] L. Berthier and G. Tarjus, *The Role of Attractive Forces in Viscous Liquids*, J. Chem. Phys. **134**, 214503 (2011).

[28] W. Kob and H. C. Andersen, *Testing Mode-Coupling Theory for a Supercooled Binary Lennard-Jones Mixture I: The van Hove Correlation Function*, Phys. Rev. E **51**, 4626 (1995).

[29] W. Kob and H. C. Andersen, *Testing Mode-Coupling Theory for a Supercooled Binary Lennard-Jones Mixture. II. Intermediate Scattering Function and Dynamic Susceptibility*, Phys. Rev. E **52**, 4134 (1995).

[30] D. Weeks, D. Chandler, and H. C. Andersen, *Role of Repulsive Forces in Determining the Equilibrium Structure of Simple Liquids*, J. Chem. Phys. **54**, 5237 (1971).

[31] S. Toxvaerd and J. C. Dyre, *Communication: Shifted Forces in Molecular Dynamics*, J. Chem. Phys. **134**, 081102 (2011).

[32] S. Toxvaerd and J. C. Dyre, *Role of the First Coordination Shell in Determining the Equilibrium Structure and Dynamics of Simple Liquids*, J. Chem. Phys. **135**, 134501 (2011).

[33] A. Paliwal, D. Asthagir, L. R. Pratt, H. S. Ashbaugh, and M. E. Paulaitis, *An Analysis of Molecular Packing and Chemical Association in Liquid Water Using Quasichemical Theory*, J. Chem. Phys. **124**, 224502 (2006).

[34] M. P. Allen and D. J. Tildesley, *Computer Simulation of Liquids* (Oxford Science Publications, New York, 1987).

[35] T. Ree, H. S. Kang, C. S. Lee, and F. H. Ree, *A Perturbation Theory of Classical Equilibrium Fluids*, J. Chem. Phys. **82**, 414 (1985).

[36] R. W. Hall and P. G. Wolynes, *Intermolecular Forces and the Glass Transition*, J. Phys. Chem. B **112**, 301 (2008).

[37] C. J. Fennell and J. D. Gezelter, *Is the Ewald Summation Still Necessary? Pairwise Alternatives to the Accepted Standard for Long-Range Electrostatics*, J. Chem. Phys. **124**, 234104 (2006).

[38] J. S. Hansen, T. B. Schrøder, and J. C. Dyre, *Simplistic Coulomb Forces in Molecular Dynamics: Comparing the Wolf and Shifted-Force Approximations*, arXiv:1108.5267.

[39] S. Nosé, *A Unified Formulation of the Constant Temperature Molecular Dynamics Methods*, J. Chem. Phys. **81**, 511 (1984).

[40] W. G. Hoover, *Canonical Dynamics: Equilibrium Phase-Space Distributions*, Phys. Rev. A **31**, 1695 (1985).

[41] D. Frenkel and B. Smit, *Understanding Molecular Simulation* (Academic, New York, 2002).

[42] All simulations were performed using a molecular dynamics code for NVIDIA graphics cards, which is available as open source at http://rumd.org.

[43] S. Toxvaerd, *Algorithms for Canonical Molecular Dynamics Simulations*, Mol. Phys. **72**, 159 (1991).

[44] T. Ingebrigtsen, O. J. Heilmann, S. Toxvaerd, and J. C. Dyre, *Time Reversible Molecular Dynamics Algorithms with Holonomic Bond Constraints in the NPH and NPT Ensembles Using Molecular Scaling*, J. Chem. Phys. **132**, 154106 (2010).

[45] S. Toxvaerd, O. J. Heilmann, T. Ingebrigtsen, T. B. Schrøder, and J. C. Dyre, *Time-Reversible Molecular Dynamics Algorithms with Bond Constraints*, J. Chem. Phys. **131**, 064102 (2009).

[46] M. E. Fisher and D. Ruelle, *The Stability of Many-Particle Systems*, J. Math. Phys. (N.Y.) **7**, 260 (1966).

[47] M. Baus and J. P. Hansen, *Statistical Mechanics of Simple Coulomb Systems*, Phys. Rep. **59**, 1 (1980).

[48] G. Wahnström, *Molecular-Dynamics Study of a Supercooled Two-Somponent Lennard-Jones System*, Phys. Rev. A **44**, 3752 (1991).

[49] R. A. Buckingham, *The Classical Equation of State of Gaseous Helium, Neon, and Argon*, Proc. R. Soc. A **168**, 264 (1938).

[50] A. A. Veldhorst, L. Bøhling, J. C. Dyre, and T. B. Schrøder, *Isomorphs in the Phase Diagram of a Model Liquid without Inverse Power Law Repulsion*, Eur. Phys. J. B **85**, 24 (2012).

[51] M. Dzugutov, *Glass Formation in a Simple Monatomic Liquid with Icosahedral Inherent Local Order*, Phys. Rev. A **46**, R2984 (1992).

[52] M. Engel and H. R. Trebin, *Self-Assembly of Monatomic Complex Crystals and Quasicrystals with a Double-Well Interaction Potential*, Phys. Rev. Lett. **98**, 225505 (2007).

[53] V. V. Hoang and T. Odagaki, *Glasses of Simple Liquids with Double-Well Interaction Potential*, Physica B (Amsterdam) **403**, 3910 (2008).

[54] F. H. Stillinger, *Phase Transitions in the Gaussian Core System*, J. Chem. Phys. **65**, 3968 (1976).

[55] F. H. Stillinger and T. A. Weber, *Amorphous State Studies with the Gaussian Core Model*, J. Chem. Phys. **70**, 4879 (1979).

[56] A. Ikeda and K. Miyazaki, *Glass Transition of the Monodisperse Gaussian Core Model*, Phys. Rev. Lett. **106**, 015701 (2011).

[57] J. P. Hansen and I. R. McDonald, *Statistical Mechanics of Dense Ionized Matter. IV. Density and Charge Fluctuations in a Simple Molten Salt*, Phys. Rev. A **11**, 2111 (1975).

[58] G. Wahnström and L. J. Lewis, *Molecular Dynamics Simulation of a Molecular Glass at Intermediate Times*, Physica A (Amsterdam) **201**, 150 (1993).

[59] L. J. Lewis and G. Wahnström, *Molecular-Dynamics Study of Supercooled Ortho-Terphenyl*, Phys. Rev. E **50**, 3865 (1994).

[60] H. J. C. Berendsen, J. R. Grigera, and T. P. Straatsma, *The Missing Term in Effective Pair Potentials*, J. Phys. Chem. **91**, 6269 (1987).

[61] C. M. Roland, S. Hensel-Bielowka, M. Paluch, and R. Casalini, *Supercooled Dynamics of Glass-Forming Liquids and Polymers under Hydrostatic Pressure*, Rep. Prog. Phys. **68**, 1405 (2005).

[62] T. S. Ingebrigtsen, T. B. Schrøder, and J. C. Dyre, *Isomorphs in Model Molecular Liquids*, J. Phys. Chem. B **116**, 1018 (2012).

[63] S. Torquato, T. M. Truskett, and P. G. Debenedetti, *Is Random Close Packing of Spheres Well Defined?* Phys. Rev. Lett. **84**, 2064 (2000).

[64] T. M. Truskett, S. Torquato, and P. G. Debenedetti, *Towards a Quantification of Disorder in Materials: Distinguishing Equilibrium and Glassy Sphere Packings*, Phys. Rev. E **62**, 993 (2000).

[65] J. R. Errington and P. G. Debenedetti, *Relationship between Structural Order and the Anomalies of Liquid Water*, Nature (London) **409**, 318 (2001).

[66] M. S. Shell, P. G. Debenedetti, and A. Z. Panagiotopoulos, *Molecular Structural Order and Anomalies in Liquid Silica*, Phys. Rev. E **66**, 011202 (2002).

[67] J. R. Errington, P. G. Debenedetti, and S. Torquato, *Quantification of Order in the Lennard-Jones System*, J. Chem. Phys. **118**, 2256 (2003).

[68] K. L. Ngai, R. Casalini, S. Capaccioli, M. Paluch, and C. M. Roland, *Do Theories of the Glass Transition, in which the Structural Relaxation Time Does not Define the Dispersion of the Structural Relaxation, Need Revision?* J. Phys. Chem. B **109**, 17356 (2005).

[69] T. S. Ingebrigtsen, L. Bøhling, T. B. Schrøder, and J. C. Dyre, *Communication: Thermodynamics of Condensed Matter with Strong Pressure-Energy Correlations*, J. Chem. Phys. **136**, 061102 (2012).

[70] S. A. Khrapak and G. E. Morfill, *Accurate Freezing and Melting Equations for the Lennard-Jones System*, J. Chem. Phys. **134**, 094108 (2011).

[71] L. Bøhling, T. S. Ingebrigtsen, A. Grzybowski, M. Paluch, J. C. Dyre, and T. B. Schrøder, *Beyond Power-Law Density Scaling: Theory, Simulation, and Experiment*, arXiv:1112.1602.

[72] D. Coslovich and C. M. Roland, *Density Scaling in Viscous Liquids: From Relaxation Times to Four-Point Susceptibilities*, J. Chem. Phys. **131**, 151103 (2009).

[73] L. Pauling, *The Nature of the Chemical Bond* (Cornell University, Ithaca, 1939).

[74] L. E. Bove, F. Sacchetti, C. Petrillo, B. Dorner, F. Formisano, and F. Barocchi, *Neutron Investigation of the Ion Dynamics in Liquid Mercury: Evidence for Collective Excitations*, Phys. Rev. Lett. **87**, 215504 (2001).

[75] C. Petrillo, F. Sacchetti, E. Guarini, L. E. Bove, and F. Demmel, *Collective Modes in a Saturated Lithium-Ammonia Solution as a Probe of the Response of the Low-Density Homogeneous Electron Gas*, Phys. Rev. B **84**, 094206 (2011).

[76] J. J. Papini, T. B. Schrøder, and J. C. Dyre, *Do All Liquids Become Strongly Correlating at High Pressure?* arXiv:1103.4954.

[77] J. Mittal, J. R. Errington, and T. M. Truskett, *Thermodynamics Predicts How Confinement Modifies the Dynamics of the Equilibrium Hard-Sphere Fluid*, Phys. Rev. Lett. **96**, 177804 (2006).

[78] J. Mittal, J. R. Errington, and T. M. Truskett, *Relationships Between Self-Diffusivity, Packing Fraction, and Excess Entropy in Simple Bulk and Confined Fluids*, J. Phys. Chem. B **111**, 10054 (2007).

[79] G. Goel, W. P. Krekelberg, J. R. Errington, and T. M. Truskett, *Tuning Density Profiles and Mobility of Inhomogeneous Fluids*, Phys. Rev. Lett. **100**, 106001 (2008).

[80] R. Chopra, T. M. Truskett, and J. R. Errington, *Excess-Entropy Scaling of Dynamics for a Confined Fluid of Dumbbell-Shaped Particles*, Phys. Rev. E **82**, 041201 (2010).

[81] J. D. Weeks, K. Vollmayr, and K. Katsov, *Intermolecular Forces and the Structure of Uniform and Nonuniform Fluids*, Physica A (Amsterdam) **244**, 461 (1997).

[82] J. D. Weeks, *Connecting Local Structure to Interface Formation: A Molecular Scale van der Waals Theory of Nonuniform Liquids*, Annu. Rev. Phys. Chem. **53**, 533 (2002).

[83] Z. Yan, S. V. Buldyrev, P. Kumar, N. Giovambattista, P. G. Debenedetti, and H. E. Stanley, *Structure of the First- and Second-Neighbor Shells of Simulated Water: Quantitative Relation to Translational and Orientational Order*, Phys. Rev. E **76**, 051201 (2007).

[84] W. P. Krekelberg, J. Mittal, V. Ganesan, and T. M. Truskett, *How Short-Range Attractions Impact the Structural Order, Self-Diffusivity, and Viscosity of a Fluid*, J. Chem. Phys. **127**, 044502 (2007).

[85] W. P. Krekelberg, J. Mittal, V. Ganesan, and T. M. Truskett, *Structural Anomalies of Fluids: Origins in Second and Higher Coordination Shells*, Phys. Rev. E **77**, 041201 (2008).

[86] W. Hujo, B. S. Jabes, V. K. Rana, C. Chakravarty, and V. Molinero, *The Rise and Fall of Anomalies in Tetrahedral Liquids*, J. Stat. Phys. **145**, 293 (2011).

[87] J. S. Rowlinson and B. Widom, *Molecular Theory of Capillarity* (Clarendon, Oxford, 1982).

[88] B. Widom, *Intermolecular Forces and the Nature of the Liquid State*, Science **157**, 375 (1967).

[89] J. A. Barker and D. Henderson, *What is "Liquid"? Understanding the States of Matter*, Rev. Mod. Phys. **48**, 587 (1976).

[90] S. Zhou and J. R. Solana, *Progress in the Perturbation Approach in Fluid and Fluid-Related Theories*, Chem. Rev. **109**, 2829 (2009).

[91] B. Bagchi and C. Chakravarty, *Interplay Between Multiple Length and Time Scales in Complex Chemical Systems*, J. Chem. Sci. **122**, 459 (2011).

IOP FTC

IOP PUBLISHING JOURNAL OF PHYSICS: CONDENSED MATTER

J. Phys.: Condens. Matter **25** (2013) 032101 (5pp) doi:10.1088/0953-8984/25/3/032101

FAST TRACK COMMUNICATION

Do the repulsive and attractive pair forces play separate roles for the physics of liquids?

Lasse Bøhling, Arno A Veldhorst, Trond S Ingebrigtsen, Nicholas P Bailey, Jesper S Hansen, Søren Toxvaerd, Thomas B Schrøder and Jeppe C Dyre

DNRF Centre 'Glass and Time', IMFUFA, Department of Sciences, Roskilde University, Postbox 260, DK-4000 Roskilde, Denmark

E-mail: dyre@ruc.dk

Received 2 November 2012, in final form 29 November 2012
Published 18 December 2012
Online at stacks.iop.org/JPhysCM/25/032101

Abstract

According to standard liquid-state theory repulsive and attractive pair forces play distinct roles for the physics of liquids. This paradigm is put into perspective here by demonstrating a continuous series of pair potentials that have virtually the same structure and dynamics, although only some of them have attractive forces of significance. Our findings reflect the fact that the motion of a given particle is determined by the total force on it, whereas the quantity usually discussed in liquid-state theory is the individual pair force.

(Some figures may appear in colour only in the online journal)

A liquid is held together by attractions between its molecules. At the same time, it is very difficult to compress a liquid because the molecules strongly resist closely approaching each other. These facts have been known for a long time, and today it is conventional wisdom that the repulsive and the attractive forces play distinct roles for the physics of liquids. The repulsive forces, which ultimately derive from the Fermi statistics of electrons, are harsh and short ranged. According to standard theory these forces are responsible for the structure and, in particular, for reducing considerably the liquid's entropy compared to that of an ideal gas at the same density and temperature. The attractive forces, on the other hand, are long ranged and weaker. These forces, which derive from induced dipolar interactions, reduce the pressure and energy compared to that of an ideal gas at the same density and temperature. We argue below that this physical picture, though quite appealing, overemphasizes the individual pair forces and does not provide a full understanding because it does not relate directly to the total force on a given particle.

The traditional understanding of the liquid state is based on pioneering works by Frenkel, Longuet-Higgins and Widom, Barker and Henderson, and Weeks, Chandler, and Andersen (WCA), and many others [1, 2]. The basic idea is that the attractions may be regarded as a perturbation of a Hamiltonian based on the repulsive forces, the physics of which is usually well represented by a hard-sphere reference system [3]. Perturbation theories based on this picture [1–4] are standard for calculating simple liquids' thermodynamics and structure as quantified, e.g., by the radial distribution function. We do not question the usefulness of perturbation theories, but will argue from theory and simulations that the repulsive and the attractive pair forces do not always play clearly distinguishable roles for the structure and dynamics of simple liquids.

This point is illustrated in the simplest possible way by studying systems of Lennard-Jones (LJ) particles. The LJ pair potential is given by $v_{\mathrm{LJ}}(r) = 4\varepsilon[(r/\sigma)^{-12} - (r/\sigma)^{-6}]$. This function is plotted in figure 1 for a number of different choices of the parameters ϵ and σ. In the following we adopt the unit system in which $\epsilon_0 = \sigma_0 = 1$ and $k_{\mathrm{B}} = 1$. We use the same unit system for all the potentials. Consider a simulation of the potential with $(\epsilon, \sigma) = (1.25, 0.947)$ at the state point

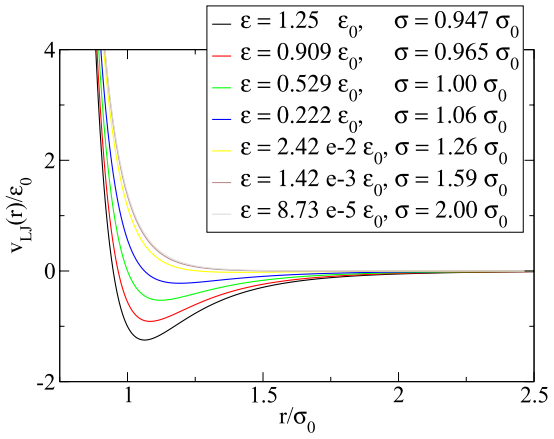

Figure 1. Lennard-Jones pair potentials $v_{\mathrm{LJ}}(r) = 4\varepsilon\,[(r/\sigma)^{-12} - (r/\sigma)^{-6}]$ predicted to give virtually the same physics at the state point $(\rho, T) = (1, 1)$ using the unit system defined by $\epsilon_0 = \sigma_0 = 1$ and $k_{\mathrm{B}} = 1$. Visually, these potentials have little in common; in particular, they have very different contributions from attractive forces. These pair potentials were constructed analytically using the isomorph theory, as detailed in the text after figure 2.

$(\rho \equiv N/V, T) = (1, 1)$. Clearly, it would lead to exactly the same structure and dynamics (after appropriate rescaling) doing a simulation of the potential with $(\epsilon, \sigma) = (8.73 \times 10^{-5}, 2.0)$ at the temperature $T = 8.73 \times 10^{-5}/1.25$ and the density $\rho = (0.947/2.00)^3$—this simply reflects the fact that the physics is determined by the two dimensionless parameters T/ϵ and $\sigma^3\rho$. We show below however that, in addition to this trivial fact, the two potentials also give (to a good approximation) the same structure and dynamics when *both* potentials are investigated at the state point $(\rho, T) = (1, 1)$. In fact, all the potentials in figure 1 were chosen to give virtually the same structure and dynamics at the state point $(\rho, T) = (1, 1)$. The paper mainly focuses on this state point, but results for a few other state points are also given, confirming the findings at $(\rho, T) = (1, 1)$.

The potentials of figure 1 all have attractive forces, but for some of the potentials the attractive forces are entirely insignificant. To show that these potentials nevertheless have virtually the same structure and dynamics, *NVT* computer simulations of systems of 1000 particles were performed using the RUMD software that runs on graphics processing units [5].

Figure 2(a) shows the radial distribution function $g(r)$ for the seven LJ pair potentials of figure 1 at the state point $(\rho, T) = (1, 1)$. For comparison, simulations at the same state point are shown in figure 2(b) for seven potentials with the same ε variation, but fixed $\sigma = 0.947$. Figure 2(c) shows the radial distribution functions at the state point (1, 1) for the pair potentials of figure 1 cut off according to the Weeks–Chandler–Andersen (WCA) recipe, i.e., by cutting the potentials at their minima and shifting them to zero there.

Figure 3 shows results for the dynamics, with (a) giving the mean-square displacement for the seven potentials of figure 1. Figure 3(b) compares the results for the diffusion constants with those of WCA simulations.

By the Henderson uniqueness theorem [6] the pair potentials of figure 1 cannot have exactly the same pair

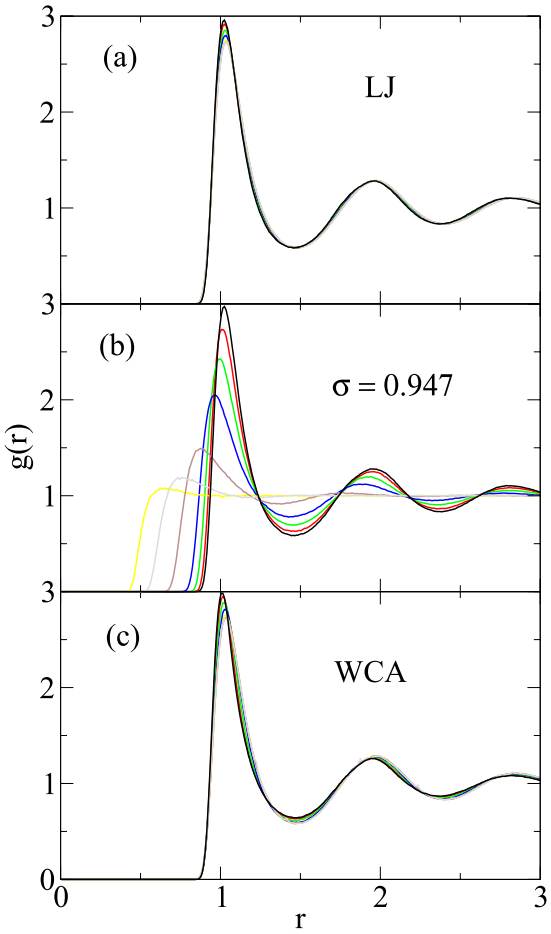

Figure 2. Radial distribution functions at the state point $(\rho, T) = (1, 1)$ for different sets of potentials: (a) the LJ pair potentials of figure 1; (b) a series of LJ pair potentials with fixed σ parameter and the ϵ-values listed in figure 1; (c) results for the series of Weeks–Chandler–Andersen (WCA) potentials corresponding to the LJ potentials of figure 1.

distribution functions. Based on figures 2 and 3 we see that, nevertheless, the potentials lead to very similar structure and very similar dynamics. In fact, both structure and dynamics among the potentials of figure 1 are closer to each other than to the WCA versions of the same potentials.

How were the pair potentials of figure 1 determined and why do they have almost the same structure and dynamics? The starting point is the existence of isomorphs in the phase diagram of liquids with strong correlations between *NVT* virial and potential-energy equilibrium fluctuations [7, 8] (which we recently argued provides a useful definition of a simple liquid [9]). Two state points with density and temperature (ρ_1, T_1) and (ρ_2, T_2) are termed isomorphic [7] if all pairs of physically relevant microconfigurations of the two state points, which trivially scale into one another, i.e., $\rho_1^{1/3}\mathbf{r}_i^{(1)} = \rho_2^{1/3}\mathbf{r}_i^{(2)}$ for all particles i, have proportional configurational Boltzmann factors: $\exp[-U(\mathbf{r}_1^{(1)}, \ldots, \mathbf{r}_N^{(1)})/k_{\mathrm{B}}T_1] = C_{12}\exp[-U(\mathbf{r}_1^{(2)}, \ldots, \mathbf{r}_N^{(2)})/k_{\mathrm{B}}T_2]$ in which the constant of proportionality is independent of the microconfiguration.

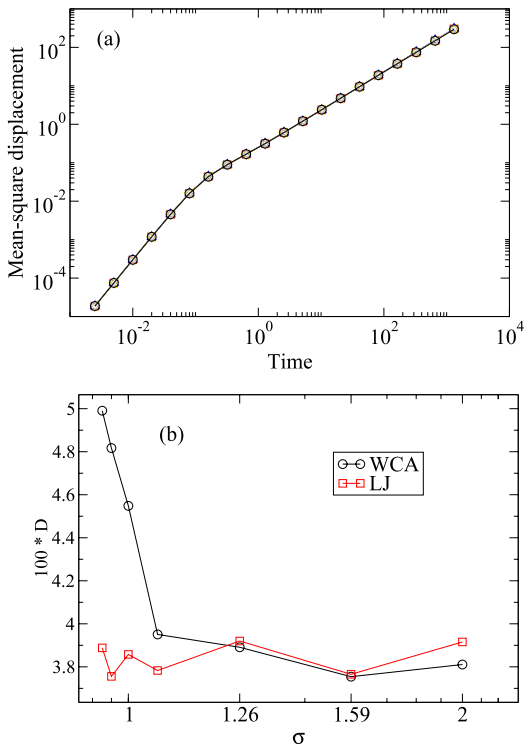

Figure 3. (a) The mean-square displacement for the LJ pair potentials of figure 1 at the state point $(\rho, T) = (1, 1)$. (b) Diffusion constants as functions of σ for the full potentials of figure 1 (red) and for the WCA versions of the potentials (black). At high σ the WCA results are accurate because these potentials are almost purely repulsive.

LJ systems are strongly correlating and thus have isomorphs to a good approximation [8]. The invariance of the canonical probabilities of scaled configurations along an isomorph has several implications [7]. Excess entropy and isochoric specific heat are both isomorph invariant, the dynamics in reduced units are invariant for both Newtonian and Brownian equations of motion, reduced-unit static density correlation functions are invariant, a jump between two isomorphic state points takes the system instantaneously to equilibrium, etc. For Newtonian dynamics, using reduced units corresponds to measuring length in units of $\rho^{-1/3}$, time in units of $\rho^{-1/3}\sqrt{m/k_BT}$ where m is the particle mass, and energy in units of k_BT. Thus the reduced particle coordinates are defined by $\tilde{\mathbf{r}}_i = \rho^{1/3}\mathbf{r}_i$.

An isomorph was generated using the recently derived result [10] that liquids with good isomorphs have simple thermodynamics in the sense that the temperature is a product of a function of excess entropy per particle s and a function of density,

$$T = f(s)h(\rho). \tag{1}$$

The function $h(\rho)$ inherits the analytical structure of the pair potential in the sense that, if the latter is given by the expression $v(r) = \sum_n v_n r^{-n}$, then $h(\rho) = \sum_n C_n \rho^{n/3}$, in which each term corresponds to a term in the pair potential [10]. Since $h(\rho)$ is only defined within an overall

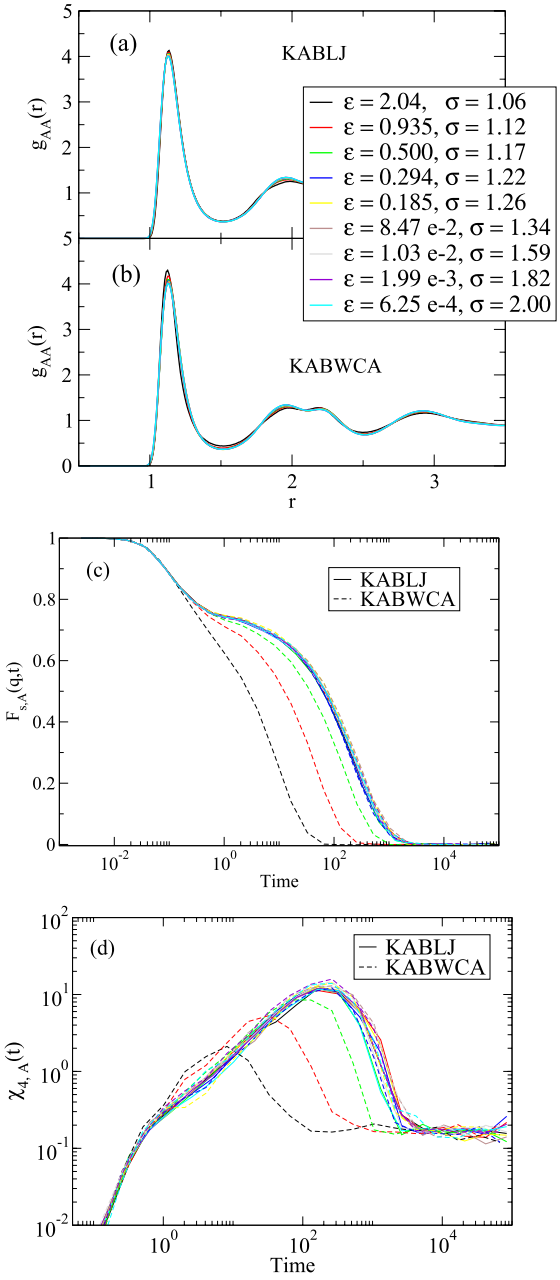

Figure 4. (a) The AA particle radial distribution function of the Kob–Andersen binary Lennard-Jones (KABLJ) mixture for a family of isomorphic pair potentials similar to those of figure 1. (b) The AA particle radial distribution function of the KABLJ mixture with the corresponding WCA potentials. (c) The A particle incoherent intermediate scattering function for the same family of potentials as a function of time at the wavevector defined from the maximum of $g(r)$ (full curves). The full dotted curves show the WCA predictions [12]. (d) The function $\chi_4(t)$ for the A particles for the same pair potentials (full curves) and the WCA predictions (dashed curves).

multiplicative constant, one can write for the LJ pair potential

$$h(\rho) = \alpha\rho^4 + (1-\alpha)\rho^2. \tag{2}$$

The constant α was determined from simulations at the state point $(\rho, T) = (1, 1)$ for $\varepsilon = 1.25$ and $\sigma = 0.947$, which is

a typical liquid state point of the LJ system. This was done by proceeding as follows [11]. We have previously [7, 10] derived the identities

$$\gamma \equiv \left(\frac{\partial \ln T}{\partial \ln \rho}\right)_{S_{ex}} = \frac{\mathrm{d}\ln h}{\mathrm{d}\ln \rho} = \frac{\langle \Delta W \Delta U\rangle}{\langle (\Delta U)^2\rangle}, \qquad (3)$$

in which W is the virial, U the potential energy, and the angular brackets denote NVT equilibrium ensemble averages. Combining equations (2) and (3) with the simulation results for the fluctuations of W and U leads to $\alpha = \gamma/2 - 1 = 1.85$.

An isomorph is a set of state points with almost the same structure and dynamics in reduced units [7]. Via appropriate rescaling, however, an isomorph can be interpreted differently: as defining a set of *different* LJ pair potentials that give invariant properties at the *same state point*. These are simply two different ways of looking at an invariant Boltzmann factor: equation (1) implies that $\exp\left(-U(\rho^{-1/3}\tilde{\mathbf{r}}_1, \ldots, \rho^{-1/3}\tilde{\mathbf{r}}_N)/[f(s)h(\rho)]\right) = \exp(-[1/f(s)]\sum_{i<j} v_{\mathrm{LJ}}(\rho^{-1/3}\tilde{r}_{ij})/h(\rho))$, where r_{ij} is the distance between particles i and j. Along an isomorph $f(s)$ is a constant; if we consider the isomorph which includes the state point $\rho = T = 1$, then given the normalization of equation (2) we have $f(s) = 1$. The shift in interpretation now comes by noticing that the same Boltzmann factor is obtained by considering a configuration at unit density and unit temperature and a family of *isomorphic pair potentials* $v_{\mathrm{LJ}}^d(r) \equiv v_{\mathrm{LJ}}\left(d^{-1/3}r\right)/h(d)$, where we have dropped the tilde from positions and replaced ρ with d to emphasize the shift in perspective. These pair potentials are still LJ potentials, but with different energy and length parameters; the potentials plotted in figure 1 were arrived at in this way.

The single-component LJ system does not have a broad dynamic range because it cannot be deeply supercooled. To test the robustness of the predicted invariance of the physics for families of 'isomorphic' pair potentials, we simulated also the Kob–Andersen binary LJ (KABLJ) mixture [13], which is easily supercooled into a highly viscous state. For this system the constant $\alpha = 1.29$ was identified from simulations of 1000 particles at the state point $(\rho, T) = (1.60, 2.00)$, using again equation (3). From the function $h(\rho)$ a family of isomorphic equivalent pair potentials was generated that looks much like those of figure 1; in particular, some of them have a vanishingly small attraction.

Figure 4(a) shows the AA particle radial distribution functions for these different pair potentials and figure 4(b) shows the same quantity for the WCA version of the potentials. Figure 4(c) shows the A particle incoherent intermediate scattering function and, with dashed lines, simulations of the corresponding WCA systems. Even though the WCA approximation has the correct repulsive forces, its physics differs considerably from the isomorphic pair potentials, as noted already by Berthier and Tarjus [12]. We also calculated $\chi_4(t)$, a measure of dynamic heterogeneities. The results shown in figure 4(d) are more noisy, but confirm the predicted invariance of the dynamics for the different pair potentials. The corresponding WCA results are shown with dashed lines.

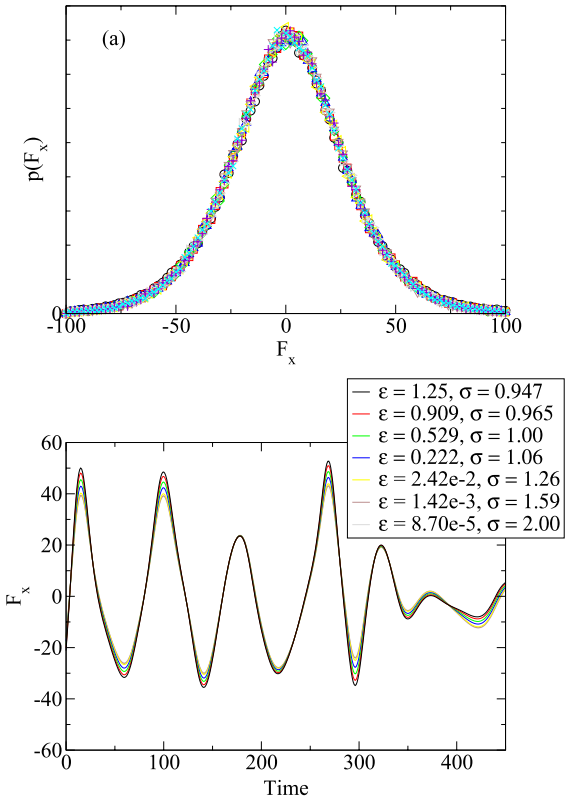

Figure 5. (a) Probability distribution of x-components of the total forces on individual particles, $p(F_x)$, for the different single-component LJ potentials of figure 1 at the state point $(\rho, T) = (1, 1)$. (b) Snapshot of the x-component of the force F_x on one particle as a function of time. The system simulated is defined by $\varepsilon = 1.25$ and $\sigma = 0.947$, and F_x was subsequently evaluated for the same series of configurations for the six other potentials. These figures show that, even though the pair potentials are quite different, the forces are virtually identical except at the extrema.

It would require extraordinary abilities to know from inspection of figure 1 that these pair potentials have virtually the same structure and dynamics. The potentials have neither the repulsive nor the attractive terms in common, so why is it that they have such similar behavior? The answer is that they result in virtually the same forces (figure 5). The force on a given particle is the *sum* of contributions from (primarily) its nearest neighbors, and plotting merely the pair potential can be misleading. We conclude that, by reference to the pair potential alone, one cannot identify separate roles for the repulsive and the attractive forces in a many-particle system. There simply are no 'repulsive' and 'attractive' forces as such.

The above reported simulations focused for each system on one particular state point. If the potentials in figure 1 are to be regarded as equivalent with respect to structure and dynamics, however, one should also test other state points. We have done this briefly, and the results are shown in figure 6. Clearly, the degree of similarity observed at the state point $(\rho, T) = (1, 1)$ is also maintained for the other state points (for comparison, figure 6(c) reproduces the $(\rho, T) = (1, 1)$ results from figure 2(a)).

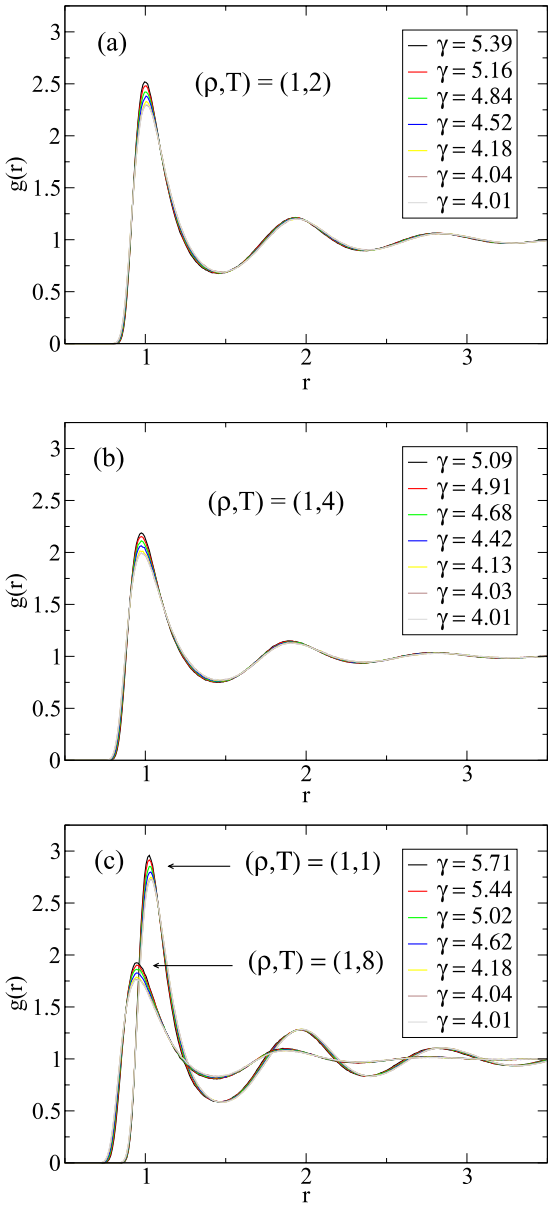

Figure 6. Radial distribution functions for the potentials of figure 1 at other state points than the state point $(\rho, T) = (1, 1)$ studied above. For reference we give in each subfigure the value of γ defined in equation (3). (a) $(\rho, T) = (1, 2)$; (b) $(\rho, T) = (1, 4)$; (c) $(\rho, T) = (1, 8)$—the γ-values reported in this subfigure are those of the state point $(\rho, T) = (1, 1)$.

What are the implications of the above results? For liquid-state perturbation theory the WCA theory is rightfully renowned for its ability to make semi-analytic predictions for thermodynamic properties of simple liquids. The focus of liquid-state theory has moved on, however, in part because modern computers make it straightforward to simulate the kinds of liquid for which WCA theory can make accurate predictions. We do not claim to have a better way to do perturbation theory in the sense of WCA. While WCA theory is based upon an *assumed* equivalence between two potentials differing by the removal of attractions, the present work describes a *predicted and observed* equivalence between apparently quite different potentials. This observation will not facilitate perturbation theory, but it could potentially be useful as a check on perturbation theories and other theories of the liquid state, for example density functional theory; such theories should be consistent with the observed invariance as the parameters of the potential are changed.

The center for viscous liquid dynamics 'Glass and Time' is sponsored by the Danish National Research Foundation (DNRF).

References

[1] Frenkel J 1955 *Kinetic Theory of Liquids* (New York: Dover)
Fisher I Z 1964 *Statistical Theory of Liquids* (Chicago, IL: University of Chicago)
Rice S A and Gray P 1965 *The Statistical Mechanics of Simple Liquids* (New York: Interscience)
Temperley H N V, Rowlinson J S and Rushbrooke G S 1968 *Physics of Simple Liquids* (New York: Wiley)
Hansen J P and McDonald J R 2005 *Theory of Simple Liquids* (New York: Academic)
[2] Longuet-Higgins H C and Widom B 1964 *Mol. Phys.* **8** 549
Barker J A and Henderson D 1967 *J. Chem. Phys.* **47** 4714
Widom B 1967 *Science* **157** 375
Neece G A and Widom B 1969 *Annu. Rev. Phys. Chem.* **20** 167
Weeks D, Chandler D and Andersen H C 1971 *J. Chem. Phys.* **54** 5237
Barker J A and Henderson D 1976 *Rev. Mod. Phys.* **48** 587
Chandler D, Weeks J D and Andersen H C 1983 *Science* **220** 787
[3] Zwanzig R W 1954 *J. Chem. Phys.* **22** 1420
[4] Sarkisov G N 1999 *Phys.—Usp.* **42** 545
Zhou S and Solana J R 2009 *Chem. Rev.* **109** 2829
[5] http://rumd.org
[6] Henderson R L 1974 *Phys. Lett.* A **49** 197
[7] Gnan N *et al* 2009 *J. Chem. Phys.* **131** 234504
[8] Pedersen U R *et al* 2008 *Phys. Rev. Lett.* **100** 015701
Bailey N P *et al* 2008 *J. Chem. Phys.* **129** 184508
Gnan N *et al* 2010 *Phys. Rev. Lett.* **104** 125902
Pedersen U R *et al* 2010 *Phys. Rev. Lett.* **105** 157801
[9] Ingebrigtsen T S, Schrøder T B and Dyre J C 2012 *Phys. Rev.* X **2** 011011
[10] Ingebrigtsen T S, Bøhling L, Schrøder T B and Dyre J C 2012 *J. Chem. Phys.* **136** 061102
[11] Bøhling L, Ingebrigtsen T S, Grzybowski A, Paluch M, Dyre J C and Schrøder T B 2012 *New J. Phys.* **14** 113035
[12] Berthier L and Tarjus G 2009 *Phys. Rev. Lett.* **103** 170601
Berthier L and Tarjus G 2011 *J. Chem. Phys.* **134** 214503
[13] Kob W and Andersen H C 1994 *Phys. Rev. Lett.* **73** 1376

THE JOURNAL OF PHYSICAL CHEMISTRY B

ARTICLE

pubs.acs.org/JPCB

Isomorphs in Model Molecular Liquids

Trond S. Ingebrigtsen,* Thomas B. Schrøder, and Jeppe C. Dyre

DNRF Centre "Glass and Time", IMFUFA, Department of Sciences, Roskilde University, Postbox 260, DK-4000 Roskilde, Denmark

ABSTRACT: Isomorphs are curves in the phase diagram along which a number of static and dynamic quantities are invariant in reduced units (Gnan, N.; et al. *J. Chem. Phys.* **2009**, *131*, 234504). A liquid has good isomorphs if and only if it is strongly correlating, i.e., if the equilibrium virial/potential energy fluctuations are more than 90% correlated in the *NVT* ensemble. Isomorphs were previously discussed with a focus on atomic systems. This paper generalizes isomorphs to liquids composed of rigid molecules and study the isomorphs of systems of small rigid molecules: the asymmetric dumbbell model, a symmetric inverse power-law dumbbell, and the Lewis–Wahnström *o*-terphenyl (OTP) model. For all model systems, the following quantities are found to a good approximation to be invariant along an isomorph: the isochoric heat capacity, the excess entropy, the reduced molecular center-of-mass self-part of the intermediate scattering function, and the reduced molecular center-of-mass radial distribution function. In agreement with theory, we also find that an instantaneous change of temperature and density from an equilibrated state point to an isomorphic state point leads to no relaxation. The isomorphs of the Lewis–Wahnström OTP model were found to be more approximative than those of the asymmetric dumbbell model; this is consistent with the OTP model being less strongly correlating. The asymmetric dumbbell and Lewis–Wahnström OTP models each have a "master isomorph"; i.e., the isomorphs have identical shape in the virial/potential energy phase diagram.

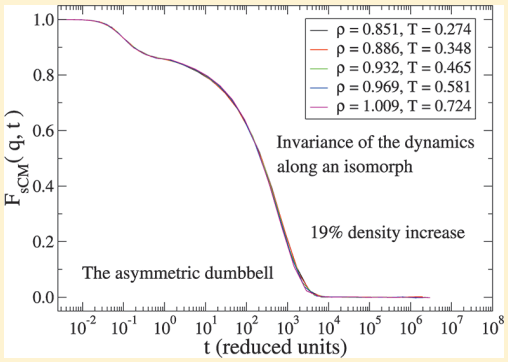

I. INTRODUCTION

For supercooled liquids near the glass transition changing slightly the density ρ or temperature T the structural relaxation time τ_α may change several orders of magnitude. In the study of these liquids[1−3] it is often found that τ_α does not change when ρ^γ/T is kept constant, where γ is a material-specific exponent. This phenomenon is called *density scaling* (or *thermodynamic scaling*) and has been established for many liquids, excluding associative liquids such as water.[3] A related observation is *isochronal superposition*,[3−5] i.e., that supercooled state points with identical τ_α have the same dielectric spectrum. A different and at first sight unrelated concept is *Rosenfeld's excess entropy scaling*.[6,7] In this procedure a relation is established between hard-to-predict dynamic properties and easier-to-predict thermodynamic quantities, here the excess entropy, via a scaling of the dynamics to so-called reduced units. Initially, this was observed for model atomic liquids,[6,7] but later it was extended to model molecular liquids[8−10] and experimental liquids.[11−14] The importance of using reduced units with regards to density scaling of experimental data has recently been pointed out.[15,16]

In a recent series of papers[17−21] a new class of liquids was identified. These liquids are characterized by having strong correlation in the *NVT* ensemble between the equilibrium fluctuations of the potential energy U and the virial W. Recall that the instantaneous energy E and pressure p can be written as a sum of a kinetic part and a configurational part: $E = K + U$ and $pV = Nk_BT + W$, respectively. The correlation between U and W is quantified via the linear correlation coefficient R defined as

$$R = \frac{\langle \Delta W \Delta U \rangle}{\sqrt{\langle (\Delta W)^2 \rangle}\sqrt{\langle (\Delta U)^2 \rangle}} \tag{1}$$

The class of strongly correlating liquids is defined by $R \geq 0.90$.[17] An inverse power-law (IPL) system r^{-n} has correlation coefficient $R = 1$, because for all microconfigurations $W = (n/3)U$, and only IPL systems are perfectly correlating. In the study of strongly correlating liquids it was discovered that they obey Rosenfeld's excess entropy scaling, isochronal superposition, as well as density scaling.[20−23] These types of scalings can be explained in the framework of so-called isomorphs (definition follows later).

Model systems that have been identified[17,18,22,24−26] to belong to this class of liquids include the standard single-component Lennard-Jones liquid (SCLJ), the Kob–Andersen binary LJ mixture[27,28] (KABLJ), the asymmetric dumbbell model,[22] the Lewis–Wahnström *o*-terphenyl model[29,30] (OTP), and others. Strong *WU* correlation has been experimentally verified for a molecular van der Waals liquid[31] and for supercritical argon.[24] The class of strongly correlating liquids includes most or all van der Waals and metallic liquids, whereas covalently, hydrogen-bonding, or ionic liquids are generally not strongly correlating.[17] The latter

Received: August 12, 2011
Revised: October 25, 2011
Published: January 17, 2012

reflects the fact that competing interactions tend to destroy the strong correlation.

An example of strong *WU* correlation is given in Figure 1 for the asymmetric dumbbell model[22] (details of this model are provided in section III). Figure 1a shows the time evolution of the equilibrium fluctuations of U and W normalized to zero mean and unity standard deviation; Figure 1b shows a scatter plot of the corresponding values of U and W. U and W are clearly strongly correlated in their equilibrium fluctuations.

References 17 and 18 identified the cause of strong *WU* correlation in the SCLJ liquid. The LJ pair potential can be well approximated from $r = 0.95\sigma$ to $r = 1.5\sigma$ (Pedersen et al.[23]) by a sum of an IPL, a linear term, and a constant via the so-called "extended IPL potential":[18] $v_{LJ}(r) \approx Ar^{-n} + B + Cr$. At moderate pressures this covers the entire first peak of the radial distribution function, i.e., the first coordination shell. The constraint of constant volume in the *NVT* ensemble has the effect that when one nearest neighbor distance increases, another one decreases; upon summation the contribution from the linear term to U and W is almost constant. The latter observation has the consequence that some of the scaling properties of pure IPL systems are inherited in the LJ system in the form of isomorphs.

Reference 20 introduced a new concept referring to a strongly correlating atomic liquid's phase diagram, namely isomorphic curves or more briefly: isomorphs. Two state points with density and temperature (ρ_1, T_1) and (ρ_2, T_2) are defined to be isomorphic[32] if the following holds: Whenever a configuration of state point (1) and one of state point (2) have the same reduced coordinates $(\rho_1^{1/3}\mathbf{r}_i^{(1)} = \rho_2^{1/3}\mathbf{r}_i^{(2)}$ for all particles $i)$, these two configurations have proportional Boltzmann factors, i.e.,

$$e^{-U(\mathbf{r}_1^{(1)},\ldots,\mathbf{r}_N^{(1)})/k_BT_1} = C_{12}e^{-U(\mathbf{r}_1^{(2)},\ldots,\mathbf{r}_N^{(2)})/k_BT_2} \quad (2)$$

Here C_{12} is a constant that depends only on the state points (1) and (2). An isomorph is defined as a continuous curve of state points that are all pairwise isomorphic. In other words, eq 2 defines an equivalence relation with the equivalence classes being the isomorphs. Only IPL systems have exact isomorphs; these are characterized by having ρ^γ/T = const where $\gamma = n/3$. Reference 20 argued analytically and demonstrated by simulations that strongly correlating atomic liquids have isomorphs to a good approximation.

From the defining property of an isomorph (eq 2) it follows that the structure in reduced units $(\tilde{\mathbf{r}}_i \equiv \rho^{1/3}\mathbf{r}_i)$ is invariant along an isomorph, because the proportionality constant C_{12} disappears when the configurational canonical probabilities are normalized.[20] Thus the reduced unit radial distribution function and the excess entropy $S_{ex} = S - S_{id}$ are isomorph invariants, where S_{id} is the ideal gas contribution to the entropy at the same temperature and density. Isomorph invariance is, however, not limited to static quantites; also the mean-square displacement, time autocorrelation functions, and higher-order correlation functions are invariant in reduced units along an isomorph. The reader is referred to ref 20 for a detailed description of isomorph invariants, as well as the proof that a liquid is strongly correlating if and only if it has good isomorphs. A brief overview of strongly correlating liquids and their isomorphs can be found in Pedersen et al.[23]

Reference 21 studied isomorphs of atomic single-component and multi-component LJ liquids with generalized exponents m and n. It was found that for given exponents (m, n) all isomorphs have the same shape in the *WU* phase diagram; i.e., a so-called master isomorph exists from which all isomorphs can be generated

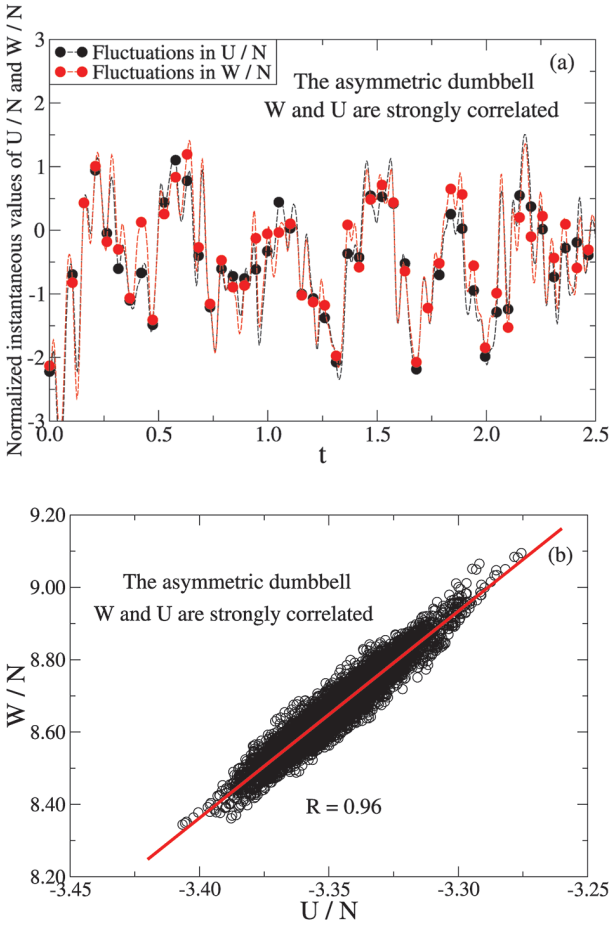

Figure 1. Two different ways of visualizing the strong virial/potential energy correlation for the asymmetric dumbbell model at $\rho = 0.932$ and $T = 0.465$ (see section III for details of the model and the units used). (a) Time evolution of U (black) and W (red) per particle normalized to zero mean and unity standard deviation. (b) Scatter plot of the instantaneous values of W and U per particle. The correlation coefficient R is 0.96.

via a simple scaling of the *WU* coordinates. For instance, the shape of isomorphs in the *WU* phase diagram of the SCLJ liquid and the KABLJ liquid are the same.

References 17−21 focused on understanding strong *WU* correlation and its implication for atomic systems. Schrøder et al.[22] in 2008 studied two rigid molecular liquids that are strongly correlating: the asymmetric dumbbell model and the Lewis−Wahnström OTP model (section III). At that time the isomorph concept had not yet been developed, and state points with the same ρ^γ/T, as inspired from the IPL system, were tested for collapse of, for instance, the reduced unit radial distribution function (note that in refs 17, 18, and 22 γ is defined slightly different from subsequent papers). The dynamics in reduced units was also found to be a function of ρ^γ/T, to a good approximation, as is the case for IPL systems.[19] Chopra et al.[10] found that the S_{ex} can be written (approximately) as a function of ρ^γ/T for rigid symmetric LJ dumbbells with different bond lengths. They also found that the reduced unit diffusion constant and relaxation time are functions of S_{ex}. These results suggest that the isomorph concept is relevant also for rigid molecular systems. In this paper we expand on earlier results by studying in detail the same systems as Schrøder et al.[22]

dx.doi.org/10.1021/jp2077402 |J. Phys. Chem. B 2012, 116, 1018–1034

The isomorph definition eq 2 must be modified for rigid molecules, because the bond lengths are fixed and cannot follow the overall scaling. A simple modification of eq 2, which is consistent with the atomic definition, is to define the mapping among configurations in terms of the molecular center-of-masses, instead of the atomic positions. We thus define two state points in the phase diagram of a liquid composed of *rigid* molecules to be isomorphic if the following holds: Whenever two configurations of the state points have identical reduced center-of-mass coordinates for all molecules,

$$\rho_1^{1/3}\mathbf{r}_{\mathrm{CM},i}^{(1)} = \rho_2^{1/3}\mathbf{r}_{\mathrm{CM},i}^{(2)} \tag{3}$$

as well as identical Eulerian angles[33]

$$\phi_i^{(1)} = \phi_i^{(2)} \qquad \theta_i^{(1)} = \theta_i^{(2)} \qquad \chi_i^{(1)} = \chi_i^{(2)} \tag{4}$$

these two configurations have proportional Boltzmann factors, i.e., [where $\mathbf{R} \equiv (\mathbf{r}_{\mathrm{CM},1}, \phi_1, \theta_1, \chi_1, ..., \mathbf{r}_{\mathrm{CM},N}, \phi_N, \theta_N, \chi_N)$]

$$\mathrm{e}^{-U(\mathbf{R}^{(1)})/k_\mathrm{B}T_1} = C_{12}\mathrm{e}^{-U(\mathbf{R}^{(2)})/k_\mathrm{B}T_2} \tag{5}$$

Again, C_{12} is a constant that depends only on the state points 1 and 2. An isomorph is defined as a set of state points that are pairwise isomorphic. It should be noted that, in contrast to what is the case for atomic systems, because the bonds do not follow the overall scaling of the system, this definition does not imply the existence of exact isomorphs for rigid molecules with IPL interactions between atoms of different molecules.

Taking the logarithm of eq 5 implies

$$U(\mathbf{R}^{(2)}) = T_2/T_1 \cdot U(\mathbf{R}^{(1)}) + k_\mathrm{B}T_2 \ln C_{12} \tag{6}$$

Equation 6 provides a convenient way of testing to what extent eq 5 is obeyed for a given system: A simulation is performed at one state point (1) and the obtained configurations are scaled to a different density ρ_2, where the potential energy is evaluated. The respective potential energies of the two state points are then plotted against each other. In the resulting plot a near straight-line *indicates*, because a liquid is usually not perfectly strongly correlating, that there exists an isomorphic state point with density ρ_2. The temperature T_2 of the isomorphic state point can be found from the slope of a linear regression fit. This procedure is termed the "direct isomorph check".[20] If this test is performed for an atomic IPL system, a correlation coefficient of $R = 1$ is obtained, consistent with these systems having exact isomorphs.

As an example, we perform a direct isomorph check for the asymmetric dumbbell model in Figure 2. A correlation coefficient of $R = 0.97$ is observed for a 15% density increase. Calculating the temperature of the isomorphic state point from the linear regression slope the result differs only 1% from the prediction by requiring constant excess entropy (see section IV).

In the present paper we show that three model liquids composed of simple rigid molecules have good isomorphs in their phase diagram as defined in eqs 3−5. Section II derives several isomorph invariants in molecular systems composed of rigid molecules. Section III describes the simulation setup and the investigated model systems. Section IV investigates the existence of isomorphs for the asymmetric dumbbell, a symmetric IPL dumbbell, and the Lewis−Wahnström OTP models. Section V investigates the existence of a master isomorph[21] for the asymmetric dumbbell and Lewis−Wahnström OTP models. Section VI summarizes the results and presents an outlook.

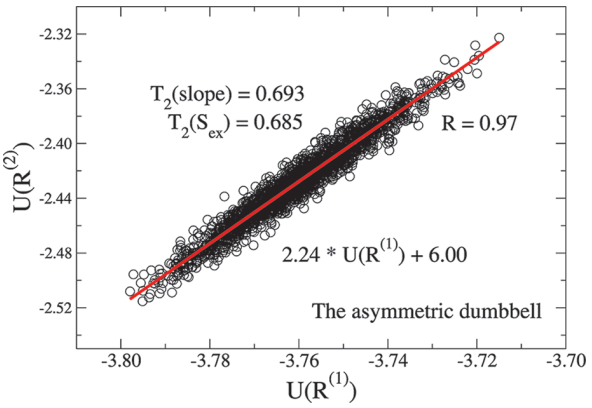

Figure 2. "Direct isomorph check"[20] for the asymmetric dumbbell model. During a simulation at state point $(\rho_1, T_1) = (0.868, 0.309)$ the center-of-mass of each dumbbell is scaled to density $\rho_2 = 0.999$, keeping the Eulerian angles fixed. The potential energy is then evaluated from the scaled configurations and plotted against the potential energy of the unscaled configurations. The temperature $T_2(\mathrm{slope})$ of the isomorphic state point at density ρ_2 is calculated by multiplying the linear regression slope with T_1 (eq 6). $T_2(S_{ex})$ is the temperature of the isomorphic state point calculated by keeping the excess entropy constant (see section IV). It should be noted that the nonzero constant in the linear regression fit reflects the fact that C_{12} in general is not unity (eq 6).

II. ISOMORPH INVARIANTS IN LIQUIDS COMPOSED OF RIGID MOLECULES

From the single assumption of curves of isomorphic state points in an atomic liquid's phase diagram, ref 20 derived several invariants along an isomorph. Because we have extended this definition in eqs 3−5 to molecular systems composed of rigid molecules, it is natural to wonder which of these invariants can be extended to molecular systems. The molecular isomorph concept is different from the atomic case in that there is no "ideal" reference system (the IPL system). Our simulations, however, show that isomorphs can nevertheless be a useful tool for understanding such liquids.

In the following we derive several invariants from exact isomorphs. We start by noting that the generalization of isomorphs to molecular systems define a bijective map among configurations of state points (1) and (2). The *NVT* configurational probability density for a system of N rigid molecules is given by[33] (where $\mathrm{d}\mathbf{R} \equiv \mathrm{d}\mathbf{r}_{\mathrm{CM},1}\,\mathrm{d}\tau_1 \ldots \mathrm{d}\mathbf{r}_{\mathrm{CM},N}\,\mathrm{d}\tau_N$ with $\tau \equiv (\phi, \theta, \chi)$ and $\mathrm{d}\tau = \sin\theta\,\mathrm{d}\theta\,\mathrm{d}\phi\,\mathrm{d}\chi$[33])

$$\hat{P}(\mathbf{R}) = \frac{\mathrm{e}^{-U(\mathbf{R})/k_\mathrm{B}T}}{\int \mathrm{e}^{-U(\mathbf{R})/k_\mathrm{B}T}\,\mathrm{d}\mathbf{R}} \tag{7}$$

In combination with eq 5 it follows that all mapped configurations of state points (1) and (2) have identical Boltzmann probabilities, i.e.,

$$\hat{P}(\mathbf{R}^{(1)})\,\mathrm{d}\mathbf{R}^{(1)} = \hat{P}(\mathbf{R}^{(2)})\,\mathrm{d}\mathbf{R}^{(2)} \tag{8}$$

For convenience we introduce two configurational distribution functions[20,33]

$$P(\mathbf{R}) = (V\Omega)^N\hat{P}(\mathbf{R}) \tag{9}$$

$$\tilde{P}(\tilde{\mathbf{r}}_{\mathrm{CM}}^N, \tau^N) = \frac{\mathrm{e}^{-U(\rho^{-1/3}\tilde{\mathbf{r}}_{\mathrm{CM}}^N, \tau^N)/k_\mathrm{B}T}}{\int \mathrm{e}^{-U(\rho^{-1/3}\tilde{\mathbf{r}}_{\mathrm{CM}}^N, \tau^N)/k_\mathrm{B}T}\,\mathrm{d}\tilde{\mathbf{r}}_{\mathrm{CM}}^N\,\mathrm{d}\tau^N} \tag{10}$$

dx.doi.org/10.1021/jp2077402 |J. Phys. Chem. B 2012, 116, 1018–1034

where Ω is the integral over the Eulerian angles for one molecule ($\Omega = \int d\tau = 8\pi^2$ for a non-linear molecule). P has been introduced to make $\hat{P}$ dimensionless. $\tilde{P}(\tilde{\mathbf{r}}^N_{CM},\tau^N)\, d\tilde{\mathbf{r}}^N_{CM}\, d\tau^N$ is the probability to observe the system represented by a point in the volume-element $d\tilde{\mathbf{r}}^N_{CM}\, d\tau^N$ located at $\{\tilde{\mathbf{r}}^N_{CM},\tau^N\} \equiv \tilde{\mathbf{R}}$. $\tilde{P}$ is invariant along an isomorph and is related to P via $\tilde{P}(\tilde{\mathbf{r}}^N_{CM},\tau^N) = (N\Omega)^{-N} P(\mathbf{R}) = \rho^{-N}\hat{P}(\mathbf{R})$. We note that the excess entropy $S_{ex} = -(\partial F_{ex}/\partial T)_{N,V}$, where F_{ex} is the excess free energy, can be written as[20]

$$S_{ex} = -k_B \int (V\Omega)^{-N} \ln P(\mathbf{R})\, P(\mathbf{R})\, d\mathbf{R} \quad (11)$$

$$S_{ex} = -k_B \int \ln \tilde{P}\, \tilde{P}\, d\tilde{\mathbf{r}}^N_{CM}\, d\tau^N - k_B N \ln(N\Omega) \quad (12)$$

From the above observations we now derive a number of isomorph invariants in liquids composed of rigid molecules.

1. *The molecular center-of-mass structure in reduced units.* For a given configuration of the molecular center-of-mass structure in reduced units, all orientations of the molecules of state points (1) and (2) by eq 8 have identical probabilities. The reduced center-of-mass structure is thus invariant along an isomorph.
2. *Any normalized distribution function describing the (relative) orientations of molecules with respect to the reduced center-of-mass structure.* This follows by analogy to statement 1 since all mapped configurations of state points (1) and (2) have identical probabilities.
3. *The isochoric heat capacity C_V.* The excess heat capacity in the NVT ensemble is given by $C_V^{ex} = \langle(\Delta U)^2\rangle/k_B T^2$. Defining $X = U/k_B T$ we may write $C_V^{ex} = k_B\langle(\Delta X)^2\rangle$. By eqs 6 and 8 it follows that C_V^{ex} is invariant along an isomorph, because the constant $k_B T_2 \ln C_{12}$ disappears when the mean is subtracted. The ideal gas contribution to C_V is independent of state point ($C_V^{id} = 6Nk_B/2$ for non-linear molecule).
4. *The translational two-body entropy*[10,34,35] $S_t/N = -\rho k_B/2\int[g_{CM}(r)\ln g_{CM}(r) - g_{CM}(r) + 1]\, d\mathbf{r}$, where $g_{CM}(r)$ is the radial distribution function for the center-of-mass of the molecules. The density dependence disappears when switching to reduced units, and by statement 1 the molecular center-of-mass structure in reduced units is invariant along an isomorph, and thus also the radial distribution function (in reduced units).
5. *The orientational two-body entropy*[10,34,35] $S_o/N = -\rho k_B/(2\Omega^2)\int g_{CM}(r)\, g(\omega^2|r) \ln g(\omega^2|r)\, d\omega^2\, d\mathbf{r}$, where ω^2 denotes a set of angles used to describe the relative orientation of two molecules, and $g(\omega^2|r)$ is the conditional distribution function for the relative orientation of two molecules separated by a distance r. Applying reduced units this invariant follows from statements 1 and 2.
6. *All N-body entropy terms.*[34,35] The excess entropy can be expanded as $S_{ex} = \Sigma_{i=2}^{\infty} S_i$. The two-body expression $S_2 = S_t + S_o$ is given above, whereas the higher-order terms are more involved.
7. *The excess entropy S_{ex}.* The excess entropy is given by eq 12, and because $\tilde{P}$ is invariant along the isomorph, so is the excess entropy. The latter also follows from statement 6, because each term is invariant.
8. *The molecular center-of-mass NVE and Nosé−Hoover NVT dynamics in reduced units.* The reduced dynamics of the individual atomic positions on account of the constraints is *not* invariant along an isomorph. Considering instead the molecular center-of-mass motion the constraint force disappears and these equations of motion are invariant along an isomorph in reduced units. The proof is given in Appendix B (a brief summary of constrained dynamics is given in Appendix A).
9. *Any average molecular center-of-mass dynamic quantity in reduced units.* This follows immediately from statement 8, because the molecular center-of-mass equations of motion in reduced units are invariant along an isomorph. In particular, this would include the reduced relaxation time $\tilde{\tau}_\alpha$.

As detailed above, it is necessary to consider the center-of-mass motion and the motion relative to the center-of-mass separately. Nevertheless, during the investigation of isomorphs we will also consider the reduced atomic quantities to examine their "invariance".

An additional consequence of isomorphs is that, because by eq 8 scaled microconfigurations have identical canonical probabilities, an instantaneous change of temperature and density from an equilibrated state point to an isomorphic state point does not lead to any relaxation. This is called an isomorphic jump.[20]

III. SIMULATION DETAILS

We studied three model systems of rigid molecules (Figure 3): the asymmetric dumbbell ($N = 500$), a symmetric IPL dumbbell ($N = 500$), and the Lewis−Wahnström OTP models ($N = 320$). The asymmetric dumbbell and Lewis−Wahnström OTP models are composed of LJ atoms, while the symmetric IPL dumbbell model is composed of IPL atoms.

For the LJ models the potential energy U and the virial W are given by (equivalent expressions apply for the symmetric dumbbell model)

$$U = U_{LJ} \quad (13)$$

$$W = W_{LJ} + W_{CON} \quad (14)$$

The first term in the virial is the LJ virial W_{LJ}, the second term is the contribution to the virial due to the constraints (fixed bond lengths), W_{CON}. U_{LJ} is a sum over intermolecular pair interactions given by the (12,6)-LJ potential

$$u(r_{ij}) = 4\varepsilon_{\alpha\beta}\left[\left(\frac{\sigma_{\alpha\beta}}{r_{ij}}\right)^{12} - \left(\frac{\sigma_{\alpha\beta}}{r_{ij}}\right)^{6}\right] \quad (15)$$

The potential energy has no contribution from the fixed bonds. A force smoothing procedure[37] was applied from $r_s = 2.45\sigma_{\alpha\beta}$ to $r_c = 2.50\sigma_{\alpha\beta}$, where r_c is the cut-off distance after which pair interactions are ignored.

The bond lengths were held fixed using the Time Symmetrical Central Difference algorithm,[38,39] which is a central difference time-discretization of the constrained equations of motion preserving time-reversibility. Appendix A gives a brief summary of constrained dynamics and the effect on the virial (see also refs 38, 40, and 41). The simulations were performed in the NVT ensemble applying the Nosé−Hoover (NH) algorithm[42−44] using RUMD,[45] a molecular dynamics package optimized for state-of-the-art GPU computing.

Figure 3. Sketch of the three model systems studied: The asymmetric dumbbell, a symmetric IPL dumbbell, and the Lewis−Wahnström OTP models. The asymmetric dumbbell is a simplistic model of toluene with the methyl side group tightly bonded to the benzene molecule. The symmetric IPL dumbbell has the same bond length as the asymmetric dumbbell model. The Lewis−Wahnström OTP model is an isosceles triangle with an angle of 75°, different from the 60° of the real 1, 2-diphenylbenzene molecule.[36]

The *NVT* simulations were performed without adjusting the time constant of the NH algorithm (see Appendix B). This choice is not expected to influence the results over the observed density and temperature range, because the dynamics is not particularly sensitive to the absolute value of the NH time constant.[46] The specific details of the investigated models follow below.

A. The Asymmetric Dumbbell. The asymmetric dumbbell model consists of a large (A) and small (B) LJ particle, rigidly bonded with a bond distance of $r_{ij} = 0.584$ (here and henceforth units are given in LJ units referring to the A particle, $\sigma_{AA} = 1$, $\varepsilon_{AA} = 1$, and $m_A = 1$). The parameters were chosen to roughly mimic toluene.[22] The asymmetric dumbbell model can be cooled to a highly viscous state without crystallizing, making it feasible to study slow dynamics. The asymmetric dumbbell model has $\sigma_{AB} = 0.894$, $\sigma_{BB} = 0.788$, $\varepsilon_{AB} = 0.342$, and $\varepsilon_{BB} = 0.117$ with $m_B = 0.195$.

B. Symmetric IPL Dumbbell. The symmetric IPL dumbbell model consists of two identical particles, rigidly bonded with bond distance of $r_{ij} = 0.584$. The atoms in different molecules interact via an IPL potential with exponent $n = 18$. The masses and IPL parameters are set to unity and a cut-and-shifted potential at $r_c = 2.50$ is applied.

C. Lewis−Wahnström OTP. The Lewis−Wahnström OTP model[29,30] consists of three identical LJ particles rigidly bonded together in an isosceles triangle with sides of $r_{ij} = 1.000$ and top-angle of 75°, i.e., different from the 60° of the real 1,2-diphenylbenzene molecule.[36] All LJ parameters (including the masses) are unity for the OTP model.

IV. NUMERICAL STUDY OF ISOMORPHS FOR THE THREE MODEL SYSTEMS

To investigate whether the three model systems have good isomorphs, we first describe how to generate an isomorph in a simulation. The excess entropy S_{ex} is invariant along an isomorph, and the method for generating an isomorph is to generate a curve of constant S_{ex} (see section II and also refs 20 and 21). A curve of constant excess entropy can be found by using the exact *NVT* ensemble relation[20]

$$\frac{\langle \Delta U \Delta W \rangle}{\langle (\Delta U)^2 \rangle} = \left(\frac{\partial \ln T}{\partial \ln \rho} \right)_{S_{ex}} \equiv \gamma \qquad (16)$$

In simulations an isomorph is generated as follows: (1) The left-hand side is calculated from the fluctuations at a given state point. (2) A new state point is identified by a discretization of eq 16 changing the density by 1%, and the new temperature is calculated from $\Delta \ln T = \gamma \Delta \ln \rho$. (3) The procedure is repeated and in this way an isomorph is generated in the phase diagram.

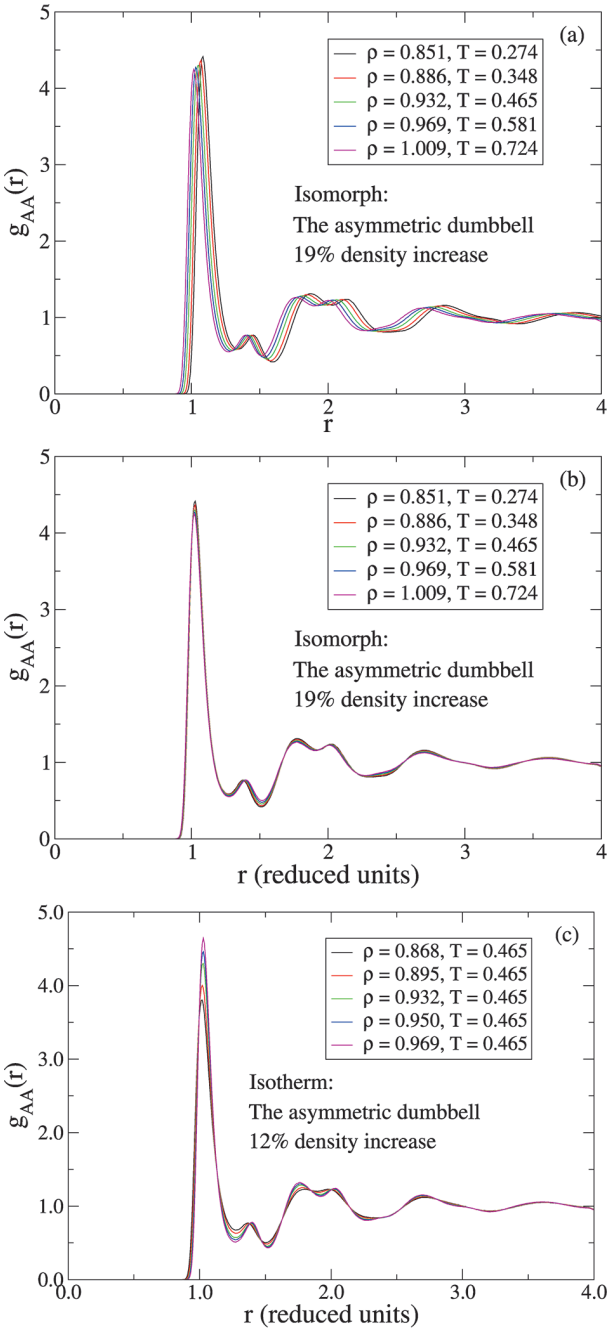

Figure 4. Radial distribution functions for the asymmetric dumbbell model. (a) AA pair-correlation function along an isomorph with 19% density increase before scaling the distance r into reduced units. (b) AA pair-correlation function along the same isomorph after scaling the distance r into reduced units. (c) AA pair-correlation function along an isotherm with 12% density increase after scaling of the distance into reduced units.

A. Isomorphs of the Asymmetric Dumbbell Model. This section investigates the asymmetric dumbbell model. Isomorphs were mapped out following the procedure described above. Figure 4 shows the AA radial distribution functions along an isomorph with 19% density increase before (a) and after (b) scaling the distance r into

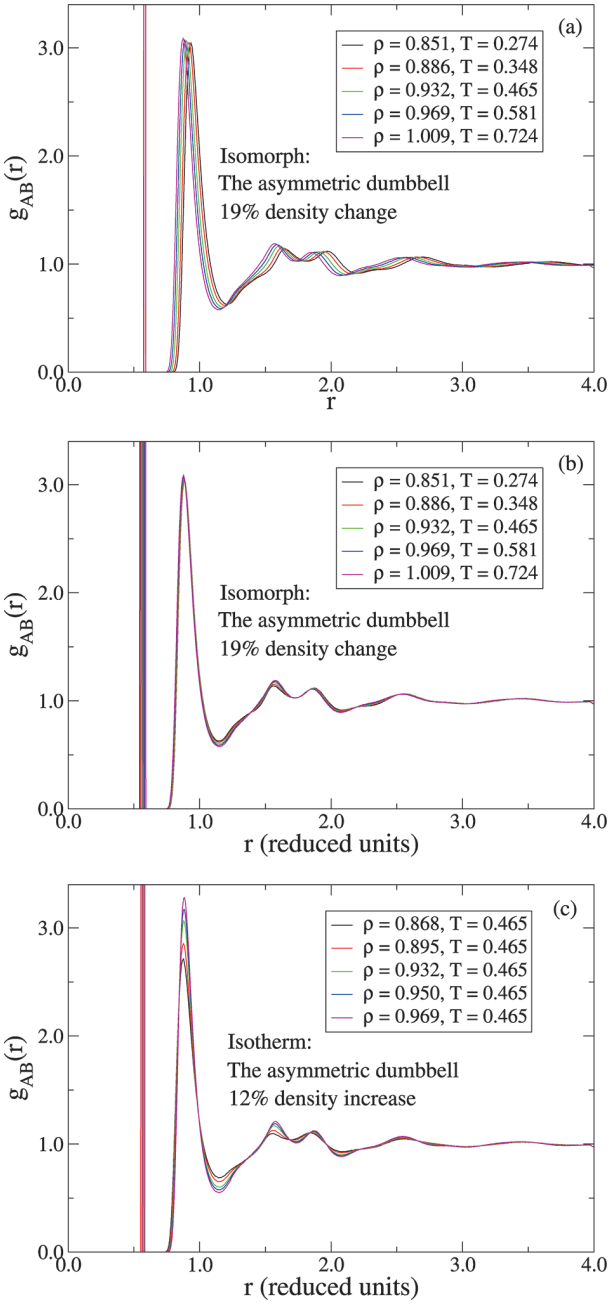

Figure 5. Radial distribution functions for the asymmetric dumbbell model. (a) AB pair-correlation function along the isomorph of Figure 4 before scaling the distance r into reduced units. (b) AB pair-correlation function along the same isomorph after scaling the distance r into reduced units. (c) AB pair-correlation function along the isotherm of Figure 4 after scaling of the distance into reduced units.

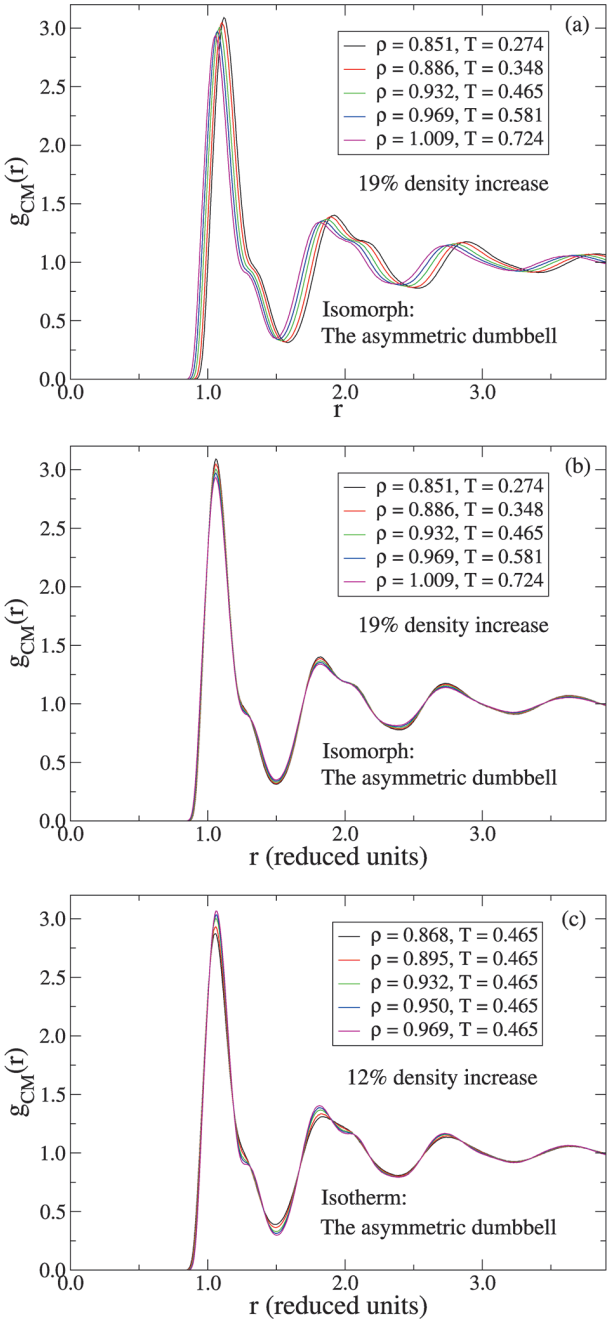

Figure 6. Molecular center-of-mass radial distribution functions for the asymmetric dumbbell model. (a) Pair-correlation function along the isomorph of Figures 4 and 5 before scaling the distance r into reduced units $\tilde{r} = \rho^{1/3} r$. (b) Pair-correlation function along the same isomorph after scaling the distance r into reduced units. (c) Pair-correlation function along the isotherm of Figures 4 and 5 after scaling of the distance into reduced units.

reduced units via

$$\tilde{r} = \rho^{1/3} r \tag{17}$$

Also shown for reference in Figure 4c is the AA radial distribution functions along an isotherm with 12% density increase. Although the reduced structure of the atomic positions, due to the fixed bonds, is predicted not to be invariant along an isomorph, Figure 4 shows that it nevertheless is so to a reasonable approximation. The reduced structure of the atomic positions is less invariant along the isotherm. Figure 5 considers the AB radial distribution functions, where the constrained bond distance shows up as a sharp peak. The analogous conclusion as with the AA distribution functions is reached, and likewise for the BB distribution functions (not shown).

Next, we consider in Figure 6 the molecular center-of-mass radial distribution functions along the isomorph and isotherm of Figures 4 and 5. This quantity is predicted to be invariant along

dx.doi.org/10.1021/jp2077402 |J. Phys. Chem. B 2012, 116, 1018–1034

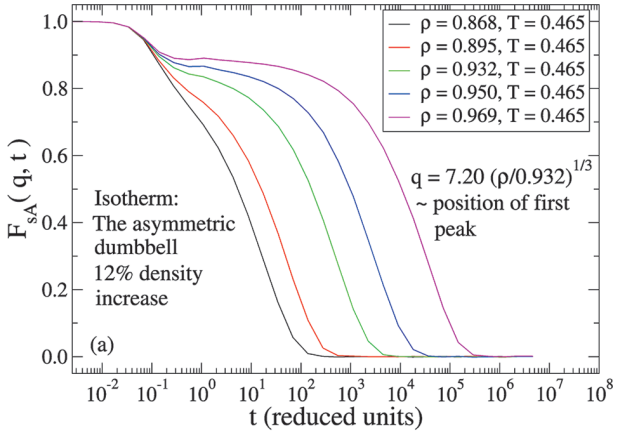

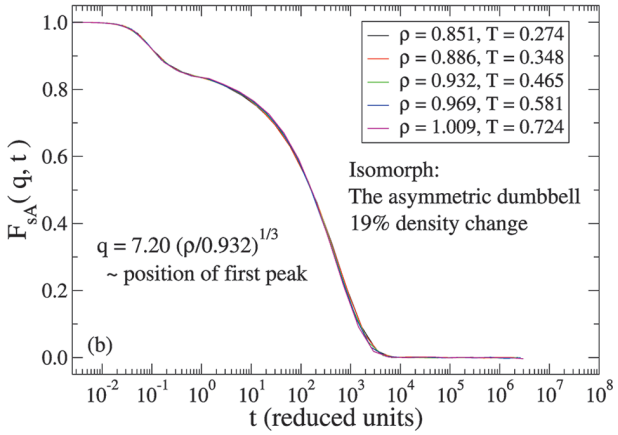

Figure 7. Reduced A-particle incoherent intermediate scattering functions for the asymmetric dumbbell model keeping the reduced wavevector q constant. (a) Along the isotherm of Figures 4−6 with 12% density increase. (b) Along the isomorph of Figures 4−6 with 19% density increase.

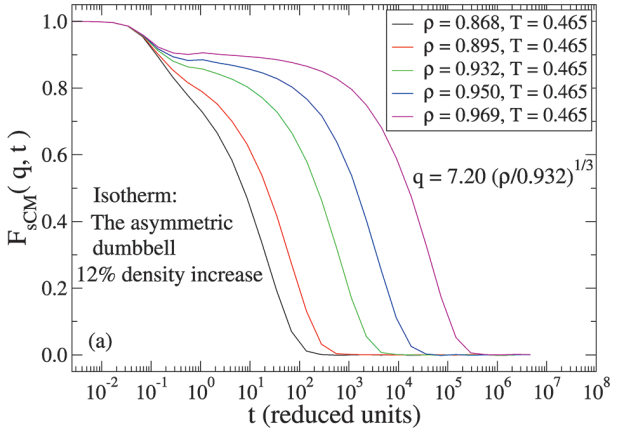

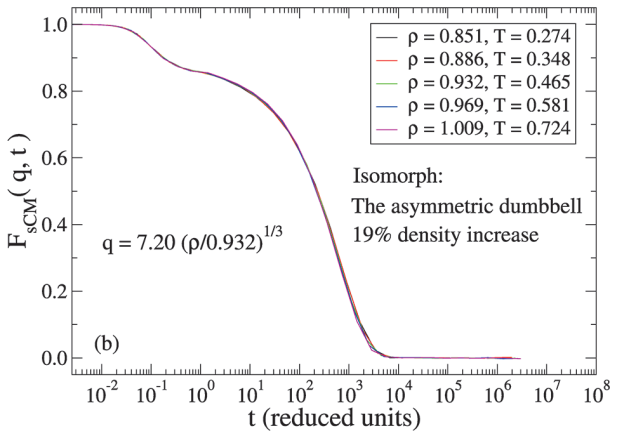

Figure 8. Reduced molecular center-of-mass incoherent intermediate scattering functions for the asymmetric dumbbell model keeping the reduced wavevector q constant. (a) Along the isotherm of Figures 4−7 with 12% density increase. (b) Along the isomorph of Figures 4−7 with 19% density increase.

an isomorph (see section II). The molecular center-of-mass structure is to a good approximation invariant in reduced units along the isomorph, but this is less so along the isotherm, as can be seen from the first and second peaks. It should, however, be noted that beyond $r \approx 2.3$ the isotherm appears more invariant than the isomorph.

We consider in Figure 7 the dynamics in terms of the reduced A-particle incoherent intermediate scattering function. The reduced dynamics of the atoms is not predicted to be invariant along an isomorph (see Appendix B); however, the figure shows that it is a good approximation. The same conclusion is reached for the B-particle (not shown). In Figure 8 we consider the reduced molecular center-of-mass self-part of the intermediate scattering function. This quantity is predicted to be invariant along an isomorph (see Appendix B), and Figure 8 clearly shows this. The dynamics is not invariant along the isotherm.

We show the variation of γ, calculated from the *NVT* fluctuations via eq 16, in Figure 9 along an isochore and along the isomorph of Figures 4−8 in two different versions. The crosses show γ calculated from the total virial W, and the asterisks show γ calculated after subtracting the constraint contribution to virial, i.e., replacing W with $W_{LJ} = W - W_{CON}$. The inset shows the corresponding correlation coefficients R. Reference 20 predicts that γ should be a function of density only $\gamma = \gamma(\rho)$. This is seen in Figure 9 to be a good approximation for both versions of γ, where the crosses are the γ used to keep the excess entropy constant. The γ calculated from the LJ virial is seen to be lower than the γ calculated from the total virial. The γ derived from the LJ virial is related to an effective IPL exponent that reproduces the structure and the dynamics of the molecular liquid (see ref 47 for more details).

As mentioned in the Introduction, density scaling[1−3] is the empirical observation that the reduced relaxation time $\tilde{\tau}_\alpha$ for many viscous liquids can be written as some function $\tilde{\tau}_\alpha = f(\rho^{\gamma_{scale}}/T)$ where γ_{scale} in experiments is a fitting exponent. If we assume that γ is constant along an isomorph, eq 16 implies that ρ^γ/T = const describes the isomorph. In this case density scaling will hold to a good approximation because the reduced relaxation time is an isomorph invariant; for the dumbbell system γ changes only moderately along an isomorph and thus density scaling is a fair approximation for this system.[22] That γ for systems with isomorphs can be identified with the density scaling exponent γ_{scale} has very recently been verified experimentially for a silicone oil.[31]

Starting from an equilibrated sample at some state point, changing either temperature or density alters the equilibrium Boltzmann distribution of states. Two isomorphic state points have identical canonical probabilities of scaled microconfigurations

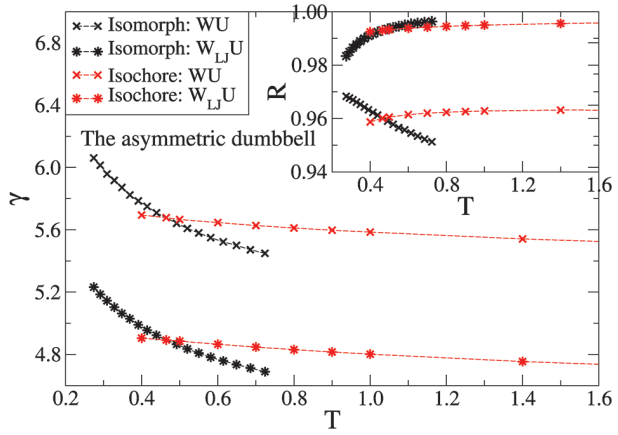

Figure 9. Variation of γ (eq 16) and the correlation coefficient R (eq 1) for the asymmetric dumbbell model in two different versions along an isochore (red, $\rho = 0.932$) and along the isomorph (black) of Figures 4−8. The crosses show γ calculated from the total virial W, and the asterisks show γ calculated after subtracting the constraint contribution to virial, i.e., $W_{LJ} = W - W_{CON}$. The corresponding R's are shown in the inset. γ is predicted in ref 20 to be a function only of density, which is seen to apply to a good approximation for both versions.

(eq 8). A sudden change of state from an equilibrated state point to an isomorphic state point should thus not lead to any relaxation. This is called an isomorphic jump, and the prediction of no relaxation was shown in ref 20 to work well for the KABLJ liquid.

A similar numerical experiment is carried out for the asymmetric dumbbell model in Figure 10. Considering three equilibrated, isochoric state points (1), (2), and (3), density and temperature are instantaneously changed to a state point (4). State point (4) is isomorphic to state point (2). The isomorph prediction is that jumps from state points (1) and (3) show relaxation, whereas jumps from state point (2) do not. This is indeed the case (Figure 10a). State point (1) ages from below because the aging scheme (1) → (4) can be described as first an instantaneous isomorphic jump to the correct density, but a lower temperature, and subsequently relaxation from this state point along the isochore of state point (4).

We finally consider the excess isochoric heat capacity per particle C_V^{ex}/N in Figure 11 along the isomorph and isotherm of Figures 4−8. The excess heat capacity increases less than 2% along the isomorph, whereas the 12% density increase on the isotherm results in a 25% increase in the excess heat capacity. This is consistent with the prediction in section II that C_V^{ex}/N is an isomorph invariant.

The previous figures show that isomorphs exists to a good approximation for the asymmetric dumbbell model. An important question is whether the specific molecular geometry determines whether or not a particular LJ model has good isomorphs. In Figure 12 the correlation coefficient R is given as a function of the bond length. The correlation coefficient decreases to $R \approx 0.65$ at unity bond length, and one might be tempted to conclude that LJ models with large bonds lengths in general do not have good isomorphs. In section IV'C we investigate the Lewis−Wahnström OTP model that have unity bond lengths and show that this model actually has good isomorphs. A theory relating the variation of R to the molecular geometry and/or bond lengths remains to be developed.

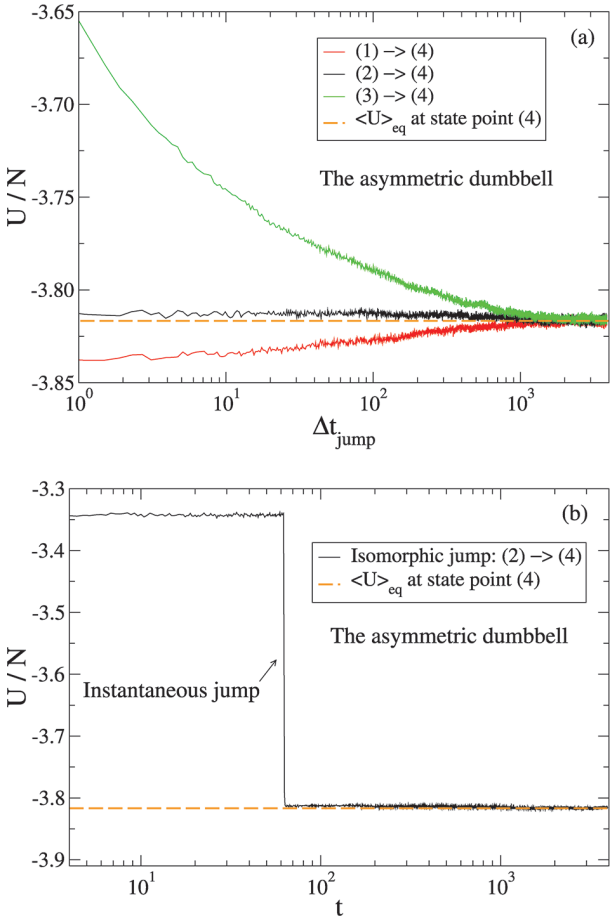

Figure 10. Four state points (1), (2), (3), and (4) corresponding to, respectively, $(\rho, T) = (0.932, 0.400)$, $(0.932, 0.465)$, $(0.932, 2.000)$, and $(0.851, 0.274)$ are given where the first three state points are on the same isochore. State points (2) and (4) are isomorphic, whereas (1) and (3) are not isomorphic to (4). After equilibrating at state points (1), (2), and (3), respectively, temperature and density are instantaneously changed to that of state point (4) via a scaling of the center-of-mass coordinates keeping the Eulerian angles of the molecules fixed. An average has been performed over 100 samples. (a) Relaxational behavior of all state points quantified by the potential energy U. The isomorph jump (2) → (4) shows no relaxation whereas the other state points do. (b) Close up of the potential energy of state point (2) before and after the jump, where the jump takes place at $t \approx 60$.

B. Isomorphs of a Symmetric IPL Dumbbell Model. In this section we briefly consider a symmetric IPL dumbbell model (see section III'B). In Figures 13a,b we show the particle radial distribution functions along an isomorph before and after scaling the distance r into reduced units. Also shown is the reduced particle incoherent intermediate scattering function in Figure 13c. The corresponding molecular center-of-mass quantities are shown in Figure 14. The atomic dynamics of Figure 13c appear slightly more invariant than the reduced molecular center-of-mass dynamics of Figure 14c, and the difference seems to be larger than what can be contributed to statistics. The latter is predicted to be invariant along an isomorph whereas the former is not. However, we have not tried to quantify this observation any further.

Atomic systems with IPL interactions have exact isomorphs. This reflects the scale invariance of the IPL potential, i.e., that it

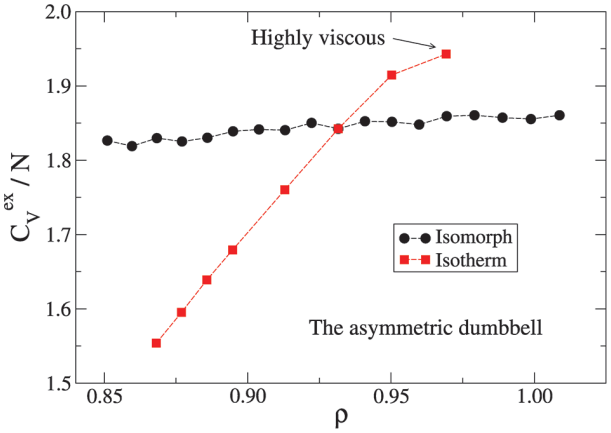

Figure 11. Excess isochoric heat capacity per particle C_V^{ex}/N for the asymmetric dumbbell model as a function of density along the isomorph (black) and isotherm (red, T = 0.465) of Figures 4−8. The density increase is 19% and 12%, respectively. Consistent with the predicted isomorph invariance, the excess isochoric heat capacity increases less than 2% along the isomorph, whereas the isotherm shows a 25% increase. For the isotherm the dynamics becomes very slow for densities higher than ρ = 0.950 and the system becomes difficult to equilibrate properly.

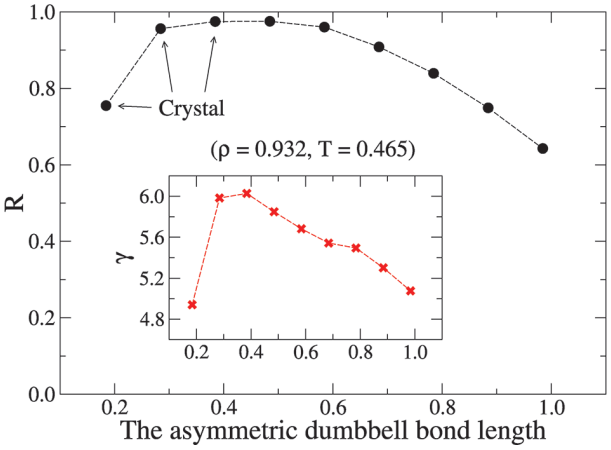

Figure 12. Correlation coefficient R as a function of the bond length in the asymmetric dumbbell model at (ρ, T) = (0.932, 0.465). The investigated model has bond length 0.584 with a correlation coefficient $R \approx 0.97$; however, as the bond length increases, the correlation coefficient decreases to $R \approx 0.65$ at unity bond length. The inset shows the corresponding values of γ as defined in eq 16. As the bond length increases, the system becomes very viscous and the statistics is poor at high bond lengths.

preserves its shape under a scaling of the argument. Because molecules by their fixed geometry define a length scale in the system, isomorphs will always be approximate. However, the previous figures show that rigid molecules with IPL intermolecular interactions can also have good isomorphs.

In Figure 15 we consider the variation of γ and R along the investigated isomorph, which shows that R decreases slightly with increasing temperature (and density). The variation of γ along the isomorph is less than for the asymmetric dumbbell, and γ is to a good approximation constant. As for the asymmetric dumbbell model (Figure 9), the effect of the constraints is to increase γ and decrease R (these are, respectively, 6 and 1 for the atomic IPL potential used).

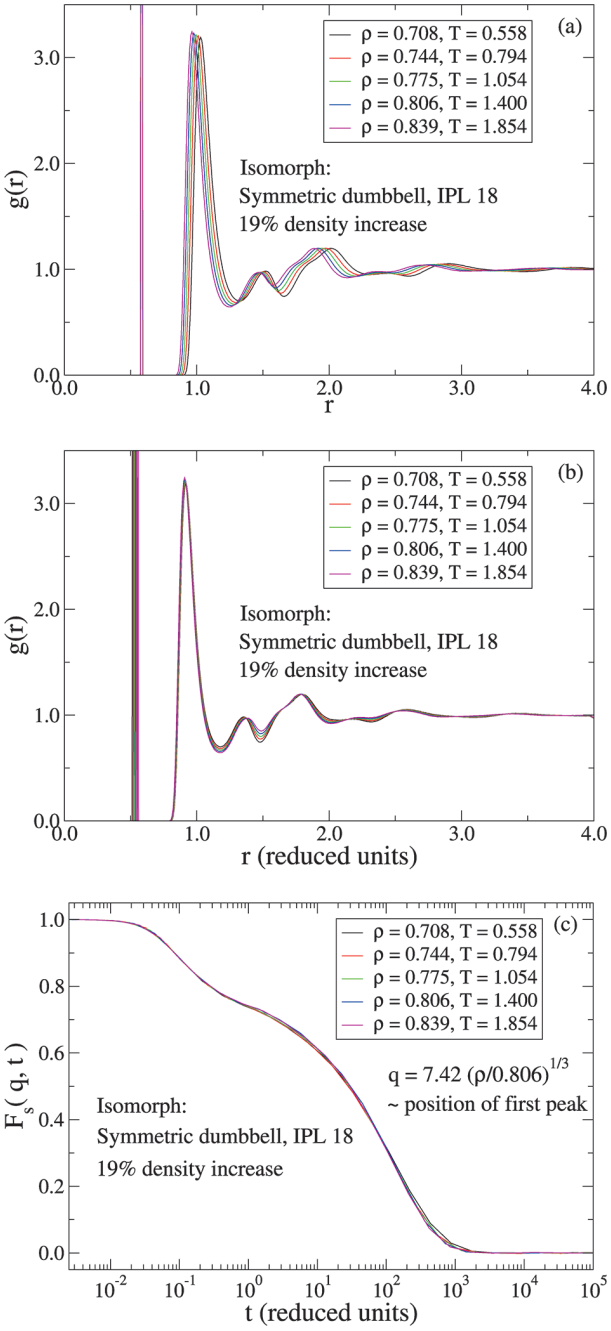

Figure 13. Structure and dynamics along an isomorph with 19% density increase for the symmetric IPL dumbbell model (n = 18). (a) Particle pair-correlation functions before scaling the distance r into reduced units. (b) Particle pair-correlation functions after scaling the distance r into reduced units. (c) The reduced particle incoherent intermediate scattering functions at constant reduced wavevector q.

C. Isomorphs of the Lewis−Wahnström OTP Model. We proceed to investigate the Lewis−Wahnström OTP model.[29,30] Figure 16 shows the particle radial distribution functions along an isomorph with 21% density increase before and after scaling the distance r into reduced units. We treat the particles as identical in the quantities probed in simulations (i.e., the radial distribution function, etc.) even though the OTP model is an isosceles triangle. Also shown for reference is an isotherm with 11%

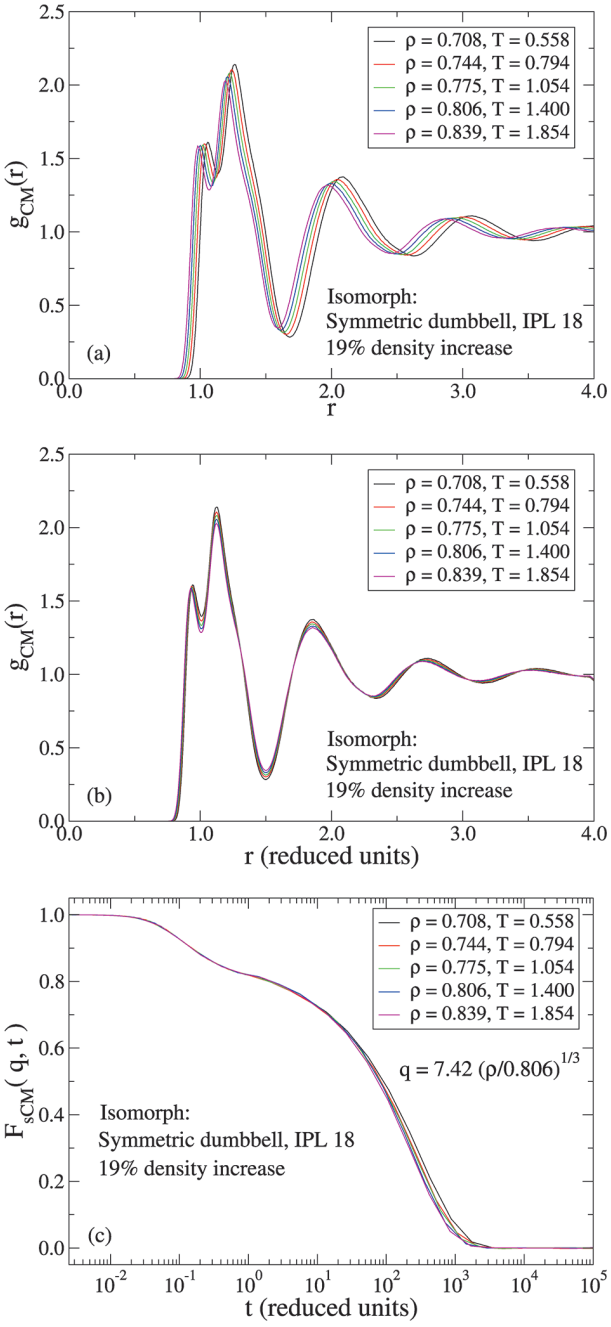

Figure 14. Structure and dynamics along the isomorph of Figure 13 for the symmetric IPL dumbbell model ($n = 18$). (a) Molecular center-of-mass pair-correlation functions before scaling the distance r into reduced units $\tilde{r} = \rho^{1/3}r$. (b) Molecular center-of-mass pair-correlation functions after scaling the distance r into reduced units. (c) Reduced molecular center-of-mass incoherent intermediate scattering functions at constant reduced wavevector q.

density increase in Figure 16c. Figure 17 shows the corresponding reduced molecular center-of-mass radial distribution functions. The reduced molecular center-of-mass structure is less invariant along the isomorph than for the asymmetric dumbbell (Figure 6), consistent with the OTP model being less strongly correlating ($R \approx 0.90$). However, comparing with the isotherm in Figure 17c, the OTP model, here, crystallizes at the highest density probed,[36] even though the density increase is just 11% compared with the 21% density increase along the isomorph.

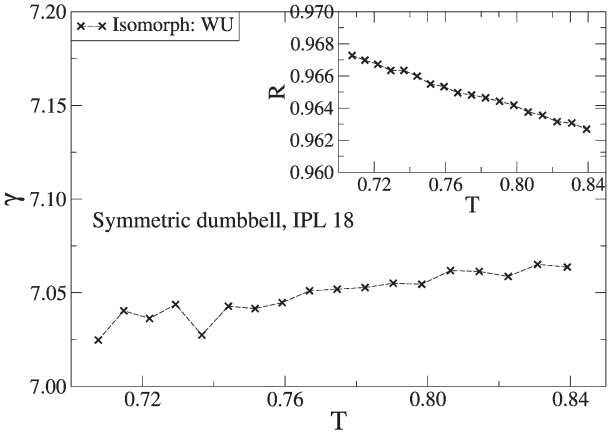

Figure 15. Variation of γ and R (inset) along the isomorph of Figures 13 and 14 with a 19% density increase for the symmetric IPL dumbbell model ($n = 18$). γ increases slightly along the isomorph. Excluding the constraints in the virial the correlation coefficient and γ are respectively $R = 1$ and $\gamma = 6$.

Comparing now with the particle quantities of Figure 16, the latter seems to be more invariant along the isomorph, even though the reduced molecular center-of-mass structure is predicted in section II to be invariant. The isomorph invariants presented in section II are exact in the case of exact isomorphs; however, the OTP model has a correlation coefficient of 0.90, and we expect this to be the cause of disagreement. This, however, does not explain why the reduced structure should be more invariant, and we currently have no explanation for this.

Figure 18 shows the reduced particle incoherent intermediate scattering functions along the isotherm and isomorph of Figures 16 and 17, while Figure 19 shows the reduced molecular center-of-mass incoherent intermediate scattering functions.
For the molecular quantities, the dynamics is roughly invariant along the isomorph but not on the isotherm, even though the density increase is 21% for the isomorph and only 11% for the isotherm. In contrast to the reduced molecular center-of-mass structure; the molecular dynamics (Figure 19b) is just as invariant as the particle dynamics (Figure 18b), consistent with the prediction of section II.

We consider in Figure 20 the variation of γ as defined by eq 16. The large variation in γ indicates that density scaling may show a breakdown sooner (for a given change in density) for the Lewis–Wahnström OTP model than for the asymmetric dumbbell where γ changes less along an isomorph. The isomorphs of the OTP model are, however, more approximative than for the asymmetric dumbbell, which is consistent with OTP model being less strongly correlating.

Next, we consider isomorph jumps for the OTP model. The setup is analogous to that of the asymmetric dumbbell model described in section IV'A. It is seen from Figure 21 that an isomorph jump shows no relaxation. The apparent larger fluctuations in the potential energy (Figure 21b) than for the asymmetric dumbbell (Figure 10b) are due to a change of scale in the figure.

We close the investigation of the OTP model by considering in Figure 22 the isochoric excess heat capacity per particle C_V^{ex}/N. This quantity increases 7% over the 21% density increase along the isomorph, whereas the 11% density increase on the isotherm results in a 34% increase in the isochoric excess heat capacity before crystallizing. These results are consistent with the prediction that C_V^{ex} is an isomorph invariant (see section II), although less so than for the asymmetric dumbbell model.

dx.doi.org/10.1021/jp2077402 |J. Phys. Chem. B 2012, 116, 1018–1034

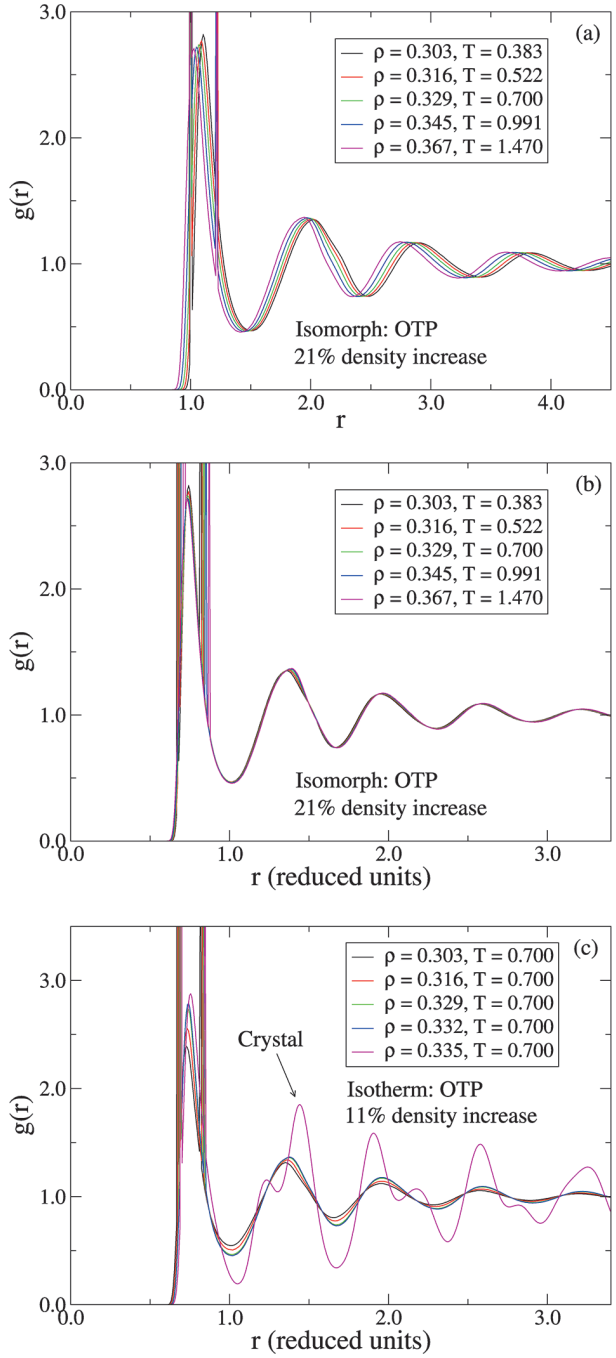

Figure 16. Particle radial distribution functions for the OTP model. (a) Along an isomorph with 21% density increase, shown prior to scaling the distance r into reduced units. (b) Along the same isomorph after scaling the distance r into reduced units. (c) Along an isotherm with 11% density increase. At the highest density probed the OTP model crystallizes[36] (magenta).

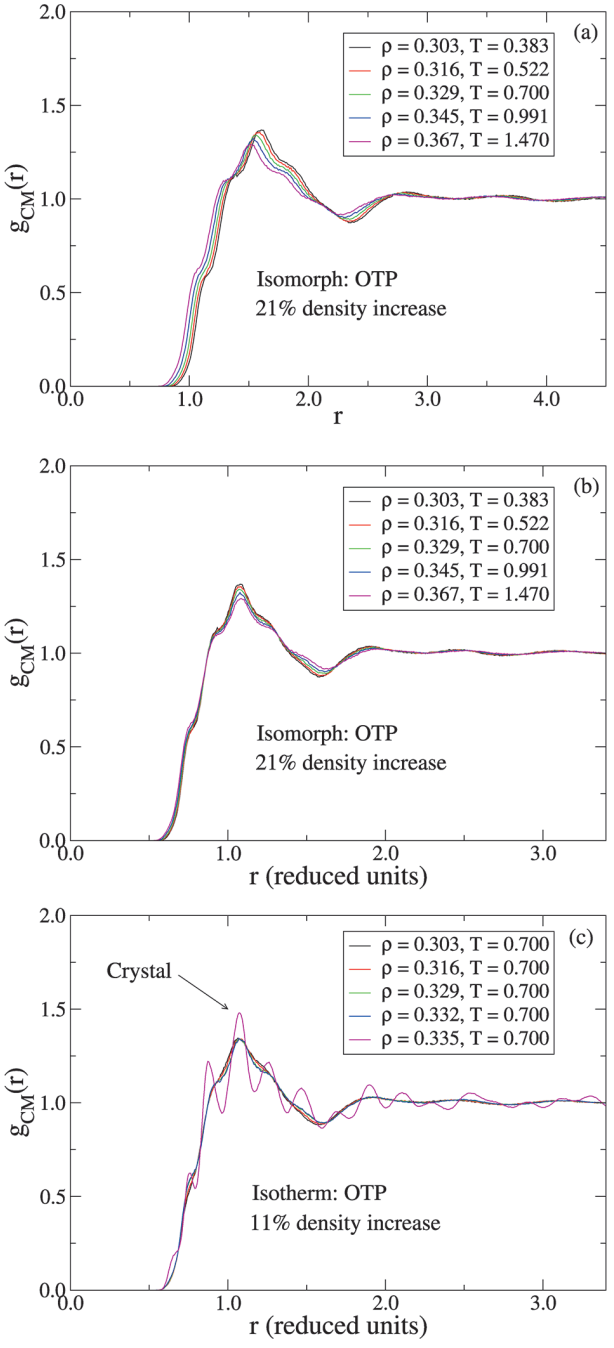

Figure 17. Molecular center-of-mass radial distribution functions for the OTP model. (a) Along the isomorph of Figure 16 with 21% density increase, shown prior to scaling the distance r into reduced units. (b) Along the same isomorph after scaling the distance r into reduced units. (c) Along the isotherm of Figure 16 with 11% density increase. At the highest density probed the OTP model crystallizes (magenta).

V. MASTER ISOMORPHS

The previous section detailed the existence of isomorphs in the phase diagram of liquids of small rigid molecules. We now investigate whether the generated isomorphs for the LJ systems have the same shape in the *WU* phase diagram, i.e., whether a so-called master isomorph exists, as has been shown for generalized LJ atomic systems.[21] It is also interesting to compare the isomorphs of the asymmetric dumbbell and OTP models, because both systems have intermolecular (12,6)-LJ interactions, but different constraint contributions to the virial (one versus three constrained distances per molecule).

Figure 23a shows three different isomorphs in the *WU* phase diagram for the asymmetric dumbbell model, in two different versions: one for the total virial W and one for the "LJ" virial, i.e., replacing W by $W_{LJ} = W - W_{CON}$. To investigate whether a master isomorph exists, Figure 23b shows the same isomorphs

dx.doi.org/10.1021/jp2077402 |J. Phys. Chem. B 2012, 116, 1018–1034

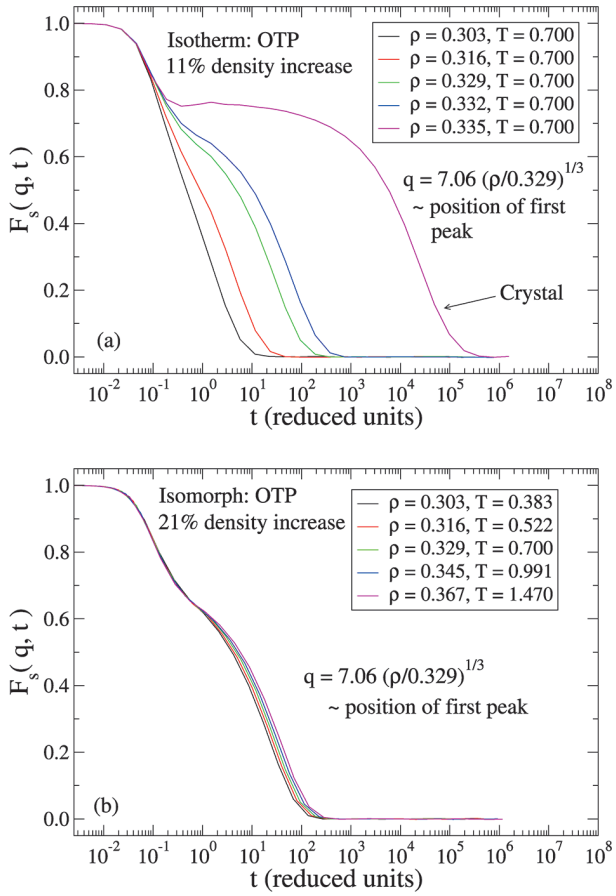

Figure 18. The reduced particle incoherent intermediate scattering functions for the OTP model keeping the reduced wavevector q constant. (a) Along the isotherm of Figures 16 and 17 with 11% density increase. (b) Along the isomorph of Figures 16 and 17 with 21% density increase and almost a factor of 4 increase in temperature. The dynamics is roughly invariant along the isomorph, but not along the isotherm.

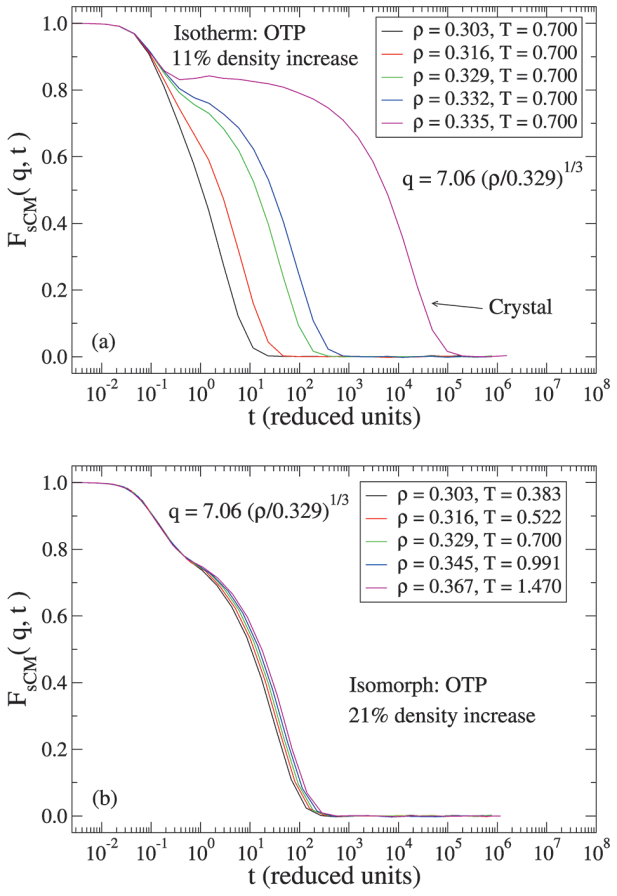

Figure 19. Reduced molecular center-of-mass incoherent intermediate scattering functions for the OTP model keeping the reduced avevector q constant. (a) Along the isotherm of Figures 16−18 with 11% density increase. (b) Along the isomorph of Figures 16−18 with 21% density increase and almost a factor of 4 increase in temperature. The dynamics is roughly invariant along the isomorph, but not along the isotherm.

after scaling of the potential energy and the virial with the *same* factor (depending on the isomorph). The best scaling factor was identified by trial and error. Corresponding figures for the OTP model are given in Figure 24. The figures show that for both models a master isomorph exists to a good approximation both with and without the constraint contribution to the virial.

Reference 21 derived predictions concerning the shape of isomorphs for *atomic* systems with pair potential given by a sum of two IPLs (the generalized LJ potential). The question arises whether $W_{LJ}U$ follows that shape? This is studied in Figure 25a where the $W_{LJ}U$ isomorphs for the asymmetric dumbbell and OTP models are scaled using the previously mentioned procedure. The two dashed curves are the isomorph prediction for an *atomic* (12,6)-LJ system[21] (where $\tilde{\rho} = \rho/\rho^*$ and ρ^* is the density of a chosen reference state point)

$$U = U_m^* \tilde{\rho}^4 + U_n^* \tilde{\rho}^2 \quad (18)$$

$$W_{LJ} = 4U_m^* \tilde{\rho}^4 + 2U_n^* \tilde{\rho}^2 \quad (19)$$

where the reference coefficients (U_m^*, U_n^*) have been calculated from two different state points along "Isomorph 1" of the asymmetric dumbbell.[21] The only assumption used in ref 21 to

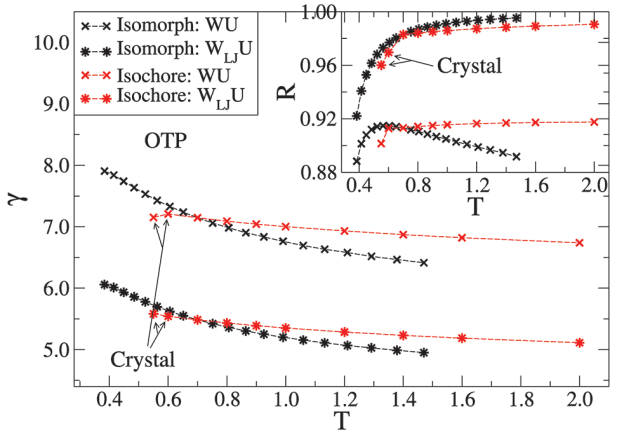

Figure 20. Variation of γ (eq 16) and the correlation coefficient R (inset, eq 1) for the OTP model in two different versions along an isochore (red, $\rho = 0.329$) and the isomorph (black) of Figures 16−19. The crosses show γ calculated from the total virial W, the asterisks show γ calculated after subtracting the constraint contribution to virial, i.e., replacing W by $W_{LJ} = W - W_{CON}$. γ is predicted in ref 20 to be a function only of density as is seen to be the case for both versions, although the variation is larger than for the asymmetric dumbbell.

dx.doi.org/10.1021/jp2077402 |J. Phys. Chem. B 2012, 116, 1018–1034

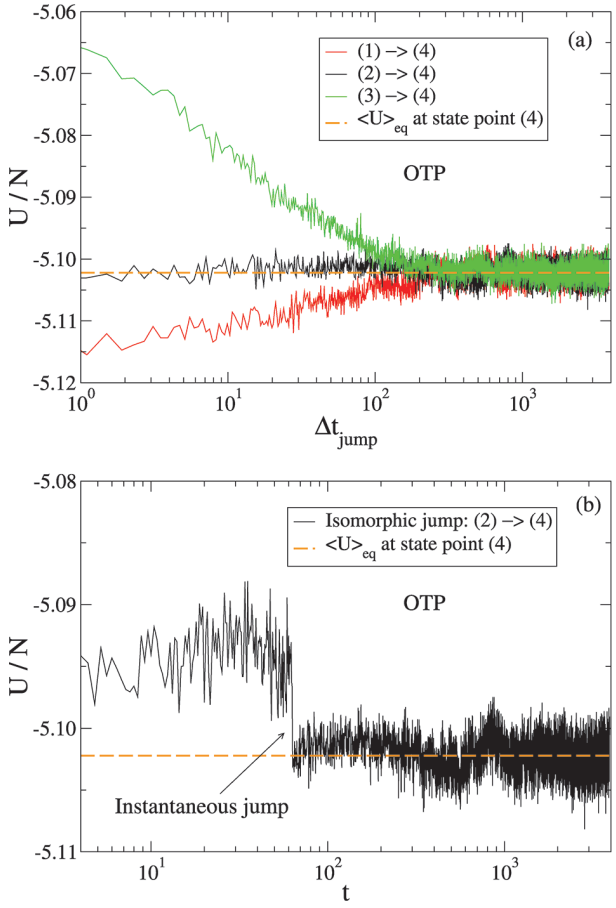

Figure 21. Four state points (1), (2), (3), and (4) corresponding to, respectively, $(\rho, T) = (0.329, 0.650)$, $(0.329, 0.700)$, $(0.329, 1.000)$, and $(0.303, 0.383)$ are given where the first three state points are on the same isochore. State points (2) and (4) are isomorphic whereas (1) and (3) are not isomorphic to (4). After equilibrating at state points (1), (2), and (3), respectively, the temperature and density are instantaneously changed to that of state point (4) via a scaling of the center-of-mass coordinates keeping the Eulerian angles of the molecules fixed. An average has been performed over 100 samples. (a) Relaxational behavior of all state points quantified by the potential energy U. The isomorph jump (2) → (4) shows no relaxation whereas the other jumps do. (b) Close up of the potential energy of state point (2) before and after the jump, where the jump takes place at $t \approx 60$.

derive these formulas is the invariance of the reduced atomic structure along an isomorph; however, this is not predicted to be the case for molecular systems with isomorphs (see section II).

It is clear that the atomic isomorph shape is not followed exactly. Nevertheless, there seems to exist not only a master isomorph in the LJ and total virial for the individual systems, but also for the LJ virial between these two different model systems. The same does not hold for the total virial, as can been seen in Figure 25b, because the constraint contributions are different.

To examine the extent of "deviation" from eqs 18 and 19, we show in Figure 26 for the asymmetric dumbbell $U/\tilde{\rho}^2$ and $W_{LJ}/\tilde{\rho}^2$ as functions of the reduced density $\tilde{\rho}^2$ ($\rho^* = 1$). The reference coefficients can be calculated from a linear regression fit of the potential energy and the estimated coefficients can be used to plot a straight line in the LJ virial plot. This is performed in Figure 26 where it is clear that even though both plots follow a

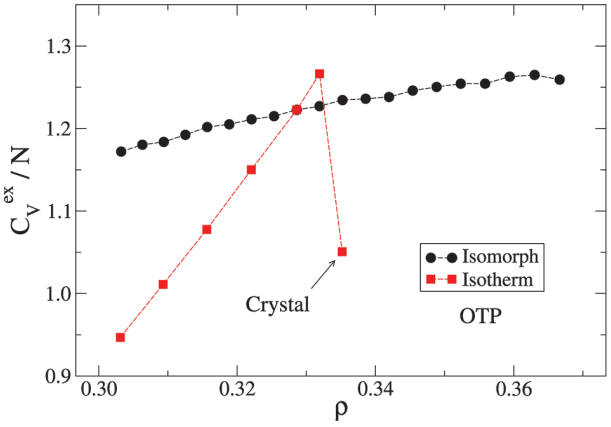

Figure 22. Isochoric excess heat capacity per particle C_V^{ex}/N for the OTP model as a function of density along the isomorph (black) and isotherm (red) of Figures 16−19. The density increase is 21% and 11%, respectively. At high densities for the isotherm the OTP model crystallizes. The isochoric excess heat capacity is to a good approximation invariant along the isomorph, whereas this is not the case for the isotherm.

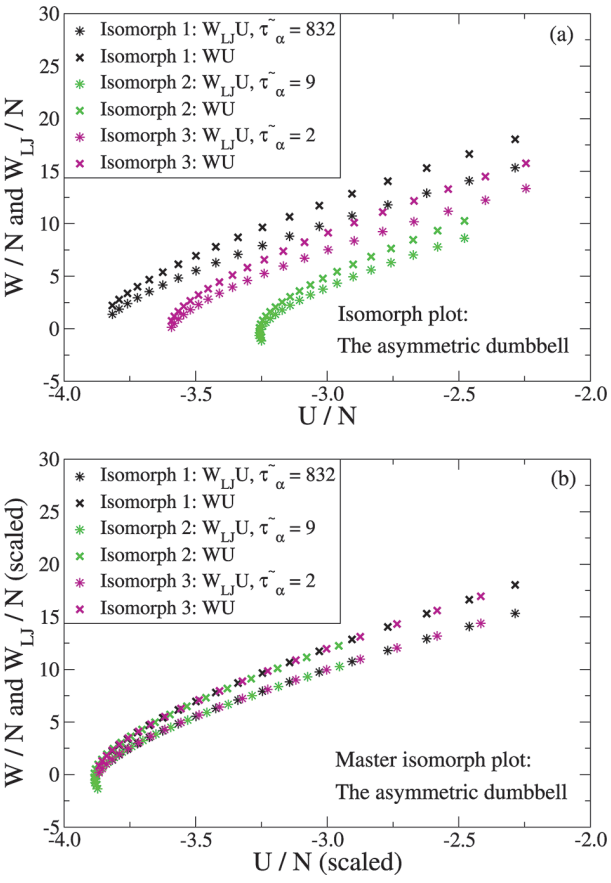

Figure 23. (a) Three different isomorphs for the asymmetric dumbbell model in two different versions with 19%, 21%, and 22% density increase, respectively (black, magenta, and green). The crosses give the total virial W, the asterisks give $W_{LJ} = W - W_{CON}$. $\tilde{\tau}_\alpha$ is the reduced relaxation time of the isomorph extracted from the self-part of the intermediate scattering function. (b) The same isomorphs as in (a) where WU and $W_{LJ}U$ are scaled to superpose with a factor identified by trial and error. The black points have unity scaling factor.

dx.doi.org/10.1021/jp2077402 |J. Phys. Chem. B 2012, 116, 1018–1034

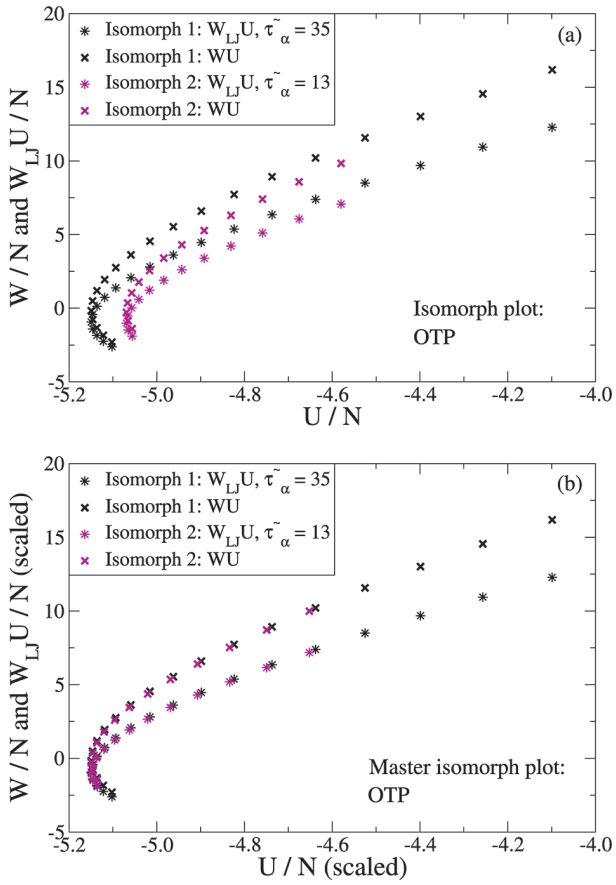

Figure 24. (a) Two different isomorphs for the OTP model in two different versions with 21% and 14% density increase (black and magenta). The crosses give the total virial W, the asterisks give $W_{LJ} = W - W_{CON}$. $\tilde{\tau}_\alpha$ is the reduced relaxation time of the isomorph extracted from the self-part of the intermediate scattering function. (b) The same isomorphs as in (a) where WU and $W_{LJ}U$ are scaled to superpose with a factor identified by trial and error. The black points have unity scaling factor.

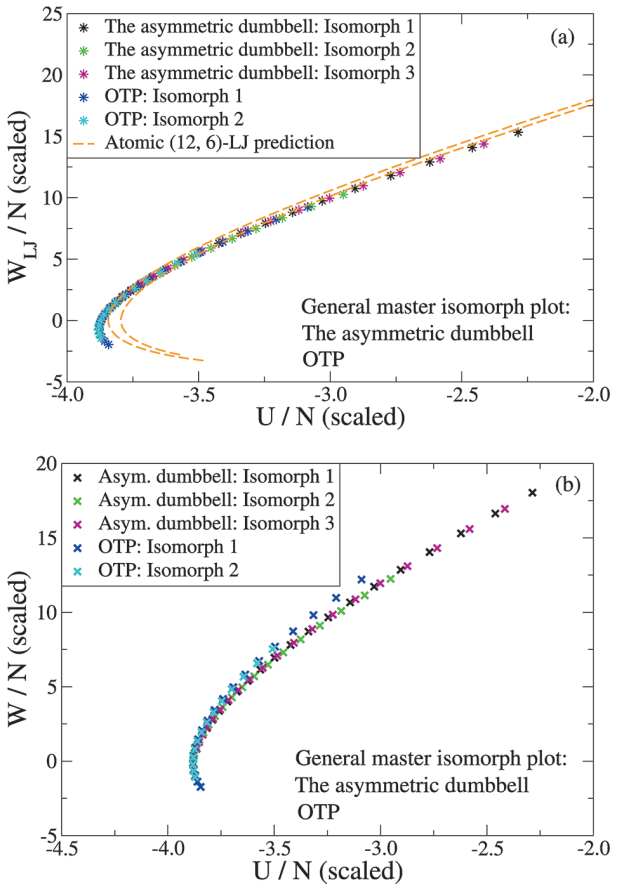

Figure 25. (a) Scaled $W_{LJ}U$ isomorphs for the asymmetric dumbbell and OTP models. The black points have unity scaling factor. Both systems have intermolecular (12,6)-LJ interactions, and the dashed curves are the isomorph prediction from ref 21 for an atomic system, where the LJ reference coefficients have been calculated from the dumbbell state points $(\rho, T) = (0.932, 0.465)$ and $(0.851, 0.274)$, respectively. (b) Scaled WU isomorphs for the systems in (a). The total virial does not show exact scaling between the asymmetric dumbbell and OTP models.

near straight line, the coefficients are not given by eqs 18 and 19. It is worth mentioning again that the prediction of ref 21 is for an atomic system and is as such not excepted to hold for rigid molecular systems.

Finally, we consider in Figure 27 for the asymmetric dumbbell how the instantaneous fluctuations of W_{CON} correlate with W_{LJ} and W, respectively. The constraint contribution to the virial at this state point does not correlate well with the contribution to the virial coming from the LJ interactions ($R = 0.31$). The correlation is higher when the total virial is considered ($R = 0.61$). The main contribution to the virial for the asymmetric dumbbell model comes from the LJ interactions; however, the LJ virial does not correlate well with the constraint virial. The latter observation may indicate a breakdown of master isomorph scaling (for the total virial) at high pressures, but this remains to be confirmed.

VI. SUMMARY AND OUTLOOK

Isomorphs are curves in the phase diagram of a strongly correlating liquid along which a number of static and dynamic quantities are invariant in reduced units. References 20 and 21 focused on understanding isomorphs in atomic systems. In this paper we generalized the isomorph concept to deal with systems of rigid molecules (eq 5) and investigated several predicted isomorph invariants for the asymmetric dumbbell, a symmetric IPL dumbbell, and the Lewis−Wahnström OTP models. We find that these rigid molecular systems also have isomorphs to a good approximation; however, the isomorphs of the OTP model were more approximative than those of the asymmetric dumbbell, which is consistent with the OTP model being less strongly correlating. Moreover, it was found that the asymmetric dumbbell and Lewis−Wahnström OTP models to a good approximation have master isomorphs, i.e., that all isomorphs have the same shape in the virial/potential energy phase diagram. This applies for the total virial, but also after subtracting the constraint contribution. A general master isomorph was identified between these two model systems after this subtraction.

A full theoretical understanding of the implications of rigid bonds remains to be arrived at. For instance, the shape of molecular isomorphs is different from the shape of ref 21 for atomic LJ systems. The rigid bonds seem in general to increase γ and decrease the correlation coefficient R with respect to the unconstrained system. More specifically, R

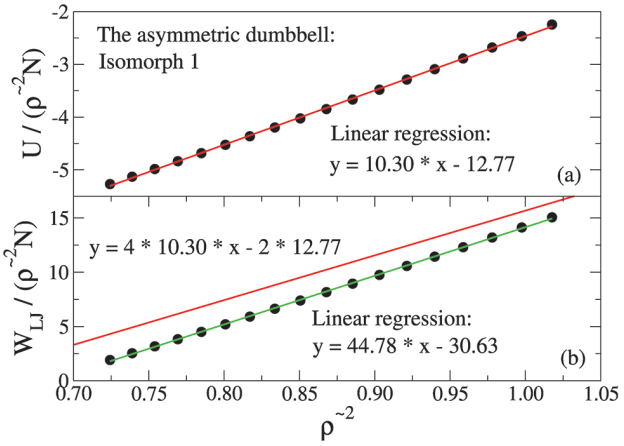

Figure 26. Potential energy and LJ virial as a function of $\tilde{\rho}^2$ for "Isomorph 1" of the asymmetric dumbbell. (a) A linear regression fit of the potential energy has been performed to calculate the reference coefficients (U_m^*, U_n^*). (b) These coefficients are then used to plot the red straight line, which according to the atomic prediction (eqs 18 and 19) should coincide with the black data points. The green line is a linear regression fit to the same data points.

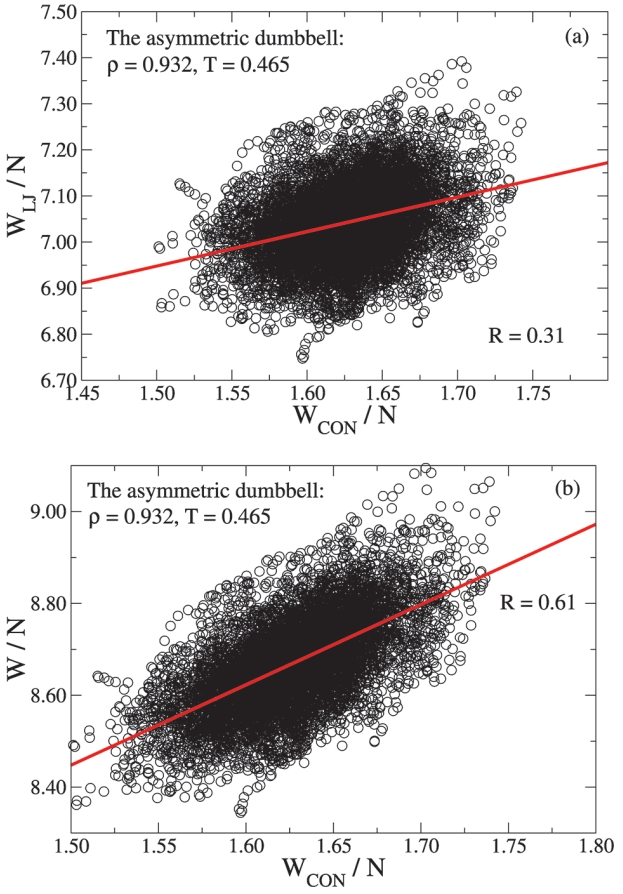

Figure 27. (a) Correlation of the instantaneous fluctuations of W_{LJ} and W_{CON}. The correlation coefficient R is 0.31. (b) Correlation of the instantaneous fluctuations of W and W_{CON}. The correlation coefficient R is 0.61.

decreases significantly with increasing asymmetric dumbbell bond length ($R \approx 0.65$ around unity bond length; see section IV'A). This is consistent with the results of Chopra et al.,[10] who noted a worse scaling of the reduced relaxation time and diffusion constant with excess entropy when the bond length of a rigid symmetric LJ dumbbell model is increased. On the other hand, it is noteworthy that strong correlation is observed for the OTP model even though it has unity bond lengths. The molecular center-of-mass structure in reduced units is predicted to be invariant along an isomorph; however, for the OTP model the reduced particle structure seems more invariant along an isomorph than the reduced molecular center-of-mass structure. The former is not predicted to be invariant along an isomorph, and the difference should be investigated in more detail to clarify this issue.

For real molecular liquids the concept of isomorphs is approximate. Thus it is natural to wonder to which extent the predicted scalings hold as the virial/potential energy correlation becomes worse. Consider for instance the supercooled regime. Here the transition states become increasingly more important as the temperature is lowered, and one might expect scalings involving dynamical quantities to be more sensitive to a decrease in the correlation coefficient than scalings based on the structure. Likewise, one could consider the breakdown of density scaling, indicated here by the study of the OTP model, as an effect of the correlation coefficient moving away from unity, because power-law density scaling is not solely based on Boltzmann factors. Quantifying how the scalings depend on the correlation coefficient is a topic that deserves more attention in future publications in connection with molecular liquids.

APPENDIX A: CONSTRAINED DYNAMICS AND THE VIRIAL EXPRESSION

Constrained dynamics is discussed in many different places, for instance refs 38, 40, and 41. We give here a brief introduction to constrained dynamics and the connection to the virial expression used in this article.

Gauss' principle of least constraint[48] states that a classic mechanical system of N particles with constraints deviates instantaneously in a least possible sense from Newton's second law, i.e., that

$$\sum_{i=1}^{N} m_i \left[\ddot{\mathbf{r}}_i - \frac{\mathbf{F}_i}{m_i}\right]^2 \tag{A1}$$

is a minimum. Here $\mathbf{r}_i$ and $\mathbf{F}_i$ are the position and interaction force of particle i. In the case of no constraints, setting the partial derivative $\partial/\partial\ddot{\mathbf{r}}_i$ to zero implies $\ddot{\mathbf{r}}_i - \mathbf{F}_i/m_i = 0$, i.e., Newtons's second law.

In the case of holonomic constraints $\psi^\alpha(\mathbf{r}^N) = 0$ where $\alpha = 1, ..., G$, the variation can be carried out by introducing Lagrangian multipliers, i.e.,

$$\sum_{i=1}^{N} m_i \left[\ddot{\mathbf{r}}_i - \frac{\mathbf{F}_i}{m_i}\right]^2 - \sum_{\alpha=1}^{G} \lambda^\alpha \ddot{\psi}^\alpha \tag{A2}$$

should be stationary. Setting the partial derivative $\partial/\partial\ddot{\mathbf{r}}_i$ to zero implies (where a factor of 1/2 has been absorbed in the Lagrangian multiplier)

$$m_i \cdot \ddot{\mathbf{r}}_i = \mathbf{F}_i + \sum_{\alpha=1}^{G} \lambda^\alpha \nabla_{\mathbf{r}_i} \psi^\alpha = \mathbf{F}_i + \mathbf{G}_i \tag{A3}$$

dx.doi.org/10.1021/jp2077402 |J. Phys. Chem. B 2012, 116, 1018–1034

Newton's second law thus remains valid if an additional force is added (called the constraint force $\mathbf{G}_i$). At this point λ^α is undetermined; however, an explicit expression[40] for λ^α can be determined from differentiating twice with respect to time the holonomic constraint. In molecular dynamics simulations it is imperative to calculate λ^α correctly to achieve a stable numerical algorithm. The reader is referred to refs 38 and 39 for details concerning this aspect.

The virial W is defined by $W = 1/3\Sigma_{i=1}^{N}\mathbf{r}_i\cdot\mathbf{F}_i$. In an atomic system with LJ pair potential interactions the virial is given by $W = W_{\mathrm{LJ}} = -1/3\Sigma_{i<j}^{N} r_{ij}u'(r_{ij})$. If the system has bond constraints $\psi^\alpha = (\mathbf{r}_{\alpha,i} - \mathbf{r}_{\alpha,j})^2/2 = r_{\alpha,ij}^{\ 2}/2 = c_{\alpha,ij}^{\ 2}/2$, it follows from eq A3 that the constraint force contributes to the virial as $W_{\mathrm{CON}} = 1/3\Sigma_{i=1}^{N}\mathbf{r}_i\cdot\mathbf{G}_i = 1/3\Sigma_{\alpha=1}^{G}\lambda^\alpha r_{\alpha,ij}^{\ 2}$.

APPENDIX B: CONSTRAINED *NVE* AND NOSÉ–HOOVER *NVT* DYNAMICS IN REDUCED UNITS ALONG AN ISOMORPH

We start our considerations from the constrained equations of motion, eq A3:

$$m_i\cdot\ddot{\mathbf{r}}_i = \mathbf{F}_i + \sum_{\alpha=1}^{G}\lambda^\alpha\nabla_{\mathbf{r}_i}\psi^\alpha = \mathbf{F}_i + \mathbf{G}_i \tag{B1}$$

Here $\mathbf{r}_i$ and $\mathbf{F}_i$ are, respectively, the position and interaction force of particle i, and λ^α is the Lagrangian multiplier for the α-th constraint ψ^α. For simulating rigid molecules[49] the constraints are in general a combination of constrained bond lengths $\psi^\alpha = (\mathbf{r}_{\alpha,i} - \mathbf{r}_{\alpha,j})^2/2 = \mathbf{r}_{\alpha,ij}^{\ 2}/2 = c_{\alpha,ij}^{\ 2}/2$ and linear constraints $\psi^\beta = \Sigma_{i=1}^{n_b}C_{\beta i}\mathbf{r}_i - \mathbf{r}_\beta = 0$, where $C_{\beta i}$ is a factor that depends on the geometry of the molecule (see ref 49 for more details). For simplicity we consider only bond constraints in the following.

The general expression for the Lagrangian multiplier λ^α is given by[40,50]

$$\lambda^\alpha = -\sum_{\beta=1}^{G}(\mathbf{Z}^{-1})_{\alpha\beta}\left[\sum_{i,j=1}^{N}\nabla_{\mathbf{r}_i}\nabla_{\mathbf{r}_j}\psi^\beta\dot{\mathbf{r}}_j\dot{\mathbf{r}}_i + \sum_{i=1}^{N}\frac{\nabla_{\mathbf{r}_i}\psi^\beta\cdot\mathbf{F}_i}{m_i}\right] \tag{B2}$$

$$Z_{\alpha\beta} = \sum_{i=1}^{N}\frac{\nabla_{\mathbf{r}_i}\psi^\alpha\cdot\nabla_{\mathbf{r}_i}\psi^\beta}{m_i} \tag{B3}$$

Defining reduced units for length, energy, and mass as follows

$$\tilde{\mathbf{r}}_i = \rho^{1/3}\mathbf{r}_i \tag{B4}$$

$$\tilde{U} = U/k_{\mathrm{B}}T \tag{B5}$$

$$\tilde{m}_i = m_i/\langle m\rangle \tag{B6}$$

reduced units for time and force follow as

$$\tilde{t} = t/(\rho^{-1/3}\sqrt{\langle m\rangle/k_{\mathrm{B}}T}) \tag{B7}$$

$$\tilde{\mathbf{F}}_i = \rho^{-1/3}\mathbf{F}_i/k_{\mathrm{B}}T = -\nabla_{\tilde{\mathbf{r}}_i}\tilde{U} \tag{B8}$$

Inserting the above definitions in eqs B1–B3 and using $\nabla_{\mathbf{r}_i}\psi^\alpha = \mathbf{r}_{\alpha,ij}$ we arrive at the constrained *NVE* equations of motion in reduced units

$$\tilde{m}_i\cdot\ddot{\tilde{\mathbf{r}}}_i = \tilde{\mathbf{F}}_i + \sum_{\alpha=1}^{G}\tilde{\lambda}^\alpha\tilde{\mathbf{r}}_{\alpha,ij} = \tilde{\mathbf{F}}_i + \tilde{\mathbf{G}}_i \tag{B9}$$

where

$$\tilde{\lambda}^\alpha = -\sum_{\beta=1}^{G}(\tilde{\mathbf{Z}}^{-1})_{\alpha\beta}\left[\sum_{i,j=1}^{N}\dot{\tilde{\mathbf{r}}}_j\dot{\tilde{\mathbf{r}}}_i + \sum_{i=1}^{N}\frac{\tilde{\mathbf{r}}_{\beta,ij}\cdot\tilde{\mathbf{F}}_i}{\tilde{m}_i}\right] \tag{B10}$$

$$\tilde{Z}_{\alpha\beta} = \sum_{i=1}^{N}\frac{\tilde{\mathbf{r}}_{\alpha,ij}\tilde{\mathbf{r}}_{\beta,ij}}{\tilde{m}_i} \tag{B11}$$

Because, in general, $\tilde{\mathbf{r}}_{\alpha,ij}^{\ 2} = \rho^{2/3}c_{\alpha,ij}^{\ 2}$, the reduced constrained equations of motion are *not* invariant along an isomorph.

Considering instead the molecular center-of-mass motion in reduced units

$$\tilde{M}_i\cdot\ddot{\tilde{\mathbf{r}}}_{\mathrm{CM},i} = \tilde{\mathbf{F}}_{\mathrm{CM},i} \tag{B12}$$

where $\tilde{\mathbf{F}}_{\mathrm{CM},i}$ and $\tilde{M}_i$ are respectively the reduced force on and mass of molecule i. Because the reduced force $\tilde{\mathbf{F}}_{\mathrm{CM},i}$ is invariant along an isomorph, it follows that the molecular *NVE* equations of motion are invariant along an isomorph. The invariance of $\tilde{\mathbf{F}}_{\mathrm{CM},i}$ can be seen as follows. The isomorph definition eq 5 implies for a fixed state point (1) and arbitrary state point (x), both along the same isomorph [where $\tilde{\mathbf{R}} \equiv (\rho^{-1/3}\tilde{\mathbf{r}}_{\mathrm{CM},1}, \phi_1, \theta_1, \chi_1, ..., \rho^{-1/3}\tilde{\mathbf{r}}_{\mathrm{CM},N}, \phi_N, \theta_N, \chi_N)$], that

$$-U(\tilde{\mathbf{R}}^{(x)})/k_{\mathrm{B}}T_x = -U(\tilde{\mathbf{R}}^{(1)})/k_{\mathrm{B}}T_1 - \ln\ C_{1x} \tag{B13}$$

Taking the gradient $\nabla_{\tilde{\mathbf{r}}_{\mathrm{CM},i}}$ it follows that

$$\tilde{\mathbf{F}}_{\mathrm{CM},i}^{(x)} = \tilde{\mathbf{F}}_{\mathrm{CM},i}^{(1)} \tag{B14}$$

This concludes the proof of the isomorph invariance of the reduced molecular center-of-mass *NVE* equations of motion. For the molecular center-of-mass *NVT* equations of motion the proof is analogous to the above and shown for atomic systems in ref 20. In this case the time constant of the Nosé–Hoover algorithm needs to be adjusted along the isomorph; otherwise, the dynamics is not invariant.[20]

ACKNOWLEDGMENT

The Centre for Viscous Liquid Dynamics "Glass and Time" is sponsored by the Danish National Research Foundation (DNRF).

REFERENCES

(1) Alba-Simionesco, C.; Cailliaux, A.; Alegría, A.; Tarjus, G. *Europhys. Lett.* **2004**, *68*, 58.
(2) Dreyfus, C.; Grand, A. L.; Gapinski, J.; Steffen, W.; Patkowski, A. *Eur. Phys. J. B* **2004**, *42*, 309.
(3) Roland, C. M. *Macromolecules* **2010**, *43*, 7875.
(4) Roland, C. M.; Casalini, R.; Paluch, M. *Chem. Phys. Lett.* **2003**, *367*, 259.
(5) Ngai, K. L.; Casalini, R.; Capaccioli, S.; Paluch, M.; Roland, C. M. *J. Phys. Chem. B* **2005**, *109*, 17356.
(6) Rosenfeld, Y. *Phys. Rev. A* **1977**, *15*, 2545.
(7) Rosenfeld, Y. *J. Phys.: Condens. Matter* **1999**, *11*, 5415.
(8) Chopra, R.; Truskett, T. M.; Errington, J. R. *J. Phys. Chem. B* **2010**, *114*, 10558.
(9) Chopra, R.; Truskett, T. M.; Errington, J. R. *J. Phys. Chem. B* **2010**, *114*, 16487.
(10) Chopra, R.; Truskett, T. M.; Errington, J. R. *J. Chem. Phys.* **2010**, *133*, 104506.
(11) Abramson, E. H. *Phys. Rev. E* **2007**, *76*, 051203.
(12) Abramson, E. H.; West-Foyle, H. *Phys. Rev. E* **2008**, *77*, 041202.
(13) Abramson, E. H. *Phys. Rev. E* **2009**, *80*, 021201.

(14) Galliero, G.; Boned, C.; Fernández, J. *J. Chem. Phys.* **2011**, *134*, 064505.
(15) Fragiadakis, D.; Roland, C. M. *J. Chem. Phys.* **2011**, *134*, 044504.
(16) López, E. R.; Pensado, A. S.; Comuñas, M. J. P.; Pádua, A. A. H.; Fernández, J.; Harris, K. R. *J. Phys. Chem.* **2011**, *134*, 144507.
(17) Bailey, N. P.; Pedersen, U. R.; Gnan, N.; Schrøder, T. B.; Dyre, J. C. *J. Chem. Phys.* **2008**, *129*, 184507.
(18) Bailey, N. P.; Pedersen, U. R.; Gnan, N.; Schrøder, T. B.; Dyre, J. C. *J. Chem. Phys.* **2008**, *129*, 184508.
(19) Schrøder, T. B.; Bailey, N. P.; Pedersen, U. R.; Gnan, N.; Dyre, J. C. *J. Chem. Phys.* **2009**, *131*, 234503.
(20) Gnan, N.; Schrøder, T. B.; Pedersen, U. R.; Bailey, N. P.; Dyre, J. C. *J. Chem. Phys.* **2009**, *131*, 234504.
(21) Schrøder, T. B.; Gnan, N.; Pedersen, U. R.; Bailey, N. P.; Dyre, J. C. *J. Chem. Phys.* **2011**, *134*, 164505.
(22) Schrøder, T. B.; Pedersen, U. R.; Bailey, N. P.; Toxvaerd, S.; Dyre, J. C. *Phys. Rev. E* **2009**, *80*, 041502.
(23) Pedersen, U. R.; Gnan, N.; Bailey, N. P.; Schrøder, T. B.; Dyre, J. C. *J. Non-Cryst. Solids* **2011**, *357*, 320.
(24) Pedersen, U. R.; Bailey, N. P.; Schrøder, T. B.; Dyre, J. C. *Phys. Rev. Lett.* **2008**, *100*, 015701.
(25) Coslovich, D.; Roland, C. M. *J. Chem. Phys.* **2009**, *130*, 014508.
(26) Coslovich, D.; Roland, C. M. *J. Phys. Chem. B* **2008**, *112*, 1329.
(27) Kob, W.; Andersen, H. C. *Phys. Rev. E* **1995**, *51*, 4626.
(28) Kob, W.; Andersen, H. C. *Phys. Rev. E* **1995**, *52*, 4134.
(29) Wahnström, G.; Lewis, L. J. *Physica A* **1993**, *201*, 150.
(30) Lewis, L. J.; Wahnström, G. *Phys. Rev. E* **1994**, *50*, 3865.
(31) Gundermann, D.; Pedersen, U. R.; Hecksher, T.; Bailey, N. P.; Jakobsen, B.; Christensen, T.; Olsen, N. B.; Schrøder, T. B.; Fragiadakis, D.; Casalini, R.; Roland, C. M.; Dyre, J. C.; Niss, K. *Nat. Phys.* **2011**, *7*, 816.
(32) In practice, it is only required that the physically relevant configurations obey this scaling, i.e., at least those that contribute significantly to the partition function.
(33) Gray, C. G.; Gubbins, K. E. *Theory of Molecular Fluids*; Oxford University Press: Oxford, U.K., 1984.
(34) Lazaridis, T.; Paulaitis, M. E. *J. Phys. Chem.* **1992**, *96*, 3847.
(35) Lazaridis, T.; Karplus, M. *J. Chem. Phys.* **1996**, *105*, 4294.
(36) Pedersen, U. R.; Hudson, T. S.; Harrowell, P. *J. Chem. Phys.* **2011**, *134*, 114501.
(37) Hess, B.; Kutzner, C.; van der Spoel, D.; Lindahl, E. *J. Chem. Theory Comput.* **2008**, *4*, 435.
(38) Toxvaerd, S.; Heilmann, O. J.; Ingebrigtsen, T.; Schrøder, T. B.; Dyre, J. C. *J. Chem. Phys.* **2009**, *131*, 064102.
(39) Ingebrigtsen, T.; Heilmann, O. J.; Toxvaerd, S.; Dyre, J. C. *J. Chem. Phys.* **2010**, *132*, 154106.
(40) Edberg, R.; Evans, D. J.; Morriss, G. P. *J. Chem. Phys.* **1986**, *84*, 6933.
(41) Ryckaert, J. P.; Ciccotti, G.; Berendsen, H. J. C. *J. Comput. Phys.* **1977**, *23*, 327.
(42) Nosé, S. *J. Chem. Phys.* **1984**, *81*, 511.
(43) Hoover, W. G. *Phys. Rev. A* **1985**, *31*, 1695.
(44) Toxvaerd, S. *Mol. Phys.* **1991**, *72*, 159.
(45) All simulations were performed using a molecular dynamics code optimized for *NVIDIA* graphics cards, which is available as open source code at http://rumd.org.
(46) Frenkel, D.; Smit, B. *Understanding Molecular Simulation*; Academic Press: New York, 2002.
(47) Pedersen, U. R.; Schrøder, T. B.; Dyre, J. C. *Phys. Rev. Lett.* **2010**, *105*, 157801.
(48) Gauss, K. F. *J. Reine Angew. Math.* **1829**, *4*, 232.
(49) Ciccotti, G.; Ferrario, M.; Ryckaert, J. P. *Mol. Phys.* **1982**, *47*, 1253.
(50) Melchionna, S. *Phys. Rev. E* **2000**, *61*, 6165.

NVU dynamics. I. Geodesic motion on the constant-potential-energy hypersurface

Trond S. Ingebrigtsen, Søren Toxvaerd, Ole J. Heilmann, Thomas B. Schrøder, and Jeppe C. Dyre[a)]

DNRF Centre "Glass and Time," IMFUFA, Department of Sciences, Roskilde University, Postbox 260, DK-4000 Roskilde, Denmark

(Received 28 March 2011; accepted 17 July 2011; published online 8 September 2011)

An algorithm is derived for computer simulation of geodesics on the constant-potential-energy hypersurface of a system of N classical particles. First, a basic time-reversible geodesic algorithm is derived by discretizing the geodesic stationarity condition and implementing the constant-potential-energy constraint via standard Lagrangian multipliers. The basic *NVU* algorithm is tested by single-precision computer simulations of the Lennard-Jones liquid. Excellent numerical stability is obtained if the force cutoff is smoothed and the two initial configurations have identical potential energy within machine precision. Nevertheless, just as for *NVE* algorithms, stabilizers are needed for very long runs in order to compensate for the accumulation of numerical errors that eventually lead to "entropic drift" of the potential energy towards higher values. A modification of the basic *NVU* algorithm is introduced that ensures potential-energy and step-length conservation; center-of-mass drift is also eliminated. Analytical arguments confirmed by simulations demonstrate that the modified *NVU* algorithm is absolutely stable. Finally, we present simulations showing that the *NVU* algorithm and the standard leap-frog *NVE* algorithm have identical radial distribution functions for the Lennard-Jones liquid. © *2011 American Institute of Physics*. [doi:10.1063/1.3623585]

I. INTRODUCTION

This paper and its companion Paper II[1] study *NVU* dynamics, i.e., dynamics that conserves the potential energy U for a system of N classical particles at constant volume V. *NVU* dynamics is deterministic and involves only the system's configurational degrees of freedom. *NVU* dynamics is characterized by the system moving along a so-called *geodesic* curve on the constant-potential-energy hypersurface Ω defined by

$$\Omega = \{(\mathbf{r}_1, \ldots, \mathbf{r}_N) \in R^{3N} | U(\mathbf{r}_1, \ldots, \mathbf{r}_N) = U_0\}. \quad (1)$$

Mathematically, Ω is a $(3N-1)$-dimensional differentiable manifold. Since it is imbedded in R^{3N}, Ω has a natural Euclidean metric and it is thus a so-called Riemannian manifold.[2] The differential geometry of hypersurfaces is discussed in, for instance, Ref. 3.

A geodesic curve on a Riemannian manifold minimizes the distance between any two of its points that are sufficiently close to each other (the curve is characterized by realizing the "locally shortest distance" between points). A geodesic is defined by the property that for any curve variation keeping the two end points $\mathbf{R}_A$ and $\mathbf{R}_B$ fixed, to lowest order the curve length does not change, i.e.,

$$\delta \int_{\mathbf{R}_A}^{\mathbf{R}_B} dl = 0. \quad (2)$$

Here, dl denotes the line element of the metric.

From a physical point of view, it is sometimes useful to regard a geodesic as a curve on a given surface along which the system moves at constant velocity with zero friction. Such motion means that at any time the force is perpendicular to the surface, and because the force performs no work, the kinetic energy is conserved. In this way, geodesic motion generalizes Newton's first law, the law of inertia, to curved surfaces. The concept of geodesic motion is central in general relativity, where motion in a gravitational field follows a geodesic curve in the four-dimensional curved space-time.[4]

A general motivation for studying *NVU* dynamics is the following. Since basically all relevant information about a system is encoded in the potential-energy function, it is interesting from a philosophical point of view to study and compare different dynamics relating to $U(\mathbf{r}_1, \ldots, \mathbf{r}_N)$. The "purest" of these dynamics does not involve momenta and relates only to configuration space. *NVU* dynamics provides such a dynamics. In contrast to Brownian dynamics, which also relates exclusively to the configurational degrees of freedom, *NVU* dynamics is deterministic. *NVU* dynamics may be viewed as an attempt to understand the dynamic implications of the potential energy landscape's geometry along the lines of recent papers by Stratt and co-workers.[5,6]

Our interest in *NVU* dynamics originated in recent results concerning strongly correlating liquids and their isomorphs. A liquid is termed strongly correlating if there is more than 90% correlation between its virial and potential energy thermal equilibrium fluctuations in the *NVT* ensemble.[7] The class of strongly correlating liquids includes most or all van der Waals and metallic liquids, whereas hydrogen-bonding, covalently bonded liquids, and ionic liquids are generally not strongly correlating because competing interactions tend to weaken the correlation. A liquid is strongly correlating if and

a)Electronic mail: dyre@ruc.dk.

only if it to a good approximation has "isomorphs" in its phase diagram.[8,9] By definition two state points are isomorphic[8] if any two microconfigurations of the state points, which can be trivially scaled into one another, have identical canonical probabilities; an isomorph is a curve in the phase diagram for which any two pairs of state points are isomorphic. Only inverse-power-law liquids have exact isomorphs, but simulations show that Lennard-Jones type liquids have isomorphs to a good approximation.[8] This is consistent with these liquids being strongly correlating.[7] Many properties are invariant along an isomorph, for instance, the excess entropy, the isochoric heat capacity, scaled radial distribution functions, dynamic properties in reduced units, etc;[8,9] the reduced-unit constant-potential-energy hypersurface $\tilde{\Omega}$ is also invariant along an isomorph.[8] Given that several properties are invariant along a strongly correlating liquid's isomorphs and that $\tilde{\Omega}$ is invariant as well, an obvious idea is that $\tilde{\Omega}$'s invariance is the fundamental fact from which all other isomorph invariants follow. For instance, the excess entropy is the logarithm of the area of $\tilde{\Omega}$, so the excess entropy's isomorph invariance follows directly from that of $\tilde{\Omega}$. In order to understand the dynamic isomorph invariants from the $\tilde{\Omega}$ perspective a dynamics is required that refers exclusively to $\tilde{\Omega}$. One possibility is diffusive dynamics, but a mathematically even more elegant dynamics on a differentiable manifold is that of geodesics. Although these considerations were our original motivation, it should be emphasized that the concept of geodesic motion on $\tilde{\Omega}$ (or Ω) is general and can be applied to any classical mechanical system, strongly correlating or not.

We are not the first to consider dynamics on the constant-potential-energy hypersurface. In papers dating back to 1986,[10] Cotterill and Madsen proposed a deterministic constant-potential-energy algorithm that is similar, but not identical, to the basic *NVU* algorithm derived below. Their algorithm was not discussed in relation to geodesic curves, but aimed at providing an alternative way to understand vacancy diffusion in crystals and, in particular, to make easier the identification of energy barriers than via ordinary MD simulations. The latter property is not confirmed in the present papers, however – in contrast, we find that *NVU* dynamics in the thermodynamic limit becomes equivalent to standard *NVE* dynamics (Paper II). Later, Scala *et al.* studied diffusive dynamics on the constant-potential-energy hypersurface Ω,[11] focusing on the entropic nature of barriers by regarding these as "bottlenecks." This point was also made by Cotterill and Madsen who viewed Ω as consisting of "pockets" connected by thin paths, referred to as "tubes," acting as entropy barriers. Reasoning along similar lines, Stratt and co-workers published in 2007 and 2010 three papers,[5,6] which considered paths in the so-called potential-energy-landscape ensemble. This novel ensemble is defined by including all configurations with potential energy less than or equal to some potential energy U_0. A geodesic in the potential-energy-landscape ensemble consists of a curve that is partly geodesic on the constant-potential-energy surface Ω, partly a straight line in the space defined by $U < U_0$.[5] Wang and Stratt's picture shifts "perspective from finding stationary points on the potential energy landscape to finding and characterizing the accessible pathways through the landscape. Within this perspective pathways would be slow, not because they have to climb over high barriers, but because they have to take a long and tortuous route to avoid such barriers. . . ."[5] Thus, the more "convoluted and labyrinthine" the geodesics are, the slower is the dynamics.[5]- Apart from these three sources of inspiration to the present work, we note that geodesic motion on differentiable manifolds has been studied in several other contexts outside of pure mathematics, see, e.g., Ref. 12.

The present paper derives and documents an algorithm for *NVU* dynamics. In Sec. II, we derive the basic *NVU* algorithm. By construction this algorithm is time reversible, a feature that ensures a number of important properties.[13,14] Section III discusses how to implement the *NVU* algorithm and tests improvements of the basic *NVU* algorithm designed for ensuring stability; this is done by single-precision simulations. This section arrives at the final *NVU* algorithm and demonstrates that it conserves potential energy, step length, and center-of-mass position in arbitrarily long simulations. Section IV briefly investigates the sampling properties of the *NVU* algorithm, showing that it gives results for the Lennard-Jones liquid that are equivalent to those of standard *NVE* dynamics. Finally, Sec. V gives a few concluding comments. Paper II compares *NVU* simulations to results for four other dynamics, concluding that *NVU* dynamics is a fully valid molecular dynamics.

II. THE BASIC *NVU* ALGORITHM

For simplicity of notation, we consider in this paper only systems of particles of identical masses (the Appendix of Paper II generalizes the algorithm to systems of varying particle masses). The full set of positions in the $3N$-dimensional configuration space is collectively denoted by $\mathbf{R}$, i.e.,

$$\mathbf{R} \equiv (\mathbf{r}_1, \ldots, \mathbf{r}_N). \tag{3}$$

Likewise, the full $3N$-dimensional force vector is denoted by $\mathbf{F}$. This section derives the basic *NVU* algorithm for geodesic motion on the constant-potential-energy hypersurface Ω defined in Eq. (1), an algorithm that allows one to compute the positions in step $i+1$, $\mathbf{R}_{i+1}$, from $\mathbf{R}_{i-1}$ and $\mathbf{R}_i$. Although a mathematical geodesic on a differentiable manifold is usually parameterized by its curve length,[2] it is useful to think of a geodesic curve on Ω as parameterized by time and we shall refer to the steps of the algorithm as "time steps."

Locally, a geodesic is the shortest path between any two of its points. More precisely: (1) For any two points on a Riemannian manifold the shortest path between them is a geodesic; (2) the property of a curve being geodesic is locally defined; (3) a geodesic curve has the property that for any two of its points, which are sufficiently close to each other, the curve gives the shortest path between them. A geodesic may, in fact, be the *longest* distance between two of its points. For instance, the shortest and the longest flight between two cities on our globe both follow great circles – these are both geodesics. In any case, the property of being geodesic is always defined by the curve length being *stationary* in the following sense: Small curve variations, which do not move the curve's end points, to lowest order do not change the curve length (Eq. (2)).

For motion on Ω, the constraint of constant potential energy is taken into account by introducing Lagrangian multipliers. For each time step j the constraint $U(\mathbf{R}_j) = U_0$ gives rise to a corresponding Lagrangian multiplier λ_j. Thus, the stationarity condition Eq. (2) for the discretized curve length $\sum_j |\mathbf{R}_j - \mathbf{R}_{j-1}|$ subject to the constraint of constant potential energy is

$$\delta\left(\sum_j |\mathbf{R}_j - \mathbf{R}_{j-1}| - \sum_j \lambda_j U(\mathbf{R}_j)\right) = 0\,. \tag{4}$$

Since $|\mathbf{R}_j - \mathbf{R}_{j-1}| = \sqrt{(\mathbf{R}_j - \mathbf{R}_{j-1})^2}$ and the $3N$-dimensional force is given by $\mathbf{F}_j = -\partial U/\partial \mathbf{R}_j$, putting to zero the variation of Eq. (4) with respect to $\mathbf{R}_i$ (i.e., the partial derivative $\partial/\partial \mathbf{R}_i$) leads to

$$\frac{\mathbf{R}_i - \mathbf{R}_{i-1}}{|\mathbf{R}_i - \mathbf{R}_{i-1}|} - \frac{\mathbf{R}_{i+1} - \mathbf{R}_i}{|\mathbf{R}_{i+1} - \mathbf{R}_i|} + \lambda_i \mathbf{F}_i = 0\,. \tag{5}$$

To solve these equations we make the *ansatz* of constant displacement length for each time step,

$$|\mathbf{R}_j - \mathbf{R}_{j-1}| \equiv l_0 \ \ (\text{all} \ \ j)\,. \tag{6}$$

If the path discretization is thought of as defined by constant time increments, Eq. (6) corresponds to constant velocity in the geodesic motion. With this *ansatz*, Eq. (5) becomes

$$(\mathbf{R}_i - \mathbf{R}_{i-1}) + (\mathbf{R}_i - \mathbf{R}_{i+1}) + l_0 \lambda_i \mathbf{F}_i = 0\,. \tag{7}$$

If $\mathbf{a}_i \equiv \mathbf{R}_i - \mathbf{R}_{i-1}$ and $\mathbf{b}_i \equiv \mathbf{R}_i - \mathbf{R}_{i+1}$, Eq. (6) implies $\mathbf{a}_i^2 = \mathbf{b}_i^2$, i.e., $0 = \mathbf{a}_i^2 - \mathbf{b}_i^2 = (\mathbf{a}_i + \mathbf{b}_i) \cdot (\mathbf{a}_i - \mathbf{b}_i)$. Since Eq. (7) expresses that $\mathbf{a}_i + \mathbf{b}_i$ is parallel to $\mathbf{F}_i$, one concludes that $\mathbf{F}_i$ is perpendicular to $\mathbf{a}_i - \mathbf{b}_i = \mathbf{R}_{i+1} - \mathbf{R}_{i-1}$. This implies

$$\mathbf{F}_i \cdot \mathbf{R}_{i-1} = \mathbf{F}_i \cdot \mathbf{R}_{i+1}\,. \tag{8}$$

Taking the dot product of each side of Eq. (7) with $\mathbf{F}_i$ one gets

$$\mathbf{F}_i \cdot (\mathbf{R}_i - \mathbf{R}_{i-1}) + \mathbf{F}_i \cdot (\mathbf{R}_i - \mathbf{R}_{i+1}) + l_0 \lambda_i \mathbf{F}_i^2 = 0\,, \tag{9}$$

which via Eq. (8) implies

$$l_0 \lambda_i = -2\,\frac{\mathbf{F}_i \cdot (\mathbf{R}_i - \mathbf{R}_{i-1})}{\mathbf{F}_i^2}\,. \tag{10}$$

Substituting this into Eq. (7) and isolating $\mathbf{R}_{i+1}$, we finally arrive at

$$\mathbf{R}_{i+1} = 2\mathbf{R}_i - \mathbf{R}_{i-1} - \frac{2[\mathbf{F}_i \cdot (\mathbf{R}_i - \mathbf{R}_{i-1})]\mathbf{F}_i}{\mathbf{F}_i^2}\,. \tag{11}$$

This equation determines a sequence of positions; it will be referred to as "the basic *NVU* algorithm."

The derivation of the basic *NVU* algorithm is completed by checking its consistency with the constant step length *ansatz* Eq. (6): Rewriting Eq. (11) as $(\mathbf{R}_{i+1} - \mathbf{R}_i) = (\mathbf{R}_i - \mathbf{R}_{i-1}) - 2[\mathbf{F}_i \cdot (\mathbf{R}_i - \mathbf{R}_{i-1})]\mathbf{F}_i/\mathbf{F}_i^2$, we get by squaring each side $(\mathbf{R}_{i+1} - \mathbf{R}_i)^2 = (\mathbf{R}_i - \mathbf{R}_{i-1})^2 + 4[\mathbf{F}_i \cdot (\mathbf{R}_i - \mathbf{R}_{i-1})]^2/\mathbf{F}_i^2 - 4[\mathbf{F}_i \cdot (\mathbf{R}_i - \mathbf{R}_{i-1})]^2/\mathbf{F}_i^2 = (\mathbf{R}_i - \mathbf{R}_{i-1})^2$. Thus, the solution is consistent with the *ansatz*.

Time reversibility of the basic *NVU* algorithm is checked by rewriting Eq. (11) as follows:

$$\mathbf{R}_{i-1} = 2\mathbf{R}_i - \mathbf{R}_{i+1} - \frac{2[\mathbf{F}_i \cdot (\mathbf{R}_i - \mathbf{R}_{i-1})]\mathbf{F}_i}{\mathbf{F}_i^2}\,, \tag{12}$$

which via Eq. (8) implies

$$\mathbf{R}_{i-1} = 2\mathbf{R}_i - \mathbf{R}_{i+1} - \frac{2[\mathbf{F}_i \cdot (\mathbf{R}_i - \mathbf{R}_{i+1})]\mathbf{F}_i}{\mathbf{F}_i^2}\,. \tag{13}$$

Comparing to Eq. (11) shows that any sequence of configurations generated by Eq. (11) $\ldots, \mathbf{R}_{i-1}, \mathbf{R}_i, \mathbf{R}_{i+1}, \ldots$ obeys Eq. (11) in the time-reversed version $\ldots, \mathbf{R}_{i+1}, \mathbf{R}_i, \mathbf{R}_{i-1}, \ldots$. A more direct way to show that the basic *NVU* algorithm is time-reversal invariant is to note that Eq. (5) is itself manifestly invariant if the indices $i-1$ and $i+1$ are interchanged.

The Appendix shows that the basic *NVU* algorithm is symplectic, i.e., that it conserves the configuration-space volume element in the same way as *NVE* dynamics does. We finally consider potential-energy conservation in the basic *NVU* algorithm. A Taylor expansion implies via Eq. (8) that

$$U_{i+1} - U_{i-1} = -\mathbf{F}_i \cdot (\mathbf{R}_{i+1} - \mathbf{R}_{i-1}) + O\left(l_0^3\right) = O\left(l_0^3\right)\,. \tag{14}$$

This ensures potential-energy conservation to a good approximation if the discretization step is sufficiently small.

The "potential energy contour tracing" (PECT) algorithm of Cotterill and Madsen[10] is the following: $\mathbf{R}_{i+1} = 2\mathbf{R}_i - \mathbf{R}_{i-1} - [\mathbf{F}_i \cdot (\mathbf{R}_i - \mathbf{R}_{i-1})]\mathbf{F}_i/\mathbf{F}_i^2$. Except for a factor of 2 this is identical to the basic *NVU* algorithm. The importance of this difference is apparent when it is realized that the PECT algorithm implies $\mathbf{F}_i \cdot (\mathbf{R}_{i+1} - \mathbf{R}_i) = 0$, whereas it does not imply the time-reversed identity $\mathbf{F}_i \cdot (\mathbf{R}_{i-1} - \mathbf{R}_i) = 0$. Thus, the PECT algorithm is not time reversible.

We end this section by reflecting on what is the relation between the *NVU* algorithm and continuous geodesic curves on Ω. Can one expect that if the step length is decreased towards zero, the discrete sequence of points traced out by the algorithm converges to a continuous geodesic curve? The answer is yes, as is clear from the current applied mathematics literature.[15] The literature deals with the analogous problem of classical mechanics where, as is well known, Newton's second law of motion can be derived from the principle of least action (Hamilton's principle). This is a variational principle. In the traditional approach, one first derives continuous equations of motion from the variational principle, then discretizes these equations to allow for computer simulations. Here, we first discretized the quantity subject to the variational principle (Eq. (4)) and only thereafter applied variational calculus. Euler himself first described discretization of time in the action integral, thus obtaining discretized versions of the Euler-Lagrange equations. There is now a large literature on this subject.[15] During the last decade, in particular, variational calculations applied *after* discretization have come into focus in connection with, for instance, the development of algorithms for the control of robots. The general consensus is the following (we quote below from Ref. 16 that provides an excellent summary of the situation): "The driving idea behind this discrete geometric mechanics is to leverage the variational nature of mechanics and to preserve this variational structure in the discrete setting... That is, if one designs a discrete equivalent of the Lagrangian, then discrete equations of motion can be easily derived from it by paralleling the derivations followed in continuous case. In essence, good numerical methods will come from discrete analogs to

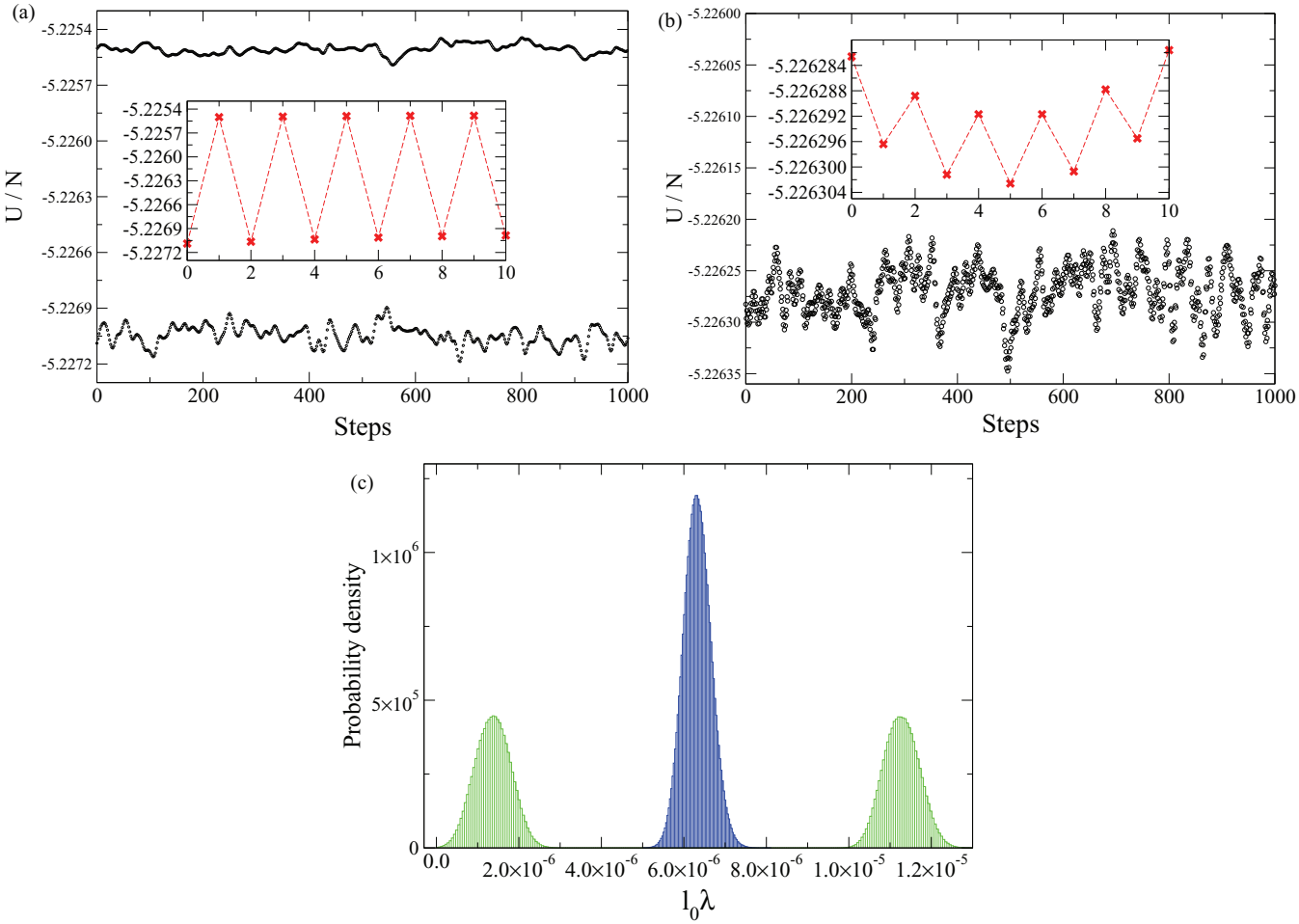

FIG. 1. (a) Evolution of the potential energy U according to the basic *NVU* algorithm (Eq. (17)) started from two consecutive configurations of an *NVE* simulation. The inset shows a snapshot of the first ten integration steps where lines connect the data points; clearly, the system jumps distinctly between two potential-energy hypersurfaces. (b) Evolution of U started from two configurations with a very small potential energy difference. The algorithm still jumps between two potential-energy hypersurfaces. (c) Probability distribution of the Lagrangian multiplier times the length l_0, $l_0\lambda$ of Eq. (10), obtained from simulations over 2.5×10^6 steps. The green distribution corresponds to (a), the blue distribution to (b).

the Euler-Lagrange equations – equations that truly derive from a variational principle… Results have been shown to be equal or superior to all other types of integrators for simulations of a large range of physical phenomena, making this discrete geometric framework both versatile and powerful."

III. TESTING AND IMPROVING THE BASIC *NVU* ALGORITHM

This section discusses the numerical implementation of the basic *NVU* algorithm and how to deal with accumulating round-off errors that arise for very long simulations. The model system studied is the standard Lennard-Jones (LJ) liquid with $N = 1024$ particles. Recall that the LJ pair potential $v(r)$ is given by

$$v(r) = 4\varepsilon\left[\left(\frac{\sigma}{r}\right)^{12} - \left(\frac{\sigma}{r}\right)^{6}\right]. \tag{15}$$

Here, ε sets the energy scale and σ sets the length scale; henceforth, the unit system is adopted in which these quantities are both unity. All simulations except those of Fig. 5 refer to the state point with density 0.85 and temperature 0.7. Initial configurations were taken from *NVE* simulations of this state point. Unless otherwise specified the forces and their derivative were adjusted to be continuous via smoothing from a value just below the cutoff distance r_c to r_c. We refer to this as a "smoothed force potential." The cutoff distance was chosen as the standard LJ cutoff $r_c = 2.5\sigma$. The simulations were performed using periodic boundary conditions. In order to easier test the numerical stability of the *NVU* algorithm, simulations were performed in single precision.[17]

A. Implementing the basic *NVU* algorithm

We rewrite Eq. (11) into a leap-frog version by introducing new variables defined by

$$\boldsymbol{\Delta}_{i+1/2} \equiv \mathbf{R}_{i+1} - \mathbf{R}_i\,. \tag{16}$$

In terms of these variables the basic *NVU* algorithm is

$$\boldsymbol{\Delta}_{i+1/2} = \boldsymbol{\Delta}_{i-1/2} - \frac{2(\mathbf{F}_i \cdot \boldsymbol{\Delta}_{i-1/2})\mathbf{F}_i}{\mathbf{F}_i^2}$$
$$\mathbf{R}_{i+1} = \mathbf{R}_i + \boldsymbol{\Delta}_{i+1/2}\,. \tag{17}$$

Equations (17) are formally equivalent to Eq. (11). Numerically, however, they are not equivalent and – as is also the

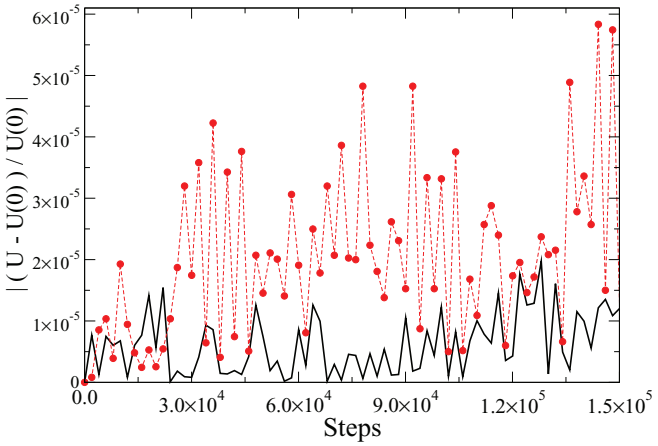

FIG. 2. Evolution of $|(U - U(0))/U(0)|$ for a simulation using the basic *NVU* algorithm. The red curve gives results from a simulation where the potential is cut and shifted at $r = 2.5\sigma$, the black curve gives results for a smoothed force potential.

case for standard *NVE* dynamics – the leap-frog version is preferable because it deals with position changes.[18]

Figure 1(a) shows the potential energy as a function of time-step number when the two initial configurations are taken from consecutive configurations of an *NVE* simulation. The system's potential energy jumps every second step, jumping between two distinct values (inset). This is also reflected in the distribution of the quantity $l_0\lambda_i$ shown in green in Fig. 1(c). *A priori* one would expect a Gaussian single-peak distribution of $l_0\lambda_i$, but the distribution has two peaks. What causes the potential energy to zig-zag in an algorithm constructed to conserve the potential energy? The answer is hinted at in Eq. (14) according to which the *NVU* algorithm implies energy conservation to a good accuracy, but only every second step. Thus, if the two initial configurations do not have identical potential energy, the potential energy will zig-zag between two values. Figure 1(b) shows that even if a simulation is initiated from two configurations with very close potential energies, the zig-zag phenomenon persists, though now on a much smaller scale.

There are further numerical issues that affect the stability of the basic *NVU* algorithm. In Fig. 2, the evolution of the potential energy is given for a long simulation, which also includes data from simulations using a non-smoothed force potential. Better numerical stability is clearly obtained for the smoothed force potential (black curve), but smoothing does not ensure constant potential energy and absolute stability.

B. Improving the algorithm to conserve potential energy and step length indefinitely

Subsection III A showed that using a smoothed force potential and ensuring that the two starting configurations have identical potential energy within machine precision, a fairly stable algorithm is arrived at. Nevertheless, absolute stability is not obtained. This is illustrated in Fig. 3(a), which shows that the potential energy for a system with a smoothed force potential over five million time steps still exhibits a slight "entropic drift" (red curve). By entropic drift, we mean the drift due to round-off errors, a drift that unavoidably takes the system to higher energies because there are many more such states – an entropic effect. Figure 3(b) shows that also the step length is not conserved. Both problems are caused by the accumulation of round-off errors. These problems are less severe if one switches to double precision, of course, but for long simulations entropic drift eventually sets in (for billions of time steps).

We would like to have an algorithm that is absolutely stable, i.e., one that does not allow for any long-time drift of the quantities which the basic *NVU* algorithm was constructed to conserve: the potential energy, the step length, and the center of mass (CM) position (just as in standard *NVE* dynamics the CM position is exactly conserved in the basic *NVU* algorithm Eq. (11) because the forces sum to zero due to the translational invariance of the potential energy: $U(\mathbf{r}_1 + \mathbf{r}^0, \ldots, \mathbf{r}_N + \mathbf{r}^0) = U(\mathbf{r}_1, \ldots, \mathbf{r}_N)$).

Drift of the CM position is trivially eliminated by adjusting the particle displacements according to $\Delta\mathbf{r}_n = \Delta\mathbf{r}_n - \sum_m \Delta\mathbf{r}_m/N$, e.g., every 100th time step. This correction

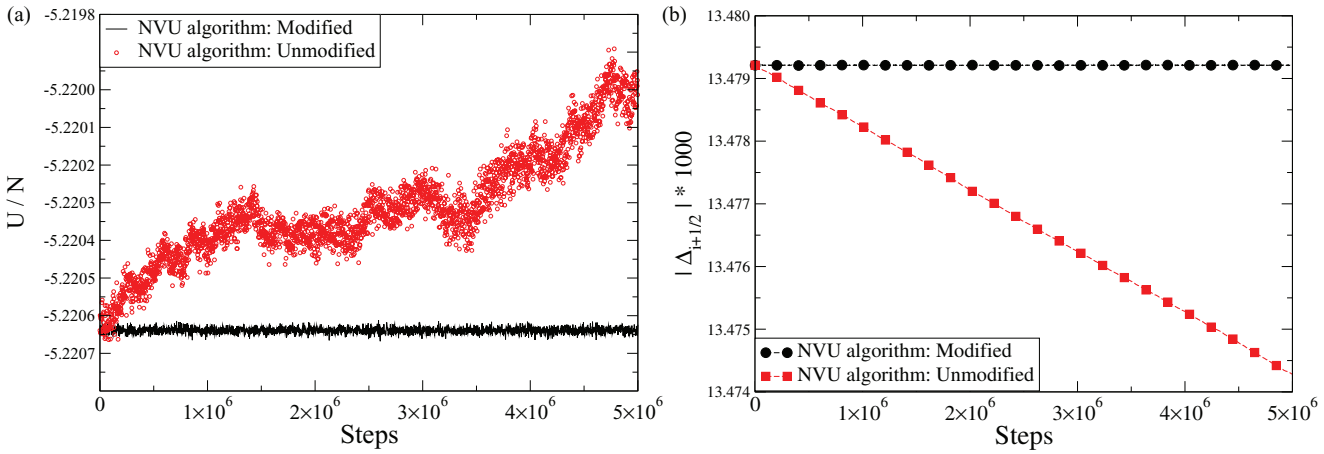

FIG. 3. (a) Evolution of U with and without the numerical stabilization (Eq. (20)): The red curve gives results using the basic *NVU* algorithm Eq. (17) with two identical initial potential energies and smoothed force potential. The black curve gives simulation results under the same conditions using the final *NVU* algorithm (Eq. (20)). (b) Evolution of the step length for the same simulations.

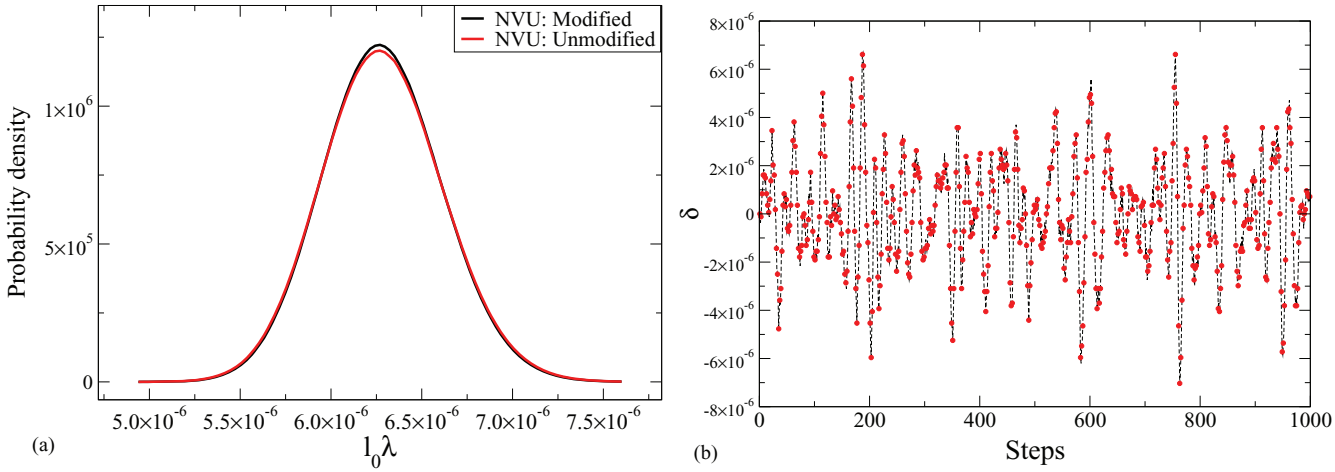

FIG. 4. (a) The distribution of the Lagrangian multiplier times l_0 with (black) and without (red) the numerical stabilization of the final *NVU* algorithm Eq. (20). (b) Evolution of the quantity δ_i defined by $l_0/D_i \equiv 1 + \delta_i$; as expected this quantity is small and averages to zero.

corresponds to setting to zero the total momentum of the system in an *NVE* simulation.

Robust potential energy conservation is obtained by adding a term that is zero if the potential energy equals the target potential energy U (this quantity was previously denoted by U_0, but to avoid confusion with the time step index we drop the subscript zero),

$$\mathbf{\Delta}_{i+1/2} = \mathbf{\Delta}_{i-1/2} + \frac{\left(-2\mathbf{F}_i \cdot \mathbf{\Delta}_{i-1/2} + U_{i-1} - \mathrm{U}\right)\mathbf{F}_i}{\mathbf{F}_i^2}. \tag{18}$$

To show that this modification of the *NVU* algorithm prevents drift of the potential energy we take the dot product of each side of Eq. (18) with $\mathbf{F}_i$, leading to $\mathbf{F}_i \cdot \mathbf{\Delta}_{i+1/2} = -\mathbf{F}_i \cdot \mathbf{\Delta}_{i-1/2} + U_{i-1} - \mathrm{U}$ or $\mathbf{F}_i \cdot (\mathbf{\Delta}_{i+1/2} + \mathbf{\Delta}_{i-1/2}) = U_{i-1} - \mathrm{U}$. Since $\mathbf{F}_i \cdot (\mathbf{\Delta}_{i+1/2} + \mathbf{\Delta}_{i-1/2}) = \mathbf{F}_i \cdot (\mathbf{R}_{i+1} - \mathbf{R}_{i-1}) = -(U_{i+1} - U_{i-1}) + O(l_0^3)$, this implies

$$U_{i+1} = \mathrm{U} + O\left(l_0^3\right). \tag{19}$$

Thus, entropic drift has been eliminated and the potential energy is conserved indefinitely except for small fluctuations.

We next address the problem of conserving step length. This is ensured by the following modification of the algorithm:

$$\mathbf{\Delta}_{i+1/2} = l_0 \frac{\mathbf{\Delta}_{i-1/2} + (-2\mathbf{F}_i \cdot \mathbf{\Delta}_{i-1/2} + U_{i-1} - \mathrm{U})\mathbf{F}_i/\mathbf{F}_i^2}{\left|\mathbf{\Delta}_{i-1/2} + (-2\mathbf{F}_i \cdot \mathbf{\Delta}_{i-1/2} + U_{i-1} - \mathrm{U})\mathbf{F}_i/\mathbf{F}_i^2\right|}. \tag{20}$$

Equation (20) gives the final *NVU* algorithm (occasionally for brevity: "the *NVU* algorithm," in contrast to Eq. (11) that is referred to as "the basic *NVU* algorithm").

In simulations, the *NVU* algorithm is implemented as follows. The target potential energy U is chosen from an *NVE* or an *NVT* simulation at the relevant state point. The step length l_0 is chosen according to the accuracy aimed for. Suppose the quantities $\mathbf{R}_i$, $\mathbf{\Delta}_{i-1/2}$, and U_{i-1} are given. From $\mathbf{R}_i$ the forces $\mathbf{F}_i$ are calculated. From $\mathbf{\Delta}_{i-1/2}$, $\mathbf{F}_i$, and U_{i-1} the quantity $\mathbf{\Delta}_{i+1/2}$ is calculated via Eq. (20). Finally, the positions are updated via $\mathbf{R}_{i+1} = \mathbf{R}_i + \mathbf{\Delta}_{i+1/2}$, and the potential energy is updated via $U_i = U(\mathbf{R}_i)$.

By construction the *NVU* algorithm Eq. (20) ensures constant step length,

$$|\mathbf{\Delta}_{i+1/2}| = l_0, \tag{21}$$

but is the potential energy still conserved for arbitrarily long runs? If the denominator of Eq. (20) is denoted by D_i, taking the dot product of each side of this equation with $\mathbf{F}_i$ leads to $\mathbf{F}_i \cdot \mathbf{\Delta}_{i+1/2} = (l_0/D_i)[-\mathbf{F}_i \cdot \mathbf{\Delta}_{i-1/2} + U_{i-1} - \mathrm{U}]$. Writing $l_0/D_i \equiv 1 + \delta_i$ in which $\delta_i = O(l_0^p)$ with $p \geq 1$, we get $\mathbf{F}_i \cdot (\mathbf{\Delta}_{i+1/2} + \mathbf{\Delta}_{i-1/2}) = \delta_i[-\mathbf{F}_i \cdot \mathbf{\Delta}_{i-1/2}] + (1 + \delta_i)[U_{i-1} - \mathrm{U}]$. Thus, since $\mathbf{F}_i \cdot (\mathbf{\Delta}_{i+1/2} + \mathbf{\Delta}_{i-1/2}) = U_{i-1} - U_{i+1} + O(l_0^3)$ and $\mathbf{F}_i \cdot \mathbf{\Delta}_{i-1/2} = U_{i-1} - U_i + O(l_0^2)$, we get $\mathrm{U} - U_{i+1} + O(l_0^3) = \delta_i[U_i - \mathrm{U} + O(l_0^2)]$. This implies again

$$U_{i+1} = \mathrm{U} + O\left(l_0^3\right). \tag{22}$$

In summary, for simulations of indefinite length the *NVU* algorithm Eq. (20) ensures constant step length and avoids entropic drift of the potential energy. Figure 3(a) shows the evolution of the potential energy using the basic *NVU* algorithm (red) and the final *NVU* algorithm (black), Fig. 3(b) shows the analogous step length evolution. Figure 4(a) shows that the distribution of the Lagrangian multiplier is only slightly affected by going from the basic (red) to the final (black) *NVU* algorithm. Figure 4(b) shows the evolution of δ_i in the final *NVU* algorithm, which as expected is close to zero.

We remind the reader that the modifications of the algorithm were introduced to compensate for the effects of accumulating random numerical errors for very long runs, and that the modifications introduced in the final *NVU* algorithm Eq. (20) vanish numerically in the mean. The prize paid for stabilizing the basic *NVU* algorithm is that the final *NVU* algorithm is not rigorously time reversible. In view of the fact that the improvements introduced to ensure stability lead to very small corrections, the (regrettable) fact that the corrections violate time reversibility is probably not important.

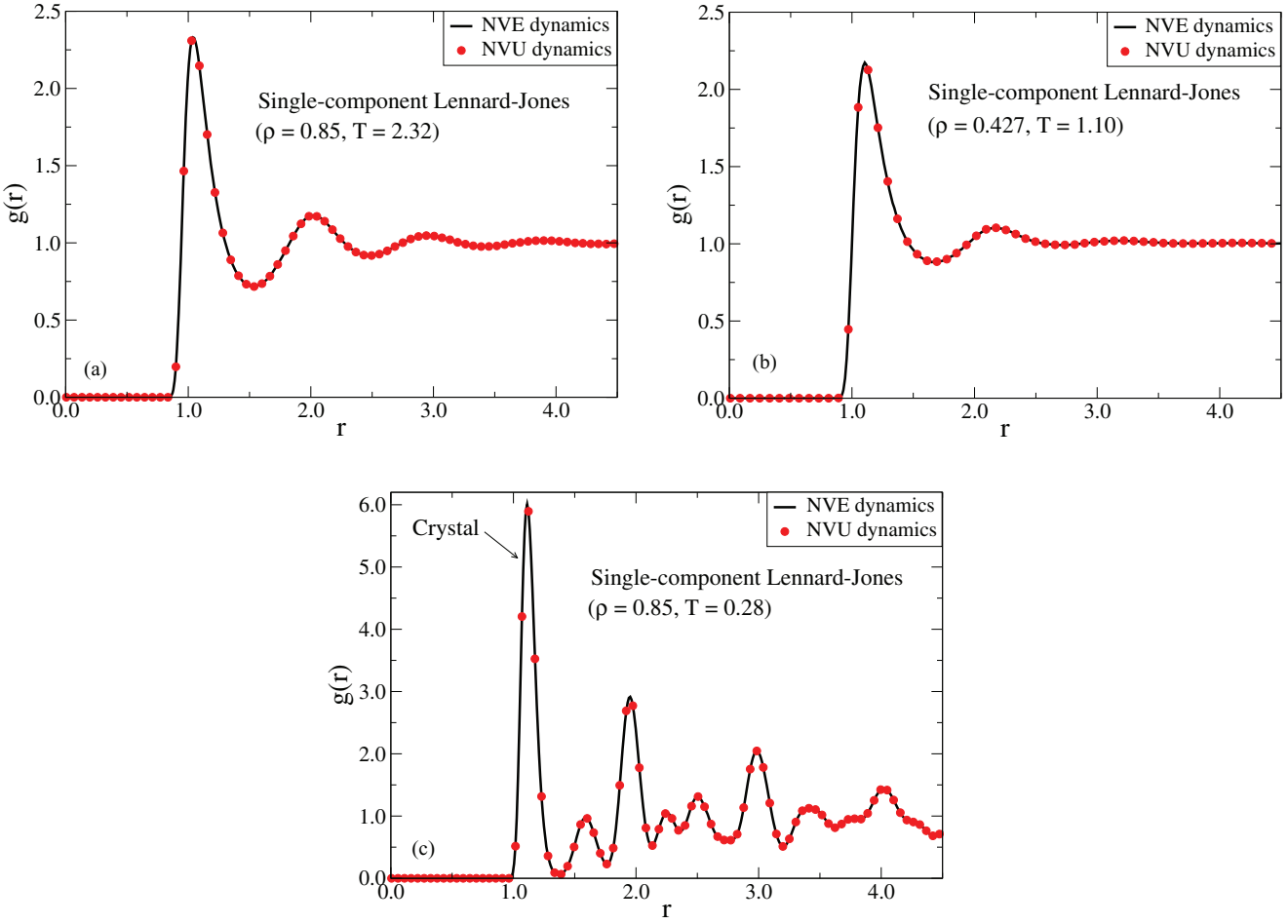

FIG. 5. Radial distribution functions $g(r)$ for a single-component Lennard-Jones system at the following state points: (a) $T = 2.32$ and $\rho = 0.85$; (b) $T = 1.1$ and $\rho = 0.427$; (c) the crystal at $T = 0.28$ and $\rho = 0.85$. The black curves show results from *NVE* simulations, the red dots show results from *NVU* simulations (Eq. (20)).

IV. SAMPLING PROPERTIES OF THE *NVU* ALGORITHM

In order to investigate whether the *NVU* algorithm gives physically reasonable results we compare results from *NVU* and *NVE* simulations for the average of a quantity that depends only on configurational degrees of freedom. This is done in Fig. 5, which shows the radial distribution function $g(r)$ at three state points. The red dots give *NVU* simulation results, the black curve gives *NVE* simulation. Clearly, the two algorithms give the same results. This finding is consistent with the conjecture that the *NVU* algorithm probes all points on Ω with equal probability. Note that this is not mathematically equivalent to conjecturing that the *NVU* algorithm probes the configuration space microcanonical ensemble, which has equal probability density everywhere in a thin energy shell between a pair of close-by constant-potential-energy manifolds. The latter distribution would imply an ensemble density of points on Ω inversely proportional to the length of the gradient of $U(\mathbf{R})$ (the force), but this distribution cannot be the correct equilibrium distribution because the basic *NVU* algorithm Eq. (11) is invariant to local scaling of the force. In the thermodynamic limit, however, the length of the force vector becomes almost constant and the difference between the configuration-space microcanonical ensemble and the Ω equal-measure ensemble becomes insignificant.

Paper II details a comparison of *NVU* dynamics to four other dynamics, including two stochastic dynamics. Here, simulation and theory lead to the conclusion that *NVU* and *NVE* dynamics are equivalent in the thermodynamic limit.

V. CONCLUDING REMARKS

An algorithm for geodesic motion on the constant-potential-energy hypersurface has been developed (Eq. (20)). Analytical arguments and single-precision simulations show that this algorithm, in conjunction with compensation for center-of-mass drift, is absolutely stable in the sense that potential energy, step length, and center-of-mass position are conserved for indefinitely long runs. The algorithm reproduces the *NVE* radial distribution function of the LJ liquid, strongly indicating that correct configuration-space averages are arrived at in *NVU* dynamics.

Although *NVU* dynamics has no kinetic energy providing a heat bath, it does allow for a realistic description of processes that are unlikely because they are thermally activated with energy barriers that are large compared to $k_B T$ (Paper II). In *NVU* dynamics, whenever a molecular

rearrangement requires excess energy to accumulate locally, this extra energy is provided by the surrounding configurational degrees of freedom. These provide a heat bath in much the same way as the kinetic energy provides a heat bath for standard Newtonian *NVE* dynamics.

Paper II compares the dynamics of the Kob-Andersen binary Lennard-Jones liquid simulated by the *NVU* algorithm and four other algorithms (*NVE*, *NVT*, diffusion on Ω, Monte Carlo dynamics), concluding that results are equivalent for the slow degrees of freedom. Paper II further argues from simulations and analytical arguments that *NVU* dynamics becomes equivalent to *NVE* dynamics as $N \to \infty$.

ACKNOWLEDGMENTS

Useful input from Nick Bailey is gratefully acknowledged. The centre for viscous liquid dynamics "Glass and Time" is sponsored by the Danish National Research Foundation (DNRF).

APPENDIX: PROOF THAT THE BASIC *NVU* ALGORITHM IS SYMPLECTIC

This Appendix proves that the basic *NVU* algorithm conserves the configuration-space volume element on the hypersurface Ω in the same sense as the *NVE* algorithm conserves the configuration-space volume element. We view the basic *NVU* algorithm (Eq. (11)),

$$\mathbf{R}_{i+1} = 2\mathbf{R}_i - \mathbf{R}_{i-1} - \frac{2\mathbf{F}_i \cdot (\mathbf{R}_i - \mathbf{R}_{i-1})}{\mathbf{F}_i^2}\mathbf{F}_i \,, \tag{A1}$$

as a mapping of R^{6N} into itself. In the $6N$-dimensional configuration space of subsequent time-step pairs $\mathbf{S}_i \equiv \{\mathbf{R}_i, \mathbf{R}_{i-1}\}$, the *NVU* algorithm is

$$\begin{aligned}\mathbf{S}_i \to \mathbf{S}_{i+1} &= \{\mathbf{R}_{i+1}, \mathbf{R}_i\} \\ &= \{2\mathbf{R}_i - \mathbf{R}_{i-1} - \frac{2\mathbf{F}_i \cdot (\mathbf{R}_i - \mathbf{R}_{i-1})}{\mathbf{F}_i^2}\mathbf{F}_i, \mathbf{R}_i\}.\end{aligned} \tag{A2}$$

The Jacobian of this map $\mathbf{J}(\mathbf{S}_i \to \mathbf{S}_{i+1})$ is given by

$$|\mathbf{J}| = \begin{vmatrix} 2 - 2\frac{\partial \frac{\mathbf{F}_i(\mathbf{R}_i - \mathbf{R}_{i-1})}{\mathbf{F}_i^2} F_{x_1,i}}{\partial x_{1,i}} & -2\frac{\partial \frac{\mathbf{F}_i(\mathbf{R}_i - \mathbf{R}_{i-1})}{\mathbf{F}_i^2} F_{x_1,i}}{\partial x_{2,i}} & \dots & -1 + 2\frac{\partial \frac{\mathbf{F}_i \mathbf{R}_{i-1}}{\mathbf{F}_i^2} F_{x_1,i}}{\partial x_{1,i-1}} & 2\frac{\partial \frac{\mathbf{F}_i \mathbf{R}_{i-1}}{\mathbf{F}_i^2} F_{x_1,i}}{\partial x_{2,i-1}} & \dots \\ -2\frac{\partial \frac{\mathbf{F}_i(\mathbf{R}_i - \mathbf{R}_{i-1})}{\mathbf{F}_i^2} F_{x_2,i}}{\partial x_{1,i}} & 2 - 2\frac{\partial \frac{\mathbf{F}_i(\mathbf{R}_i - \mathbf{R}_{i-1})}{\mathbf{F}_i^2} F_{x_2,i}}{\partial x_{2,i}} & \dots & 2\frac{\partial \frac{\mathbf{F}_i \mathbf{R}_{i-1}}{\mathbf{F}_i^2} F_{x_2,i}}{\partial x_{1,i-1}} & -1 + 2\frac{\partial \frac{\mathbf{F}_i \mathbf{R}_{i-1}}{\mathbf{F}_i^2} F_{x_2,i}}{\partial x_{2,i-1}} & \dots \\ \vdots & \vdots & & \vdots & \vdots & \\ 1 & 0 & \dots & 0 & 0 & \dots \\ 0 & 1 & \dots & 0 & 0 & \dots \\ \vdots & \vdots & & \vdots & \vdots & \end{vmatrix}. \tag{A3}$$

This may be regarded as a two-by-two block matrix consisting of blocks $\mathbf{A}, \mathbf{B}, \mathbf{C}, \mathbf{D}$. The determinant of this block matrix is $|\mathbf{J}| = |\mathbf{AD} - \mathbf{BC}| = |-\mathbf{BC}| = (-1)^M|\mathbf{B}|$, giving (where the index i is dropped for brevity and $M = 3N$)

$$|\mathbf{J}| = (-1)^M \begin{vmatrix} -1 + 2\frac{F_{x_1}^2}{\mathbf{F}^2} & 2\frac{F_{x_2}F_{x_1}}{\mathbf{F}^2} & 2\frac{F_{x_3}F_{x_1}}{\mathbf{F}^2} & 2\frac{F_{x_4}F_{x_1}}{\mathbf{F}^2} & \dots \\ 2\frac{F_{x_1}F_{x_2}}{\mathbf{F}^2} & -1 + 2\frac{F_{x_2}^2}{\mathbf{F}^2} & 2\frac{F_{x_3}F_{x_2}}{\mathbf{F}^2} & 2\frac{F_{x_4}F_{x_2}}{\mathbf{F}^2} & \dots \\ 2\frac{F_{x_1}F_{x_3}}{\mathbf{F}^2} & 2\frac{F_{x_2}F_{x_3}}{\mathbf{F}^2} & -1 + 2\frac{F_{x_3}^2}{\mathbf{F}^2} & 2\frac{F_{x_4}F_{x_3}}{\mathbf{F}^2} & \dots \\ 2\frac{F_{x_1}F_{x_4}}{\mathbf{F}^2} & 2\frac{F_{x_2}F_{x_4}}{\mathbf{F}^2} & 2\frac{F_{x_3}F_{x_4}}{\mathbf{F}^2} & -1 + 2\frac{F_{x_4}^2}{\mathbf{F}^2} & \dots \\ \vdots & \vdots & \vdots & \vdots & \end{vmatrix} = (-1)^M(\pm 1). \tag{A4}$$

Defining the unit-length vector along the direction of the force vector $\mathbf{n}$, the last equality of Eq. (A4) follows from $\mathbf{B} = -\mathbf{1} + 2\mathbf{n}\cdot\mathbf{n}^T \Rightarrow \mathbf{B}^2 = \mathbf{1} + 4\mathbf{n}\cdot\mathbf{n}^T - 4\mathbf{n}\cdot\mathbf{n}^T = \mathbf{1}$. Since $|B|^2 = |B^2| = 1$, one has $|B| = \pm 1$. Thus, the volume element transforms as

$$d\mathbf{R}_i d\mathbf{R}_{i-1} = d\mathbf{R}_{i+1} d\mathbf{R}_i \,. \tag{A5}$$

This means that the basic *NVU* algorithm conserves the volume element in the $6N$-dimensional configuration space, i.e., that the algorithm is symplectic just as the *NVE* algorithm is.

[1] T. S. Ingebrigtsen, S. Toxvaerd, T. B. Schrøder, and J. C. Dyre, J. Chem. Phys. **135**, 104102 (2011).

[2] S. Gallot, D. Hulin, and J. Lafontaine, *Riemannian Geometry*, 3rd ed. (Springer, Berlin, 2004).

[3] N. J. Hicks, *Notes on Differential Geometry* (van Nostrand Reinhold, New York, 1965); P. Dombrowski, Math. Nacthr. **38**, 133 (1968).

[4] S. Weinberg, *Gravitation and Cosmology* (Wiley, New York, 1972); L. D. Landau and E. M. Lifshitz, *The Classical Theory of Fields*, 5th ed. (Pergamon, London, 1975).

[5] C. Wang and R. M. Stratt, J. Chem. Phys. **127**, 224503 (2007); **127**, 224504 (2007).

[6] C. N. Nguyen and R. M. Stratt, J. Chem. Phys. **133**, 124503 (2010).

[7] U. R. Pedersen, N. P. Bailey, T. B. Schrøder, and J. C. Dyre, Phys. Rev. Lett. **100**, 015701 (2008); U. R. Pedersen, T. Christensen, T. B. Schrøder, and J. C. Dyre, Phys. Rev. E **77**, 011201 (2008); T. B. Schrøder, U. R. Pedersen, N. P. Bailey, S. Toxvaerd, and J. C. Dyre, Phys. Rev. E **80**, 041502 (2009); N. P. Bailey, U. R. Pedersen, N. Gnan, T. B. Schrøder, and J. C. Dyre, J. Chem. Phys. **129**, 184507 (2008); N. P. Bailey, U. R. Pedersen, N. Gnan, T. B. Schrøder, and J. C. Dyre, J. Chem. Phys. **129**, 184508 (2008); T. B. Schrøder, N. P. Bailey, U. R. Pedersen, N. Gnan, and J. C. Dyre, J. Chem. Phys. **131**, 234503 (2009); U. R. Pedersen, T. B. Schrøder, and J. C. Dyre, Phys. Rev. Lett. **105**, 157801 (2010).

[8] N. Gnan, T. B. Schrøder, U. R. Pedersen, N. P. Bailey, and J. C. Dyre, J. Chem. Phys. **131**, 234504 (2009); N. Gnan, C. Maggi, T. B. Schrøder, and J. C. Dyre, Phys. Rev. Lett. **104**, 125902 (2010); T. B. Schrøder, N. Gnan, U. R. Pedersen, N. P. Bailey, and J. C. Dyre, J. Chem. Phys. **134**, 164505 (2011).

[9] U. R. Pedersen, N. Gnan, N. P. Bailey, T. B. Schrøder, and J. C. Dyre, Non-Cryst. Solids **357**, 320 (2011).

[10] R. M. J. Cotterill and J. U. Madsen, Phys. Rev. B **33**, 262 (1986); R. M. J. Cotterill and J. U. Madsen, in *Characterizing Complex Systems*, edited by H. Bohr (World Scientific, Singapore, 1990), p. 177; J. Li, E. Platt, B. Waszkowycz, R. Cotterill, and B. Robson, Biophys. Chem. **43**, 221 (1992); R. M. J. Cotterill and J. U. Madsen, J. Phys.: Condens. Matter **18**, 6507 (2006).

[11] A. Scala, L. Angelani, R. Di Leonardo, G. Ruocco, and F. Sciortino, Philos. Mag. B **82**, 151 (2002); L. Angelani, R. Di Leonardo, G. Ruocco, A. Scala, and F. Sciortino, J. Chem. Phys. **116**, 10297 (2002).

[12] V. Caselles, R. Kimmel, and G. Sapiro, Int. J. Comput. Vis. **22**, 61 (1997); R. Kimmel and J. A. Sethian, Proc. Natl. Acad. Sci. U.S.A. **95**, 8431 (1998); J. A. Sethian, *Level Set Methods and Fast Marching Methods* (Cambridge University Press, Cambridge, England, 1999); L.-T. Cheng, P. Burchard, B. Merriman, and S. Osher, J. Comput. Phys. **175**, 604 (2002); A. Rapallo, J. Chem. Phys. **121**, 4033 (2004); L. Ying and E. J. Candes, J. Comput. Phys. **220**, 6 (2006); A. Rapallo, J. Comput. Chem. **27**, 414 (2006); A. Spira and R. Kimmel, J. Comput. Phys. **223**, 235 (2007); H. Schwetlick and J. Zimmer, J. Chem. Phys. **130**, 124106 (2009).

[13] S. Toxvaerd, Phys. Rev. E **50**, 2271 (1994).

[14] S. Toxvaerd, O. J. Heilmann, T. Ingebrigtsen, T. B. Schrøder, and J. C. Dyre, J. Chem. Phys. **131**, 064102 (2009).

[15] J. E. Marsden and M. West, Acta Numerica **10**, 357 (2001); R. Elber, A. Cardenas, A. Ghosh, and H. A. Stern, Adv. Chem. Phys. **126**, 93 (2003); A. Lew, "*Variational time integrators in computational solid mechanics*," Ph.D. dissertation, California Institute of Technology, 2003; C. G. Gray, G. Karl, and V. A. Novikov, Rep. Prog. Phys. **67**, 159 (2004); A. Lew, J. E. Marsden, M. Ortiz, and M. West, Int. J. Numer. Methods Eng. **60**, 153 (2004); M. West, "*Variational integrators*," Ph.D. dissertation, California Institute of Technology, 2004; T. J. Bridges and S. Reich, J. Phys. A **39**, 5287 (2006); E. Hairer, C. Lubich, and G. Wanner, *Geometric Numerical Integration - Structure-Preserving Algorithms for Ordinary Differential Equations*, 2nd ed. (Springer, Berlin, 2006); R. I. McLachlan and G. R. W. Quispel, J. Phys. A **39**, 5251 (2006).

[16] A. Stein and M. Desbrun, in *Discrete Differential Geometry: An Applied Introduction*, edited by M. Desbrun, P. Schroeder, and M. Wardetzky (Columbia University, New York, 2008), p. 95.

[17] All simulations were performed using a molecular dynamics code optimized for NVIDIA graphics cards, which is available as open source code at http://rumd.org.

[18] M. P. Allen and D. J. Tildesley, *Computer Simulation of Liquids* (Oxford Science, Oxford, 1987); D. Frenkel and B. Smit, *Understanding Molecular Simulation* (Academic, New York, 2002).

NVU dynamics. II. Comparing to four other dynamics

Trond S. Ingebrigtsen, Søren Toxvaerd, Thomas B. Schrøder, and Jeppe C. Dyre[a)]
DNRF Centre "Glass and Time," IMFUFA, Department of Sciences, Roskilde University, Postbox 260, DK-4000 Roskilde, Denmark

(Received 28 March 2011; accepted 17 July 2011; published online 8 September 2011)

In the companion paper [T. S. Ingebrigtsen, S. Toxvaerd, O. J. Heilmann, T. B. Schrøder, and J. C. Dyre, "*NVU* dynamics. I. Geodesic motion on the constant-potential-energy hypersurface," J. Chem. Phys. (in press)] an algorithm was developed for tracing out a geodesic curve on the constant-potential-energy hypersurface. Here, simulations of NVU dynamics are compared to results for four other dynamics, both deterministic and stochastic. First, NVU dynamics is compared to the standard energy-conserving Newtonian NVE dynamics by simulations of the Kob-Andersen binary Lennard-Jones liquid, its WCA version (i.e., with cut-off's at the pair potential minima), and the Lennard-Jones Gaussian liquid. We find identical results for all quantities probed: radial distribution functions, incoherent intermediate scattering functions, and mean-square displacement as function of time. Arguments are presented for the equivalence of NVU and NVE dynamics in the thermodynamic limit; in particular, to leading order in $1/N$ these two dynamics give identical time-autocorrelation functions. In the final part of the paper, *NVU* dynamics is compared to Monte Carlo dynamics, to a diffusive dynamics of small-step random walks on the constant-potential-energy hypersurface, and to Nosé-Hoover NVT dynamics. If time is scaled for the two stochastic dynamics to make single-particle diffusion constants identical to that of NVE dynamics, the simulations show that all five dynamics are equivalent at low temperatures except at short times. © *2011 American Institute of Physics*. [doi:10.1063/1.3623586]

I. INTRODUCTION

In the companion paper (Paper I[1]), we developed a stable numerical algorithm for tracing out a geodesic curve on the constant-potential-energy hypersurface Ω of a system of N classical particles. If $U(\mathbf{r}_1, \ldots, \mathbf{r}_N)$ is the potential energy as a function of the particle coordinates, for a given value U_0 of the potential energy Ω is the $(3N-1)$-dimensional Riemannian differentiable manifold defined by (where $\mathbf{R} \equiv (\mathbf{r}_1, \ldots, \mathbf{r}_N)$ is the position in the $3N$-dimensional configuration space)

$$\Omega = \{\mathbf{R} \in R^{3N} \,|\, U(\mathbf{R}) = U_0\}\,. \tag{1}$$

Geodesic motion on Ω is termed NVU dynamics in analogy with standard Newtonian NVE dynamics, which conserves the total energy E. Motivations for studying NVU dynamics were given in Paper I. The present paper compares NVU dynamics to four other dynamics, two deterministic and two stochastic, concluding that NVU dynamics is a fully valid molecular dynamics.

The path of shortest distance between two points on a Riemannian manifold is a so-called geodesic curve. By definition a geodesic is a curve of stationary length, i.e., one for which small curve variations keeping the two end points $\mathbf{R}_A$ and $\mathbf{R}_B$ fixed, to lowest order do not change the curve length,

$$\delta \int_{\mathbf{R}_A}^{\mathbf{R}_B} dl = 0\,. \tag{2}$$

By discretizing this condition and carrying out the variation, keeping the potential energy fixed by introducing Lagrangian multipliers, the following "basic NVU algorithm" was derived in Paper I ($\mathbf{F}$ is the $3N$-dimensional force vector and i is the time-step index):

$$\mathbf{R}_{i+1} = 2\mathbf{R}_i - \mathbf{R}_{i-1} - 2\,\frac{\mathbf{F}_i \cdot (\mathbf{R}_i - \mathbf{R}_{i-1})}{\mathbf{F}_i^2}\mathbf{F}_i\,. \tag{3}$$

This algorithm works well, but for very long simulations numerical errors accumulate and U drifts to higher values ("entropic drift," see Paper I). This problem is also encountered for the total energy in NVE algorithms,[2] and it is not more severe for NVU than for NVE dynamics. A fully stable NVU algorithm was developed in Paper I, which may be summarized as follows. If one switches to the leap-frog representation and defines the position changes by $\mathbf{\Delta}_{i+1/2} = \mathbf{R}_{i+1} - \mathbf{R}_i$, the stable NVU algorithm is: $\mathbf{\Delta}_{i+1/2} = l_0\,\mathbf{A}_{i+1/2}/|\mathbf{A}_{i+1/2}|$ where l_0 is the step length and $\mathbf{A}_{i+1/2} = \mathbf{\Delta}_{i-1/2} + (-2\mathbf{F}_i \cdot \mathbf{\Delta}_{i-1/2} + U_{i-1} - U_0)\mathbf{F}_i/\mathbf{F}_i^2$. Just as for standard NVE dynamics a final stabilization introduced is to adjust the position changes slightly, e.g., every 100th step, in order to eliminate numerical drift of the center of mass coordinate. In the simulations reported below, we used the fully stable NVU algorithm. However, since the stabilization is merely a technicality, the basic NVU algorithm Eq. (3) is used for theoretical considerations.

Constant-potential-energy algorithms were previously considered in papers dating back to 1986 by Cotterill and Madsen *et al.*[3] and in 2002 by Scala *et al.*[4] In the same spirit, but in a slightly different context, Stratt and co-workers in 2007 and 2010 considered geodesic motion in the space of

a)Electronic mail: dyre@ruc.dk.

points with potential energy less than or equal to U_0.[5] In the thermodynamic limit these points are almost all of potential energy very close to U_0. We refer to Paper I for further discussion of how NVU dynamics relates to these earlier works.

NVU dynamics invites to an alternative view of molecular motion. Instead of focusing on the standard potential-energy landscape in $3N+1$ dimensions,[6] NVU dynamics adopts the configuration-space microcanonical viewpoint and focuses on the $(3N-1)$-dimensional Riemannian hypersurface Ω. The classical potential-energy landscape picture draws attention to the stationary points of the potential-energy function, in particular its minima, the so-called inherent states.[6] In contrast, all points on Ω have the same probability in NVU dynamics and there are no energy barriers – all barriers are of entropic nature defining unlikely parts of Ω that must be passed.[3–5] Despite the absence of energy barriers in the ordinary sense of this term, NVU dynamics is fully able to describe locally activated events (hopping processes between local potential-energy minima). The NVU "heat bath" is provided by the multitude of configurational degrees of freedom.[3–5]

The present paper compares NVU dynamics to other molecular dynamics, including stochastic ones. We first compare to NVE dynamics, which is also deterministic, and conclude that for large systems the two dynamics are basically equivalent. We proceed to compare to other kinds of dynamics, inspired by previous works: The first investigation providing long-time simulations that compared different dynamics (Newtonian versus Langevin) was presented by Gleim *et al.*[7] They studied the Kob-Andersen binary Lennard-Jones (KABLJ) mixture[8] at different temperatures and found that below a certain temperature ($T < 0.8$), the temperature dependence of the diffusion constant and of the structural relaxation time was identical for the two dynamics. This type of investigation was extended by Szamel *et al.*[9] to Brownian dynamics, i.e., stochastic dynamics without the momentum degrees of freedom. They found power-law fitting exponents for the temperature dependence of the diffusion constant and relaxation time very close to those of NVE dynamics. Subsequently, Berthier *et al.*[10] investigated Monte Carlo dynamics for which agreement with Newtonian dynamics was also established, both for a strong and a fragile model glass former (an SiO_2 model and the KABLJ model). This, however, did not apply for higher-order time-correlation functions, a fact contributed to the presence of different conservation laws.[10]

We compare below NVU dynamics to the following four other dynamics: Newtonian dynamics (NVE), Nosé-Hoover NVT dynamics,[11] Monte Carlo dynamics (MC),[12] and a diffusive small-step random-walk dynamics on the constant-potential-energy hypersurface (RW). Section II compares NVU dynamics with the "true" (NVE) time evolution defined by Newton's second law. This is done by simulations of the KABLJ liquid, as well as of the Weeks-Chandler-Andersen (WCA) approximation[13] to the KABLJ liquid (KABWCA) and the Lennard-Jones Gaussian liquid. Section III gives arguments for the equivalence of NVU and NVE dynamics in the thermodynamic limit. Section IV compares NVU dynamics with NVT, MC, and RW dynamics. Section V gives a brief summary and outlook.

II. SIMULATIONS COMPARING *NVU* DYNAMICS TO *NVE* DYNAMICS

In NVU dynamics a geodesic is traced out in configuration space. Physically, this curve may be traversed with any velocity; comparing however to NVE dynamics suggests an obvious time measure for NVU dynamics, as we shall see now. Limiting ourselves for simplicity to systems of particles with identical masses m, the Verlet algorithm for NVE dynamics with time step Δt_{NVE} is[2,14]

$$\mathbf{R}_{i+1} = 2\mathbf{R}_i - \mathbf{R}_{i-1} + \frac{(\Delta t_{NVE})^2}{m}\mathbf{F}_i . \tag{4}$$

Comparing to Eq. (3) suggests the following identification of a NVU time step $\Delta t_{i,NVU}$

$$\frac{(\Delta t_{i,NVU})^2}{m} = -2\frac{\mathbf{F}_i \cdot (\mathbf{R}_i - \mathbf{R}_{i-1})}{\mathbf{F}_i^2} . \tag{5}$$

This quantity is identical to $l_0\lambda_i$ of Paper I. Our simulations show that the average of the right-hand side is always

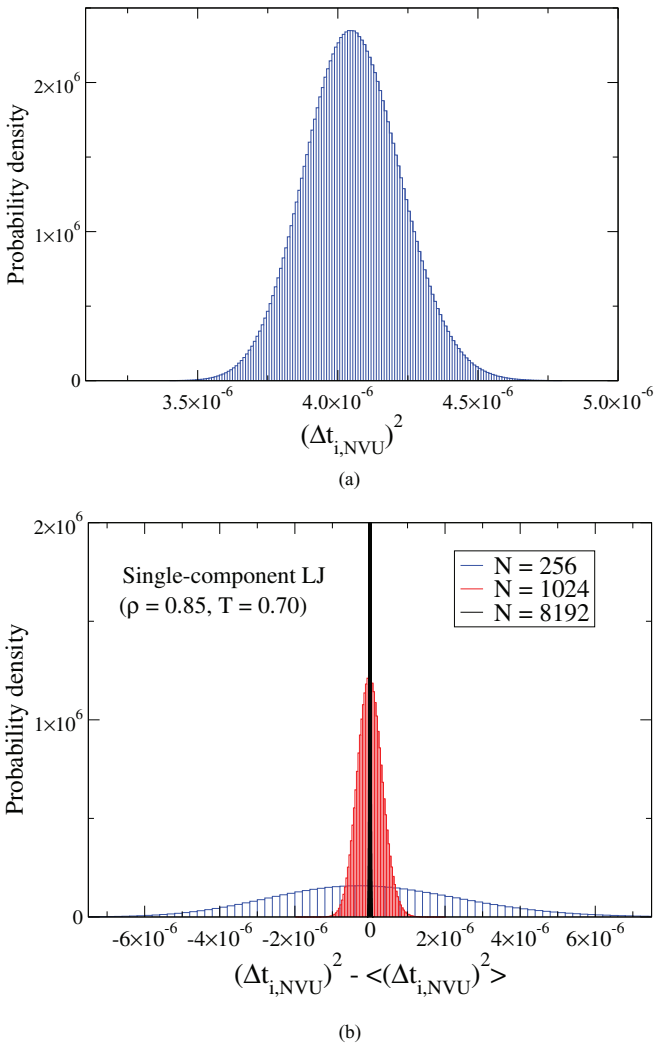

FIG. 1. (a) Probability density of $(\Delta t_{i,NVU})^2$ given by Eq. (5) for the Kob-Andersen binary Lennard-Jones (KABLJ) liquid at $\rho = 1.2$ and $T = 0.44$; (b) Probability density for $(\Delta t_{i,NVU})^2 - \langle(\Delta t_{i,NVU})^2\rangle$ for 256, 1024, and 8192 particles of the single-component LJ liquid ($T = 0.70$, $\rho = 0.85$), showing a narrowing as the particle number increases.

positive for small l_0. We have no proof of this, but presumably it applies rigorously in the thermodynamic limit.

Data are given below in terms of the natural units for the Lennard-Jones pair potential; for the KABLJ and KABWCA system length and energy are given in units of the large-particle parameters σ_{AA} and ϵ_{AA}, respectively. The system sizes are $N = 1024$, 1000, and 1024 for KABLJ, KABWCA, and Lennard-Jones Gaussian, respectively.

The probability distribution of $(\Delta t_{i,NVU})^2$ is given in Fig. 1(a) for an $N = 1024$ KABLJ liquid at $\rho = 1.2$ and $T = 0.44$.[15] The simulations behind this, as well as all below figures, were initiated by choosing the two initial configurations from a well-equilibrated NVE simulation. The target potential energy U_0 in the NVU simulation was chosen as $U_0 = \langle U \rangle_{NVE}$ at the relevant state points. The probability distribution of Fig. 1 is a Gaussian, which is consistent with the fact that $(\Delta t_{i,NVU})^2$ is a sum of many terms that are uncorrelated for large spatial separations.

In view of the above, for comparing NVU and NVE generated sequences we define the NVU time step length Δt_{NVU}

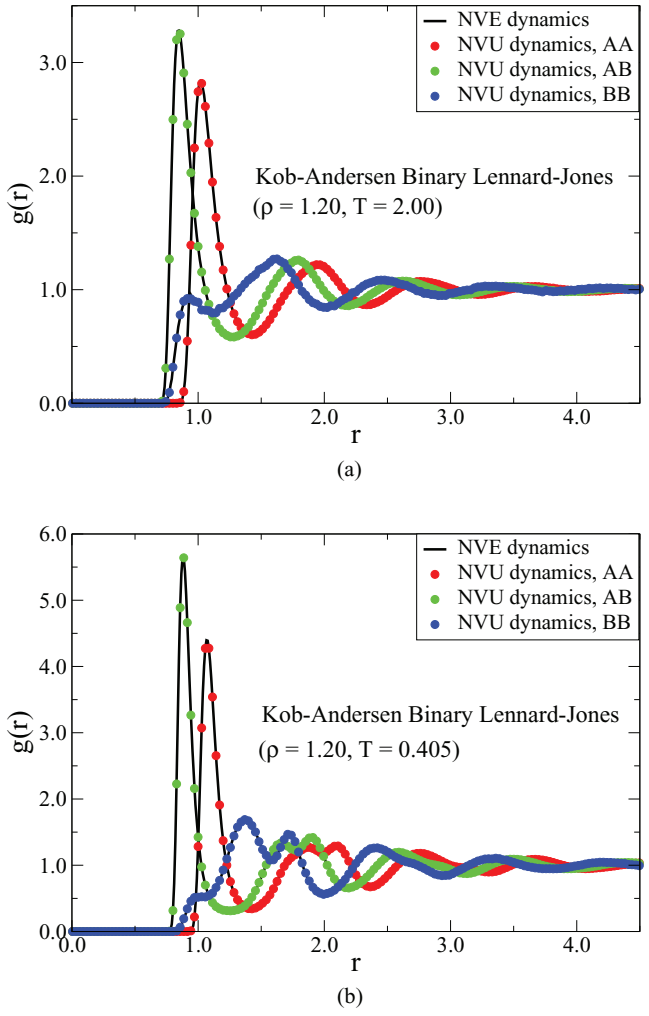

FIG. 2. Radial distribution functions for the KABLJ system at $\rho = 1.2$. The black lines give results from NVE simulations, colored circles from NVU simulation where green, red, and blue denote, respectively, AB, AA, and BB pairs for: (a) $T = 2.0$ and (b) $T = 0.405$.

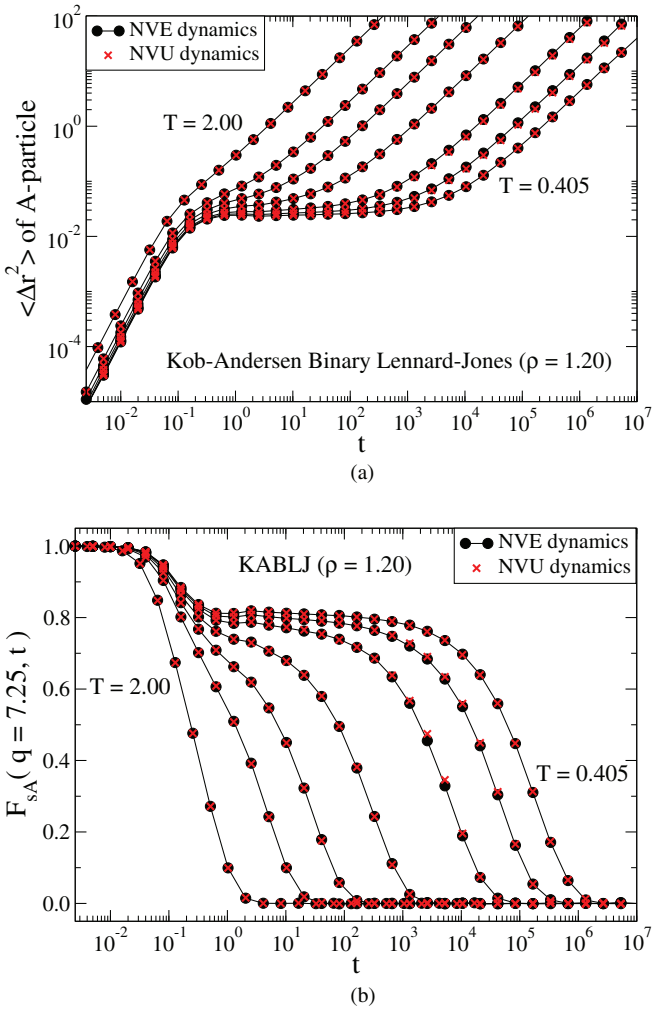

FIG. 3. (a) Mean-square displacement and (b) incoherent intermediate scattering function at the wave vector of the first peak of the AA structure factor. Both simulations were performed at $\rho = 1.2$ for $T = 2.0$, 0.80, 0.60, 0.50, 0.44, 0.42, and 0.405 (left to right) for the KABLJ liquid (1024 particles). NVE dynamics is given by the filled black circles connected by straight lines, NVU dynamics by the red crosses.

as the average of Eq. (5), i.e.,

$$\frac{(\Delta t_{NVU})^2}{m} \equiv -2 \left\langle \frac{\mathbf{F}_i \cdot (\mathbf{R}_i - \mathbf{R}_{i-1})}{\mathbf{F}_i^2} \right\rangle . \tag{6}$$

First, we compare static averages of NVU and NVE simulations. Figure 2 shows the three radial distribution functions for the KABLJ liquid at two different state points. Clearly, the two algorithms give identical results. Next, Fig. 3 shows NVU and NVE results for the mean-square displacement and the incoherent intermediate scattering function of the KABLJ liquid at density $\rho = 1.2$ over a range of temperatures. The mean-square displacement and the incoherent scattering function are both identical for NVU and NVE dynamics.

Corresponding figures are shown in Fig. 4 for the Weeks-Chandler-Andersen (WCA) approximation, which cuts off interactions beyond the energy minima, i.e., keep only the repulsive part of the potential. The WCA version of the system has a similar structure, but a much faster dynamics in the su-

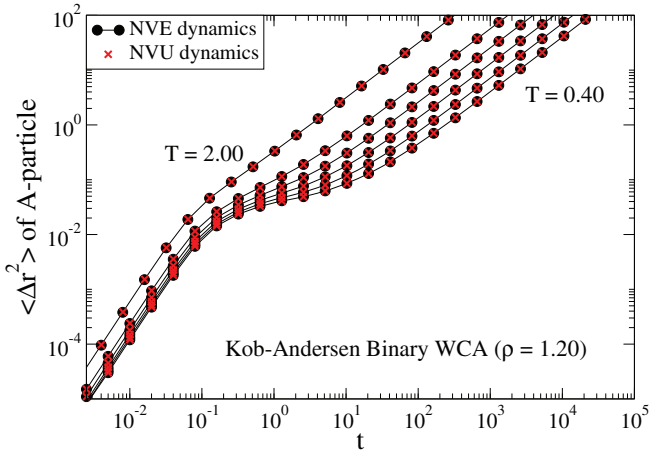

(a)

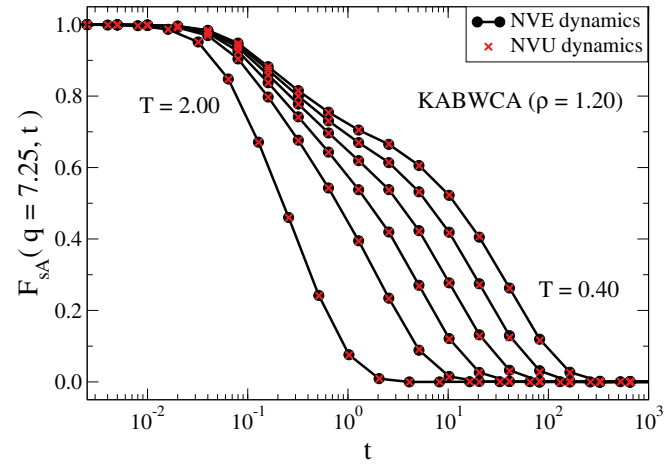

(b)

FIG. 4. (a) Mean-square displacement and (b) incoherent intermediate scattering function at the same wave vector as in Fig. 3. Both simulations were performed at $\rho = 1.2$ for $T = 2.0$, 0.80, 0.60, 0.50, 0.44, and 0.40 (left to right) for the WCA approximation to the KABLJ liquid. NVE dynamics is given by the filled black circles connected by straight lines, NVU dynamics by the red crosses.

percooled regime.[16,17] Again, NVU and NVE dynamics give identical results.

We also studied the so-called Lennard-Jones Gaussian system defined by a pair potential that adds a Gaussian to a LJ potential,[18] a liquid that is not strongly correlating.[16] Figure 5 shows that for this model the incoherent intermediate scattering function is also the same for NVU and NVE dynamics. In summary, for all systems simulated, we found $NVU = NVE$. This applies even for $N = 65$ particles of the KABLJ liquid ($T = 0.8$, $\rho = 1.2$).

III. ARGUMENTS FOR THE EQUIVALENCE OF *NVU* AND *NVE* DYNAMICS AS $N \to \infty$

The above results raise the question: Are NVU and NVE dynamics mathematically equivalent in some well-defined sense? The two algorithms are not identical, of course; that would require no variation in the quantity $\Delta t_{i,NVU}$ (Fig. 1). On the other hand, the $\Delta t_{i,NVU}$

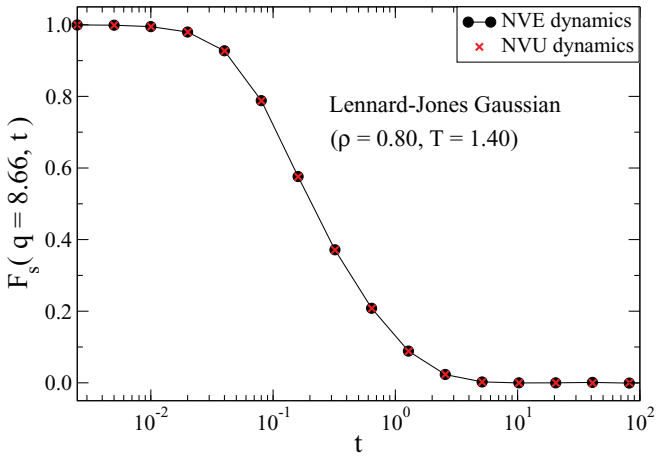

FIG. 5. The incoherent intermediate scattering function at $\rho = 0.8$ and $T = 1.4$ for the Lennard-Jones Gaussian system.[18] The black circles represent a NVE simulation, the red symbols represent a NVU simulation.

distribution narrows as the particle number increases [Fig. 1 (b)]. From this NVU and NVE dynamics are expected to become equivalent for $N \to \infty$ in the following sense: For any configurational quantity A with zero average, to leading order in $1/N$ there is identity of dynamic quantities such as the time-autocorrelation function $\langle A(0)A(t)\rangle$ or the mean-square change $\langle \Delta^2 A(t)\rangle$ (i.e., the relative deviations go to zero as $N \to \infty$). Consider the time-autocorrelation function of an extensive quantity A with zero average. In this case, the time-autocorrelation function scales in both ensembles as N, and the proposed equivalence of the dynamics means that $|\langle A(0)A(t)\rangle_{NVU} - \langle A(0)A(t)\rangle_{NVE}| \propto N^0$ as $N \to \infty$. Intuitively, what happens is that since in NVE dynamics the relative potential-energy fluctuations go to zero as $N \to \infty$, it becomes a better and better approximation to regard the potential energy as conserved.[5]

There exists in analytical mechanics a variational principle that does not involve time. This is the Maupertuis principle from 1746,[20,21] a variational principle that is originally due to Jacobi and for this reason is sometimes referred to as "Jacobi's form of the least action principle."[19,21] This states that a classical-mechanical system of fixed energy E follows a curve in configuration space obeying (with fixed end points)

$$\delta \int_{\mathbf{R}_A}^{\mathbf{R}_B} \sqrt{2m(E-U)}\, dl \;=\; 0\,. \tag{7}$$

One may argue that the relative variations of the integrand go to zero as $N \to \infty$. Thus, the integrand in this limit becomes effectively constant and can be taken outside the variation, implying Eq. (2) for motion which in the same limit effectively takes place on the constant-potential-energy hypersurface.[5]

If l is the path length parametrizing the path, Eq. (7) implies[19,20] $d^2\mathbf{R}/dl^2 = [\mathbf{F} - (\mathbf{F}\cdot\mathbf{t})\mathbf{t}]/2(E - U(\mathbf{R}))$ where $\mathbf{t} = d\mathbf{R}/dl$ is the unit vector tangential to the path. The term $\mathbf{F} - (\mathbf{F}\cdot\mathbf{t})\mathbf{t}$ is the (vector) component of the force normal to the path. In the thermodynamic limit the path as mentioned approaches more and more the constant-potential-energy hypersurface Ω, i.e., $\mathbf{F}\cdot\mathbf{t} = 0$. In this limit, one has also $dl \propto dt$ because the relative kinetic energy fluctuations go to

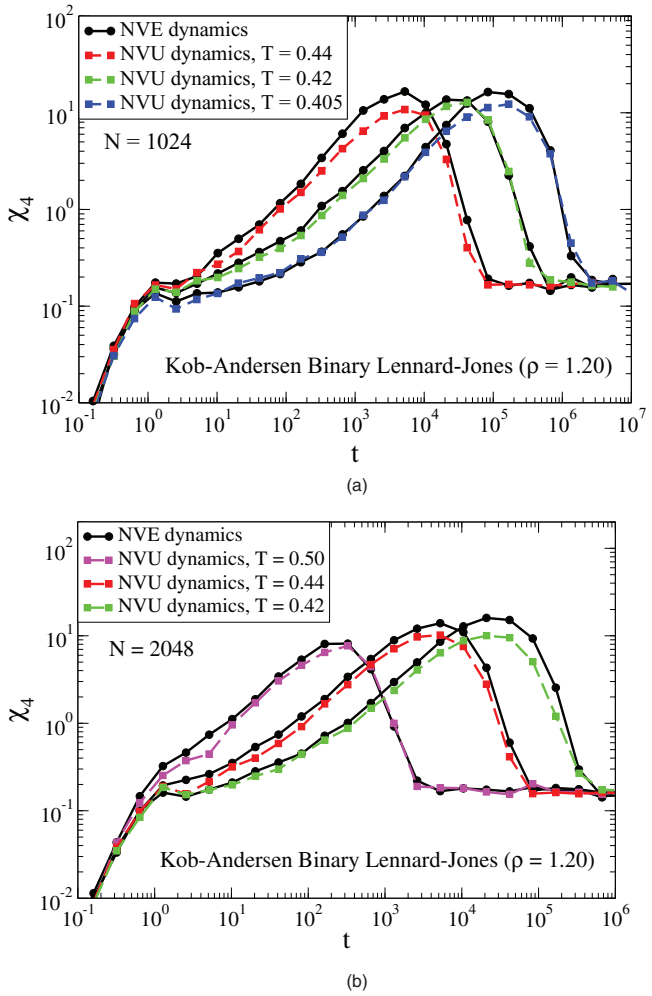

FIG. 6. (a) The dynamical fluctuations quantified by $\chi_4(t)$ for the A particles at $\rho = 1.2$ for a KABLJ liquid with 1024 particles. The black circles give results for an NVE simulation, the red, green, and blue symbols represent NVU simulations at, respectively, $T = 0.44,\ 0.42,\ 0.405$. (b) The dynamical fluctuations quantified by $\chi_4(t)$ for the A particles at $\rho = 1.2$ for the KABLJ system with 2048 particles. The black circles give results for a NVE simulation, the violet, red, and green symbols represent NVU simulations of, respectively, $T = 0.50,\ 0.44$, and 0.42. Increasing the number of particles does not appear to decrease the deviation between the two dynamics.

zero. In this way, in the thermodynamic limit the Maupertuis principle is equivalent to both the geodesic equation Eq. (2) and to Newton's second law $\ddot{\mathbf{R}} = \mathbf{F}/m$.

The equivalence of NVU and NVE dynamics in the thermodynamic limit relates to static averages as well as to time-autocorrelation functions of extensive quantities with zero average. Just as one must be careful when comparing fluctuations between different ensembles, fluctuations relating to the dynamics need not be the same for NVU and NVE dynamics. As an example, Fig. 6 shows the quantity $\chi_4(t)$ defined by $\chi_4(t) = N_A\,[\,\langle F_{sA}^2(\mathbf{k},t)\rangle - \langle F_{sA}(\mathbf{k},t)\rangle^2\,]$ for the KABLJ system at three temperatures and two values of N. χ_4 quantifies the incoherent intermediate scattering function fluctuations.[22] For $\chi_4(t)$, NVU and NVE dynamics do not appear to give identical results. A related observation was made by Berthier *et al.*, who showed that $\chi_4(t)$ is not the same in NVE and NVT dynamics.[10]

IV. COMPARING *NVU* DYNAMICS TO *NVT*, MONTE CARLO, AND DIFFUSIVE DYNAMICS ON Ω

This section compares simulations using NVU dynamics to results for three other dynamics, two of which are standard. We focus on the viscous regime. One dynamics is the Nosé-Hoover NVT dynamics, a deterministic sampling of the NVT canonical ensemble that may be derived from a "virtual" Hamiltonian.[11,23] The second standard dynamics considered is the Metropolis Monte Carlo (MC) algorithm, which generates a stochastic sequence of states giving the correct NVT canonical ensemble distribution. The third dynamics employed below is also stochastic; it simulates diffusion on the constant-potential-energy hypersurface Ω by a small step-length random walk (RW) on Ω. This was discussed by Scala *et al.*,[4] who proposed the following equation of motion:

$$\frac{d\mathbf{R}_i}{dt} = \Delta\boldsymbol{\eta}_i - \frac{\Delta\boldsymbol{\eta}_i \cdot \mathbf{F}_i}{\mathbf{F}_i^2}\mathbf{F}_i\,, \tag{8}$$

where $\Delta\boldsymbol{\eta}_i$ is a $3N$-dimensional random vector (see below). Equation (8) implies $\mathbf{F}_i \cdot \dot{\mathbf{R}}_i = 0$, which ensures the potential-energy conservation required for staying on Ω.

The RW algorithm was discretized and implemented as a "predictor-corrector" algorithm in the following way. A vector $\Delta\boldsymbol{\eta}_i$ was chosen from a cube with length $L = 0.01\sigma$. This is small enough to ensure that the dynamics generates the correct NVE radial distribution function and at the same time has no effect on the average dynamical quantities. Positions were updated via

$$\mathbf{R}_{i+1} = \mathbf{R}_i + \Delta t\,\Delta\boldsymbol{\eta}_i - \frac{\Delta t\,\Delta\boldsymbol{\eta}_i \cdot \mathbf{F}_i}{\mathbf{F}_i^2}\mathbf{F}_i\,. \tag{9}$$

Finally, $\mathbf{R}_{i+1}$ was corrected by applying two iterations of $\mathbf{R}_{i+1} \equiv \mathbf{R}_{i+1} - \frac{U_{i+1}-U_0}{\mathbf{F}_{i+1}^2}\mathbf{F}_{i+1}$ in order to eliminate long-time entropic drift of the potential energy.

MC and RW dynamics involve no generic measures of time. We compared their results to NVU dynamics by proceeding as follows. At any given state point the time-scaling factor was determined from the long-time behavior

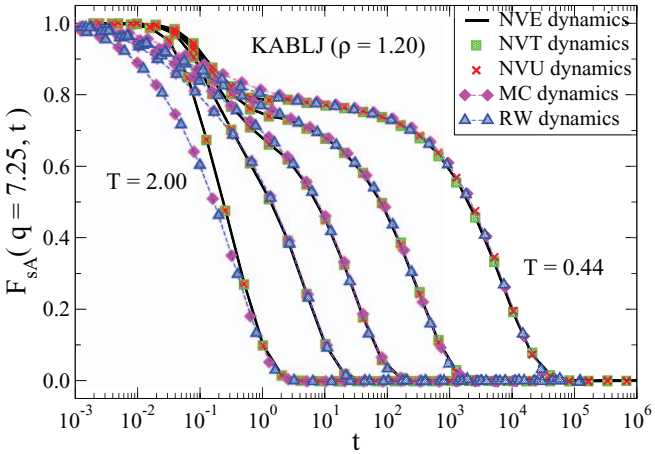

FIG. 7. The incoherent intermediate scattering function for all five investigated dynamics for the KABLJ liquid at $\rho = 1.2$ and $T = 2.0,\ 0.80,\ 0.60,\ 0.50$, and 0.44. The black curve is the NVE simulation, red crosses: NVU, green squares: NVT, magenta diamonds: MC, blue triangles: RW.

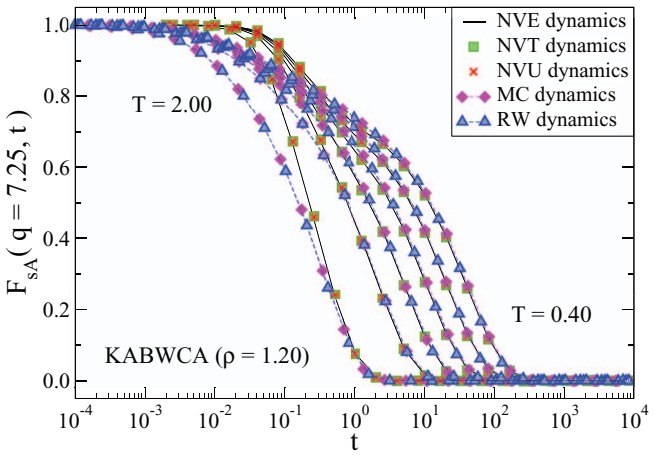

FIG. 8. The incoherent intermediate scattering function for all five investigated dynamics for the KABWCA system at $\rho = 1.2$ and $T = 2.0$, 0.80, 0.60, 0.50, 0.44, and 0.40. The black curve is the NVE simulation, red crosses: NVU, green squares: NVT, magenta diamonds: MC, blue triangles: RW.

of the mean-square displacement by requiring that the single-particle displacement obeys $\langle \Delta x^2(t) \rangle = 2Dt$ for $t \to \infty$ with the NVE diffusion constant D. By construction, this ensures agreement with the long-time mean-square displacement of NVE dynamics.

In Fig. 7, we show the incoherent intermediate scattering function of the KABLJ liquid for all investigated dynamics at several state points. A corresponding figure for the KABWCA system is shown in Fig. 8.

NVU and NVT dynamics agree quantitatively for all investigated state points. This is not surprising given the results of Secs. II and III and the well-known fact that NVE and NVT dynamics give the same time-autocorrelation functions to leading order in $1/N$.[24] The incoherent intermediate scattering functions of MC and RW agree at all investigated temperatures. This is consistent with the recent results of Berthier *et al.*,[10] who compared Langevin to MC dynamics. For lower temperatures ($T < 0.80$) quantitative agreement is found among all five dynamics investigated in the α-relaxation regime.

V. SUMMARY AND OUTLOOK

NVU dynamics traces out geodesic curves on the $(3N-1)$-dimensional potential-energy hypersurface Ω. We have compared NVU dynamics with four other dynamics. Simulations supplemented by non-rigorous analytical arguments showed that NVU and NVE dynamics are equivalent in the thermodynamic limit, i.e., typical autocorrelation functions become identical to leading order in $1/N$. Furthermore, NVU dynamics was compared to two stochastic dynamics, standard Monte Carlo dynamics and a small-step random walk on the constant-potential-energy hypersurface Ω representing diffusion on Ω. Agreement was established for all dynamics, including also NVT dynamics, in the α-relaxation regime where inertial effects are unimportant. We conclude that NVU dynamics is a fully valid molecular dynamics.

It is interesting to note that NVU dynamics, like any geodesic motion on a Riemannian manifold, can be formulated as a Hamiltonian dynamics based on the curved-space purely kinetic energy Hamiltonian $H = 1/2 \sum_{a,b} g_{ab}(x) p^a p^b$ where x is the manifold coordinate, g_{ab} is the corresponding metric tensor, and p_a are the generalized momenta.[25] Indeed, long ago Hertz argued that one should focus exclusively on the kinetic energy and describe classical mechanics as a geodesic motion on a high-dimensional Riemannian manifold (along the "geradeste Bahn" of this manifold, the straightest curve).[26] Hertz' idea was to eliminate the force and potential energy concepts entirely from mechanics and replace particle interactions by constraints among the coordinates; the relevant manifold is defined by these constraints. This is not what we have done here. There is nevertheless the fundamental similarity between the Hertz and the NVU approaches that both are built on the conceptual simplification of "replacing Newton's second law by Newton's first law." Moreover, as shown in the Appendix, the effect of masses enters into the metric of the Riemannian manifold in precisely the same way as we need for NVU dynamics when this is generalized to deal with systems of varying masses. Thus, NVU dynamics realizes Hertz's ideas to a large extent.

From a technical point of view NVU dynamics offers few advantages because it is not faster than NVE or NVT dynamics. However, by referring directly to the properties of a Riemannian differentiable manifold, NVU dynamics leads to an alternative way of thinking about the classical mechanics of many-particle systems. Future work should focus on relating the mathematical properties of Ω to the physical properties of the system in question. It is our hope that in this way new insights into liquid dynamics may be arrived at by adopting the NVU viewpoint.

ACKNOWLEDGMENTS

Useful inputs from Ole J. Heilmann and Nick Bailey are gratefully acknowledged. The centre for viscous liquid dynamics "Glass and Time" is sponsored by the Danish National Research Foundation (DNRF).

APPENDIX: GENERALIZATION OF THE *NVU* ALGORITHM TO DEAL WITH SYSTEMS OF DIFFERENT PARTICLE MASSES

Papers I and II deal with systems of particles with identical mass m. The basic NVU algorithm Eq. (3), however, is well defined and works perfectly well for any classical mechanical system. The algorithm traces out a geodesic on Ω that is independent of the particles' masses, a geometrical path entirely determined from the function $U(\mathbf{r}_1, \ldots, \mathbf{r}_N)$. Equation (5), which ensures $NVU = NVE$ in the thermodynamic limit, only works if all particles have mass m. On the other hand, the question arises if a generalization of Eq. (3) is possible ensuring that $NVU = NVE$ as $N \to \infty$ also for systems of particles with different masses.

If the kth particle mass is m_k, we seek to modify the basic NVU algorithm such that it, for the kth particle as $N \to \infty$, converges to (where $\mathbf{r}^{(k)}$ is the coordinate of the kth particle,

$\mathbf{F}^{(k)}$ is the force on it, and the subscript j is the time step index)

$$\mathbf{r}_{j+1}^{(k)} = 2\,\mathbf{r}_j^{(k)} - \mathbf{r}_{j-1}^{(k)} + \frac{(\Delta t)^2}{m_k}\mathbf{F}_j^{(k)}\,. \tag{A1}$$

If the average mass is denoted by $\langle m\rangle$, we define reduced masses by

$$\tilde{m}_k \equiv \frac{m_k}{\langle m\rangle}\,. \tag{A2}$$

A geodesic is defined by giving the shortest distance between any two of its close-by points. In Paper I and in Eq. (2) of the present paper the distance measure is given by the standard Euclidian distance $dl^2 = \sum_k d\mathbf{r}^{(k)} \cdot d\mathbf{r}^{(k)}$. A change of metric leads to different geodesics. Consider the following metric:

$$dl^2 = \sum_k \tilde{m}_k\, d\mathbf{r}^{(k)} \cdot d\mathbf{r}^{(k)}. \tag{A3}$$

This is precisely the metric discussed by Hertz in his mechanics long ago.[26] In the "Hertzian" metric the discretized path length used in deriving the NVU algorithm is (Paper I) $\sum_j \sqrt{\sum_k \tilde{m}_k(\mathbf{r}_j^{(k)} - \mathbf{r}_{j-1}^{(k)})^2}$ (j is the time step index). Thus, the variational condition becomes

$$\delta\left(\sum_j \sqrt{\sum_k \tilde{m}_k\left(\mathbf{r}_j^{(k)} - \mathbf{r}_{j-1}^{(k)}\right)^2} - \sum_j \lambda_j U(\mathbf{R}_j)\right) = 0\,. \tag{A4}$$

From this it follows via the *ansatz* of constant step length that

$$\mathbf{r}_{j+1}^{(k)} = 2\mathbf{r}_j^{(k)} - \mathbf{r}_{j-1}^{(k)} - \frac{2[\mathbf{F}_j \cdot (\mathbf{R}_j - \mathbf{R}_{j-1})]\mathbf{F}_j^{(k)}}{\tilde{m}_k \mathbf{F}_j^2}. \tag{A5}$$

This translates into Eq. (A1) for a suitably chosen Δt; likewise, the relative fluctuations of the term $2[\mathbf{F}_j \cdot (\mathbf{R}_j - \mathbf{R}_{j-1})]/\mathbf{F}_j^2$ go to zero in the thermodynamic limit ($N \to \infty$) such that $NVU = NVE$ in this limit.

[1] T. S. Ingebrigtsen, S. Toxvaerd, O. J. Heilmann, T. B. Schrøder, and J. C. Dyre, J. Chem. Phys. **135**, 104101 (2011).

[2] M. P. Allen and D. J. Tildesley, *Computer Simulation of Liquids* (Oxford Science, Oxford, 1987); D. Frenkel and B. Smit, *Understanding Molecular Simulation* (Academic, New York, 2002).

[3] R. M. J. Cotterill, Phys. Rev. B **33**, 262 (1986); R. M. J. Cotterill and J. U. Madsen, in *Characterizing Complex Systems*, edited by H. Bohr (World Scientific, Singapore, 1990), p. 177; J. Li, E. Platt, B. Waszkowycz, R. Cotterill, and B. Robson, Biophys. Chem. **43**, 221 (1992); R. M. J. Cotterill and J. U. Madsen, J. Phys.: Condens. Matter **18**, 6507 (2006).

[4] A. Scala, L. Angelani, R. Di Leonardo, G. Ruocco, and F. Sciortino, Philos. Mag. B **82**, 151 (2002).

[5] C. Wang and R. M. Stratt, J. Chem. Phys. **127**, 224503 (2007); C. Wang and R. M. Stratt, **127**, 224504 (2007); C. N. Nguyen and R. M. Stratt, J. Chem. Phys. **133**, 124503 (2010).

[6] M. Goldstein, J. Chem. Phys. **51**, 3728 (1969); F. H. Stillinger, Science **267**, 1935 (1995); F. Sciortino, J. Stat. Mech.: Theory Exp. **2005**, 35 (2005); A. Heuer, J. Phys.: Condens. Matter **20**, 373101 (2008).

[7] T. Gleim, W. Kob, and K. Binder, Phys. Rev. Lett. **81**, 4404 (1998).

[8] W. Kob and H. C. Andersen, Phys. Rev. E **51**, 4626 (1995); **52**, 4134 (1995).

[9] G. Szamel and E. Flenner, Europhys. Lett. **67**, 779 (2004); E. Flenner and G. Szamel, Phys. Rev. E **72**, 011205 (2005).

[10] L. Berthier and W. Kob, J. Phys.: Condens. Matter **19**, 205130 (2007); L. Berthier, Phys. Rev. E **76**, 011507 (2007).

[11] S. Nosé, J. Chem. Phys. **81**, 511 (1984); W. G. Hoover, Phys. Rev. A **31**, 1695 (1985).

[12] N. Metropolis, A. W. Rosenbluth, M. N. Rosenbluth, A. H. Teller, and E. Teller, J. Chem. Phys. **21**, 1087 (1953).

[13] J. D. Weeks, D. Chandler, and H. C. Andersen, J. Chem. Phys. **54**, 5237 (1971).

[14] L. Verlet, Phys. Rev. **159**, 98 (1967).

[15] All simulations were performed using a molecular dynamics code optimized for NVIDIA graphics cards, which is available as open source code at http://rumd.org.

[16] U. R. Pedersen, N. P. Bailey, T. B. Schrøder, and J. C. Dyre, Phys. Rev. Lett. **100**, 015701 (2008); U. R. Pedersen, T. Christensen, T. B. Schrøder, and J. C. Dyre, Phys. Rev. E **77**, 011201 (2008); T. B. Schrøder, U. R. Pedersen, N. P. Bailey, S. Toxvaerd, and J. C. Dyre, Phys. Rev. E **80**, 041502 (2009); N. P. Bailey, U. R. Pedersen, N. Gnan, T. B. Schrøder, and J. C. Dyre, J. Chem. Phys. **129**, 184507 (2008); N. P. Bailey, U. R. Pedersen, N. Gnan, T. B. Schrøder, and J. C. Dyre, J. Chem. Phys. **129**, 184508 (2008); T. B. Schrøder, N. P. Bailey, U. R. Pedersen, N. Gnan, and J. C. Dyre, J. Chem. Phys. **131**, 234503 (2009); N. Gnan, T. B. Schrøder, U. R. Pedersen, N. P. Bailey, and J. C. Dyre, J. Chem. Phys. **131**, 234504 (2009); N. Gnan, C. Maggi, T. B. Schrøder, and J. C. Dyre, Phys. Rev. Lett. **104**, 125902 (2010); T. B. Schrøder, N. Gnan, U. R. Pedersen, N. P. Bailey, and J. C. Dyre, J. Chem. Phys. **134**, 164505 (2011).

[17] U. R. Pedersen, T. B. Schrøder, and J. C. Dyre, Phys. Rev. Lett. **105**, 157801 (2010).

[18] V. V. Hoang and T. Odagaki, Physica B **403**, 3910 (2008). The Lennard-Jones Gaussian pair potential is $\varepsilon\left[(\sigma/r)^{12} - 2(\sigma/r)^6 - \varepsilon_0 \exp((r-r_0)^2/2\sigma_0^2)\right]$ where $\sigma_0 = 0.14$, $\varepsilon_0 = 1.5$, and $r_0 = 1.47$.

[19] E. T. Whittaker, *A Treatise on the Analytical Dynamics of Particles and Rigid Bodies*, 4th ed. (Cambridge University Press, Cambridge, England, 1999); H. Goldstein, *Classical Mechanics* (Addison-Wesley, Reading, MA, 1950).

[20] L. D. Landau and E. M. Lifshitz, *Mechanics*, 2nd ed. (Pergamon, Oxford, 1969).

[21] Wikipedia article "Maupertuis' principle," see http://wikipedia.org.

[22] C. Toninelli, M. Wyart, L. Berthier, G. Biroli, and J.-P. Bouchaud, Phys. Rev. E **71**, 041505 (2005).

[23] S. Toxvaerd, Mol. Phys. **72**, 159 (1991); T. Ingebrigtsen, O. J. Heilmann, S. Toxvaerd, and J. C. Dyre, J. Chem. Phys. **132**, 154106 (2010).

[24] D. J. Evans and B. L. Holian, J. Chem. Phys. **83**, 4069 (1985).

[25] Wikipedia article "Geodesics as Hamiltonian flows," see http://wikipedia.org.

[26] H. Hertz, *Die Prinzipien der Mechanik, in Neuem Zusammenhange Dargestellt* (Johann Ambrosius Barth, Leipzig, 1894); J. Lützen, Arch. Hist. Exact Sci. **49**, 1 (1995); J. Lützen, *Mechanistic Images in Geometric Form: Heinrich Hertz's "Principles of Mechanics"* (Oxford University Press, Oxford, 2005); J. Preston, Stud. Hist. Philos. Sci. **39**, 91 (2008).

NVU dynamics. III. Simulating molecules at constant potential energy

Trond S. Ingebrigtsen[a] and Jeppe C. Dyre
DNRF Centre "Glass and Time," IMFUFA, Department of Sciences, Roskilde University, Postbox 260, DK-4000 Roskilde, Denmark

(Received 12 September 2012; accepted 12 November 2012; published online 26 December 2012)

This is the final paper in a series that introduces geodesic molecular dynamics at constant potential energy. This dynamics is entitled *NVU* dynamics in analogy to standard energy-conserving Newtonian *NVE* dynamics. In the first two papers [T. S. Ingebrigtsen, S. Toxvaerd, O. J. Heilmann, T. B. Schrøder, and J. C. Dyre, J. Chem. Phys. **135**, 104101 (2011); T. S. Ingebrigtsen, S. Toxvaerd, T. B. Schrøder, and J. C. Dyre, *ibid.* **135**, 104102 (2011)], a numerical algorithm for simulating geodesic motion of atomic systems was developed and tested against standard algorithms. The conclusion was that the *NVU* algorithm has the same desirable properties as the Verlet algorithm for Newtonian *NVE* dynamics, i.e., it is time-reversible and symplectic. Additionally, it was concluded that *NVU* dynamics becomes equivalent to *NVE* dynamics in the thermodynamic limit. In this paper, the *NVU* algorithm for atomic systems is extended to be able to simulate the geodesic motion of molecules at constant potential energy. We derive an algorithm for simulating rigid bonds and test this algorithm on three different systems: an asymmetric dumbbell model, Lewis-Wahnström o-terphenyl (OTP) and rigid SPC/E water. The rigid bonds introduce additional constraints beyond that of constant potential energy for atomic systems. The rigid-bond *NVU* algorithm conserves potential energy, bond lengths, and step length for indefinitely long runs. The quantities probed in simulations give results identical to those of Nosé-Hoover *NVT* dynamics. Since Nosé-Hoover *NVT* dynamics is known to give results equivalent to those of *NVE* dynamics, the latter results show that *NVU* dynamics becomes equivalent to *NVE* dynamics in the thermodynamic limit also for molecular systems. © *2012 American Institute of Physics*. [http://dx.doi.org/10.1063/1.4768957]

I. INTRODUCTION

In two recent papers[1,2] (henceforth, Papers I and II), molecular dynamics at constant potential energy was introduced, tested, and compared to well-known molecular dynamics algorithms. This new molecular dynamics is entitled *NVU* dynamics in analogy to standard energy-conserving Newtonian *NVE* dynamics. The conclusion was that *NVU* dynamics is a fully valid molecular dynamics, which for sufficiently large systems can be used interchangeably with *NVE* dynamics for calculating most quantities of interest. *NVU* dynamics is not faster than standard *NVE* or *NVT* dynamics, but introduces a new way of thinking about molecular dynamics. Molecular dynamics at constant potential energy was previously considered by Cotterill and co-workers,[3–6] by Scala *et al.*,[7] and most recently by Stratt and co-workers,[8–11] who, however, allowed also lower potential energy values. Our motivation for studying *NVU* dynamics derive from recent work on strongly correlating liquids and their isomorphs[12–19] (see the Introduction of Paper I).

NVU dynamics is defined by geodesic motion on the constant-potential-energy hypersurface Ω defined by

$$\Omega = \{\mathbf{R} \in R^{3N} \mid U(\mathbf{R}) = U_0\}. \tag{1}$$

Here, $\mathbf{R} \equiv \{\mathbf{r}^{(1)}, \ldots, \mathbf{r}^{(N)}\}$ in which $\mathbf{r}^{(k)}$ is the position vector of the k'te particle (we follow the notation of the Appendix of Paper II), and U is the potential-energy function of an N-particle classical system. A geodesic on Ω is a curve that satisfies the condition of stationary length for fixed endpoints $\mathbf{R}_A$ and $\mathbf{R}_B$, i.e.,

$$\delta \int_{\mathbf{R}_A}^{\mathbf{R}_B} dl \Big|_{\Omega} = 0, \tag{2}$$

where dl is the line element of the metric. The shortest path between any two points is a geodesic. On a sphere, geodesics are great circles, the "straightest lines" of the surface. Traversing a geodesic at constant velocity thus corresponds to a generalization of Newton's first law to a curved space (the surface itself).

In Paper I, the *NVU* algorithm was developed via a discretization of Eq. (2), subsequently carrying out the variation. This technique, which is known as variational integration,[20–23] resulted in a "basic" *NVU* algorithm that is similar to the well-known Verlet algorithm $\mathbf{R}_{i+1} = 2\mathbf{R}_i - \mathbf{R}_{i-1} + (\Delta t)^2 \mathbf{F}_i/m$ for Newtonian (*NVE*) dynamics (m is the particle mass, which is here the same for all particles, and $\mathbf{F}_i \equiv -\nabla_{\mathbf{R}_i} U$ is the $3N$-dimensional force vector); the index i refers to step i of the integration sequence. In the Verlet algorithm, Δt is a fixed time step length. In comparison, the basic *NVU* algorithm is given by (Paper I)

$$\mathbf{R}_{i+1} = 2\mathbf{R}_i - \mathbf{R}_{i-1} - \frac{2\mathbf{F}_i \cdot (\mathbf{R}_i - \mathbf{R}_{i-1})}{\mathbf{F}_i^2}\mathbf{F}_i. \tag{3}$$

If the number of particles N increases, the relative variation of the term $-2\mathbf{F}_i \cdot (\mathbf{R}_i - \mathbf{R}_{i-1})/\mathbf{F}_i^2$ decreases, and this is why equivalence with Newtonian *NVE* dynamics is established in

[a]trond@ruc.dk.

the thermodynamic limit. This equivalence should be understood in the sense that the relative deviations between, for instance, *NVE* and *NVU* time auto-correlation functions go to zero as $N \to \infty$.

Paper I additionally developed a "stabilized" version of the basic *NVU* algorithm to prevent the accumulation of numerical errors. This version of the algorithm is given by (defining the position changes $\mathbf{\Delta}_{i+1/2} \equiv \mathbf{R}_{i+1} - \mathbf{R}_i$)

$$\mathbf{\Delta}_{i+1/2} = l_0 \frac{\mathbf{A}_{i+1/2}}{\|\mathbf{A}_{i+1/2}\|}, \tag{4}$$

$$\mathbf{R}_{i+1} = \mathbf{R}_i + \mathbf{\Delta}_{i+1/2}, \tag{5}$$

where l_0 is the step length and

$$\mathbf{A}_{i+1/2} = \frac{\mathbf{\Delta}_{i-1/2} + (-2\mathbf{F}_i \cdot \mathbf{\Delta}_{i-1/2} + U_{i-1} - U_0)}{\mathbf{F}_i^2} \mathbf{F}_i. \tag{6}$$

All simulations in Papers I and II were performed with the stabilized algorithm. The basic algorithm was used, however, for theoretical considerations. Note that the basic *NVU* algorithm has the same excellent stability as the Verlet algorithm, and the accumulation of numerical errors is no more serious.

In this article, we extend the stabilized *NVU* algorithm to deal with simulations of molecular systems. Molecular systems are simulated by introducing rigid and/or flexible bonds between the atoms in the modelling. Flexible bonds introduce merely an additional contribution to U, for instance, harmonic spring potentials. The *NVU* algorithm conserves the total potential energy and can readily simulate flexible bonds. The focus in this paper is thus on implementing rigid bonds in the framework of *NVU* dynamics.

Section II considers *NVU* dynamics with rigid bonds. Introducing rigid bonds in the simulations lead to Lagrangian multipliers in addition to those introduced in order to keep the potential energy constant (Paper I). Section II is fairly technical and easiest to read after reading Paper I. Section III gives simulation and model details. Section IV tests the rigid-bond *NVU* algorithm, and Sec. V investigates the *NVU* sampling properties by comparing the *NVU* results to Nosé-Hoover *NVT* results[24,25] on three different systems: the asymmetric dumbbell model,[26] Lewis-Wahnström OTP,[27] and rigid SPC/E water.[28] Nosé-Hoover *NVT* dynamics is known to give results equivalent to *NVE* dynamics in the thermodynamic limit,[29] and we refer to these dynamics interchangeably in the forthcoming sections. Finally, Sec. VI concludes.

II. RIGID-BOND *NVU* ALGORITHM

The rigid bonds[30,31] introduce constraints among the particle coordinates of the system. Each constraint $\alpha = 1, \ldots, G$ is of the form

$$\sigma_\alpha(\mathbf{R}) \equiv (\mathbf{r}^{(k_\alpha)} - \mathbf{r}^{(l_\alpha)})^2 \equiv (\mathbf{r}^\alpha)^2 = C_\alpha^2; \tag{7}$$

it expresses that the distance between particles k_α and l_α is a constant, C_α. In Papers I and II, the integral of Eq. (2) was merely restricted to the constant-potential-energy hypersurface Ω. Each rigid bond constraint introduces a function σ_α to be kept constant, and thus the integral of Eq. (2) is now further restricted to the sub-manifold ω of Ω where the bond constraints are satisfied,

$$\omega = \{\mathbf{R} \in \Omega \mid \sigma_\alpha(\mathbf{R}) = C_\alpha^2,\ \alpha = 1, \ldots, G\}. \tag{8}$$

If the bond constraints are independent, as assumed throughout the paper, ω is a (3N - G - 1)-dimensional compact Riemannian manifold. The variational principle defining *NVU* dynamics with rigid bonds is given by

$$\delta \int_{\mathbf{R}_A}^{\mathbf{R}_B} dl = 0 \Big|_\omega. \tag{9}$$

Most of Papers I and II dealt with the case of identical particle masses, but we wish here to develop a completely general molecular *NVU* algorithm. The line element dl is defined by

$$dl^2 \equiv \sum_k \tilde{m}_k (d\mathbf{r}^{(k)})^2, \tag{10}$$

where $\tilde{m}_k = m_k/\langle m \rangle$ is the "reduced" mass of particle k. Equation (10) is not the standard Euclidean line element, but a mass-weighted line element that goes back to Hertz.[32,33] We shall refer to this metric as the "Hertzian" metric. This metric ensures equivalence between *NVU* and *NVE* dynamics for systems of atoms and molecules of varying mass. In the Appendix, we derive the variable-mass atomic *NVU* algorithm applying the Hertzian metric (correcting also a typo of the Appendix of Paper II).

Applying the variational integration technique to Eq. (9) gives

$$\delta \left(\sum_i \sqrt{\sum_k \tilde{m}_k \left(\mathbf{r}_i^{(k)} - \mathbf{r}_{i-1}^{(k)}\right)^2} - \sum_i \lambda_i U(\mathbf{R}_i) + \sum_{i,\alpha} \Lambda_{\alpha i} \sigma_\alpha(\mathbf{R}_i) \right) = 0. \tag{11}$$

In Eq. (11), the path is divided into a number of discrete points and one Lagrangian multiplier $\Lambda_{\alpha i}$ is introduced for each constraint α at every point i. Following standard notation for constraint molecular dynamics,[30,31] the Lagrangian multipliers of the bond constraints are chosen with a positive sign. As in Papers I and II, we now make the Ansatz of constant step length l_0, i.e.,

$$\sum_k \tilde{m}_k \left(\mathbf{r}_i^{(k)} - \mathbf{r}_{i-1}^{(k)}\right)^2 \equiv l_0^2. \tag{12}$$

Carrying out the variation of Eq. (11) using Eq. (12) leads to (compare the derivation in Paper I)

$$\mathbf{r}_{i+1}^{(k)} = 2\mathbf{r}_i^{(k)} - \mathbf{r}_{i-1}^{(k)} + \frac{l_0}{\tilde{m}_k} \lambda_i \mathbf{f}_i^{(k)} + \frac{l_0}{\tilde{m}_k} \nabla_{\mathbf{r}_i^{(k)}} \sum_\alpha \Lambda_{\alpha i} \sigma_\alpha, \tag{13}$$

where $\mathbf{f}_i^{(k)} = -\nabla_{\mathbf{r}_i^{(k)}} U$ is the force on particle k at step i. This equation constitutes the *NVU* algorithm with rigid bonds. It has a close resemblance to the Lagrangian equations of motion with holonomic constraints,[31] i.e., rigid-bond *NVE* dynamics.[30] Equation (13) contains $G + 1$ Lagrangian multipliers for each integration step, which must be determined to complete the algorithm.

TABLE I. Definitions and nomenclature of the text.

Symbol	Definition
$\sigma_\alpha(\mathbf{R})$	The α'th bond constraint between particles k_α and l_α with $\alpha = 1, \ldots, G$. ($\sigma_\alpha = (\mathbf{r}^\alpha)^2 = C_\alpha^2$).
$\tilde{m}_k$	The mass of particle k divided by the average mass of the system. ($\tilde{m}_k = m_k/\langle m \rangle$).
	3-dimensional vectors
$\mathbf{r}_i^{(k)}$	Position of particle k at step i.
$\boldsymbol{\delta}_{i+1/2}^{(k)}$	Displacement of the position of particle k between step i and $i+1$. ($\boldsymbol{\delta}_{i+1/2}^{(k)} = \mathbf{r}_{i+1}^{(k)} - \mathbf{r}_i^{(k)}$).
$\mathbf{f}_i^{(k)}$	Force on particle k at step i. ($\mathbf{f}_i^{(k)} = -\nabla_{\mathbf{r}_i^{(k)}} U$).
$\mathbf{g}_i^{(k)}$	Constraint force on particle k at step i. ($\mathbf{g}_i^{(k)} = \nabla_{\mathbf{r}_i^{(k)}} \sum_\alpha \Lambda_{\alpha i}\sigma_\alpha$).
$\mathbf{r}_i^\alpha$	Displacement of the positions of particles k_α and l_α at step i. ($\mathbf{r}_i^\alpha = \mathbf{r}_i^{(k_\alpha)} - \mathbf{r}_i^{(l_\alpha)}$).
$\delta_{i-1/2}^\alpha$	Displacement of the velocities of particles k_α and l_α at step $i-1/2$. ($\delta_{i-1/2}^\alpha = \boldsymbol{\delta}_{i-1/2}^{(k_\alpha)} - \boldsymbol{\delta}_{i-1/2}^{(l_\alpha)}$).
$\mathbf{s}_i^\alpha$	Sum of displacements of positions and velocities of particles k_α and l_α at, respectively, step i and $i-1/2$. ($\mathbf{s}_i^\alpha = \mathbf{r}_i^\alpha + \delta_{i-1/2}^\alpha$).
$\tilde{\mathbf{f}}_i^\alpha$	Displacement of the forces on particles k_α and l_α at step i divided by their reduced particle mass. ($\tilde{\mathbf{f}}_i^\alpha = \mathbf{f}_i^{(k_\alpha)}/\tilde{m}_{k_\alpha} - \mathbf{f}_i^{(l_\alpha)}/\tilde{m}_{l_\alpha}$).
$\tilde{\mathbf{g}}_i^\alpha$	Displacement of the constraint forces on particles k_α and l_α at step i divided by their reduced particle mass. ($\tilde{\boldsymbol{g}}_i^\alpha = \mathbf{g}_i^{(k_\alpha)}/\tilde{m}_{k_\alpha} - \mathbf{g}_i^{(l_\alpha)}/\tilde{m}_{l_\alpha}$).
	3*N*-dimensional vectors
$\mathbf{R}_i$	Position of all particles at step i. ($\mathbf{R}_i = \{\mathbf{r}_i^{(1)}, \ldots, \mathbf{r}_i^{(N)}\}$).
$\boldsymbol{\Delta}_{i+1/2}$	Displacement of the positions between step i and $i+1$. ($\boldsymbol{\Delta}_{i+1/2} = \mathbf{R}_{i+1} - \mathbf{R}_i$).
$\mathbf{F}_i$	Force on all particles at step i. ($\mathbf{F}_i = -\nabla_{\mathbf{R}_i} U$).
$\tilde{\mathbf{F}}_i$	Force on all particles at step i divided by the reduced particle mass. ($\tilde{\mathbf{F}}_i = \{\mathbf{f}_i^{(1)}/\tilde{m}_1, \ldots, \mathbf{f}_i^{(N)}/\tilde{m}_N\}$).
$\tilde{\mathbf{G}}_i$	Constraint force on all particles at step i divided by the reduced particle mass. ($\tilde{\mathbf{G}}_i = \{\mathbf{g}_i^{(1)}/\tilde{m}_1, \ldots, \mathbf{g}_i^{(N)}/\tilde{m}_N\}$).

A. Determining the *NVU* Lagrangian multipliers

This section shows how to calculate the Lagrangian multipliers. Since the algorithm is to be implemented on a computer (with finite-precision), we shall proceed directly to a "stabilized" algorithm conserving for indefinitely long runs potential energy, bond lengths, and step length (in 3*N*-dimensions). The resulting algorithm reduces to the stabilized atomic *NVU* algorithm of Eqs. (4)–(6) in the case of no bonds constraints.

Some notation used in the following derivation is now introduced (the nomenclature of text is summarized in Table I). Defining $\boldsymbol{\delta}_{i+1/2}^{(k)} \equiv \mathbf{r}_{i+1}^{(k)} - \mathbf{r}_i^{(k)}$ and $\mathbf{g}_i^{(k)} \equiv \nabla_{\mathbf{r}_i^{(k)}} \sum_\alpha \Lambda_{\alpha i}\sigma_\alpha$ the "Leap-frog"[34] version of the rigid-bond *NVU* algorithm Eq. (13) reads

$$\boldsymbol{\delta}_{i+1/2}^{(k)} = \boldsymbol{\delta}_{i-1/2}^{(k)} + \frac{l_0}{\tilde{m}_k}\lambda_i \mathbf{f}_i^{(k)} + \frac{l_0}{\tilde{m}_k}\mathbf{g}_i^{(k)}, \tag{14}$$

$$\mathbf{r}_{i+1}^{(k)} = \mathbf{r}_i^{(k)} + \boldsymbol{\delta}_{i+1/2}^{(k)}. \tag{15}$$

In analogy to rigid-bond *NVE* dynamics we call $\mathbf{g}_i^{(k)}$ the "constraint force" on particle k at step i. Introducing the notation $\tilde{\mathbf{F}}_i \equiv \{\mathbf{f}_i^{(1)}/\tilde{m}_1, \ldots, \mathbf{f}_i^{(N)}/\tilde{m}_N\}$ and $\tilde{\mathbf{G}}_i \equiv \{\mathbf{g}_i^{(1)}/\tilde{m}_1, \ldots, \mathbf{g}_i^{(N)}/\tilde{m}_N\}$, the *NVU* algorithm in the full 3*N*-dimensional coordinate space reads

$$\boldsymbol{\Delta}_{i+1/2} = \boldsymbol{\Delta}_{i-1/2} + l_0\lambda_i\tilde{\mathbf{F}}_i + l_0\tilde{\mathbf{G}}_i, \tag{16}$$

$$\mathbf{R}_{i+1} = \mathbf{R}_i + \boldsymbol{\Delta}_{i+1/2}, \tag{17}$$

The Lagrangian multipliers are calculated by combining a result derived in Paper I with the method applied in the *SHAKE* algorithm[30] for rigid bonds in *NVE* dynamics.[30,35,36] The *SHAKE* algorithm calculates the Lagrangian multipliers from the equations $(\mathbf{r}_{i+1}^\alpha)^2 = C_\alpha^2$. In doing so, the target value of the constraints C_α appears explicitly in the algorithm, making the bond lengths insensitive to numerical error. The expression for $\mathbf{r}_{i+1}^\alpha$ is supplied by the integration algorithm containing herein the Lagrangian multipliers. In our case, this gives G equations with $G+1$ unknowns. The missing equation is supplied by an expression derived in Paper I, namely that $U_{i+1} = U_{i-1} - \mathbf{F}_i \cdot (\mathbf{R}_{i+1} - \mathbf{R}_{i-1})$ to third order in the step length. In the discrete sequence of points, U_{i+1} is set equal to U_0 (the constant defining Ω), making the constraint of constant potential energy also insensitive to numerical errors. We thus have the following $G+1$ equations for calculating the Lagrangian multipliers

$$U_{i-1} - \mathbf{F}_i \cdot (\mathbf{R}_{i+1} - \mathbf{R}_{i-1}) - U_0 = 0, \tag{18}$$

$$\left(\mathbf{r}_{i+1}^\alpha\right)^2 - C_\alpha^2 = 0, \ (\alpha = 1, \ldots, G). \tag{19}$$

By Eqs. (16) and (17); $\mathbf{R}_{i+1} - \mathbf{R}_{i-1} = \boldsymbol{\Delta}_{i+1/2} + \boldsymbol{\Delta}_{i-1/2} = 2\boldsymbol{\Delta}_{i-1/2} + l_0\lambda_i\tilde{\mathbf{F}}_i + l_0\tilde{\mathbf{G}}_i$. Defining $\delta_{i-1/2}^\alpha \equiv \boldsymbol{\delta}_{i-1/2}^{(k_\alpha)} - \boldsymbol{\delta}_{i-1/2}^{(l_\alpha)}$, $\tilde{\mathbf{f}}_i^\alpha \equiv \mathbf{f}_i^{(k_\alpha)}/\tilde{m}_{k_\alpha} - \mathbf{f}_i^{(l_\alpha)}/\tilde{m}_{l_\alpha}$, and $\tilde{\boldsymbol{g}}_i^\alpha \equiv \mathbf{g}_i^{(k_\alpha)}/\tilde{m}_{k_\alpha} - \mathbf{g}_i^{(l_\alpha)}/\tilde{m}_{l_\alpha}$, since by Eqs. (14) and (15); $\mathbf{r}_{i+1}^\alpha = \mathbf{r}_{i+1}^{(k_\alpha)} - \mathbf{r}_{i+1}^{(l_\alpha)} = \mathbf{r}_i^{(k_\alpha)} - \mathbf{r}_i^{(l_\alpha)} + \boldsymbol{\delta}_{i+1/2}^{(k_\alpha)} - \boldsymbol{\delta}_{i+1/2}^{(l_\alpha)} = \mathbf{r}_i^\alpha + \boldsymbol{\delta}_{i-1/2}^\alpha + l_0\lambda_i\tilde{\mathbf{f}}_i^\alpha + l_0\tilde{\mathbf{g}}_i^\alpha$, it follows that

$$U_{i-1} - \mathbf{F}_i \cdot [2\boldsymbol{\Delta}_{i-1/2} + l_0\lambda_i\tilde{\mathbf{F}}_i + l_0\tilde{\mathbf{G}}_i] - U_0 = 0, \tag{20}$$

$$\left[\mathbf{r}_i^\alpha + \boldsymbol{\delta}_{i-1/2}^\alpha + l_0\lambda_i\tilde{\mathbf{f}}_i^\alpha + l_0\tilde{\mathbf{g}}_i^\alpha\right]^2 - C_\alpha^2 = 0, \ (\alpha = 1, \ldots, G). \tag{21}$$

The above coupled quadratic equations for the Lagrangian multipliers are now solved following the produce of the *MILC-SHAKE* algorithm,[37] which starts by neglecting the second order terms in the Lagrangian multipliers and solving the resulting linear equations. Afterwards, the second order terms are taken into account in an iterative manner—the details of which are described below.

For each integration step i, the linearized equations are given as

$$\mathbf{A}_i\boldsymbol{\lambda}_i = \mathbf{b}_i, \tag{22}$$

where $\mathbf{A}_i$ is a $(G+1)\times(G+1)$ matrix, $\boldsymbol{\lambda}_i \equiv \{\lambda_i, \Lambda_{1i}, \ldots, \Lambda_{Gi}\}$, and $\mathbf{b}_i$ a $G+1$ column vector. We start by calculating explicitly the first few elements of the matrix $\mathbf{A}_i$. A_{11} consists merely of the factor in front of λ_i in Eq. (20), i.e., $A_{11} = -l_0\tilde{\mathbf{F}}_i \cdot \mathbf{F}_i$. The second element A_{12} appears after expansion of the dot product $\mathbf{F}_i \cdot \tilde{\mathbf{G}}_i$. Noting that $\nabla_{\mathbf{r}_i^{(k_\alpha)}}\sigma_\alpha = 2\mathbf{r}_i^\alpha$, we have $\mathbf{F}_i \cdot \tilde{\mathbf{G}}_i = \mathbf{f}_i^{(1)} \cdot \mathbf{g}_i^{(1)}/\tilde{m}_1 + \ldots + \mathbf{f}_i^{(N)} \cdot \mathbf{g}_i^{(N)}/\tilde{m}_N = 2\Lambda_{1i}(\tilde{\mathbf{f}}_i^1 \cdot \mathbf{r}_i^1) + \ldots + 2\Lambda_{Gi}(\tilde{\mathbf{f}}_i^G \cdot \mathbf{r}_i^G)$. The last equation follows as the Lagrangian multipliers appear in pairs, differing only by the sign from $\nabla_{\mathbf{r}_i^{(k_\alpha)}}\sigma_\alpha$ and the term $\mathbf{f}_i^{(k_\alpha)}/\tilde{m}_{k_\alpha}$. We thus find $A_{12} = -2l_0\tilde{\mathbf{f}}_i^1 \cdot \mathbf{r}_i^1$, $A_{13} = -2l_0\tilde{\mathbf{f}}_i^2 \cdot \mathbf{r}_i^2$, etc. In the second row of $\mathbf{A}_i$, the short-hand notation $\mathbf{s}_i^\alpha \equiv \mathbf{r}_i^\alpha + \boldsymbol{\delta}_{i-1/2}^\alpha$ is introduced, making $A_{21} = 2l_0(\mathbf{s}_i^1 \cdot \tilde{\mathbf{f}}_i^1)$, i.e., the factor in front of λ_i after squaring of the parentheses. The next element A_{22} appears after expanding $\mathbf{s}_i^1 \cdot \tilde{\mathbf{g}}_i^1 = \boldsymbol{s}_i^1 \cdot \sum_\beta \Lambda_{\beta i}(\frac{1}{\tilde{m}_{k_1}}\nabla_{\mathbf{r}_i^{(k_1)}}\sigma_\beta - \frac{1}{\tilde{m}_{l_1}}\nabla_{\mathbf{r}_i^{(l_1)}}\sigma_\beta)$. In this sum, we identify the factor in front of Λ_{1i}, giving $A_{22} = 2l_0\boldsymbol{s}_i^1 \cdot (\frac{1}{\tilde{m}_{k_1}}\nabla_{\mathbf{r}_i^{(k_1)}}\sigma_1 - \frac{1}{\tilde{m}_{l_1}}\nabla_{\mathbf{r}_i^{(l_1)}}\sigma_1)$, and similarly for the remaining elements of the second row.

Altogether, the elements of $\mathbf{A}_i$ are thus given by

$$\mathbf{A}_i = 2l_0\begin{pmatrix} -\tilde{\mathbf{F}}_i \cdot \mathbf{F}_i/2 & -\tilde{\mathbf{f}}_i^1 \cdot \mathbf{r}_i^1 & \cdots & -\tilde{\mathbf{f}}_i^G \cdot \mathbf{r}_i^G \\ \boldsymbol{s}_i^1 \cdot \tilde{\mathbf{f}}_i^1 & \boldsymbol{s}_i^1 \cdot \left(\frac{1}{\tilde{m}_{k_1}}\nabla_{\mathbf{r}_i^{(k_1)}}\sigma_1 - \frac{1}{\tilde{m}_{l_1}}\nabla_{\mathbf{r}_i^{(l_1)}}\sigma_1\right) & \cdots & \boldsymbol{s}_i^1 \cdot \left(\frac{1}{\tilde{m}_{k_1}}\nabla_{\mathbf{r}_i^{(k_1)}}\sigma_G - \frac{1}{\tilde{m}_{l_1}}\nabla_{\mathbf{r}_i^{(l_1)}}\sigma_G\right) \\ \vdots & \vdots & \ddots & \vdots \\ \boldsymbol{s}_i^G \cdot \tilde{\mathbf{f}}_i^G & \boldsymbol{s}_i^G \cdot \left(\frac{1}{\tilde{m}_{k_G}}\nabla_{\mathbf{r}_i^{(k_G)}}\sigma_1 - \frac{1}{\tilde{m}_{l_G}}\nabla_{\mathbf{r}_i^{(l_G)}}\sigma_1\right) & \cdots & \boldsymbol{s}_i^G \cdot \left(\frac{1}{\tilde{m}_{k_G}}\nabla_{\mathbf{r}_i^{(k_G)}}\sigma_G - \frac{1}{\tilde{m}_{l_G}}\nabla_{\mathbf{r}_i^{(l_G)}}\sigma_G\right) \end{pmatrix}. \tag{23}$$

The column vector $\mathbf{b}_i$ consists of all zeroth-order terms in Eqs. (20) and (21)

$$\mathbf{b}_i = \begin{pmatrix} U_0 - U_{i-1} + 2\mathbf{F}_i \cdot \boldsymbol{\Delta}_{i-1/2} \\ C_1^2 - \left(\mathbf{s}_i^1\right)^2 \\ \vdots \\ C_G^2 - \left(\mathbf{s}_i^G\right)^2 \end{pmatrix}. \tag{24}$$

Turning now to the iteration procedure, the second-order terms in the Lagrangian multipliers (Eq. (21)) are taken into account by iterating the right-hand side of Eq. (22) via the scheme ($\alpha = 1, \ldots, G$)

$$b_\alpha^{j+1} = b_\alpha^j + \left[C_\alpha^2 - \left(\left(\mathbf{r}_{i+1}^\alpha\right)^2\right)^j\right]. \tag{25}$$

The superscript j refers here to iteration j, and $((\mathbf{r}_{i+1}^\alpha)^2)^j$ are the positions associated with iteration j. The element b_0 is not updated as it derives from the constraint of constant potential energy. For each iteration j, the term $C_\alpha^2 - ((\mathbf{r}_{i+1}^\alpha)^2)^j$ is expected to become smaller as the bonds are satisfied better and better, and indeed, convergence was achieved within a few iterations.[37]

For each integration step i, the algorithm for determining the *NVU* Lagrangian multipliers thus proceeds as follows:

1. The Lagrangian multipliers of iteration j, $(\boldsymbol{\lambda}_i)^j$, are calculated from Eq. (22).
2. $((\mathbf{r}_{i+1}^\alpha)^2)^j$ is calculated via Eqs. (14) and (15) using $(\boldsymbol{\lambda}_i)^j$.
3. $\mathbf{b}_i$ is updated via Eq. (25) from $((\mathbf{r}_{i+1}^\alpha)^2)^j$.
4. The above steps are repeated until convergence is established (we used a preset number of iterations, typically 3–5).

How is constant step length l_0 ensured numerically after determining the Lagrangian multipliers? Generalizing the approach of Paper I, we introduce a normalizing factor such that

$$\boldsymbol{\delta}_{i+1/2}^{(k)} = l_0\frac{\boldsymbol{\chi}_{i+1/2}^{(k)}}{\sqrt{\sum_k \tilde{m}_k\left(\boldsymbol{\chi}_{i+1/2}^{(k)}\right)^2}}, \tag{26}$$

$$\mathbf{r}_{i+1}^{(k)} = \mathbf{r}_i^{(k)} + \boldsymbol{\delta}_{i+1/2}^{(k)}, \tag{27}$$

where

$$\boldsymbol{\chi}_{i+1/2}^{(k)} \equiv \boldsymbol{\delta}_{i-1/2}^{(k)} + \frac{l_0}{\tilde{m}_k}\lambda_i\mathbf{f}_i^{(k)} + \frac{l_0}{\tilde{m}_k}\mathbf{g}_i^{(k)}. \tag{28}$$

The normalizing factor is close to unity[1] and ensures trivially $\sum_k \tilde{m}_k(\boldsymbol{\delta}_{i+1/2}^{(k)})^2 = l_0^2$, i.e., that the step length is conserved. The algorithm is now absolutely stable, conserving potential energy, bond lengths, and step length for indefinitely long runs. The stability of the *NVU* algorithm is tested numerically in Sec. IV.

B. Alternative determination of the *NVU* Lagrangian multipliers

Section II A followed the traditional way of calculating the Lagrangian multipliers. The *NVU* Lagrangian multipliers may also be calculated by Taylor expanding the constraints σ_α in analogy to the method sketched above for the potential energy. In this way, the constraints of constant potential energy and constant bond lengths are treated on equal footing. The set of equations to be solved is the following (recall that $\mathbf{R}_{i+1} - \mathbf{R}_{i-1} = 2\boldsymbol{\Delta}_{i-1/2} + l_0\lambda_i\tilde{\mathbf{F}}_i + l_0\tilde{\mathbf{G}}_i$),

$$U_{i-1} - \mathbf{F}_i \cdot (\mathbf{R}_{i+1} - \mathbf{R}_{i-1}) - U_0 = 0, \tag{29}$$

$$\sigma_{\alpha(i-1)} + \nabla_{\mathbf{R}_i}\sigma_{\alpha i} \cdot (\mathbf{R}_{i+1} - \mathbf{R}_{i-1}) - C_\alpha^2 = 0, \ (\alpha = 1, \ldots, G). \tag{30}$$

The equations for the Lagrangian multipliers are now linear and thus no iterations are needed. The bond constraints σ_α are obeyed to the same order $O(l_0^3)$ as the constraint of constant potential energy. The sampling properties of this alternative determination method is tested briefly in Sec. V. It appears to be a promising new way of determining the Lagrangian multipliers in connection with rigid bonds, which might also be useful for standard bond-constraint *NVE* or *NVT* simulations.

III. SIMULATION DETAILS AND MODEL SYSTEMS

We investigated three systems: the asymmetric dumbbell model, the Lewis-Wahnström OTP model, and rigid SPC/E water. For all simulated pair potentials, the shifted-force truncation scheme was applied at a cut-off radius r_c. If the pair potential is $v(r)$ and the pair force is $f(r) = -v'(r)$, the shifted force is given by[34,38]

$$f_{\mathrm{SF}}(r) = \begin{cases} f(r) - f(r_c) & \text{if} \quad r < r_c\,, \\ 0 & \text{if} \quad r > r_c\,. \end{cases} \tag{31}$$

This corresponds to using the following pair potential below r_c: $v_{\mathrm{SF}}(r) = v(r) - v'(r_c)(r - r_c) - v(r_c)$. All simulations were performed with the *NVT* and *NVU* algorithms. Recall that *NVE* and *NVT* dynamics give equivalent results;[29] for this reason, no simulations are presented for *NVE* dynamics. The Roskilde University Molecular Dynamics (RUMD) code[39] was used for molecular dynamics simulations (an optimized open-source GPU code). The *NVT* ensemble is generated via the Nosé-Hoover algorithm,[24,25,40] and the bonds held fixed using the time-reversible constraint algorithm of Refs. 35 and 36. The *NVU* algorithm is described in Sec. II. The starting files for *NVU* dynamics were taken from an equilibrated *NVT* simulation. The positions and velocities of the *NVT* configuration do not correspond perfectly to motion on ω, since the potential energy and step length are not those of $U_0 = \langle U \rangle$ and l_0, respectively. As all the constraints are to be satisfied simultaneously, this results in numerical problems when starting the simulation from the particular *NVT* configuration. A more gentle procedure is thus applied, where the atomic *NVU* algorithm is used for a couple of integration steps to ensure the correct values of U_0 and l_0. Afterwards, the rigid-bond *NVU* algorithm is used.

A. *NVU* iteration procedure

The quadratic equations (Eq. (25)) were iterated with a fixed number of iterations (between 3 and 5). The linear systems were solved utilizing Cusp,[41] a library for solving systems of linear equations on the *GPU*. More specifically, the stabilized biconjugate gradient algorithm with a Jacobi preconditioner[42] was used with the initial value $\boldsymbol{\lambda}_i = \boldsymbol{\lambda}_{i-1}$ ($\boldsymbol{\lambda}_0 = 0$ for the start of the simulation). The relative tolerance τ of the solver for the asymmetric dumbbell and Lewis-Wahnström OTP models was chosen as $\tau = 10^{-7}$ and for rigid SPC/E water as $\tau = 3 \times 10^{-7}$. A larger tolerance was chosen for rigid SPC/E water due to convergence issues in connection with the shifted-force Coulomb interactions (see below).

The maximum number of allowed iterations was 50. A restart scheme was applied when the solver did not converge within the chosen tolerance. In this case, the solver (and quadratic iteration) was restarted from the partially estimated "solution" adding 2×10^{-7} to the tolerance. It should be noted that the stabilized biconjugate gradient algorithm may get trapped, resulting in a break-down of the Cusp linear solver. If this happens, it is detected by our program, and the solver and quadratic iteration are restarted with a smaller number (10) of maximum allowed iterations for the solver.

B. The asymmetric dumbbell

The asymmetric dumbbell model[26] consists of a large (A) and a small (B) Lennard-Jones (LJ) particle, rigidly bonded with bond distance of $r_{AB} = 0.29/0.4963$ (here and henceforth units are given in LJ units referring to the A particle such that $\sigma_{AA} = 1$, $\epsilon_{AA} = 1$, and $m_A = 1$). The asymmetric dumbbell model has $\sigma_{BB} = 0.3910/0.4963$, $\epsilon_{BB} = 0.66944/5.726$, and $m_B = 15.035/77.106$. The AB interaction between different molecules is determined by the Lorentz-Berthelot mixing rule.[34] $n = 500$ molecules (here and henceforth n denotes the number of molecules and N the number of atoms) were used in the simulations with a pair-potential cut-off of $r_c = 2.5$. The step length l_0 was fixed in the range 0.125–0.138 depending on the state point.

Simulations were also performed where the rigid bonds were replaced by stiff harmonic springs. The spring constant was $k = 3000$, while all other model parameters remained unchanged.

C. Lewis-Wahnström OTP

The Lewis-Wahnström OTP model[27] consists of three identical LJ particles rigidly bonded in an isosceles triangle with sides of $r_{AA} = 1$ and top angle of 75°. All parameters (including the masses) are unity for the OTP model. $n = 320$ molecules were simulated and a pair-potential cut-off of $r_c = 2.5$ was used. The step length was 0.100.

D. SPC/E water

The SPC/E water model[28] is an isosceles triangle with sides $r_{\mathrm{OH}} = 1/3.166$ and top angle 109.47°. The OO intermolecular interactions are given by the LJ pair potential ($\epsilon_{\mathrm{OO}} = 1$, $\sigma_{\mathrm{OO}} = 1$, and $m_{\mathrm{O}} = 15.9994/1.00794$). The three

TABLE II. Potential energy, deviation of bond lengths and step length as functions of integration step number in the *NVU* algorithm for Lewis-Wahnström OTP ($\rho = 0.329$, T = 0.700). Single-precision floating-point arithmetic was used for the simulations.

Integration steps	U/N	$(1/G\sum_\alpha (r^\alpha - C_\alpha)^2)^{1/2}$	$\sum_k \tilde{m}_k (\boldsymbol{\delta}_{i+1/2}^{(k)})^2$
10^1	−4.42550	2.81207×10^{-7}	0.0999999
10^2	−4.42552	3.03535×10^{-7}	0.1000000
10^3	−4.42552	2.81128×10^{-7}	0.1000000
10^4	−4.42552	2.95078×10^{-7}	0.1000000
10^5	−4.42550	3.08793×10^{-7}	0.1000000
10^6	−4.42551	2.90477×10^{-7}	0.1000000

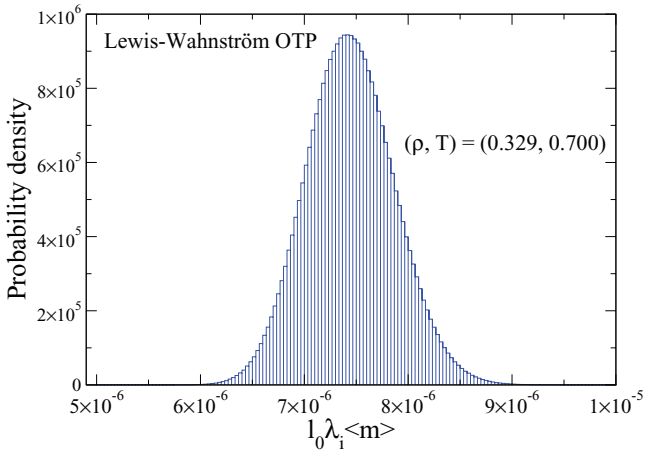

FIG. 1. The probability density of the "time step" length $(\Delta t_{i,NVU})^2 \equiv l_0\lambda_i\langle m\rangle$ of the rigid-bond *NVU* algorithm for Lewis-Wahnström OTP at $\rho = 0.329$ and T = 0.700. $n = 320$ molecules were simulated.

particles are charged with $q_O = -22.0$ and $q_H = |q_O|/2$. $n = 2000$ molecules were simulated and a pair-potential cut-off of $r_c = 6.28$ for both LJ and Coulomb interactions was applied.[43,44] The step length was fixed in the range 0.06–0.07 depending on the state point. For this system, the numerical stability is sensitive to the cut-off used in the Coulomb interactions, but a larger shifted-force cut-off improves this behavior.[44]

IV. TESTING THE STABILITY OF THE RIGID-BOND *NVU* ALGORITHM

This section tests the conservation properties of the rigid-bond *NVU* algorithm. Table II shows the potential energy, the deviation of bond lengths, and step length as functions of integration step number for Lewis-Wahnström OTP at $\rho = 0.329$ and T = 0.700. It is clear that these quantities are conserved by the algorithm and that no drift occurs. The step length is conserved to the highest accuracy since it is not prone to numerical error in determining the Lagrangian multipliers.

Figure 1 shows the distribution of the term $l_0\lambda_i\langle m\rangle$ in Eq. (13) ($\tilde{m}_k = m_k/\langle m\rangle$). In *NVU* dynamics there is, as such, no notation of time; a geodesic on the manifold can be traversed with any velocity. Comparing the *NVU* algorithm of Eq. (13) to the rigid-bond Verlet algorithm[30] $\mathbf{r}_{i+1}^{(k)} = 2\mathbf{r}_i^{(k)} - \mathbf{r}_{i-1}^{(k)} + ((\Delta t)^2/m_k)[\mathbf{f}_i^{(k)} + \mathbf{g}_i^{(k)}]$, we can define the term $l_0\lambda_i\langle m\rangle$ as a varying "time step" length of the *NVU* algorithm (see also Paper II), i.e.,

$$(\Delta t_{i,NVU})^2 \equiv l_0\lambda_i\langle m\rangle. \tag{32}$$

The integration steps of the *NVU* algorithm are thus henceforth referred to as "time steps." The average of Eq. (32) is used in Sec. V when comparing to *NVT* dynamics. As was the case for the atomic *NVU* algorithm (Paper I), $l_0\lambda_i\langle m\rangle$ is Gaussian distributed for large systems and its relative variation decreases as the number of particles increases. It thus becomes a better and better approximation to treat this term as constant, implying equivalent sampling properties of *NVU* and *NVE* dynamics also when rigid bonds are included in the simulations.

V. SAMPLING PROPERTIES OF THE RIGID-BOND *NVU* ALGORITHM

The *NVU* algorithm is now compared to *NVT* dynamics for the three different models. First, we consider the asymmetric dumbbell model,[26] both rigid and flexible. Afterwards, the Lewis-Wahnström OTP model,[27] and finally the rigid SPC/E water model.[28]

A. The asymmetric dumbbell model

In Figs. 2(a) and 2(b) are shown, respectively, the molecular center-of-mass (CM) radial distribution functions and the CM incoherent intermediate scattering functions for the rigid asymmetric dumbbell model[26] for different temperatures at $\rho = 0.932$. The black circles and curves give *NVT* simulation results while the red crosses give the *NVU* simulation results. The two radial distribution functions in Fig. 2(a) agree very well, and this is also the case for the dynamics in Fig. 2(b).

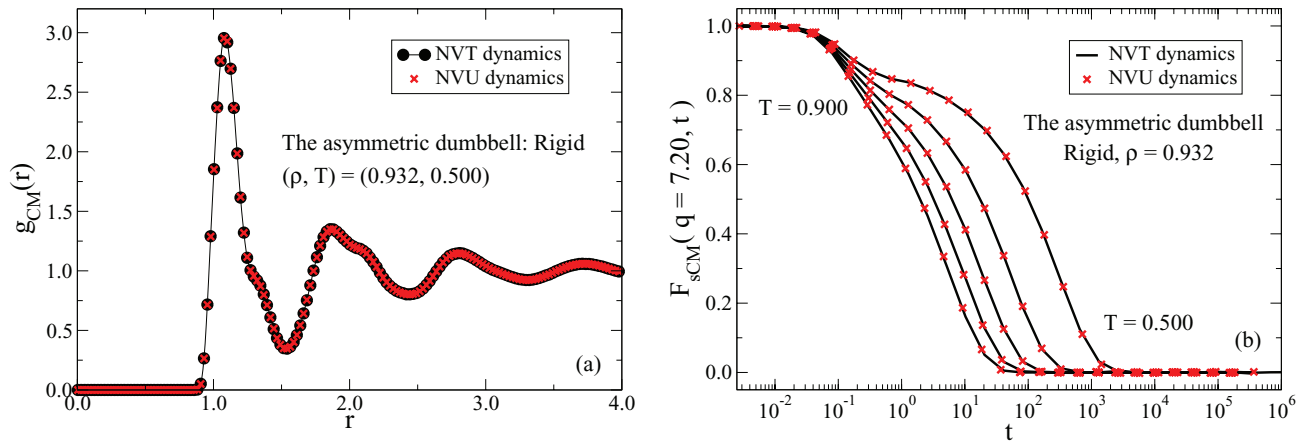

FIG. 2. Comparison of structure and dynamics in *NVU* and *NVT* simulations of the rigid asymmetric dumbbell model. The black circles and curves give *NVT*, the red crosses *NVU* simulation results. (a) The molecular CM radial distribution functions at $\rho = 0.932$ and T = 0.500. (b) The molecular CM incoherent intermediate scattering functions at $\rho = 0.932$ and T = 0.500, 0.600, 0.700, 0.800, 0.900.

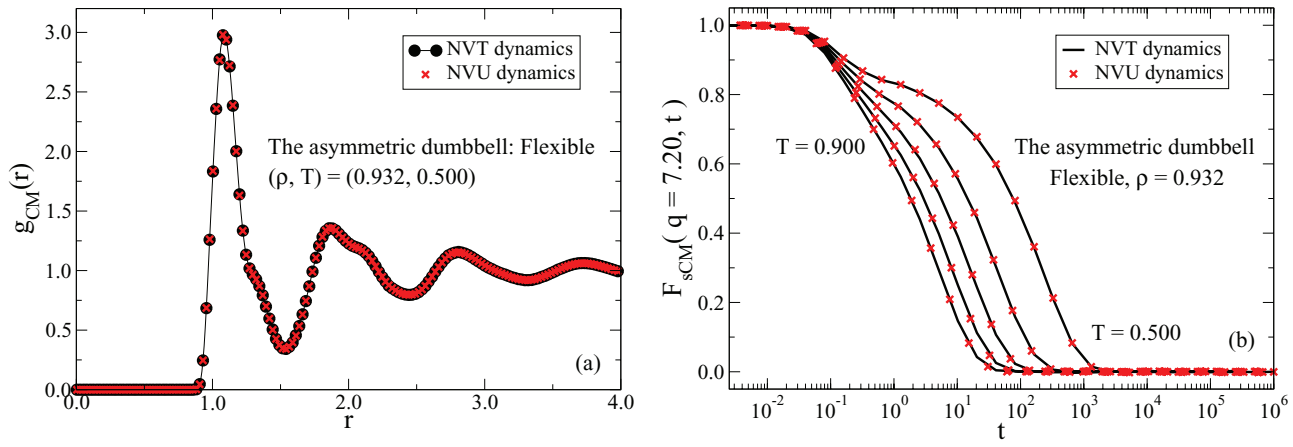

FIG. 3. Comparison of structure and dynamics in *NVU* and *NVT* simulations of the flexible-bond asymmetric dumbbell model. The black circles and curves give *NVT*, the red crosses *NVU* simulation results. The same state points as in Fig. 2 were simulated. (a) The molecular CM radial distribution functions at $\rho = 0.932$ and T = 0.500. (b) The molecular CM incoherent intermediate scattering functions at $\rho = 0.932$ and T = 0.500, 0.600, 0.700, 0.800, 0.900.

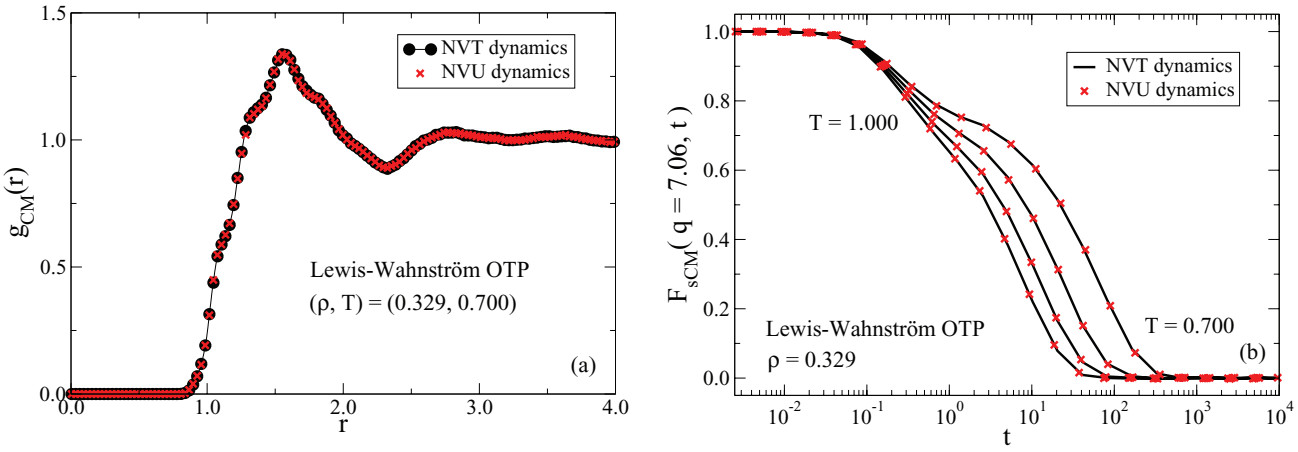

FIG. 4. Comparison of center-of-mass structure and dynamics in *NVU* and *NVT* simulations of the Lewis-Wahnström OTP model. The black circles and curves give *NVT*, the red crosses *NVU* simulation results. (a) The molecular CM radial distribution functions at $\rho = 0.329$ and T = 0.700. (b) The molecular CM incoherent intermediate scattering functions at $\rho = 0.329$ and T = 0.700, 0.800, 0.900, 1.000.

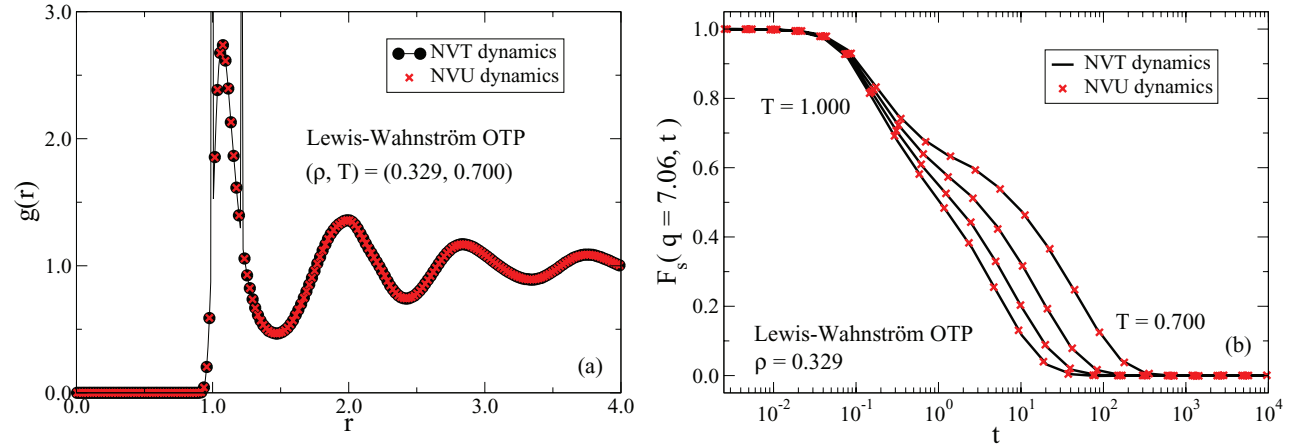

FIG. 5. Comparison of particle structure and dynamics in *NVU* and *NVT* simulations for the Lewis-Wahnström OTP model. The black circles and curves give *NVT*, the red crosses *NVU* simulation results. (a) The particle radial distribution functions at $\rho = 0.329$ and T = 0.700. (b) The particle incoherent intermediate scattering functions at $\rho = 0.329$ and T = 0.700, 0.800, 0.900, 1.000.

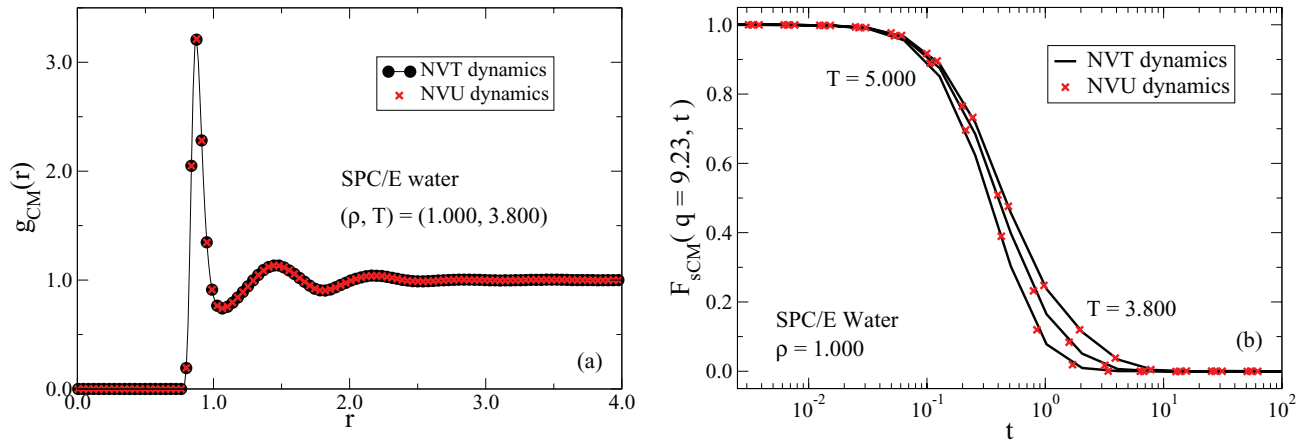

FIG. 6. Comparison of structure and dynamics in *NVU* and *NVT* simulations of rigid SPC/E water. The black circles and curves give *NVT*, the red crosses *NVU* simulation results. (a) The molecular CM radial distribution functions at $\rho = 1.000$ and T = 3.800. (b) The molecular CM incoherent intermediate scattering functions at $\rho = 1.000$ and T = 3.800, 4.200, 5.000.

For reference, we also simulated (Fig. 3) the corresponding quantities for the flexible-bond asymmetric dumbbell model at the state points of Fig. 2. Again, there is a very good agreement between *NVU* and *NVT* dynamics.

B. Lewis-Wahnström OTP

We show in Figs. 4(a) and 4(b), respectively, the molecular CM radial distribution functions and CM incoherent intermediate scattering functions for the Lewis-Wahnström OTP model.[27] The same symbols and meanings as in the preceding section are used. Again, the *NVU* and *NVT* simulations agree very well for both structure and dynamics.

For comparison, we also show in Fig. 5 the corresponding particle quantities for the OTP model.

C. SPC/E water

Finally, we consider in Fig. 6 the same quantities as above for the (not strongly correlating) rigid SPC/E water model.[28]

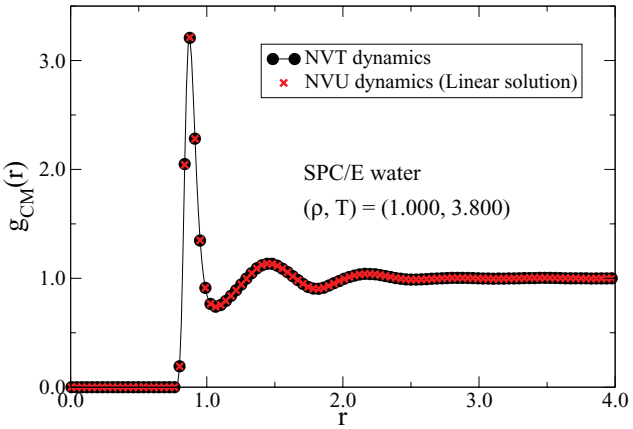

FIG. 7. Comparison of structure in *NVU* and *NVT* simulations of rigid SPC/E water at $\rho = 1.000$ and T = 3.800 applying the linear method to determine the Lagrangian multipliers (Eqs. (29) and (30)). The bond lengths are here conserved to order 10^{-6} in the standard deviation of the bonds (using single-precision).

Again, full equivalence between *NVU* and *NVT* dynamics is found.

The linear algorithm for determining the Lagrangian multipliers presented in Sec. II B (Eqs. (29) and (30)) is tested in Fig. 7 by probing the molecular CM radial distribution functions. *NVU* and *NVT* dynamics also here give identical results.

We conclude from the presented results that for sufficiently large molecular systems with flexible and/or rigid bonds, *NVU* dynamics is equivalent to Nosé-Hoover *NVT* dynamics (and, by implication, to Newtonian *NVE* dynamics).

VI. SUMMARY

NVU dynamics is molecular dynamics at constant potential energy realized by tracing out a geodesic on the constant-potential-energy hypersurface Ω (Eq. (1)). In Papers I and II,[1,2] a "basic" and a "stabilized" atomic *NVU* algorithm for simulating geodesics on Ω were developed. The basic *NVU* algorithm has excellent stability and it is time-reversible and symplectic; the stabilized algorithm was developed only to prevent accumulation of numerical error as also happens for *NVE* dynamics. It was found that atomic *NVU* dynamics becomes equivalent to atomic *NVE* dynamics in the thermodynamic limit.

In this paper, the stabilized *NVU* algorithm has been extended to simulate molecules at constant potential energy. Molecules are generally simulated by introducing rigid and/or flexible bonds in the models. The atomic *NVU* algorithm keeps the potential energy constant and can thus right away simulate flexible bonds. The focus here was on incorporating rigid bonds in the framework of *NVU* dynamics, which leads to the introduction of additional Lagrangian multipliers beyond those of the constraint of constant potential energy. This is completely analogous to the approach for simulating rigid bonds in standard Newtonian *NVE* dynamics.[30,35,36] In the *NVU* algorithm, a set of coupled quadratic equations was constructed for calculating the Lagrangian multipliers and solved in an iterative manner as a linear system, a procedure developed for rigid-bond *NVE* dynamics in the *MILC-SHAKE*

algorithm.[37] In addition, a set of linear equations was presented for calculating the Lagrangian multipliers, which appears to be a promising new way of simulating rigid bonds.

The rigid-bond *NVU* algorithm reduces to the atomic *NVU* algorithm when there are no rigid bonds. The algorithm was tested on three different model systems: the asymmetric dumbbell model, Lewis-Wahnström OTP, and rigid SPC/E water. The probed quantities in the simulation gave identical results to those of Nosé-Hoover *NVT* dynamics. We conclude that also for molecular systems, *NVU* dynamics becomes equivalent to *NVE* dynamics in the thermodynamic limit (since *NVE* and *NVT* dynamics are known to give equivalent results[29]).

ACKNOWLEDGMENTS

The centre for viscous liquid dynamics "Glass and Time" is sponsored by the Danish National Research Foundation (DNRF). The authors are grateful to Ole J. Heilmann for pointing out the alternative method for determining the Lagrangian multipliers (Sec. II B).

APPENDIX: DERIVATION OF THE ATOMIC *NVU* ALGORITHM FOR THE HERTZIAN METRIC

According to Newtonian dynamics, heavy particles move slower than light particles in thermal equilibrium. The standard Euclidean metric does not involve the particle masses, and thus applying this metric to geodesic motion for systems of varying masses will not produce dynamics equivalent to Newtonian dynamics in a thermal system. The mass-weighted metric of Hertz,[32] however, ensures that *NVU* dynamics becomes equivalent to *NVE* dynamics in the thermodynamic limit, as is clear from the derivation below. The Hertzian metric is given by (where $\tilde{m}_k = m_k/\langle m\rangle$)

$$dl^2 \equiv \sum_k \tilde{m}_k (d\mathbf{r}^{(k)})^2. \tag{A1}$$

We here derive the discrete *NVU* algorithm applying this metric (this appendix also corrects a typo in Eq. (A5) of Paper II). The discretized variational condition for geodesic motion on Ω is

$$\delta\left(\sum_i \sqrt{\sum_k \tilde{m}_k \left(\mathbf{r}_i^{(k)} - \mathbf{r}_{i-1}^{(k)}\right)^2} - \sum_i \lambda_i U(\mathbf{R}_i)\right) = 0\,. \tag{A2}$$

Assuming a constant step length l_0, i.e.,

$$\sum_k \tilde{m}_k \left(\mathbf{r}_i^{(k)} - \mathbf{r}_{i-1}^{(k)}\right)^2 \equiv l_0^2, \tag{A3}$$

it follows by differentiation with respect to $\mathbf{r}_i^{(k)}$ from Eq. (A2) that

$$\tilde{m}_k \left(\mathbf{r}_i^{(k)} - \mathbf{r}_{i-1}^{(k)}\right) + \tilde{m}_k \left(\mathbf{r}_i^{(k)} - \mathbf{r}_{i+1}^{(k)}\right) + l_0 \lambda_i \mathbf{f}_i^{(k)} = 0. \tag{A4}$$

Defining $\mathbf{a}_i^{(k)} \equiv (\mathbf{r}_i^{(k)} - \mathbf{r}_{i-1}^{(k)})$ and $\mathbf{b}_i^{(k)} \equiv (\mathbf{r}_i^{(k)} - \mathbf{r}_{i+1}^{(k)})$, Eq. (A3) expresses that $\sum_k \tilde{m}_k((\mathbf{a}_i^{(k)})^2 - (\mathbf{b}_i^{(k)})^2) = \sum_k \tilde{m}_k(\mathbf{a}_i^{(k)} + \mathbf{b}_i^{(k)}) \cdot (\mathbf{a}_i^{(k)} - \mathbf{b}_i^{(k)}) = 0$, and thus via Eq. (A4)

$$\sum_k \tilde{m}_k \left(-l_0/\tilde{m}_k \lambda_i \mathbf{f}_i^{(k)}\right) \cdot \left(\mathbf{r}_{i+1}^{(k)} - \mathbf{r}_{i-1}^{(k)}\right) = 0. \tag{A5}$$

Equivalently,

$$\sum_k \mathbf{f}_i^{(k)} \cdot \mathbf{r}_{i+1}^{(k)} = \sum_k \mathbf{f}_i^{(k)} \cdot \mathbf{r}_{i-1}^{(k)}. \tag{A6}$$

Combining Eq. (A6) with the discrete *NVU* algorithm (Eq. (A4)) gives the following result

$$l_0 \lambda_i = \frac{-2\sum_k \mathbf{f}_i^{(k)} \cdot (\mathbf{r}_i^{(k)} - \mathbf{r}_{i-1}^{(k)})}{\sum_k \frac{(\mathbf{f}_i^{(k)})^2}{\tilde{m}_k}}. \tag{A7}$$

The atomic *NVU* algorithm with varying masses is thus given by

$$\mathbf{r}_{i+1}^{(k)} = 2\mathbf{r}_i^{(k)} - \mathbf{r}_{i-1}^{(k)} + \frac{l_0}{\tilde{m}_k} \lambda_i \mathbf{f}_i^{(k)}, \tag{A8}$$

$$l_0 \lambda_i = \frac{-2\sum_k \mathbf{f}_i^{(k)} \cdot (\mathbf{r}_i^{(k)} - \mathbf{r}_{i-1}^{(k)})}{\sum_k \frac{(\mathbf{f}_i^{(k)})^2}{\tilde{m}_k}}. \tag{A9}$$

Equation (A9) fluctuates relatively less and less as the number of particles increases, and equivalence with *NVE* dynamics is established in the thermodynamic limit.

[1] T. S. Ingebrigtsen, S. Toxvaerd, O. J. Heilmann, T. B. Schrøder, and J. C. Dyre, J. Chem. Phys. **135**, 104101 (2011) (Paper I).
[2] T. S. Ingebrigtsen, S. Toxvaerd, T. B. Schrøder, and J. C. Dyre, J. Chem. Phys. **135**, 104102 (2011) (Paper II).
[3] R. M. J. Cotterill, Phys. Rev. B **33**, 262 (1986).
[4] R. M. J. Cotterill and J. U. Madsen, *Characterizing Complex Systems*, edited by H. Bohr (World Scientific, Singapore, 1990), p. 177.
[5] J. L. E. Platt, B. Waszkowycz, R. Cotterill, and B. Robson, Biophys. Chem. **43**, 221 (1992).
[6] R. M. J. Cotterill and J. U. Madsen, J. Phys.: Condens. Matter **18**, 6507 (2006).
[7] A. Scala, L. Angelani, R. D. Leonardo, G. Ruocco, and F. Sciortino, Philos. Mag. B **82**, 151 (2002).
[8] C. Wang and R. M. Stratt, J. Chem. Phys. **127**, 224503 (2007).
[9] C. Wang and R. M. Stratt, J. Chem. Phys. **127**, 224504 (2007).
[10] C. N. Nguyen and R. M. Stratt, J. Chem. Phys. **133**, 124503 (2010).
[11] C. N. Nguyen, J. I. Isaacson, K. B. Shimmyo, A. Chen, and R. M. Stratt, J. Chem. Phys. **136**, 184504 (2012).
[12] N. P. Bailey, U. R. Pedersen, N. Gnan, T. B. Schrøder, and J. C. Dyre, J. Chem. Phys. **129**, 184507 (2008).
[13] N. P. Bailey, U. R. Pedersen, N. Gnan, T. B. Schrøder, and J. C. Dyre, J. Chem. Phys. **129**, 184508 (2008).
[14] T. B. Schrøder, N. P. Bailey, U. R. Pedersen, N. Gnan, and J. C. Dyre, J. Chem. Phys. **131**, 234503 (2009).
[15] N. Gnan, T. B. Schrøder, U. R. Pedersen, N. P. Bailey, and J. C. Dyre, J. Chem. Phys. **131**, 234504 (2009).
[16] T. B. Schrøder, N. Gnan, U. R. Pedersen, N. P. Bailey, and J. C. Dyre, J. Chem. Phys. **134**, 164505 (2011).
[17] T. S. Ingebrigtsen, T. B. Schrøder, and J. C. Dyre, J. Phys. Chem. B **116**, 1018 (2012).
[18] T. S. Ingebrigtsen, L. Bøhling, T. B. Schrøder, and J. C. Dyre, J. Chem. Phys. **136**, 061102 (2012).
[19] T. S. Ingebrigtsen, T. B. Schrøder, and J. C. Dyre, Phys. Rev. X **2**, 011011 (2012).
[20] J. E. Marsden and M. West, Acta Numerica **10**, 357 (2001).
[21] R. Elber, A. Cardenas, A. Ghosh, and H. Stern, Adv. Chem. Phys. **126**, 93 (2003).
[22] A. Lew, "Variational time integrators in computational solid mechanics," Ph.D. dissertation (California Institute of Technology, 2003).
[23] M. West, "Variational integrators," Ph.D. dissertation (California Institute of Technology, 2004).

[24]S. Nosé, J. Chem. Phys. **81**, 511 (1984).
[25]W. G. Hoover, Phys. Rev. A **31**, 1695 (1985).
[26]T. B. Schrøder, U. R. Pedersen, N. P. Bailey, S. Toxvaerd, and J. C. Dyre, Phys. Rev. E **80**, 041502 (2009).
[27]L. J. Lewis and G. Wahnström, Phys. Rev. E **50**, 3865 (1994).
[28]H. J. C. Berendsen, J. R. Grigera, and T. P. Straatsma, J. Phys. Chem. **91**, 6269 (1987).
[29]D. J. Evans and B. L. Holian, J. Chem. Phys. **83**, 4069 (1985).
[30]J. P. Ryckaert, G. Ciccotti, and H. J. C. Berendsen, J. Comput. Phys. **23**, 327 (1977).
[31]H. Goldstein, C. Poole, and J. Safko, *Classical Mechanics*, 3rd ed. (Addison-Wesley, 2002).
[32]H. Hertz, "Die Prinzipien der Mechanik," in *Neuem Zusammenhange Dargestellt* (Johann Ambrosius Barth, Leipzig, 1894).
[33]J. Lützen, *Mechanistic Images in Geometric Form: Heinrich Hertz's "Principles of Mechanics"* (Oxford University Press, Oxford, 2005).
[34]M. P. Allen and D. J. Tildesley, *Computer Simulation of Liquids* (Oxford Science, 1987).
[35]S. Toxvaerd, O. J. Heilmann, T. Ingebrigtsen, T. B. Schrøder, and J. C. Dyre, J. Chem. Phys. **131**, 064102 (2009).
[36]T. Ingebrigtsen, O. J. Heilmann, S. Toxvaerd, and J. C. Dyre, J. Chem. Phys. **132**, 154106 (2010).
[37]A. G. Bailey, C. P. Lowe, and A. P. Sutton, J. Comput. Phys. **227**, 8949 (2008).
[38]S. Toxvaerd and J. C. Dyre, J. Chem. Phys. **134**, 081102 (2011).
[39]All simulations were performed using a molecular dynamics code optimized for *NVIDIA* graphics cards, which is available as open source code at http://rumd.org.
[40]S. Toxvaerd, Mol. Phys. **72**, 159 (1991).
[41]N. Bell and M. Garland, "Cusp: Generic parallel algorithms for sparse matrix and graph computations," (2012), version 0.3.0; available also at http://cusp-library.googlecode.com.
[42]W. H. Press, S. A. Teukolsky, W. T. Vetterling, and B. P. Flannery, *Numerical Recipes*, 3rd ed. (Cambridge University Press, 2007).
[43]C. J. Fennell and J. D. Gezelter, J. Chem. Phys. **124**, 234104 (2006).
[44]J. S. Hansen, T. B. Schrøder, and J. C. Dyre, J. Phys. Chem. B **116**, 5738 (2012).